This is an open access article published under an ACS AuthorChoice License, which permits copying and redistribution of the article or any adaptations for non-commercial purposes.

CHEMICAL REVIEWS

Review

pubs.acs.org/CR

Downloaded via US EPA OFFICE OF ENVIRONMENTAL INFO on August 28, 2019 at 20:06:39 (UTC).
See https://pubs.acs.org/sharingguidelines for options on how to legitimately share published articles.

New Insights into Perfluorinated Sulfonic-Acid Ionomers

Ahmet Kusoglu* and Adam Z. Weber

Energy Conversion Group, Energy Technologies Area, Lawrence Berkeley National Laboratory, 1 Cyclotron Road, MS70-108B, Berkeley, California 94720, United States

ABSTRACT: In this comprehensive review, recent progress and developments on perfluorinated sulfonic-acid (PFSA) membranes have been summarized on many key topics. Although quite well investigated for decades, PFSA ionomers' complex behavior, along with their key role in many emerging technologies, have presented significant scientific challenges but also helped create a unique cross-disciplinary research field to overcome such challenges. Research and progress on PFSAs, especially when considered with their applications, are at the forefront of bridging electrochemistry and polymer (physics), which have also opened up development of state-of-the-art in situ characterization techniques as well as multiphysics computation models. Topics reviewed stem from correlating the various physical (e.g., mechanical) and transport properties with morphology and structure across time and length scales. In addition, topics of recent interest such as structure/transport correlations and modeling, composite PFSA membranes, degradation phenomena, and PFSA thin films are presented. Throughout, the impact of PFSA chemistry and side-chain is also discussed to present a broader perspective.

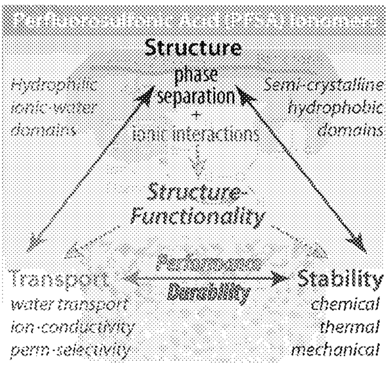

CONTENTS

1. Introduction 988
  1.1. PFSA State 991
    1.1.1. Impact of EW and Side-Chain Chemistry 991
    1.1.2. Thermal Treatment and Processing Effects 992
    1.1.3. Definition of Quasi-Equilibrium and Long-Term Effects 992
    1.1.4. Casting Effects 993
    1.1.5. Durability issues and New Developments 993
  1.2. Applications 993
2. Sorption and Solvent Uptake 994
  2.1. Overview 994
  2.2. Sorption from Vapor versus Liquid 998
  2.3. Dimensional Change and Swelling 999
  2.4. Density and Free Volume 1000
  2.5. Nature of Water and Freeze 1000
  2.6. Modeling of Water Uptake 1002
    2.6.1. Governing Equations 1002
    2.6.2. Swelling Pressure 1004
    2.6.3. Effect of Constraints and Compression 1004
    2.6.4. Interaction Parameter and Solubility 1005
    2.6.5. Morphology and Variations 1006
3. Morphological Features 1007
  3.1. Nanomorphology 1009
    3.1.1. Scattering with X-ray and Neutrons 1011
    3.1.2. Direct Imaging 1012
    3.1.3. Crystallinity 1012
    3.1.4. Thermal History 1014
    3.1.5. Mechanical Deformation 1014
  3.2. Multiscale Swelling 1015
  3.3. Mesoscale Models and Simulations 1017
    3.3.1. Impact of EW and Side-Chains 1018
  3.4. Surface Morphology and AFM Studies 1020
4. Transport Properties and Mechanisms 1021
  4.1. Water Transport 1021
    4.1.1. Steady-State Diffusion 1022
    4.1.2. Transient Water Uptake and Diffusion 1024
    4.1.3. NMR Studies and Self-Diffusion 1025
    4.1.4. Liquid Transport 1027
    4.1.5. Liquid/Vapor Transport and Interfacial Resistance 1027
    4.1.6. Modeling and Membrane Water Profiles 1028
  4.2. Proton Transport 1030
    4.2.1. Conductivity Values 1031
    4.2.2. Structural Interactions 1033
    4.2.3. Conduction Mechanisms 1034
  4.3. Cross-Correlation Phenomena 1036
    4.3.1. Electro-osmosis 1036
    4.3.2. Thermo-osmosis 1037
  4.4. Nanoscale Correlations 1038
    4.4.1. Nanoscale Proton Transport 1038
    4.4.2. Nanostructure/Conduction Interplay 1039
    4.4.3. Molecular Dynamic Models 1040
  4.5. Gas Transport 1041
  4.6. Impact and Transport of Alcohols 1043
  4.7. Temperature Effects and Activation Energies 1045
  4.8. Other Transport Properties 1047
5. Mechanical and Thermal Properties 1047
  5.1. Stress–Strain Behavior 1047

Received: February 29, 2016
Published: January 23, 2017

ACS Publications © 2017 American Chemical Society

DOI: 10.1021/acs.chemrev.6b00159
Chem. Rev. 2017, 117, 987−1104

5.2. Young's Modulus and Strength: Hydration Effects 1049
5.3. Time-Dependent Behavior 1050
5.4. Thermal-Mechanical Transitions 1051
5.5. Fracture and Fatigue Behavior 1053
6. Thin Films and Interfaces 1057
6.1. Swelling and Sorption Behavior 1058
6.2. Morphology, Interactions, and Properties 1060
6.3. Implications 1062
7. Other Topics 1063
7.1. PFSA Stability and Durability Issues 1063
7.1.1. Chemical and Mechanical Degradation 1064
7.1.2. Contamination Effects 1065
7.1.3. Hygrothermal Aging 1065
7.1.4. Thermal Decomposition 1067
7.2. Composite Membranes and Modifications 1067
7.2.1. Mechanical Reinforcements 1069
7.2.2. Performance Additives 1070
7.3. Different Ionic Forms and Interactions 1072
7.3.1. Different Cationic Forms 1073
7.3.2. Interfacial and Electrolyte Effects: Anions 1076
7.3.3. Interfacial and Electrolyte Effects: Multiple Cations 1077
8. Concluding Remarks and Future Directions 1078
Author Information 1080
Corresponding Author 1080
ORCID 1080
Notes 1080
Biographies 1080
Acknowledgments 1080
References 1081

1. INTRODUCTION

Perfluorinated sulfonic-acid (PFSA) ionomers are members of a class of ion-conductive polymers known for their remarkable ion conductivity and chemical-mechanical stability. PFSAs are commonly used as the solid-electrolyte in electrochemical technologies, especially as the proton-exchange membrane (PEM) in polymer-electrolyte fuel cells (PEFCs) and the sodium-ion conductor in the chlor-alkali industry, which have been driving forces behind PFSA research since the 1970s, when the first commercial PFSA ionomer, Nafion was developed by DuPont.[1] [Nafion is a registered trademark of E. I. DuPont De Nemours & Co. Nafion membrane is a commercially available PFSA-based membrane commonly used in fuel cell applications.] Even after decades of research into alternate PEMs, Nafion still serves as the canonical solid electrolyte for most energy-storage and -conversion devices due to its inherent electrochemical functionalities of efficient ion and solvent transport in a chemically inert mechanically robust matrix that inhibits the transport of electrons and reactants/products.

Nafion is a random copolymer composed of an electrically neutral semicrystalline polymer backbone (polytetrafluoroethylene (PTFE)) and a randomly tethered side-chain with a pendant ionic group, SO_3^- (polysulfonyl fluoride vinyl ether), that is associated with a specific counterion (e.g., $SO_3^- + H^+ \rightarrow SO_3H$). The dissimilar nature of the covalently bonded pendant group and backbone results in natural phase separation, which is enhanced by solvation (upon introduction of water or solvent molecules). It is this phase-separated morphology that gives PFSAs their unique ion- and solvent-transport capabilities. As such, PFSAs are, in essence, multifunctional polymers with transport and mechanical functionalities governed by their morphology in the presence of electrostatic interaction. This morphology however is also dependent on the various interactions and balance between the mechanical (deformation) energy associated with the hydrophobic backbone and the chemical/entropic energy associated with hydration of the hydrophilic ionic groups their side chains. This balance is controlled and impacted by wide range of environmental and material parameters that govern the structure/property relationship of PFSAs, as summarized in Figure 1.

For a given application, improving the membrane's overall stability requires an understanding of how different stressors (e.g., mechanical, electrochemical, environmental) impact the ionomer. Any effort to improve the transport functionalities (performance) is likely to undermine the mechanical stability (device longevity); the challenge to enhance the transport without compromising the latter, i.e. mechanical integrity, requires optimization of the phase-separated morphology.

The most impactful route to control the morphology is through the ionomer chemistry. PFSAs can be characterized by

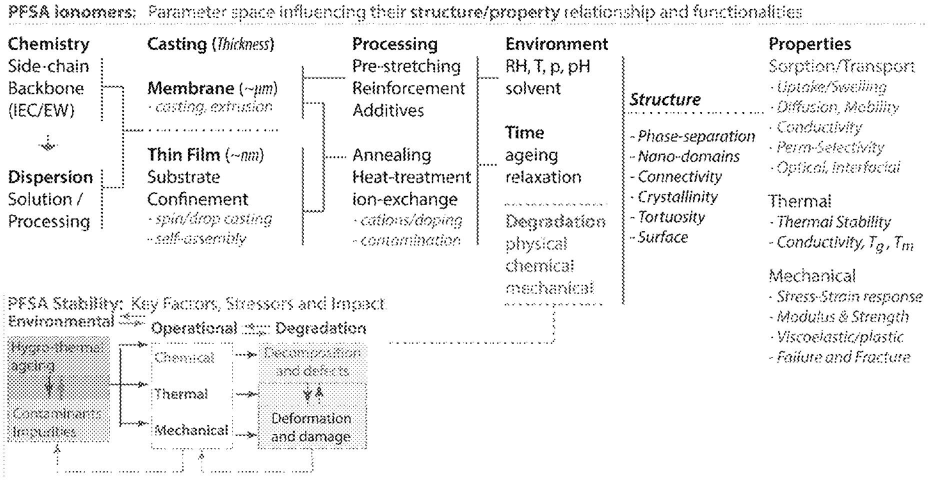
PFSA Ionomers: Parameter space influencing their structure/property relationship and functionalities
Chemistry
Side-chain
Backbone
(IEC/EW)
Dispersion
Solution /
Processing
Casting (Thickness)
Membrane (~μm)
- casting, extrusion
Thin Film (~nm)
Substrate
Confinement
- spin/drop casting
- self-assembly
Processing
Pre-stretching
Reinforcement
Additives
Annealing
Heat-treatment
ion-exchange
- cations/doping
- contamination
Environment
RH, T, p, pH
solvent
Time
ageing
relaxation
Degradation
physical
chemical
mechanical
Structure
- Phase-separation
- Nano-domains
- Connectivity
- Crystallinity
- Tortuosity
- Surface
Properties
Sorption/Transport
- Uptake/Swelling
- Diffusion, Mobility
- Conductivity
- Perm-Selectivity
- Optical, Interfacial
Thermal
- Thermal Stability
- Conductivity, T_g, T_m
Mechanical
- Stress-Strain response
- Modulus & Strength
- Viscoelastic/plastic
- Failure and Fracture
PFSA Stability: Key Factors, Stressors and Impact
Environmental
Operational
Degradation
Hygro-thermal ageing
Contaminants Impurities
Chemical
Thermal
Mechanical
Decomposition and defects
Deformation and damage

Figure 1. Material, processing, and environmental parameter space controlling the structure/property relationship of PFSA ionomers and their stability and degradation.

DOI: 10.1021/acs.chemrev.6b00159
Chem. Rev. 2017, 117, 987−1104

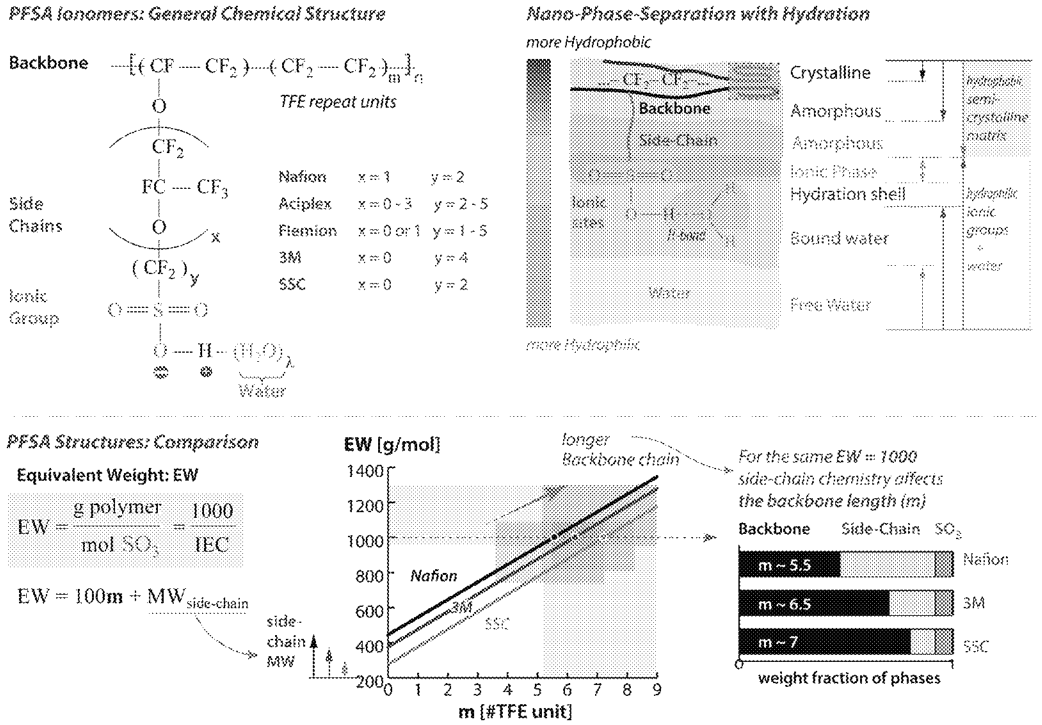
PFSA Ionomers: General Chemical Structure
Backbone
TFE repeat units
Side Chains
Ionic Group
Water
Nafion x = 1 y = 2
Aciplex x = 0 - 3 y = 2 - 5
Flemion x = 0 or 1 y = 1 - 5
3M x = 0 y = 4
SSC x = 0 y = 2
Nano-Phase-Separation with Hydration
more Hydrophobic
Backbone
Side-Chain
Ionic sites
H-bond
Water
Crystalline
Amorphous
Amorphous
Ionic Phase
Hydration shell
Bound water
Free Water
hydrophobic semi-crystalline matrix
hydrophilic ionic groups + water
more Hydrophilic
PFSA Structures: Comparison
Equivalent Weight: EW
EW = g polymer / mol SO3 = 1000 / IEC
EW = 100m + MWside-chain
side-chain MW
EW [g/mol]
1400
1200
1000
800
600
400
200
0 1 2 3 4 5 6 7 8 9
m [#TFE unit]
Nafion
3M
SSC
longer Backbone chain
For the same EW = 1000 side-chain chemistry affects the backbone length (m)
Backbone Side-Chain SO3
m ~ 5.5 Nafion
m ~ 6.5 3M
m ~ 7 SSC
weight fraction of phases

Figure 2. General chemical formula for the PFSA ionomers of various forms, shown with key chemical structural parameters governing their phase-separated morphology and properties. Impact of EW and side-chain chemistry is highlighted for selected commercial PFSAs.

a combination of (1) equivalent weight, EW, grams of dry polymer per ionic group, i.e., $g_{polymer}/mol_{ionic\text{-}group}$, which is inversely proportional to the ion-exchange capacity (IEC), and (2) side-chain chemistry and length (Figure 2). EW is directly related to the number of TFE units in the backbone, m, via EW = $100m + MW_{side\text{-}chain}$, which is the side-chain molecular weight. For a given EW, the shorter the side-chain (or the lower its MW) of the PFSA, the higher its backbone fraction. Thus, both side-chain length (size) and backbone length (m) control the EW and chemical structure of the PFSA ionomer, and its phase-separation behavior. In addition, the counterion that neutralizes its SO_3^- groups is also critical in determining the ionomer's structure, with the protonated form being the most common.

Despite the unequivocal dominance of Nafion in literature studies, PFSAs with IECs and short(er) side-chain chemistries, have gained considerable attention in an effort to optimize functionalities. In particular, those by 3M, Solvay Specialty Polymers (i.e., Aquivion, formerly known as Dow SSC ionomer by Dow Chemical Company), and Asahi Glass (i.e, Flemion), as well as reinforced composite PFSAs by W. L. Gore and Associates (i.e, Gore-SELECT, GORE-SELECT and GORE and designs are trademarks of W. L. Gore & Associates, Inc.). Sharing the same backbone chemistry, these PFSA ionomers are sometimes categorized according to their side-chain length and EW. For example, Aquivion (formerly Dow) PFSAs are commonly classified as short-side-chain (SSC) PFSAs, while Nafion could be considered a long-side chain (LSC) PFSA. [This terminology is less common, and generally speaking, length-based classification of side-chains could change depending on the context. For example, 3M PFSA has a shorter-side chain compared to Nafion, but it is not known as an SSC, which usually indicates Dow/Aquivion PFSA.] As seen in Figure 3, the PFSA ionomers with shorter-side chains and higher IECs have been increasingly studied,[3−9] due to their increased transport properties and performance in devices.[3−7,10] It is not just the length of the side-chain but also its chemistry that governs a PFSA's properties, which could be even more relevant and important when studying the ionomers in a dispersion state or the interfaces they form with the other materials (such as thin films or in electrode structures).

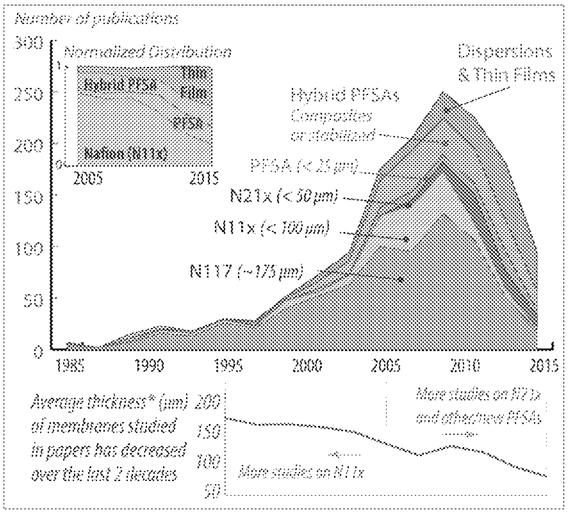

Figure 3. Changes in PFSA material thickness and types over the decades in terms of journal publications showing an increased interest in thinner membranes, stabilized/composite PFSAs as well as dispersion and thin films. Inset shows the fraction of papers published over the past decade on selected categories of PFSAs (Nafion membrane, newer generation PFSAs, Hybrid PFSAs, and thin films). The plot at the bottom shows the change in the average thickness of the membranes used in these studies over the years.

Another trend is that the thicknesses of PFSA membranes have been decreasing (Figure 3) driven by the need to reduce overall transport resistances, which, however, tends to accelerate gas crossover, subsequently reducing system efficiency.[11] This trend is especially seen for polymer-electrolyte fuel cells (PEFCs) where there is a need for thinner but stable ionomers that can withstand the aggressive chemical and environmental conditions, while meeting the durability targets for commercializaiton.[1,12]

Figure 3 clearly shows that there is a substantial amount of research activity in PFSAs; thus, a review on this topic is timely. [Due to increasing number of papers in the literature, a significant effort has been made by the authors to search, select, and include all the relevant references available on the web by early 2016, with a focus on the past decade, yet still considering the historically important papers and seminal works from earlier decades. Over 2500 papers on the topic have been reviewed and analyzed for content and key findings.] In terms of previous reviews, the most complete review on Nafion was published by Mauritz and Moore in 2004.[1] That paper contains an extensive review of the literature on Nafion to that date and covers an overview of Nafion's chemical structure, morphological descriptions based on small- and wide-angle X-ray scattering (SAXS, WAXS), microscopy studies, nature of water and solvents in the membrane, conductivity, and molecular-level structure based on molecular-dynamics simulations. While most of the studies prior to 2005 used the 175-μm thick Nafion 117 membrane (or a similar generation N11x but with different thickness), there has been a shift in the past decade to new generation of dispersion-cast Nafion (NR-21x) membranes of 25 to 50 μm thick, as well as stabilized membranes that impart different functionality, especially with regard to transport and durability properties. [In these Nafion membranes, x indicates the thickness in mil (e.g., N112, x = 2 mil, 50 μm nominal thickness).] Thus, a vast collection of newer studies on PFSAs can be classified as (i) new modeling and diagnostic studies of Nafion thanks to the advances in the field, (ii) new PFSA ionomers, including the new generation and alternative chemistries, and (iii) new applications beyond PEFCs, with different ionomer behavior.

As seen in Figure 3, an ever-growing number of studies on Nafion have accumulated over the past decade, which have provided significant improvements on the understanding of it, its morphology, and interrelations of its structure/function properties. In addition, specific reviews have also been published on topics of chemical structure within the context of other sulfonated ionomers[13] or PFSAs,[4] transport mechanisms,[13−18] morphology,[19] modeling,[14,20] and durability[11,12] from a PEFC perspective. The ones that contain a critical mass of information on Nafion and/or PFSA ionomers are summarized in Table 1. It is interesting to note that the changing topics and focuses of these reviews reflect the broadening interest in PFSA ionomer for various applications. The growing literature also resulted in reviews with very specific topics that were not of significant interest just a decade ago (e.g., alternative membranes, stabilizers, and advanced in situ diagnostics). Hence, while the understanding of PFSAs have been evolving with an ever-expanding property database, new demands and applications continuously present new challenges, resulting in a very dynamic research field.

Table 1. Summary of Previous Review Papers and Book Chapters Containing Information on Nafion and PFSA Membranes Studied either from Polymers or PEM Perspective within the Context of Fuel-Cells and Other Applications[a]

topic (or relevance to PFSA)	focus (context or applications)	ref
structure/property	Nafion	Mauritz and Moore[1]*
scattering techniques (structure)	PFSA (PEM)	Gebel and Diat[19]
electro-osmosis	PFSA (PEM)	Pivovar[21]
structure/property	ionomers (PEM)	Hickner and Pivovar[13]
transport modeling	PFSA–PEM (PEFC)	Weber and Newman[14]*
transport in proton conductors	PFSA (PEM)	Kreuer et al.[16]*
membrane properties	PEM (PEFC)	Doyle et al.[22]
proton conduction and modeling	PFSA (PEM)	Paddison[23]
conductivity	ionomer	Kim and Pivovar[24]
structure/property	Nafion	Duncan et al.[25]
durability/ degradation	durability, including PEM (PEFC)	Borup et al.[12]*
water uptake and diffusion	Nafion (ionomer transport)	Kusoglu and Weber[17]
transport: solubility/ diffusivity	Nafion (water electrolysis)	Ito et al.[15]
durability/ degradation	durability, including PEM (PEFC)	Rodgers et al.[26]*
durability/ degradation	PFSA degradation (PEFC)	Gittleman et al.[11]
water transport in ionomers	ionomers (Clean water applications)	Hickner[18,27]
techniques for water distribution	PFSA–PEM (PEFC)	Deabate et al.[28]
hybrid PFSAs with stabilizers	PFSA–PEM (PEFC)	Subianto et al.[29]
composite PFSAs with inorganic fillers	PFSA–PEM (PEFC)	Herring[30]
structure/property	PFSA–PEM with EWs and side-chain effects	Hamrock and Yandrasits[4] and Hamrock and Herring[9]
property characterization	PFSA–PEM (PEFC)	Kim and Lee[31]

[a] Asterisk (*) denotes ones in *Chemical Reviews*. Reviews focused on fuel-cell durability and modeling or other ion-conductive polymers with limited data and discussion on PFSAs are omitted.

Since the early 2000s, several new topics have emerged including the understanding of the quasi-equilibrium states of PFSA ionomers, importance of thermal and manufacturing history, and examination of the PFSA as a thin film. The recent advances include the impact of side-chain and moieties, characterization of interface and surfaces, more advanced understanding of Schröder's paradox, impact of casting and solvent, incorporation of additives and stabilizers to mitigate degradation, time-dependent transport and mechanical properties, thin films (<100 nm thick), effect of stretching and compression, additional diagnostic techniques including QENS, PALS, neutron and X-ray imaging, BES, and grazing-incidence SAXS (GISAXS), and more detailed ab initio and molecular-dynamics simulations. Such studies and techniques are visualized in Figure 4. It is interesting to note that the studies and focuses therein have shifted from more traditional techniques (macroscopic water-uptake and transport, as well as SAXS, DSC) to more advanced techniques that can probe the structure-transport correlations of PFSAs at various time and length scales. Thus, in essence, PFSAs have become widely used benchmark materials in new investigations and adoption of advanced characterization techniques for foundational science. The above-mentioned studies need to be compared

DOI: 10.1021/acs.chemrev.6b00159
Chem. Rev. 2017, 117, 987−1104

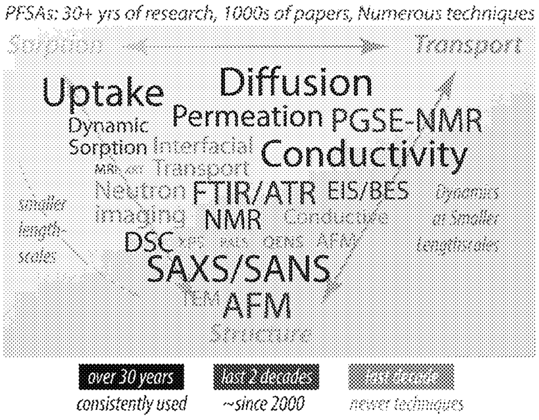

Figure 4. Evolution and expansion of techniques used to study PFSA membranes, based on our literature survey,* presented in the form of word cloud showing the periods each technique was adopted (font color) and to which extent they were used in papers (font size).

critically and collated such that the general trends and insights can be identified; it is the purpose of this article to accomplish this objective. Moreover, in this comprehensive review, we will also provide a new perspective for structure−function relationship of PFSA, by correlating various data sets from sorption, transport, mechanical property measurements, and morphological features for both Nafion and related PFSAs.

The outline of this review is as follows: First sorption behavior and related physical properties of PFSA will be discussed with experimental and modeling studies, followed by the current state of understanding of PFSA morphology studied by various techniques and simulations. Then, an overview of PFSA transport and thermomechanical properties will be provided based on sorption and morphological properties. It will then be discussed how these properties change when PFSA ionomers are confined to thin films. Lastly, factors influencing the correlations among morphology, stability, and transport will be discussed, including degradation, aging, contamination effects, as well as mitigation strategies used to develop composite and hybrid PFSA membranes. It should be noted that many of the sections and properties are highly interrelated and thus cross-referenced. Before proceeding, it is worthwhile to explore some underlying principles.

1.1. PFSA State

It is increasingly becoming recognized how EW, formation, and processing influence PFSA properties. These effects are being recognized in terms of contributing to various literature observations, or the inconsistencies among them, and are at the foundation for the rest of the review.

1.1.1. Impact of EW and Side-Chain Chemistry.

As noted above, EW, along with side-chain chemistry, is a critical parameter influencing ionomer behavior and its transport-stability relationship, yet the question remains how they affect an ionomer's other transport properties, dynamic behavior, mechanical properties, and its surface and structure in confined geometries, such as a thin film. EW is an average measurement of distribution in m (see Figure 2) and is measured by acid−base titration, elemental analysis (of S), or infrared (IR) spectroscopy. A large variation (~10%) in measured EW has been observed, which could be attributed to variation among batches and to morphological complexities arising from the dispersion nature.[32] EW of PFSA ionomers studied in the literature are in the range of 600 to 1500 g/mol, with 1100 g/mol being the most common for Nafion. EW plays a critical role in balancing transport and stability. For example, 3M ionomers begin to lose significant stiffness in water and act more like a gel as the EW decreases below 800 g/mol,[5,6,8] as shown in Figure 5. Even though the most commonly studied PFSA is 1100 EW Nafion, which dominates the published property data sets, the impact of EW on membrane properties and structure have always been of an interest, yet overlooked, in part due to the lack of a wide range of EWs among commercially available PFSAs. Earlier studies by researchers at DuPont reported properties of Nafion of various EWs, including, nanostructure, crystallinity, water uptake, and conductivity.[33−35] These were followed by similar studies on the effect of EW on PFSA's swelling and structure−property relationship,[36−38] including those of shorter side-chain (SSC Dow) PFSAs.[38−41] Relatively more recent investigations on EW and side-chain effects include investigation of water uptake,[5,6,10,42−48] morphology,[2,8,42,43,48,49] conductivity, diffusion and other transport properties,[2,4−7,9,10,39,43,44,48−60] thermal and mechanical properties,[2−4,7,34,38,40,49,61] and molecular modeling and simulations.[62−73] More recent studies have moved toward exploring alternative PFSA chemistries, such as multiacid

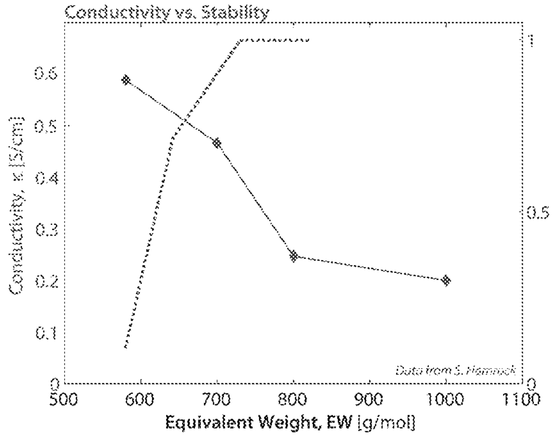

Figure 5. Conductivity-stability correlation as a function of EW for 3M PFSA ionomers, where the stability was quantified by the membrane's ability to withstand water-boiling process and conductivity was measured in liquid water.[77] (Data courtesy of Steve Hamrock of 3M).

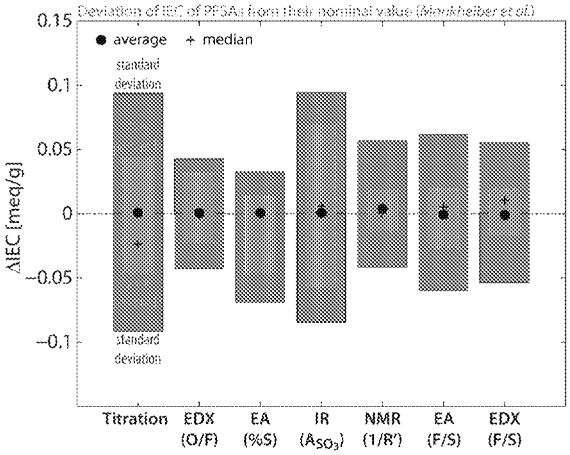

Figure 6. Variation in IEC of PFSA ionomers with respect to their nominal value reported by the manufacturer determined from various techniques (data are from Moukheiber et al.[3]).

ionomers containing multiple acid groups per side-chain (e.g., based on aromatic sulfonic acids (ortho bis acid) or perfluorinated side-chains (perfluoro imide acids, or PFIAs).[4,5,9,74,75] and additives and reinforcement strategies (see section 1.1.5). Regardless of its EW and side-chain chemistry, a PFSA's chemical and mechanical properties are interrelated through their phase-separated morphology, where the transport properties could be due to the hydrophilic water domains, while the hydrophobic backbone controls the thermal/mechanical properties, although it must be noted that all these properties are dependent on each other.

Improvements in membrane chemistry and additives and reinforcements have paved the way for thinner membranes that are chemically and mechanically stable. This can be seen in the continuous reduction in thicknesses of commercial PFSA membranes (Figure 3); unlike the 175 μm (μm)-thick N117 that was commonly studied in 90s and early 2000s, and therefore extensively discussed in the 2004 M&M review,[1] many recent studies investigated thinner PFSA ionomers, and the field is moving toward membranes that are 25 μm or thinner (N211, 3M ionomers, Aquivion etc.) and/or reinforced (Nafion XL and Gore-Select) with the newer reinforced membranes approaching 5 μm.[76]

1.1.2. Thermal Treatment and Processing Effects.

It has been well documented that the morphology and properties of PFSA membranes (whether extruded or cast) are strongly influenced by their thermal history, which can be altered through heat-treatment processes such as pretreating (PT) or preboiling (PB), a.k.a. expanded form, in liquid water or heating at higher temperatures to induce annealing (i.e., higher crystallinity).[17,78−91] PFSA membranes stored and used as-received (AsR, from the manufacturer) are prone to containing contaminates and may exhibit continuous changes in structure and properties over time (i.e., physical aging phenomenon). Thus, it has been a common practice to pretreat the membrane to set a baseline by erasing its thermal history via boiling in peroxide agents (cleaning), sulfuric acid (reprotonating), and water (boiling-induced rehydration), with the exact duration and concentrations changing from one study to another, although with similar end states. Such heat-treatment processes have been shown to alter the water uptake,[6,81−83,90,92−98] and transport coefficients (e.g., diffusivity),[49,83,97] density,[99] permeability,[93,100,101] ionic conductivity,[49,80,83,90,93,94,96−98,100−105] selectivity,[100,105,106] mechanical properties,[81−83,88−90,98,103] thermal stability,[107] phase-separated nanostructure and/or crystallinity,[42,81−84,89−91,97,98,103,107−111] surface topology and energy.[78−81,112] Such changes make it hard to compare literature studies if the pretreatment conditions have not been noted. For example, surface ionic activity of extruded Nafion membranes is lower in AsR or annealed form, however, it increases upon treatment in acid solutions.[78,96] In addition, in situ SAXS experiments showed that preboiling a PFSA membrane increases and (pre)sets its water-domain spacing at a maximum value compared to an AsR membrane, consistent with its water uptake behavior.[42,82,94,113] Overall, there is a consensus that the appropriate pretreatment process establishes a quasi-equilibrium state and sets a standard baseline. However, with new dispersion-cast and/or stabilized membranes as well as lower EW ones, the nature of the solvent, casting, additives, and postannealing processes still need to be studied and optimized as they strongly affect the membrane properties controlled by the physicochemical interactions and morphology.

1.1.3. Definition of Quasi-Equilibrium and Long-Term Effects.

When an ionomer is in equilibrium, a balance exists between the chemical and mechanical energies, which, continuously change with time as a result of the complex nanophase separation of semicrystalline backbone and ion-rich water domains. Overall, relaxation or equilibrium time measured for many PFSA properties are much larger than the typical experimental observation times; changes in water uptake and morphology have been after equilibrating for weeks, months, or even years,[88,114−117] and mechanical relaxation was shown to exhibit time-, temperature-, and humidity-dependent response over the course of days.[118] Thus, even after a PFSA membrane reaches steady state, it is not in a true thermodynamic equilibrium in typical experiments and could be at best in quasi-equilibrium, depending on the pretreatment and measurement conditions. A slow, continuous change in properties has been observed at longer time scales (up to days and years), which are accompanied by changes in morphology. This long-term relaxation of the polymer matrix leads to additional water uptake and associated reorganization possibly affecting the structure and connectivity of the hydrophilic network. Time-dependent relaxation processes in PFSAs have been reported to occur for conductivity,[119−122] stress and elastic modulus,[119,123−127] and polymer backbone stretching.[128,129] Relaxation phenomena have also been discussed within the context of morphological changes even over weeks based on SAXS studies,[84,115−117,130,131] dielectric measurements,[2,34,132−135] and dynamical mechanical analysis (see section 5.4). When the polymer backbone relaxes, it also relaxes the constraints it enforces onto the water domains it surrounds by means of reduced swelling pressure, and therefore changes the chemical-mechanical balance in favor of swelling (see section 2.6). As a result, additional increases in water uptake have been observed even after the membrane seemingly reached quasi-equilibrium,[13,94,114,128,136] accompanied by continues changes in nanostructure, albeit at a very slow rate, even for weeks.[115−117]

Relaxation phenomena, similar to electrostatic interactions, reflect and bridge the unique properties of PFSA ionomers: transport ←→ morphology ←→ thermo-mechanical response. For example, conductivity was shown to change with time,[104,119−121] which was influenced by applied pressure during the measurements.[120] As such, interpretation of the measured time-dependent response is rather intriguing as it is likely to be governed by a combination of chemical, mechanical and structural factors. To account for relaxation, one can define a time-dependent change in a property, $\psi(t)$, as

$$\psi(t) = \psi_{\infty} + \sum_{r} a_r \exp\left(-\frac{t}{\tau_r}\right)^{\beta_r} \qquad (1)$$

where ψ_{∞} is the final, quasi-equilibrium value, a_r and β_r are the fitting parameters, and τ_r is the time-constant for the relaxation process, r. When $\beta_r = 1$, the usual exponential decay function is recovered, whereas values of $\beta_r < 1$ indicates a stretched exponential function. One must note that, when multiple mechanisms are involved in relaxation process ($r > 1$), a single characteristic time constant for PFSA phenomenon cannot be identified, especially when these processes and time constants also change with temperature and humidity.

The real challenge associated with determining τ_r is that the actual relaxation time is most times longer than the experimental observation for a property, τ_{exp}. The ratio of the time constant is defined as Deborah number; $De \equiv \tau_r/\tau_{\mathrm{exp}}$. Interestingly, De for PFSA has not been studied in detail, although it has been mentioned.[128,137] If the process of interest is diffusion (see section 4.1), then the Deborah number can be written as

$$De \equiv \frac{\tau_r}{\tau_{\mathrm{exp}}} = \frac{\tau_{\mathrm{relaxation}}}{\tau_{\mathrm{diffusion}}} = \frac{\tau_{\mathrm{relaxation}}}{L^2/D} \tag{2}$$

If $De \ll 1$, then the relaxation process is not dominant, whereas high De indicates processes for which relaxation becomes relevant and important. Based on long-term experiments in the literature, the estimated time constants for relaxation processes in vapor phase are on the order of 10^3 to 10^4 s for conductivity,[119] 10^4 to 10^5 s for water-uptake,[114] 10^5 to 10^6 s for water domain spacing,[115−117] and 10^3 to 10^7 s for mechanical relaxation.[118,127,138] Clearly, there is a huge gap among the measured τ, mainly driven from the limited time scale of observations. A noteworthy exception is in mechanical relaxation studies, which invokes the time−temperature−superposition (TTS), which, by its virtue, could overcome this limitation of time of observation by shifting time scales using temperature (see section 5.4). Hence, low De could be associated with more viscous (mechanical) response and transient (diffusion) behavior, whereas a high De is more relevant to elastic (mechanical) response and steady-state and mutual diffusion.

1.1.4. Casting Effects. Most ionomers are now cast from dispersion due to the possibility of going to smaller thicknesses and easy incorporation of additives and/or reinforcements. Casting PFSA ionomers from dispersions and the resultant impact on membrane properties is a long-standing challenge, especially for thin films in complex electrode structures.[1,139,140] As will be discussed in the morphology section, PFSAs do not form a true solution but rather exhibit dispersion-like behavior with rod-like cylindrical aggregates, the nature of which affects the properties of the as-cast membranes.[1,141−147] Since Moore and Martin demonstrated that casting PFSAs from a high-boiling point (BP) fluid resulted in improved properties, i.e., closer to that of extrusion-cast AsR membrane,[148] the role of dispersion fluids and thermal treatments in ionomer structure/property relationship has been of great interest. Casting with different solvents changes conductivity,[149,150] and casting at higher temperatures usually results in a more entangled network of chains and higher crystallinity and better solvent resistance and overall mechanical properties.[1,108,139] Recently, Kim et al.[139] demonstrated using over 25 dispersion fluids that mechanical toughness (inversely proportional to brittleness) of the dispersion-cast PFSA membrane is governed by the dispersion fluid's critical gelation concentration through chain entanglements induced during evaporation rather than the crystallinity, with additional effects that can be imposed by the high fluid's BP thermal treatment. It is clear that casting conditions and solvents can impact overall properties significantly, as well as membrane's performance, and this is an active area of investigation currently.[139,140,151−153]

1.1.5. Durability issues and New Developments. The past decade has witnessed significant efforts on mitigation strategies targeted at improving an ionomer's ability to withstand these chemical-mechanical stressors (Figure 1), resulting in hybrid composite membranes with chemical and mechanical stabilizers. The latter was achieved by the researchers at W. L. Gore & Associates by incorporating a strong hydrophobic reinforcement layer into a PFSA ionomer to improve its dimensional stability in response to hydration (i.e., GORE-SELECT membranes). Such reinforcements could also be used to compensate for the deterioration of mechanical stability in PFSA ionomers of lower EW. Over the decades, many other strategies have been adopted to mitigate degradation problems, whether they are mechanical and/or chemical, and to develop more durable PFSA membranes. Such strategies include, but are not limited to, impregnating the ionomer with (i) radical scavengers such as cerium/cerium oxide to prevent radical formation, (ii) inorganic fillers to improve water-retention capacity especially at higher temperature and lower humidities, and (iii) chemically inert hydrophobic mechanical support layers, such as PTFE mesh, to improve the mechanical properties and dimensional stability in response to humidity changes. Thus, an ionomer filled intentionally with secondary particles can be considered and treated as a composite membrane. However, given that PFSA ionomers exhibit a phase-separated morphology, inclusion of additional particles or support layers creates an even more complex multiphase material where the interactions of these newly added particles and the ionomer's hydrophilic and hydrophobic phases become critical in controlling not only the efficacy of the hybrid structure but also the overall functionality of the membrane.

1.2. Applications

Finally, we should note many of the applications that contain ionomers as critical components (Table 2). PFSA ionomers and their analogues exhibit good performance and durability, and have become the industry standard for automotive fuel-cell applications.[11,154,155] However, continuously improving cost and durability targets for commercial applications drives the interest in improving PFSAs functionalities further and/or developing alternative membranes. Since 2004, Nafion and related PFSA ionomers, thanks to their attractive electrochemical and thermal properties, have gained increasing interest for devices that require rapid ion- and water-transport rates and robust mechanical and chemical properties. Despite gaps in the current state of understanding and modeling of structure-transport relationships, PFSA ionomers continue to find themselves as the benchmark and baseline materials.

Moreover, their success in PEFCs as the electrolyte/separator[21,155−157] has made them of interest for other solid-state energy-conversion and -storage devices, such as flow batteries[158,159] and solar-fuel generators and electrolyzers,[160−164] for which the ionomer behavior and functionalities are expected to differ (Table 2). In addition, they have been employed in other applications, as microfluidic devices and soft actuators,[165−169] humidifiers[170] or dryer membranes to remove moisture in many applications,[171,172] chlorine-tolerant gas-separation membrane,[173] and considered for electrodialysis and water-purification systems.[27,174] These applications take advantage of various properties of the membrane, most usually conductivity, water transport and chemical stability, albeit sometimes at the expense of other properties (e.g., improved transport properties vs lower mechanical stability), therefore demonstrating the importance of the controlling and optimizing the complex structure−function relationship for a given application. For example, while actuators exploit the swelling-induced deformation of the membrane under applied voltage,[167] shape-memory applications focus on the thermo-mechanical properties that could be controlled with deformation and thermal treatments.[175] All of these studies have

Table 2. Broad Range of Applications Employing PFSAs Listed along with Ionomer's Role and Functionalities and Application-Specific Material Needs

application/system	role	functionality (for transport)	functionality (for stability)	optimize for/key parameters	refs
polymer-electrolyte fuel cells (PEFC)	ion-conducting electrolyte/separator	ion-conductivity, water transport, perm-selectivity with low reactant crossover (e.g., H_2 and O_2)	mechanical robustness, chemical stability against radicals	thinner stable membranes with reduced gas crossover and high conductivity at low RH	1,21,22,31,154−156,176
catalyst layers (in PEFC)	Pt binder, electrolyte	ion-conductivity, gas permeability	Pt/C coverage and stability	catalyst particle coverage, oxidation kinetics, transport	136,177−179
chlor-alkali	ion-exchange membrane	perm-selective ion-exchange	chemical stability	solution concentration, transport (selectivity)	180−182
passive water vapor transfer device	humidifer membrane	water permeability, gas impermeable	chemical stability, gas barrier functionality over lifetime	high water-permeance, reduced aging and contamination effects	170,183
water desalination	perm-selective membrane	water permeability (reverse osmosis), limited ion-permeability (salt rejection)	chlorine-tolerance stability/longevity	selectivity	27
shape-memory devices	shape-memory material	reversible thermo-mechanical deformation	shape recovery upon thermal effects/loads	thermal history, mechanical and thermal properties	175
ionic polymer metal composite (IPMC)	actuator/sensor	deformation (swelling gradient) under applied electric field (actuation), voltage generation if deformed (sensing)		bending stiffness, ability to maintain deformation and hydration (repeated loadings)	25,167−169
biomimetic pumps	soft actuator	reversible deformation under voltage	membrane stability (flexible yet robust)	adequate water under voltage without electrolysis to maintain deformation (swelling)	165
redox flow battery	electrolyte membrane	selective ion-conductivity, separator of reactants	mechanical integrity, product impermeability	selectivity	105,158,159
artificial solar fuel generator	electrolyte membrane	gas separation, ion-exchange	photostability, chemical stability	optical transparency effective light absorption, balance gas blockage vs conductivity	163,893

provided new data sets as well as widened the window for understanding and tuning the structure−property relationship of PFSA membranes, the discussion of which were mainly absent in previous review(s) since the properties of interest in those applications are not always the same as with traditional ones such as PEFCs and other electrochemical-conversion technologies.

2. SORPTION AND SOLVENT UPTAKE

2.1. Overview

As noted above, the sorption behavior of PFSA ionomers is the most important phenomenon affecting their phase-separated morphology and, hence, their overall transport and structural properties. Thus, the starting point with any PFSA characterization is the determination of its water-uptake capacity, or any other solvent for that matter. Although the overall concepts and modeling approaches are applicable to other solvents, in the following, the emphasis will be given to water, followed by a discussion on other solvents. The amount of water in the hydrated membrane can be quantified in a number of ways, which are all interrelated, even though the most commonly used quantity is the *water content*, λ (= mol H_2O/mol SO_3^-), defined as the number of water molecules per mole of sulfonic-acid groups, introduced first in a paper by Springer et al.,[184] although the concept of quantifying water locally in sites or clusters predate this paper.[33,34,185] The water content, λ (the terminology "λ" is now ubiquitous in PFSA research and was introduced by researchers working at University of California, Berkeley and Los Alamos National Laboratory around 1990), related to the macroscopic mass uptake using the EW of the membrane

$$\lambda \equiv \frac{n(H_2O)}{n(SO_3)} = \underbrace{\left(\frac{\Delta M_{H_2O}}{M_p}\right)}_{\text{water-mass uptake}} \frac{EW}{\bar{M}_{H_2O}} \tag{3}$$

where M_{H_2O} (M_p) and $\bar{M}_{H_2O}$ ($\bar{M}_p$) are the mass and molar mass of water (dry polymer), respectively. The water content can also be related to the water volume fraction, ϕ_w, and concentration, c_w by

$$c_w = \frac{\lambda}{\lambda\bar{V}_w + \bar{V}_p} \text{ and } \phi_w = c_w V_w = \frac{\lambda\bar{V}_w}{\lambda\bar{V}_w + \bar{V}_p} = \frac{V_w}{V_w + V_p} \tag{4}$$

where $\bar{V}_p$ and ρ_p are the molar volume and density of dry polymer, respectively. The above relationships hold as averages across the membrane (i.e., not local sites) and assumes additive molar volumes for the total volume of membrane, an assumption that will be addressed in subsequent sections (section 2.4).

In most experimental setups, the change in membrane weight is measured gravimetrically, at a controlled water-vapor activity, a_w, (or relative humidity) at a given temperature. This weight change can be used to relate the λ and a_w to generate a sorption isotherms (Figure 7). The water-uptake behavior of 1100 EW Nafion membranes have been under investigation over the past few decades with over 100 papers published since the 80s reporting isotherms that are similar in shape but different in absolute values as summarized in Figure 8 and in Table 3. As for the $\lambda = f(\text{RH})$ relationship, the observed differences have been attributed to, and in some cases carefully explained by, the

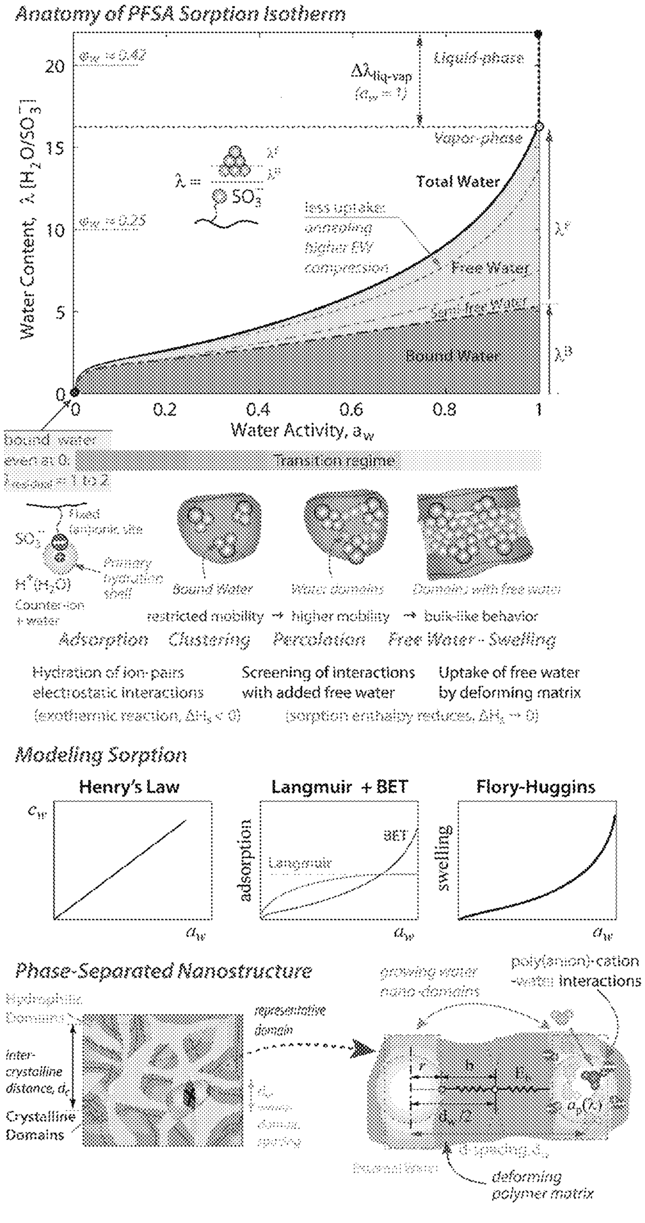
Anatomy of PFSA Sorption Isotherm
$\phi_w \approx 0.42$
$\Delta\lambda_{liq\text{-}vap}$ ($a_w = 1$)
Liquid-phase
Vapor-phase
$\lambda = \frac{\lambda^F, \lambda^B}{SO_3^-}$
Total Water
$\phi_w \approx 0.25$
less uptake: annealing higher EW compression
Free Water
Semi-free water
Bound Water
λ^F
λ^B
Water Content, λ [H_2O/SO_3^-]
0
5
10
15
20
0
0.2
0.4
0.6
0.8
1
Water Activity, a_w
bound water even at 0: $\lambda_{residual} \approx 1$ to 2
Transition regime
Fixed (anionic) site
SO_3^-
Primary hydration shell
$H^+(H_2O)$
Counter-ion + water
Bound Water
Water domains
Domains with free water
restricted mobility → higher mobility → bulk-like behavior
Adsorption
Clustering
Percolation
Free Water - Swelling
Hydration of ion-pairs electrostatic interactions
Screening of interactions with added free water
Uptake of free water by deforming matrix
(exothermic reaction, $\Delta H_s < 0$)
(sorption enthalpy reduces, $\Delta H_s \to 0$)
Modeling Sorption
Henry's Law
Langmuir + BET
Flory-Huggins
c_w
adsorption
BET
Langmuir
swelling
a_w
a_w
a_w
Phase-Separated Nanostructure
Hydrophilic Domains
inter-crystalline distance, d_c
Crystalline Domains
representative domain
d_w water-domain spacing
growing water nano-domains
poly(anion)-cation -water interactions
r
h
E_b
$d_w/2$
$a_p(\lambda)$
d-spacing, d_w
External Water
deforming polymer matrix

Figure 7. Representative sorption isotherm for a PFSA ionomer illustrating the distinct regimes governed by the electrostatic interactions as well as chemical/mechanical energy balance in the phase-separated nanostructure.

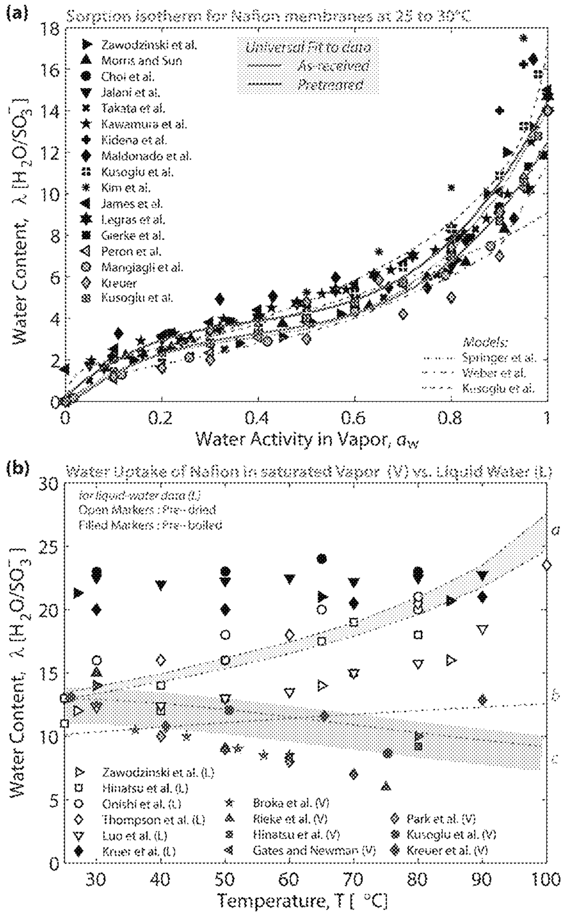

Figure 8. (a) Membrane water content, λ, as a function of water activity measured at 25 or 30 °C from various experimental data [see refs 6, 33, 82, 83, 95, 191, 199, 206, 207, 217, 221, 241, and 244−248] and models[82,184,201,204] and (b) as a function of temperature in vapor- and liquid-equilibrium [refs 33, 59, 82, 92, 94, 95, 113, 121, 239, 249, and 250]. The curves in (a) are polynomial expression from Springer et al.,[184] the lower and upper boundaries of models by Kusoglu et al.[82,194,204] and Weber and Newman.[201] (See Table 3 and section 2.6 for details.) The solid lines are generated from the best fit polynomial to all the data points in the plot. The lines are model prediction from refs 82 and 194: *a*, liquid water; *b* and *c*, saturated water vapor for the case of increasing and decreasing uptake with temperature, respectively (see section 2.6 for model details).

effects of pretreatment and thermal history (as mentioned earlier). It should be noted that there is a significant difference depending on whether it is the vapor or liquid phase, something that will be addressed in detail below.

The water uptake of a PFSA membrane decreases with increasing EW,[6,33,34,38,40,46−48,55,82,90,186,187] (see Figure 9), decreasing solvent polarity[188,189] (e.g., alcohols[190]), increasing heat-treatment temperature,[81−83,92,114,191] aging and contamination[85,170,192,193] (also see section 7.1), and mechanical compression.[194] Although seemingly irrelevant, all of these factors, at a fundamental level, are a result of changes in the chemical-mechanical energy balance of the ionomer's phase-separated nanostructure. In this sense, all of the above effects can be considered to either increase the backbone's resistance to deformation (e.g., crystallinity, compression, etc.) or the propensity for dissolution (e.g., lowering EW). This chemical-mechanical balance has long been a key aspect of equilibrium-swelling modeling of ionomers, albeit with many different approaches and formulations, starting with early studies by Eisenberg,[195] Mauritz et al.,[196] Dreyfus et al.,[197] and Hsu et al.,[198] and more recently revisited by Choi et al.,[199,200] Weber,[201] Freger,[202,203] Kusoglu et al.,[82,204,205] and Kreuer,[206] and associated with PFSAs' structure-transport[117,137,207,208] (see section 4) and swelling-mechanical response[61,82,122,126,204,209] (section 5) correlations. In addition, although explored more qualitatively, such a balance also changes with the cations,[210,211] due to changing electrostatic interactions altering not only the chemical properties but also the mechanical response (see section 7).

The swelling or sorption process of PFSA ionomer membranes is a multistep, multiscale phenomenon governed by complex interactions between the water, hydrophilic ionic moieties, and hydrophobic polymer matrix, resulting in a highly nonlinear water-uptake profile as demonstrated in Figure 7.

Table 3. Selected Studies on the Sorption Behavior of PFSA Ionomers, Including the Modeling Studies[a]

ref	year	investigation	studied effects and discussions	model/analysis*
Yeo[189]	1977	λ_{liq} (solvent)	solubility and interaction	FH and χ fitted
Gierke et al.[33]	1981	λ_{liq} (RH, EW, cation)	cluster coalescence and λ-domain spacing correlation	
Roche et al.[110]	1981	λ_{liq} (PT), H, Na	counterion and pretreatment	
Starkweather and Chang[34]	1982	λ_{liq} (EW)	bound/free water	
Escoubes and co-workers[214,251]	1984,1985	λ (RH,cation)	counterion effect and freeze	thermodynamics*
Mauritz and Rogers[196]	1985	λ (RH), Na^+, H^+	swelling equilibrium and pressure	thermodynamics
Springer and co-workers[47,95,184]	1991,1993	λ (RH), λ_{liq} (T, EW)	swelling regimes	polynomial fit
Hinatsu et al.[92]	1994	λ_{liq} (T, EW, RH)	ionomer type, pretreatment	
Futerko and Hsing[240]	1999	λ (RH,T)	analysis using FH model	FH and χ fitted
Laporta et al.[226]	1999	λ (RH)	solvation and free water	
Morris and Sun[246]	1993	λ (RH,T)	Henry's sorption	*
Gates and Newman[239]	2000	λ (RH, alcohol)	swelling equilibrium: methanol, H_2O	swelling
James et al.[221]	2000	λ (RH)	cluster coalescence	
Thampan et al.[252]	2000	λ (RH)	swelling equilibrium	BET
Reucort et al.[212]	2002	λ (RH)	enthalpy of sorption	*
Legras et al.[247]	2002	λ (RH)	Henry + Langmuir modes	*
Freger[202]	2002	λ (RH)	swelling pressure model	swelling pressure
Choi and Datta[253,199]	2003	λ (RH,T), SP	swelling model: solvation + FH	FH + BET + P_s, χ fitted
Weber and Newman[201,254]	2004	model	effect of constraints	macrohomogeneous
Bass and Freger[255]	2006	liq/vap	Schröder's paradox exists for $a_w < 1$	thermodynamics*
Onishi et al.[94]	2007	λ_{liq} (T), SP	pretreatment effect	
Takata et al.[241]	2007	λ (RH)	comparison of models: FH, Langmuir, Henry's, clustering	BET
Alberti et al.[88,114]	2007,2009	λ_{liq} (T, time), λ(H,T)	equilibrium time, pretreatment, explained using matrix elasticity	*
Kreuer et al.[6]	2008	λ (RH), λ_{liq} (T)	impact of side-chain, EW and temperature	
Collette et al.[85]	2009	λ (RH, aging)	impact of anhydrides, Langmuir + Henry contributions	
Zhao et al.[236]	2008,2011	λ (RH, alcohol)	solvation + matrix deformation, relaxation-driven increase in λ	thermodynamics*
Satterfield et al.[137]				
Kusoglu et al.[82,204]	2009,2012	λ (RH,PT)	swelling pressure model based on nanodeformation of the matrix	FH + BET + P_s, χ is fitted
Kusoglu et al.[194,257]	2011,2012	λ_{liq} (compression)	modified swelling pressure based on d-spacing of compressed membrane	FH + BET + P_s, χ is fitted
Kidena et al.,[191]	2010	λ (RH)	predrying temperature	
Maldonado[83]	2012	λ (RH,T), λ_{liq} (T)	predrying temperature	
Wadso and Jannasch[227]	2013	λ (RH)	predrying, enthalpy of mixing	
Kreuer[206]	2013	λ (RH,T)	Langmuir + swelling pressure related to the modulus	Langmuir + P_s
Shi et al.[211]	2016	λ (RH,cations)	impact of cation size and charge	dual-mode adsorption model

[a] λ_{liq} and λ indicates water uptake in liquid and vapor phase, respectively. "λ(X)" indicates sorption behavior is studied as a function of "X", where X can be RH, T, EW, and PT (pretreatment), alcohol/solvent, cation, compression, and ageing time. SP indicates studies where Schröder's Paradox was discussed. FH, BET, and P_s indicated models or analysis based on Flory-Huggins, Brunauer-Emmett-Teller, and swelling pressure formulations, respectively. Asterisk (*) indicates studies that analyzed data based on swelling equilibrium or other theories rather than proposed predictive models..

The water-uptake process is governed by the solvation energy of the ionic groups and chemical potential driving the external water molecules to attach to the hydrophilic ionic moieties of the membrane, which are counterbalanced by the deformation of the ionomer's hydrophobic matrix (i.e., the chemical-mechanical energy balance). During the hydration process, the first water molecule (H_2O) ionizes and binds to the sulfonic acid group via hydrogen bonds to form hydronium ions ($SO_3H + H_2O \rightarrow SO_3{\cdot}(H_3O)^+$). The initial water molecules continue solvating the ionic moieties by forming a stable hydration shell and allow the dissociation of the bound counterion; such water is termed bound water (Figure 7). This is driven by the fact that the hydration enthalpy of the proton is much higher than that of the conjugated base ($-SO_3^-$). Thus, water could form hydration shells around the cations and not just the tethered sulfonic-acid groups, and such cation-dependent hydration can impact interactions and PFSA properties (see section 7.3).

As the membrane uptakes water, protons (H^+) disassociate from the sulfonate sites, $-SO_3^-$, become solvated and mobilized by the water molecules (forming ions such as $H_9O_4^+$) reducing the hydration enthalpy of additional water sorption. This bound water and its solvation process is associated with reducing the hydration enthalpy, ΔH_s, due to the exothermic adsorption process of water.[206,212,213] The enthalpy change is the highest within $\lambda = 1$ to 2, corresponding to the ionization of SO_3H by water, with $\Delta H_s = -20$ to -25 kJ/mol.[190,206,212,214−216] After this bound-water regime, additional water molecules enhance the phase separation and form hydrophilic, ion-rich domains in the backbone matrix (see Figure 7).[35,217−226] With the adsorption of 2 or more water molecules, an interconnected network of domains are believed

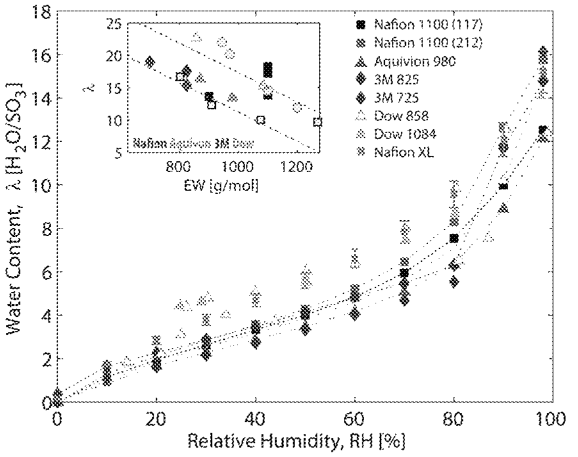

Figure 9. Sorption isotherms measured by gravimetric water uptake at 25 °C for various PFSA membranes. (Data shown are for Nafion,[48,82,90] Nafion XL,[98] 3M PFSAs,[48] and Dow SSC PFSAs,[47,187] all pretreated.) Inset shows λ values at saturation (taken from the plot) as a function of membrane EW along with those reported by Gierke et al.[33] for Nafion (open squares) and Moore and Martin for SSC PFSA (open circles).[38] (Lines are guide for-the-eye.)

to form, which marks the percolation threshold, giving the membrane its ion- and water-transport functionalities (see section 4). The adsorption process continues for up to 5 to 6 water molecules that form multiple solvation shells around a fixed sulfonic acid site ($SO_3^-H^+$), and after dissociation around $(H_3O)^+$. At higher RHs, additional water molecules cause further growth and connectivity of the hydrophilic domains as shown in Figure 7, leading eventually to a more bulk-like water region where water molecules freely move. In this regime ($\lambda > 6$), hydration enthalpy plateaus to −40 to −45 kJ/mol,[190,206,212,214−216] and approaches the heat of condensation of water (40 kJ/mol), which exhibits liquid-like properties, although confinement effects within nanodomains are still present (see section 4). Thus, the total water content in the ionomer at a given water activity, a_w, and T, can be expressed as

$$\lambda(a_w) = \underbrace{(\lambda_0)}_{\text{Residual(primary solvation)}} + \underbrace{\lambda_B(a_w)}_{\text{Bound}} + \underbrace{\lambda_F(a_w)}_{\text{Free}} \qquad (5)$$

where the residual water is a strongly bound water molecule participating in the primary hydration shells that can be removed only at elevated temperatures, i.e., $\lambda_0 = 1$ to 2 at 120 °C,[82,83,89,92,227] with a small trace of water possibly surviving up to 200 °C,[228−232] at the onset of SO_3 decomposition (section 7.1). Existence of a strongly bound water molecule is also consistent with a single immobile water determined in dynamic QENS studies.[233,234] (also see section 4.4).

Figure 8 summarizes the literature data on water uptake of Nafion membranes demonstrating the characteristic features of the sorption isotherms discussed above and illustrated in Figure 7. In plotting this data, the residual water is ignored for simplicity (i.e., $\lambda_0 = 0$ in eq 5), the nonzero value of which was discussed only in limited studies, usually in conjunction with drying effects[82,89,235] (see section 7.1.4 on TGA). Although only the sorption (humidification) data are plotted, PFSA membranes exhibit comparable sorption and desorption response, in terms of uptake, λ,[216,236,237] albeit with quite different kinetics, as discussed in section 4.1. Even though the plotted data exhibit some scatter, in part due to various experimental apparati and methodologies employed, they exhibit similar trends. Moreover, a closer examination of the membranes used in these studies reveal that preboiled membranes tend to uptake more water than the AsR (or predried) membranes, especially at greater than 60% RH, signifying the important role of thermal history and membrane pretreatment. At higher RHs, N21x membranes uptakes slightly more water than the older generation N11x membranes, (not listed in the legends for brevity) which can be associated with processing effects. It is worth noting that the high-humidity window, in which the thermal and processing effects manifest themselves in controlling the membrane's sorption capacity, also corresponds to the transition from bound to free water regime (per eq 5). Thus, up to 50 to 60% RH, membranes water uptake is mainly governed by Langmuir-type absorption of water molecules creating hydrations shells around the ionic groups, thereby creating a nanoscale local swelling, which appears to be less impacted by the side-chain length, EW, and thermal history of the membrane (Figures 7−9). Only in the free-water regime do these effects coming come into play. This increased effect is due to the accommodation of the absorbed water molecules in the growing hydrophilic domains deform the phase-separated morphology, resulting in a network swelling at multiple length scales, where the crystallinity, thermal history, and processing effects becomes more relevant. This can be seen better in Figure 9 which shows that increasing EW lowers the water-uptake capacity and changes the upturn of the isotherm, especially at high hydration levels (from 75% RH to liquid water), where uptake of free water molecules is controlled by the polymer matrix's resistance, which increases with EW (for a given side-chain).

In terms of temperature effect, sorption isotherms at elevated temperatures are relatively scarce in the literature, which could be attributed more to the difficulty in obtaining and accurately measuring values under high temperature, high humidity conditions. For a given membrane, nearly all of the studies report a similar water-uptake profile up to 70% RH, regardless of the temperature (25 to 90 °C).[83,92,98,156,191,206,238] However, under vapor conditions, especially close to saturation, the water content decreases with increasing temperature,[88,92,98,239−241] with the notable exception of a study by Kreuer,[206] who reported a trend of decreased λ with temperature below 80% RH, but an increased λ at higher RH (see Figure 8). In fact, from purely a mechanics perspective, the reduced modulus of the backbone at higher temperatures is expected to reduce the pressure it exerts on growing water domains, thereby allowing uptake of more water molecules (see section 2.6), and this is the case in liquid water (Figure 8b). Thus, a lower uptake at high RH for higher temperature could only be driven by the chemical interactions that oppose water uptake in the vapor phase. Although seemingly counterintuitive, this reduced swelling with temperature has been discussed in many studies and attributed to the changing hydrophilicity due to the surface interactions[85,92,95] and the changes in the role of the entropic term of water and polymer−solvent interactions[82,83,92,194,242,243] (also see section 2.6.4). An indiscernible change in λ with temperature below 70% RH was associated with the exothermal nature of hydration within this regime, where chemical interactions persist.[206] While the underlying phenomenon for reduced water uptake at elevated temperatures is still not definitively known or explained for PFSA membranes, it has been observed in other polymers and discussed within the context of cross-links or water retention

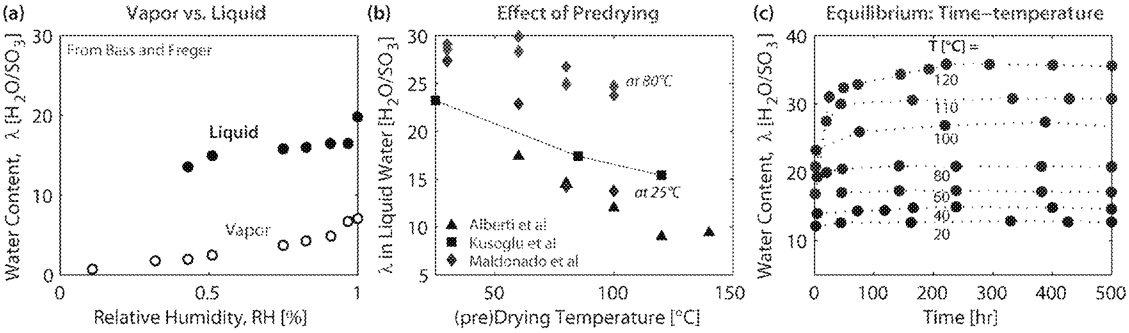

Figure 10. Impact of various factors on Nafion membrane's water uptake in liquid water, λ, (a) water content of Nafion equilibrated in saturated liquid and saturated vapor phase for a wide range of activities (from ref 203) (b) effect of (pre)drying temperature on measured water content,[82,83,114] and (c) effect of equilibrium time and temperature in water (from Alberti et al.[114]).

(or release) through condensation (or evaporation) controlled by the nanodomain size.[121,207]

2.2. Sorption from Vapor versus Liquid

Water content at saturation is of great interest as it provides the maximum hydration state, although with distinct water-uptake values depending on whether the water at the membrane boundary is vapor or liquid; these states are termed vapor- and liquid-equilibrated, respectively (see Figure 7). However, the water molecules inside the domains are always in a condensed or liquid-like phase. A similar effect is also seen with uptake from different solvents.[255,258] The existence and cause of the difference between λ measured in saturated vapor and in liquid water, i.e., $\Delta\lambda_{\text{liq-vap}} = \lambda_{\text{liq}} - \lambda_{\text{vap}}$, has been a long-lasting debate, as the membrane is in the same thermodynamic equilibrium in both cases, i.e., $a_w = 1$, and therefore a nonzero $\Delta\lambda_{\text{liq-vap}}$ implies an anomaly with the assumption of a single-phase system. This phenomenon has been termed "Schröder's paradox", based on the work of Schröder,[259] who reported that gelatins swell more in liquid water than in saturated water vapor. It has been a subject of great controversy in swelling of gels and other cross-linked polymer networks[255,260−262] and remains an intriguing problem both from theoretical (phase-equilibrium thermodynamics) and experimental (achieving a true liquid- and vapor-equilibrium) studies. Schröder's paradox for PFSA community has stimulated a number of systematic investigations that attempted to provide solutions both from modeling[194,201,203,253,263] and experimental[94,95,115,255,262,264,265] perspectives. While the former modeling approaches have employed various treatments to redefine thermodynamic equilibrium through interfacial effects and morphological changes (see section 2.6), experimental studies have examined whether the saturated membrane is in true equilibrium (kinetic effects), and the reversibility of the paradox,[94,95,115,116] as well as exploring the membrane's surface and morphological changes between vapor and liquid.[59,115,116,264,266,267] (See section 3.4.)

The specific origins of this change due to vapor/liquid conditions is still not fully understood or satisfactorily explained, although significant progress has been made leading to new investigations focusing on the membrane interface. The underlying origins of the liquid/vapor interactions are thought to be of either interfacial origin or thermal history, where the former induces a different morphology at the interface and the latter throughout the bulk. As for the latter, the fact that a predried membrane absorbs a similar amount of water whether it is in saturated vapor or liquid water ($\lambda_{\text{vap}} \approx \lambda_{\text{liq}} \approx 14 \pm 1$), but a preboiled membrane does not ($\lambda_{\text{vap}} = 14 \pm 1 < \lambda_{\text{liq}} = 22 \pm 1$),[82,88,92,94,95,114,255] has led some research to conclude that the difference is a matter of equilibrium, or lack thereof. However, as the paradox is of a thermodynamic origin, the focus should be on the membrane that is closer to quasi-equilibrium, which is the preboiled membrane, which does exhibit a vapor/liquid difference ($\Delta\lambda_{\text{liq-vap}} > 0$). For example, it is known that as the temperature of the liquid water is increased, the water content increases and approaches the preboiled membrane value for both Nafion[6,47,82,92,94,100,113,114,248−250] and other PFSA ionomers[6,47,92,98,100] (see Figure 10). For a membrane that was not preboiled (e.g., AsR), its λ in water increases with temperature.[94,95,222,268,269] However, once the membrane is (pre)boiled, its liquid-water uptake does not change with temperature,[82,94,113] indicating that the membrane is already in quasi-equilibrium.

Thus, the observed increase in sorption capacity of (AsR or heat-treated) membranes with temperature is related to their morphology, which could be in a kinetically trapped state, and is in agreement with the longer times for stabilization as shown in Figure 10c. Alberti et al.[88,114] showed that it took up to 200 h for predried membranes to reach equilibrium, and the higher the predrying temperature the longer the equilibrium time becomes, once again indicating that heat-treatments preset a restricted morphology even at temperatures below the cluster-transition temperature (see section 5.4). In fact, it was shown that as the (pre)drying temperature of the membrane increases, its subsequent water uptake decreases in both vapor[82,83,88,92,114,191] and liquid water,[6,47,83,92,191,227] which affect related transport properties as well. (See section 3.)

In an effort to elucidate the origins and nature of Schroder's paradox, Bass and Freger[203] carried out a systematic study of Nafion's water uptake for activities below $a_w = 1$ using solutions of a polyelectrolyte (polyvinylsulfonic acid salts) as an osmotic stressor, which allowed measuring isopiestic sorption isotherms in vapor- and liquid-equilibration modes for different water activities (Figure 10a). Their findings demonstrated Schröder's paradox is not an anomaly at 100% RH but extends to the water activities down to 50%, confirming the difference between vapor and liquid-equilibrium, which is strongly related to the membrane morphology, especially at the surface. As will be discussed in section 3.4, the surface of a PFSA membrane change with hydration, something that was well acknowledged through contact angle,[112,266,270] AFM,[74,271−279] electrochemical mass-transport[280] measurements, and X-ray studies.[48,281] Bass and Freger[266,267] investigated the morphology of Nafion membrane and showed that the surface morphology is hydrophobic in nature in vapor but becomes hydrophilic in liquid, an observation in agreement with other observed surface changes as a function of humidity, as discussed in section 4. Kusoglu et al.[115] later showed using time-resolved SAXS that a membrane's d-spacing reaches steady-state in seconds when in liquid water, yet in vapor, d-spacing does not reach a steady-state even after a month and is still lower than that in liquid water. Gebel et al.[116] reported similar morphological differences and kinetic effects between vapor and liquid using SANS. The same group also showed that the ionomer peak in vapor-equilibrium was changing even after a year, with linear dependence of d-spacing on log(time) suggesting a slow continuous reorganization and relaxation of the water network.[116,117] Hence, accurate characterization of the membrane water uptake requires an understanding of its surface morphology thermal history, and long-term sorption behavior as well as relaxation phenomena, which will be discussed in section 3. The observed differences in morphology between the vapor/liquid conditions have not only improved the current state of PFSA understanding, in a large part due to more advanced in situ morphological characterization, but also provided convincing evidence for the changes in the surface under saturated vapor/liquid conditions and its key role in delineating the Schröder's paradox. It must be noted that it is challenging to achieve a true unit vapor activity ($a_w = 1$) in the absence of thermal fluctuations and liquid–water condensation on the surface, since the latter effect, if occurring, would change the membrane's state from vapor to liquid.

Finally, it should be noted that uptake experiments with different solvent vapors and different solvent solutions show a strong trend that the more polar the solvent,[190,239] the higher the values and larger the discrepancy between liquid and vapor values.[188,189,282] This suggests that these environmental interactions have similar impacts on membrane morphology and hence solvent uptake.

2.3. Dimensional Change and Swelling

A direct consequence of sorption in PFSA membranes is the change in their dimensions, i.e., swelling, to accommodate the absorbed water molecules, which, as described in section 2.1, mainly occurs in the free-water regime of uptake. The volume change can be defined as the volumetric swelling strain, which can be decomposed into the swelling strains in three directions (in-plane, x, and y and through-the-thickness, z):

$$\varepsilon_V^{\text{sw}} = \frac{\Delta V_{\text{w}}}{V_{\text{P}}^{\text{dry}}} = (1 + \varepsilon_x^{\text{sw}})(1 + \varepsilon_y^{\text{sw}})(1 + \varepsilon_z^{\text{sw}}) - 1 \tag{6}$$

which can be related to the water uptake as follows (assuming isotropic swelling, the accuracy of which will be discussed below, and constant molar volumes)

$$\frac{L_{\text{s}}(\lambda)}{L_{\text{dry}}} = \left(1 + \frac{\Delta V_{\text{w}}}{V_{\text{dry}}}\right)^{1/3} = \left(1 + (\lambda - \lambda_{\text{ref}})\frac{\overline{V}_{\text{w}}}{\overline{V}_{\text{P}}}\right)^{1/3} \text{ or} \varepsilon_{\text{swe}} \approx \frac{1}{3}\frac{\overline{V}_{\text{w}}}{\overline{V}_{\text{P}}}(\lambda) = \beta_{\text{swe}}\lambda \tag{7}$$

where L_S and L_{dry} are the swollen and dry (initial) dimension length, respectively, and λ_{ref} is the reference water content at which dimensional changes start, usually at $\lambda_{\text{ref}} \geq 2$. A simplified expression for the swelling strain, ε_{swe}, can also be written as a linear function of λ, where the calculated swelling-expansion coefficient, $\beta_{\text{swe}} = 0.009 \pm 0.002$, is in good agreement with the experimental data taken from various resources[283−285] (Figure 11). Similarly, a thermal expansion coefficient, α_T, can be defined to relate the thermal strain to temperate change, i.e. $\varepsilon_{\text{the}} = \alpha_T \Delta T$.

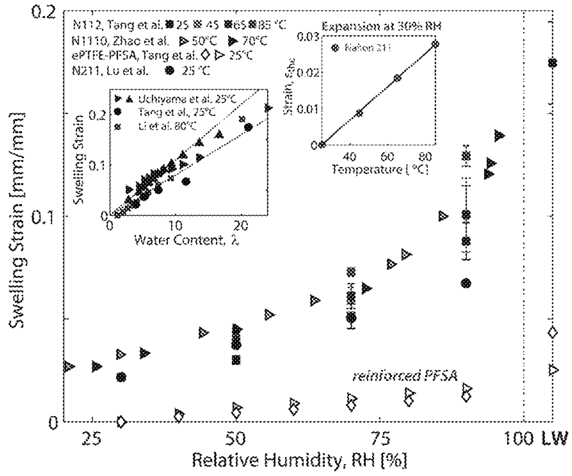

Figure 11. Dimensional change (swelling strain) of PFSA membranes as a function of relative humidity, shown for the in-plane direction, for Nafion[61,123,127,190,283−285] and for ePTFE-reinforced PFSA.[286] (See section 7.2.) The inset on the left shows the swelling strain vs water content, from Uchiyama et al.,[283] Tang et al.,[284] and Li et al.[285] (The lines in the inset are the lower and upper bounds for the best-fit to the data.) The other inset plots dimensional change at 30% RH for Nafion 211 membrane as a function of temperature, i.e., thermal strain (from ref 127).

The studies on dimensional change of PFSA membranes can roughly be classified into humidity-dependent swelling strain at constant temperatures[61,127,190,246,285−290] and swelling in liquid water at different temperatures with a focus on swelling anisotropy, i.e., thickness vs in-plane swelling,[98,123,188,248,283,291−293] as highlighted in Figure 11. Even though PFSAs exhibit discernible anisotropy in terms of thickness vs in-plane swelling, there is evidence to suggest that thickness swelling could be higher than the swelling in one of the in-plane directions, albeit only slightly.[98,123,188,283,284,286] In addition, membranes that are reinforced with ePTFE exhibit a 10-fold decrease in in-plane swelling (i.e., lower β_{swe}) since swelling in the plane is hindered in favor of thickness swelling due to the reinforcement strategy.[98,284,287,294] (Figure 11). As discussed earlier, the impact of pretreatment can be seen here as well, in that pretreatment can exhibit a significant impact on swelling strains measured in liquid water, resulting from not only the thermal-history effects but also due to changes in reference length depending on whether the membrane is predried and later humidified or preboiled with the swelling calculated after the membrane is dried. Anisotropic swelling is induced upon (i) extrusion of PFSA membranes, which swell less in the direction of extrusion (machine direction) resulting in machine/transverse swelling ratio of $\varepsilon_{\text{swe}}^{\text{TD}}/\varepsilon_{\text{swe}}^{\text{MD}} = 1.1$ to 1.4,[98,123,127,286−288,293] (ii) prestretching,[295,296] and (iii) constrained-drying, which causes a heat-reversible increase in the thickness/length swelling ratio from 1.4 to 5.8.[293]

Information on swelling of various PFSA chemistries is also scarce, with notable exceptions of Aquivion[61] and 3M,[7] both of which exhibited higher swelling (but still directly proportional with water content) than a Nafion membrane. Lastly, thermal expansion (coefficient), α_T, in PFSA membranes is much less than the swelling expansion (coefficient) and is not significant in typically operating device conditions (i.e., < 100 °C). Existing literature suggests anywhere from 0.00014 to 0.00046[99,127,297] to 0.0023[298] below T_g, and 0.0030−0.0085[99,298] above T_g, which also changes in different cationic forms.[99]

2.4. Density and Free Volume

The density of a hydrated PFSA ionomer membrane can be approximated from its density in the dry state and fraction of water by using a rule-of-mixture

$$\rho_p(\phi_w, \mathrm{EW}) = \phi_w\rho_p^{\mathrm{dry}}(\mathrm{EW}) + \phi_w\rho_w, \text{ with } \phi_w = 1 - \phi_p \qquad (8)$$

where the dry density $\rho_p^{\mathrm{dry}}(\mathrm{EW})$ is 2.05 ± 0.05 g/cm^3 for most PFSA membranes but changes with EW as shown in Figure 12.[33,213,246,299] The figure clearly shows that the density of a hydrated PFSA membrane decreases with water uptake and approaches a value of 1.5 for a liquid-equilibrated membrane ($\phi_w \approx 0.5$).

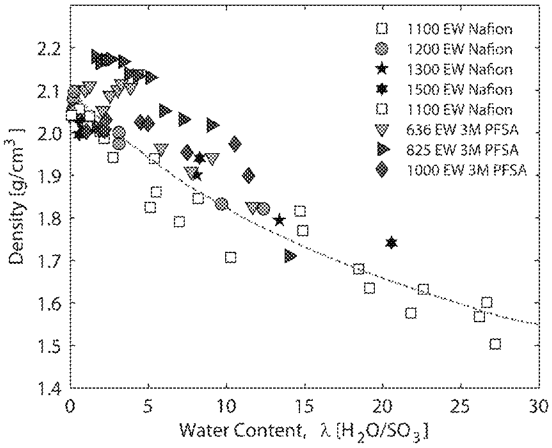

Figure 12. Density of Nafion[99,246] and 3M PFSA[213] ionomers of various EWs plotted as a function of water content at 25 °C. The line shows the prediction from the rule-of-mixture for Nafion 1100 EW membrane (eq 8, for a dry density of 2.1 g/cm^3).

The density is also related to the free volume in the PFSA ionomer. This free volume has been investigated via positron annihilation lifetime spectroscopy (PALS) that relies on the annihilation of a positron through its interaction with electrons. By probing the lifetime of positrons (*o*-Ps) in various states, one can determine the radius of free-volume holes, i.e. shorter lifetime indicates smaller volumes.[300−303] The size of the free volume in Nafion as a function of temperature and humidity is summarized in Figure 13 based on PALS data by Mohamed et al.[303] The increase in free volume with temperature is indicative of thermal expansion that marks the beta-transition (of the main-chain) around 20 °C at which a change in slope is observed (i.e., a thermal expansion coefficient similar to that from macroscopic expansion). Nevertheless, in K$^+$ and Na$^+$ form, PFSA does not exhibit this transition due to a shift in its beta-temperature as discussed in section 5.[301] Moreover, the gradual decrease in free volume with increasing humidity, especially after 60% RH (around the bound-to-free water transition), was attributed to the more positron annihilating in the aqueous phase due to the large uptake of water.[303] This free volume is key for transport processes such as gas permeability as it provides pathways for molecular jumps.[303] The free volume of dry Nafion 212 detected by PALS at ambient temperature was reported to be between 0.175 and 0.219 nm^3,[300,301,303] which is smaller than that of PTFE (0.297 nm^3).[303] It is interesting to note that the fraction of total free volume (all cavities) in the polymer is approximately 0.028 (or 2.8%),[300] a rather small value compared membrane's overall macroscopic volume change. Hence, despite nonideal mixing governed by the solvation of ions by bound water in the early stages of hydration and associated nanoscopic free volume therein, a PFSA membrane's hydration behavior and total volume change for high λ (or RH) can still be approximated, at least macroscopically, as additive molar volumes of water and polymer.

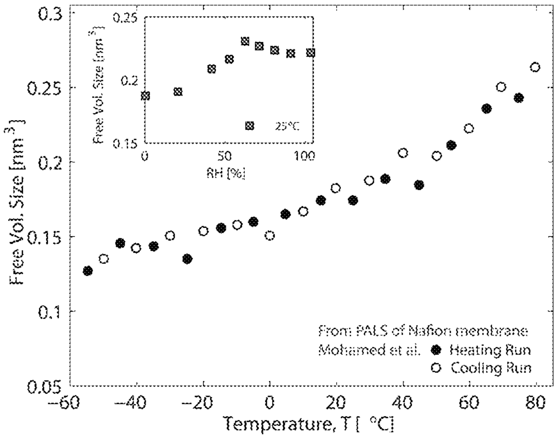

Figure 13. Change in free volume with temperature and humidity at 25 °C (inset) in terms of hole volume measured by PALS. (Data from Mohamed et al.[303])

2.5. Nature of Water and Freeze

Sorption isotherms measured at subzero temperatures show similar behavior as those measured at RT, albeit with less overall water uptake due to less free water (Figure 14).[251,304] Less free water at subzero temperatures is a result of changing the energy balance in the membrane via increased backbone modulus as shown by Kusoglu et al.[305] Nevertheless, adsorption of bound water in the membrane does not change in the subzero regime, as these water molecules do not freeze due to their strong electrostatic interactions with the ionic groups. In fact, it has been acknowledged that, unlike free water molecules that have been observed to be freezable, bound water molecules were shown to be not freezable and, thus, are associated with nonfreezable water. Thus, subzero temperature behavior of ionomers is commonly used to identify and investigate bound vs free water molecules in the system. Using such information from dynamic scanning calorimetry (DSC), a number of studies correlated the amount of freezable (free) water, λ^{F}, in the hydrated membrane with the total water content:

$$\lambda = \lambda^{\mathrm{F}} + \lambda^{\mathrm{NF}} \text{ with } \lambda^{\mathrm{NF}} \approx \lambda_{\mathrm{B}} \qquad (9)$$

A further relationship can be established from the plot of total water vs free (freezable) water based on the reported values (Figure 14), where the intercept gives a rough estimate of $\lambda^{\mathrm{NF}} \approx \lambda_{\mathrm{B}}$.

$$\lambda = 1.7\lambda^{\mathrm{F}} + 4.75 \qquad (10)$$

It must be noted that, the above expression, while quantitatively capturing the measured data, simplifies the state of water into two distinct states. DSC studies on freezable

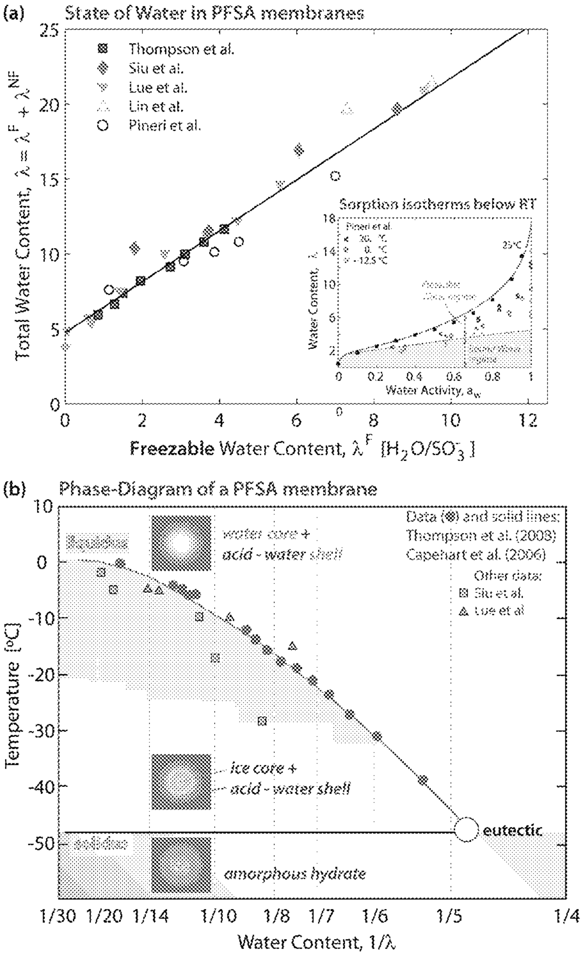

Figure 14. (a) Correlation between the freezable water, λ^F, and total water (freezable + nonfreezable), based on the reported values in the literature.[52,58,214,251,296,309,310] Solid line is a linear fit to the data. Inset shows the sorption isotherm of Nafion at 25 °C[17] and below room temperature from Pineri et al.[214,251] and Gallagher et al.[311] (b) Phase diagram for hydrated Nafion at subzero temperatures, modified from Thompson et al.[309] with added data from refs 52, 58, 309, and 310.

water, however, indicates a third type of semifree water, which is bound but still freezable, occupying the outer solvation shells of the polymer-$SO_3^-\cdot H_3O^+$ region (Figure 7).[269,306−308] In fact, this type of water is sensitive to the nature of cations in the PFSA, which not only impacts the amount of total and freezable water, but also the intermediate-states of water.[186,269,306,308] (See section 7.3.) Nevertheless, the fact that sorption isotherm at subzero temperatures approaches a Langmuir-type adsorption curve for the bound water supports the notion that nonfreezable water can be treated as bound water (Figure 14a, inset). Finally, while one can distinguish between freezable and nonfreezable water, the water in a PFSA ionomer is a continuous condensed phase with varying properties depending on molecular interactions from the backbone wall and not a true solid/liquid multiphase system.

Thanks to the nonfreezable, mobile water molecules, species transport in the membrane is possible even below the freezing point (and expected due to concentrated ion solution), another intriguing property of PFSA ionomers.[312] Water content, transport, thermal, and mechanical properties of PFSA ionomers below 0 °C have been investigated using a variety of techniques, including sorption,[214,251,311] DSC,[34,214,251,307−309,313] DMA,[34,214,251] and NMR,[251,304,313,314] not only in H^+ form but also with various counterions (K^+, Na^+, Li^+).[186,251,269,306,308] In DSC studies, an endothermic peak around 0 °C due to the melting of water is observed for high water content (saturated or liquid), but as the initial λ goes down the peak becomes broader shifting to lower temperatures, indicative of freezing-point depression.[58,214,309,310] Thus, the higher the water content, the closer to bulk water temperature (0 °C) the phase-transition occurs.[58,309,312] The maximum water a PFSA membrane can uptake also reduces with decreasing temperature in the freezing regime, from $\lambda = 15$ at 0 °C to $\lambda = 8$ at −15 °C and to $\lambda = 6$ below −35 °C, at which a limiting value is reached regardless of the initial water content (e.g., at ambient temperature).[304,309,311]

Ice formation followed by desorption was confirmed by the morphological investigations using X-rays.[315−317] Therefore, decreasing the temperature continuously below 0 °C not only decreases the total water (desorption) but also reduces the amount of free water (freezing), thereby restricting transport functionalities. Despite the existence of nonfrozen water molecules at as low as −50 °C, significantly slower mobility is observed via NMR with a 1 order of magnitude decrease in the water tracer-diffusion coefficient.[304,313,314] Hence, water molecules demonstrate more coordination with the ionic sites at these temperatures, resulting in restricted but finite mobility.[52,58,304,309,312,313] In addition, compared to ambient temperature, PFSAs at subzero temperatures exhibit higher activation energy for conductivity,[58,102,250] and higher modulus[305,318] but not a significant change in electro-osmosis coefficient.[311] All of these changes are traditionally attributed to the depression of the freezing point due to confinement of water interactions with ions in nanodomains.[312] Due to its potential to unveil the nature of water and associated transport mechanisms, quantifying freezable/nonfreezable water has been employed to examine various factors, such as mechanical stretching,[296] degradation,[319] nanostructure,[315,317,320] as well as transport (e.g., refs 58, 186, 250, 264, 311, 312, and 314 also see section 4).

Recent X-ray[315,317] and neutron[320] studies based on crystallization of water and change in ionomer peak (domain size) of PFSA below 0 °C revealed that water desorbs without freezing in the membrane and becomes glassy below −53 to −60 °C.[315,317,320] Moreover, water remains amorphous even at $\lambda = 22$, or a domain size of ~3 nm, only crystallizing for $\lambda = 50$ (hyper-swollen state) and/or domain size of 5 nm.[317] Thus, freezing-point depression is attributed to both confined and acidic nature of the water nanodomains in a hydrated PFSA.[309,312,317,320] Moreover, this effect of confinement could also be confirmed by the increase in the fraction of nonfreezable water in PFSA upon stretching which creates less tortuous and smaller domains.[296] Despite the consensus on the temperature-λ range in which the water molecules are nonfrozen and mobile, their nature in mixed state, i.e., intermediate λ, can be delineated better with the help of transport studies. Such an effort was undertaken by Thompson et al.,[309] who, through a systematic study on conductivity and DSC of Nafion at temperatures down to −50 °C during heating/cooling cycles, constructed a phase diagram for water/Nafion that exhibits similarities to molecular acid/water mixtures (Figure 14). Overall, the water domains in a "frozen" PFSA contain an ice core surrounded by concentrated acid/water solution and bounded by the λ-dependent liquidus and

Table 4. Selected Studies on the Modeling of Sorption-Related Phenomena in PFSA Ionomers, with Brief Summary of the Methodology Employed and Key Findings[a]

ref	method and approach	predicts/analyzes
Eikerling and co-workers[206,350,351]	random pore-network with idealized pores having surface and bulk-like water and poro-electroelasticity with pore size distribution	sorption, conductivity, aging
Gavish et al.[353]	phase flow model, Cahn-Hiliard functionalization	sorption, morphology
Wu and Paddison[63,67]	dissipative particle dynamics, coarse-grained mesoscale model	morphology and transport
Hwang et al.[347]	bimodal porous domains + MD (canonical Monte Carlo)	sorption, conductivity
Weber and Newman[201]	macro-homogeneous membrane model	sorption, transport
Kusoglu et al.[82,257]	microhomogenous model based on domain spacing data (SAXS)	sorption, compression effects
Li et al.[354]	free energy perturbation using density functional theory (DFT)	sorption, diffusion
Voth and co-workers[348,355−357]	coarse-grained with smoothed particle hydrodynamics to capture the morphology and transport based on the chemical potential with various morphologies (cluster, cylindrical, lamellar)	macroscopic transport and conductivity, electrostatic interactions and ionic group distribution impacts transport
Gostick and Weber[352]	resister- and pore-network model, with mesoscale distributions of domains	effective conductivity and percolation
Daly et al.[349]	molecular dynamics with a thermodynamic and transport model	λ(RH, T), role of water-sulfonate interactions

[a] Additional MD/DPD studies focusing on proton transport mechanisms and morphologies are discussed in sections 3.3 and 4.4, respectively.

solidus phase lines. According to their findings, formation of ice cores in hydrophilic domains does not strongly affect their percolation and, thus, conductivity. Rather, they help stabilize the network (connectivity) where the mobile water molecules are pushed and connected through the unfrozen walls of the domains and connection pathways. Due to these morphological differences and the state of the water, freezing and dehydration cannot be considered to be governed by the same phenomena, even at the same λ. Based on Poisson−Boltzmann models, differences between the conductivity and calorimetry are attributed to gradients in the proton concentration that result in a proton-depleted core in the hydrated domains, which freezes first and contributes minimally to conductivity, although such models do not account rigorously for solvation and other changes to the water and proton chemical potentials.

2.6. Modeling of Water Uptake

Despite a tremendous amount (~100s) of experimental studies on PFSA water uptake, the modeling of their sorption behavior is rather less explored (on average, 1 out of every 10 papers with water-uptake data attempt to model/explain the data). Table 4 lists some of the modeling studies along with some experimental ones, in which a systematic investigation and analysis were conducted [see refs 47, 85, 88, 92, 94, 95, 114, 121, 184, 191, 196, 199, 210, 211, 214, 221, 226, 239−241, 244−246, 249−251, 253, 254, 258, 304, and 321−323] It should be noted that the majority of the modeling studies are not aimed at predicting the uptake by solving physics-based governing equation(s) and instead are employed in a context to analyze other properties and phenomena. Despite notable attempts for a unified model, none thus far has satisfactorily explained the complete sorption phenomena, including effects such as thermal history (annealing, predrying), EW, vapor/liquid transitions, multiscale swelling, morphological changes, etc.

As the water content is a critical variable for transport and other properties and describing the membrane state, extensive efforts have been undertaken to predict λ based on measurable properties and environmental conditions (e.g., RH, T). A majority of the efforts resort to a thermodynamic, equilibrium-based energy-balance approach to explain the sorption phenomena based on the contributions from the elastic forces and electrostatic interactions.[82,88,194,196,198,202−204,206,251,255] These models typically either assume a nanoscale morphology or calculate one. In addition, sorption isotherms have been analyzed or modeled using empirical curve-fits,[83,92,184,210] Henry's law,[85,210,246,247] adsorption isotherms,[85,199,206,210,211,241,247,252,253,255,324] Flory−Huggins theory,[199,204,240,241] and/or equilibrium between water in the membrane and vapor.[201,252,325,326] Due to the distinct physiochemical processes each model represents, they typically only model a specific phase of the PFSA's water uptake (see Figure 7), which have led researchers to combine models or modify them to account for the very complex nature of PFSA water uptake. A commonly used approach is to model bound-water (Langmuir-type) and free-water (high-RH) regimes separately and then linearly superimpose the solutions to predict the total water uptake (Figure 7) or to extend an adsorption model to account for swelling pressure (matrix deformation),[82,194,199,200,206,210,241] as discussed below. The complexity of the multiscale multiphysics phenomena makes it a challenge to develop a comprehensive, self-consistent model that accounts for all aspects discussed above. Thus, the early models based on thermodynamic equilibrium of a hydrated PFSA have been modified or expanded over the years to include the ionomer's electrostatic interactions and bound water, matrix deformation and swelling pressure, as well as its phase-separated nanostructure (growth of water nanodomains). Despite their differences, a general framework can still be outlined for many of these models.

Before proceeding with the detailed modeling of water uptake in PFSAs, it should be noted that many device models utilize a polynomial expression for the sorption isotherm of Nafion (such as the seminal one by Springer et al.).[184]

$$\lambda(a_{\mathrm{w}}) = \lambda\left(\frac{RH}{100}\right) = b_3{a_{\mathrm{w}}}^3 + b_2{a_{\mathrm{w}}}^2 + b_1a_{\mathrm{w}} + b_0 \tag{11}$$

where b_i are the coefficients of the polynomial. While useful due to its simplicity, such an expression is not predictive for conditions outside of which it was measured and lacks physical insight. A more general set of coefficients can be determined from a single polynomial fit to all the literature data shown in Figure 8a. [b_3 = 36.00 ± 2.45, b_2 = −42.8 ± −2.4, or b_1 = 20.45 ± 0.65, b_3 = 0.05 ± 0.20, where higher and lower values of b_i correspond to the as-received and preboiled membranes, respectively.]

2.6.1. Governing Equations.

The equilibrium swelling of a membrane in an environment at a given water activity, a_{w}, is governed by the chemical potentials of the membrane, $\Delta\mu_{\mathrm{w}}^{\mathrm{P}}$, and the environment exterior to the membrane, e.g., humid air, which is simply, $\Delta\mu_w^e = \mu_w^e - \mu_0^e = RT\ln a_w$, where μ_0^e is the chemical potential of the reference state (typically unit activity). This change in chemical potential of the water in the membrane, with respect to its reference value, $\mu_{\text{ref}}^{\text{P}}$, is

$$\Delta\mu_w^{\text{P}} = \mu_w^{\text{P}} - \mu_{\text{ref}}^{\text{P}} = RT\ln a_p + \bar{V}_w P_s \tag{12}$$

where T is the absolute temperature, R is the universal gas constant, a_p is the activity of water in the membrane, and P_s is the swelling pressure (or osmotic stressor, Π) arising in the polymer matrix as it deforms with the swelling of domains. Thermodynamics dictates that the chemical potential of water internal and external to the ionomer must be the same at equilibrium, i.e.

$$\left.\begin{aligned} \Delta\mu_w^e &= RT\ln a_w \\ \Delta\mu_w^{\text{P}} &= RT\ln a_p + \bar{V}_w P_s \end{aligned}\right\} \rightarrow \ln a_w - \ln a_p = \frac{\bar{V}_w}{RT}P_s \tag{13}$$

This expression has been commonly used as the starting point of swelling equilibrium of PFSA ionomers. Alternatively, the equilibrium can be stated in terms of total change in the free energy with respect to a reference state

$$\Delta G = \underbrace{\Delta G_s}_{\text{swelling/osmotic}} + \underbrace{\Delta G_e}_{\text{elasticity/deformation}} \quad \text{and} \Delta\mu_w(a_p) = \left(\frac{\partial}{\partial n_w}\Delta G\right)_{p,T} \tag{14}$$

where the first two terms represent the swelling (osmotic) and elastic energy associated with the elastic deformation of the matrix opposing swelling. One point at which the models begin to deviate is the description of a_p. The simplest form for a_p is the mole fraction of water in the hydrophilic domains, $a_p = \lambda/(1 + \lambda)$, which however neglects molecular interactions. Specific expressions can be adopted to describe a_p, or μ_w^{P}, depending on the physiochemistry of the sorption phenomenon. As discussed in section 2.4, due to the distinct nature of free and bound water molecules in the ionomer, it is appropriate to treat and model these regimes separately. Thus, it has been customary to model water content as $\lambda(a_w) \equiv \lambda^{\text{B}}(a_w) + \lambda^{\text{F}}(a_w)$. Note that this approach does not consider the water to be in separate thermodynamic phases, but it acknowledges that the water continuum exhibits different properties due to its local conditions of ion concentration, dielectric constant, etc. The bound- and free-water regions of an isotherm can be predicted using the following modeling approaches (Figure 7).

For the bound water, a Langmuir isotherm is commonly employed.[199,241,253] Langmuir adsorption of the first water molecule at a given partial pressure, p_w, is expressed in terms of fraction of surface (monolayer) coverage, θ

$$\theta_1^{\text{w}} = \frac{K_{\text{eq},1}^{\text{w}} p_w}{1 + K_{\text{eq},1}^{\text{w}} p_w} \tag{15}$$

where $K_{\text{eq},1}^{\text{w}}$ is the equilibrium constant for the adsorption reaction of the first water molecule forming the solvation shell. When applied to adsorption of bound water molecules to the ionic groups in a PFSA, a multistep expression is adopted for bound water, λ^{B}, as follows $(n(\text{H}_2\text{O}) \overset{K_{\text{eq}}^{\text{w}}}{\longleftrightarrow} (\text{H}_2\text{O})_n)$

$$\lambda^{\text{B}}(a_w) = \sum_{i=1}^{\nu} \lambda_i^{B}(a_w) = \sum_{i=1}^{\nu} \left(\prod_{j=1}^{i} \theta_j^{\text{w}}\right) \text{ and } \theta_j^{\text{w}} = \frac{K_j^{\text{w}} a_p}{1 + K_j^{\text{w}} a_p}, \; K_j^{\text{w}} = \exp\left(-\frac{\Delta G_j}{RT}\right) \tag{16}$$

where ΔG_j is the hydration (solvation) energy of reaction step j and ν is the total number of equilibrium steps or the number of bound water molecules ($\nu = 4$ to 5). The above equation represents the multilayer adsorption of water molecules by clustering on the primary monolayer, based on the BET theory,[327] which yields the following general form in terms of water concentration:

$$c_w = C_m \frac{A_S a_w}{(1 - a_w)(1 - (C_m - 1)a_w)}, \quad (a_w = \text{RH}/100) \tag{17}$$

where C_m is the sorption capacity of the monolayer and A_s is related to the difference in heats of sorption between the first monolayer ($j = 1$) and all other (j^{th}) layers, which are assumed to be the same as that of a pure liquid (H_L), i.e., $A_s \propto \exp((H_1 - H_L)/RT)$.[327] Assuming that the energy of interaction is higher for the first step (i.e., K_1) and decreases thereafter, a modified form for PFSA was proposed by Choi and Datta[199,200,253]

$$\lambda^{\text{B}}(a_w) = \frac{K_1 a_w}{1 - a_w}\left[\frac{1 - (\nu + 1)a_w + (\nu)a_w^{\nu+1}}{1 - (K_1 - 1)a_w - K_1(\nu)a_w^{\nu+1}}\right], \quad (a_w = \text{RH}/100) \tag{18}$$

Thus, the sorption (or solubility) of a water molecule (or any specie) can also be related to its enthalpy of hydration, ΔH_s, through $S \propto S_0 \exp(\Delta Hs/RT)$, which has been investigated in a number of studies.[206,212,214,215,328] Enthalpy of sorption, ΔH_s, during vapor-uptake reduces at lower humidities, for $0 < \lambda < 7$, indicating exothermic reaction with the strongest enthalpy change occurring for the first 1 to 2 water molecules, reflecting the highly hydrophilic nature of PFSAs.[213,328−330] Thus, hydration enthalpy is also dependent on the cation, which is the most negative for H^+ and Li^+ form PFSAs, and increases for larger cations, resulting in lower swelling (see section 7.3).[328−330] These models have been shown to be applicable for analyzing the water-uptake of PFSAs exchanged with other cations, the interaction (energy) of which could be related to the change in swelling.[210,211]

For the free-water part of the uptake isotherm ($\lambda > 6$), a commonly used approach is based on Flory−Huggins theory, which is traditionally used to study the thermodynamics of mixing and swelling of gels[331]

$$\ln a_p = \ln(1 - \phi_p) + \left(1 - \frac{\bar{V}_w}{\bar{V}_p}\right)\phi_p + \chi\phi_p^2 \tag{19}$$

where the entropy of mixing is combined with the enthalpy interactions through the Flory−Huggins interaction parameter, χ, which is related to the solubility of the polymer, δ_p, and the water, δ_w, as

$$\chi = \frac{\bar{V}_w}{RT}(\delta_w^2 - \delta_p^2) \tag{20}$$

Thus, as the solubility of the water approaches that of the polymer, χ decreases, meaning that enthalpic interactions opposing mixing become weaker and swelling is more favorable (see section 2.6.4). Equation 12 can be rearranged in terms of driving or opposing mixing

$$\underbrace{\ln \underbrace{a_w}_{\mathrm{RH}/100} - \ln(1-\phi_p) - \left(1 - \frac{1}{\bar{V}_p/\bar{V}_w}\right)\phi_p}_{\text{drives mixing}} = \underbrace{\chi(\phi_p, T)\phi_p^2 + \left(\frac{\bar{V}_w}{\mathrm{RT}}\right)P_s(\phi_p, T)}_{\text{opposes mixing}} \tag{21}$$

Here the assumption is also made that both the interaction parameter and swelling pressure change with temperature and swelling (ϕ_p). Hence, the tendency of water nanodomains to swell due to favorable water/ionic-group interactions, represented by the chemical energy of solvation and hydration (left-side of eq 21), is opposed by the deformed hydrophobic backbone that acts against swelling (i.e., mechanical energy, right-side of eq 21). Thus, it is a common practice to interpret swelling equilibrium as a balance between the entropic forces driving the swelling and the exergonic effects including the mechanical deformation of the matrix, which acts as a resistance by generating a swelling pressure (see Table 3, Figure 7).

FH models can successfully predict the swelling of cross-linked gels in the absence of electrostatic interactions that are amply present in PFSA ionomers. Thus, FH theory could be applicable, at best, to the swelling of membrane with free water, and a complete model must account for the nature of water, i.e., whether it is free or bound, as they are governed by different physicochemical process. For this reason, the volume fraction of polymer for FH expression is usually modified to include the bound water that are strongly attached to the polymer's ionic moieties[241,253,332]

$$\phi_p = (\bar{V}_p + \lambda^B\bar{V}_w)/(\bar{V}_p + \lambda\bar{V}_w) \tag{22}$$

Unequivocally, as the water activity increases, the contribution from Langmuir adsorption to the sorption isotherm decreases in favor of the clustering of free water (Figure 7).[82,199,206,247] In a similar fashion, one can calculate the fraction of hydrophilic ionic water domains as $\phi_{hf} = \phi_{SO_3} + \phi_w = \phi_p\phi_{SO_3}^{dry} + \phi_w$, where the volume fraction of SO_3^- groups in the dry polymer is roughly equal to $\phi_{SO_3}^{dry} = \bar{V}_{SO_3}/\bar{V}_p$ and $\bar{V}_{SO_3}$ can be taken to be 40.94 cm^3/mol.[33]

2.6.2. Swelling Pressure.

The swelling pressure in eqs 12 and 13 is directly related to the elastic modulus of the polymer matrix acting against the swelling (Figure 7). The concept of deforming the polymer backbone with the swelling of water nanodomains has been discussed both from modeling and structural characterization perspectives.[146,194−198,201,202,206,332] Thus, it is unequivocal that swelling-pressure formulations involve the modulus of the polymer, but the deformation of the matrix is rather difficult to calculate. The simplest approach has been correlating deformation to macroscopic volume change (fraction), even though it is questionable if matrix deformation at the nanoscale can be represented by a macroscopic term,[196,206,253] given that the nanoscopic swelling of water domains is different than the membrane's macroscopic swelling, i.e., nonaffine swelling, as discussed in section 3.2. Inspired by this difference, swelling pressure formulations based on microscopic[202,203] and nanoscopic[82,204] swelling have been proposed. In both models, the swelling pressure calculated for the nonaffine swelling case was higher than that for the affine swelling one. Even though swelling pressure formulations exist in classical theories, they yield a finite pressure at zero swelling, as discussed by Freger,[202] who developed an alternative expression based on the nonaffine swelling of phase-separated PFSA network, which relates the swelling pressure to shear modulus, G, of dry polymer network

$$P_s(\phi_p) = \frac{2}{3}G(\phi_p^{1/3} - \phi_p^{7/3}) \tag{23}$$

Kusoglu et al.[82,204] proposed a different swelling-pressure expression based on the deformation of the hydrophobic backbone (of modulus E_b) being compressed between growing water domains (of diameter, d, and spacing, d_w) with hydration, i.e., $P_s \propto E_b \times (d_w - d)$ (Figure 7):

$$P_s(T, \phi_w) = E_b(T) \times \left(\frac{b}{b_{dry}} - 1\right) \text{ and } \frac{b(\phi_w)}{b_{dry}} = \frac{d_w(\phi_w) - 2r_w(\phi_w)}{(d_{dry} - 2r_{dry})} = \frac{d_w(\phi_w)}{d_{dry}}\left(\frac{1 - \phi_w^{1/n} - 1}{1 - \phi_{dry}^{1/n}}\right) \tag{24}$$

where b and b_{dry} are the swollen and dry thickness of the backbone ("wall") between the water domains, respectively, which can be related to the spacing, d_w, and radius, r_w, of the hydrophilic domain, both of which increase with hydration (ϕ_w). This concept is in agreement with the backbone wall thickness inferred from the morphological studies.[33,333] The advantage of this approach is it incorporates the domain spacing as the deformation parameter, which can be measured from SAXS, and therefore provides a flexible model that predicts the decrease in water uptake due to annealing, compression, and higher EW, all of which increase the swelling pressure either by inducing higher matrix modulus (EW and annealing), and/or additional deformation in the matrix (compression), as confirmed by SAXS studies.[82,194,204,257] We note that both expressions above yield comparable trends, although derived through different approaches. Hence, despite idealizations of the disordered morphology of the PFSA and simplification of its complex multiscale swelling process, structure-based models for thermodynamic equilibrium can help analyze and elucidate the measured uptake data. However, the true nature of water inside the ionomer is still not understood completely due to complex interactions with the spatially distributed ions, confinement effects and the role of the penetrant pendant side-chains.

2.6.3. Effect of Constraints and Compression.

Ionomer membranes in most applications are constrained and/or under compression due to the nature of the multicomponent system design and geometry (e.g., clamping of the membrane electrode assembly for gasketing purposes and to ensure minimal contact resistance). In addition, there could be other internal constraints developed in the membrane during the manufacturing process (e.g., extruded or stretched membranes exhibit structural anisotropy due to the preferential orientation during processing).[123,334,335] Moreover, membranes that are macroscopically reinforced with ePTFE have almost negligible swelling in the plane (reinforcement) direction and much higher mechanical properties.[286,287] These internal constraints result in effects that are inherent properties of the membrane. For example, reinforcing the membrane with a stiffer material would generate additional internal resistance to the swelling in the direction of the reinforcement. This effect is similar to, at least theoretically, externally constraining an unreinforced membrane in one direction and letting it hydrate; it will swell less in the constrained direction compared to the unconstrained direction.

The change in water content of Nafion with compression has been observed using in situ neutron imaging of an operating PEFC[336,337] and ex situ compression tests.[194,214,338] These tests showed that the change in water content was negligible upon compression unless the membrane was in liquid water and compressed by more than 4 MPa, at which point more than 10% reduction in λ was reported.[194,214,338] Also, the internal pressure in the hydrated ionomer membrane measured using compression fixtures is 30 to 100 MPa.[185,214,338] Such high values have been attributed to the swelling pressure within the swollen domains of the membrane at the nanometer length scale.[196,202,204] Unlike hydrogels, ionomer membranes require high pressures to lose their (free) water (25 MPa required for 50% reduction in λ) due to their intrinsic semicrystalline morphology, highly concentrated ionic domains and strong electrostatic interactions. The effect of compression has been studied using macrohomogeneous models.[194,254,257,339] The model by Kusoglu et al.[194] accounted for the nanodomian deformation under compression from SAXS, and used it to determine the change in swelling pressure, chemical-potential equilibrium, and water content.[194] Conceptually, the compression effect can be implemented into the swelling equilibrium by extending eq 5[194,254]

$$\begin{aligned}\Delta\mu_{\mathrm{w}}^{\mathrm{e}} = \Delta\mu_{\mathrm{w}}^{\mathrm{p}} = \Delta\mu_{\mathrm{w}}^{\mathrm{p,c}} \Rightarrow RT\Delta\ln a_{\mathrm{w}} = RT\Delta\ln a_{\mathrm{p}} + \bar{V}_{\mathrm{w}}\Delta P_{\mathrm{s}} \\ = RT\Delta\ln a_{\mathrm{p}} + \bar{V}_{\mathrm{w}}\Delta P_{\mathrm{s}}^{\mathrm{c}}\end{aligned} \tag{25}$$

where $\Delta\mu_{\mathrm{w}}^{\mathrm{p,c}}$ and P_s^{c} are the chemical potential and swelling pressure of the compressed/constrained membrane, respectively. It is of note that if a hydrated membrane is subjected to hydrostatic pressure, p, its volume also decreases by $dV = p/K_{\mathrm{b}}(\lambda)$, affecting the molar volume of the membrane (K_{b} is the λ-dependent bulk modulus).

2.6.4. Interaction Parameter and Solubility. A key parameter characterizing the interactions in FH model (see eq 26) is χ, which has significance beyond being a model parameter due its relation with solubility. As the interaction parameter of a solvent/polymer network decreases, solvent uptake becomes more favorable. χ can be determined either from measured solubility,[188,189,340] or by fitting a sorption isotherm using an FH expression,[82,199,204,240,340] or predicted from ab initio computations.[63,66,67] Interaction parameter, χ, computed from MD simulations, and determined from uptake data are summarized in Table 5 and Figure 15, respectively. Most of these studies agree on a hydration-dependent interaction parameter (which is composed of the various independent individual interactions) as plotted in giving a range from 0.9 and 2.5.[189,240,332] The interaction parameter has been shown to decrease (favor swelling) with hydration, with expressions $\chi \approx {\varphi_{\mathrm{p}}}^{1.5}$ or φ_{p},[82,240] and $\exp(-\varphi_{\mathrm{w}})$.[199] The data collected from the literature, when plotted as a function of solvent (and water) fraction, fall between two trends with ${\varphi_{\mathrm{p}}}^{1.5}$ and ${\varphi_{\mathrm{p}}}^{2}$ dependence, although the exponential form could capture the swelling in water-vapor regime fairly well, as discussed in Kusoglu et al.[82,194]

Table 5. Computed Interaction Parameters for Nafion, 3M, and SSC PFSA Ionomers from DPD[a]

	interaction parameter, χ		
pair	3M[67]	SSC[66]	Nafion[63]
backbone–side-chain	−0.03	0.15	1.23
backbone–$CF_2SO_3H{\cdot}3H_2O$	7.07	6.86	7.44
backbone–$6H_2O$	3.30	3.28	3.36
side-chain–$CF_2SO_3H{\cdot}3H_2O$	7.04	6.24	2.70
side-chain–$6H_2O$	3.47	3.15	1.53
$CF_2SO_3H{\cdot}3H_2O$–$6H_2O$	1.53	1.24	1.48

[a] Data taken from Wu, Paddison, and co-workers.[63,66,67] DPD beads for the backbone is $6(CF_2)$ units for all cases and the side-chains are –$CF_2CF(OCF_2CF_2CF_2)$– for 3M; – $CF_2CF_2CF_2CF(OCF_3)$– for SSC; and $OCF_2C(CF_3)FOCF_2$– for Nafion (also section 3.3 for details on simulations).

In addition, by definition, χ is expected to decrease with increasing temperature,[331] thereby favoring thermodynamics of mixing (swelling), which has been observed in other polymers.[243,341] However, in water vapor, increasing temperature could reduce λ at very high RHs (as discussed in section 2.1, Figure 8), which, within the context of this discussion, implies a χ that increases with temperature, as also suggested in other studies.[83,240] The resultant expression for the interaction parameter can be written as[82,194]

$$\chi(\phi_{\mathrm{p}}, T) = \chi_{\mathrm{S}}{\phi_{\mathrm{p}}}^{1.5} + \chi_{\mathrm{T}}\left(1 - \frac{T_{\mathrm{ref}}}{T}\right) \tag{26}$$

where the parameter χ_{T} (and its sign) can be attributed to the polymer–solvent interactions arising from the change in the phase of water and membrane morphology due to thermal history;[85,94,95,114,258] the expression above at 25 °C is plotted in Figure 15, and its prediction of water uptake is shown in Figure 8b (cases b and c, for negative and positive χ_{T}, respectively). The fact that the opposite trend is observed in liquid water, i.e., higher λ and lower χ with increasing temperature, suggests either an interaction parameter cannot be extracted from classical FH theory for vapor-equilibrated PFSAs at higher temperatures (e.g., due to very small free water), or its behavior is controlled by the increasing morphological differences between vapor and liquid-equilibrium with temperature. In the latter case, the interaction parameter could provide an intriguing link between $\Delta\lambda_{\text{liq-vap}}$ and pairwise interactions among water and PFSA moieties, including surface interactions, which could be used to elucidate Schröder's paradox. Another interesting interplay is observed for the temperature-dependent water uptake: While temperature reduces the modulus of the polymer backbone, and therefore its resistance to swelling giving rise to a higher λ, a positive dependence of χ on temperature tends to reduce λ. Thus, once again, the equilibrium uptake is governed by the mechanical-chemical energies, with an intriguing effect of temperature on interactions. However, it is still unclear as to how the interaction parameter varies with certain thermodynamic variables such as pressure; this is an active area of research.

In liquid solvents, however, uptake values change significantly depending on the solvent (polarity and dielectric constant),[188,189,282] which was summarized in Figure 15. Overall, solvent-uptake capacity of PFSA appears to be correlated with the solvent's dielectric constant or solubility parameter, although a universal trends exists in that higher solvent uptake usually leads to higher conductivity.[188,343,344]

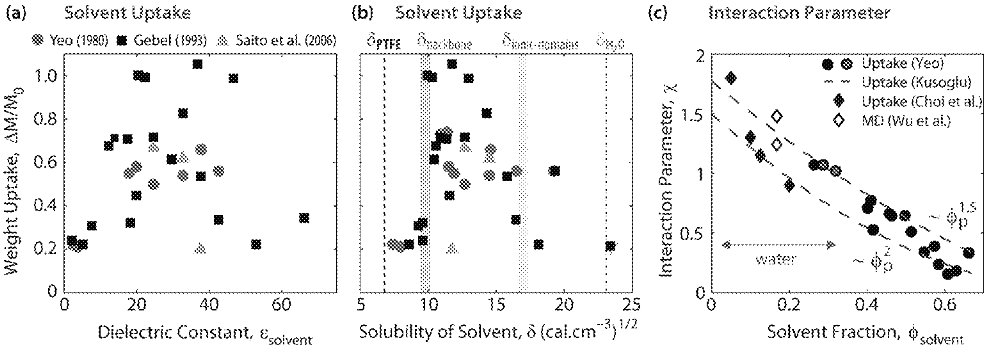

Figure 15. Weight change of PFSA equilibrated in various solvents plotted as a function of (a) dielectric constant and (b) solubility parameter of the solvent based on data from refs 186, 188, and 342. (c) Interaction parameter plotted as a function of fraction of water[82,194,199,342] and other solvents (from Yeo et al.[342]) Calculated values for water from MD simulations are included for comparison.[63]

The solvent uptake vs solubility data create a "swelling envelope" controlled by the two solubility values of PFSA; one for its hydrophobic backbone, $\delta \approx 10$ (cal cm^{-3})$^{1/2}$ and another one associated with the hydrophilic ionic groups, $\delta \approx 17$ (cal cm^3)$^{1/2}$, as discussed by Yeo.[342] As seen from the figure, all the data are bounded between the solubility of PTFE and pure water, elucidating the origin of two distinct solubility values for PFSAs. Gebel and co-workers[188] published an in-depth investigation on the swelling of Nafion 117 membranes in various solvents and reported that it correlates best with the donor number of the solvent, compared with dielectric constant and solubility. Doyle et al. later presented a similar correlation,[343] and PFSAs swell more in polar solvents,[188,343,345] which was supported by the applicability of the group contribution theory.[345] It has been reported that the solvent influences PFSA's uptake,[188−190,245,282,345] conductivity,[190,282,344] and domain spacing.[141,142,346] Studies on vapor uptake in other solvents are rather limited.[190,245] A recent study by Zhao et al. reported that Nafion's swelling strain is higher in ethanol and methanol compared to that in water, despite the fact that number of solute molecules in water is higher compared to the alcohols.[190]

2.6.5. Morphology and Variations.

Even though a strong link exists at a fundamental level between sorption and transport, they tend to be modeled exclusive of each other, and in seemingly disparate fields, with only a few efforts trying to bridge them.[201,206,208,347−349] While the sorption models (for water uptake) are interpreted as "equilibrium" models, the transport models involve the uptake and mobility of water and other species (e.g., conductivity), sometimes also with time dependence (e.g., diffusivity). An effective approach to bridge the water-uptake and transport phenomena is through the phase-separated morphology (discussed in section 3), by using the size, shape, and connectivity of the hydrophilic domains. In such models, a membrane nanostructure is usually assumed (usually spherical or cylindrical "pore", representing the hydrophilic domain) and dependent properties are predicted. Such geometric idealization of water domains is commonly used for the interpretation of the broad-peaked SAXS data and measured domain spacing, from which one can estimate parameters such as the domain diameter, domain size and number of ionic sites per domain as a function of water content (see section 3.1.1). Although useful for interpretation of the morphology for modeling purposes, such approaches lack the nuances of the real structure and its responsiveness, because in reality, phase-separated nanodomains and their geometrical features result from hydration. It must be noted that various morphological descriptions have been adopted in the literature, from spherical clusters to locally flat morphologies, as discussed in section 3.1, nevertheless, a domain can still be defined as essentially the smallest observable repeated structural unit at the nanoscale. [Historically, a domain has been frequently associated with a (spherical) cluster, due to the cluster-network geometry that was adopted in early studies; however, the current state of understanding of PFSA morphology necessitates a more general description without a prescribed geometric shape.]

Moreover, due to the evolution of the phase separation during sorption, it is not possible to preset a certain morphology and geometry for PFSA ionomers. In fact, these morphological changes have been discussed and used in modeling studies to explain the unique sorption properties of PFSA ionomers. Inspired from idealized two-phase morphologies, such as the cluster-network model, similar geometric descriptions have been adopted to explain or model the nanostructure based on available SAXS data,[82,204,223,226,305] swelling pressure and sorption,[82,196,204] sorption and transport,[199,201,350] or pore-network ensemble.[208,347,350] Pore-network models either construct idealized rigid pores[208,347] or use a pore-size distribution.[351,352] One shortcoming of idealizing the water domains as rigid voids and pore-wetting phenomena is the lack of nanoswelling and backbone deformation, which do not necessarily reflect the true nature of PFSA, which has hydrophilic domains growing and perhaps coalescing with water uptake, and deforming the hydrophobic domains.

Moreover, the shape and connectivity of the domains, whether they are spherical or cylindrical, have been discussed in conjunction with these models: Weber and Newman proposed that the connection between the spherical domains become cylinders in liquid water which explains the vapor-to-liquid transition.[201] In a similar fashion, but using a different approach, Kusoglu et al. showed that measured hydration-dependence of both water uptake and mechanical properties can be reproduced better, especially at higher humidities, with random cylinder-like domains in the nanostructure.[82,194] In fact, it was shown using such idealized domains that the membrane's actual water uptake is bounded between the uptake of a hypothetical membrane of fully spherical and cylindrical domains.[82,194,204,226] Recently, Kreuer[333] discussed possible morphologies for the water domains and concluded that only locally flat regions agree with multiple sources of experimental data, a description that agrees with recent cryo-TEM tomographs of hydrated Nafion;[353] ionomer morphology is addressed in more detail in section 3.

Distinct from the aforementioned models, the models of Freger and co-workers[202,203] and Promislow and co-workers,[64,65] both use an expression for the free energy of the system and minimize it among possible geometries to derive a description of the hydrophilic domain nanostructure. In this fashion, they predict the impact of environment on water uptake and provide a domain distribution that can be used to run transport simulations. The vapor–liquid transition was also explained with this type of model but using the (change) in surface energies.[203] Thus, in all of the models, the key is that the thermodynamic equilibrium is governed by a mechanical/chemical energy balance where the sulfonic acid moieties would like to dissolve but this is hindered by the backbone, hydrophobic moieties that generate a swelling pressure.[202,204]

As noted, most models attempt to explain Schröder's paradox by asserting that the membrane undergoes a morphological change from vapor- to liquid-equilibrium, especially starting with its surface or specific surface phenomena.[208,253,263,359] Such a treatment eliminates the "paradox" by virtue of adopting distinct structures even when the water activity is $a_w = 1$ (similar to liquid and vapor phase transitions). The early models were based on the assertion that a PFSA membrane has a hydrophobic surface in vapor-saturation but becomes hydrophilic when in contact with liquid water, an observation that is now accepted based on experimental evidence from contact-angle,[112,266,270] and mass-transport[280] measurements and more recently supported by water-sorption,[206,258,267] conductive AFM,[274,275] SAXS,[115,266] and GISAXS[266,360] experiments (see section 3.4). Similarly, in vapor, PFSA's the hydrophobicity of the surface reduces with increasing RH,[221,271,276,361−363] accompanied by higher ionic activity.[271−274,279]

Inspired by these observations, researchers proposed to represent the swelling pressure in thermodynamic models with another term that is present in vapor phase due to the "hydrophobic skin" at the membrane surface but absent in liquid water thereby lowering the counter pressure.[206,208,274,275] As a result of reduced swelling pressure at the surface, the membrane's water-uptake capacity increases at the same water activity. In one approach, the additional term was proposed to be arising from the capillary effect in vapor, which is quantified by adding a capillary pressure term to a pore representing the water domains, which is positive due to the hydrophobic surface, to the regular pressure term in the polymer matrix.[199,208,253] Eikerling and Berg[208] used a pore-ensemble model involving capillary, osmotic, and elastic pressure effects that can account for the surface charge density reorganization and relate the pore swelling to macroscopic uptake through pore-filling. Their model also resolved Schröder's paradox using capillary arguments which change the pressure equilibrium within the pores. However, using capillary pressure and pore-wetting mechanisms for the water nanodomains that are open to the surface is debatable, and has been proposed to be energetically unstable.[262] In the other approach,[255,359] a modified Laplace pressure is added in terms of a surface energy term which exists for vapor equilibrium but vanishes for liquid equilibrium. While the former approach associates the capillary pressure term with internal matrix/external medium interface, the latter energy approach does so with the interface between the internal liquid and polymer matrix. Although mathematically different, both approaches are conceptually similar, and use a thermodynamic force in swelling equilibrium that changes with the phase of the external water, thereby resolving the paradox. Freger[203] proposed another term, G_L, to be added to the free energy, $\Delta G' = \Delta G + \Delta G_L$, to account for the interfacial energy at the ionic-aggregate/matrix interface, and defined the chemical potential by minimizing the total energy per ionic group, g, with respect to λ

$$g = g_s + g_e + \gamma\sigma \rightarrow \mu_w(\lambda) = \left(\frac{\partial}{\partial\lambda}g\right)_\sigma = \mu_s(\lambda) + \upsilon p_e(\lambda) + \upsilon p_L(\lambda, \sigma) \quad (I)$$

where an additional term comes from the surface tension, γ, and σ and υ are the surface area and polymer volume per ionic group, respectively. The chemical potential of water has then a swelling term and two osmotic terms opposing the swelling, the usual swelling pressure, p_e, arising from elastic deformation of the matrix, and a new Laplace pressure, p_L, involving both interfacial and elastic contributions. In vapor equilibrium, the membrane surface would be covered by a matrix-vapor interface with a nonzero Laplace pressure. However, in liquid water, this interfacial pressure term vanishes, thereby releasing the pressure by the amount of excess pressure, p_L, which drives more swelling. This phenomenon has been suggested to explain Schröder's paradox. According to this approach, a higher pressure develops around the domains of the membrane equilibrated in vapor phase, hence limiting the water uptake therein.

3. MORPHOLOGICAL FEATURES

A hydrated PFSA phase separates at nanoscales with various disordered complex morphologies having mesoscale connectivity to form a hydrophilic ion-conducting phase and a hydrophobic, nonconductive phase controlling the mechanical integrity. [As per convention: hydrophilic domains are used to describe the regions with solvent and cations, although in some studies they are described as clusters or aggregates, and pores in molecular models.] Morphological features of sulfonated polymers have been studied extensively over the past few decades using small- and wide-angle scattering with X-rays and neutrons (i.e., SAXS, WAXS, and SANS; see refs 33, 35, 36, 84, 108, 110, 117, 130, 141, 144, 146, 157, 217−220, 224, 225, 334, 335, and 364−371) as discussed in section 3.1.1.

X-ray scattering has historically been a useful tool to study the morphology of dry and hydrated PFSA and similar random copolymers (Figure 16).The most commonly used information from the scattering is the single, broad, so-called, ionomer peak corresponding to a structural correlation length for hydrophilic domains, and interpreted as the spacing between water domains on the order of nanometers. This is followed by additional information that can be extracted from the whole q-range, including the matrix knee (intercrystalline domain spacing) at lower-q (larger scales), the Porod-regime at higher q (lower scales), which is related to internal interface (surface to volume ratio, S/V), and crystallinity at the highest q (diffraction regime) referring to atomic distances. Overall, due to the relative random phase separation, peaks are often broad without reflections and therefore the interpretation of the data (e.g., peak behavior during humidification) has been a challenging task attacked by researchers over the past decades stating that findings are over interpreted and not definitive. The analysis is also burdened by the fact that scattering techniques provide data in Fourier space, the conversion of which to real-space for a 3D morphology is ambiguous, and open to interpretation, especially for a disordered polymer such as a

DOI: 10.1021/acs.chemrev.6b00159
Chem. Rev. 2017, 117, 987−1104

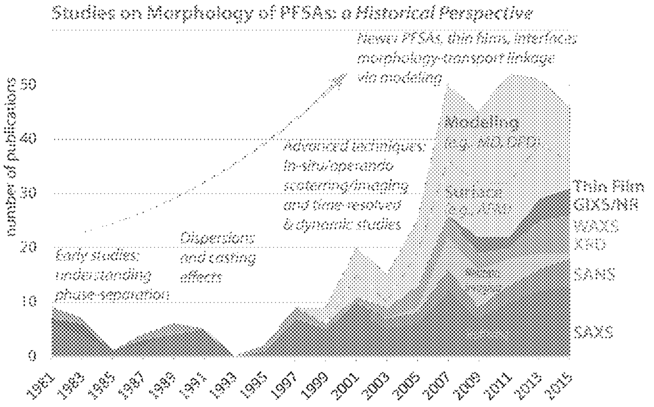

Figure 16. Historical perspective on morphological studies on PFSA (membranes, dispersion, and thin films) from scattering and imaging techniques with X-rays and neutrons. Computational simulations of morphology are also included. Only publications with strong focus on PFSAs are included.

PFSA. This criticism is somewhat overcome thanks to the vast amount of structural data obtained through SAXS/WAXS, and more recently by SANS, QENS, of these ionomers, investigating the effect of time, humidity, temperature, crystallinity, mechanical loads, and to a certain extent thickness and ion-exchange capacity, on ionomer-peak behavior and associated macroscopic water uptake and conductivity. Furthermore, these techniques remain robust and powerful tools to elucidate and compare the structural features of PFSAs, especially with advances in in situ and operando diagnostics. Nevertheless, the debate over the exact nanostructure and connectivity of these domains, and their interactive role in species transport still continues, in part driven by the desire to improve and optimize material functionalities (e.g., conductivity vs stability) through understanding the interrelation between transport mechanisms and morphological behavior.

Key to that understanding as well is the local environment, which has been probed by various spectroscopic techniques.[1,18] Such spectroscopic techniques have been employed to study

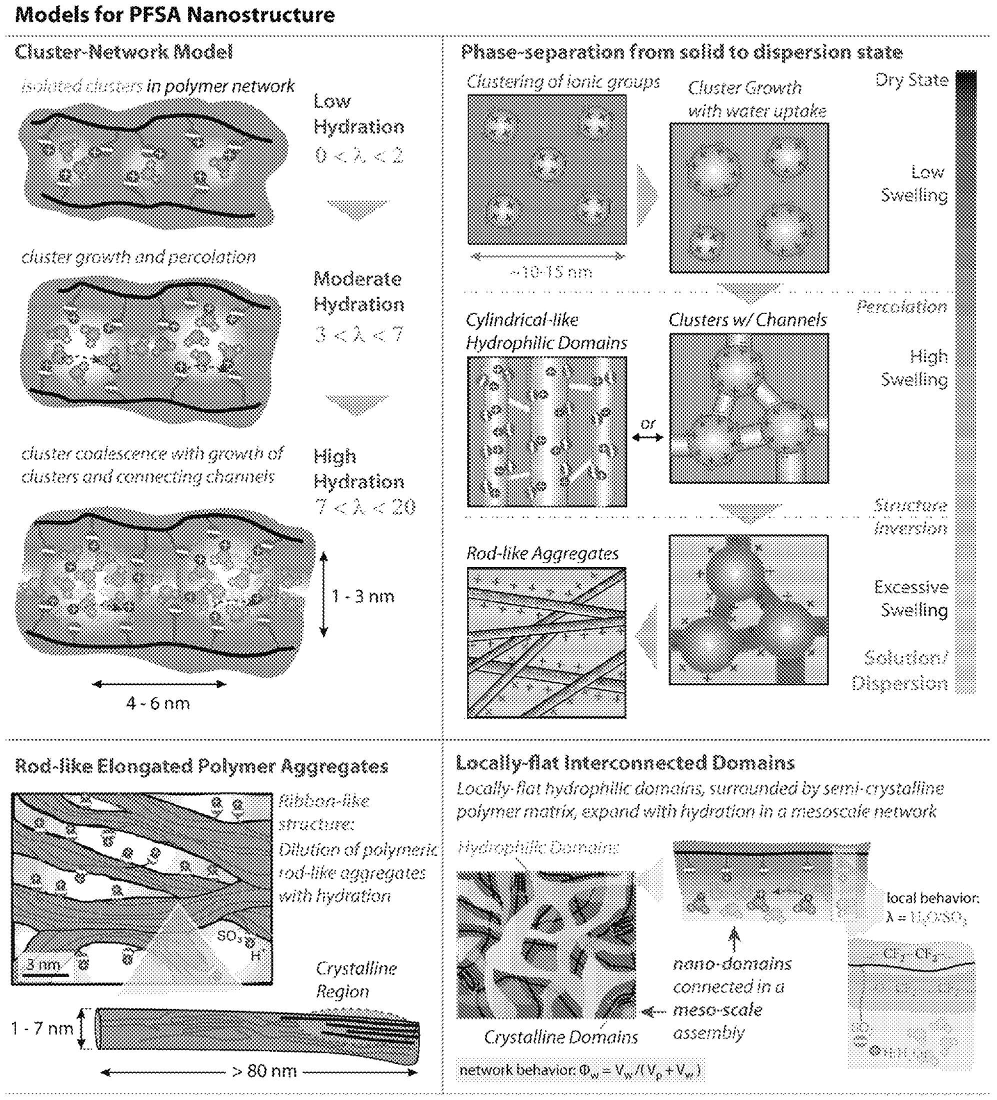
Models for PFSA Nanostructure
Cluster-Network Model
isolated clusters in polymer network
Low Hydration
0 < λ < 2
cluster growth and percolation
Moderate Hydration
3 < λ < 7
cluster coalescence with growth of clusters and connecting channels
High Hydration
7 < λ < 20
1 - 3 nm
4 - 6 nm
Phase-separation from solid to dispersion state
Clustering of ionic groups
Cluster Growth with water uptake
Dry State
Low Swelling
~10-15 nm
Percolation
Cylindrical-like Hydrophilic Domains
Clusters w/ Channels
or
High Swelling
Structure Inversion
Rod-like Aggregates
Excessive Swelling
Solution/ Dispersion
Rod-like Elongated Polymer Aggregates
Ribbon-like structure: Dilution of polymeric rod-like aggregates with hydration
SO_3^-
H^+
3 nm
Crystalline Region
1 - 7 nm
> 80 nm
Locally-flat Interconnected Domains
Locally-flat hydrophilic domains, surrounded by semi-crystalline polymer matrix, expand with hydration in a mesoscale network
Hydrophilic Domains
local behavior: $\lambda = H_2O/SO_3$
CF_2-CF_2
nano-domains connected in a meso-scale assembly
Crystalline Domains
network behavior: $\Phi_w = V_w/(V_p + V_w)$

Figure 17. Proposed morphological descriptions for Nafion (or PFSA): Cluster-network model (by Gierke, Hsu, and co-workers[33,35]), evolution of morphology from spherical domains to rod-like aggregates in dispersion (by Gebel[146]), as well as cylindrical or layered model,[217,225,411,420] rod-like elongated polymeric aggregate model,[144,146,364,366] and the locally flat ribbon-like model, discussed by Kreuer,[333] as well as Gebel and co-workers (CEA group)[364,409,429] and later by Kusoglu et al.,[48] which is also in agreement with the direct imaging from cryo-TEM (Figure 21).

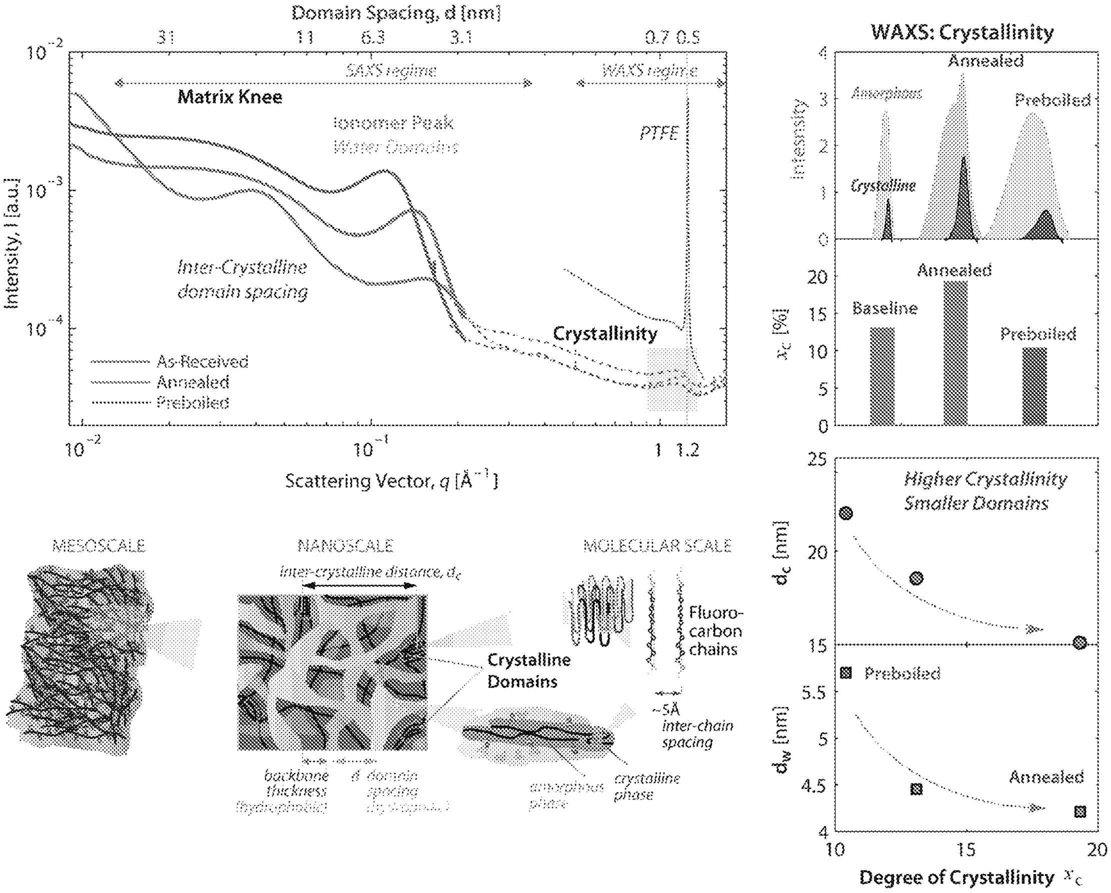

Figure 18. Scattering of Nafion: Typical SAXS/WAXS profiles for Nafion membrane in liquid water at room temperature in AsR (baseline), preboiled, and annealed forms. Characteristic peaks and their values are shown in the plot along with the WAXS peaks for amorphous and crystalline phases. The schematic below is added only to illustrate the length scales, not the exact morphology. (Data taken from Kusoglu et al.[82])

PFSAs since the 1980s, starting with FTIR by Falk et al.[372,373] and Mauritz, Moore and co-workers,[41,374] and followed by various techniques including Raman,[133,222,375,376] FTIR/ATR[3,41,85,128,193,226,372,374,377−383] and solid-state NMR.[3,193,384−387] The assignment of IR spectra bands to specific molecular interactions is key to their analysis.[133,222,226,319,373,377,382] In these studies, the characteristic IR fingerprints of PFSA are associated with the polymer chains (stretching bands for C−O−C and CF_2 between 950 to 1425 cm^{-1}), ionic groups ($-SO_3^-$ exhibiting symmetric $\nu_s(SO_3^-) \sim$ 1060 cm^{-1} and antisymmetric $\nu_{as}(SO_3^-) \sim 1130$ cm^{-1} S−O stretching modes as well as $\nu(SO_3H)$ at 2200−2720 cm^{-1}),[41,222,226,372,374,388] and interacting and free water (H−O−H bending at 1620−1740 cm^{-1}, ν(O−H) stretching at 3000−3450 cm^{-1}).[41,222,226,372−374,382,383,388−392] The shifts in the latter bands, ascribed to changes in local water environment, are used to analyze water-uptake behavior.[45,222,226,373,378,393,394] Thus, spectroscopic analysis of PFSAs provides information related to proton dissociation from SO_3^- groups and hydration-induced changes in sulfonate-water local environment, with implications on conductivity,[2,133,319,378] diffusion[128,379,380,395] sorption,[226,228] cation/sulfonate-group interactions,[75,373,385,392,394,396,397] annealing,[81,96,107,398,399] and conformational changes in the main-chain within the context of the semicrystalline PTFE backbone.[2,226,384,387] For example, the SO_3^- vibrational mode is influenced by its local chemical environment, where strong cationic interactions polarize the S−O dipole, from which interaction energies can be determined.[394] For this reason, spectroscopy is commonly employed to elucidate the substructures of water in response to many phenomena (see section 4.4), from aging and cation-contamination[170,183,192,193,392,397,400] to interactions of inorganic fillers with the host ionomer matrix.[382,401,402] (see section 7).

3.1. Nanomorphology

Since the early SAXS works by Roche et al.,[110,224] Gierke and co-workers,[33,35] and Fujimura et al.[36,218] reported a humidity-dependent ionomer peak associated with a phase-separated nanostructure, a large number of studies have employed SAXS/SANS to delineate PFSA morphological features. Such investigations include the effect of hydration,[8,17,19,33,35,36,48,82,98,117,146,193,217,219−221,223,225,257,333,364] temperature and thermal history,[82,84,87,90,91,108,109,117,131,147,333] freeze,[317,320] aging,[90,193,400] mechanical loads, stretching and orientation,[33,36,84,295,296,334,335,365,367,370,403,404] time,[115−117,217,405] cations,[33,109,131,211,346] solvents,[142,346,406,407] and PFSAs in dispersion state.[1,141−147] Early studies employed thermodynamics-based models to predict the hydrophilic domain formation in the hydrophobic matrix based on an energy balance between the electrostatic interactions and deformation of the surrounding matrix as mentioned in section 2.6.[35,197,198,408] While the energy of dipole interactions favor aggregation of hydrophilic ionic sites, the polymer backbone opposes it. Other works include interpretation based on scattering theory,[37,146,217,219,221,225,333,364,366,409] simulation studies to reproduce experimental observa-

DOI: 10.1021/acs.chemrev.6b00159
Chem. Rev. 2017, 117, 987−1104

tions,[66,67,355,368,410−412] direct imaging via TEM,[358] and macroscopic models based on nanostructure to determine sorption,[82,201,204,413] transport,[201,257,350,413] and mechanical[414] properties. Even though determining the spacing of domains (their correlation length) from SAXS peak is straightforward, the same is not true for their shape, structure, or connectivity.

Based on structural idealizations (see Figures 17 and 18), a hydrophobic "wall" of 2 to 3 nm separating 2 to 4 nm hydrophilic primary domains that are interconnected by secondary domains (0.5 to 1 nm) have been estimated,[33,35,65,146,204,219,221,223,333,334,415,416] although these values depend on the shape of the domains (either spherical or cylindrical) prescribed in the calculations, and become ambiguous when quantifying secondary interconnections and for other morphological representations (such as locally flat domains; see section 3.1.2 for further discussion). Nevertheless, they are in reasonable agreement with similar analysis from porosimetry[417−419] and cryoporometry,[111] which suggest that majority of water in hydrated Nafion are within domains of 1 to 3 nm, with larger (>5 nm) domains in the size distribution were also reported.[417−419] As noted, one typically assumes a domain shape to do the analysis, and commonly used geometries (i.e., spherical, cylindrical, and lamellar) and their possible connectivity were evaluated or discussed in studies by Gebel and co-workers,[19,146,364,409] Litt,[420] Rollet,[409] Weber and Newman,[413] Schmidt-Rohr and co-workers,[411,421] Kusoglu et al.,[194,204] Feng, Savage and Voth,[355,356] and recently by Kreuer et al.[333] (see Figure 17). While assuming structures can provide some insight, direct imaging is required due to the ambiguous data issues discussed above. Such imaging demonstrates a locally flat, highly branched structure at full hydration as described in section 3.1.2. Even so, quantification of morphology with an accurate geometric representation of domains, their shape, distribution, and connectivity, especially across water contents, is a remaining challenge.

An integral component of morphological investigations is the structure of PFSAs in the dispersion state (as mentioned in section 1.1.5), with studies dating back to late 80s.[1,141−145,147] The topic has drawn more attention in recent years, in part driven by the use of dispersion-cast PFSAs in electrochemical applications. It has been well accepted that in a dispersion, a PFSA is not a true solution (although the term is still used) but rather a colloidal suspension due to the strong role of polymer/solvent interactions.[141] In a series of SAXS/SANS studies of PFSA in various solvents and cations, Gebel, Loppinet and coworkers[141−144] developed a morphological picture of aggregated PFSA colloids in polar solvents (see Figure 17). The size of the aggregates is determined by the elastic energy required to form the rod-like structure, and the interfacial energy associated with the polymer−solvent interactions that tends to decrease by minimizing the surface area.[142−144,146] SANS data of solutions was used to extract (i) Bragg spacing of aggregates via ionomer peak, (ii) radii of the scattering particles via Guinier analysis, or (iii) information about the particle interface the study of the asymptotic behavior (large-q at Porod's limit).[371] In the low-q regime, intensity (I) scales with q^{-1} indicating elongated objects,[19,364,366,367,422] whereas in the asymptotic regime, I scales as q^{-4}, which indicates that the aggregates present a well-defined interface with the solvent.[142−144,146,364,366] Thus, in dilute solutions of polar solvents, the SANS/SAXS spectra indicates rod-like elongated aggregates with a radius of 20 to 25 Å and a persistence length of $l_p = 3$ to 5 nm.[144] For solvents with low interfacial energy, the radii are independent of the solvent, whereas at high interfacial energy, the radii increase to minimize the specific area per polar head. Also, an increase in dielectric constant of the solvent favors the existence of a local order but does not have a strong effect on rod radius.[142,143] Increasing the size or the valence of the counterion significantly reduce the electrostatic repulsions between particles and favors interparticle aggregation. Compared to LSC ionomers, the value of the radius in short-side chain PFSAs was found to be slightly smaller due to the lower EW (15 to 17 Å vs 20 to 25 Å), while the effect of the nature of the terminal ionic group was found to be negligible.[144] All of these studies on PFSAs from membrane to dispersion form contribute significantly to the current morphological understanding (Figure 17). A number of morphological models have been proposed since the cluster-network model proposed by Gierke, Hsu and co-workers,[33,35] where the water attached to the ionic groups form interconnected spherical hydrophilic clusters of 4 to 6 nm diameter, which are distributed in the polymer network (Figure 17). Investigations by Gebel and coworkers of CEA group on PFSAs from dry state to solution phase combined several features of previous models in that an interconnected network of domains would convert into a rod-like polymer structure in colloidal solution with a structure inversion due to excessive swelling of water domains.[141,144,146,220,371] Later, Rollet, Rubatat and co-workers described the morphology of PFSAs as elongated polymeric rod-like aggregates with water pools residing among them,[364,366,409] following up on the previous studies from the same group.[144,371] According to their model, the scattering peak is associated with the interaggregate distance and hydration is interpreted as the dilution of these aggregates without structural reorganization.[364,366] Since then, alternative descriptions for the hydrated PFSA morphology have been proposed,[217,225,368,410,411] including a sandwich model, where the water is embedded in the polymer matrix,[225] a disordered network of polymer chains and water pools,[217] platelet- to ribbon-like structure of polymer domains with ionic sites on their surface,[410] parallel-cylindrical water channels embedded in a semicrystalline polymer matrix,[411] and a bicontinuous network of ionic clusters in a matrix of fluorocarbon chains.[368] However, the structure at full hydration is akin to ribbons, i.e., locally flat, of hydrophilic domains interspersed among backbone crystallites,[333,366] although the structure under different hydration levels is not definitively known, with perhaps more discontinuous cluster-like behavior at very low water contents. Such a picture is also consistent with surface-morphology (e.g., AFM) studies, which suggest a humidity-dependent fluorocarbon-rich skin within a wormlike network of elongated[423] or locally flat[51] domains (see section 3.4).

Similar structural interpretation of SAXS data comes from the Porod regime, from which one can obtain the polymer−water interface S/V.[19,146,333,421,424] After an initial increase, S/V continuously decreases with hydration in order to minimize the interfacial energy of the system (from ~600 to 400 m^2/cm^3).[146,333,421] While Kong et al.[421] explained this S/V vs φ_w trend in two regimes, arguing a transition from spherical domains in dry state to ribbons in hydrated state, Kreuer[333] argues that local flattening is still energetically more favorable than cylinders or spheres, as long as the separated charges are not completely screened by the high dielectric solvent. This makes it possible for a PFSA to adopt a rod-like morphology in dispersion state, due to very high hydration levels. In a recent MD study, Savage and Voth[356] examined large-scale morphologies of PFSA and found that a bundle-like structure flattens into ribbons thereby creating a locally flat model, in better agreement with transport data than lamellar and random models. They also found that the hydrophobic/hydrophilic interface is key for transport phenomena, with lower surface areas (S/V) showing higher H^+ diffusion coefficients.[356]

More recent studies in various solutions and counterion forms revealed that PFSA dispersions form primary aggregates at low PFSA concentrations, and then secondary aggregations with increasing concentration, leading to a more disordered chain segments that do not participate in the cylindrical rods; the number and length of molecular chains in the rod and the rod size both decrease with increasing concentration.[425] Overall, these studies suggest a transition with increasing PFSA concentration from a coil-like disordered aggregated structure, where ionic interactions still persist, to more ordered rod-like aggregates with secondary ionic clusters.[425−427] The phase-separation of the aggregates is controlled by the solvent's compatibility with the PFSA backbone, where favorable electrostatic interactions also influence their interaggregate distance.[428]

3.1.1. Scattering with X-ray and Neutrons. Scattering is a robust tool that probes the morphology based on the scattering of an incident beam of known wavelength, λ_{wave}, upon its interaction with the material's scattering entities' electronic (X-rays) or nuclear (neutrons) structure, across a wide range of distances. The intensity is recorded as a function of the scattering wave vector, q, which characterizes the distance in Fourier space, and is related to the scattering angle, θ by $q = 4\pi/\lambda_{\text{wave}} \sin(\theta/2)$. Depending on the q-range, and the regime, various analysis could be performed to extract specific structural information, including, but not limited to the scattering entity shape/size and their spatial distribution (form and structural factor, respectively).[19]

Figure 18 shows the SAXS/WAXS spectra for Nafion membrane hydrated in liquid water and summarizes the characteristic peaks and structural features. Typically, there are three commonly studied q-regimes from which structural information can be obtained, three of which are shown in Figure 18. The small-angle upturn ($q < 0.01$ Å^{-1}) provides information about larger-scale structural features (which was mentioned above). The other three peaks shown the figure are (i) a broad peak between 0.02 Å^{-1} < q < 0.1 Å^{-1}, corresponding to intercrystalline spacing, d_c (10 to 25 nm), between the crystalline domains of the polymer matrix, the so-called matrix knee; (ii) a stronger ionomer peak, the most characteristic peak arising from the mean correlation spacing between the hydrophilic water-domains, d (= 3 to 6 nm); and (iii) the amorphous and crystalline WAXS peaks at q = 1.24 and 2.6 Å^{-1}, respectively, corresponding to the inter- and intracrystalline spacing of the fluorocarbon ($-CF_2-$) chains in the crystalline structure, and from which the degree of crystallinity, x_c, can be estimated (which is discussed in section 3.1.3). There is also a Porod regime between SAXS (ii) and WAXS (iii) peaks, which manifest itself as a strong continuous decrease in intensity with a characteristic slope as noted above.[19] It should also be mentioned that the obtained circular scattering spectra of PFSA indicates morphological isotropy, at least in the plane; through-thickness isotropy was confirmed by edge-on scattering studies performed by Rubatat[364] and Kusoglu et al.[257] Nevertheless, in-plane anisotropy can be induced due to membrane processing or stretching (see section 3.1.5).

As seen from the insets, all of the peaks are strongly interrelated in that there exists a balance between the semicrystalline matrix and hydrophilic water domains that governs the degree of phase separation. Figure 18 shows how this balance changes with thermal history, which shifts all of the peaks in concert resulting in inverse relationships between the hydrophilic and hydrophobic properties ($d_c \propto d \propto 1/x_c$). Thermal annealing of a membrane increases its crystallinity and reduces d_c (more crystalline domains), which in turn decreases the water-domain spacing. Similarly, preboiling a membrane disrupts crystalline order to a certain extent, thereby enhancing water-domain spacing. Such changes in the phase-separated nanostructure with thermal history are the underlying cause for the observed changes in the structure−property relationships discussed throughout this review. The fact that the matrix knee changes with thermal annealing supports its assignment to the crystalline domains, as discussed in references.[82,87,146,217,430]

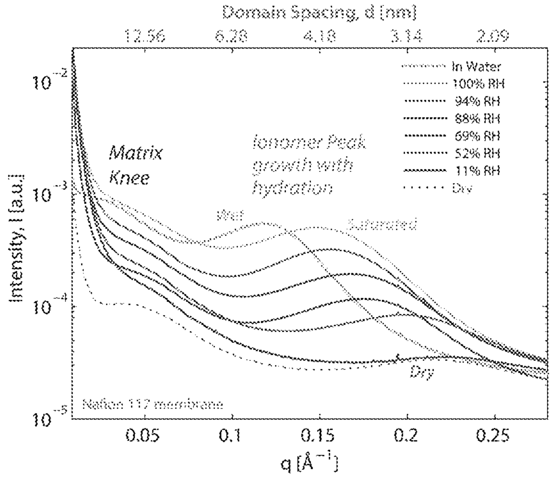

Figure 19. Changes in ionomer peak of Nafion 117 during humidification (from 0 to 100% RH) and in liquid water (at 25 °C) determined from in situ SAXS spectra.[82]

Perhaps the most important aspect of PFSA morphology is the growth and shift of the ionomer peak during humidification, which is an indication of nanoscale swelling of the hydrophilic domains with water uptake (Figure 19). It has been well documented that d-spacing increases with hydration, which has also been used to explain many of the observed hydration-driven structure−property relationships (such as conductivity, see section 4). Although used mainly to determine the water d-spacing, namely the hydrophobic/hydrophilic correlation length, additional information can be extracted from the SAXS profiles, as shown in Figure 20. First of all, there exists a linear relationship between d_c and d during hydration, indicating that the crystallites in the matrix are also moving apart slightly to accommodate the growth of the water domains (Figure 20a). Interestingly, the changes in d_c with hydration are dissimilar for extruded and dispersion-cast Nafion membranes, suggesting that processing influences their response to hydration, with potentially different larger lengthscale reorganization. Moreover, the full-width half-max (fwhm) of the ionomer peak decreases with hydration, indicating a slightly less disordered nanostructure. Figure 20f also shows that d-spacing of a hydrated PFSA increases with IEC (or reduced EW) at a given water content, λ, which increases the size and spacing of the hydrophilic domains and enhances phase separation, in

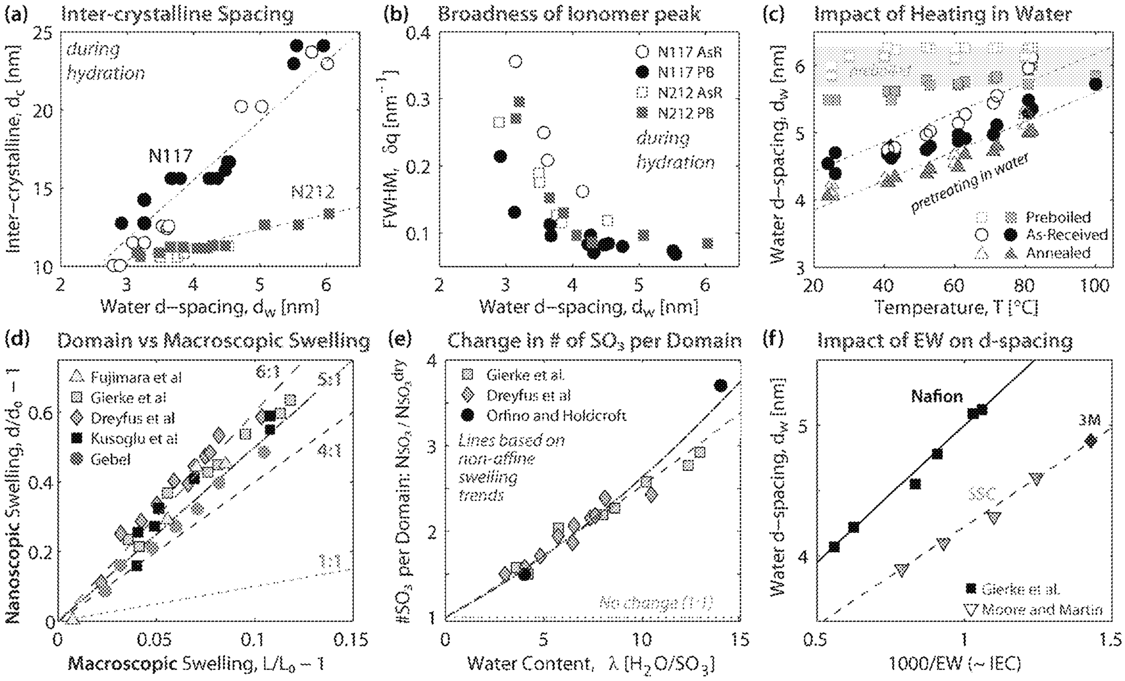

Figure 20. Characteristic spacing in PFSAs: Change in (a) intercrystalline spacing and (b) full-width half-max (fwhm) of ionomer peak with hydration (our data and ref 82). (c) Impact of heating on water d-spacing for as-received, annealed and preboiled membranes (from refs 82 and 90). (d) Nonaffine swelling behavior of PFSA shown as change in water d-spacing (nanoscopic swelling) vs membrane length (macroscopic swelling; data from refs 33, 82, 146, 218, and 223). (e) Number of ionic SO_3^- sites in a water domain from various refs 33, 219, and 223 along with estimated values from volume analysis based on nonaffine swelling trends shown in d. (f) Impact of EW on water d-spacing in liquid water for Nafion,[33] SSC,[38] and 3M.[38]

agreement with mesoscale simulation studies (see section 3.3). [It must be noted that, for a given water volume fraction, the trend reverses slightly, i.e., d-spacing decreases, since increasing IEC at a constant λ indicates a higher volume fraction, which tends to increase d-spacing due to swelling.] The intensity of the matrix knee also decreases for higher IEC ionomers, especially if their crystallinity decreases. Hence, d-spacing of a PFSA remains to be the single most important structural property to characterize its phase-separated morphology, albeit open to various interpretations; for a historical perspective and earlier discussions on the interpretation of the ionomer peak, see the review by Mauritz and Moore.[1]

3.1.2. Direct Imaging. Definitive visualization is required to unambiguously ascertain the correct morphology, although it is a difficult experiment due to sample preparation, beam damage if using electron microscopy,[358,431] possible cation contamination if using metal support grids[358,431] etc. A phase-separated nanostructure comprised of 3 to 8 nm circular domains has been visualized in the dry state with TEM.[248,296,430,431] However, it is of greater interest to examine the hydrated morphology, which only recently was visualized successfully. Allen et al.[358] obtained the first direct 3-D nanoscale image of hydrated Nafion film using cryo-TEM tomography, which is shown in Figure 21. This nanostructure provides direct evidence of the 3-D structure and illuminates some of the previously discussed descriptions based on SAXS, in particular, the locally flat or elongated domains, interconnected via varying size secondary domains (or channels). It must be noted that this direct structure was obtained at maximum hydration and does not necessarily invalidate other morphologies that may form at lower hydrations levels, including spherical domains with weaker connections (as seen in dry TEMs). Still, an interesting outcome of this study is that the Fourier-transform of the images yielded a scattering peak ($q \approx 1$ nm^{-1} (= 0.1 Å^{-1}), similar to the experimentally observed ones (see Figure 18), and also in agreement with predicted structures from mesoscale simulations.

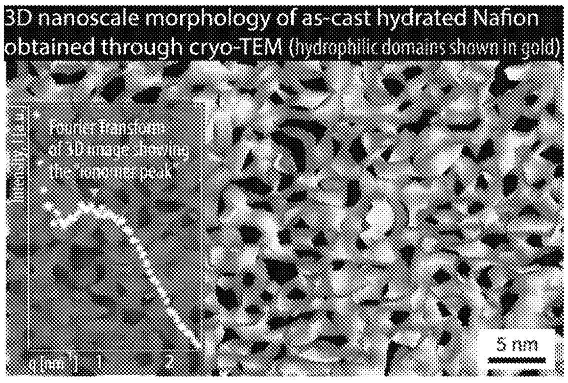
3D nanoscale morphology of as-cast hydrated Nafion obtained through cryo-TEM (hydrophilic domains shown in gold)
Fourier Transform of 3D image showing the "ionomer peak"
Intensity [a.u.]
q [nm^{-1}]
1
2
5 nm

F.I. Allen, et al. ACS Macro Letters, 4 (2015) 1-5 | DOI: 10.1021/mz500606

Figure 21. 3D Nanostructure of hydrated Nafion film obtained through cryo-TEM tomography (from Allen et al.[358]). Inset on the left shows the scattering profile obtained via Fourier transform. Reproduced from ref 358. Copyright 2015 American Chemical Society.

3.1.3. Crystallinity. Crystallinity of PFSAs is the most critical property governing its structural integrity, which gives them their remarkable stability even at high degrees of swelling. Increased crystallinity of PFSA has been studied in relation to its impact on properties, such as dielectric relaxation,[104] smaller d-spacings,[33,36,38,82,97] reduced water uptake,[33,38,81,82,89,96,97] and swelling,[99] lower gas permeability[97] and free volume (which is associated with the amorphous regions),[301] improved mechanical and thermal stability,[40,81,82,107,295] as well as conductivity.[49,81,97,101,103,104] High crystallinity manifests itself by the amount and size of the crystallites with more ordering, which tends to enhance mechanical stability but could limit transport of species.[82,89,97,430] The crystalline properties of PFSA are commonly determined by WAXS (or XRD), from which one can obtain a scattering/diffraction pattern arising from the crystalline and amorphous phases of the PFSA's semicrystalline PTFE matrix. By deconvoluting the WAXS peaks, the relative degree of the crystallinity, x_c, can be calculated as (Figure 18)[432]

$$x_c = \frac{\int q^2 I_c(q)\,dq}{\int (q^2 I_c(q) + q^2 I_a(q))\,dq} \tag{27}$$

The crystalline peak corresponds likely to the diffraction from the ⟨100⟩ plane of hexagonal PTFE lattice that has a 15/7 helical formation of CF_2-CF_2 chains.[415,433,434] In fact, the lattice structure of PTFE chains in PFSAs was discussed in analogy to the PTFE hexagonal lattice model, which may hold especially at higher EWs,[2,222,367,384,415] where the crystalline spacing decrease slightly with EW and approaches the value for PTFE, 4.93 Å.[433,434] Some studies on PFSAs also reported a secondary broad peak (a.k.a. third WAXS peak), with 2.4 ± 0.2 Å distance, which was attributed to intrachain distances and associated with the overlapping diffractions along the chain axis from both amorphous- and crystalline-phase intramolecular correlations.[367,403] More recently, another peak corresponding to the C–C bond length of 1.29 Å was also reported.[403]

x_c values of PFSA were determined either from WAXS[2,33,36,38,40,81,82,98,108,145,367,403,415] or DSC.[38,40,89,415] In the latter, crystallinity is related to the heat of fusion, as calculated from the melting peak. The relative degree of crystallinity of Nafion membranes has been reported to be x_c = 7–17% for extruded (e.g., N112 and N117)[82,217] and 14–20%[82,90,103,281,295,301] for dispersion-cast membranes (e.g., N212), which can be compared with that of PTFE of 55–75%.[433–435] (see Figure 22). The lower crystallinity of PFSA compared to pure PTFE can be attributed to the side-chains and ionic sites acting as "defects" that disrupt crystallization.[108,217] This was shown by a decrease in crystallinity of PFSA precursor (SO_2F) after it was hydrolyzed, which resulted in the formation of ionic aggregates.[33,81] It is important to realize that x_c calculated from WAXS patterns could change from one sample or setup to another, and the reported values are in fact a relative degree of crystallinity, and therefore are used here for qualitative comparisons only. Thus, despite the presence of crystallites, they do not necessarily have long-range order, and are randomly distributed in the matrix, thus giving rise to the broad matrix knee. However, through annealing, a more ordered crystalline structure can be obtained (i.e., a narrower matrix knee) (Figure 18).

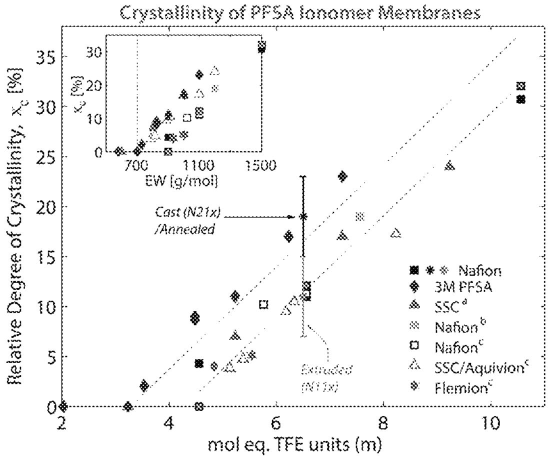

Figure 22. Relative degree of crystallinity for various PFSA membranes plotted as a function of backbone length (TFE repeat unit), based on literature data from various studies [(a) ref 40, (b) ref 36 (c) ref 3; the symbol * with the error bar represent the average of all reported values in the literature for 1100 EW Nafion extruded (gray) and dispersion-cast/annealed samples (black)].

Earlier works on crystallinity were motivated by understanding solution-processing and annealing effects for developing a more stable membrane.[145] Crystallinity in PFSA can be induced (or improved) by thermal annealing process, which involves heating the membrane above its cluster (T_α) transition temperature, thereby giving the polymer chains enough mobility to reorient and pack themselves to form crystallites.[40] Annealing in the literature has been done with a rather wide range of temperatures, from 130 to 250 °C.[33,36,82,108] In temperature-dependent WAXS studies, disappearance of the crystalline peak was observed above the melt temperature and around 250–300 °C, depending on the counter-ion,[33,38,40,108,131] as well as formation of a (stronger) crystalline peak during annealing and cooling.[36,82,131]

With increasing EW, the crystalline peak narrows and its intensity increases, reflecting the more ordered structure, as was inferred from TEM studies.[430] Crystallinity increases with EW, but is also affected by the side-chains, which tend to disrupt packing efficiency and crystallite formation.[2,3,36,38,40,415,430] Thus, the extent of crystallinity can be enhanced if desired through a more effective packing of polymer main-chain (crystallization), which can be achieved either by shortening the side-chains or increasing their separation (or fraction, i.e., increasing EW).[3,38,40] Thus, at the same EW, a PFSA with a shorter side-chain has higher crystallinity, as shown in Figure 22. However, care must be taken when comparing different PFSA ionomers due to competing effects: a low-EW SSC ionomer may tend to pack better (due to short side-chain) but has also more side-chains (due to low EW) compared to Nafion.[40] [Rather limited data on density of shorter-side chain PFSAs indicates slightly higher density at low hydration levels (see Figure 12).]

In an effort to explore the chemistry/crystallinity relationship, the available data[2,3,38,40,82,430] for various PFSAs are plotted in Figure 22 as a function of backbone length, in terms of # TFE repeat units, m, instead of EW (see Figure 2), which shows a linear correlation of the form: $x_c \propto (m_{TFE} - m_{TFE}^{min})$. There appears to exist a minimum backbone length of m_{TFE}^{min} = 3.5–5 (or 7–10 CF_2 units) for a PFSA to exhibit semicrystallinity. Below this value, the ionomer exhibits a gel-like behavior with weak stability, albeit with good transport properties, in agreement with the fact that 3M PFSA of less than 725 ± 25 EW ($m_{TFE} \approx$ 3–4) and Nafion of less than 900 ($m_{TFE} \approx$ 4) begin to dissolve in boiling water.[2,5,77] Previous studies reported a minimum EW of 965 g/mol for Nafion,[33,40] 800 g/mol for SSC[38] and recently for 3M PFSA,[2,48,77] all of which correspond to a minimum of 3–4 TFE units required to induce packing order. Thus, there is a trade-off between transport and structure since even though lowering EW increases proton conductivity[3−7,10] it also lowers crystallinity,[2,3] as shown in Figure 5.

Efficient packing of chains in SSC ionomers also reduces their free volume available for chain motion, which is the origin of transition temperatures,[40] and will be discussed, along with mechanical properties, in section 5. Overall, higher crystallinity and shorter side-chains tend to lower mobility of the main- and side-chains, thereby increasing the transition temperatures and mechanical properties.[2−4,9,38,40,77] Thus, by its nature, crystallinity and backbone conformation states are strongly related to the ionomer's thermo-mechanical relaxations and transitions.[2,3,415,436] (See sections 3.3, 4, and 5).

3.1.4. Thermal History.

Thermal annealing not only induces crystalline order for backbone main chains but also allows a membrane's ionic moieties to rearrange themselves when the electrostatic interactions holding ionic groups in aggregates are overcome by the thermal energy. Since such rearrangements occur above the cluster-transition temperatures (see section 5.4), electrostatic interactions also influence the morphological changes; thus, different counterions can results in different effects.[89,91,103,437] For example, annealing Nafion in Na^+ form results in increased stabilization of SO_3 groups, which could persist after protonation and enhance the proton transport.[101,103] An interesting effect of heat-treatments is, however, on the membrane surface concurrent with the higher crystallinity in the bulk. While AFM suggests an increase in PFSA's surface hydrophobicity,[80] ATR/FTIR techniques revealed that annealing increases crystallinity with reduced internal energy that pushes SO_3^- group toward the surface to minimize the surface energy and reorient polymer chains parallel to the surface,[80,81,103,399] which persists in subsequent humidification as evidenced by reduced conductivity[80,81,103] and free water.[398]

An interesting aspect of thermal history is the relationship between thermal annealing and heat-treatments in water (e.g., boiling), as discussed and demonstrated in Figure 18. Although *d*-spacing measured in water is lower for an annealed membrane, it increases upon heating in water and approaches that of a pretreated membrane (see Figure 20c) as mentioned above in section 1.1.2. The reduced effect of annealing and crystallinity via acid and water pretreatments has been shown in terms of transport and mechanical properties as well.[82,96] Nevertheless, the true impact of annealing on transport properties is still not completely understood due to inconclusive results on whether annealing enhances conductivity or not (for a given water content).[18,49,81,97,101,103,104] In fact, when the effects of annealing time,[80,104,107] membrane thickness, and cooling rates (crystallization kinetics)[49,82,217,437] are combined and the impact of activated chain-motions on transport is considered,[104] (section 4.4) the observed deviations in different membrane studies are not unexpected. Moreover, given that annealing increases crystalline order and changes the surface activity, where ionic groups and side-chains orient differently than in the bulk, thermo-mechanical relaxations during heat-treatment process are expected to be strong functions of annealing time, temperature, counterion, and more importantly, on the kinetics and crystallization during cooling,[49,80,82,104,217,437] all of which are interrelated (e.g., counterions can influence crystallization rate due to different side-chain mobility and electrostatic interactions).

It was observed in a few SAXS studies that extruded or processed membranes have an intrinsic orientation, similar to those observed during stretching as discussed in section 3.1.5. This intrinsic orientation could be eliminated by stretching the membrane in a perpendicular orientation,[84,131] thermal annealing,[84,131] and to a certain extent by boiling in water.[82,84] However, the intrinsic orientation induced during extrusion sets a residual morphology that cannot be completely eliminated even with pretreatment.[84] The fact that processing and external deformation causes similar structural changes reveals an intriguing link between the thermal history and mechanical deformation (see section 5). Xie et al.[87,175] showed that when Nafion is deformed, its subsequent strain-recovery rate (or temperature) is strongly related to its initial deformation temperature, reminiscent of a shape-memory effect. This morphology-thermal history link could also explain, partially, the observed differences in transport properties between extruded and cast membranes (see section 4).

3.1.5. Mechanical Deformation.

To develop a better morphological picture with deformation behavior, the nanostructure of PFSA membranes has been investigated under mechanical stretching (tensile loads).[33,36,84,334,335,365,367,370] When macroscopically stretched, the domains elongate in the stretching direction, causing (nano)structural anisotropy.[33,36,84,130,335,365,367,404] Morphology of stretched PFSA has been studied in conjunction with conductivity (which increases in stretching direction),[335] crystallinity,[367,403] orientation of domains,[36,84,365,367,370,422] thermal relaxation behavior,[131] as well as birefringence experiments to study nanostructural orientation and relaxation.[130,438] The stretching-induced orientation has also been evidenced by Raman spectroscopy[375] and supported by MD simulations.[439]

From the data of stretched membranes, nanoscopic changes in *d*-spacing (nanostrain) follows the macroscopic deformation (externally applied macro-strain), with a linear correlation.[365,367,422] However, the ratio of nano- and macro-deformations were not the same, indicating nonaffine behavior. Interestingly, the ratio of the nonaffinity of deformation is smaller than that observed for swelling (see section 3.2),[194,257] which again reveals differences in the underlying mechanism of swelling-induced matrix deformation vs externally induced deformation. It must be noted that various modeling attempts to link multiscale deformation mentioned the importance of mesoscale deformation, and necessity of its inclusion in a model to explain fully PFSA morphology.[194,257,422] van der Heijden et al.[367] observed that the orientation of ionomer, amorphous, and crystalline peaks differ during stretching, with the latter being less sensitive. Also, even stronger effects in the crystalline phase was evidenced by the change in lattice dimensions and anisotropy.[403] They explained this by describing the deformation at the mesoscale in terms of the rotation of bundles comprised of rod-like polymeric aggregates and the subsequent orientation and elongation of the polymer-chains within the bundles upon further stretching,[367] in accord with the morphology discussed above[130,364,366,422] and shown in Figure 23c. In fact, strain-induced deformation occurring at multiple length scales (from nanodomains[257,367] to larger length scales (e.g., ~70 nm[404]) are strongly intertwined with the mechanical stress−strain response of the PFSA (as discussed in section 5). While deformation at lower strains is an average response of polymeric aggregates, thus giving rise to a more or less elastic modulus, the preferential orientation of domains at larger strains are strongly related to the postyield hardening behavior.

When deformed, the ionomer peak in the SAXS spectra of a PFSA becomes elliptical, indicating reorganization of hydrophilic domains, wherein the *d*-spacing increases in the

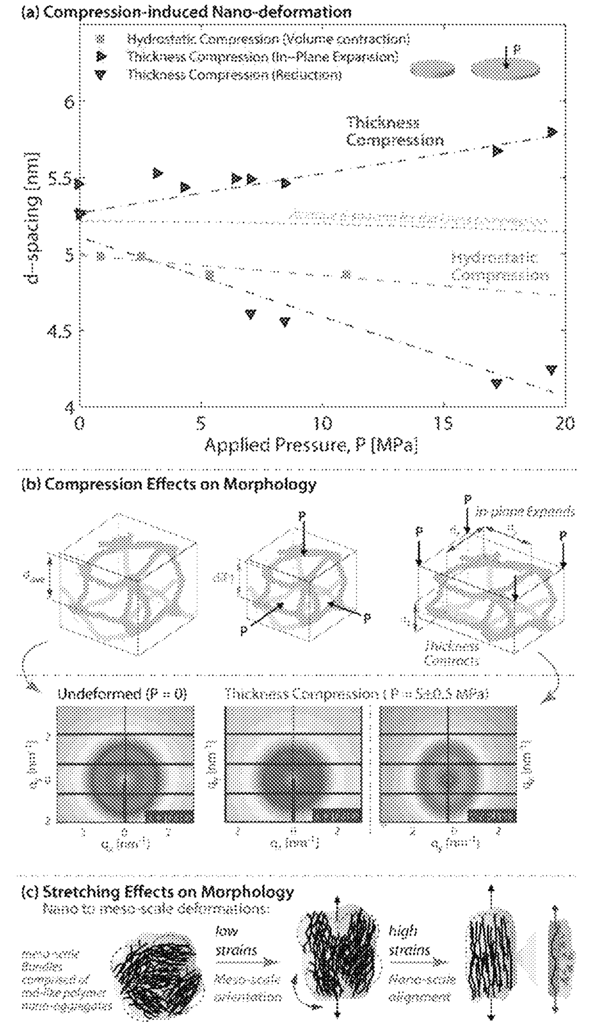

Figure 23. Nafion morphology under deformation inferred from SAXS studies: (a) Change in *d*-spacing as a function of pressure for thickness and hydrostatic compression cases and (b) corresponding 2D SAXS images with an pictorial depiction of deformed nanomorphology (Kusoglu et al).[257] (c) Below shown is the evolution of multiscale deformation mechanisms in Nafion during stretching, based on studies by CEA group (from van der Heijden et al.[367] and related works from the same group[19,130,366,438]).

stretching direction and decreases perpendicular to the stretching direction (Figure 23). A similar phenomenon is observed under compression, which brings the domains closer (reduced *d*-spacing) in the compression direction, but increases their separation (higher *d*-spacing) in the perpendicular direction, as illustrated in Figure 23. Such domain orientation in the stretching direction was shown to align well with the improvement in transport properties measured in the same direction, including conductivity[369,439] and self-diffusion,[369] which was attributed to the reduced resistance to transport (i.e., tortuosity) due to preferential alignment of transport pathways. However, changes in transport or mechanical properties usually come with an opposite effect in the perpendicular direction.[257,335,369] Such changes were also confirmed using molecular simulations[439] predicting that the side chains orient perpendicular to the stretching direction, thus enhancing their nanophase separation with longer hydrophilic channels, which increases proton conductivity along the stretching direction but decreases it along the transverse one. It was demonstrated that conductivity in the thickness direction also increases when the membrane is compressed, albeit at a rather small rate and with possible contact-resistance effects,[440] which was attributed to a closer proximity of water-domains, despite slight water loss under compression (see sections 2.6.3 and 5.2).[257] For a fully hydrated membrane, the relative change in *d*-spacing is stronger than the relative decrease in water content, λ, revealing an interesting interplay among uptake, morphology, and deformation.[257] Therefore, regardless of the deformation mode (tension/compression), any orientation induced in the membrane results in anisotropy not only in the morphology but also in the transport properties, leading to changes that could be stronger than changes in water uptake.

Inspired from these effects, Lin et al.[295,296] developed a prestretched (PS) Nafion membrane, which was stretched with a heat-treatment process to set an oriented morphology that can possess some of the transport-property anisotropy discussed above. Prestretching was found to reduce the water-domain size, but increase their number leading to a more uniform distribution compared to recast Nafion.[296] Moreover, prestretching was found to increase crystallinity,[295,403] mechanical properties,[295] and reduce the amount of freezable water,[296] and methanol permeability,[441] but does not affect much the water uptake and conductivity.[296] Interestingly, in PS Nafion, the crystallites strongly align along the stretching direction, while the amorphous phase remains isotropic, which helps explain the property improvement and anisotropy.[403]

3.2. Multiscale Swelling

The swelling behavior of a PFSA membrane results from its structures' response to hydration effects at multiple length scales: from nanoswelling of domains to a possible supramolecular organization at mesoscales to accommodate the growth and reorganization of water domains as well as semicrystalline polymer aggregates (Figure 7 and Figure 18). Hydrophilic (or water) *d*-spacing, d, in PFSAs increase with water content, λ, exhibiting a linear relationship, confirming the nanoscale swelling of water domains (Figure 24a),[33,82,146,217,364] which was shown to hold for other solvents as discussed in section 2.3.[346] A plot of *d*-spacing vs λ, or $\Delta V_w/V_p$, exhibits a linear relationship, signifying the local-swelling of hydrophilic domains. Thus, the hydration dependence of *d*-spacing can be expressed in various ways

$$d(\lambda) = d_{dry} + s_n\lambda \text{or} \frac{d(\lambda) - d_{dry}}{d_{dry}} = s_n'\lambda = s_n''\frac{\Delta V_w}{V_p} \qquad (28)$$

where s_n (or s_n', s_n'') is the nanoscale swelling coefficient,[82] in analogy to the macroscopic swelling coefficient discussion in section 2.3, the value of which changes depending on the descriptions used. Figure 24 depicts that this linear $d-\lambda$ holds for all PFSAs, but with a slight dependence of d_{dry} on the ionomer chemistry and EW. While such linearity was originally observed by Gierke et al.,[33,35] who associated it with growth of hydrated domains, the mathematical insight of this relationship nevertheless was not satisfactorily explained in the early studies.[218] Litt[420] suggested, based on the proportionality of nanoswelling with $\Delta V_w/V_p$ ($s_n'' = 1$ in eq 28), that the packing of the hydrophilic domains should be lamellar. Similar considerations followed later, albeit with different structural interpretations, in the works by Gebel[146] and co-workers at CEA[19,364,366,409] (ribbon-like morphology), and Haubold et al. (sandwich-like morphology).[225] Recently, Kreuer revisited the same concept in conjunction with structural analysis of SAXS

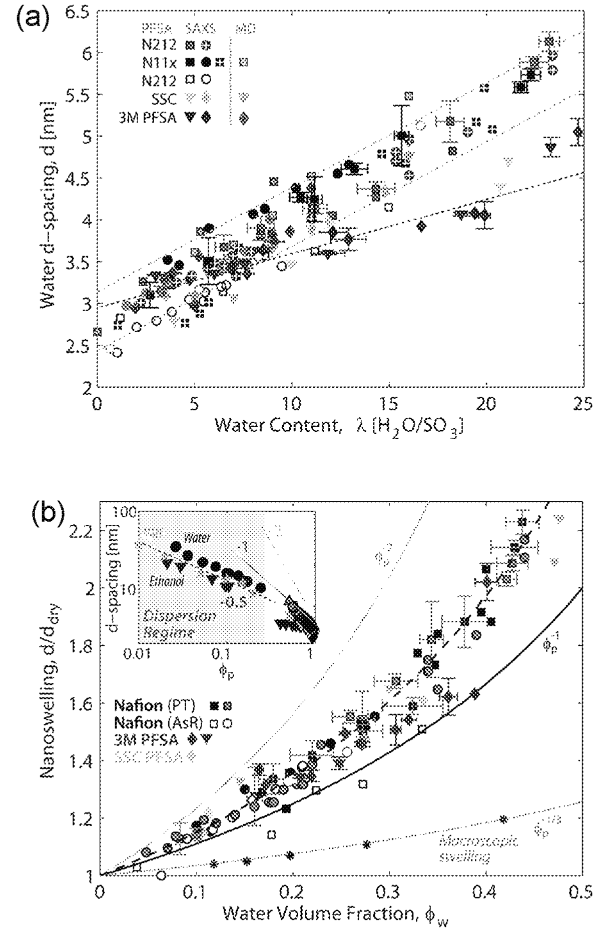

Figure 24. (a) Water domain spacing, *d*, of PFSA membranes as a function of water content. (b) Normalized *d*-spacing with respect to its initial value in dry state as a function of water volume fraction. Inset includes the data from dispersion form ($\varphi_p < 0.6$, or $\varphi_w > 0.4$), and shows the transition from membrane (solid) state to dispersion state with a change in slope. Open symbols in (b) represent data from MD and DPD simulations. Data are compiled from refs 33, 82, 146, 193, 218, 223, and 333 for Nafion, ref 42 for 3M PFSA, and for SSC[6] Dispersion data are from refs 141, 142, and 146.

data to confirm locally flat domain structure, which follows $d = d_{dry} + \Delta V_w/V_p$ ($s_n'' = 1$),[333] which was confirmed in other studies.[429] Moreover, Kusoglu et al. showed that the linearity of $d-\lambda$ extends to 3M PFSAs,[48] and heating in liquid water[82] (Figure 20). The fact that $d-\lambda$ relationship is valid during humidification,[33,35,48,82,333,420] ($d_{dry} = 2.7$ to 3.2, $s_n = 0.125$ to 0.135), heating in liquid water ($d_{dry} = 2.75$; $s_n = 0.135$),[82] and dehydrating at subzero temperatures ($d_{dry} = 2.75$; $s_n = 0.145$),[320] suggests a universal correlation across the temperature and hydration ranges with similar nanoscale swelling. Recently, $d - \lambda$ trends were shown to hold for 3M PFSAs as well, although with a lower nanoscale swelling, s_n, which was attributed to better packing of hydrophilic domains at a given λ, owing to their shorter side-chains. In fact, such nanoswelling behavior has also been observed in MD/DPD simulations, including the similar effect of PFSA EW and chemistry[63,65−67,410,412,442,443] (Figure 24a).

An interesting correlation appears when the change in *d*-spacing with hydration, $d(\lambda)/d_{dry}$, is plotted against the macroscopic swelling, $L(\lambda)/L_{dry}$, (discussed in section 2.3 and Figure 11) as demonstrated in Figure 20. Such a plot shows a linear correlation, albeit with a slope around 4 to 6 (instead of 1, which is affine), indicating a nonaffine swelling behavior across these length scales.[33,146,198,217,218,220,334,364,370] This phenomenon, first reported in early studies in 1980,[33,35] has been a subject of controversy and attributed to various mechanisms,[33,35,370] usually in conjunction with the structural changes in the proposed morphological descriptions (Figure 17). For instance, Hsu and Gierke proposed that such structural changes accompany coalescence of water-swollen clusters during water uptake that lead to higher increase in their spacing that would be expected from an affine relationship.[33,35] In a dry PFSA membrane, ionic SO_3^- sites cluster to minimize the free energy and grow with water uptake by deforming the surround polymer matrix, which, in turn, exerts a counter pressure to the growing domains.[146,195−199,201,218,253,350,444] As a result of this interplay between hydrophilic and hydrophobic domains, a structural reorganization and coalescence of the water-filled domains has been proposed to occur across the length scales, as discussed in refs.[33,146,194,204,219,223,334] If such a structural reorganization occurs, then the number of SO_3^- sites per domain is also expected to increase (as the total number of domains decreases upon coalescence), as calculated from the modeling analysis of scattering data,[33,219,223] (as shown in Figure 20e). Nevertheless, such analysis and the controversial nature of nonaffine swelling has been in part due to the nanostructural descriptions adopted and could be resolved if one considers swelling of locally flat domains, which swell proportional to the volume of water (Figure 17). This was shown by Kreuer,[333] who also argued that, while at low hydration the locally flat morphology must persist as the water helps establish ionic cross-links, there is still the mesoscale assembly of these domains. The overall morphology is governed by the conformation degrees of freedom of the polymer chains and interactions. Therefore, an assembly at mesoscales is possible, which could be more dependent on processing and thermal history, and give the characteristic properties of the macroscopic polymer.

Thus, while one would expect affine swelling due to the lamellae type nanomorphology, at the macroscale, one is probing more the mesoscale assembly of these flat domains. Such an assembly is expected to respond in a different fashion than the individual nanodomains, which is consistent with the broadness in the scattering peak, as shown by Kreuer.[333] This was further detailed recently by Kusoglu et al.[48] in that the nonaffine swelling response of the PFSA membrane can be reduced to an affine behavior, if the ionomer is cast as a very thin film (<100 nm), which also exhibits a stronger local ordering reminiscent of locally packed flat domains. The fact that such affinity in swelling is lost at macroscales and the membrane exhibit nonaffine swelling suggests that there is indeed some intriguing assembly of locally flat domains at mesoscales, which may or may not undergo a structural reorganization.

Given the morphological changes across a wide range of hydration levels, researchers attempted to extend the *d*-spacing regime to dispersion state to explore the underlying origins of hydration and solvation effects.[141,142,146,333,429] Studies by CEA group,[141,142,146,364,429] showed a transition in the hydration dependence of *d*-spacing around water volume fraction, $\varphi_w = 0.45$, after which PFSAs exhibit a different swelling behavior in the dispersion-regime (as discussed in section 3.1.1). Thus, one can rewrite eq 8 in the following form

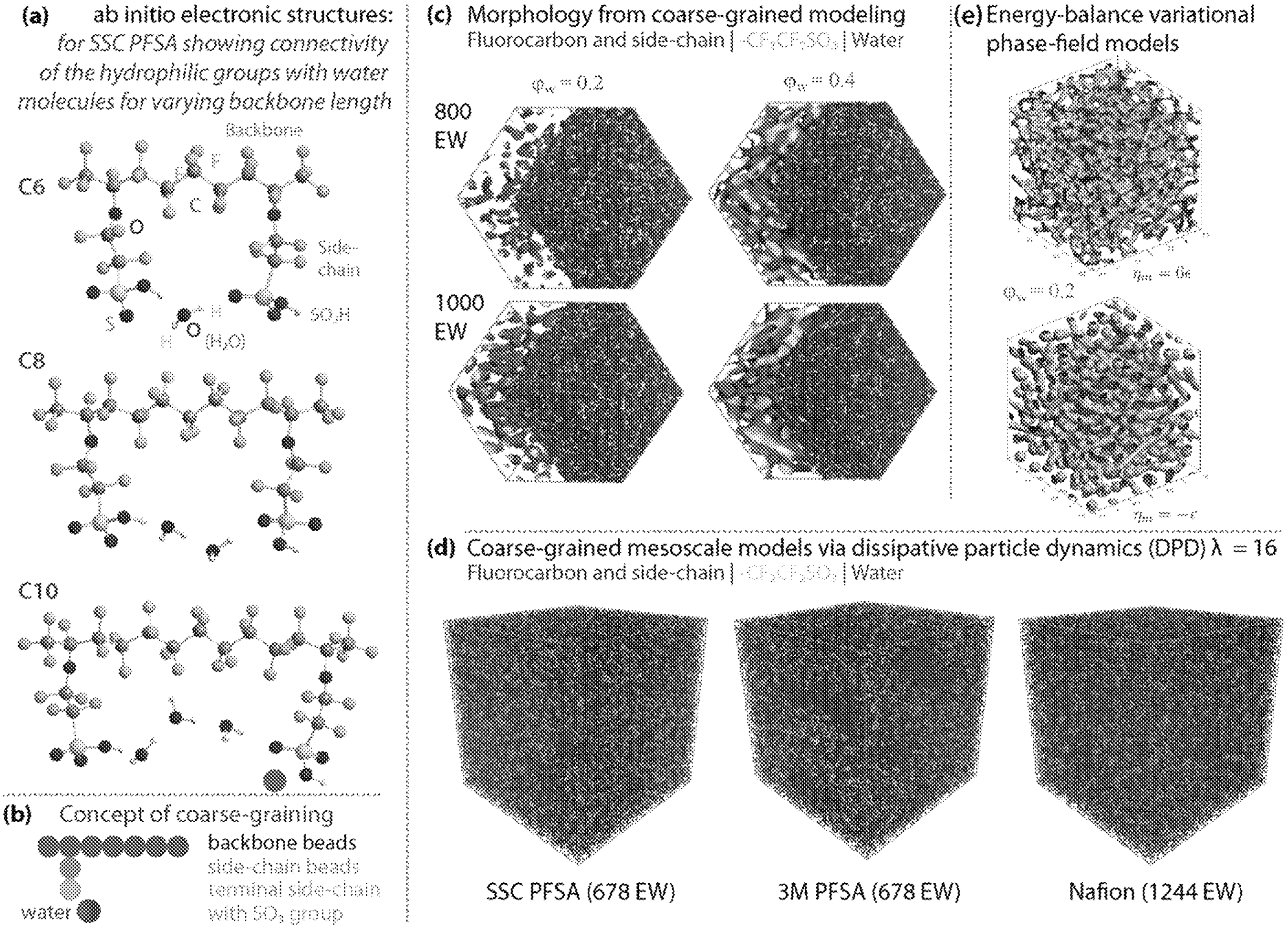
(a) ab initio electronic structures: for SSC PFSA showing connectivity of the hydrophilic groups with water molecules for varying backbone length
Backbone
C6
F
C
O
Side-chain
S
H
O
H
(H_2O)
SO_3H
C8
C10
(b) Concept of coarse-graining
backbone beads
side-chain beads
terminal side-chain with SO_3 group
water
(c) Morphology from coarse-grained modeling
Fluorocarbon and side-chain | $-CF_2CF_2SO_3$ | Water
$\varphi_w = 0.2$
$\varphi_w = 0.4$
800 EW
1000 EW
(e) Energy-balance variational phase-field models
$\eta_m = 6\epsilon$
$\varphi_w = 0.2$
$\eta_m = -\epsilon$
(d) Coarse-grained mesoscale models via dissipative particle dynamics (DPD) λ = 16
Fluorocarbon and side-chain | $-CF_2CF_2SO_3$ | Water
SSC PFSA (678 EW)
3M PFSA (678 EW)
Nafion (1244 EW)

Figure 25. Simulated morphology of PFSAs at various length scales as determined from (a) ab initio models (Paddison et al.[62]), (c and d) mesoscale (coarse-grained) models, and (e) phase-field models.[353,468] Panel a demonstrates the impact of backbone length on min number of water molecules required to bridge SO_3^- sites. Panel b illustrates the concept of coarse-graining. Panel c shows the effect of EW for Nafion at two hydration levels (from ref 469) and panel d shows a comparison of three PFSAs at the same water content (Wu and Paddison[63]). Also see Table 5 for the computed interaction parameters for these structures. (e) Possible morphologies obtained from variational model for low high and low mixing energies corresponding to the strength of segregation of phases (from Promislow[353,468]). ((a) Reproduced from ref 62. Copyright 2005 American Chemical Society. (e) Reproduced from ref 353. (c) Reproduced from ref 469. Copyright 2011 American Institute of Physics. (d) Reproduced from ref 63. Copyright 2008 Royal Society of Chemistry.)

$$\frac{d(\lambda)}{d_{\mathrm{dry}}} = (1 - \phi_{\mathrm{w}})^{-m} = \phi_{\mathrm{P}}^{-m} = \left(\frac{V}{V_{\mathrm{P}}}\right)^{m} = \left(\frac{\Delta V_{\mathrm{w}} + V_{\mathrm{P}}}{V_{\mathrm{P}}}\right)^{m} \tag{29}$$

where the exponent m is related to the morphology of the hydrated domains, i.e., $m = 0.5$ for rod-like elongated aggregates, which occurs in the dispersion state. In the solid regime, $m = 1$ has been reported, indicative of locally flat 1D domains.[141,142,146,193,333,364,429] (as shown in Figure 17) Nevertheless, when the literature data plotted together, Figure 20 suggests a deviation from $m = 0.5$, to values toward $m = 2$, perhaps reflecting the interconnected disordered morphology of the PFSA in the regular hydration regime. The best fit to the data, however, appears to be $m = 1.33$, which is slightly different than 1, perhaps indicating the morphological imperfections in locally flat domains but still significantly different than the isotropic value of $m = 1/3$, as is the case of macroscopic (3D) swelling of PFSA membranes. This underlines the point that locally, PFSA nanodomains do not exhibit isotropic expansion over the whole hydration regime, and their mesoscale hierarchy cannot be ignored.

Thus, in light of many recent evidence providing a better picture on multiscale swelling and hydrated morphology, completing the morphological picture of PFSA necessitates the explanation, imaging, and modeling of the evolution of nanostructure from dry to hydrated state, and its linkage to the mesoscale morphology.

3.3. Mesoscale Models and Simulations

A large body of computational work on PFSAs exists in the literature including classical MD,[445−452] ab initio MD (AIMD),[62,70,73,453−455] empirical-valence-bond (EVB) models,[355−357,456−459] self-consistent mean field (SCMF),[460,461] and mesoscale modeling (e.g., coarse-graining) studies.[63,65,460] These simulations report a large data set on radial distribution functions between various atoms (hydrated morphology), domain(pore)-size distributions, and self-diffusion of species. As mentioned, for simulations, "pore" is the oft-used term for hydrophilic water domain and "cluster" refers to larger length scales. For a discussion of MD models, most of which focus on transport phenomena see section 4.4.3; below we examine coarse-grained and higher-level models that use MD in part to determine structure.

Key findings from the earlier studies using electronic structure calculations,[23,62,462−465] as reviewed and discussed in studies by Kreuer and Paddison,[16,23,73] could be summarized as follows: the dissociated state is a result of the excess positive charge being stabilized in the H-bonding network of water, and the excess electron density (due to breaking of the SO_3−H bond) being delocalized by the neighboring chemical group. H-bonding between water solvating the SO_3^- groups is favored, which creates a continuous water network (within the first hydration shell) even under minimal hydration conditions (protons begin to dissociate at λ values of as low as 3). Later MD studies by Vishnakov and Neimark suggested that protons could travel even in the absence of such continuous pathways by forming short-lived dynamic bridges (100 ps) between more concentrated water domains.[201,451,466] (See section 4.1.3 for related discussion on diffusion.)

To predict the water distributions and morphology, higher-level models than MD are required due to the larger sizes (10−200 nm) and number of atoms, which are comparable to experimental SAXS[368] and TEM data.[430] To overcome the limitations of conventional MD, coarse-grained methods have been employed to model mesoscale morphologies, where one can examine length and time scales that are several orders of magnitude greater and longer than MD simulations.[412,443,460] A commonly adopted method is dissipative particle dynamics (DPD),[63,65−67,71,348,368,412] which relies on dynamical evolution of coarse-grained clusters of atoms (beads), whose response is driven by dissipative (molecular friction) and stochastic (Brownian-like) forces.[71] In DPD, a mesoscopic structure is obtained where the Flory−Huggins interaction parameter, χ_{ij}, (characterizing repulsion) between the beads (which represent a group of atoms, as shown in Figure 25b) are estimated from the mixing energy computed using Monte Carlo calculation.[71,412] In these models, a PFSA is represented as a chain of beads connected by harmonic springs, with short-range conservative interaction forces acting between the beads. The topology of the Nafion chain for example could then be composed of a backbone particle *A* (representing the $(CF_2)_m$), decorated at regular intervals by side chains consisting of a ***B*** particle ($-OCF_2C(CF_3)FOCF_2-$, for Nafion) terminated by the hydrophilic end group, C ($-CF_2SO_3H\cdot 3H_2O-$).[63,65−67,71,348,412] Then the water bead, W, comprised of a number of water molecules, is added. The interaction parameters among these groups have been calculated in many studies, which quantitatively characterizes the degree of phase-separation among the hydrophobic and hydrophilic groups, and water particles.[63,65−67,412] Figure 25c,d shows simulation results where one can clearly delineate the water domains from the backbone and start to analyze specific morphologies and transport pathways. One can then determine using these morphologies the self-diffusion of water (section 4.1.3), or even conductivity,[348] if the electrostatic interactions are introduced.

From the figure, one can compare the distributions to those obtained from SAXS (see section 3.2). *d*-spacing computed for various PFSA membranes all suggest a similar increase with hydration (λ)[63,65−67,410,412,442,443] (Figure 24a) and qualitatively agree with the experimental data in terms of side-chain and EW effects with a linear functionality. Nevertheless, the computed *d*-spacing in some cases are larger than those measured, which can be explained by the smaller volume of simulation boxes, for which the MWs are lower than realistic values, and lack of crystallites, which would exert additional forces driving domains toward smaller sizes.[65,67,456,460,467] In fact, *d*-spacing was shown to decrease with increasing MW[67] and is expected to approach measured values with larger length scales in simulations, which could also reveal new topologies and larger-scale architectures.[65,66,456,460] Also, most simulation studies correctly reproduced the experimental SAXS profiles, albeit through different methods and phase-separated structures,[368,411,442] which demonstrates that capturing SAXS data alone is not sufficient to identify unambiguously a PFSA's morphology due to its nonunique nature.

Comparison of spacing and radius of domains, along with cluster-size distribution provide additional insight into the connection and geometry of the domains. A number of studies reported a change in cluster-size distribution with hydration from many small isolated water domains to fewer but larger water-domains (i.e., coalescence as discussed in section 3.2).[443,449,451,452] In fact, substantial rearrangement of SO_3^- groups and conformational changes in polymer chain was suggested to result in nonaffine swelling correlations, even in the absence of mesoscale organization of domains of lower dimensionality.[71,73,368]

Other approaches that can be used to predict the morphology are energy-balance-variational and phase-field models[353,468] that utilize a functionalized Cahn−Hilliard (FCH) energy, as discussed by Promislow et al. In these simulations, an overall expression for the free-energy of the system is minimized among possible geometries to derive a description of the hydrophilic domain microstructure as introduced in section 2.6.[353,468] In this fashion, they can predict the impact of environment on water uptake and provide a domain distribution that can be used to run transport simulations as shown in Figure 25. The figure shows the structures for various mixing energies, η_{mix}, which reflect the entropic penalty for high densities of interspersed ions and counterions, with larger values leading to segregation of charge groups on the length scale of the domain.[468] At higher water contents, the appearance of the network starts to mimic that observed using the cryo-TEM (Figure 21), composed of flat, worm-like small channels. Finally, these models naturally predict changes due to liquid and vapor boundaries in terms of an inversion of the morphology that occurs due to a vanishing surface-tension energy term.

3.3.1. Impact of EW and Side-Chains. Coarse-grained techniques have been especially helpful for delineating the effect of side-chain length and EW on morphological features for Nafion,[63,461,469] SSC,[62,63,69,70,449,461] and 3M PFSA,[63,67−69,456] as shown in Figure 25. Peterson et al.[457] stated that while a SSC could prevent SO_3 groups from penetrating the hydrophobic regions, favoring transport in the bulk-like phase, it could also enable the hydrated protons to interact more with the backbone, enabling transport at the hydrophilic/hydrophobic interface.[457] According to Devanathan and Dupuis,[72] shortening side-chains, while retaining the same backbone, offers no significant benefit for transport because the longer side-chain is bent and becomes effectively equivalent to a SSC, and any improvement in conductivity of SSC could be originated from reducing its EW, i.e. increasing the concentration of acid groups. On the other hand, simulation studies by Cui et al. found more connected and dispersed water clusters in SSC PFSA, while Nafion's longer and flexible side-

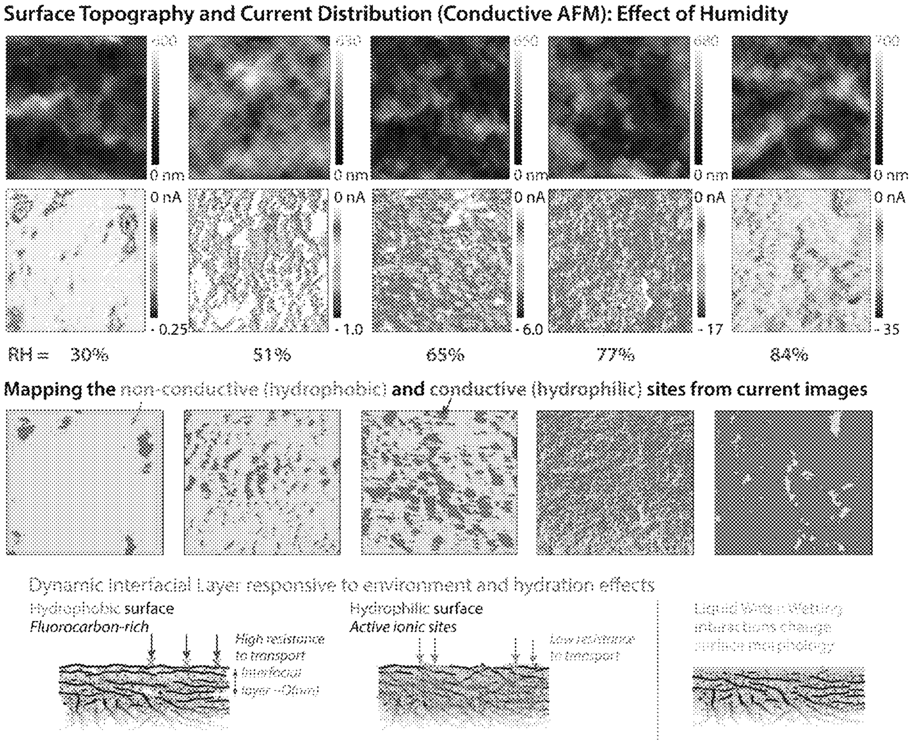
Surface Topography and Current Distribution (Conductive AFM): Effect of Humidity
600
630
650
680
700
0 nm
0 nA
- 0.25
- 1.0
- 6.0
- 17
- 35
RH = 30%
51%
65%
77%
84%
Mapping the non-conductive (hydrophobic) and conductive (hydrophilic) sites from current images
Dynamic Interfacial Layer responsive to environment and hydration effects
Hydrophobic surface
Fluorocarbon-rich
High resistance to transport
Interfacial layer ~0(nm)
Hydrophilic surface
Active ionic sites
Low resistance to transport
Liquid Water Wetting interactions change surface morphology

Figure 26. Humidity-dependent surface topography and current distribution of Nafion 212 membrane based on conductive AFM, shown with the evolution of conductive and nonconductive regions. Shown below is a schematic representation of the change in surface morphology with humidification and in liquid water. (AFM images and surface mapping modified from He et al.[275] Reproduced from ref 275. Copyright 2012 American Chemical Society.)

chain tend to cause more aggregated and disconnected clusters.[449]

In a series of ab initio MD calculations on SSC PFSAs, Paddison and Elliott[62,70,73] demonstrated that the side-chains and their separation by means of the backbone length (m_{TFE}) affects the extent and nature of H-bonding between terminal SO_3^- groups and the number of water molecules needed for H^+ dissociation. There also exists a critical backbone length for SSC PFSAs ($m_{\mathrm{TFE}} = 4$), for which no H-bonding forms between adjacent SO_3H groups in the dry state due to the larger separation. The minimum number of water molecules required to transfer the proton to the water in the first hydration shell and transfer it both scale with the number of backbone CF_2 groups[70,73] (see Figure 25a). The simulations revealed that when the backbone is folded partially, it brings sequential SO_3^- groups closer, thereby allowing water to bind strongly to the protogenic groups. With such conformational changes in backbone, the number of water molecules required for proton dissociation is reduced and it is more likely to be associated with Zundel ions at higher λ, indicating a link between chain flexibility and dissociation. In another AIMD study,[455,470] a hypothetical carbon nanotube structure functionalized by $-CF_2SO_3H$ was modeled with and without fluorine, which showed dissociated protons are stabilized as Eigen-like (H_3O^+) cation in the former case, and as a Zundel in the latter configuration ($H_5O_2^+$), owing to the fact that F atoms stabilize H-bonds and enhance proton dissociation. In addition, proton dissociation was found to increase as the distance between the SO_3H groups decreased.[455,470]

In terms of side-chain effects on phase-separation, shorter backbone and side-chains both lead to better connectivity with more dispersed water-domains, while longer/larger side-chains result in larger domains and stronger segregation.[63,65,67,72,449,461,467,471] Although most of these results were obtained from comparisons of Nafion and SSC,[72,449,472] recent studies reached a similar conclusion for Nafion vs 3M PFSA[456] and 3M PFSA vs SSC (3M PFSA side-chains are more flexible).[67] Shorter pendant chain of 3M simplifies its conformational states, where it is either full extended to form a hook, whereas Nafion's LSC is more delocalized.[456] These effects also manifest themselves when it comes to a membrane's response to hydration; at low hydration levels, high EW and LSCs (such as Nafion) tend to have more aggregated and disconnected domains, while SSCs have better-connected networks (see Figure 25c,d).[63,66,449] Nafion's longer chains also makes them more flexible, which increases mobility especially in the hydrated state.[72,467,472] Thus, for a given λ, d-spacing was computed to be in the order: Nafion > 3M > SSC, in agreement with the experimental observations indicating higher d-spacing for Nafion (Figure 24a), although values are comparable for 3M and SSC in the latter.[63]

Changing the EW for the same side-chain also impacts the phase-separation and transport, in a manner consistent with experimental observations. Increasing EW or backbone length leads to stronger aggregation resulting in fewer but more spread out domains due to the stronger repulsion between the hydrophobic and hydrophobic domains, with higher specific pore area.[65,67,350] Thus, while calculated domain size decreases with higher EW, d-spacing increases,[63,65,67] resulting in a structure with reduced connectivity and thus slower transport (Figure 25c). (See section 4.2.2 for further discussion.)

3.4. Surface Morphology and AFM Studies

Changes in the PFSA surface during hydration and associated interfacial phenomena are key aspects of the transport/nanostructure interplay. The membrane surface, representing the interface between the bulk membrane and environment external to the membrane, not only influences the transport mechanisms as discussed in section 4.1, but is also interrelated to the nanostructural changes within the membrane. Thus, surface morphology and compositions, and their dependence on environmental factors, are strongly coupled to mechanisms controlling the membrane's behavior.

To probe the interface, surface techniques are used. These include X-ray photoelectron spectroscopy (XPS), which probes the chemical composition of PFSA surface from the binding energies of chemical bonds: e.g., for Nafion C:O:F:S = 30 ± 1:60 ± 1:8.6 ± 0.03:1.4 ± 0.1.[473−475] Those studies have shown that hot-pressing reduces the S:F ratio at the surface.[476] The most commonly used technique to characterize the membrane surface is atomic force microscopy (AFM), which can provide useful surface topography data especially when accomplished under humidification. Nevertheless, the true potential of AFM for elucidating PFSA's surface behavior has been unveiled in the past decade when combined with current sensing, so-called conductive AFM (CAFM).[80,272,278,279,477−479] Such electrochemical scanning-probe techniques are powerful tools for imaging the surface morphology, as well as localized electrochemical activity therein, and thus are particularly well-suited for ionomers.[480,481]

Earlier AFM studies observed a hydrophobic fluorocarbon-rich surface depleted of ionic groups in dry PFSA, and a stronger phase-separation with humidification.[221,271,344,361,481] In addition, based on the evolution of the inhomogeneous distribution of current mapping images in CAFM studies,[74,271−279] the fraction of conductive, hydrophilic (active) area increased with increasing humidity, which was associated with enhanced surface hydrophilicity (Figure 26). In these studies, phase-separation at the surface has been evidenced in the form of 25 to 45 nm size conductive, hydrophilic "active" sites comprised of 3 to 15 nm domains, surrounded by PTFE-rich "inactive" regions[51,74,274,363,423] (see also Figure 26). In CAFM, a distribution of current is obtained, which shows an increase in average current as well as broadening of the distribution with increasing humidity, reflecting the enhanced active sites.[272,275−277,279,481,482] Thus, while these active sites are isolated at low RHs, they grow in size and become more connected and conductive with humidity,[51,74,272,274,275,423] which was further enhanced in liquid water.[50] Interestingly, both single-domain conductivity and the number (or fraction) of conductive sites increases with hydration (Figure 26),[275,277,482] although it is difficult to assess whether a hydrophilic site is also electrochemically-active given the nano- to mesoscale variations at the surface.[275,279] Yet, RH-dependent average surface conductivity from CAFM was shown to correlate, at least qualitatively, with bulk conductivity of the ionomer.[74,275] In fact, a monotonic increase in current with RH has also been observed.[74,275,276] The increased fractional area for water entry through the surface has been correlated with mass-transport at the surface, which reveals that the wetting and sorption interactions at interfaces aid in understanding transport mechanisms in bulk membranes, as will be discussed in section 4.1. Such wetting interactions have been shown to have significant effects in water uptake of bulk membranes, where polymer reorganization as well as interfacial resistance at the membrane/vapor interface can limit transport.[137,256,483−487] However, it should also be noted that the strong correlation between the mass transport properties and fraction of surface ionically conducting area is relative in that the magnitudes of the mass-transfer coefficient and/or conductivity cannot be obtained unambiguously without a reference experimental measurement.

Recent CAFM studies also allowed for comparison of various PFSAs. Compared to Nafion, SSC and lower EW PFSAs have more connected, larger water-rich regions with a broader distribution,[50] but interestingly their total conductive area are all similar, regardless of the PFSA.[50,51,274] Thus, while individual nanodomain sizes and their mesoscale distribution appear to be highly dependent on chemistry, the (macroscopic) fraction of conductive area is mainly governed by the environment.

Another property characterizing the surface hydrophilicity of the PFSA membrane is the contact angle. Advancing contact angle of Nafion is 113 to 116° in drier conditions ($\lambda < 5$), which is close to that of PTFE (110°), and decreases to below 100° in saturated vapor,[59,112] and to 83 to 87° when in contact with liquid water.[59,112,270] These values tend to decrease further with lower EWs.[112] Thus, there is a switch from hydrophobic to hydrophilic surface from vapor to liquid saturation, whereas a secondary transition occurs between $\lambda = 5$ to 9,[59,112] where a bound-to-free water transition takes place (see section 2.1). Daly et al.[488] supported this via MD simulations showing a more hydrophobic surface at the membrane/vapor interface than the membrane/liquid one. Thus, in addition to the AFM studies, existence of an interfacial layer has also been studied from the perspective of vapor vs liquid transitions (as discussed in section 4.1.5), in that, interfacial resistance effects are vanished or minimized in liquid water. GISAXS studies of Nafion also confirmed the hydrophobic nature of the membrane surface in water vapor.[266,267] In marked contrast, the surface of a liquid-equilibrated membrane was found to be completely hydrophilic or wetting.[266,267] RH-dependent interfacial effects were observed for O_2 transport as well.[489,490] Gargas et al.[491] employed a pore-directed nanolithography to determine the connectivity of hydrophilic domains through Nafion, which was used as a mask to etch electrochemically the silicon surface underneath leaving a footprint at the Nafion-silicon interface, and found that only 48% of hydrophilic domains beginning at one surface are connected to the other surface. Despite its unequivocal role in understanding surface and transport phenomena, there are still gaps between the quantitative correlation of nanostructural features of bulk membrane and surface (e.g., SAXS vs AFM). Recent studies on PFSA thin films by Krtil et al.,[492] Kusoglu et al.,[493] Davis et al.,[129] Ogata et al.,[494] and Kongkanand[487] all showed distinctly different transport mechanisms due to confinement and surface effects, which will be discussed in section 6.

All of these studies lend credence to the concept of a RH-dependent dynamic interfacial layer at the membrane/vapor interface, a.k.a. "skin layer",[51,206,255,256,274,275,280,360,395,484,487] as illustrated in Figure 26. At low hydration levels, this layer is highly hydrophobic and resistive, with the fluorocarbon chains oriented parallel to the membrane/vapor interface and thereby limiting mass-transport of water and possibly ions. In a hydrated state, however, the wetting interactions make the surface highly hydrophilic and conductive, where the ionic moieties are randomly oriented with more of them facing outward thereby facilitating transport by activating conductive pathways. The thickness of such a skin layer has been under debate despite values estimated be on the order of 10 nm,[51,274,281] yet its influence and effective thickness can be elucidated in conjunction with transport and thin-film studies (sections 4 and 6). This surface (skin) layer can be modified through aging,[277] annealing,[80,398] and other surface treatments.[271] For example, the hydrophobic skin effects can be minimized/removed through surface treatments such as plasma etching with Argon gas causing a more hydrophilic surface with higher ionic activity.[271]

4. TRANSPORT PROPERTIES AND MECHANISMS

Transport phenomena in polymers comprise multiple mechanisms and species moving throughout the matrix at various time- and length scales. These processes are often coupled and generally investigated using a wide range of diagnostic techniques that provide complementary data to define and elucidate the governing mechanisms and structure/function relationships. While there is a rich literature pertaining to these phenomena, there is a need to coalesce the studies to uncover the underlying transport mechanisms, especially as the literature is often contradictory. In this section, all aspects of transport will be reviewed and detailed.

In general, transport in these systems typically considers a linear relationship between the flux of a species and its driving force[495] (see Table 6 and Figure 27)

$$\mathbf{N}_i = -L_{i,j} \nabla \mu_i \tag{30}$$

Table 6. Summary of Transport Mechanisms, Driving Force, and Flow in PFSA Membranes[a]

	gradient or driving force			
flux	hydraulic head	temperature	electrical	chemical
fluid	hydraulic conduction *Darcy's law*	thermo-osmosis	electro-osmosis	chemical osmosis
heat	heat convection	thermal conduction *Fourier's law*	*Peltier effect*	*Dufour effect*
current	streaming current	thermo-electricity *Seebeck effect*	electric conduction *Ohm's law*	diffusion/ potentials
ion	streaming potential	thermal diffusion *Soret effect*	electrophoresis	diffusion *Fick's law*

[a] Adapted from J. S. Newman transport notes.

where $\mathbf{N}_i$ and μ_i are the molar flux density and chemical potential of species i, respectively, and $L_{i,j}$ is related to the frictional interactions between species i and j. The most commonly used measurements techniques in PFSAs for studying transport phenomena and determining the various $L_{i,j}$'s are listed in Table 7, which include (i) transient diffusivity from dynamic vapor sorption (DVS); (ii) steady-state (SS) diffusion or permeation (usually under an applied chemical-potential driving force); (iii) self-diffusivity or local mobility from pulsed-field gradient spin−echo (PGSE) nuclear magnetic resonance (NMR) or quasi-elastic neutron scattering (QENS) (usually exciting a molecule and tracking its interactions and relaxation in the absence of concentration gradient); (iv) electro-osmotic transport of water under applied potential; (v) indirect techniques probing correlated structural changes using time-resolved techniques, such as SAXS, SANS, or Fourier transform infrared-attenuated total reflectance (FTIR-ATR) or dielectric spectroscopy; (vi) and ionic conductivity from AC impedance, broadband dielectric spectroscopy (BES) or electrochemical impedance spectroscopy (EIS). The findings in these studies provide useful information on the processes of transport in PFSA membranes, yet a complete understanding of the transport mechanisms (e.g., water transport) is elusive due to the complex and ill-defined nanostructure of the membrane and its surfaces.

For example, water diffusivity reported in the literature varies up to 4 orders of magnitude, from $D \approx 10^{-8}$ to 10^{-5} cm^2/s (Figure 28) due mainly to the varying testing methods, which could be probing distinct water-transport mechanisms and focusing on certain time- and length scales. Although some of these coefficients can be related by thermodynamic factors for example (section 4.1), others are fundamentally different due to a lack of external gradient (e.g., PGSE NMR), different driving forces (Table 6), or additional phenomena occurring (e.g., transient sorption). Similarly, relaxation times vary depending on the length scales and species tracked (Table 7). Thus, understanding the water-transport mechanisms requires a systematic investigation that bridges the studies conducted at multiple length- and time scales via different experimental techniques (Figure 28). As demonstrated in Figure 28 however, water diffusivity does correlate very well with the length scales over which it is measured.[504] This finding highlights the key role of the morphology/transport interplay that occurs over multiple length scales, from molecular-level fast motions of water and protons to their mesoscale transport restricted by tortuosity and network effects, with an overall impact on macroscopic diffusion and conductivity. Although transport in PFSAs has been widely studied, challenges still remain, especially understanding the underlying mechanisms for simultaneous movement of water and ions within the polymer's phase-separated, dynamically fluctuating structure (see section 3).

4.1. Water Transport

The water-transport mechanisms and techniques can be classified depending on whether it is a steady-state or transient measurement (under a constant concentration-related driving force) or whether it provides information about the (molecular) mobility of water at the meso- or nanoscales (i.e., inter- and intradomain transport). The literature is rich with studies on steady-state and transient water diffusion in PFSA membranes (see Figure 28 and Table 7) including: steady-state transport measurements,[238,298,299,486,497,499,500] internal water profiles,[405,505,506] gravimetric water uptake,[17,137,207,216,238,246,298,484,507,508] time-resolved FTIR,[45,128,379,380] evolution of water-domain spacing using SAXS/SANS,[17,115,116,217] and XRD.[509] Tracer or self-diffusion is commonly measured using NMR as a function of temperature,[95,186,191,244,256,297,298,304,510−512] water content,[47,53,83,95,191,244,256,297,304,395,502,503,513,514] cationic form (as discussed in section 7.3),[44,180,186,510,515−518] pretreatment and annealing,[49,83,191] as well as to investigate various ionomers such as SSC Dow/Aquivion,[6,47,55] Flemion,[44,53,186,503] 3M PFSA,[56,519] and Gore-Select Membranes.[314] It should be noted that water transport in this section refers to only water under water gradients (i.e., diagonal components in Table 6) and not the cross-correlated ones discussed in section 4.3.

As mentioned, transient studies involve water uptake in addition to water transport (Figure 29), and to distinguish this

Table 7. List of Commonly Used Techniques to Study Transport Phenomena in PFSA Membranes

property and probed species	technique	studied phenomena
water transport		
steady-state diffusion, D_{ss}	diffusion	transport driven by concentration gradient in the absence of Δp (= 0) and $\Delta\Phi$ (= 0)
transport coefficient, α	diffusion	transport driven by chemical potential gradient in the absence of Δp (= 0) and $\Delta\Phi$ (= 0)
liquid-water permeability, k	pressure differential	water transport driven by pressure gradient in the absence of Δc_w (= 0) and $\Delta\Phi$ (= 0)
transient (dynamic) diffusion	weight uptake, DVS	diffusivity (dynamic) due to transient weight changes
ion/water transport		
self-diffusion coefficient of protons or water and their mobility	pulsed-field-gradient (PGSE)-NMR	self-diffusion of H^+ or H_2O based on their attenuation in applied magnetic field, in the absence of Δc_w (= 0)
	radio-tracer	self-diffusion based on the isotopic-exchange of radioactivity tagged water internal and external to membrane
	QENS	self-mobility of species in confined molecular geometry based on their interaction and energy exchange with neutrons
"diffusivity" from time-dependent spectra of molecules	time-resolved FTIR	molecular level information from change in vibrations of chemical bond at different wavelength during swelling
"diffusivity" from time-resolved nanodomain response	time-resolved SAXS/SANS	time-dependent changes in nanostructure, e.g., ionomer peak
bulk conductivity	EIS	proton transport and mobility under applied voltage, $\Delta\Phi$
local conductivity	conductive AFM	
dielectric properties and ionic relaxation	broadband dielectric spectroscopy (BES)	dielectric properties and impedance as a function of frequency
electroosmotic coefficient, water transport number	streaming potential/current	transport of solvent and species due to potential gradient in the absence of Δc_w (= 0) and Δp (= 0)
gas transport		
gas permeation	crossover, constant-volume gas permeator	transport of gaseous species due to partial pressure gradient

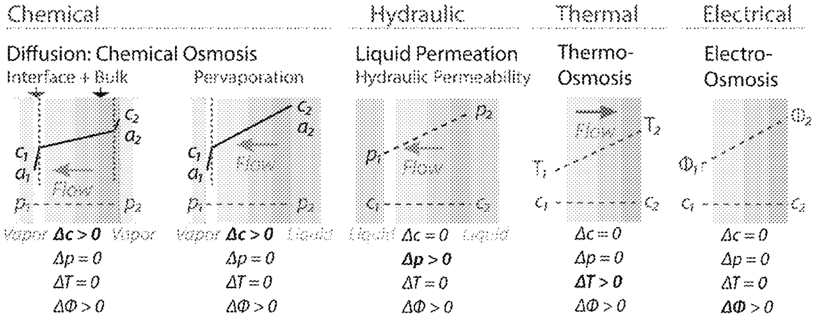

Figure 27. Illustration of transport mechanisms in a membrane for various driving forces. (See Table 6.)

fact, the term dynamic diffusivity is used if the study reports only a single diffusivity (i.e., does not account explicitly for the two processes). Hence, the membrane's nanostructure has to accommodate the nanoswelling and growth of water domains as well as any solvation effects of the polymer chains (see sections 2.2 and 3.2), while providing a pathway for water molecules to move. Thus, the time to reach the equilibrium water-uptake at a given humidity provides information on the time scales for the water transport and interactions inside the polymer. For example, the decrease in dynamic diffusivity with water content compared to steady-state diffusion could be attributed to growth and relaxation of water clusters reducing the water mobility, whereas within the time scale of observation, interfacial mass-transport effects could significantly impact steady-state measurements. Thus, as seen in Figure 28, the values for the dynamic studies are often much lower than those for the steady-state ones. In the following subsections, steady-state and transient water diffusion will be discussed including secondary issues such as interfacial mass-transport resistance and relaxation.

4.1.1. Steady-State Diffusion.

Steady-state diffusion in a PFSA is generally investigated using a diffusion cell where the membrane is subjected to a chemical-potential gradient of water, $\nabla\mu_w$, by controlling the water activity or concentration at both surfaces. Under such conditions, the molar water flux through the membrane is related to the imposed driving force through the characteristic transport property of water, i.e.

$$\mathbf{N}_w = -\alpha_T \nabla\mu_w \tag{31}$$

where α_T is the transport coefficient, and $\nabla\mu_w$ can be expressed as (at constant temperature)

$$\nabla\mu_w = RT\nabla \ln a_w + \bar{V}_w \nabla p \tag{32}$$

In the absence of a pressure gradient ($\nabla p = 0$), eq 31 yields

$$\mathbf{N}_w = -\alpha_T RT \nabla \ln a_w \tag{33}$$

and α_T can be related to the thermodynamic diffusion coefficient using a molarity concentration scale by[254]

$$D_\mu = \alpha_T \frac{RT\lambda}{c_w(\lambda + 1)} \tag{34}$$

Often, Fick's law is used for the water-transport equation, for which, the driving force is concentration gradient, i.e.,

(a) Water Diffusion in Nafion Membrane

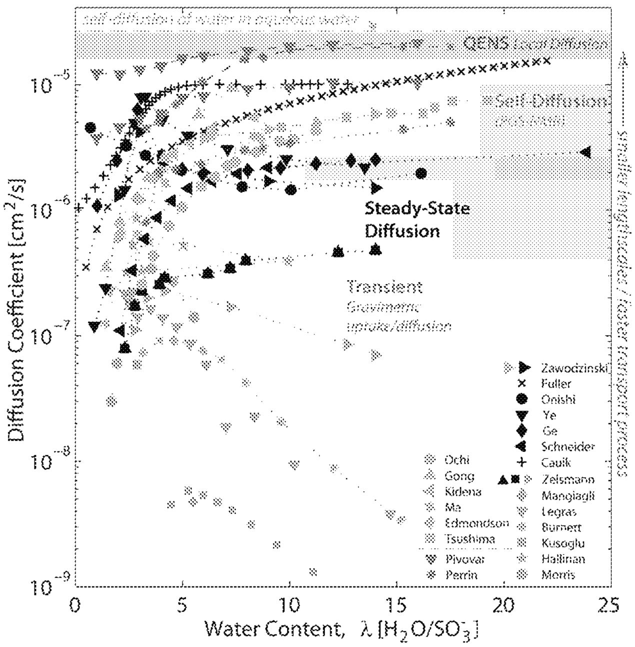

(b) Comparison of water diffusion across time- and length-scales

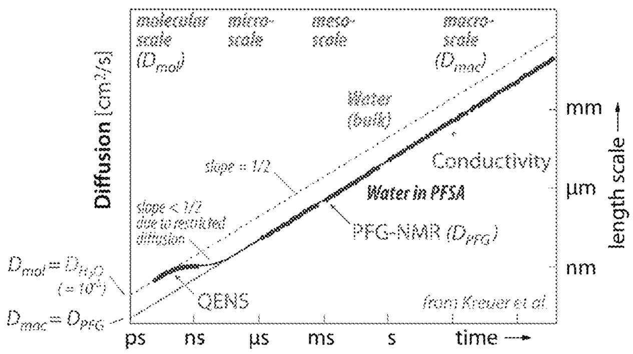

(c) Structure-Transport interplay in PFSAs

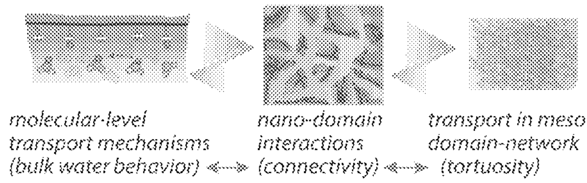
molecular-level transport mechanisms (bulk water behavior)
nano-domain interactions (connectivity)
transport in mesoscale domain-network (tortuosity)

Figure 28. (a) Water diffusion coefficient in Nafion membranes reported in the literature based on dynamic,[128,207,236,246,247,380,496] steady-state diffusion,[483,496−502] self-diffusion (NMR),[53,95,191,244,297,314,502,503] and QENS[233,234] measurements. (b) Plot below shows diffusion of water in aqueous solution and in PFSA, which were measured from various techniques probing water transport across time- and length scales (from Kreuer et al.[504]). (c) Illustration of structure-transport interplay across the length scales (also see section 3.1 for further discussion of morphology).

$$\mathbf{N}_{\mathrm{w}} = -D_{\mathrm{f}} \nabla c_{\mathrm{w}} \tag{35}$$

where D_f is the (Fickian) diffusion coefficient for steady-state diffusion and is concentration-dependent (i.e., $D_f = D_f(c_w)$). The two diffusivities defined above are related by the Darken factor, which accounts for the change in concentration with water activity (arising from the nature of the sorption isotherm, $c_w(a_w)$, discussed in section 2) and relates the thermodynamic diffusion coefficient to the Fickian one

$$D_{\mathrm{f}} = \frac{\partial \ln a_{\mathrm{w}}}{\partial \ln c_{\mathrm{w}}} D_{\mu} \tag{36}$$

It should be noted that this factor is somewhat of a simplification of accounting for activity coefficients and nonideal behavior of these systems as well as the use of only a single solvent and treatment of the PFSA as a single-ion conductor.

Steady-state diffusivities reported for Nafion membrane are generally consistent within the same order-of-magnitude, and increase with water content or humidity (see Figure 28). An interesting observation common among studies is that the steady-state Fickian diffusivity exhibits a sharp peak around $\lambda = 3-5$, whose decrease is followed by a slow increase with additional water, indicating a nonmonotonic dependence on concentration.[128,184,238,483,520] This has been a subject of debate over the decades, since it was discussed in papers by Springer, Zawodzinski and co-workers,[184,502] and has been attributed to the Darken correction, as the derivative term in eq 35 is also nonmonotonic.[238,395,483,500,501,520] Such a behavior was linked to the distinct regimes during water uptake (see section 2.1): very fast diffusion and hydration with initial water molecules where strong ionic interactions persist ($1 < \lambda < 4$), followed by a decrease with the formation of sparsely connected water domains that inhibit water transport. Although such trend was initially associated with steady-state measurements, it was later shown to exist in transient diffusion experiments as well.[17,207,236,238,246]

Determining the steady-state water diffusivity is actually measuring the resistance to water transport through the membrane. However, as the test setups and cell designs vary among these studies, careful attention must be used to ascertain that the correct value is being reported and analyzed, not a combination of effects (e.g., it includes membrane/vapor interfacial resistances). The interfacial resistance and the bulk resistance to water transport can be determined from a steady-state diffusion experiment by measuring the water flux through the membrane at different water activity gradients, $\Delta a_w = a_{w1} - a_{w2}$, and using samples with different thicknesses (L) (Figure 29a). The diffusivity can then be determined as a function of average water activity in the membrane from the measured flux

$$\mathbf{N}_{\mathrm{w}} = \frac{\text{activity difference}}{\text{resistance}} = \bar{c}_{\mathrm{w}} \frac{\Delta a_{\mathrm{w}}}{R} = \bar{c}_{\mathrm{w}} \frac{a_{\mathrm{w1}} - a_{\mathrm{w2}}}{\frac{1}{k_{\mathrm{m,1}}} + \frac{L}{D_{\mathrm{ss}}} + \frac{1}{k_{\mathrm{m,2}}}} \tag{37}$$

where the resistance is the sum of the interfacial resistances ($1/k_m$) at both sides of the membrane and the bulk resistance, which is inversely proportional to the steady-state diffusivity ($1/D_{ss}$) (Figure 29a), and $\bar{c}_w$ is the average water concentration in the membrane between the two activities. Although it is perhaps more appropriate to use the chemical-potential difference, the above is the preferred data analysis method in the literature. Thus, a plot of the measured membrane resistance as a function of membrane thickness, L, gives a straight line where the slope yields the diffusivity and the nonzero intercept, if it exists, gives the interfacial resistance. Note that if the intercept is zero, the interfacial resistance does not exist, and eq 37 reduces to the original expression, $\mathbf{N}_w = \bar{c}_w D_{ss} \Delta a_w / L$, meaning that the diffusion process is not limited by interfacial mass transport. Also, care must be taken to ensure

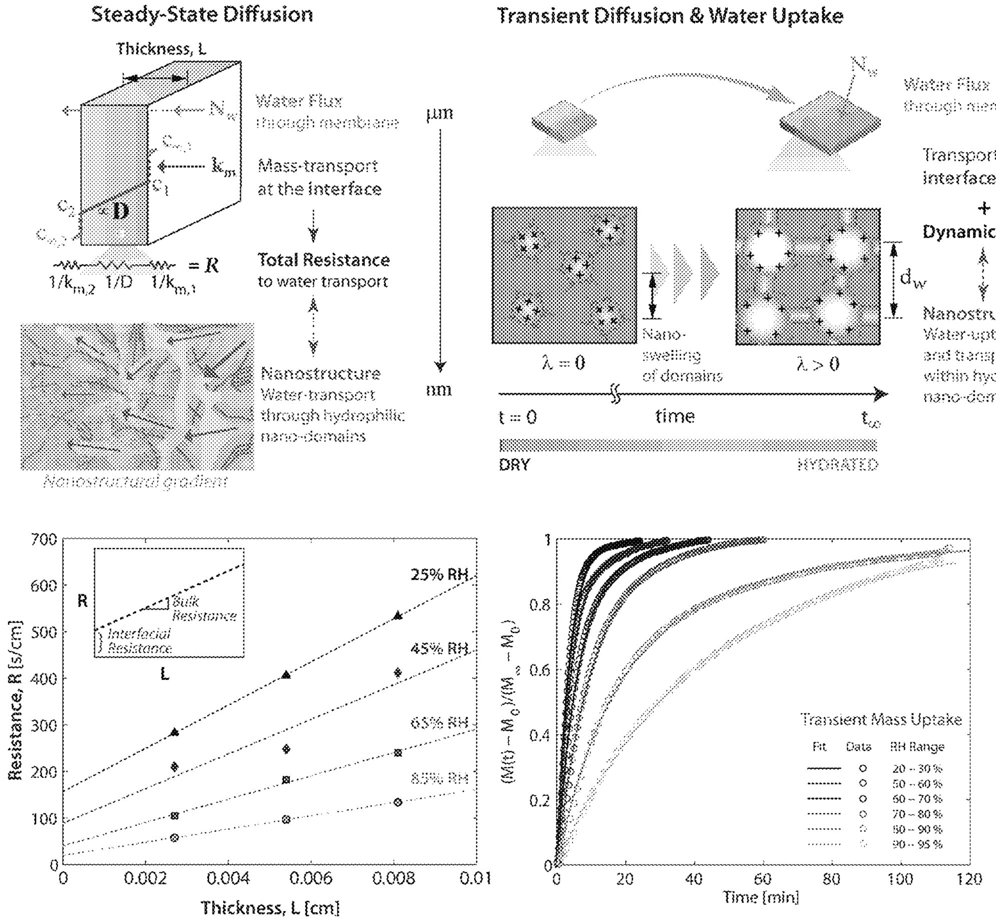

Figure 29. Comparison of steady-state and transient water transport: (a) Resistance to steady-state water transport in the membrane as a function of membrane thickness showing the mass-transport resistance at the interface. (b) Dynamic-vapor-sorption curves at different humidity intervals showing the normalized mass change with time. (The figure is inspired and modified from Kusoglu and Weber.[17])

any external influences such as water-vapor access to the polymer surface or gas-phase boundary layers are minimized and/or considered. A typical resistance vs thickness plot is demonstrated in Figure 29a.[17,486] As discussed later (section 4.1.5), there is an interfacial resistance that changes with activity and must be considered.

4.1.2. Transient Water Uptake and Diffusion.

Unlike steady-state diffusion, transient diffusion involves the incorporation of water and any polymer relaxation or multiscale swelling and is related morphological changes that occur (see section 2.2). These processes result in different functional forms and values for the diffusivity as seen in Figure 28. The dynamics of water transport in PFSA membranes are commonly investigated using time-dependent gravimetric measurements, for example using a dynamic-vapor-sorption (DVS) analyzer. Most studies rely on measuring the change in the mass of the membrane with time at a given temperature and humidity from which the diffusivity of water can be determined (see Figure 29b).

Determination of the diffusion coefficient from a DVS of a membrane going from dry to saturated conditions can be cumbersome. Mathematical modeling of dynamic water transport in PFSA membranes requires a careful examination of thickness, mass-transport coefficients, relaxation, and diffusivity, the competition among which determines the dominant (or limiting) process in the membrane. Moreover, all of these parameters change with concentration and time, which makes it challenging to characterize the dynamics of diffusion. For time-dependent, transient water transport, Fick's second law is often assumed,

$$\frac{dc_w}{dt} = -\nabla \cdot \mathbf{N}_w = -\nabla \cdot D_d(c_w)\nabla c_w \qquad (38)$$

where D_d is considered a concentration-dependent dynamic diffusivity, which, as mentioned above, accounts for both sorption and diffusion, and thus is different than the concentration-dependent diffusivity determined from steady-state experiments. The equation above can be solved with the initial and boundary conditions that are either concentrations internal or external to the membranes or relating the flux of water into the membranes (i.e., Dirichlet or Neumann conditions, respectively). For membranes whose thickness is much smaller than the other dimensions, diffusion in the plane is negligible and diffusion in the thickness direction controls the overall (water) mass uptake. Therefore, it is a common practice to use the membrane thickness, L, as the characteristic length for the diffusion process. The solution to eq 38 results in a characteristic time constant of $\tau_{\text{diffusion}}$ ($= L^2/D_d$). If multiple time constants or transport and sorption processes exist for the system, the above analysis becomes very complicated and it is easiest and more straightforward to assume a phenomenological approach of additive time constants with each term representing different time-dependent process for water transport and uptake

$$\frac{M(t) - M_0}{M_\infty - M_0} = 1 - \sum_m A_m \exp\left(-\frac{t}{\tau_m}\right) \text{ with } \sum_{m=1} A_m = 1 \qquad (39)$$

where A_m is an empirical constant showing the contribution of the process, m, and τ_m is the characteristic time constant for that process. While useful for comparing data, such analysis is not necessarily directly correlated to the governing physical processes. This form can also be used to characterize the diffusion-relaxation process in the membrane by associating a second time constant with the relaxation of the polymer backbone during water sorption. Doing so generally results in a two- to three- orders-of-magnitude higher value than the diffusion time constant,[521] meaning that the overall transport process becomes controlled by the polymer morphological rearrangement. Alternatively, interfacial resistance can be implemented into the equation by setting $\tau_2 = \tau_{\text{interface}} = k_m/L$. Lastly, swelling of the PFSA membrane with water uptake (discussed in section 2.3) must be considered for incorporating the true diffusion length in the analysis (in eqs 30–37).

Unlike steady-state measurements, transient experiments rely on longer time scales of observation during which the same final state can be achieved through various intervals of humidity (or activity). A consequence of using humidity intervals is that two types of transient measurements can be undertaken: (i) integral diffusion, where the sample is instantaneously exposed to a target RH (e.g., 100% RH), and (ii) differential diffusion, where the sample is equilibrated within smaller humidity intervals (e.g., steps of 10% up to 100% RH).[17,137,207,216,238,380,499] By conducting a differential experiment, the humidity or concentration dependence of the diffusivity can be determined. The results of a DVS experiment conducted by measuring the water-vapor uptake by increasing the humidity step by step up to the saturation vapor pressure are shown in Figure 29b.[17] The data suggest that this diffusivity decreases with increasing humidity and reaches its lowest value (10^{-9} cm^2/s) at 100% RH.[128,207,216,247,499] The decrease in diffusivity at high humidities is opposite to those observed in steady-state and NMR experiments, in which it generally increases with increasing RH. The underlying origins of this opposite trend have been attributed to the secondary mechanisms present in dynamic measurements, including water-uptake and longer relaxation times, greater absolute amounts of water necessary at high RH (sorption), or smaller differentials in the chemical-potential gradient (although the RH interval is fixed). Mangliagli et al. explained the slower sorption at high RH by the smaller enthalpy of solvation in an already-hydrated membrane, which effectively reduces the rate of additional water uptake.[207] Related to this is the observation that PFSAs exhibit non-Fickian diffusion at very low humidification (0–20%),[380] undoubtedly related to the impacts of solvation energies under those conditions (see section 2.6). The slower diffusion at higher RH intervals is consistent with observations of stiffer backbones exhibiting slower water-uptake responses[207] and can be correlated to nanodomain swelling and related structural properties.[17] Thus, the nature of diffusion process in PFSA is strongly dependent on the type of the measurement and the transport mechanisms it probes, which become more complex over larger concentration gradients and time scales.

Dynamically, both sorption and desorption processes can be examined, and desorption has been shown to be faster,[17,207,236,256,380,483,508] with up to an-order-of-magnitude higher diffusion,[483,484,492] (for methanol as well[190]) and attributed to either water organization,[207] interfacial effects,[137,483,484,487] or heat of condensation.[508] As for the latter, during sorption, there is an increase in temperature due to the heat of condensation of the vapor, which has the effect of lowering the water-vapor activity relative to the higher membrane temperature and, therefore, decreasing the sorption rate.[508] Interestingly, no rate difference was observed in FTIR-based molecular diffusion studies[380] or when diffusion was measured under vacuum,[238] while interfacial effects during sorption/desorption have been shown to be effective at low flow rates[380] and for thin films.[487,492] This observation is probably due to differences in polymer surface and internal structure (i.e., initial state), which is dominant in thin films. For example, one can explain a faster desorption rate based on the notion that it is easier to expel and contract the water domains rather than expand them (i.e., larger domains facilitate water removal).

4.1.3. NMR Studies and Self-Diffusion.

The thermodynamic diffusion coefficient, D_μ, can be determined by pulsed field gradient spin–echo (PGSE) NMR. Benefits include probing the internal movement of the water, and thus minimizing impacts of boundary conditions and interfacial phenomena. In PGSE NMR, an intradiffusion coefficient for species bearing the detected nucleus is determined from the diffusional dephasing of (or loss of phase coherence in) a gradient-encoded magnetization. Thus, with varying field gradients, one can detect the diffusive transport of this tracer species (i.e., tracer-diffusion) at various diffusion times and length scales (Δ = 4−600 ms).[44,53,186,244,297,369,502,504,511,512,522−526] While shorter times (ms) give the molecular diffusivity of water molecules within shorter length scales (μm), longer times could probe diffusion, and restrictions to it, over longer length scales (e.g., multiple domains at the mesoscale) providing information on morphological features and tortuosity of the percolation pathway.[256,502] It must be noted, that NMR measures the ensemble of ^{1}H nuclei and therefore is a weighted average of all diffusion coefficients in the different environments. In addition, NMR measures a tracer diffusion and not a true self-diffusion, although they can be correlated for the larger length scales with appropriate interpretation and evaluation (see section 4.4). [Throughout the text, we use tracer and self-diffusion interchangeably, although the former is for NMR experiments exclusively.]

NMR studies of Nafion investigated the dynamic water behavior by means of the relaxation time, which increases with increasing hydration (λ) (from ~10 to 200 ms),[47,55,502,522] and temperature.[297,313,435,522,524,527,528] At low hydration levels, the molecular motion of water is influenced by the acidity and mobility of the SO_3H groups to which the water molecules are coordinated, which makes water reorientation easier in confined hydrophilic domains, as evidenced by the low NMR relaxation time (T_1).[55,519,528,529] At higher hydration levels, their behavior is more controlled by the size of the hydrophilic domains and approach bulk-water.

A frequently reported property from PGSE-NMR of PFSA membranes is the tracer-diffusion coefficient, D′, as a function of hydration and temperature,[44,47,53,55,186,297,304,313,314,502−504,517,519,530] as well as cation effects. In PGSE-NMR, one cannot distinguish between the neutral or charged species (e.g., H_2O vs H_3O^+), and thus the mobility calculated from tracer diffusion is a related but ambiguous representative measure of conductivity[502,504,530] (see section 4). In fact, tracer diffusion in cation-exchange membranes provides insight into the separation of such mechanisms (see section 7.3). For example, Saito et al.[44] reported that, in PFSA-Li^+ membranes, self-diffusion for Li^+ (D_{Li+}) does not changes as a function of diffusion time, Δ, but self-diffusion for H_2O decreases; indicating slower mobility over longer length scales due to the heterogeneous nature of the water-transport pathways. The fact that the self-diffusion of water in aqueous water is constant over Δ further supports the role of contributions from interacting (bound) water molecules with H-bonding in PFSA-H^+ membrane.

Figure 30 shows diffusivity data for several PFSAs including Dow, Aquivion,[47,55] Flemion,[44,53,186,503] 3M PFSA,[56,519] and Gore-Select Membranes.[314] Even though the tracer-diffusivity slightly increases for lower EW ionomers,[44,47] it does not change significantly for reinforced membranes, implying that macroscopic reinforcement does not restrict mobility at the length scales probed by NMR.[525] At subzero temperatures, D' reduces significantly, indicating that water molecules still exists in a mobile state but with slower diffusion, in accord with the presence of bound water but a reduced amount of free water[304,313,314] (see section 2.5). At low λ, water has a lower mobility due to its strong interaction with the ions (i.e., bound water), giving rise to a low D'. With increasing λ (or φ_w), water mobility and D' increase and approach the self-diffusivity of bulk water, D'_{aq}, which can be expressed as

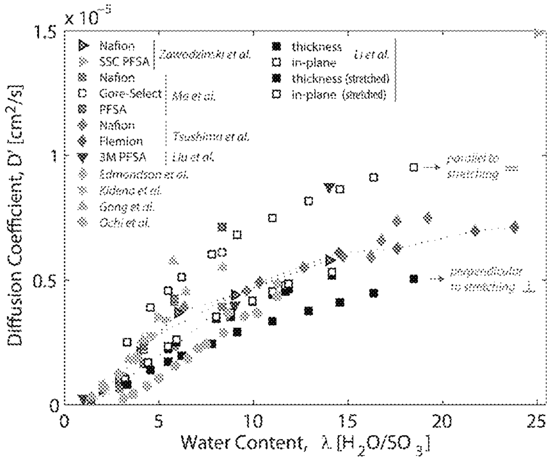

Figure 30. Water tracer-diffusion coefficient of PFSA membranes as a function of water content (25−30 °C), compiled from the PGS-NMR data in the literature: Nafion (1100 EW),[53,191,244,297,314,502,503] Dow,[502] Flemion,[503] 3M,[10] Gore-Select,[314] as well as anisotropy of D′ and stretching effect for Nafion membrane (from Li et al.[369,525]).

$$D'(\phi_w) = \frac{D'_{aq}}{\tau}\phi_w \tag{40}$$

where τ is the tortuosity. Although the general trend is to interpret the diffusivity data with respect to a tortuosity or increased path length,[256,531] the self-diffusion of water has also been analyzed using free volume theory. In this analysis, the diffusion process is described based on a diffusing species of free volume, v_f, moving through a hole that is larger than a critical volume, v^*, i.e., $D \propto \exp(-gv^*/v_f)$.[53,297,510,531] Such a (free) volume effect was shown to capture the measured data by accounting for the size effect of the diffusing species, in particular for water and alcohols.[53,297,510,531]

Another phenomenon studied by combined NMR and conductivity experiments is the activation volume measured under high pressure, which can be interpreted as the volume change when a diffusing species transfers from a "normal" position to an "activated" position.[289,514,532] When a proton transfers from a H_3O^+ ion to a separate water molecule, it moves from a high volume to a low volume (where H^+ is shared by 2 water molecules), thus the negative activation volume. The activation volume decreases with increasing λ, where transport is dominated by bulk/free water similar to aqueous solutions, whereas at very low λ (i.e., bound-water regime), the activation volume is high and transport is controlled polymer-chain motions and interactions.[289,514,532]

Self-diffusion of water and hydronium ions in PFSA has also been calculated from MD simulations from the mean-square displacement of species at various hydration levels.[72,357,442,449,533] MD studies by Vishnakov and Neimark suggested that water could travel even in the absence of continuous pathways by forming short-lived dynamic bridges ($\tau_{br} \approx O(100\text{ ps})$) that create temporary connection between the nanodomains if they are sufficiently close.[413,451,466] These values are in the same order as discussed in modeling[446,447,534] and QENS[233,234,429,529] studies, which helps elucidate the coupled nature of water-proton transport via hydronium (H_3O^+) or larger solvated ions (see section 4.4.2). This time scale for an intermolecular bridge of $l_{br} \approx 0.3$ to 0.5 nm gives a diffusivity 10^{-5} cm/s, close to that of bulk water.[451] Devanathan et al.[446] and Cui et al.[449] calculated that self-diffusion for H_2O is higher than that for H_3O^+ ($D_{H2O} > D_{H3O^+}$). Also, compared with the experimental data, the former was higher while the latter was much lower, due probably to the existence of proton hopping mechanisms.[446,449] Cui et al. found higher diffusivity in Nafion compared to SSC PFSAs, due to its larger nanodomains, although less well-connected at the mesoscale.[449]

In addition to the tracer-diffusion coefficient, NMR relaxometry also provides information related to the mobility of water molecules and their interactions with SO_3^-. For example, the activation energy for reorientation of water molecules in confined domains (inferred from NMR) increases with hydration due to a reduced probability of H-bonding with the neighboring SO_3^- sites.[55,522,528,529,535] Perrin et al.[529] showed using NMR relaxation that the diffusion is more anisotropic and 2-D at lower hydration, due to more locally structured water therein, and becomes more 3-D at higher water contents. Hickner and co-workers[55] reported shorter NMR relaxation time of SSC compared to Nafion, which was attributed to ability of its flexible short side-chains to promote reorientation of $O - {}^2H$ bonds around the water molecules, in line with its higher conductivity at given λ. In a recent study, lowering the EW in 3M PFSA was found to reduce the relaxation times of water, indicating faster mobility.[519]

Finally, while Nafion 212 membranes exhibit nearly an isotropic diffusion inferred from D′ measured in the plane and thickness directions,[512,525] there is an anisotropy in Nafion 112 membranes that are extruded, with faster diffusion (up to 18%) in the extrusion direction.[525] Madsen, Moore and co-workers[369] carried out a systematic investigation on the self-diffusion of water in each direction in a stretched Nafion membrane as a function of draw ratio. D′ was observed to increase in the draw direction, and decrease in the transverse direction in such a way that D′ averaged from the three directions falls on the same curve for all of the draw ratios (Figure 30).[369,536] These results support the morphological picture of interconnected locally flat hydrophilic domains that could exhibit preferential orientation under a macroscopic deformation. This finding was supported in later NMR studies,[404,537] exemplifying the structure-diffusion interplay, and a structural anisotropy on the order of 70 nm was observed upon stretching.[404] A rather interesting behavior was observed by Lin et al.[296] on prestretched Nafion membranes (see section 3.1.5), where water mobility reduced with increasing (pre)draw ratio but its self-diffusion remained unaffected, demonstrating the separate effects of meso- and nanoscale transport processes.

4.1.4. Liquid Transport.

Unlike the above analysis with water diffusion that depends on a difference in concentration (e.g., humidity or water partial pressure), transport of liquid water across the membrane does not involve concentration changes. It is pressure-driven, which can be related to a chemical-potential driving force

$$\nabla\mu_{\mathrm{w}} = \bar{V}_{\mathrm{w}}\nabla p \rightarrow \mathbf{N}_{\mathrm{w}} = -\frac{k}{\mu_{\nu}\bar{V}_{\mathrm{w}}}\nabla p = L_{\mathrm{P}}\nabla p \tag{41}$$

where μ_{v} is the viscosity, L_{P} is the hydraulic permeability coefficient,[340,538] and k is the membrane permeability (in the range of 3 to 5 × 10^{-16} cm^2).[137,269,484,498,501,508,539−542] The assumption above is that the flow across the membrane due to a liquid pressure gradient follows a Darcy's-law type expression, something common in porous media and commonly used to analyze pressure-driven flow in PFSA membranes.[93,485,518,540−548] Using this formalism, the transport coefficient from eq 30−31 can be related to the permeability as

$$\alpha_{\mathrm{T}} = \frac{k}{\mu_{\nu}\bar{V}_{\mathrm{w}}^{\,2}} \tag{42}$$

Similar to diffusivity, the value of the hydraulic permeability coefficient depends on membrane pretreatment effects[93] and mechanical modifications,[485,541,542,547,549] and increases with temperature.[540,542,549−551] Also, due to the nature of the experiment, dynamic liquid-transport experiments are not conducted and those that probe related processes (e.g., SAXS for domain spacing and water-profile analysis in section 4.1.6),[115,116,405,552] demonstrate much more rapid changes and hence faster time constants than in vapor experiments. The effect of water phase on sorption behavior has been attributed to the thermal history[94] and the distinct processes for water transport from liquid and vapor phases,[95,253,254] where the latter is related to the interfacial resistance at the membrane/vapor interface[253,266] and surface nanostructure.[266,267]

4.1.5. Liquid/Vapor Transport and Interfacial Resistance.

As noted in section 2.2, there is a change in water content and morphology depending on the phase of water that is contacts the PFSA membrane surface (i.e., Schröder's paradox).[1,94,95,203,254,255,258,262,521] Similarly, as discussed above, there are also different values for the transport coefficients and even their meaning depending on how the chemical-potential gradient is interpreted due to the phase of water. Thus, there is a natural difficulty in analyzing data with both liquid and vapor boundaries (i.e., pervaporation).[520,541,544,553] In these experiments, a higher flux is achieved when liquid is present on one surface.[540−542,544] Adachi et al.[541,544] measured the water flux though the membrane with vapor/vapor, vapor/liquid, and liquid/liquid boundaries and found that the liquid-equilibrated transport coefficient (determined from the slope of flux vs chemical potential) was the highest for the membrane exposed to liquid water on both sides, and lowest for the vapor-exposed membrane as shown in Figure 31. These results also suggest a difference in the nature of the transport mechanism and the mesostructure it is transporting within (e.g., changes in surface structure).

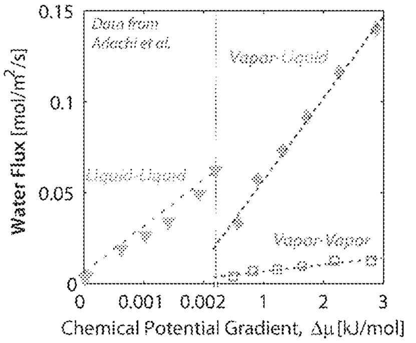

Figure 31. Measured flux as a function of chemical potential gradient for various cases (from Adachi et al.[544]).

Related to the issue of liquid versus vapor boundaries is the existence of an interfacial resistance to mass transport. Such a phenomenon can be derived from steady-state measurements by varying the membrane thickness as shown in Figure 29a and described in section 4.1.1. A nonzero intercept, as shown in the figure, allows for the calculation of the mass-transport coefficient (see eq 37), which is written as a serial resistance for water transport

$$\mathbf{N}_{\mathrm{w}} = k_{\mathrm{m}}(\mu_{\mathrm{int}} - \mu_{\mathrm{ext}}) \tag{43}$$

where int and ext represent internal and external to the membrane, respectively. The mass-transport coefficient is a function of temperature and humidity, where it increases almost exponentially with humidity or slightly greater than linearly with λ (Figure 32).[275,486] Various values of k_{m} are given in Table 8.[275,484−486,500,540]

The increase in mass-transfer coefficient or decrease in interfacial resistance with humidity can be rationalized based on the existence of a varying PFSA surface morphology. As discussed in section 3.4, and illustrated in Figure 26, the surface morphology adopts configurations that are humidity dependent with increased hydrophilicity and open channels with higher humidities. This change in surface morphology is in agreement with studies on vapor vs liquid effects, where interfacial resistance effects are vanished or minimized in liquid water[137,485,501,541,549] and at higher humidities as measured by various means including diffusion and transport,[256,395,483,485,487,489,508,549] and water uptake,[255] in situ X-ray tomography,[405] Raman spectroscopy,[395] MRI,[555] and time-resolved SAXS.[115] In addition, Daly et al.[488] supported this via MD simulations showing more hydrophobic surface at the membrane/vapor interface with a mass-transport resistance comparable to that of Teflon, and higher than the bulk resistance of the membrane (beneath its surface). There is compelling evidence to suggest that that hydrophilicity of the surface has a direct role in transport properties across the surface including ion conductivity and water transport.[275,556] For the latter, He et al. directly related the increased fractional surface area for conduction (f_a) to the mass-transport coefficient with a simple power-law expression, $k_{\mathrm{m}} \propto f_{\mathrm{a}}^{0.5}$,

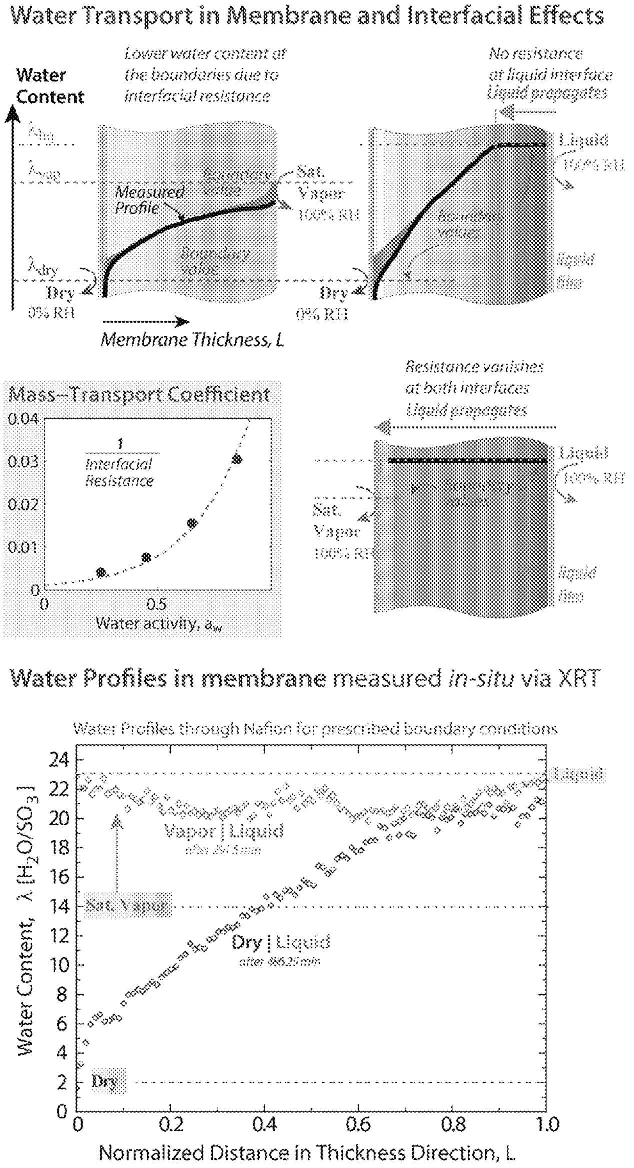

Figure 32. Illustration various water profiles that can form in the membrane depending on the boundary conditions and the associated surface morphology controlling the interfacial resistance. As shown in the inset, the mass-transport coefficient, k_m, increases, and interfacial resistance decreases, with increasing humidity[486] and disappears in liquid water, which impacts the water profile when one surface is liquid-equilibrated. Shown below is the water profile across a membrane under dry/liquid and vapor/liquid boundary conditions measured using computed X-ray tomography (from Hwang et al.[405]). Interfacial mass-transport data are taken from ref 275.

demonstrating the linkages between resistance, surface morphology, and humidity.[275]

An effective way to illustrate the dominant transport mechanism for steady-state water transport, and in which membrane relaxation does not play a role, is through the Biot number, which is the ratio of the characteristic time for bulk diffusion of water, $\tau_{\text{diffusion}}$, to that for mass transport through the membrane surface, $\tau_{\text{interface}}$

$$Bi = \frac{k_m L}{D} = \frac{L^2/D}{L/k_m} = \frac{\tau_{\text{diffusion}}}{\tau_{\text{interface}}} \tag{44}$$

Table 8. Studies on the Vapor/Liquid Interface, Interfacial Resistance, and Mass-Transport of PFSA Membranes[a]

ref	method and analysis	mass-transport coefficient, k_m [cm/s]
Okada et al.[554]	model	$1 - 9 \times 10^{-4}$
Ge et al.[483]	steady-state permeability	sorption: $3.53 \times 10^{-3}\ \phi_w$, desorption: $1.42 \times 10^{-2}\ \phi_w$
Ye et al.[501]	steady-state	$\sim P_w^{\ 1.5}$
Satterfield et al.[137]	sorption	2.8 to 10.6 (50 to 250 μm thick)
Kienitz et al.[486]	steady-state	$k_m \approx 10^{-3}\phi_w$
He et al.[275]	conductive AFM	$k_m \approx 10^{-4} \times$ conductive area (Figure 26)
Kongkanand[487]	sorption in thin films	sorption: 2×10^{-4} desorption: 5.9×10^{-4}
Zhao et al.[256]	permeability	$1.2 - 3.8 \times 10^{-3}$ (30 to 80 °C)
Adachi et al.[541]	permeability	4.5×10^{-4} 70 °C
Tabuchi et al.[395]	Raman spectroscopy	$1.25 - 10 \times 10^{-4}$ at 70 °C
Monroe et al.[485]	permeability	0.63–0.75

[a] Temperature is 25 °C unless otherwise noted.

If, for example, water transport is limited by the interfacial resistance at the membrane/vapor interface ($k_m \to 0$), then the characteristic time constant for mass-transport becomes high ($\tau_{\text{interface}} \gg \tau_{\text{diffusion}}$) making the Biot number small ($Bi \ll 1$). If, on the other hand, interfacial resistance is negligible ($k_m \gg 1$), then Bi becomes large indicating diffusion limited. Note that, with the other properties remaining constant, reducing the thickness also decreases Bi thereby creating interface-limited transport. In fact, for very thin films ($L \to O(\text{nm})$), transport resistance is thought to be of interfacial origins (see sections 6 and 3.4). In fact, one can consider that some of the reported diffusion coefficients or rate-constants for PFSA thin-films could be interpreted as, and correlated to, the interfacial mass-transport coefficient. On the other hand, for $\tau_{\text{diffusion}} \gg \tau_{\text{interface}}$, water transport is limited by the bulk diffusion and interfacial effects are negligible. This often occurs in dynamic measurements since the studies exhibit small diffusivities due to additional sorption behavior and polymer relaxations (see section 4.1.2), thus yielding large Bi. In general, the critical value for Bi that determines which process dominates is around 10.

Finally, as noted above, one must be careful to ensure that gas-phase boundary layers are accounted for and not influencing the determination of the interfacial mass-transfer coefficient. For example, Onishi et al.[499] and Mittelstad[238] measured water-diffusivity under varying pressures to eliminate boundary-layer effects. In particular, the discrepancy between the steady-state and transient diffusivity values was shown to disappear when measured in vacuum.[238] However, this is not unexpected since the nature of the interaction with the surface is more hydrophilic due to the greater number of collisions of water molecules and perhaps existence of a liquid-water film on the surface. Thus, while one can minimize traditional gas-phase boundary layers, the influence of the inert on the surface structure plays a role.

4.1.6. Modeling and Membrane Water Profiles. Due to the complex transport mechanisms with interfacial resistance and concentration-dependent diffusivity, mathematical modeling has been used to predict the water profiles in PFSAs under various conditions including in electrochemical applications. Incorporating the various effects makes the model challenging as it becomes highly nonlinear, especially if one is solving

Table 9. Summary of the Water-Distribution Measurement Studies in the PFSA Literature Listed with the Technique Used, Its Resolution and Environmental Conditions[a]

study	Nafion	technique		spatial (μm[c])	temporal (seconds)	T (°C)	RH (%)
Hwang et al.[405]	N117	X-ray tomography	ex situ	1.3	~600	25	0−100[b]
Morin et al.[552,565]	N117	neutron scattering	in situ	~10		80	100
Huguet et al.[566]	N115	confocal Raman spectroscopy	in situ	~7	~900	25−50	25−100
Hara et al.[567]	N212		in situ	~5		40−110	0−90
Peng et al.[46]	N212, Aquivion	Raman microspectroscopy	in situ	~7	~3600	60−70	0−100
Zhang et al.[568]	N1110	magnetic resonance imaging (MRI)	ex situ	~8	~120	15−19	0−100
Ouriadov et al.[569]	N117		ex situ	~5	~600	25	~30[d]
Tsushima et al.[570]	N1110	EMRI[e]	in situ	50.8	~3600	70	40−92
Suzuki et al.[555]	N1110	MRI	ex situ	25.0		25	0−80
Albertini et al.[571]	N117	X-ray diffraction	in situ	8.6	75	RT	100
Quan et al.[572]	N117	neutron radiography	in situ	25.0	~60	60, 80	100
Hussey et al.[506,573]	N1140, N117		in situ[f]	~15	~60	80	0−100[b]
Bellows et al.[574]	N117 (×4)		in situ	~40		80	69−93
Hickner et al.[575]	N112		in situ	~16.4	~1200	40−80	100

[a] Adapted from ref 405 and updated. [b] Vapor vs liquid conditions are also studied. [c] Size that each data point covers. Unless it is specified in the original paper, the spatial resolution is calculated based on the sample thickness and the data points shown in the original papers unless it was addressed. [d] Ambient humidity, ~30% is approximated. [e] EMRI: environmental magnetic resonance imaging. [f] Also studied transport in situ in fuel cells.

water-uptake morphological models simultaneously (see section 2.6). In addition to the steady−steady state resistance models discussed earlier,[275,484−486,500,540] nearly all transient models start with Fickian diffusion (eq 38), and either modify the governing equation to account for water-uptake during transport, or the boundary conditions to reflect better the mass-transport effects at the surface. Such boundary conditions include using mass-transport[238,507,557] or vaporization-exchange rate constant at the membrane/gas interface,[557,558] additional terms to represent the water transfer reaction in and out of the water domains,[492] and mass-transfer coefficient at the boundaries to analyze time-dependent swelling based on water uptake,[137,483,484] reflection absorption spectroscopy IR,[129] and FTIR data.[559] For example, the diffusion-reaction model by Hallinan et al.[380] incorporated additional first-order concentration-dependent terms to account for water-uptake of domains, which also participate in diffusion. This phenomenon was also discussed by Kusoglu and Weber[17] based on transient SAXS observations that seem to be a key feature for separating steady-state and dynamic diffusion as illustrated in Figure 29. One way to express the various transport mechanisms mathematically is to use a phenomenological multiple-term relaxation model defined in eq 39. Even though additional terms can easily be incorporated to include other processes controlling the water transport, a two-term expression has been shown to be sufficient to reproduce the time-dependent water-uptake behavior of Nafion membranes,[17,137,487,521] which has also been adopted in some works[17,115,137,360,487] including to identify differences between sorption and desorption kinetics.[137,485,487]

Beyond just understanding water transport, an important reason modeling is used is to visualize the water profile inside the typically relatively thin PFSA membrane (<100 μm). Elucidating water profiles in the membrane for various boundary conditions have been an integral part of transport studies and models, in most cases related to PEFCs modeling.[14] In early modeling work, Springer et al.[560] calculated a nonlinear water distribution due to a concentration-dependent diffusivity. Later Buchi and co-workers measured the water content by probing resistance via interlayered electrodes in between stacked Nafion membranes and modeled the 1D profile.[505] Weber and Newman developed a mathematical model, which accounted for the above-mentioned internal vapor/liquid interfaces in the membrane including different transport modes. Weber and Hickner[561] and Hussey et al.[506] later determined the membrane's water profile using neutron imaging and mathematically modeled it. It must be noted that these models also account for electroosmosis (which is discussed in section 4.3.1) to predict water profiles under operation; such simulations are commonly employed in transport-property studies on PFSAs[6,506] and reviewed elsewhere.[14,20]

In situ determination of the internal water distribution in PFSA membranes has been of interest (Table 9), yet challenging due to technique limitations, in particular low spatial and temporal resolutions (~10 to 40 μm).[28] Similarly, despite neutron imaging's potential for noninteracting and nondestructive imaging, blurring effects limit exhaustive studies on water behavior.[506,561−564] In contrast, transmission-scattering-based techniques provide information averaged over the volume of the material along the beam path with better spatial resolution (~1 μm),[28,405] suffer from low water sensitivity which makes it challenging to visualize the water profiles. The range of the spatial resolution and water sensitivity of the other techniques lie between the two. Details of previous studies on the water-distribution measurement using various techniques are listed in Table 9.

From neutron imaging, the membrane's water content was found to be dependent on the level of compression in the fuel cell (e.g., caused by clamping force[336]), as well as on the humidity, where it was found that only by matching the phase in contact with the membrane could agreement between model and experiments be reached in terms of water content.[194,506,561] Most of these in situ measurements, however, bring two challenges: (i) the measured distribution is a result of the convolution of water phenomena from diffusion- and/or permeation-driven flow and also electro-osmotic and other flows, and separating their contributions is difficult, and (ii) the boundary conditions of the membrane are difficult to control

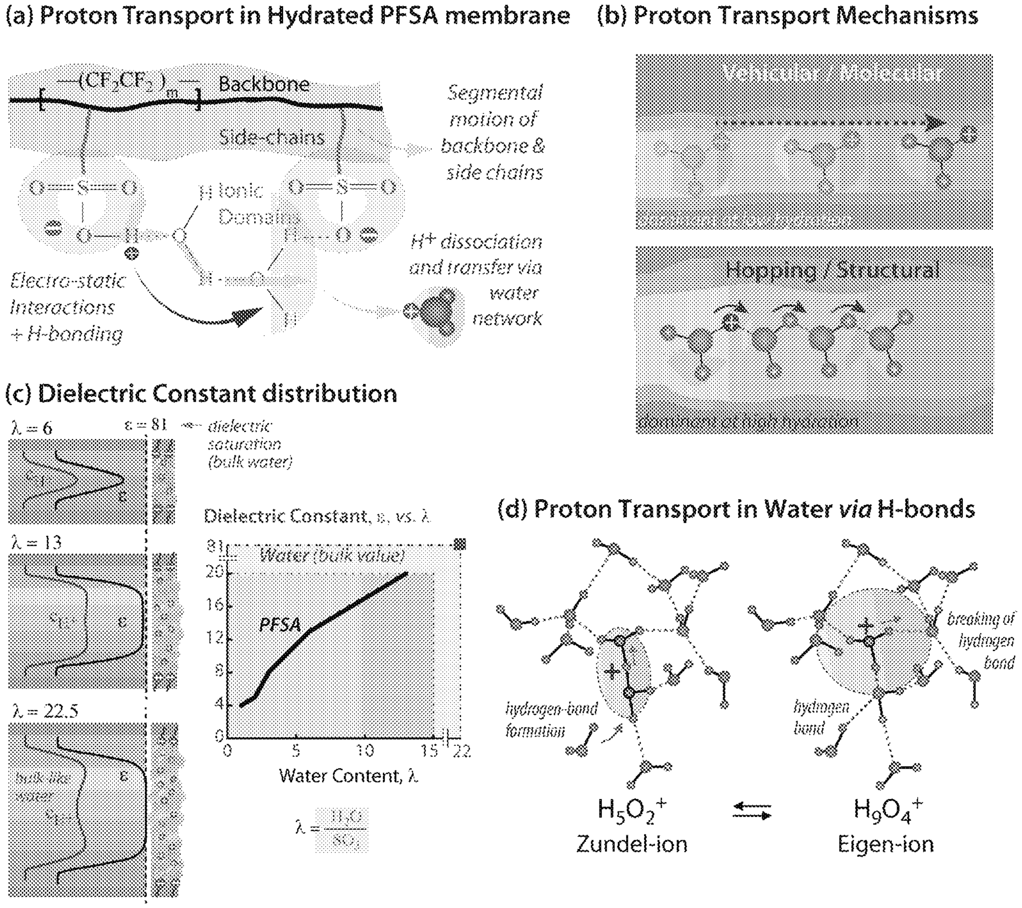
(a) Proton Transport in Hydrated PFSA membrane
(b) Proton Transport Mechanisms
—(CF2CF2)m— Backbone
Side-chains
Segmental motion of backbone & side chains
Ionic Domains
H+ dissociation and transfer via water network
Electro-static Interactions + H-bonding
Vehicular / Molecular
dominant at low hydration
Hopping / Structural
dominant at high hydration
(c) Dielectric Constant distribution
λ = 6
ε = 81
dielectric saturation (bulk water)
λ = 13
λ = 22.5
bulk like water
Dielectric Constant, ε, vs. λ
Water (bulk value)
PFSA
Water Content, λ
λ = H2O / SO3
(d) Proton Transport in Water via H-bonds
hydrogen-bond formation
breaking of hydrogen bond
hydrogen bond
H5O2+
Zundel-ion
H9O4+
Eigen-ion

Figure 33. Proton conduction mechanism in hydrated PFSA; (a) chemical structure and key structural factors influencing the proton transport, (b) illustration of vehicular and hopping mechanisms, (c) distribution of proton concentration and dielectric constant across a hydrated domain for three water contents, λ. The plot shows dielectric constant as a function of water content, λ (from ref 578). (d) Role of Zundel-ion and Eigen ions in facilitating proton transfer via hydrogen-bond breaking and formation in the second hydration shell. (c) and (d) are inspired from studies by Kreuer et al.[16,579,580] Paddison,[23,581] Tuckerman et al.,[582] and Pintauro.[583]

since it is assembled with the electrochemical components such as porous electrodes.

Recently, Hwang et al.[405] used computed X-ray microtomography to examine water distributions within PFSA ionomers with high spatial (~1 μm) and temporal (~10 min) resolutions under different surface concentrations. An interesting observation shown in Figure 32 is that a membrane that is equilibrated with liquid water on one side ($\lambda = 22$) and with saturated vapor ($\lambda = 14$) on the other side exhibits a flat profile at $\lambda = 22$, which is probably due to a liquid film of water formed on the vapor side due to crossover of water. Such flat profiles were observed by Morin et al. using scanning SANS.[28,552,565] However, when one vapor-saturated surface is dried ($\lambda = 2$), the liquid interface cannot transport fully across the membrane and thus a flat region exists within the membrane. Figure 32 also clearly shows a complex and slower evolution for the water profile with a gradient if a difference of saturated vapor-to-dry vs liquid-to-dry is applied across the membrane. Although in these cases the surface has the same water activity, $a_w = 1$, the existence of interfacial resistance for the vapor case (but not for the liquid case) is clearly evident in the water-content drop at the interface in the vapor case and not the liquid one. Overall, more research into the water profiles and associated modeling of the various transport mechanisms will enable greater understanding of the underlying processes that occur related to water transport in PFSAs.

4.2. Proton Transport

The transport of water and ions is highly coupled. Transport of ions in PFSA is not only dependent on water, but also governed by the nature of water, its interaction with the SO_3^- sites, by the side-chain (its length and hydrophilicity), as well as the segmental motions of the polymer chains in terms of defining the mesoscale transport network as shown in Figure 33. Thus, proton conduction involves multiple sequential and interrelated processes, starting with the dissociation of the proton and formation of an ion-pair with water (or solvent) at the molecular scale, water-mediated transport through the hydrated domains at the nanoscale, and long-range mobility within the water network at the mesoscale, where restrictions to transport and tortuosity impact overall macroscopic conductivity. Therefore, proton transport in PFSAs is linked to water behavior at multiple length- and time scales, wherein correlations between conductivity and water diffusivity could be established (as will be discussed in section 4.4, Figure 28).

Owing its widespread use to its remarkable conductivity, ion transport and conductivity of PFSA ionomers have been the most widely investigated and measured property, spanning over 3 decades of work. In the ensuing discussions, conductivity will refer to proton conductivity, unless otherwise noted. Other ions and ionic forms are discussed in section 7.3, including selectivity. Finally, it should be noted that the impact of

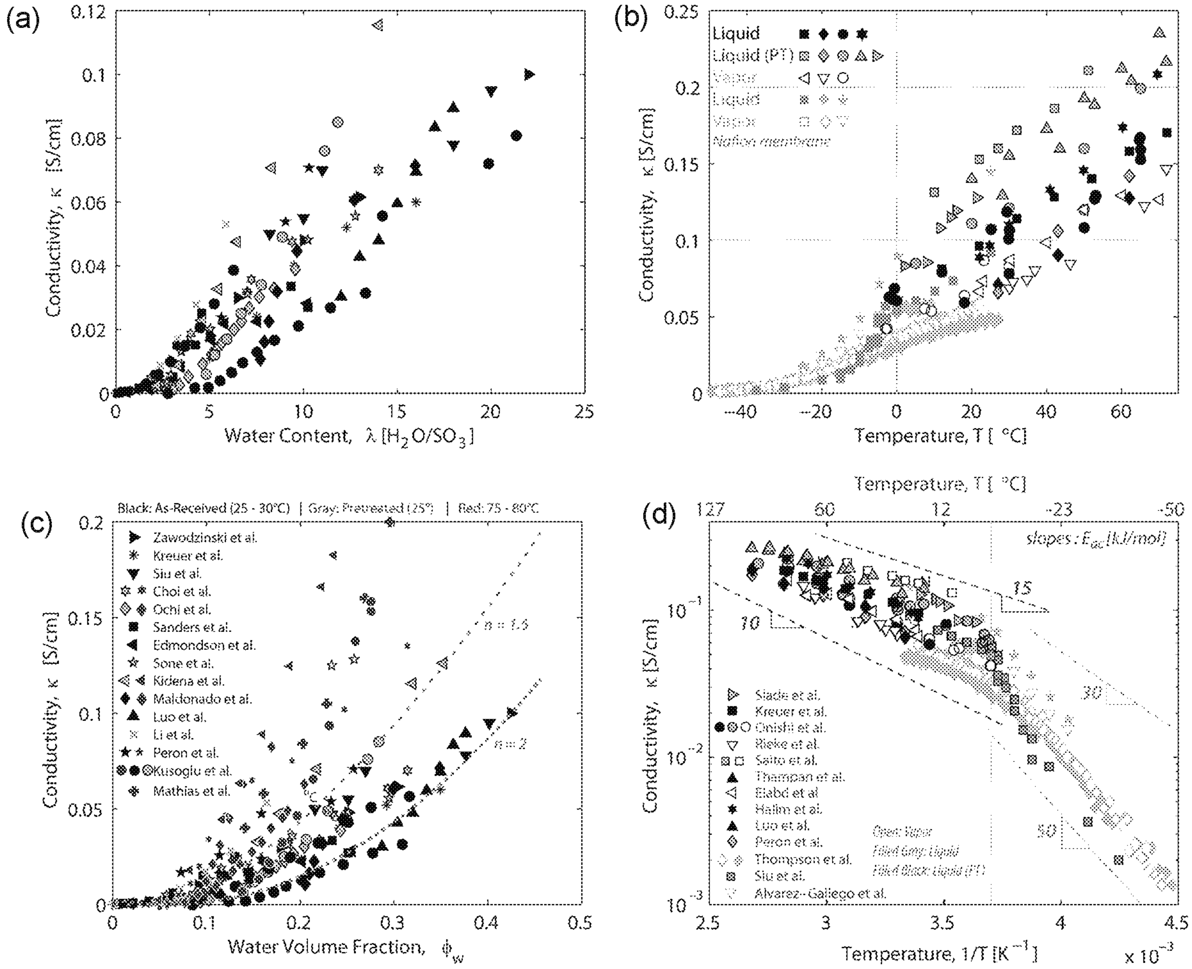

Figure 34. Conductivity of Nafion Membranes: Hydration effect shown in terms of (a) water content, λ, at 25 to 30 °C, and (b) water volume fraction, including high-temperature data, shown in red (75 to 85 °C). The lines in (b) are conductivity expressions based on fraction-scaling for various scaling exponents. Data are compiled from references in the literature [refs 6, 48, 53, 58, 59, 83, 95, 113, 156, 186, 191, 244, 248, 289, 332, 525, 580, 586, 587, and 594]. Impact of temperature on conductivity is demonstrated in (c) linear and (d) log scale.[54,58,94,186,248,252,264,309,504,524,587,591] Lines in (d) represent the trends based on shown activation energy values (also see section 4.7 for details). Conductivity data obtained at low and subzero temperatures are shown in light blue.[52,58,309] Open (white) and black symbols correspond to measurements for membranes that were equilibrated with saturated water vapor and liquid water, respectively, and gray symbols represents liquid-water data for samples that were pretreated (PT) by boiling in water.

possible interfacial resistance on conductivity is inconclusive due to the measurement techniques and decoupling with contact resistances.[440,559,576,577]

4.2.1. Conductivity Values. The proton conductivity of various PFSAs has been measured, discussed, and modeled in over 200 papers. It is commonly measured using electrical impedance, electrochemical cells, dielectric spectroscopy, or (indirectly) determined from self-diffusion (e.g., from ^{1}H NMR, see section 4.1.3). As for the latter, however, the obtained value is vehicular conductivity and fails to represent conductivity if structural diffusion (i.e., hopping) is present (as discussed in section 4.2.3). Ionic conductivity, κ, can be calculated by measuring the resistance, R, either in the plane or through the thickness

$$\kappa = \frac{L}{RA} \tag{45}$$

where L is the characteristic length through which the resistance is measured and A is the active area of the specimen. Studies on Nafion conductivity include investigations on, in addition to hydration, thickness,[584,585] interfacial resistance,[440,576,577] pretreatment[49,81,83,98,586] and annealing,[18,49,81,96,97,101,103,104] subzero temperatures,[52,58,102,309,312] compression,[257,440] stretching,[296,335] and EW effects and PFSA ionomers,[3,5,47,54,191,532] such as 3M PFSA,[2,4,5,7,9,56] SSC PFSAs,[6,50,54,55,57,59,282] Nafion XL,[98] Flemion, and Gore-Select membrane.[287] (Contamination and aging effects on conductivity are discussed separately in section 7.1.) From these studies, it can be determined that the conductivity increases as the EW is lowered, an effect that is more pronounced at higher hydration levels and temperatures consistent with the higher water uptake of low EW PFSAs (see sections 2.2 and 3.3).

As with the other transport properties, PFSA membrane conductivity increases with hydration and temperature as summarized in Figure 34. The hydration and temperature dependence of conductivity can be expressed as

$$\kappa(T, \phi_w) = \kappa_0(T)(\phi_w - \phi_0)^n \tag{46}$$

where ϕ_w is the water volume fraction, ϕ_0 is the water-volume-fraction percolation threshold (i.e., where an interconnected network of conductive domains forms, see Figure 7), $\kappa_0(T)$ is a material parameter that can include temperature effects through

Table 10. Summary of the Conductivity Expressions Based on Its Scaling with Volume Fraction of Water

scaling exponent, n	φ_0	κ_0	ref	membrane
1.38, 1.31	0.030, 0.035	0.272, 0.259	Edmondson et al.[53]	N117, Dow 800
1.95	0.060	0.125	Morris and Sun[246]	N117
1.5	0.100	0.160	Hsu et al.[35]	N117
0.88, 1.10	0.042,0.045		Ochi et al. (NMR)[244]	N117
1.5	0.060		Weber and Newman[201]	Nafion
1.6, 1.5	0.100		Wodzki[595]	N120, N427
1.2 (2D)	0.450		Gierke et al.[593] (Percolation theory)	Nafion
1.5 (3D)	0.150			
1.5 (upper bound, PB)	0.060 ± 0.010		fit to data in Figure 34 for Nafion	N11x, N21x
2.0 (lower bound, AsR)				
1.5 (high EW)	0.100 ± 0.010	0.50	fit to data in Figure 35 for PFSA	Nafion, 3M, SSC
1.0 (low EW)	0.100 ± 0.010	0.40		

an Arrhenius expression (see section 4.7; see refs 2, 6, 54, 56, 58, 102, 134, 186, 287, 289, 290, 309, 312, 314, 504, and 587−592) or under subzero conditions, and n is the critical exponent that accounts for the morphological domain connectivity and alignment. As shown in Table 10, n is empirically determined to be between 1.0 and 1.95,[35,53,201,244,246,309] where the values are around 1.5, which is expected for a 3-D isotropic system.[593] Also from Table 10, the average percolation threshold is close to 0.10 and below 0.15, which is expected for a random and continuous system, thus indicating some degree of preferential alignment. Such a local orientation in a nano-morphology stems from the nature of the hydrophilic domains and their connectivity as discussed in section 3.1 and shown in Figure 21.

Since the conductivity does not follow a purely random expression and there is some morphological orientation, it could be expected that the conductivity is not entirely isotropic. The anisotropy of conductivity has been well studied for various types of PFSA membranes, measuring conductivity in the plane, κ_{IP}, (four-probe) and through-plane, κ_{TP}, (cell assembly).[250,268,440,536,559,576,577] Differences between these techniques were investigated by Cooper,[576,577] who reported similar conductivities in two directions, with a ratio of $\kappa_{IP}/\kappa_{TP} = 1.00 \pm 0.07$ if the through-plane conductivity is corrected for the cell resistance. Thompson et al.[250] and Jiang et al.[440] reported that the conductivity of Nafion is slightly higher in the plane than in the thickness direction.[250] Such anisotropy was shown to be more pronounced in extruded and composite membranes, where significant preferential orientation could be induced at multiple length scales relevant to the ion-transport mechanism. Furthermore, one can enhance this anisotropy through mechanical means similar to the effect of stretching on water self-diffusion.[369,525,536] For both stretching[335] and compression,[257] the conductivity tends to increase in the direction of applied force, albeit at different magnitudes, due to chain and domain alignment. Kusoglu et al.[257] showed that compression has minimal effect on conductivity up to 75% RH, after which increasing the applied pressure reduces conductivity at high temperatures, but increases it at lower temperatures. Although seemingly counterintuitive, this experiment demonstrates the interplay between temperature (increases κ, but reduces λ, in vapor), hydration (increases κ), and pressure (increases κ, but reduces λ due to water loss) that all stem from altered morphology (see section 3.1.5). In terms of interface, the electronic resistance was found to be higher during compression than during decompression, and this difference becomes smaller as the compression pressure is increased. The resistance value levels off when the applied compression pressure is higher than 2.5 MPa.[440]

In terms of conductivity values, it should be noted that pretreatment alters the conductivity concomitant with the change in water-uptake capacity (section 2.2), where annealing or predrying tends to reduce a membrane's uptake and conductivity, and preboiling enhances these properties (see Figure 34).[83,94,97,312,586] However, as will be shown in the next section, when plotted as a function of water content, λ, the conductivity at a given λ is still higher for a preboiled membrane due to the induced morphological changes.

Finally, although the literature is rich with conductivity data of Nafion 1100 EW (dominating over 95% of papers on the topic), the impact of EW and chemistry on conductivity has been overlooked. The liquid-water conductivity of PFSA membranes are plotted in Figure 35a based on the available data in the literature. A universal trend in PFSA studies is the increase in conductivity with lower EW, primarily due to an increase in ion-exchange capacity, i.e., charge carriers, as witnessed with SSC,[6,47,50,52,55,57,61] Nafion,[156] 3M PFSA,[2,4,7] and Flemion.[282] Increasing IEC also permits more water uptake, which improves percolation and therefore long-range diffusion of ions. However, when comparing EWs of different PFSA (side-chain) chemistries, one must be careful as it is the backbone length and side-chain length/chemistry that change, not just the number of SO_3^-. Despite the scatter in data, the figure shows an unequivocal trend of higher conductivity with lower-EW membranes. Since the water uptake is also expected to change with EW (see section 2.1 and Figure 9), conductivity is plotted as a function of water volume fraction of the membrane, which exhibits a surprisingly strong correlation, signifying the key role of water uptake and mesoscale network.

As shown in Figure 35, lower-EW PFSAs have greater ion conductivity compared to that of Nafion membranes for the same nominal water uptake. Since the d-spacing is smaller for these lower-EW PFSAs compared to Nafion at a given water content (Figure 24a), this implies a better distribution of sulfonic-acid groups and decreased ion-pathway tortuosity, thereby explaining their improved ion conductivity.[2,5,9] In addition, the improved backbone flexibility of the 3M ionomers enhances the proton dissociation and mobility and thus leads to higher conductivity.[70,71,73] This effect is shown in Figure 35b and is in agreement with recent studies showing how EW, nanostructure, and crystallinity affect the proton-conduction mechanisms.[2,6,519] To describe these changes, one can correlate the proton conductivity with the mobility of the carrier protons, u_{H^+}, by

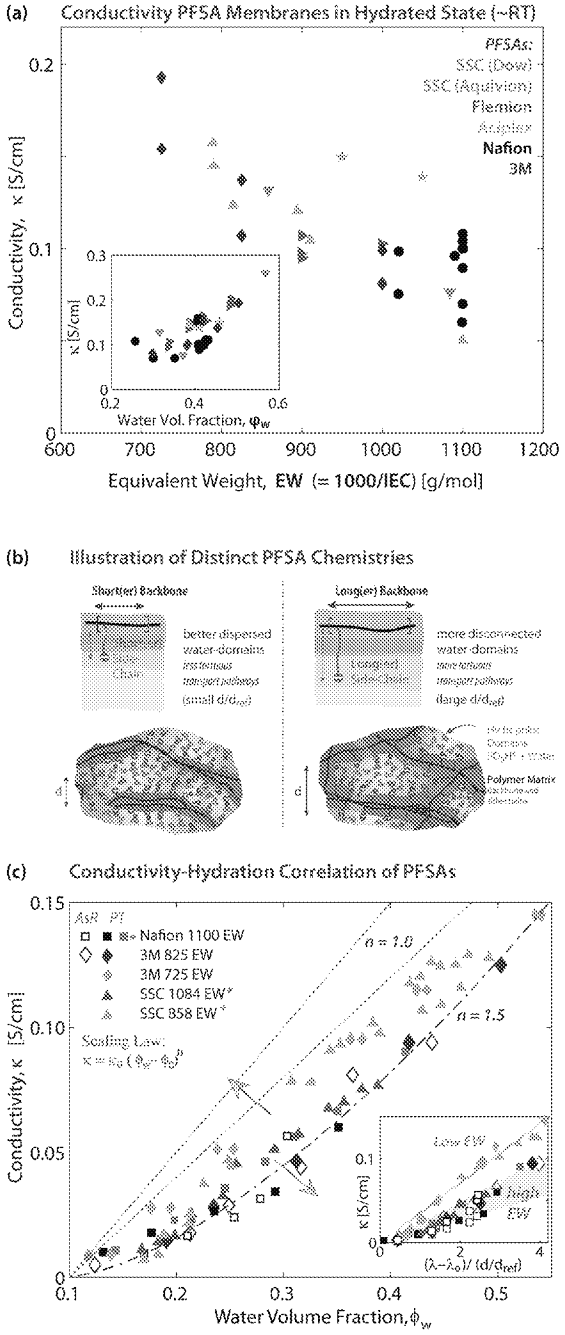

Figure 35. (a) Conductivity-EW relationship for various PFSA membranes measured in liquid water at 25° (from refs 3, 6, 44, 48, 52, 59, and 282) (c) Nafion, 3M and SSC PFSA conductivity in humidified environment as a function water volume fraction. Data marked (*) are from Kreuer et al.[6] and the others are from Kusoglu et al.[48] Inset shows the same data as a function water content normalized by transport length (see the text, eq 45) Lines are predicitons based on various scaling exponents (eq 44). Data are shown for both as-received (open symbols) and preboiled (filled symbols) membranes. (b) Illustration of two PFSA structures; SSC and LSC and backbone representative of distinct trends in (c).

$$\kappa_i = z_i F C_i u_i \tag{47}$$

which, for H^+, simplifies to $\kappa_{H^+} = FC_{H^+}u_{H^+}$, where the concentration of protons can be approximated from that of SO_3^- groups, which can be estimated from the EW and dry-polymer density,

$$C_{H^+} = C_{SO_3^-} = \frac{1}{\bar{V}_p + \lambda \bar{V}_w} = \frac{1}{\frac{EW}{\rho_p} + \lambda \bar{V}_w} \tag{48}$$

Thus, increasing EW tends to reduce the fractional proton concentration and impact the conductivity. While this suggests that EW impacts conductivity through water-uptake, this should not rule out additional role chemical structure could play, which will be examined next.

4.2.2. Structural Interactions.

As seen in Figure 34 and eq 46–48, there is an interplay between the structure and the conductivity that involves the water content. To examine this interplay better, the conductivities of PFSAs membranes with different chemical structures (i.e., Nafion, 3M, and SSC, see Figure 2) are plotted as a function of water volume fraction (Figure 35c). [While λ has proven to be a useful parameter that probes the local behavior of water, ϕ_w is a better representation of the network-level properties. The difference between the two appears only when the side-chain and EW changes due to changing molar volumes, and using both reveals insight into the local vs network and mesoscale properties.] It follows from the figure that while conductivity increases with hydration, there appears to be two distinct trends: Higher-EW membranes all fall on the same curve represented by $\kappa \propto (\phi_w - \phi_0)^{1.5}$, similar to that expected and predicted for Nafion (Table 10), whereas the lower EW SSC and 3M PFSAs demonstrate an almost linear dependence on hydration with $\kappa \propto (\phi_w - \phi_0)^1$. An exponent of $n = 1$ indicates locally flat transport pathways discussed in section 3.2. A closer examination of the chemical structures reveal that, despite different EWs and side-chains of SSC and 3M PFSA, what they have in common is the short backbone (m_{TFE}). The change in scaling exponent suggests a strong change in morphology or at least transport pathways, and it is not the hydration alone that determines the conductivity, but also the polymer-chain structure and conformation. This is in agreement with studies reporting the effect of side-chain and segmental motions on conductivity as discussed in section 4.4. This was in also in accord with recent studies on transport,[2,6,519] dielectric spectroscopy,[2,133,436] and molecular modeling,[63,65,66,68−71,73,348,449,455,456,534,596] pointing out the roles of backbone and side-chain conformation in conductivity (see section 4.4) and the favorable impact of a shorter backbone on better-dispersed domains. In particular, the role of a shorter backbone (low EW) in enhancing proton mobility at the same λ has been identified recently[519] and attributed to the formation of more continuous water network, wherein the associated bound water molecules could be loosened due to the closely spaced sulfonate groups,[519] thereby increasing the mobility by enhancing formation of water-sulfonate bridges and stabilizing the hydrogen-bond network.[68,69,348,353,356,456,534,596] In addition, more continuous and better-connected hydrophilic domains have been revealed in these modeling studies[63,65−67,449,456] (also see section 4.4.3). The fact that conductivity of these lower-EW PFSAs differ more than their self-diffusion, as shown in Figure 30 and supported by simulations,[449,456] indicates a change in conduction mechanism related to the proximity of ionic groups. One must recognize that reducing the PFSA backbone length, while advantageous for increasing the proximity of SO_3^--terminated side-chains, could make it closer to Bjerrum length of water (~0.70 nm at RT), increase the counterion concentration, and affect the proton dissociation (i.e., causing Manning counterion condensation), which may offset some of the above-mentioned achievements. The distance between side-chains of Nafion was shown via molecular modeling to be ~1 nm and increases to 1.5 nm with hydration.[443] It must be pointed out that lower-EW PFSAs possess shorter side-chains, which also impact proton dissociation[62−64,70,72,73,377,449] and transport,[2,6,9,48,50,55,282] the effect of which manifests itself even at lower hydration levels, where the proton transport relies on the hydronium bridges between sulfonate sites and side-chain.[63,69,348,446,447,534] The controversial nature of high conductivity in short-backbone PFSAs in consideration of counterion condensation could be resolved if one considers, in light of aforementioned results, the more-flat continuous water domains with less-tortuous interfacial area.

To explore the conductivity/structure relationship, the conductivity data is correlated with a parameter that can capture both the hydration and side-chain proximity (or separation) effects[24,257]

$$\kappa \propto \frac{\text{hydration}}{\text{separation}} \propto \frac{h(\lambda)}{s(\delta_{\mathrm{SO_3}})}, \text{ and } \kappa \propto \frac{\lambda - \lambda_0}{d_{\mathrm{w}}(\lambda)/d_{\mathrm{ref}}(\mathrm{EW})} \tag{49}$$

which could be generalized as the ratio of a hydration function, $h(\lambda)$, and structural-proximity function, s. In the above expression, λ_o is the water content in a reference state, which can be interpreted another way to represent a percolation threshold, and δ_{SO_3} represents the barrier for ion transport. Due to fluctuations and reorganization, and increase in δ_{SO_3} with hydration, for the lack of a better term, one can instead use the PFSA *d*-spacing, d_w, as it is a measurable quantity (see section 3.2). As can be seen from the Figure 35, the PFSA membranes' ion conductivity scales linearly with the "hydration/separation" parameter. In plotting the data, d_w is normalized by a d_{ref}, which could be interpreted as a characteristic transport length, i.e., representing how long a proton could move at nanoscales without a significant resistance along its path, reminiscent of a persistence length in a polymer. [This was set to 1 nm based on QENS data discussed in section 4.4.1, due to the lack of a better value.] The resistance can therefore be interpreted as a collection of structural defects that can hinder proton transport, which is linked to the proximity of side-chains (which affects local water behavior and confinement) at molecular levels and to tortuosity, τ, at the mesoscale (interconnection of nano-domains at a length scale on the order of 10 to 100 nm). The fact that shorter-backbone PFSAs possess closely packed side-chains can impact both of the above effects, thereby leading to the observed lower scaling exponent ($n = 1$) as illustrated in Figure 35b. Note that this approach of linking transport to hydration and measurable structural parameters can be considered a precursor to more advanced structure-based models, where a realistic distribution of domains sizes and connectivities could be employed to generate an accurate representation of transport pathways in the membrane[208,352] (also see Table 4).

In terms of an overall morphology, a more continuous transport pathway with less clustering such as a lamellar or cylindrical one is preferred in an ionomer, which has been supported by a MD models,[355,356] and also explored in ion-conductive blockcopolymers[597−599] and other sulfonated ionomers,[598,600,601] where one aims for smaller transport lengths and lower tortuosity.[406,598,600] Factors such as domain-alignment and side-chain chemistry and acidity play key roles in modifying the structure/transport relationship.[598,599,601] PFSAs other than Nafion exhibit the potential to offer such a morphology with even better transport properties, albeit at the cost of stability (as the shorter backbone tends to reduce the crystallinity, see Figure 22). Nevertheless, such negative effects could be minimized by modification through side-chain chemistry. PFSA's macroscopic conductivity is therefore more dependent on the mesoscale or network than on transport at the domain scale, especially at lower hydration, investigation of which warrants further studies.

Since *d*-spacing scales linearly with λ, the above expression somewhat represents water volume fraction although can account for cases wherein d and λ do not change equally.[352] For example, during membrane compression the conductivity increases, since the loss of water due to the applied external force is more than offset by the changes in terms of alignment and overall *d*-spacing which increases conductivity (see section 3.1.5 and section 2.6).[24] Even though hydration enables formation of a water-network for ion transport, it also increases the separation distance between the ionic domains, thereby establishing a higher barrier for ion-hopping and transport among the ion-exchange sites, especially at low hydration. No universal ionomer relationship is observed for the κ−λ lines, which do not overlap for different ionomers (see the inset of Figure 35). Thus, the mechanisms underlying ion transport are more accurately captured by the hydration-driven morphological changes rather than by hydration alone.

As noted, a PFSA exists in a quasi-equilibrium wherein long-term relaxation occurs. Thus, even though one might expect higher conductivity in a membrane that relaxes and absorbs more water, such a trend has not been shown, at least not in a systematic fashion. This is because ion transport depends on not only water content but also morphological features, which are expected to change, especially in the presence of long-term backbone relaxation and associated changes in water-domain connectivity, along with possible impact of aging-induced changes (see section 7.1). All time-dependent conductivity measurements demonstrated a decay with time.[120,121,602] In addition, Casciola reported that conductivity decay is related to the applied pressure during the measurements.[120] Moreover, Liu et al.[119] showed that both conductivity and stress in Nafion membrane relaxes with time, albeit at different rates; stresses relax faster than the proton conductivity. As such, the interpretation of the measured time-dependent response is rather intriguing as it is likely governed by a combination of chemical (e.g., ion and water transport and interactions), mechanical (e.g., compression and matrix relaxation effects), and structural (phase-separation and hydrophilic domains) factors.

4.2.3. Conduction Mechanisms.

The current state of understanding of proton conduction in PFSAs has evolved over the years, thanks to many developments in the field evidenced by advanced diagnostics and supported by simulation studies.[16,18,71] Proton transport can be explained in conjunction with water (or solvent) uptake and related morphological changes. Conductivity in a hydrated PFSA occurs via protonic charge carriers. For proton conductivity, the key is the formation of the hydrogen-bonded water network[16,18,349,535,579,603,604] and the nature of water, which displays amphotericity (i.e., acts as both a proton donor (as hydronium) and proton acceptor). In addition, PFSAs owe their remarkable proton conductivities to their acidity, the determination of which, however, is not straightforward as PFSA is not soluble in water (see its dispersion nature in section 3.1). Nevertheless, a low pK_a value of −5.5 to −6 has been assigned to PFSAs, owing to the strong electron-withdrawing nature of its fluorine side-chains stabilizing the negative charge, meaning that their protons could easily dissociate in water and become available to facilitate proton transport, for example as hydronium ions ($SO_3H + H_2O \rightarrow SO_3^+ + H^+(H_2O)$).[9,55,235,604,605] Studies suggest that Nafion has an acid strength higher than CH_3SO_3H, and comparable to CF_3SO_3H and even to concentrated H_2SO_4 solutions.[235] It must be noted then, in dry conditions, most of the protons reside on SO_3H sites, reducing their solvation and increasing the pK_a. Thus, a PFSA's acidity can be defined within its hydrophilic nanodomains and is different than its surrounding solution (i.e., dispersion). In fact, in dry form, Nafion is even more acidic than solutions of H_2SO_4, in which H_3O^+ are solvated unlike in PFSAs, when their $-SO_3H{\cdot}H_2O$ (or $-SO_3^-{\cdot}H_3O^+$) pairs are not solvated.[235] This acidity also allows larger complex ion formation (e.g., Zundel and Eigen ions, see Figure 33d)[16,311,454,579,604,606] at higher water contents, where more solvation occurs (see section 2.1). When a proton is separated from the SO_3^- groups ($SO_3H^+ \rightarrow SO_3^- + H^+$), it is solvated by water molecules, forming a hydronium ion, H_3O^+. Addition of more water molecules create a larger hydration shell ultimately resulting in more complex protonic species such as Eigen or Zundel ions (see Figure 33).[16,226,311,381,454,504,579,604,606] With the increase in λ, hydrophilic nanodomains grow and eventually become connected, thereby forming a percolated network ($\lambda \sim$ 2 to 3) as discussed in section 2.1. With increasing hydration, proton conductivity increases because of higher proton dissociation and mobility, and the evolution of the hydrogen-bond network.

The nature of proton conduction is due to one of two mechanisms: Grotthuss hopping (structural diffusion) and vehicular (Figure 33). The former mechanism is attributed to a sequence of proton-transfer reactions across an array of water molecules. In the pioneering work of Agmon,[607] it was described how a series of bond breaking and forming steps transfer protons across the hydrogen-bond network (see Figure 33d).[16,18,349,535,603] Such a coordinated transfer of the positive charge through the hydrogen-bond network via (re)-orientational motion of water molecules occur on a time scale of 1.5 ps.[607] This hopping requires a faster rotation and reorientation of water molecules, which is possible in fully hydrated conditions, and results in faster conduction since the proton that enters the network is not the one that leaves and its translational movement across the domain is not limiting, unlike in the vehicular mechanism, as explained in detail by Kreuer and co-workers.[16,321,504,579,604] It is this water-mediated increase in proton transport that imparts hydrated PFSA its remarkable conductivity, especially compared to other cationic forms (see transport discussion in section 7.3.1).

At low hydration and with an incomplete hydrogen-bond network, the vehicular mechanism dominates and conductivity occurs through a vehicular mechanism of the transport of the solvated proton (Figure 33c). The key to understanding the mechanisms is the competition between the proton's solvation energy and electrostatic interactions, where solvation energy can be interpreted as proportional to the inverse of dielectric constant (high ε reduces solvation energy of protons; see sections 3.3 and 4.4). Pintauro and co-workers[583,608] developed a molecular-level equilibrium model which showed that the balance between the electric field generated by the fixed anionic sites, represented by the dielectric constant, ε, and ion solvation free energy dictates the distribution of the cations (charges) within a hydrophilic domain, with highly structured (i.e., bound) water concentrated in the vicinity of the interface ("wall"). Far from the interface, however, ε approaches the value of bulk (i.e., free) water. Kreuer, Paddison and co-workers[16,23,581] demonstrated that the dielectric constant (relative permittivity) and proton concentration, c_{H^+}, of the hydrated hydrophilic phase are strongly coupled and both are reduced near the hydrophobic/hydrophilic interface, where the interaction of the SO_3 groups with water also reduces the dielectric constant (Figure 33c). A reduced dielectric constant near the interface then results in a relative stabilization of the dissociated protons in the central region of the domain. Therefore, the spatial distribution of the dielectric constant within the hydrated domains is dependent on the size of the hydrophilic domains (which changes with λ) and the separation of the dissociated sulfonic-acid functional groups (Figure 33b).[16] At high degrees of hydration, the dielectric constant becomes bulk-like in the center of the water domain (~80).[578,581,583,608] Such trends can also rationalize the observed trends with alcohols, where lower-dielectric solvents reduce conductivity (κ scales with $1/\varepsilon$ also in alcohol solutions[344]) and other cations as discussed in sections 4.6 and 7.3, respectively.

The mechanism of conduction is perhaps temperature dependent as well, which can be seen in the coupling with electro-osmosis and the activation energy for conduction (see sections 4.3.1 and 4.7, respectively). The more interesting aspect is conduction under subzero conditions,[52,102,186,251,309,311−313,609] as it provides insight into the mechanisms. Although water slows down and partially crystallizes below freezing, there is still sufficient mobility to promote transport of proton (and water,[251,313,314,512,528] also see section 2.5), albeit at a slower rate[609] and thus the decrease in conductivity as shown in Figure 34b,d. As Thompson et al.[309] demonstrated, under freezing conditions the proton distribution is expected to change and allow conduction in a thin region next to the side chains that does not freeze unlike the center of the water domain (Figure 14b). Thus, the free-water content decreases but hopping can still occur for conduction. Such studies demonstrate that the percolated network connectivity is maintained even under these conditions and protons can still transport.

In terms of EW, it is expected that the conductivity changes not only due to structural reasons as mentioned above, but perhaps due to mechanistic changes as well. For example, Giffin et al.[2] showed that EW affects the hopping- and proton-conduction mechanisms, which are accompanied by changes in the crystallinity and conformation of the PTFE backbone. MD simulations suggest that short(er) side-chain ionomers have improved backbone flexibility, which enhances the proton dissociation and leads to higher conductivity.[70,71,73] Similarly, due to the water network, the ratio of Grotthuss/vehicular transport is expected to increase with lower EWs.[186]

Spectroscopic[2,133,382] and computational[63,65,67,72,449,456,461,467,471] studies collectively suggest that EW affects the hopping- and proton-conduction mechanisms, which are accompanied by changes in the crystallinity and conformation of the PTFE backbone, indicating the critical role of EW in facilitating proton transport and controlling the structure/function relationship. Similarly, it has been shown that SSC PFSA have shorter relaxation times, as measured by NMR, than Nafion, especially, at low levels of hydration. Thus, the water motion is influenced by the acidity and mobility of the sulfonic-acid groups around which water molecules are coordinated.[55] Furthermore, the flexibility of shorter pendant chains promote reorientation of the O−D bonds.[55] MD simulations suggest that these short(er) side-chain ionomers have improved backbone flexibility, which enhances the proton dissociation and leads to higher conductivity, especially at lower hydration levels.[70,71,73] At higher water contents, however, a PFSA membrane's conductivity is pretty much dominated by its water-uptake capacity and mesoscale network.

The relationship between the water and ion transport is commonly illustrated from comparison of self-diffusion, or intradiffusion, of water, D_μ (determined from ^{1}H NMR, see section 4.1.3) and ionic diffusion/mobility, D_κ, determined from the Nernst−Einstein relationship for protons in this system[610]

$$D_\kappa = \kappa \frac{RT}{F^2} \frac{1}{c_{\mathrm{H}^+}} \tag{50}$$

where F is Faraday's constant and c_{H^+} is the proton concentration. Although rigorously valid only for infinitely dilute solutions, the above relationship is commonly employed to compare water and ionic mobilities and to provide an understanding on the role of water in ion transport (see Figure 36).[502] At low λ, both D_μ and D_κ are similar, yet they differ with increasing λ, where D_κ becomes higher than D_μ, which has been traditionally attributed to the distinct proton-transport mechanisms in the hydrated membrane as described above (Figure 33b). A decrease in dissociation of SO_3H groups and associated dielectric screening leads to a stronger exclusion of protons from the transport in the water domains and the excess protons tend to be more localized in the vicinity of the sulfonic-acid functional groups (see Figure 33c), which leads to a higher reduction in D_κ compared to D_μ.[604] Therefore, proton mobility at intermediate and low degrees of hydration is essentially vehicular in nature. The higher values of ionic mobility compared to water mobility at high water contents, $D_\kappa > D_\mu$, indicates that hopping mechanism is more dominant.[16,53,59,95,191,244,502,536,604] Overall, a striking result of Figure 36 is that the ratio $D_\kappa/D_\mu = 2$ is constant, especially at high hydrations, but is closer to 1, at lower hydration levels. This underscores the fact that ion and water transport are related through the chemical structure. Recently, Kreuer[504] showed that the ratio D_κ/D_μ, what he called an amplification factor, is 2.5 in hydrated Nafion, and decreases with increasing temperature (probably due to the different activation energies enhancing the vehicular mechanism) and lower water contents. For the latter, values of less than 1 were measured, indicative of negligible structural diffusion.

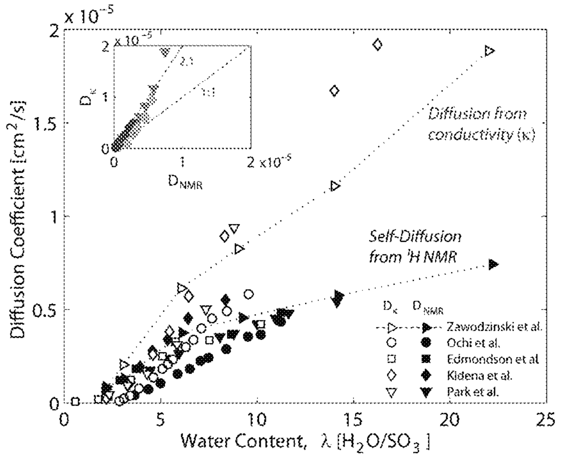

Figure 36. Hydration dependence of diffusion coefficient of water and protons in Nafion membrane measured from NMR or D_κ as determined from measured proton conductivity, κ (using the Nernst−Einstein relationship, eq 47).[53,95,191,244,502,536] A filled and open symbol of the same type refer to D_{NMR} and D_κ, respectively, taken from the same study. The inset plots these values against each other showing their correlation.

4.3. Cross-Correlation Phenomena

As noted from Table 6, different driving forces can cause changes in the off-diagonal components, thereby demonstrating a coupling of the transport phenomena. Such cross-correlation phenomena are expected in the concentrated and dynamic environments that PFSAs represent, and are naturally accounted for using a concentrated-solution theory framework. The prototypical case for this is electro-osmosis. However, other effects including thermo-osmosis, thermo-electric effect, etc. have been observed and will be mentioned in more detail in this section. Before proceeding, one cross-correlation that has been reported in only a single article is that of the Seebeck effect, where the temperature gradient induced a potential with a Seebeck coefficient of 0.76 mV K^{-1}, which was measured between platinum and Nafion.[611]

4.3.1. Electro-osmosis. Electro-osmosis relates the movement of the solvent (water) due to the electric field. It is the inverse of the streaming current. In a rigorous sense, the electro-osmotic coefficient, sometimes termed the electro-osmotic drag coefficient, is the transport number of water in the membrane

$$\xi \equiv \left(\frac{N_w}{N_+}\right)_{\Delta c_w = 0} = \frac{t_\mathrm{w}^\mathrm{m}}{z_\mathrm{w}} / \frac{t_+^\mathrm{m}}{z_+} \tag{51}$$

where it is assumed that the proton flux carries all of the ionic charge, i.e., $t_+^\mathrm{m} = 1$, and t_w^m/z_w is the transport number of water (see section 7.3 for other cases). The electro-osmotic coefficient is a measure of the number of water molecules that are carried with each proton, by its solvation shell, in the absence of a concentration gradient. This last aspect is critical since many measurements induce concentration gradients either without knowing (e.g., due to membrane swelling) or on purpose (e.g., in an operating cell) and use the terminology electro-osmotic coefficient; in either case, the value reported is a net electro-osmotic coefficient. This highlights the need to be careful when measuring this coefficient. For example, Cheah et al. showed that the effective (net) coefficient decreases compared to the intrinsic one due to interfacial effects.[556]

Electro-osmosis has been one of the more controversial issues in PFSA studies, in part due to the complex nature of coupled ion/water transport, and also due to the difficulty in measuring it as mentioned above. A number of techniques have been adopted, including electric-field measurements,[269,612] streaming potentials,[269,330,612] electrochemical cells[95,605,613] including fuel-cell setups,[60,614−617] and electrophoretic NMR[606] in various aqueous solutions and in vapor (also see reference[21] for a discussion and comparison of methods). Since the early studies by Zawodzinski and co-workers[95,184] and Fuller and Newman,[613] some consensus has been reached with values of 0.9 to 1.4 in vapor ($\lambda < 14$) and 2.5 to 2.9 in liquid water ($\lambda > 20$) as shown in Figure 37. In general, there appears to be an average monotonic increase in the electro-osmotic coefficient with increasing λ, although various dependences, or lack thereof, could be suggested when investigated on a case by case basis. Temperature also increases the electro-osmotic coefficient up to a value of 5 in liquid water (Figure 37b).[60,95,113,269,606,613−615,617]

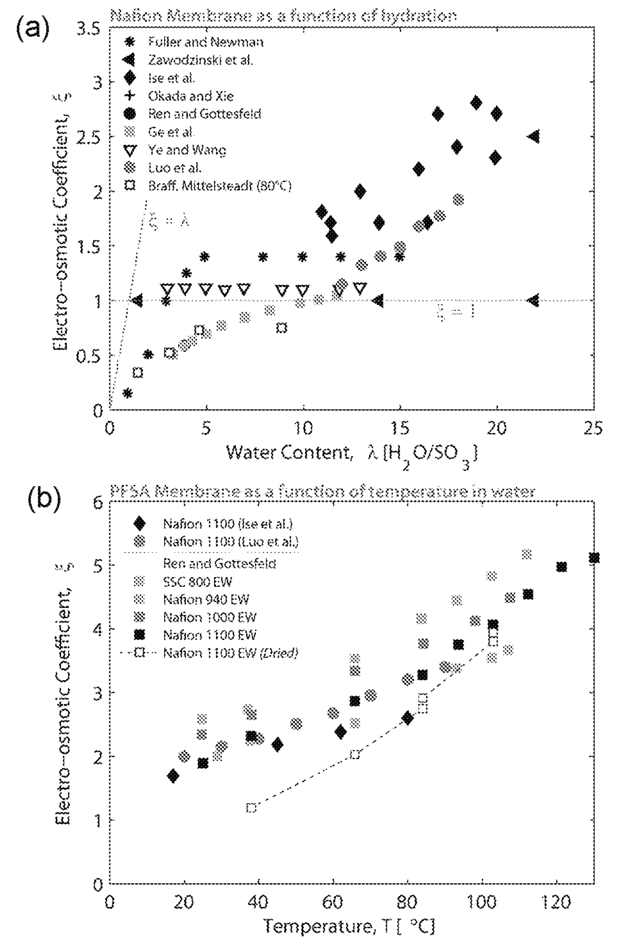

Figure 37. Electro-osmotic coefficient as a function of (a) water content (for Nafion at 25 °C unless otherwise noted) and (b) temperature in liquid-water (for Nafion and SSC PFSA).[60,95,113,269,606,613−615,617]

Electro-osmosis is integrally related to the water/proton dynamics and transport mechanisms as described in sections 4.2 and 4.4, where there exists a strong correlation between electro-osmosis and proton hopping (see Figure 33).[605] However, the true correlation between the two is an inverse one in that, in a strict sense, an electroosmotic coefficient of zero should occur for pure hopping mechanism.[605] However, some recently measured coefficients have demonstrated values less than one.[617] As soon as a water molecule also moves with a proton, i.e. vehicular mechanism, the coefficient should be one assuming a hydronium ion (H_3O^+) is the transporting species. At higher temperature and higher water contents, the increase in the electro-osmotic coefficient is commonly attributed to the presence of ions larger than H_3O^+ (such as Eigen or Zundel),[311,454,606] and increased hydrodynamic flow with hydration and/or temperature. (Also see section 3.3). Such issues are also compounded by the analysis of the mesoscale network, wherein the tortuosity and interdomain transport can impact measured values.[618] One should note that the coefficient cannot exceed λ (i.e., $0 < \xi < \lambda$).[498,613]

The above mechanism is in agreement with ab initio calculations that suggested the coefficient value to be 1 and constant in vapor, due to coupling between the water and ion transport processes. They also suggested that more water increases hopping, which reduces the electro-osmotic coefficient.[454] Finally, Ise et al.[606] proposed the following modified hydrodynamic model where the electro-osmotic coefficient is related to the hydrodynamic rate for hydrated proton, Γ_{hydro}, and rate for proton transfer, Γ_{transfer}, and λ_{H_3O} is the water molecules hydrating and associated with protons (e.g., hydronium ions).

$$\xi = \frac{\Gamma_{\text{hydro}}}{\Gamma_{\text{hydro}} + \Gamma_{\text{transfer}}}\left(\lambda_{H_3O} + (\lambda - \lambda_{H_3O})\frac{\overline{v}_{H_2O}}{v_{H+}}\right) \tag{52}$$

where $\overline{v}_{H_2O} v_{H+}$ is the drift velocity for protons and mean velocity for water. At lower temperatures, more of the H^+ transfer processes occur without contributing to the water flux, and the hydration effect is due to increased hydrodynamic pumping.

As for other PFSAs, studies by Kreuer[6] and Ren and Gottesfeld[60] showed that the electro-osmotic coefficient decreases for a lower EW or SSC PFSA. While the former (EW) effect could be associated with higher concentration of ionic sites, the latter (side-chain) effect is thought to be related to lower spacing between the domains resulting in smaller bulk-like domains where water transport is inhibited compared to proton transport, thus the increase in the coefficient.

4.3.2. Thermo-osmosis.

Another interesting, but rather less explored, transport phenomena is thermal-osmosis, i.e., water flux due to a temperature gradient in the absence of other gradients[584,619]

$$\mathbf{N}_w = -D_{\text{TO}}\nabla T \text{ with } D_{\text{TO}} = (\overline{s}_w - s_w)D_{\text{TO}}^{*} \tag{53}$$

where D_{TO} is the thermo-osmotic coefficient and can be expressed as the difference between the partial molar entropy of water in and external to the membrane, and $D_{\text{TO}}^{*} = L_p/\overline{V}_w$ is related to the hydraulic permeability of the water and its partial molar volume (see eq 41).[584] Kim and Mench[619] investigated this phenomenon using Nafion, Flemion, and Gore-Select membrane, and showed that the thermo-osmotic coefficient exhibits an Arrhenius-type temperature dependence, with values in the range of $D_{\text{TO}}(T) = (-)\ 1$ to $1.5 \times 10^{-5} \exp(-2300 \pm 100/T)$ kg/m^{2}sK. The water flux increased with lower EWs and thinner membranes, due to a higher temperature gradient. Villaluenga et al. reported that the thermo-osmotic coefficient for water is lower than that for methanol (0.7 vs 1.4×10^{-6} kg/m^{2}sK), which can be attributed to the solvent uptake capacity of the membrane and solvent mobility at that temperature as discussed in section 4.6.[584] Thermo-osmosis is distinct from other transport mechanisms discussed earlier in that it cannot be easily represented by a chemical-potential driving force; it is rather the entropy of water that governs the transport of water under a temperature gradient, which becomes complicated since one cannot define a partial molar entropy of a single ion. A rigorous treatment of the chemical potential of water using a reference of the triple point may be able to incorporate thermo-osmosis into the chemical potential changes,[558,620] although this needs to be proven. Finally, it should be noted that thermo-osmosis is

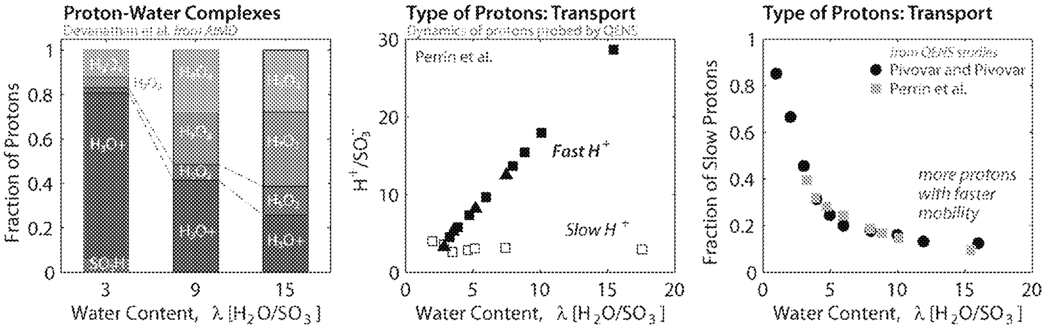

Figure 38. Nature of proton in hydrated PFSA: (from left to right), fraction of protons occupying various molecular configurations based on AIMD (Devanathan et al.[453]); two types of protons, fast and slow, in the membrane as a function of hydration obtained from the water dynamics probed by QENS (Perrin et al.[234]) and fraction of slow protons from these QENS studies (refs 234 and 233).

typically only witnessed with PFSAs that are sandwiched between electrodes, thereby insinuating that swelling, surface tension, local ionic fields, and concentration effects may exist and impact the results; more research is required to delineate and study this phenomenom.

4.4. Nanoscale Correlations

In the last sections, the various transport properties have been reviewed and discussed; in this section, we examine some of the possible relationships between transport and structural features, especially at the nanoscale. The complex nature structure-transport interplay in PFSAs has also stimulated investigations on various aspects of transport-property correlations, including, but not limited to, diffusion/relaxation,[128,380] self-diffusion/conductivity (i.e., ion and water transport, see section 4.2.3),[44,53,95,191,244,269,502,603,621] diffusion/free-volume effects,[297,510,531,622] diffusion/nanostructure (e.g., nanoswelling of domains),[17,116,217,429] diffusion/interfacial effects (e.g., conductive AFM, see section 4.1.5),[256,275,486,487] diffusion/permeability,[518] permeation/electro-osmosis,[548] coupling of stretching and (anisotropic) self-diffusion/conductivity (section 3.1.5 and 4.2.2),[296,369,404,536] structure/conductivity under compression[257] and tension,[335] chain dynamics and transport (e.g., dielectric spectroscopy[2,133,603,623]) as well as structure/water dynamics (e.g., QENS or water relaxation).[233,234,429,529,535,623] As seen above, such phenomena couplings are pervasive in PFSAs and are discussed throughout this review; in this section, we focus on those that are mainly derived from or use transport-related diagnostics and analyses.

4.4.1. Nanoscale Proton Transport. Stemming from the need for unraveling the complex interplay between structure and transport mechanisms, advanced diagnostic techniques have also been employed. One such technique is quasi-elastic neutron scattering (QENS), a powerful tool capable of simultaneously probing the time scale (through frequency space) and length scale (through q-space, as discussed in section 3.1) and thus allowing study of dynamic correlations.[233,234,624] When energy is exchanged between molecules and neutrons, they either accelerate or slow down while scattering, which results in a weak (quasi-elastic) energy transfer as a function of momentum transfer, related to the molecular motions.[19] Thus, from the broadening of the quasi-elastic scattering ($I(q)$) one can obtain information on moving scattering particles, which, for the case of PFSA, are H^+ molecules that characterize the self-motion of protons.[19,233,234,429,624] QENS is in particular well-suited for PFSA, due to larger incoherence neutron scattering cross-section of ^1H allows observation of self-correlated motion of hydrogen (diffusion), from Å to nm length scales at picosecond resolution. Therefore, QENS combines the features of NMR (ms, μm) and XS/NS, i.e., by inferring not only the nanostructural features of hydrophilic domains, but also the molecular motion of water therein, as discussed in a series of in-depth investigations by CEA group.[234,429,624]

Volino et al.[624] demonstrated the potential of QENS for capturing the fast water motions in Nafion membranes. The key finding was that the water molecules could move as fast as in bulk water in a restricted volume of 1 nm size, but their longer-range motions are much slower. In a later QENS study, Pivovar and Pivovar[233] explored the dynamic behavior of water in Nafion and determined that the residence time for water molecules decreased with hydration, thereby indicating faster diffusion, albeit in two different regimes: (i) one was attributed to confinement residence time, i.e., time between successive jump motions within a sphere (10−4 ps, for $q > 0.7$ Å^{-1}), and (ii) a longer residence time (25−10 ps for $q < 0.7$ Å^{-1}) corresponding to diffusion confined in a sphere. The radius of this dynamic sphere was shown to increase with hydration up to $\lambda = 7$ and then saturates slowly indicating that additional (free) water molecules do not experience the same confinement (Figure 38). Based on this data, they calculated two types of diffusion: confined, local, diffusion D_{local} and a faster jump diffusion, D_{jump}. The ratio $D_{\mathrm{jump}}/D_{\mathrm{local}}$ decreases to a constant value of 2 after $\lambda > 5$. In a more recent study, Perrin et al.[234] reported similar observations, but with different interpretation of diffusion mechanisms: a local diffusion (inside a sphere) D_t, and a slower long-range diffusion, D_{lr}, where the ratio D_t/D_{lr} also becomes constant at higher hydration levels.

Even though interpretations of QENS data changes depending on the analysis and models adopted, the qualitative trends are the same (Figure 38). [Due to some discrepancies in values and interpretation among studies herein, the terminology used by the authors was adopted as is.] As the number of water molecules (λ) in the membrane increases, the additional water molecules move faster, and their residence time decreases, hence diffusion increases.[233,234,429,446] Another similar finding is the existence of a $3H^+$ species in the dry state (which can be correlated with a nondiffusing hydronium ion, H_3O^+) that does not exchange and participate in transport, regardless of λ (see Figure 38). This is in agreement with the fact that three bonds in the first solvation shell of H_3O^+ cannot participate in proton transfer in water,[607] which was observed for PFSAs.[62,71,72,447] These interpretations agree with MD models and uptake studies wherein there are two characteristic regimes: initial water molecules form a hydration shell around SO_3^- sites with additional water molecules behaving more bulk-like far from the polymer–water interface with less restricted motion (see section 4.4.3 and Figure 38). The transition between the two regimes, occurring around $\lambda = 5$ to 7, happens to be the transition in dynamic behavior of water as well (see Figure 7, Figure 28). Thus, a general finding is that with hydration, the characteristic sizes increase and the characteristic times decrease, both approaching asymptotic values at higher water contents. In addition, water dynamics studied at subzero temperatures revealed that proton jump diffusion in PFSA is lower than that in bulk water at 25 °C but decays slower during cooling and becomes higher once temperature goes below −13 °C owing to the stable H-bond network in confined acidic environment.[609] Recently, Page et al. studied the polymer-chain dynamics, which was found to increase with temperature and water content, although the latter reaches a plateau after $\lambda = 6$, similar to the local dynamic behavior of water.[603] These studies collectively indicates a coupling between the dynamics of water and the polymer chains through the side-chains.

Berrod et al.[429] examined the structure-transport interplay in PFSAs by means of surfactants to create hydration-dependent mesoporous phases and investigate their dynamic behavior via NMR and QENS. In the low q-range, the water residence time, $\tau_{\mathrm{residence}}$, was around 30 ps and hydration independent, while a hydration dependent residence time was observed of $\tau_{\mathrm{residence}} =$ 15 to 3 ps, with increasing λ (in accord with previous findings discussed above). The $\tau_{\mathrm{residence}}$ for water also decreases with increasing confinement size of the water domains, and reach a constant value for sizes over 1 nm, approaching bulk-water values.[429] Below 1 nm, water domains are confined, and their behavior is governed by the size and local environment; after 1 nm, is like an assembly of hydrophobic obstacles that limit long-range transport only, reminiscent of tortuosity. Since the $\tau_{\mathrm{residence}}$ is related to the proton hopping and H-bonding reorientation (rotational motions), such findings reveal insight into the conduction mechanisms occurring at molecular level within the nanodomains.

4.4.2. Nanostructure/Conduction Interplay.

When it comes to the structure-conduction interplay, one must recognize that various time- and length scales exist in the PFSAs influencing the transport mechanisms. As discussed in refs 429 and 504, one probes smaller length and time scales going from conductivity (κ) to NMR (D') and to QENS (local diffusion). While the former techniques characterize the microscopic transport within millisecond (ms), the latter provides information into transport in confined (nm) spaces with picosecond (ps) resolution. Thus, the differences in transport properties measured via these techniques elucidates the underlying mechanisms of the structure-transport interplay, but also resolves some of the differences in the measured diffusion coefficients, as highlighted in Figure 28. For example, Berrod et al.[429] reported that, upon hydration, local diffusion (from QENS) increased by a factor of 2, while the residence time decreased by a factor of 7. In contrast, self-diffusion (D') changes by more than an order-of-magnitude. Such changes are in accord with the analysis by Kreuer et al.,[504] who articulated that the molecular-level environment (<1 nm) of PFSA is more of an acidic-solution-like, while the microscopic length scale depends on the mesoscale network as discussed in section 3.1 (also see Figure 28). Therefore, it is critical to understand water transport across the length scales and changes, with higher length scales causing more morphological restrictions to transport arising from the morphology, grain boundaries, and mesoscale domain connectivities (see sections 3.1 and 3.2).

The transport of water and protons is correlated as well to structural variations within the polymer. An effective tool to characterize and probe these interactions is dielectric spectroscopy,[2,18,134,147,298,344,578,588,590,603] which enables the investigation of polarization and dielectric strengths as well as the temperature-dependence of ion transport and associated relaxation mechanisms over a range of frequencies.[2,18,34,132,134,298] In dielectric spectroscopy, the measured complex permittivity is the superposition of all of the phenomena, such as polarization and dielectric relaxation events, characterizing the electrical response of a material.[34,134,298,578] The dielectric constant (relative permittivity) is also related to chemical polarity (as discussed in section 2.6) and water uptake. The stronger the confinement of water in hydrophilic domains/channel, the lower the dielectric constant.[16,578,604] Thus, the dielectric constant of PFSAs increases with both water uptake, λ, and frequency (Figure 33c).[578]

In an early study, Paddison et al.[578] reported, using the dielectric spectroscopy in GHz range (0.045 to 30 GHz), that the dielectric constant increases with increasing water content and decreases with increasing frequency, much like the behavior of water. Conductivities extracted below 5 GHz are in agreement with other conductivity measurements. Interestingly, when compared to PTFE, dry Nafion exhibit comparable dielectric constant but much stronger loss, due to presence of side-chains possibly with a residual water molecule. While GHz relaxations are observed for bulk-like properties of free water,[578] lower frequencies are associated with the restricted motion of water molecules in confined spaces, such as the bound water at lower λ. In the bulk-like regime, (free) water molecules have more rotational freedom, which increases polarization (or polarizability). Thus, shifts to higher relaxation frequencies indicate faster movement of water molecules, which happens as λ increases.[2,132,133,298,578] Frequency shifts to higher values also occurs with increasing temperature, in which increased chain dynamics also play a role.[2,34,133,134,603] The dielectric loss peak, tan δ, is related to interfacial polarization between hydrophilic and hydrophobic phases in the polymer, where short-range ion migration occurs. The loss peak shifts to higher frequency with increasing water content due to faster polarization at the interfaces.

Using broadband dielectric spectroscopy (BES), Di Noto and co-workers have investigated the nature of transport mechanisms and various relaxation events in PFSAs of various EWs.[2,133,436] The overall long-range conductivity was shown to have three components: electrode polarization (κ_{EP}) and two interfacial (κ_{IP_1} and κ_{IP_2}) polarizations, representing the proton exchange within the hydrophilic domains, and proton migration along the hydrophilic/hydrophobic interfaces, respectively. These values also change a few orders of magnitude from dry or (subzero temperatures) to wet and high temperatures, controlling the long-range total conductivity; formation of a water-network with interfaces upon hydration activates interfacial polarizations. The total conductivity can be expressed and simplified as[2]

$$\kappa = \kappa_{\mathrm{EP}} + \kappa_{\mathrm{IP}_1} + \kappa_{\mathrm{IP}_2} \approx \kappa_{\mathrm{EP}} \tag{54}$$

which implies that it is the proton exchange between hydrophilic domains that limits the proton conduction. Similarly, for lower EW membranes, the contribution from

κ_{IP} becomes more pronounced due to the larger fraction of ionic groups (and side-chains) creating new interfaces, thereby reducing the hopping distance for protons.[2] On the other hand, larger, but less interconnected, domains in high EW membranes facilitate proton transport mainly via migration through the percolated channels (e.g., bridging sites) connecting the domains. These findings are also in good agreement with picture emerged in section 4.2.2, where the reduced interdomain distance with continuous transport pathways enhances conductivity in low-EW PFSA (Figure 35). BES has also been shown to be valuable for analyzing composite membranes with secondary particles (see section 7.2) due to its ability to identify the interfaces between the polymer and hydrophilic domains and their role in facilitating transport.[70,71,73133,436,590]

Dielectric relaxation behavior of PFSA also reveals the thermal transitions (e.g., α, β) in the membrane,[2,18,34,132,133,298] similar to those obtained by DMA (see section 5.4) and other techniques.[91,131,603,623] This highlights the existence of interrelated relaxation mechanisms for polymer chains and ionic associations (see section 3.3). While the former is related to the segmental motion of polymer chains (including the actual glass transition of the fluorocarbon backbone), the latter is governed by the time that an ion pair resides in an aggregate before hopping to another site. This ion-hopping transition has been attributed to the cluster transition, or α transition, but not the glass transition[18,91,603,623] (see section 5.4 for further discussion). A manifestation of this phenomenon was realized during annealing of a PFSA, which was found to increase the α- and β-relaxation times from BES by lowering their frequency due to desorption and diminished free volume.[104] Nevertheless, annealing, while reducing network connectivity, increases conductivity via hopping between the SO_3H groups along the interface.[104]

Another technique to probe these interactions is FT-IR, which can be used to explore the nanoscale relationships as it can quantitatively measure the molecular interactions between the solvents and polymer through shifts in the infrared spectra obtained across wavelengths or vibrational bond energies.[128,380] A key fingerprint of IR Spectra of PFSA is that with hydration, the band ascribed to stretching vibrational modes of the nondissociated $-SO_3H$ groups disappears, while that of $-SO_3^-$ band gradually increases and shifts to lower frequencies, indicative of proton dissociation.[41,222,226,372,374,381,383,388,625] This hydration effects are associated with reduced interactions between $-SO_3^-$ and H_3O^+, and accompanied by increasing H-bonding, which raises − OH bending frequency but lowers − OH stretching frequency.[222,226,372,373,383,625] Thus, spectroscopic techniques have been proven to be powerful to distinguish the structured (H_3O^+) and free water (H_2O), due to their distinct vibration modes that changes with hydration levels.[222,226,372,373] While water becomes increasingly bulk-like in a fully hydrated PFSA, it is still less strongly H-bonded than in aqueous water solutions.[372,381] Such changes in behavior of water spectra (e.g., S−O and −OH stretching bands) have also been studied as a function of hydration to examine the diffusion mechanisms[379,383,567] (see section 4.1). In addition, since early studies demonstrating the changes in bands associated with the polymer (e.g., CF_2 and C−O−C) during hydration indicative of side-chain contribution,[41,381,388,391] the role of polymer−water interface and side-chains have been studied to examine the substructures in various PFSAs.[2,41,374,377,391] In fact, these structure−transport correlations have been further exploited to investigate the dynamics of backbone motions and ion mobility[2,133,384] and the impact of side-chain chemistry[2,3,45,75,377] (also see section 3.3.1). Moreover, Hallinan and Elabd demonstrated that FTIR can be used to probe water diffusion (O−H band) accompanied by polymer chain relaxation (C−F band).[128,379,380] Conductivity was also shown to be correlated well with the O−H bending band, revealing the key role H^+-dissociation, which occurs even at low hydration levels,[2,226,378] and subsequent H-bonding plays in proton transport.[319,378]

4.4.3. Molecular Dynamic Models. Molecular dynamics (MD) simulations can possibly provide guidance into the morphology/transport interplay at the nanoscale, especially with the complex proton conduction. Since the mid-1990s, an increasing number of MD simulations have been conducted, concurrent with the ever increasing experimental investigations on transport and morphology of PFSAs. It should be noted that interest in modeling of proton transport predates these studies, such as the work of Tuckerman et al.,[582] who showed the key role fluctuations of hydronium and Eigen and Zundel ions play in transferring a proton in liquid water. Thanks to advances in modeling techniques and computational power, simulation studies of PFSAs have increased significantly, as well as their contribution to the current understanding of PFSAs (for further information see the reviews and discussions by Kreuer,[16] Paddison,[23] Elliott and Paddison,[71] and Voth[459]). Early studies by Paddison and co-workers explored the nature of the side-chain and its role in proton dissociation at minimum and higher hydration levels.[462] These studies also allowed the calculation of properties in a water-filled pore domain, which revealed a bulk-like structure in the center where transport is facilitated by proton hopping, whereas, at the polymer/water interface (within <1 nm of pore wall), transport is vehicular in nature.[23,463−465] Such changes are driven by the dielectric properties within the pore, where the permittivity of water at the center varies from 70% to 100% of bulk value ($\varepsilon = 80$) with increasing water content.[23] Consequently, diffusion and mobility of water and ions is faster in the center of the domain and increases with λ.[463−465,467,533] As summarized by Kreuer and Paddison,[16,23,73] these studies also demonstrated that the dissociated state is a result of the excess positive change being stabilized in the H-bonding network of water, and the excess electron density (due to breaking of the SO_3-H bond) is delocalized by the neighboring chemical group. H-bonding between the SO_3^- groups are favored, which creates a continuous water network (within the first hydration shell) even at minimal hydration where partial dissociation of protons starts with λ values as low as 3.

A number of studies confirmed that a minimum hydrated state of $\lambda = 3$ is necessary for protons to dissociate.[62,71,72,447] In such a low hydration state, water molecules occupy the first hydration shell and have exceptionally high residence time (almost 1 ns, in line with QENS), restricting their mobility (low diffusion).[72,446] With increasing hydration, SO_3^- groups move apart (which results in an increase in cluster spacing), and the residence time of water molecules decrease by 1 order of magnitude (~50 ps), accompanied by reduced relaxation time, which improves their mobility and diffusion.[72,349,446−448,452,534]

Hence, another critical water content appears to be around $\lambda \approx 7$, below which most hydronium ions remain within the first hydration shell around the SO_3^- sites.[71,72,349,357,446,452,459] Not surprisingly, this region of higher mobility coincides with the transition from bound water to free water in the sorption isotherm (see section 2.5 and Figure 7). At higher levels of hydration, $\lambda > 7$, water accumulates beyond the first hydration shell where it is more mobile, for it is less affected by the strong water-sulfonate electrostatic interactions. In this state, the separation between the SO_3^- and H_3O^+ increases and their interactions are mediated by water (which pulls H_3O^+ away from SO_3^-), which increases the mobility of H_3O^+.[71,72,349,357,446,447,452,459] In this state ($\lambda > 6$ to 7), water molecules rotational mobility also increases, which facilitates structural diffusion (i.e., proton hopping).[71,349,357,446,447,459] Hydrogen bonding is the most fundamental feature of the proton transport in PFSAs, and therefore its understanding is an integral aspect of structure-transport interplay in them. Paddison and Elliott summed up the essential ingredients of proton transport as complexity, connectivity, and cooperativity.[71,73] Complexity of proton conduction encompasses the mechanism discussed above, dissociation of H^+ (from the acidic site), transfer (to the water molecules), separation of the hydrated proton (H_3O^+) from the conjugate base (SO_3^-) and its diffusion in confined water. Proton transfer also requires a cooperative hopping diffusion process with transition between Zundel and Eigen-like moieties (or configurations).[16,23,62,68,70,71,73,357,457,459,472] At this point, it is also worth differentiating the direction of hopping, as it could be forward (constructive) or backward (nonconstructive, i.e., coming back to the oxygen site of the original water molecule).[357,453,454] The net proton hopping is controlled by the electrostatic interactions between excess protons and SO_3^- groups, dominant within the first solvation shell (low λ) and the repulsion with other protons, resulting in greater occurrence of forward hopping.[357]

As discussed in studies by Voth and co-workers,[348,357,456,459] since the hydrated proton is a dynamical electronic charge defect transferring through multiple water molecules, the simulation method must account for dynamically readjustable chemical bonding topology.[459] While AIMD could capture such processes, where, the electronic degrees of freedom are treated explicitly, it is computationally expensive. Another method that can capture the reactive nature of chemical process is reactive multistate MD, which uses a combination of multiple binding topologies to describe the chemically reactive system.[357,456,459] These studies indicated that the most likely structure in the hydrated state are Eigen-type complexes, in which a proton charge defect resonates between three possible distorted states of the complex until a successful hopping occurs. An interesting finding in these studies is the anti/negative-correlation between hopping and vehicular diffusion, in that their sum is less than the total proton diffusion calculated.[357,458]

The molecular modeling techniques, which were initially performed for Nafion, have been systematically extended to other PFSA ionomers over the years, in order to investigate the effect of EW and side-chain (length/chemistry) including SSC/Dow,[6,62,63,66,69,70,72,73,449,472] Aciplex,[472] 3M PFSA,[63,67−69,430,456,596] and Hyflon.[467] Most of these studies agree on the critical role the side-chain plays in facilitating proton conduction, where shorter pendant chains result in better proton conduction due to the water molecular rearrangement and hydrophilic domain connectivity. In particular, charge delocalization and dynamic chemical bonding governs the solvation and transport of protons. Side-chain connectivity through H-bonding impacts dissociation and transfer of protons and associated diffusion of water and hydronium ions, and how they transform from dry to hydrated conditions (from vehicular to hopping in nature).[62,68,70,71,73,348,357,472] For instance, with hydration, side-chains also relax and deform with changes in their conformation, from *gauche* to *trans*, which was shown to be impacted by EW.[534] In an MD study of 3M PFSAs, Clark and Paddison showed for ultralow EW (<600 g/mol), where proximity of SO_3^- groups are reduced, the proton dissociation starts as low as $\lambda = 1$, and resistance to deprotonation was reduced owing to more stable, continuous H-bond network.[68,69,596] In a recent study, Giffin et al.[2] showed that EW affects the hopping- and proton-conduction mechanisms, which are accompanied by changes in the crystallinity and conformation of the PTFE backbone. The MD simulations suggest that short(er) side-chain ionomers have improved backbone flexibility, which enhances the proton dissociation and leads to higher conductivity (see also section 4.2.2).[70,71,73,449,455,456]

Once an equilibrium morphology is obtained, self-diffusivities of water and hydronium are calculated from their mean-square displacement, which increases with hydration, similar to the experimental observations (see section 4.1.3).[65,72,357,443,446,448,449,452,456,464,465,533,626,627] Also, these studies consistently report lower diffusion for H_3O^+ than H_2O diffusion,[72,357,446,448,449,451,452,464,465] which can be explained by the stronger interactions H_3O^+ has with the SO_3^- groups, compared to H_2O, which is, however, slowly released with hydration due to increasing solvation of hydronium ions and their increased lability.[357,448] Despite variations in reported data, the difference in self-diffusion between various PFSAs (Nafion vs SSC vs 3M)[449,456] is much lower compared to the difference in their measured conductivities, which implies that the effect of PFSA chemistry and EW on conductivity is more pronounced for the hopping mechanism. Backbone conformation, side-chain flexibility, degree of aggregation, and association of SO_3^- all collectively determine the fate of proton transport (dissociation of protons and formation of Zundel and Eigen cations).[71] Recent MD-EVB studies demonstrated that proton transport primarily occurs through the hydrophobic/hydrophilic interface in a hydrated PFSA, where low surface areas are favorable.[355,356] This is in agreement with the improved conductivity observed for lower-EW PFSAs owing to their more continuous transport pathways, as discussed in section 4.2.2 (Figure 35b). Thus, given that EW and side-chain chemistry, along with processing methods, directly impacts the nature and fraction of polymer/water interface (see section 3.3.1), one would expect strong implications on transport mechanisms, in agreement with BES studies (section 4.4.1).

Finally, it should be noted that there have also been studies in which multiple physical phenomena were combined (such as equilibrated mesoscale structures from DPD with kinetic Monte Carlo, or thermodynamic data and chemical potentials[348,354]) to study various other aspects of transport, including electro-osmosis,[454] conductivity,[348,627,628] gas permeability,[469,626,629] sorption,[349,354] or glass transition temperature.[630]

4.5. Gas Transport

Permeation of gases through polymeric membranes obeys a solution-diffusion mechanism by which sorbed gas molecules dissolved at the upstream side of membrane diffuse through the membrane and desorb at the downstream face. The permeability of a gas i, P_i, can be described as a product of its intrinsic physical property of the gas-polymer pair diffusion coefficient, D_i, (kinetic or mobility term) and its solubility coefficient, S_i, (equilibrium or thermodynamic factor)

$$P_i = D_i S_i \tag{55}$$

The gas diffusivity is a function of penetrant gas size, available free volume (nano/microcavity) within the polymer matrix, polymer structure and morphology, polymer polarity, gas concentration, and operating temperature. Gas solubility is influenced by the penetrant gas condensability, gas-polymer pair interactions, and polymer morphology. Thus, the permeability of a gas is a result of a complex, and sometimes competing, interplay that is strongly related to the polymer's phase-separated morphology. For example, while O_2 diffusivity increases with temperature and humidity, its solubility decreases.[280,301,631] These trade-offs often result in the gas permeability being less sensitive to various parameters than either the diffusivity or solubility. Gas permeability through a PFSA membrane has been measured in the literature using a number of techniques,[15,632] including the volumetric method (measuring permeation under pressure),[633−636] time-lag study,[394] gas chromatography,[249,301,637] and electrochemical cells.[280,632,638−641]

Generally speaking, gas permeability in PFSAs increases with relative humidity[249,280,303,632−634,637,638,640,642−644] and temperature,[249,303,631−634,636−640,643−646] and decreases with thermal annealing[97,647] and aging.[648] The latter effects could be associated with the morphological changes driven by increased crystallinity and reduced domain-connectivity. The humidity-dependent increase in selected gases are shown in Figure 39, and the temperature dependence (which follows an Arrhenius behavior) is discussed in more detail in section 4.7. Some of these studies systematically investigated a wide range of gases,[394,635,641] including cation effects[301,394,636,641,646] and membrane thickness effects.[646,647] In these studies, the most commonly investigated gases are O_2 and H_2, followed by CO_2,[394,635,643,647,649,650] N_2,[394,634,635,643] He,[394,634,635,643] CO,[639] Ar,[635] CH_4,[394,635] and ammonia.[636]

Despite variations in measured values, the following generalized trends can be found: Permeability decreases in the order: He ≫ H_2 ≫ CO_2 > O_2 > Ar > N_2 > CH_4 (Figure 39), while gas diffusivity decreases in the order: He ≫ H_2 > O_2 > Ar > N_2 > CO_2 > CH_4, and solubility increases in the order: CO_2 > CH_4 > Ar ≈ O_2 > N_2 > H_2 > He. The solubility could be attributed to condensability of the gases: CO_2 is the most condensable gas, with a high critical temperature, making it highly soluble, whereas He is least condensable gas (196 vs 10 K).[394] Permeability of a gas, on the other hand, scales inversely with its kinetic diameter (KD).[394,643] This results from the opposite effects on S (increases with KD) and D (decreases with KD). Given that the activation energy for P also increases with KD,[394] this signifies an overall higher barrier for transport of larger gas molecules. It must be noted that CO_2 permeability through PFSA is rather unique,[634,644,649,650] comparable to high He permeability, especially at higher humidities,[649] due to its polar nature and strong interaction with the fluorocarbon chains, which it plasticizes.[634,651] Due to plasticization of the matrix, CO_2, unlike other gases, exhibits a pressure-dependent permeability.[635] A direct consequence of this is seen when the PFSA membrane is swollen with an alcohol, which plasticizes the membrane, reducing its free volume, and further restricting the diffusion of gases, in particular nonpolar gases such as CO_2.[652]

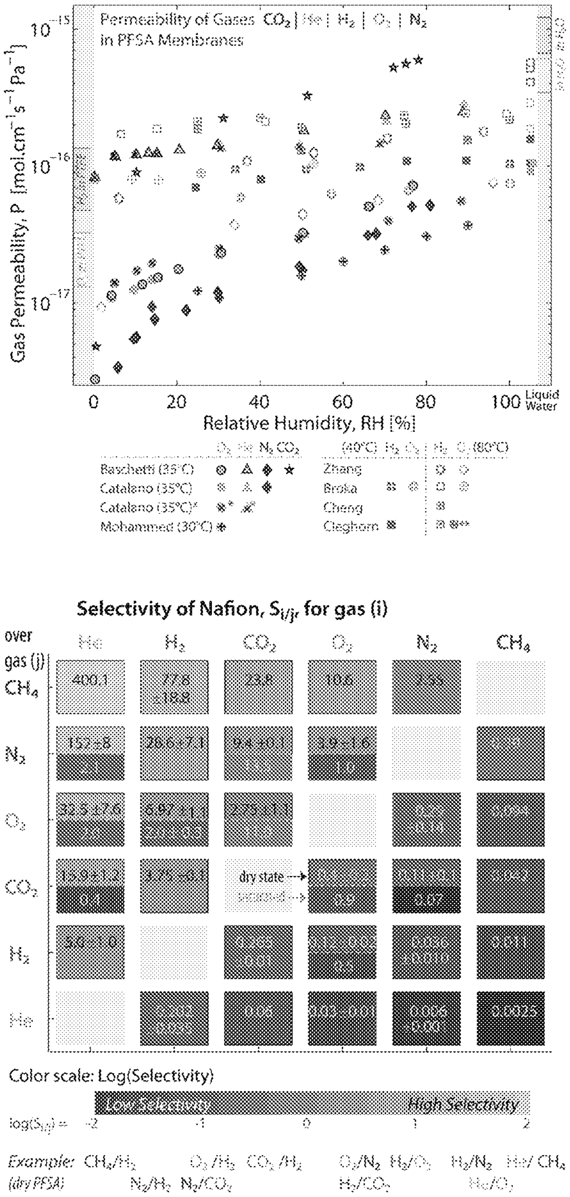

Figure 39. Permeability of various gases in PFSA membranes as a function of relative humidity. Data taken from refs 249, 287, 303, 634, 638, 643, and 655. The range shown on left and right side of the figure are for permeability (of O_2 and H_2) in PTFE and water, respectively.[15,249] All of the data shown are for Nafion membranes, except two cases: Aquivion (* by Catalano et al.[634]) and Gore-Select Membranes (**, by Cleghorn and Kolde[287]). Bottom diagram displays a selectivity matrix for the selectivity of PFSA for various gases, S_{ij}, in dry and saturated state, at 25 to 35 °C, based on measured data from refs 303, 394, 634, 635, 643, 645, 646, and 656.

As seen from Figure 39, the gas permeability in PFSA increases with humidity and is bounded between its low permeability in PTFE (similar to dry PFSA) and high permeability in aqueous water (similar to wet PFSA). Such a trend clearly shows the unique role of the hydrophobic and hydrophilic phases on permeability. While at lower hydration levels, higher gas solubility in the hydrophobic backbone contributes to permeability, with increasing hydration, diffusion through the hydrophilic (water) domains becomes the dominant factor. It is these water-rich domains and their interface with the backbone that create the interactions responsible for the gas transport behavior in PFSAs. For example, the higher permeability of H_2 compared to that of O_2 is attributed to its small size and weak interaction with the PFSA, and for the very same reason O_2 is affected more by these interactions and exhibits a stronger dependence on hydration (vs H_2).[626,634] Similarly, Nafion has a higher activation energy for gases than PTFE, again owing to its interactions and ionic groups.[394]

The nature of interactions and contributions from these phases is still not completely resolved, due in part to the presence of an intermediate region where the gas transport is influenced by the interactions and motion of the side-chains. For example, MD and DPD studies have shown that gas molecules tend to diffuse through this interfacial region, and, with increasing hydration, they shift their adsorption locations to the hydrophilic domains.[626] Thus, while diffusion increases with λ, solubility decreases.[626] Another study showed that at the same water volume fraction, PFSA membrane with the lowest EW exhibited the highest permeation, and gas permeability increases linearly with domain spacing.[469] These predictions are also in line with the measured reduction in gas permeability with increasing crystallinity.[97,249,653,654] An increase in the PFSA hydrophobic amorphous fraction due to high EW results in an increase in gas solubility, while reducing the size and connectivity of the hydrophilic domains, which are the main transport pathways, leading to an overall decrease in permeability.[97] On the other hand, a decrease in the amorphous domains induced by heat-treatments resulted in a decrease in gas solubility and created larger crystallites that increased gas-barrier properties via more tortuous diffusive pathways.[14] As a result, heat-induced crystallinity results in a decrease in gas permeability.

Since gas permeability is traditionally attributed to free volume in polymers, this correlation has been investigated in PFSAs as well.[300,301,303,626,642] These studies revealed that a correlation between the free volume and gas permeability holds only in dry state,[301,303] enforcing the key role of water (domains) in gas permeability. It is worth noting that this deviation from free-volume theory starts around 60% RH, which happens to be the transition from bound to free water molecules, at which a disordered water-network could form that enhances gas diffusion (Figure 13).

Lastly, gas selectivity of PFSA for gas i with respect to gas j is usually defined as the ratio of their permeability: $S_{i/j} = P_i/P_j$, which is, by definition, related to their ratios of diffusivity and solubility. The selectivity of PFSA membranes for mixed gases reported in the literature exhibits a large variation (from 0.1 to 100), but overall the following trends can be deduced as summarized in Figure 39: $He/CH_4 > CO_2/CH_4 \gg He/N_2 \approx He/O_2 > O_2/N_2 \approx N_2/CH_4$.[634,635] CO_2 selectivity is in the order of CO_2/N_2[647] > CO_2/CH_4[635] > $CO_2/O_2 > CO_2/He$.[643,647] Overall, Nafion exhibits exceptionally high selectivity for He and H_2 or ammonia/N_2[636] and low selectivity for CH_4 or for Cl_2/N_2.[173] Nafion was also shown to be selectively permeable to ammonia compared to N_2 or O_2, with strong temperature dependence over 100 °C, although ammonia reacts to form ammonium ions inside the PFSA.[636] Catalano et al.[634] and Baschetti et al.[643] demonstrated that while permeability increases with RH, selectivity goes down but still remains higher than their values in pure water,[634,643] with the exception of CO_2, for which selectivity increases with hydration.[643] Similar to its effect on permeability, annealing decreases selectivity,[647] as with any other factor that tends to reduce hydrophilic domain size/connectivity and increase crystallinity or ionic cross-linking (such as doping with cations or inorganic fillers, see section 7).

Lastly, any factor affecting the morphology is expected to change the gas permeability, including cation exchange. Among all other cations, PFSA in H^+ form has the lowest permeability and solubility, and is also the most sensitive to temperature changes.[394] Thus, exchanging H^+ with larger cations in a PFSA tends to reduce diffusivity due to changes in connectivity and domain size and increase solubility as a result of lower entropy due to stronger cation/sulfonate interactions.[301,394] Naudy et al.[648] showed that cross-links formed between the sulfonate groups of PFSA during aging or contamination, reduce both diffusivity and overall gas permeability by restricting gas mobility and creating more tortuous pathways (see section 7.1 for aging and cation effects). Similarly, confinement effects are expected to change the gas-transport properties in thin films (see section 6). Overall, gas permeability and selectivity of a PFSA membrane are governed by (i) backbone (EW, crystallinity), (ii) side-chain chemistry (amorphous regions and polymer/SO_3 interface), and last (iii) ionic groups and hydration (cation interactions and hydrophilic domain size and connectivity), along with hydration and temperature effects. Despite a wide spectrum of gases investigated in Nafion membranes, there is still a strong need to examine gas transport and selectivity in PFSAs, especially with hydration effects, given the expanding application-base and ionomer (side-chain) chemistries.

4.6. Impact and Transport of Alcohols

The transport of nonwater neutral species through PFSAs is of interest for different applications, especially alcohols used in direct-alcohol fuel cells; Nafion/methanol systems have been investigated the most. Due to the various setups and alcohol concentrations used in the studies, measured values tend to differ and must be interpreted in conjunction with species (ion, water, and alcohol) that are tracked and the membrane system employed. Studies include permeability,[190,545,551,657−660] pervaporation,[659] diffusion,[190,239,379,508,661] self-diffusion (e.g., NMR),[282,297,661−665] electroosmosis,[661,665] conductivity,[343,344,662,666,667] cation selectivity,[666] as well as uptake (methanol,[190,239,282,340,346,664,667,668] ethanol,[190,282,346,508,667,668] ,668 and propanol[282,346,508,668]). Although solvent uptake was discussed in section 2 from a sorption perspective, it will be revisited here within the context of transport since uptake (i.e., solubility) and diffusion are closely interrelated in controlling permeation and transport in PFSAs in water/alcohol mixtures.

PFSA membrane prefers alcohol over water and absorbs more by weight,[190,340,545,658,664] which could be explained by a number of phenomena such as higher affinity of alcohols in PFSAs and their lower hydration energy,[188,190] higher viscosity of alcohols,[658] and the alcohols' ability to solvate the fluoroether side-chains.[508,669] At the same external concentration, the uptake decreases in order: propanol > ethanol > methanol > water,[190,245,508,658] which is the same order as their viscosity.[658] In terms of transport properties, generally speaking, water diffusivity is higher than methanol diffusivity by up to three times depending on methanol concentration.[190,508,661,665] Also, for a given volume fraction of solvent, diffusivity follows the trend: from high to low is water > Methanol > Ethanol > Propanol,[508] which is the reverse order of uptake, suggesting that swelling-mediated morphological changes hinder solvent transport. It has been observed that the

Table 11. Activation Energies for Various Processes Measured for PFSA Listed Based on the Measurement Type[a]

property/process		range [kJ/mol]	PFSAs
proton conductivity	κ	9−22	Nafion[54,102,134,186,289,290,309,312,314,504,524,587−592]
		12−27	3M[2,56]
		10−11	Dow[6,54]
		15−25	Gore-Select[287,314]
		7−10	Flemion[186]
		36−65	Nafion, freezing range (−50 to 0 °C)[55,309]
proton conductivity	κ	20−45	thin film Nafion[487,679,680]
		115 (<20% RH)	thin film Nafion[487,679,680]
self-diffusion (PSGE-NMR)	D'	11−23 (RH)	Nafion,[39,186,191,256,282,297,304,310,511]
		14−26*	Nafion, from WLF[297]
		20−23	Nafion, freezing range (−50 to 0 °C)[186,304,512]
		20−25	Nafion, in alcohol mixtures[282]
		20−30	Flemion[186]
self-diffusion (MD simulation)	D'	11−20	Nafion[357,533]
permeation and diffusion	k	15−30	Nafion[328,591,661]
sorption and diffusion	D_d	20−31	Nafion[137,246,251,298,299,551,588]
gas permeation	P	15−49	Nafion,[394,631,633,634,643,645] depending on the gas[34,132,435,522,681]
DMA, mechanical properties	E	10−12	Nafion[34,284,305]
	E	40	Nafion, with WLF[118]
dielectric spectroscopy and relaxation (time)	τ	40−60	Nafion[2,34,132,134,524,590,603] some with VTF
	τ	10−25 (low EW)	3M, with VTF[2]

[a] Asterisk (*) indicates studies in which non-Arrhenius forms of temperature-dependence were examined (see section 7.3 for trends with various cations).

kinetics of alcohol uptake and subsequent diffusivity decrease with alcohol concentration.[379,508] Despite a lower diffusivity in alcohols, preferential solvation of fluoroether side-chains by the alcohol[190,406,435,669,670] (which is less repulsive to TFE) results in structural changes such that the effective diffusivity for alcohol increases more rapidly in a narrow concentration range.[508] This additional interaction results in additional swelling and assumed lower tortuosity. However, due to their larger size, alcohol molecules diffuse slower in the hydrophilic-domain network especially when large ionic hydrophilic domains are present, as discussed elsewhere.[190,282,379,660,668,671]

To characterize the solvent uptake in a mixture, a partition coefficient or selectivity value is typically used,

$$S = \frac{\mathrm{mol(H_2O)}}{\mathrm{mol(solvent)}}_{\mathrm{membrane}} \Big/ \frac{\mathrm{mol(H_2O)}}{\mathrm{mol(solvent)}}_{\mathrm{solution}} \qquad (56)$$

For water/methanol mixtures, the selectivity is around $S = 1$ to 2.5,[659,668] with higher values for thinner membranes.[659] Additionally, one is concerned about selectivity in terms of transport (see section 7.3). It should also be noted that selectivity alone is not an adequate descriptor since one must also be concerned about the absolute magnitude of the transport property. Selectivity of water in alcohol mixtures depends on the size of the domains and the cationic interactions and increases with stronger interactions between the cations and water, for a given domain size.[306] To assess the nature of conductivity in alcohols, an alternative definition of selectivity out of a need for a practical metric has also been adopted based on the ratio of the protonic conductivity to permeability of the solvent, P_S,[672]

$$\alpha_S = \frac{\kappa_{H^+}}{P_S} = \frac{D_{H^+} c_{H^+} F^2}{D_S K_S RT} \qquad (57)$$

where D_S and K_S are the diffusivity and partition coefficient of the solvent. The above expression has practical use especially in applications where high conductivity−low permeability trade-off is essential, such as DMFCs. The expression above indicates that the proton conductivity (diffusivity and concentration) and solvent diffusivity are intrinsically related making it difficult to increase one while decreasing the other. This selectivity defined above has been adopted in many studies where the goal was to minimize solvent crossover (permeability) without sacrificing proton conductivity (even for non-PFSA membranes).[672] Such a trade-off has motivated research into hybrid membranes with inorganic fillers and inert additives, including those for DMFCs, where minimization of methanol crossover is a key issue,[406,651,673−677] or in redox flow batteries where inactive (undesired) cation crossover is problematic.[406,678] Elucidating the nature of the coupling among various active charged and uncharged species, and altering them to enhance selectivity through additives and fillers, are key motivations behind many studies on cation-PFSA interactions and hybrid membrane modification, which are discussed in section 7.

Solvent permeability and selectivity also depend on the cationic form of the PFSA, as demonstrated in several studies.[406,546,550,660,666,670,673] In general, methanol permeability decreases with increasing cation size and valence, with PFSA-Na^+ exhibiting the highest permeability.[546,550]

In alcohol/water mixtures, the uptake-transport interplay is also strongly dependent on the alcohol fractional amount. For example, one observes a transport-property maximum as a function of mole fraction, where, at lower fractions, the alcohol transport increases with fraction up to around 0.4 to 0.6 and causes a change in repulsion between the charges and subsequent reduced diffusion, permeability, and proton mobility.[545,659,660,664,671] In the presence of other cations, this maximum becomes less evident; for example, for trivalent ions, the permeability decreases monotonically with methanol concentration.[660] In mixtures, it has also been seen that the transient diffusivity in Nafion was $D_d = 1.01 \times 10^{-7}$ cm^2/s for methanol uptake compared to $D_d = 4.87 \times 10^{-8}$ cm^2/s for water uptake, indicating faster diffusion of methanol into the membrane from the mixture.[239] In a recent study, selectivity was shown to exhibit a 10-fold decrease upon boiling compared to AsR (or heat-treated) Nafion membranes.[100]

PFSA proton conductivity also decreases in the presence of alcohol, in the order: water > methanol > ethanol > propanol, which is the same order in which the dielectric constant decreases, leading to lower polarity, reduced ionization of SO_3^- groups, and also reduced proton hopping (see section 4.3).[190,282,344,379,508,661,667,671] In fact, Saito et al. demonstrated that proton mobility is the dominant factor on conduction in alcohols, with a smaller ratio of Grotthuss to vehicular transport due in part to the lower interaction energy of protons with alcohols compared to water.[282]

Higher swelling in alcohols also opens up more space in the nanostructure, thereby increasing the diffusion rate (vehicle mechanism) whereas some protons are still transported through Grotthuss.[282] Similarly, activation energy for conductivity follows the order: methanol < ethanol < 2-propanol.[282] As in the case of water transport, the activation energy for methanol transport also decreases with methanol uptake.[551] Overall, the transport of alcohols and other solvents is still an area of future work, especially with new PFSAs being used in multiple applications.

4.7. Temperature Effects and Activation Energies

There is universal agreement on the positive impact of temperature on transport (properties), whether it is water-diffusion and permeability, self-diffusion, or ion conductivity. Due to the similarity of the effects, the impact of temperature for the various transport processes described above are summarized in this section. The temperature dependence for a PFSA property of interest, Ψ, is most commonly represented by an Arrhenius expression

$$\Psi(=D, D_\mu, \kappa) \propto \exp\left(-\frac{E_{a,\psi}}{RT}\right), \text{ or } \ln\frac{\Psi}{\Psi_{\text{ref}}} = \frac{E_{a,\psi}}{R}\left[\frac{1}{T} - \frac{1}{T_{\text{ref}}}\right] \tag{58}$$

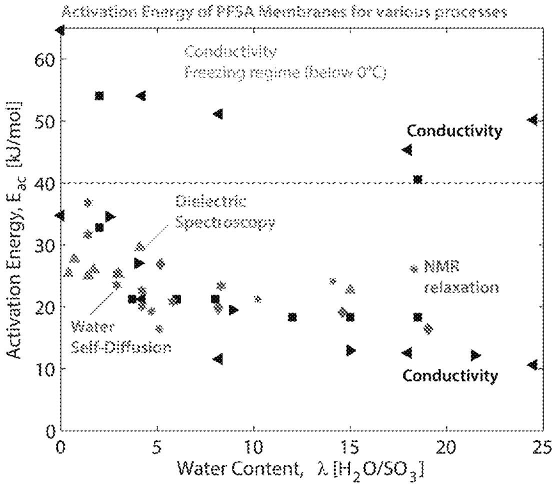

Figure 40. Activation energy of Nafion for various processes/properties as a function of water content. Data are compiled from conductivity,[102,290,309] self-diffusion,[191,297,314] NMR,[132,522] and dielectric measurements.[298] Hydration-dependence of activation energy is also shown based on conductivity measurements in the freezing regime (Thompson et al.[309]).

where $E_{a,\psi}$ is the activation energy for the relevant property (or process). The activation energies have been reported for a wide range of processes and are summarized in Table 11. Although values reported in these studies are close, it is still difficult to assign a single value for the activation energy of a given process in a PFSA due to various pretreatments, experimental differences, and the strong coupling between hydration and temperature dependence (i.e., the range of temperature in which $E_{a,\psi}$ is defined), although both effects are interrelated through the hydrated morphology. For example, trends for temperature-dependent on conductivity of PFSA membrane can be seen in Figure 34d, where the slopes represent the activation energy ranging between $E_{a,\kappa}$ = 10 to 15 kJ/mol above 0 °C, and 30 to 50 kJ/mol for temperatures below 0 °C. It must be noted that, $E_{a,\kappa}$ exhibits a strong dependence on water content, which is likely to change with temperature (see Section 2.2). [For this reason, the activation energy for conductivity may be the most accurate for preboiled membranes heated in liquid water (Figure 34d) since its water content does not change with temperature (see Figure 8b).] Thus, most activation energies provide a phenomenological property and may not represent an accurate measure of activation for proton transport. As Figure 40 demonstrates, overall, the activation energy decreases with increasing water content due to its ability to enhance thermally activated motion of water, ions, and polymer chains. Nevertheless, the effect of hydration on thermal activation is the strongest for proton conductivity, while the activation energy for self-diffusion of water appears to be less dependent on water content. In fact, the complex nature of conductivity involving water-mediated transport, proton hopping, and segmental motion of chains, all contribute to the thermally activated kinetics of proton mobility that changes significantly with water content. For this reason, the temperature-dependence of conductivity and self-diffusion have been shown in a few studies to be non-Arrhenius, and described by two other theories: Willams-Landel-Ferry (WLF),[297,622] similar to time–temperature superposition (see section 5.4), and Vogel–Tammann–Fulcher (VTF), which is given by[2,133,134,436,603]

$$\Psi(=D_\mu, \kappa) \propto \exp\left(-\frac{E_a'}{R}\frac{1}{T - T_0}\right) \tag{59}$$

where E_a' is the pseudo (or apparent) activation energy and T_0 is the thermodynamic ideal glass transition temperature at which the configurational entropy becomes zero and "free volume" vanishes.[2] It should be noted that although this expression is discussed in terms of classical polymer physics, it applies to aqueous acid-solutions as their conductivity and water diffusivity also show non-Arrhenius behavior (VTF). In the instances herein, the configurational-entropy model seems to describe well the data, thus suggesting some impact of polymer chain mobility on conductivity, which could be due to barriers moving across domains or mechanistic changes from vehicle to hopping mechanism at higher temperatures. The non-Arrhenius behavior has been commonly observed for relaxation times measured by NMR and BES.[2,133,436,524]

The temperature dependence of conductivity in Nafion and 3M PFSAs was studied in detail by Giffin et al.[2] using BES. They reported that when the conductivity follows an Arrhenius form the dominant mechanism can be considered as hopping. At higher temperatures (>120 °C) conductivity of hydrated

Table 12. Summary of Studies on Mechanical Properties of PFSA Membranes[a]

study	year	materials	reported properties	studied effects or focus
Dynamic Mechanical Response and Thermal Transitions				
Yeo and Eisenberg[298]	1977	N1100	E = f(T,λ), relaxation, T_g	temperature and counter ions
Phillips and Moore[385]	2006	N112-M$^+$	T_g shift with M$^+$, DSC	mixed counter ions
Bauer et al.[288]	2004	N117, H, Na	E = f(T,RH)	
Kreuer[206]	2013	N117	DMA, E = f(T,RH)	viscoelastic response and hydration
Shi et al.[211]	2016	N212	DMA, E = f(cation)	impact of mono- an multivalent cations
Stress−Strain Behavior and Constitutive Response				
Kawano et al.[689]	2002	Nafion-X	SS, E = f(T), dry/wet	counter ion and pretreatment
Tang et al.[284]	2006	N112	SS, E, PLS, BS = f(RH, T, direction)	RH, T, in-plane anisotropy
Tang et al.[286]	2008	PFSA + ePTFE		RH, T, reinforcement
Kusoglu et al.[123,305,690]	2009 2012	N112/PFSA	SS = f(RH, T) and relaxation	constitutive models for nonlinear response in vapor and liquid water
Ballengee et al.[7,691]	2011	e-spun PFSA	SS, PLS, E	PFSA fraction in composite
Collette et al.[193]	2013	N112,N212	SS = f(aging time)	hygrothermal aging
Kusoglu et al.[82]	2013	N212,N117	SS in dry, wet	compression behavior and pretreatment
Lin et al.[295]	2008	N212	SS = f(draw ratio)	prestretching and orientation
Time-Dependent Behavior and Visco-Elastic/Plastic Response				
Liu et al.[692]	2006	N117−H	SS, YS, TS, BS	strain rate effects
Satterfield et al.[122,126]	2006	N115-TiO_2	E, creep = f(RH, λ,T)	creep and viscoelasticity
Majsztrik et al.[124]	2008	N1110	creep, f(T, RH)	creep and viscoelasticity
Lai et al.[693]	2009	N111	creep, f(T, RH)	WLF model for t-T-RH superposition
Silberstein and Boyce et al.[694,695]	2010 2011	N212 N211	SS = f(T, RH, rate) DMA	elastic-viscoplastic model with back stress under cyclic loading
Yoon and Huang[696]	2011	N111	SS = f(RH, T)	nonlinear visco-elastic model
Shi et al.[90,697]	2015	N212	SS = f(aging, ε-rate)	aging effect on creep, moduli and T_g
Khattra[698] Lu[127] et al.	2012	N211	SS, E, PLS = f(RH,T,rate)	viscoelastic-plastic response[127] model[698]
Zhao and Benziger[61]	2013	Nafion, SSC	creep, E = f(T,RH)	EW/side-chain and creep
Mechanics of PFSAs Coated with Electrodes				
Kai et al.[699]	2013	N211	SS, E, YS, BS = f(T, RH)	fatigue and crack initiation behavior
Park et al.[700]	2007	N1110	DMA: T_g, E = f(T)	electrode material (IPMC) and DSC
Uchiyama et al.[283]	2012	N211	SS, E = f(RH) at 80 °C	deformation model and buckling
Lu et al.[701]	2014	N211	SS, PLS, E = f(RH, T,rate)	nonlinear elastic-plastic model
Goulet et al.[702]	2013	Cast-PFSA	SS, E, YS = f(RH,T)	catalyst coating
Other Studies Relevant to Mechanical Properties				
Roberti et al.[682]	2010	N115	light scattering to measure moduli; $E = E(T)$ dry/sat	
Alberti et al.[114]	2008	N117	pretreatment effect on modulus and hydration	
Kusoglu et al.[305,414] 2010	2008	PFSA	modulus; micromechanics models with hydration and freeze effects	
Moukheiber et al.[703]	2014	N111,XL,SSC	double edge notched tensile test (DENT) for fracture energy	
Grohs et al.[704]	2010	N211, N111 Gore-Select	pressure-loaded blister test to measure membrane's burst strength and cyclic fatigue response	
Li et al.[705]	2009			
Li et al.[706]	2008	N211, N11, Gore-Select	Knife-Slit test to measure fracture energy as a function cutting rate, temperature and humidity	
Patankar et al.[707]	2010			
Patankar et al.[118,138]		N211, Gore-Select	Long-term stress-relaxation and creep compliance experiments with time−temperature−humidity superposition	
Page et al.[209]	2014	Nafion films	buckling method to measure moduli of thin films of 20 to 50 nm	
Kim et al.[139]	2015	PFSA	toughness of dispersion cast-PFSAs influenced by the casting fluid	
Page et al.[91,131] 2005	2006	N117	mechanical and thermal relaxations (DMA) with various cations	
Di Noto et al.[133,436]	2009	N117	DMA with BDS for dynamic transition and mechanical relaxation	
Melchior et al.[404]	2016	N117	structural interactions controlling the viscoelasticity at high/low RH/T	
Shi et al.[708]	2016	N212, NXL	impact of reinforcement on anisotropic mechanical properties (DMA)	

[a] For additional information on properties of stabilized/composite PFSAs, see section 7.2, and on deformation in conjunction with morphology studies, see section 3.1.5. (SS, stress-strain; E, modulus; YS or PLS, proportional limit stress; BS, break stress/strain.).

PFSA exhibits VTF behavior, which suggests long-range segmental motion of the polymer chains and their viscosity were also involved in the transport process, thus mediating proton exchange.[2] In this case, E_a' characterizes the probability of a large increase in free-volume formation in the polymer matrix for ion migration and relaxation events.[2] In fact, it was shown in BES studies[2,133,436] that frequency peaks (in the transition regimes) also exhibit a VTF dependence, similar to conductivity, revealing the link between ion transport and relaxation through the morphology. Such a combined effect of ion migration and polymer-chain motion manifests itself even stronger for the activation energy of conductivity measured in the freezing regime (0−50 °C),[52,58,102,250,309] where distinct changes are observed not only in conductivity, but also in its temperature dependence (see Figures 34 and 40).

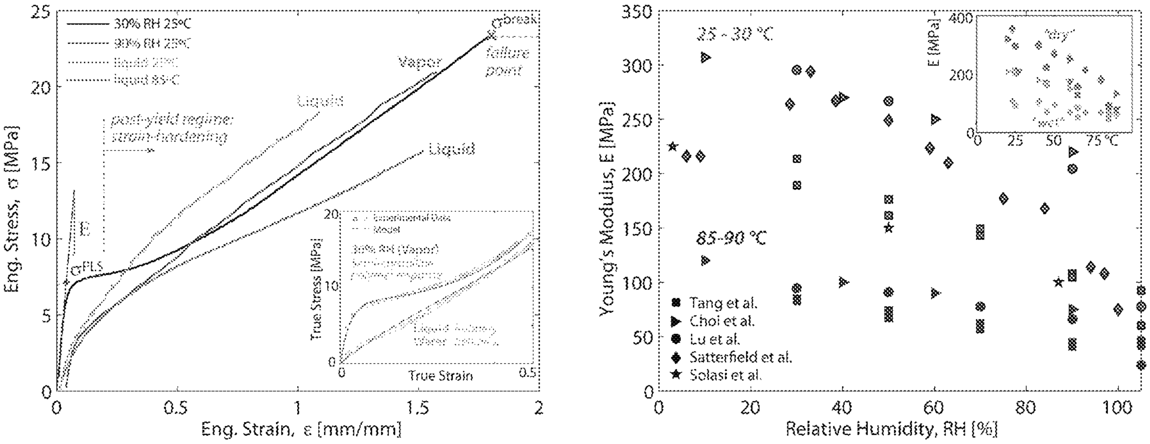

Figure 41. Stress–strain response of a Nafion membrane at 25 °C in vapor and liquid water, with the true-stress true-strain response shown in the inset, from Tang et al.[284] and Kusoglu et al.[123] Young's modulus of Nafion as a function of relative humidity at low (blue) and high (red) temperatures.[123,125−127,200,204,284,305] Inset shows the temperature dependence of the moduli measured in the literature: dry (gray) and vapor-saturated (blue) Nafion membrane.

4.8. Other Transport Properties

Besides the main properties discussed above, some studies, although scarce, have focused on other transport phenomena in PFSAs and especially Nafion. These studies include optical, acoustic, and thermal properties and are included here for reference. The refractive index for Nafion is 1.35−1.38 for the range of 400−1000 nm wavelength,[438,682−684] with a slight temperature-dependent increase toward 1.4,[682] and hydration-dependent decrease toward 1.34.[684] Nafion is almost transparent with over ~90% light transmission and close to 10% reflection, within the same wavelength range,[163,685] a property that is of interest for solar-fuels applications.[163,686,687] When hydrated, however, transmissivity decreases to ~60% with a stronger wavelength dependence.[687] Also, in a study by van der Heijden et al.,[438] birefringence was shown to be originated from orientation of the backbone chain, which could be caused by the manufacturing extrusion process or drawing, but not from the bond angles.

The thermal conductivity of Nafion has been measured to be between 0.12 and 0.19 $\mathrm{Wm^{-1}K^{-1}}$ in the temperature range from 10 to 70 °C, with a slight dependence on temperature.[688] The thermal conductivity increases with increasing humidity, reaching 0.29 ± 0.03 $\mathrm{Wm^{-1}\ K^{-1}}$ at 100% RH, 65 °C.[688] The thermal diffusivity of Nafion was measured to be 1.3×10^{-3} and $1.3 \pm 0.1 \times 10^{-2}$ $\mathrm{cm^2/s}$, at 280 and 240 K, respectively.[316]

A study on the propagation of acoustic waves in Nafion reported that the speed of sound in hydrated Nafion is lower than that in dry Nafion and water, which was attributed to the water-hydrated phase-separated nanostructure dampening the sound 10 times stronger than pure water.[316] Below freezing temperatures, however, the damping capacity decreased with ice formation.

5. MECHANICAL AND THERMAL PROPERTIES

A PFSA membrane's hydration-driven morphology (see section 3) is integrally linked with its mechanical and thermal properties. Unlike transport phenomena (see section 4), it is primarily the hydrophobic (PTFE-like) matrix that controls the mechanical stability and properties, with the additional effects arising from the ionic interactions (cross-links), thus the effective properties of a hydrated PFSA are still controlled by its phase-separated nanostructure. Mechanical deformation of a membrane can be characterized by measuring its strain (stress) in response to an applied stress (strain) under different configurations, resulting in a stress–strain (σ–ε) curve. Since deformation of an ionomer involves collective motions of its constituent chains, along with other moieties, which are all temperature dependent, mechanical and thermal properties of PFSA membranes are strongly linked via their morphology (for a given hydration level). Hence, the mechanical and transport behavior of a PFSA membrane is governed by almost the same underlying factors, in that, any parameter that changes its transport alters its mechanical properties, which is the focus of this section.

Almost all of the early studies on mechanical stability, briefly discussed in a 2004 review,[1] used dynamic mechanical analysis (DMA), which characterizes the viscoelastic response of a polymer across a range of temperatures. DMA, although useful for such thermomechanical transitions, is not always practical to predict deformation behavior with plasticity. Thus, in the past decade, an increasing number of studies characterized a broader range of PFSA mechanics, including their stress–strain behavior and plastic deformation, time-dependent viscoplasticity, and fracture behavior, as illustrated in Table 12. In addition, computational studies have explored their constitutive response and Young's modulus, all of which have expanded significantly the understanding of their mechanical properties.

5.1. Stress–Strain Behavior

Stress–strain behavior is most commonly measured using uniaxial tensile testing, ideally, at a controlled strain-rate, temperature, and humidity. An important factor that had not been clearly addressed in earlier studies is that the calculation of strain and stress relies on length (L) and cross-sectional area, respectively, both of which change with hydration. Thus, depending on the reference state used for the dimensions (i.e., initial or hydrated), stress–strain curves change. As such, deformation can be quantified in different ways, and the most common ones for polymers are

$$\varepsilon = \frac{\Delta L}{L_{\mathrm{ref}}},\ \varepsilon_{\mathrm{true}} = \ln\left(1 + \frac{\Delta L}{L_{\mathrm{ref}}}\right),\ \text{and } \Lambda = 1 + \frac{\Delta L}{L_{\mathrm{ref}}} \qquad (60)$$

which are (engineering) strain, true (log) strain, and stretch ratio, respectively, with the latter being more common for elastomers. Due to these differences, stress−strain curves for the same PFSA could appear qualitatively different.[123] Typical stress−strain curves for Nafion membrane under different environmental conditions are shown in Figure 41, along with key mechanical properties that can be determined: Young's modulus (E) from the initial slope of the linear elastic region; proportional limit stress (PLS, or σ^{PLS}), calculated from the onset of nonlinearity; failure or break strain (BS); and maximum stress at the point of failure. Even though σ^{PLS} is associated with the yield limit or strength (YS or σ^{Y}), which marks the onset of plastic (permanent) deformation, it is impossible to know when a membrane actually begins to deform plastically during loading unless loading−unloading cycles are carried out to examine deformation elasticity. Thus, PLS is a more appropriate term in this context, unless plastic yielding is identified, although PLS and YS are used interchangeably in the literature. Lastly, Poisson's ratio for Nafion membranes was reported to be around 0.4 in ambient conditions[689,690,709] and increases with hydration due to the increasing fraction of uncompressible water molecules.[414]

The overall stress−strain response of a PFSA membrane can be characterized, in accord with the mechanically-induced morphological changes discussed in section 3.1.5, as consisting of the following regimes:[123,126,690,692] (i) elastic, recoverable, deformation, with molecular-level bond stretching at lower strains, where the load is carried through the polymer aggregates that might rotate and reorient around the ion-rich water domains (within their local bundles at mesoscales, see Figure 23c), (ii) at/after onset of plasticity, (i.e., yielding) further stretching causes sliding and disentangling of the aggregates, (iii) at higher strains, (i.e., postyield) stretching causes collective motion of chains with preferential orientation of aggregates in the direction of applied load, which increases resistance to load, i.e., strain-hardening, and finally (iv) breakup of interaggregate interactions and entanglements between the aggregates that exhibit localized yielding, i.e., crazing, leading to ultimate failure with bond breaking. Nevertheless, it is the time-dependent deformation due to viscous behavior that governs a PFSA's overall mechanical response in which relaxation mechanisms and ionic interactions in the morphology all play key roles, as discussed in many recent studies.[122,123,126,404,698,61,127,693] For example, stress relaxation, i.e., reduction in stress when the membrane is held at a constant strain, can be explained by the continuous movement of chains and their disentanglements within these mesoscale bundles, i.e., molecular-level relaxation.[692]

The stress−strain behavior of a PFSA exhibits characteristic features of semicrystalline polymers: a linear regime followed by an onset of nonlinearity and strain-hardening at higher strains. These regimes have been identified for PFSAs and discussed elsewhere, along with hydration and temperature effects,[123,125,126,284,295,689,690,692,694] cation effects,[91,131,689,710,711] in relation to morphological changes,[19,82,90,91,131,192,257,295,367] and also under compression.[82] Moreover, as discussed in previous sections, thermal treatment induces higher crystallinity in the polymer matrix, leading to enhanced mechanical properties,[82,114] which are reflected as higher strength and Young's modulus. Such changes are opposite in trend to transport properties (i.e., reduced uptake and conductivity, see section 4). Similarly, for subzero temperatures, the stress−strain response changes significantly with a more brittle response and higher modulus, owing to enhanced backbone stiffness as well as reduced chain motion within the domains with possible ice formation from freezable water.[305,318] As such, reduced hydration with limited mobility of ionomer moieties collectively restrict transport mechanisms (see sections 4.1 and 4) and increase ionomer stiffness, consistent with a chemical/mechanical balance motif.

As seen from Figure 41, the stress−strain response and mechanical properties are highly sensitive to environment, and modulus, strength, and break stress all decrease with increasing temperature and hydration.[123,126,284,295,689,690,692,694] Strain at failure, for example, decreases with hydration and increasing temperature.[286,689,699,701] The effect of temperature on break strain can be better understood when the subzero temperature data are considered, that is, lowering temperature makes the membrane more brittle due to reduced mobility of the polymer aggregates. The temperature effect on deformation is governed via the main-chain motion, as with other polymers, and also by the mobility of the PFSA's pendant chains and ionic sites, which makes a hydrated ionomer's deformation more complex. The humidity effect, on the other hand, is governed by a PFSA's unique hydration-induced morphology. At low hydration levels, PFSA membranes exhibit a semicrystalline-like response with an apparent onset of nonlinearity and strain-hardening, features that are reminiscent of PTFE's deformation response. However, the onset of nonlinearity becomes less pronounced as membrane water uptake increases, with a very low PLS in liquid water. In fact, at maximum hydration, a PFSA membrane exhibits a rubber-like response (especially in true stress−strain form, see Figure 41). Stemming from this distinct deformation nature, Kusoglu et al.[690] demonstrated that the stress−strain response of a Nafion membrane can be accurately captured using models for semicrystalline polymers and swollen hydrogels, with a transition from the former to the latter at very high water uptake and temperature. The following expression was shown to predict (true) stress as a function of strain, ε, and strain rate, $\dot{\varepsilon}$

$$\sigma(\varepsilon, \dot{\varepsilon}, H, T) = \sigma^{\mathrm{Y}}(1 - \mathrm{e}^{-E\varepsilon/\sigma^{\mathrm{Y}}})(\dot{\varepsilon}^{m})(e^{h\varepsilon^{2}}) \qquad (61)$$

where m and h are the humidity- and temperature-dependent material parameters characterizing the strain-rate sensitivity and the strain-hardening behavior, respectively. They also showed that other formulations based on deformation of elasticity of gels could capture PFSA membranes deformation behavior in liquid water quite well, but not in vapor.[123,690] Thus, a PFSA membrane's stress−strain behavior changes dramatically from vapor to liquid water, which can be predicted using the appropriate models (see Figure 41 inset).[123,690]

These distinct deformation mechanisms could also explain the various factors controlling the stress−strain behavior. First of all, processing-induced changes could cause intrinsic orientation of polymer aggregates, thereby increasing the membrane's strength, albeit with anisotropy. For example, extruded Nafion membranes have better mechanical properties in the direction of machining (MD) compared to that in the transverse direction,[123,284,286,690,703] which is in accord with the nanostructural orientation observed in AsR extruded membranes.[84,131,334] This structural orientation was shown to be eliminated upon boiling in water, or thermal annealing.[84,131,334] Cast membranes, on the other hand, exhibit less in-plane anisotropy in both mechanical properties and nanostructure.[257,364] Similarly, Lin et al.[295] showed that prestretching a PFSA membrane induces even stronger anisotropy in mechanical properties, where the stress at a given strain

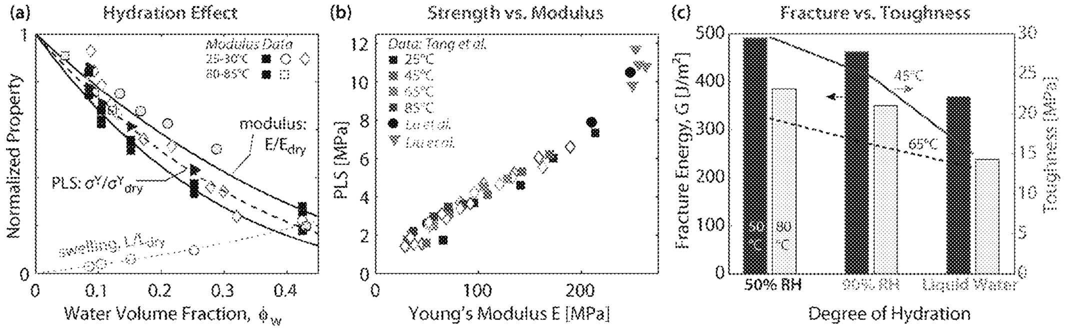

Figure 42. (a) Hydration effect on mechanical properties shown by normalized Young's modulus (E) and proportional limit stress (PLS) as a function of water volume fraction. Swelling strain is also shown for comparison. Symbols are experimental data from refs 126, 200, and 284. Lines are model predictions by Kusoglu et al.[305,414,708] (b) Relationship from E and PLS based on data from Tang et al.,[284] Li et al.,[692] and Lu et al.[701] (c) Fracture energy measured by Patankar et al.[707] compared with toughness calculated from stress−strain curves[123,284] of Nafion membrane at selected temperature and humidities.

increases in the stretching direction with increasing draw ratio. Recently, preconstraining a PFSA membrane was shown to increase yield strength and hardening, but not modulus, which was attributed to a higher degree of chain orientation induced during the preconstraining process affecting large-strain deformation.[293] Thus, regardless of the process, a membrane's mechanical response is strongly linked to the changes in nanostructure.

Moreover, nearly all literature works have focused on PFSA membranes' mechanical properties under tensile deformation, even though membranes are usually constrained and compressed in most devices. A few studies have measured the (hydrostatic) compressive behavior of membrane in liquid water in an effort to quantify the swelling pressure (see section 2.6.2), and reported pressures between 30 to 100 MPa depending on the compression ratio.[185,206,214,257,338] Budinski et al.[338] measured swelling pressure through membrane hydrostatic compression, which was extended and modeled by Kusoglu et al.,[82,194] who showed these changes are consistent with the nanostructural deformation, and the local pressures therein, consistent with the swelling-pressure-concept formulation. Such a high swelling pressure developing internal to a membrane has been shown to be key for understanding its swelling-equilibrium, as discussed by Freger,[203] Eikerling and Berg,[208] and Kreuer[206] in conjunction with surface-layer effects and vapor/liquid equilibrium (see sections 2.2 and 3.4). Naturally, a PFSA membrane under compression can accommodate larger stresses than the break stress under tension. Similarly, dehydration of a full-hydrated membrane under external compression was shown to be negligible (<10%) under stresses lower than 10 MPa.[194,257]

Composite PFSA membranes also exhibit improved mechanical properties, depending on the nature of the reinforcement or filler.[4,7,118,122,286,287,436,691,705,712−715] For example, PFSA membranes reinforced with the hydrophobic ePTFE layer exhibit a more than 2-fold increase in yield strength, modulus,[286] and tear stress[287] (see section 7.2 for more detail). However, the real impact of such hydrophobic reinforcement layers is that the membrane's modulus and strength becomes less sensitive to RH, and therefore becomes mechanically more robust in a hydrated state. As such, Young's modulus increases from ~270 MPa for Nafion to over 600 MPa for ePTFE reinforced PFSA[691] and Nafion:Nanofiber e-spun composite.[691] (See section 7.2).

5.2. Young's Modulus and Strength: Hydration Effects

As noted, hydration reduces both modulus and strength of the membrane, which is attributed to its plasticization of the polymer matrix. However, water's role is more complex. For example, at very low humidities (0 to 10% RH), water actually increases the modulus, especially at higher temperatures,[61,126,138,206,288] which is explained by its role in stabilizing the ionic sites through strong electrostatic interactions (ionic cross-links), i.e., antiplasticization effect. In fact, Bauer et al. showed that this modulus increase occurs only in protonated form, implying the role of hydrogen bonding and formation of O−H bonds that can act as cross-links, thereby improving membrane stiffness.[288] Only after $\lambda = 2$ does the plasticization effect dominate the mechanical response. A similar effect of water is seen at larger strains, where the PFSA exhibits a stronger hardening behavior,[123,690] which again could be attributed to the stiffening caused by water molecules locally restricting the mobility of oriented polymer aggregates. Naturally, these effects of water cannot be isolated from the role of electrostatic interactions. As a result of this interaction, stress−strain curves and mechanical properties of PFSA are strongly dependent on the cation type and size, which increase these properties (see section 7.3).[211,689,710,711] Thus, at low hydration levels, PFSA exhibits antiplasticization arising from the strong water-sulfonate interactions, whereas at high hydration levels, the decrease in Young's modulus is driven by its high fraction of water domains (conceptually like a hydrogel, although still with crystallinity). This phenomenon has manifested itself in various studies.[61,126,138,288,404] Benziger group,[61,126] using creep tests, identified a transition temperature of 70 to 80 °C, below which elastic modulus decreases with humidity, whereas at higher temperatures, elastic modulus exhibits an increase with a small increase in humidity from 0 to 20%, which was also supported by DMA results of Kreuer.[206] This observation was validated after a few RH cycles for both Nafion and SSC PFSA.[61] More recently, Melchior et al.[404] have investigated this phenomenon via NMR under stretching. They proposed that, under high RH, mechanical stress is transferred through the polymer backbone, whereas at lower RH and higher temperatures (i.e., dry/hot conditions), the trend is reversed such that the role of weakly hydrated ionic domains contribute to the load transfer. This reversal in RH-dependent modulus at higher temperatures was attributed in the former study[61,126] to the stronger ionic cross-links due to the cluster formation at higher temperatures, while the latter study[404] explained it by the stronger role of the Coulomb structure formed in weakly hydrated ionic domains. Since the modulus of the polymer backbone decreases at higher temperatures, (similar to that of dry PFSA in Figure 41) at low water contents, the stronger ionic interactions could dominate the mechanical response. In fact, the results from the above-mentioned studies comply with the fact that modulus of a dry membrane at a given temperature increases in the presence of cations owing to their stronger ionic interactions.[211,711] Finally, one must note that the above-mentioned effects should be considered for a given PFSA, and changing its EW and/or side-chain could induce stronger changes in mechanical stability.

The modulus/hydration relationship of PFSA membranes and factors influencing it are summarized in Figure 42a based on literature data. As noted above, Young's modulus is the single most commonly used mechanical property. In addition to the stress–strain tests summarized in Table 12, the PFSA modulus has been measured using tapered element oscillating microbalance, optoelectronic holography technique,[199,237] light scattering,[682] and nanoindentation[273] for bulk membranes, and buckling[209] and cantilever beam bending[716] for supported thin films. Young's modulus of a Nafion membrane of 1100 EW in ambient conditions has been reported to be 250 to 300 MPa,[414] depending on strain-rate.[127,692] The modulus decreases to as low as 100 MPa at higher temperatures[114,122,126,127,200,204,284,682,689] and humidities.[122,126,127,200,204,284] Despite a large scatter in measured moduli, when the RH-dependent modulus is normalized by the modulus of the dry membrane, E_{dry}, and plotted as a function of water volume fraction, all of the data follow a universal hydration dependence (see Figure 42a). Inspired from this relationship, Kusoglu et al.[305,414] employed a mechanics model to propose the following scaling expression for PFSA Young's modulus and yield strength as a function of temperature and water volume fraction, ϕ_w:

$$E = E(T, \phi_p) = E_{dry}(T)\phi_p^{\ n}, \text{ and } \frac{\sigma^Y(T, \phi_p)}{\sigma^Y_{\ dry}} = \phi_p^{\ m} \tag{62}$$

where $\phi_p = 1 - \phi_w$, and n and m are power-law exponents. These relationships were shown to arise from the PFSA's phase-separated nanostructure, in which the reduced fraction of load-carrying hydrophobic backbone with hydration reduces the effective modulus. By idealizing the shape of the hydrophilic domains as interconnected spheres or cylinders, an exponent of $n = 3.6$ or 2.4 was calculated, respectively, which are in agreement with the measured data (see Figure 42a). Also, the modulus' temperature dependence in dry state was shown to obey an Arrhenius type relationship down to −20 °C,[305] with an activation energy of 10.7 kJ/mol, very close to that reported for PTFE.[435]

The scaling exponent can be interpreted as mechanistically analogous to scaling expressions developed for conductivity (see section 4.2.1). While for conductivity, the scaling represents the increasing fraction of the water-domain network, for modulus, the scaling represents the inverse structure, i.e., the reduced fraction of hydrophobic backbone domains. This observation suggests that water's role in ion-containing, semicrystalline PFSA's mechanical response cannot be solely explained by classical plasticization observed in other polymers. In fact, earlier mechanical models also treated PFSA as a two-phase medium to determine the change in its modulus with water, which constitutes one of the phases.[35,198,717] Hsu and Gierke[35,198] presented a semiphenomenological elastic theory for ionic clustering in PFSA membranes, and proposed an expression for the cluster (domain) diameter corresponding to the minimization of the free energy. Their studies are based on the assumption that the domain shape is determined by the electro-elastic interaction energy between the ionic domainss and the fluorocarbon matrix, and the surface energy of the domain.

The phase-separated nanostructure is expected to control other mechanical properties, or their interrelation, as well. This can be seen from a plot of yield strength vs modulus, where all data pairs fall on the same line regardless of temperature and humidity. The slope of the line, which is the strength-to-modulus ratio (PLS/E) appear to be constant, regardless of the hydration and temperature. Such a findings reveals the existence of a morphology-mechanics interplay that concurrently change both modulus and strength in response to environmental changes. Thus, similar to modulus, yield strength or PLS also follows a power-law dependence, albeit with a different exponent: $m = 2.67$ (Figure 42a).[123]

Lastly, studies suggest that cations reduce the modulus in the order of $Rb^+ > Cs^+ > K^+ > Na^+ \approx Mg^{2+} > Li^+$,[196,211,689,710] and $Fe^{3+} > Mg^{2+} > Cu^{2+}$,[710,711] again with strong dependence on hydration. The impact of cations on modulus are exacerbated in dry/hot conditions or diminished with hydration,[710] which could be explained by hindered electrostatic interactions in the presence of more solvation (also see section 7.2). The increase in mechanical properties with larger cations is attributed to physical (cation-sulfonate) cross-links formed within the hydrophilic domains, which reduce mobility and thereby increase the resistance to deformation.

5.3. Time-Dependent Behavior

A convenient and useful way to study the time-dependent mechanical behavior of PFSA membranes is by means of their viscoelastic or viscoplastic response. Recent studies investigated them by using either relaxation and creep,[61,119,123,126,693,697,718] within the context of viscoelasticity, or strain-rate-dependent stress–strain response,[125,127,692,697,698,719] for viscoplasticity.[125,696,698,719] In these latter modeling studies, the measured time-dependent stress–strain data are reproduced using rheological models, typically composed of time-independent (spring element with a modulus) and time-dependent (dashpot with a viscosity) stress components, as illustrated in Figure 43 for uniaxial behavior. While viscoelasticity could be captured in relatively simple systems (i.e., Maxwell and Voigt elements), modeling of elastic-viscoplastic response requires more comprehensive models with a number of material elements that are functions of temperature and humidity.[698,720] In these multilayer models, stress is interpreted as the sum of an elastoplastic network, where yield stress and strain-hardening response are represented by a slider and spring elements, respectively, and a viscous network characterizing the dissipative behavior with a dashpot element. With such a network model, one can capture the strain-rate dependence and creep/relaxation response, under various environmental conditions. Other rheological models were also developed for PFSAs, including a multiparameter viscoplasticity model by Silberstein et al.[694] that can capture the nonlinear loading–unloading under cyclical loads. In addition, the tensile creep behavior of Nafion was investigated by Satterfield et al.[122,126] and Majsztrik et al.,[124] who reported the creep rate as a

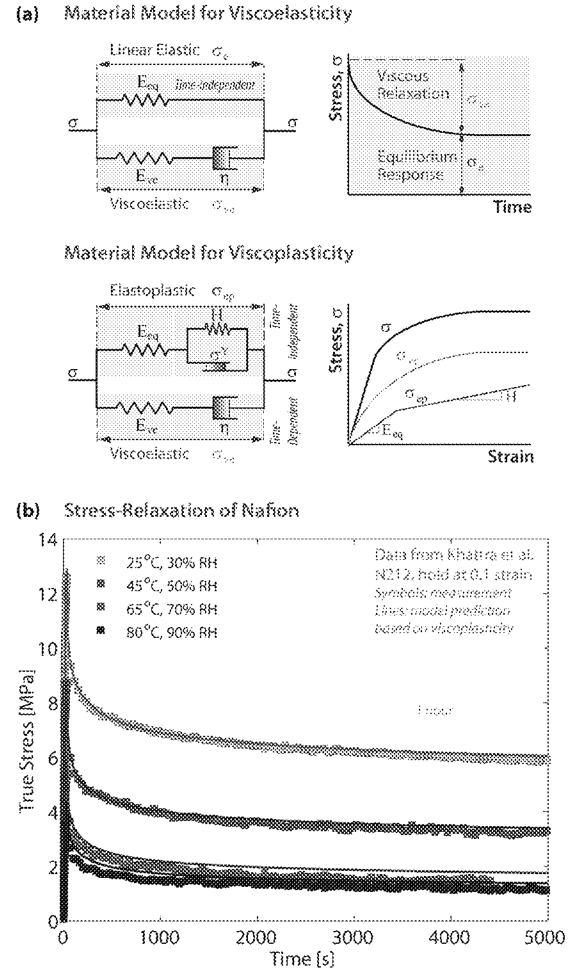

Figure 43. Representative rheological material models used in the literature to characterize the viscoelastic and viscoplastic mechanical response of PFSA membranes,[123,125,698] and stress-relaxation response of Nafion 212 membrane under various environmental conditions (measured data are modeled based on the viscoplastic model shown above, from Khattra et al.[698]).

function of temperature and humidity and discussed the membrane's viscoelastic response.

5.4. Thermal-Mechanical Transitions

DMA relies on measuring a membrane's stress response under an applied sinusoidal strain at a controlled frequency, ω, across a wide range of temperature. DMA yields the following key properties: storage modulus, E′, representing the stored energy (elastic); loss modulus, E″, representing the dissipated energy (viscous); and loss tangent, tan δ, which is the ratio of two moduli and a measure of damping factor. tan δ is a rather unique feature of DMA and shows a peak at a temperature when the material undergoes a thermo-mechanical transition. A typical temperature-scan DMA of Nafion membrane is demonstrated in Figure 44, with the characteristic transition temperatures noted. Despite being one of the oldest techniques used for Nafion, the molecular origins of the transition temperatures, in particular the "glass transition temperature" has been a subject of great interest and discussion. Most of the early discussions centered around the assignment of the peaks observed in DMA and DSC studies to particular (e.g., glass) transition temperatures or relaxation mechanisms, starting with earlier papers by Yeo, Eisenberg, and co-workers,[135,298] Moore and Martin,[38,40] and Mauritz and co-workers,[91,131,385,721] (some of which were summarized in a 2004 review[1]), and a consensus appears to have been reached thanks to these studies in the past decade or so.

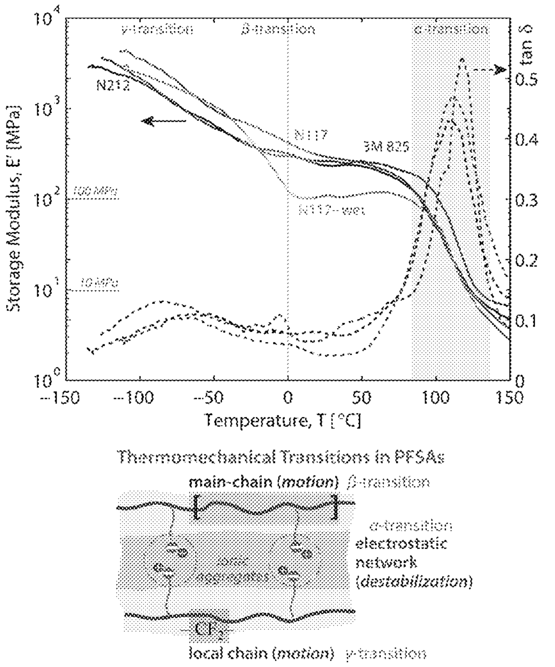

Figure 44. Typical temperature scan profiles from DMA showing the storage modulus and tan(δ) for Nafion[98,211] and 3M PFSA membranes, and an illustration of thermomechanical transitions associated with PFSA morphology.

As demonstrated in Figure 44, PFSA membranes exhibit 3 thermal transitions ($\gamma < \beta < \alpha$) corresponding to distinct relaxation mechanisms: (i) a γ relaxation around $T_\gamma = -120$ to -90 °C, (ii) a broader β relaxation between $T_\beta = -40$ to $+20$ °C and (iii) an α relaxation, so-called, ionic-cluster transition temperature, which is around $T_\alpha = 90$ to 120 °C for acid-form (H^+) and over 200 °C for the other salt forms (see Table 13). However, both α and β relaxation temperatures increase by over a 100 °C when the protonated PFSA is exchanged with alkali salts but not the γ-relaxation, which indicates the intrinsic role electrostatic interactions in these relaxation mechanisms (see section 7.3).[1,91,135,211,298] Also, the fact that the impact of cation on both thermal and stress relaxations is reduced with increasing water amount due to its shielding of ionic species and their interactions supported the assignment of T_α to ionic groups.[135] Interestingly, when Nafion was exchanged with two counterions of varying compositions, both β and α relaxation were observed at the intermediate temperatures of the corresponding two fully-exchanged ionomers with composition-dependent shifts in their positions, as expected from the changes in electrostatic interactions.[385] However, while α-relaxation followed Fox equation based on this rule-of-mixing, β-relaxation deviated from such a trend, which was attributed to plasticization of the ionomer by the bulky cations.

In a series of studies on the molecular origins of thermal transitions in Nafion, Page et al.,[91,131,387,623] compared the transition temperatures via temperature-dependent DMA, DSC, SAXS, and ^{19}F NMR experiments with different alkylammonium ions. An interesting finding was that the single transition temperature observed around 0 °C for the Nafion precursor (SO_2F form) shifts to over 100 °C once the polymer

Table 13. Summary of Reported Transition Temperatures in °C for Various PFSAs in Selected Cation Forms

DMA			DSC		
T_γ	T_β	T_α	T_1	T_2	notes
refs 34,307,318	refs 38,91,131,298,318,722	refs 90,211,288,298,318,722	refs 38,40,145,229,298,301	refs 38,40,229	
−108,−132	−62 to 23	95−115	104−152	230	Nafion-H^+
			201−218	320−333	SSC-H^+
	158−177		275−288	335−338	SSC-Na^+
−114	140	225	213 ± 20,226		Nafion-K^+
−97	130,150	235	238 ± 25,211,262		Nafion-Na^+
−81	147	217	212 ± 18		Nafion-Li^+
	130	240			Nafion-TMA^+[91,131,385]
	73	100			Nafion-TBA^+[91,131,385]
		~0			precursor[91]

is converted into SO_3H form (via hydrolysis and neutralization). This is due to the strong association of the SO_3H groups limiting the main-chain mobility, and a further increase to 250 °C occurs upon conversion to SO_3Na, owing to their stronger dipole−dipole interactions between the SO_3^--Na^+ groups.[1,91,131] As authors noted, this ionomer, unlike the precursor, cannot be melt-processed due to the strong Coulombic interactions giving rise to a dynamic electrostatic network with a physically cross-linked system that can persist at the high temperatures. In another study, authors found that transition temperatures were similar from DMA ≈ SAXS ≈ ^{19}F NMR (main-chain), and counterions acts like a polar ionic plasticizers,[91,387,623] impacting both α and β transitions, which indicates the existence of interrelated relaxation mechanisms for polymer chains and ionic associations. While the former is related to the segmental motion of polymer chains (including the actual glass transition of the fluorocarbon backbone, T_γ), the latter is governed by the time that an ion pair resides in an aggregate before hopping to another site. This ion-hopping transition has been attributed to the cluster transition, or α transition, but not the glass transition.[91,603,623] Similarly, the fact that the β transition, T_β, also shifts with larger counterions to lower temperatures (accompanied by reduced relaxation time) indicates that main-chain motions and electrostatic cross-links are coupled through the side-chains.[91,387,603,623] Thus, at T_α, the electrostatic interactions ("cross-links") become unstable and move from a static state to a dynamic state at the onset of ion hopping (Figure 44). In fact, this transition has been termed in BES studies the "dynamic glass transition" and also related to the segmental-chain motion caused by the conformational changes in main-chains.[2,133,436] As the temperature increases, the amplitude of counterion motion increases and approaches length-scales that facilitate ion-hopping between sulfonate groups.[131,623] On the other hand, at subzero temperatures, the backbone motions and ion mobility are both restricted accompanied by partially crystallized water. In accord with these changes, the activation behavior was suggested to change from Arrhenius (hopping) to VTF at higher temperatures,[2,436] where segmental dynamics of polymer chains are also activated (see section 4.7).

Considering that the formation of ionic aggregates (cluster) is a balance between dipole−dipole interactions favoring, and elastic forces opposing, at high temperatures when SO_3H groups are no longer ionized, the reduced Coulombic barrier to reorientation makes it easier to disintegrate the ionic aggregates.[95,195] While such disappearance reflects as a transition temperature in DMA between 100 to 200 °C, heating at higher temperatures could yield a shift from thermal transition and decomposition (see section 7.1.4).

A series of investigations by various groups[2,18,91,104,131,133,603,623] reported similar transitions from a wide range of studies (DMA, QENS, NMR, DSC, and BES), indicating a strong correlation between the mechanical and dielectric properties influenced by the polymer backbone, side-chains, and morphology. In summary, as illustrated in Figure 44, (a) T_α is a dynamic ionic-cluster transition associated with the onset of long-range mobility of the chains surrounding the ionic domains as a result of a destabilization (weakening) of the electrostatic network, disrupting the polar domains therein, (b) T_β is the glass transition of the PFSA matrix attributed to the onset of segmental main-chain motion, facilitated by the side-chains, within a physically cross-linked static network of amorphous fluorocarbon matrix, while (c) the low-temperature transition T_γ is associated with the local motions of the PTFE backbone.[2,3,91,104,131,145,298] For this reason, T_α and T_β are more sensitive to hydration,[135,229,288,711] EW,[5,38,436,703,711] side-chain chemistry[38,40,703] and cation-form[91,131,135,211,229,385,394,396,711] of the PFSA. Hydration tend to reduce the T_α due to the plasticization effect of water further enhancing the mobility of ionic domains reducing the onset of ion-hopping.[229,288,298,436,711] Change in T_α with cations is due to their stronger interactions that stabilizes the electrostatic network via ionic cross-linking, thereby locally stiffening the ionomer and restricting its chain mobility (Figure 44b), which increases the relaxation temperature.[131,229,394] However, the impact of cations on thermal transition diminished as the degree of hydration increases, due to the shielding effect of water weakening the cation−sulfonate interactions[135] (see section 7.3).

The effect of low EW or backbone length (distance between side-chains) and/or increasing fraction of side-chains in the PFSA on reducing T_α,[3,5,38,40] can be interpreted as side-chains acting as plasticizers, with the longer side-chains having a more profound effect; thus, the lower α-transition of Nafion compared to SSC[3,38] and 3M PFSAs.[2,4,5,9] Even for the same PFSA, however, higher EWs increase crystallinity, which tend to reduce main-chain mobility and increase and broaden the transition temperature.[38,40] A recent study by Moukheiber et al.[3] reported that increasing the backbone length (CF_2 repeat unit) increases T_α for SSC PFSA, but reduces it for Nafion, which was explained by the higher crystallinity of SSC (for a given n) restricting the chain motions (see section 3.1.3). For Nafion membranes, however, the (higher) mobility of the side-chains is further enhanced if their separation (backbone length) is higher, thereby reducing the relaxation temperature. In fact, such effects persist at lower temperatures affecting the T_β, which has been shown to be controlled by side-chain dynamics.[2,3,38,133] These effects of side-chain chemistry have recently been investigated via dielectric spectroscopy (see section 4.4), which have not only demonstrated transition temperatures similar to those from DMA,[2,34,132,133,298] but also revealed the role of dynamic side-chain motions in coupling the α and β transitions, with a shift of both relaxation temperatures and frequencies to higher values with lower EW and/or higher uptake. Similarly, BES studies reported a higher activation energy for β-relaxation for higher-EW PFSAs, where the increase in crystallinity in the polymer matrix restricts the side-chain mobility.[2]

Transition temperatures have also been investigated by DSC, where studies in the freeze regime all report an (exothermic) peak around $T = -20$ °C[58,132,186,251,264,307,309,681] and an (endothermic) melting peak around −3 to 0 °C.[58,214,264,309,310] The shift of freezing point to a lower temperature compared to the melting transition is associated with the supercooling phenomenon of water, as detected through various means.[58,264,309,320,723] In a few DSC studies, higher temperature peaks around 275 to 350 °C were also reported,[38,46,229] and associated with the melting of the crystallites, in accordance with WAXS investigations.[33,36,82,103] Nevertheless, due to its chemically heterogeneous structure, PFSA has a lower melting point and broader transition temperature compared to PTFE.[229]

Thus far, the relaxation phenomena in PFSA have been discussed in terms of thermal transitions and time-dependent mechanical response, both of which change with hydration. A powerful feature of mechanical-relaxation experiments is its ability to link these mechanisms through time−temperature superposition (TTS) principle, the applicability of which for PFSA was shown by Kyu and Eisenberg,[135] and more recently investigated systematically by Patankar et al.[118,138,707] TTS relies on the fact that viscoelastic relaxation (stress-time) response of a polymer can be superimposed by increasing its temperature, which effectively shifts current time, t, to a new reduce time, t'. TTS can be mathematically expressed as

$$E(t,\ T) = E\left(\frac{t}{a_T},\ T_{\mathrm{ref}}\right) = E'(t',\ T_{\mathrm{ref}}) \text{ where } t' = \int_0^t \frac{\mathrm{d}\xi}{a_H[\lambda(\xi)]a_T[T(\xi)]} \tag{63}$$

where $E(t,T)$ is the modulus at a given time and temperature, T, and $E'(t',T_{\mathrm{ref}})$ is the equivalent modulus that can be obtained at reduced time at a reference temperature. Thus, the change in temperature is equivalent to a shift in time, via a temperature-shift factor a_T. By conducting relaxation experiments at various temperatures, one can shift the modulus data to match and form a "master curve", from which the shift factors can be extracted. Given the similar effect of hydration on relaxation, one expects a similar superposition with humidity. By performing a set of relaxation experiments (under controlled RH, T), Patankar et al.[118,138,707] demonstrated that a hygrothermal curve can be generated for Nafion and Gore-Select Membranes by shifting the measured data from which not only a_T, but also a hygral-shift factor, a_H, was obtained, thus affirming the applicability of a time−temperature-hydration superposition (TTHS). Although both temperature and humidity reduce modulus, by increasing the mobility of ionomer chains and moieties, the effect of humidity was found to be less pronounced with an a_H of 1.5 decades (30 to 90% RH) versus an a_T of 7 decades (40 to 100 °C). The observed lack of TTHS for PFSA in the low-hydration regime (<5% RH),[138] can be attributed to the aforementioned antiplasticization effects, which cannot be captured with the classical TTS behavior that does not account for electrostatic interactions. Another interesting but convenient use of TTS was demonstrated for aged PFSAs, which result in cross-link formations (see section 7.1.3) thereby increasing its stiffness as a function of aging time.[138,697]

5.5. Fracture and Fatigue Behavior

Having discussed the stress−strain response and mechanical stability (e.g., strength), one other important mechanical property is the fracture failure (or membrane's resistance to it, i.e., toughness), which has not been investigated except for a few notable recent studies. Fraction failure is studied in the context of membrane lifetime, and thus this topic can be considered part of fatigue-failure and defect initiation and propagation process in PFSA membranes, as recently discussed by Kusoglu and Weber.[205] In fact, as discussed in section 7.1, the mechanical failure in PFSAs cannot be isolated from chemical degradation and aging, during which the PFSA mechanical behavior and properties of change significantly.[90,193,319,697,724−729]

Here we briefly highlight the recent findings on PFSA's fracture energy,[703,706,707] fatigue behavior,[693] and toughness. While the determination of fracture energy in ionomers is not trivial and difficult to determine, toughness can actually be estimated from the total area under the stress−strain curve, which yields the deformation energy (i.e., $\int_0^{\varepsilon_{\mathrm{break}}} \sigma(\varepsilon)\ \mathrm{d}\varepsilon$). The first set of studies on fracture behavior was by Li et al.[706] and Patankar et al.[707] who reported a comprehensive set of data on the critical strain-energy release rate, G_c, or fracture energy, of Nafion and reinforced PFSA membranes using a "knife-slit test". Their findings suggest that the fracture energy of Nafion decreases with increasing humidity and/or temperature. However, the temperature effect on the fracture energy is larger than the humidity effect,[707] which almost vanishes in the highest temperature range investigated (up to 80 °C). Interestingly, in liquid water, the fracture energy of the membrane decreases significantly such that a smooth humid-to-wet transition of the data and the corresponding hygrothermal master curve could not be obtained.[707] This rapid transition in the fracture energy of the membrane upon immersion in water is consistent with the observations on the semicrystalline-to-hydrogel-like transition in Nafion's stress−strain behavior.[123,690] It must also be noted that the effects of liquids and humidity on yield strength (controlling the shear plasticity) and fracture energy (controlling the rupture through crazing plasticity) are different in nature: From 50% to 90% RH at elevated temperatures, the fracture energy for Nafion decreases by 15 to 20%,[707] while the yield strength decreases by more than 60%.[284] For example, the fracture energy of a Nafion 211 membrane was reported to be between 450 and 550 J/m^2 (0 to 90% RH) at 50 °C, compared with 350 to 400 J/m^2 at 80 °C.[707] These values are shown in Figure 42c along with toughness (from the stress-strain curve), and both properties appear to decrease with hydration. More recent studies reported that tearing energy (2 to 3 kJ/m^2) decreases when H$^+$ is exchanged with other cations,[710] in striking contrast with their effect on increasing the elastic modulus.

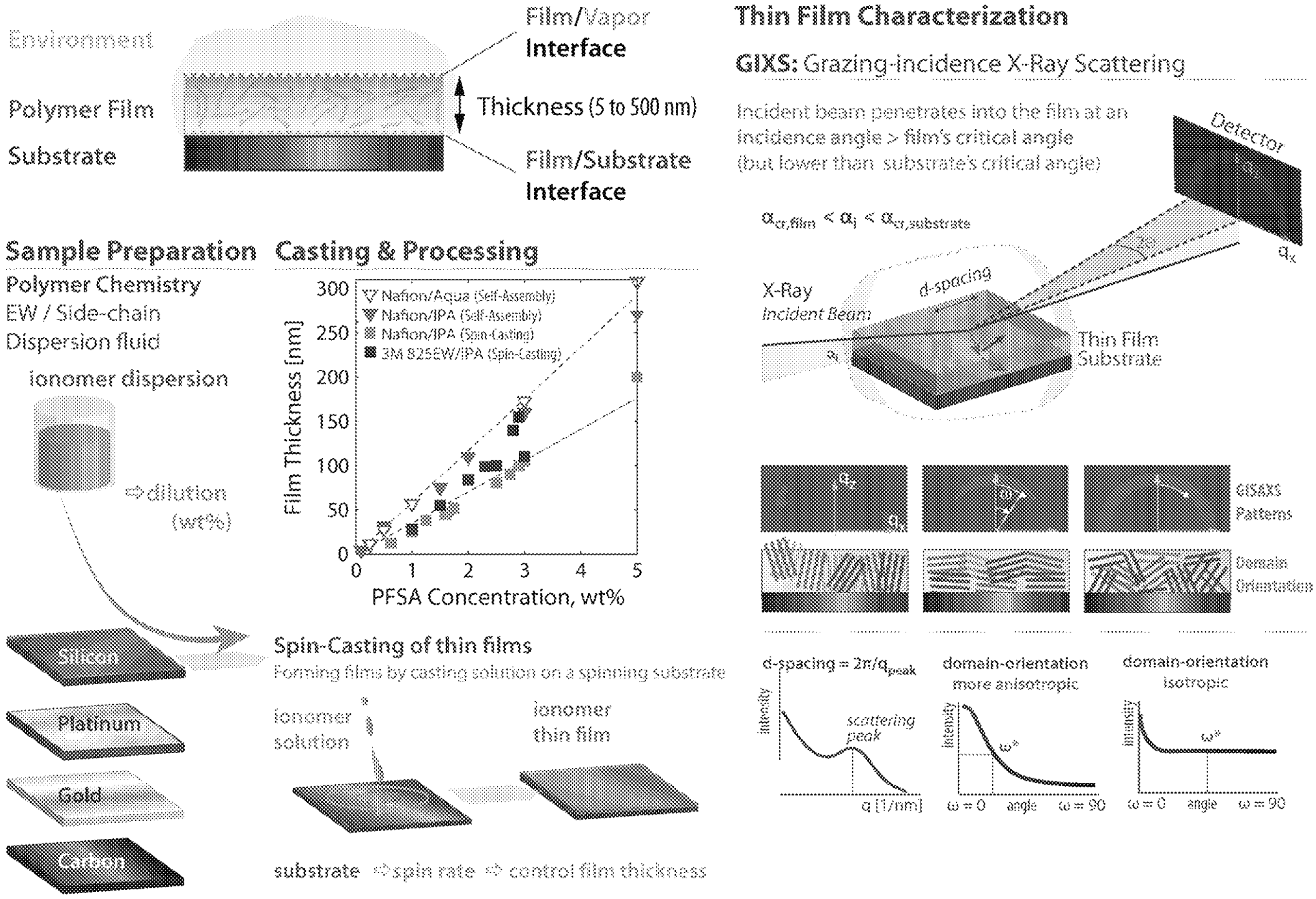
Environment
Polymer Film
Substrate
Film/Vapor
Interface
Thickness (5 to 500 nm)
Film/Substrate
Interface
Sample Preparation
Polymer Chemistry
EW / Side-chain
Dispersion fluid
ionomer dispersion
⇨dilution
(wt%)
Silicon
Platinum
Gold
Carbon
Casting & Processing
Film Thickness [nm]
300
250
200
150
100
50
0
0
1
2
3
4
5
PFSA Concentration, wt%
Nafion/Aqua (Self-Assembly)
Nafion/IPA (Self-Assembly)
Nafion/IPA (Spin-Casting)
3M 825EW/IPA (Spin-Casting)
Spin-Casting of thin films
Forming films by casting solution on a spinning substrate
ionomer
solution
ionomer
thin film
substrate ⇨spin rate ⇨ control film thickness
Thin Film Characterization
GIXS: Grazing-incidence X-Ray Scattering
Incident beam penetrates into the film at an
incidence angle > film's critical angle
(but lower than substrate's critical angle)
$\alpha_{cr,film} < \alpha_i < \alpha_{cr,substrate}$
Detector
q_z
q_x
X-Ray
Incident Beam
α_i
d-spacing
Thin Film
Substrate
q_z
q_x
ω
GISAXS
Patterns
Domain
Orientation
d-spacing = 2π/q_{peak}
intensity
scattering
peak
q [1/nm]
domain-orientation
more anisotropic
intensity
ω*
ω = 0
angle
ω = 90
domain-orientation
isotropic
intensity
ω*
ω = 0
angle
ω = 90

Figure 45. Material (substrate), processing (casting and thickness), and environmental (interfaces) parameters controlling the structure/property relationship of PFSA thin films and along with a brief description of the structural characterization (GIXS) techniques. (The inset in the casting shows the film thickness as a function of the PFSA concentration for various dispersions, taken from refs 48 and 762)

Similarly, fracture behavior is history dependent as a recent studied demonstrated that peel strength (i.e., the stress required to separate (peel off) a bilayer Nafion hot-pressed specimen) increased with hot-pressing time and temperature.[730] Also, the fracture energy is direction-dependent, especially in reinforced PFSAs, which exhibit higher toughness perpendicular to the preferential orientation of the chains (e.g., machine or reinforcement direction). These findings reinforce the idea that toughness and strength are not always correlated, especially in PFSA membranes where hydration and electrostatic effects are present; care must be taken when the mechanical stability of the membrane is characterized by modulus alone, as usually done in most studies. In fact, this idea was utilized recently by Kim et al.,[139] who demonstrated that the improvements in mechanical stability of PFSAs cast from different solvents can be best characterized by mechanical toughness.

Li et al.[705] investigated the ex situ fatigue response of PFSA membrane under biaxial loading using pressure-loaded blisters and stress-at-leaking as the failure criterion. They obtained typical fatigue-lifetime curves that consisted of a crack formation-dominated zone at high stress levels and a crack propagation-dominated zone at low stress levels. In the crack formation-dominated zone, cyclic stresses have been found to decrease faster than in the propagation-dominated zone, which is attributed to crack/craze formation.[705] Crazes in polymers are regions of a highly localized yielding zone that nucleates and grows in regions with stress concentrations such as crack-tips, pinholes, and surface defects, when the hydrostatic tension is sufficiently large. Crazes form usually behind a defect by localized fibrils that are nucleated from voids and stretch under tension, which temporarily holds the crack, but then breaks, resulting in a cleavage similar to crack propagation (see Kusoglu et al.[731] and refs therein). Thus, craze growth can be considered as a precursor to crack propagation in PFSA membranes,[731] in line with observations from stress-cycling and fatigue-failure tests.[693,705,732] However, the in situ effects (e.g., chemical degradation during cell operation and local imperfections) could further accelerate the failure by degrading the intrinsic properties and opening new surfaces at the membrane interface. One strategy that has been shown to be effective at improving mechanical toughness and fatigue-lifetime is reinforcing the PFSA membrane with ePTFE fibrils (see section 7.2.1),[98,287,733,734] which has been discussed to act as an effective blunting mechanism slowing down the propagation of cracks by creating a higher resistance to craze formation.[731,733] This is consistent with the higher fracture energy of reinforced PFSA membranes,[703,707] and delayed formation of cracks/crazes during fatigue tests,[154,705] and in numerical simulations.[735] This increase in fracture energy could be attributed to strength of the ePTFE fibrils within the crack tip inhibiting craze formation.[154,733,736]

Table 14. Summary of Previous Studies on PFSA Ionomer Thin Films[a]

ref	year	methods	study and key findings	compared to bulk	thickness [nm]	preparation method	substrate	ionomer/EW
Blanchard et al.[391]	2000	IR	hydration effects on IR spectra for various cations		~100	spin-cast	ZnSe	N 1100
Krtil et al.[492]	2001	QCM, AFM	water content and sorption kinetics with humidity	lower D	20 to 80	drop casting	Ag	N
Siroma et al.[742]	2002	EIS (conductivity)	interdigitated electrode-substrate (Si/Pt) conductivity vs temperature	lower κ	70	drop casting	Si/Pt interdigitated	N 1100
Hill et al.[774]	2003	AFM, ellipsometry	annealing effect: no dewetting over 2 weeks of annealing surface morphology, bundles of micelles of 20 nm size		200–400 (rms = 3)	self-assembly annealing effect	Si	SSC 800EW
Ugo et al.[789]	2004	QCM, CV voltammetry	Langmuir isotherms mass change during deposition		<100 (?60)	Langmuir–Blodgett	Au	N 1100
Pantelic et al.[683]	2005	ellipsometry	optical properties, refractive index, dynamic response		400–560	spin-cast	glass	N 1100
Bertoncello et al.[748,765]	2006	AFM, QCM, CV voltammetry	apparent diffusion film impregnated with different redox mediators	lower D	1.3–17	Langmuir-Schafer	Si, glass, ITO	N 1100
Umemura et al.[773]	2006	AFM	modulus from AFM, surface clusters, phase-separation at the surface (~20 nm)	higher modulus	230 + / 36 rms =1.9	drop casting		N 1100
Maeda et al.[79]	2008	AFM	annealing effect: surface root-mean-square (rms) decreases after annealing		<200	drop casting annealing effect	μ-patterned glass	N 1100
Wood et al.[745]	2009	NR voltammetry	aging effects: irreversible swelling (increase in thickness) Pt: hydrophobic, PtO: hydrophilic	substrate interaction	60	spin-cast, annealed 140 to 210 °C	Pt, Si, GC	N 1100
Siroma et al.[680]	2009	conductivity	conductivity as a function of humidity and temperature	higher E_{ac} lower κ	14–1121	spin-cast	Si/Pt,interdigitated	N 1100
Dura et al.[768]	2009	NR	RH-dependent lamellar structure at the interface for7 nm		~60	spin-cast, annealed	Si, Au, Pt	N 1000EW
Noguchi et al.[273]	2010	SFGS	RH-dependent, more hydrophilic surface at high RH		500	spin-cast	quartz prism	N 970EW
Bass et al.[266,267]	2010/2011	AFM, GISAXS, contact angle	surface orientation and hydrophilicity depending on interface: vapor vs liquid		100	spin-cast, annealed	Si, Si-OTS	N 1100
Kongkanand[487]	2011	QCM	water uptake and kinetics, temperature effect, interfacial transport, relaxation, E_{ac}	lower uptake	33–3000	spin-cast, annealed	Au, Pt	N 1100
Paul et al.[679]	2011	EIS (conductivity)	conductivity with temperature and RH effects	lower κ higher E_{ac}	50	self-assembly	Si/Au interdigitated	N 1100
Ahmed et al.[790]	2011	CV	voltammetry		0–3.3		Pt	N 1100
Modestino et al.[360]	2012	GISAXS, ellipsometry	time-resolved GISAXS and swelling; effect of annealing	lower swelling	100	spin-cast, annealed	Si, Si-OTS	N 1100
Eastman et al.[752]	2012	QCM, NR, GISAXS, QCM, PM-IRRAS	swelling, uptake, domain spacing, diffusion, less phase-separation	lower swelling lower D	20–222	spin-cast	Si	N 1100
Modestino et al.[747]	2013	GISAXS, TEM, conductivity, ellipsometry	less phase-separation. transport limitations	lower κ higher λ less phase-separation	4–160	self-assembly	Si	N 1100
Ogata et al.[494]	2013	surface plasmon resonance, NR	diffusion, restricted mobility, interfacial effects	lower D	~50	spin-cast	Ag, Si, quartz	N 1100
Ohira et al.[744]	2013	e-AFM, ellipsometry, contact angle	surface morphology differs from bulk; current mapping: better conductivity on Pt	lower surface current density	12–221	spin-cast	GC, Pt	N 1100
Abuin et al.[770]	2013	QCM, ellipsometry	substrate and aging effect; lower swelling with aging	lower λ	17–1000	spin-cast	Si, Au, glass, graphite	N 1100
Dishari et al.[746,749]	2012/2013	QCM, ellipsometry, fluorescence	antiplasticization, substrate-dependent, interfacial confinement and cation effects	lower λ lower mobility	70–600	spin-cast, annealed	Au, Si	N 1100
Mohamed et al.[302]	2013	XPS, AFM, PALS, contact angle	enrichment of O at the Si interface for thinner films, and hydrophilic film surface Stronger interaction on Pt with SO_3H	impact of substrate (interactions)	10–256	spin-cast	Si, glassy carbon, Pt	N 1100

Table 14. continued

ref	year	methods	study and key findings	compared to bulk	thickness [nm]	preparation method	substrate	ionomer/EW
Paul et al.[762]	2013/2014	AFM, XPS, ellipsometry, EIS, contact angle	RH and thickness-driven conductivity; wettability changes with thickness (<55 nm), annealing, and liquid-water exposure	more hydrophilic surface, higher capacitance, higher E_{ac} lower κ	4–300	self-assembly annealing effect	Si/Pt interdigitated	N 1100
Kim et al.[763]	2013	QCM,NR,X-ray porosimetry	substrate hydrophilicity affects the film's nanostructure: Interfacial layering on Si but not on hydrophobic analogue		~60 nm	spin-cast	Si, Si-OTS	N 1100
Page et al.[209]	2014	buckling, ellipsometry, GIXD	elastic modulus, confinement-driven stiffening	higher modulus	20–158	spin-cast	Si, PDMS	N 1100
Kusoglu et al.[493]	2014	QCM, ellipsometry, GISAXS GIWAXS	impact of substrate, thickness, annealing, casting; swelling dimension and structural anisotropy on metal substrates	less swelling lower λ less phase-separation	5–210 18–270	self-assembly spin-cast annealing effect	Au, Si, C, Pt	N 1100
Davis et al.[129]	2014	PM-IRRAS	diffusion and relaxation. Slower chain dynamics in films	lower D	153	spin-cast	Si	N1100
DeCaluwe et al.[776]	2014	NR	lamellar structure with a water-rich layer on hydrophilic substrate		5–42	spin-cast	Si	
De Almeida et al.[393]	2015	ellipsometry, NMR	temperature-independent chemical shift in ultrathin film unlike thicker films	restricted H^+ mobility	160 10	spin-cast self-assembly	Si	N1100
Nadermann et al.[766]	2015	nanoindentation, ellipsometry	poroelastic relaxation, effective diffusion, intrinsic permeability	lower D, lower water permeability	55–950	spin-cast, annealed	Si	N1100
Kalisvaart et al.[791]	2015	NR	swelling (RH, T), large hysteresis during T cycle		15	spin-cast	Si	N1100
Page et al.[716]	2015	cantilever, XR, Ellipsometry	stress-thickness and modulus due to humidity change	higher modulus	200	flow coating	glass/Au cantilever	N1100
Kudo et al.[490]	2016	electrochemical permeation cell	oxygen transport resistance and permeability	lower O2 permeability	20–100	solution casting, annealed	Pt	N1100
Paul et al.[764]	2016	AFM, EIS, contact angle	surface hydrophilicity and annealing effect: thermally-induced changes in surface wettability	higher hydrophilicity	4–300	self-assembly	Si	N1100
Zimudzi et al.[767]	2016	FTIR (ATR)	molecular ordering evidenced by shifts In FTIR spectra	molecular ordering at interface	5–250	spin-cast	Si	N1100
Kusoglu et al.[48]	2016	Ellipsometry, GISAXS, GIWAXS	structural anisotropy and multi-scale swelling, effect of EW and side-chain; lower-EW films exhibit better phase-separation, stronger nanodomain alignment and swelling	lower swelling, stronger nanodomain alignment	20–100	spin-cast	Si	N 1100EW 3M 660EW 3M 825EW

[a] Property changes in thinner films in comparison to bulk ionomer are given to demonstrate the overall trends, which could change also with the substrate, processing and environmental variables. Readers are urged to read the original references for detailed information on materials, preparation methods, processing and results. VASE: variable angle spectroscopic ellipsometry; AFM: atomic force microscopy; QCM: quartz-crystal microbalance; XPS: X-ray photoelectron spectroscopy; EIS: electrochemical impedance spectroscopy; SFGS: sum frequency generation spectroscopy; CV: cyclic voltammetry; SXR: specular X-ray reflectivity; NR: neutron reflectivity; GI-SAXS/WAXS: grazing-incidence small- and wide-angle X-ray scattering; GIXRD: grazing-incidence X-ray diffraction; PM-IRRAS: polarization-modulation infrared reflection–absorption spectroscopy.

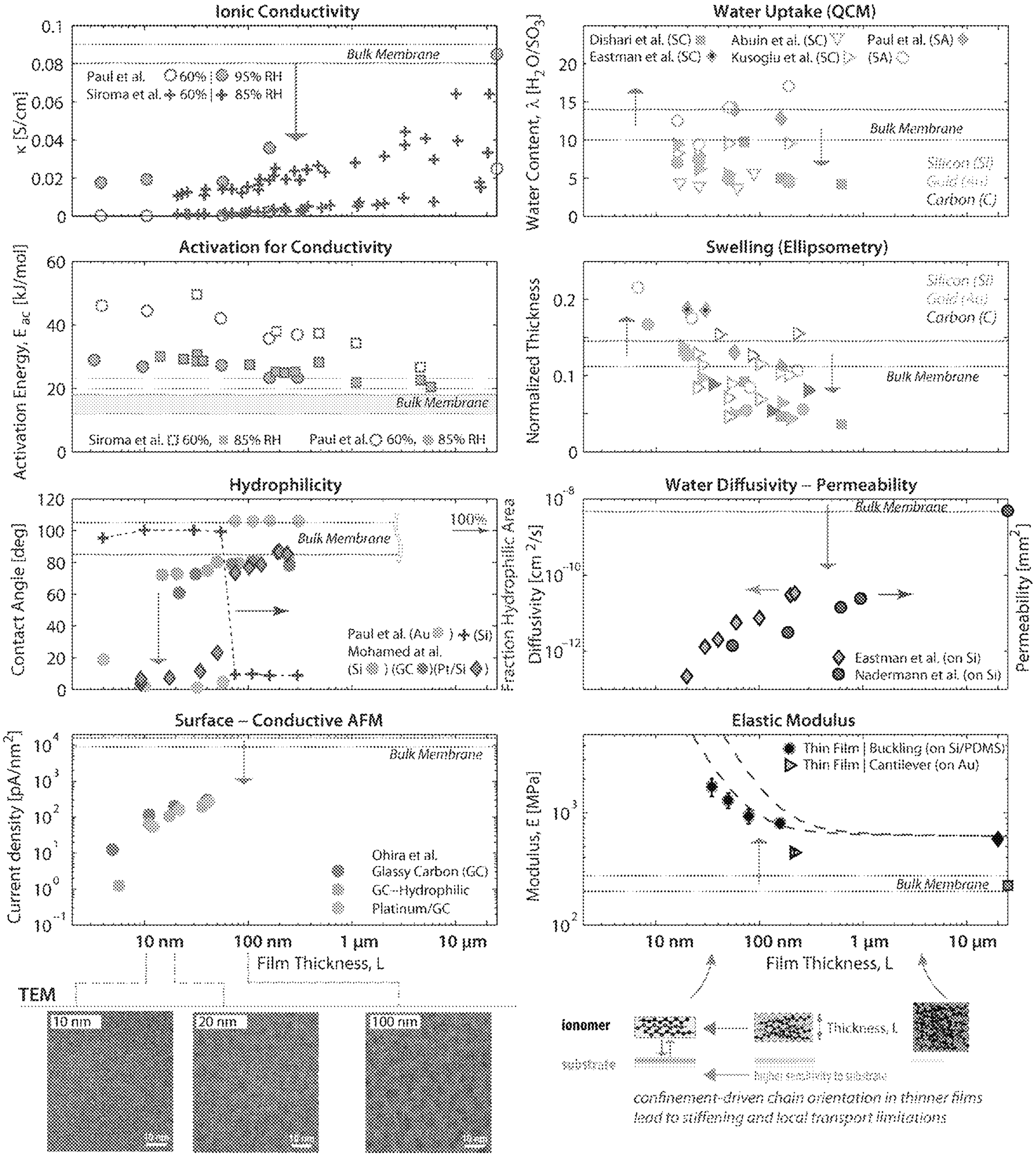

Figure 46. Impact of thickness on properties of PFSA thin films; conductivity and activation energy,[680,751,762,769] contact angle,[302,762,764] associated fraction of hydrophilic area,[764] conductive AFM,[744] QCM (water uptake),[493,746,762,770] ellipsometry (thickness swelling),[493,746,752,762,770] water diffusivity[752] and permeability,[766] and modulus measured with buckling[209] and cantilever beam bending methods,[716] as well as TEM images.[747] Legends are the same for QCM and Ellipsometry data, and open and closed symbols correspond to unannealed and annealed films, respectively (see also Figure 47). Bulk values and deviations from them are depicted as shaded areas and arrows, respectively, based on values reported and discussed throughout this review. (TEM images reproduced from ref 747. Copyright 2013 American Chemical Society.)

6. THIN FILMS AND INTERFACES

PFSA ionomers have been continuously studied as a "bulk" membrane (e.g., PEM) with a thickness on the order of micrometers (25 to 175 μm); yet, increasingly important, but less explored, is the role of ionomers as thin films and the interfaces they form within composite structures (e.g., electrodes where they interact with catalysts).[177−179,737−740] In PEFC catalyst layers, ionomers are found as nanometer-thick "thin films" binding the catalyst particles together and facilitating proton transport through the layer and gas and water transport to and from the catalytic sites.[177−179,490,737,739,741−743] Similarly, in solar-fuel generators, they interact with semiconducting substrates to form heterojunctions.[160−162] As the ionomer enters the thin-film regime, its properties are influenced by film thickness and become sensitive to specific substrate interactions.[178,302,493,744,745] In recent years, significant effort has been expended toward understanding PFSA thin films, primarily Nafion ones, which exhibit reduced transport properties compared to those of bulk films due to confinement effects when the film thickness approaches the characteristic domain size of the ionomer (i.e., order of nm).[178,267,487,493,494,680,744,746−752] The magnitude of these reductions change with several factors, including processing conditions (treatment), thickness, substrate type, and operating

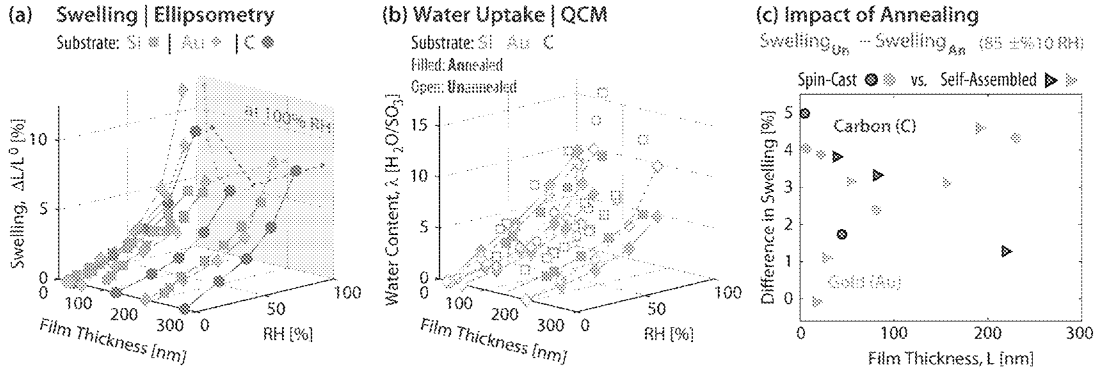

Figure 47. PFSA Thin Film Hydration: (a) swelling (from ellipsometry) and (b) water-uptake (from QCM) as a function of RH at RT on Si, C, and Au substrates, compiled from the literature (refs 487, 493, 679, 746, and 752) and (c) change in swelling upon thermal annealing of thin film shown for spin-cast and self-assembled films (from ref 493).

environments (e.g., humidity), resulting in a wide material-parameter space that remains to be explored fully in order to elucidate the governing and dominant interactions and phenomena (Figure 45).[360,493,679,744,746,751,752]

Thin-film confinement is known to affect the phase behavior of uncharged block copolymer systems.[753−758] In thin films, surface interactions and confinement can cause anisotropy in domain orientation and pose significant limitations to self-assembly. Even though confinement effects in polymer films have long been of interest, films of naturally phase-separated ionomers, such as those used in PEFCs, have gained attention only recently, especially in the past few years.[360,487,493,679,680,739,743,744,746−749,752,759,760] This interest has been driven primarily by two needs: (i) to understand the surface morphology and interfacial properties of bulk membranes, where the ionomer is believed to form a distinct layer and act more like a thin film (see sections 3 and 4) and (ii) to understand the formation and behavior of ionomer films in PEFC electrodes,[177−179,490,738,743,761] and other microfluidic devices.[160]

PFSA thin films are prepared by casting a diluted dispersion onto a model substrate via various methods (spin-casting, self-assembly, drop-casting, doctor blade, etc.), followed by thermal treatments. Thus, the PFSA thin-film structure/property relationship is affected by the processing methods as well as the specific substrate interactions. The key aspects of thin films, their preparation, and traditional diagnostics are illustrated in Figure 45. It is evident that there is a large parameter space including solvent, concentration, drying conditions and post-treatments, substrate (interactions), as well as confinement (thickness) that governs the structure and properties of PFSA thin films. To probe these thin films, techniques such as quartz-crystal microbalance (QCM) and ellipsometry for weight and thickness change, respectively, are used and grazing-incidence X-ray scattering (GIXS) experiments and neutron reflectivity (NR) for morphological characterization (see Figure 45).

Due to challenges with the direct measurement of transport properties, most studies rely on swelling measurements supplemented by nanostructural characterization for understanding ionomer thin−film functionalities. Table 14 summarizes the current studies on PFSA thin films, along with sample preparation and thicknesses used, and the key findings. Overall, these recent studies have consistently demonstrated that as the thickness of a Nafion thin film approaches 10s of nanometers, significant deviations in its properties occur compared to a bulk Nafion (membrane), yet the magnitude of these deviations largely depends on the thickness and substrate, as highlighted in Figure 46. Both dynamics and static properties are impacted. Compared to bulk membrane, Nafion films of ∼100 nm or thinner have been shown to exhibit reduced swelling, water-uptake amounts and rates,[48,129,360,487,493,494,679,744,746,748,751,752] reduced ionic conductivity and increased activation energy,[679,680,742,744,747,751,763,764] lower water diffusion rates,[129,492,494,748,752,765] lower intrinsic permeation,[766] higher modulus,[209,716] and lower oxygen permeability.[490,761] These trends are exacerbated as the film thickness approaches 20 nm,[48,487,493,494,680,744,746−752] as shown in Figure 46 (also see Table 14). Confinement, along with the substrate/surface specific interactions affect the molecular ordering of the backbone chains as evidenced from FTIR,[767] NR,[494,760,768] and GISAXS[48,493] data, where orientation of the backbone chains and ionic domains resulted in reduced water uptake[267,360,746,752] and transport processes.[267,360,746,752] All of these observed limitations in transport properties can be explained by the thin film's reduced swelling and morphology with more anisotropy and a less well-defined phase separation.

6.1. Swelling and Sorption Behavior

There are various techniques that could be used for thin films in terms of thickness and mass changes including profilometry and AFM, that probes thickness profiles via surface mapping as well as X-ray scattering, although the most prevalent are QCM and ellipsometry and are discussed in detail below. QCM measures the mass change or solvent uptake of a thin film on a substrate and ellipsometry infers the thickness swelling, $\Delta L/L_0$, by measuring the change in the optical response of the thin film (Figure 45). PFSA thin films' mass uptake can be characterized by QCM,[487,493,746,749,759,760,763] is accurately described by the Sauerbrey analysis, where Nafion films of less than 600 nm show no dissipation or viscoelastic losses.[746,749] Ellipsometry data on the other hand provides parameters such as the refractive index of the material, which must be modeled for the specific conditions. To do this, a Cauchy model is often employed[683,771]

$$n(\lambda_{\text{wave}}) = A + \frac{B}{{\lambda_{\text{wave}}}^2} + \frac{C}{{\lambda_{\text{wave}}}^4} \tag{64}$$

where $n(\lambda_{\text{wave}})$ is wavelength-dependent refractive index and A, B, and C are coefficients determined through the data modeling. Ellipsometry and QCM measurements can be compared[493]

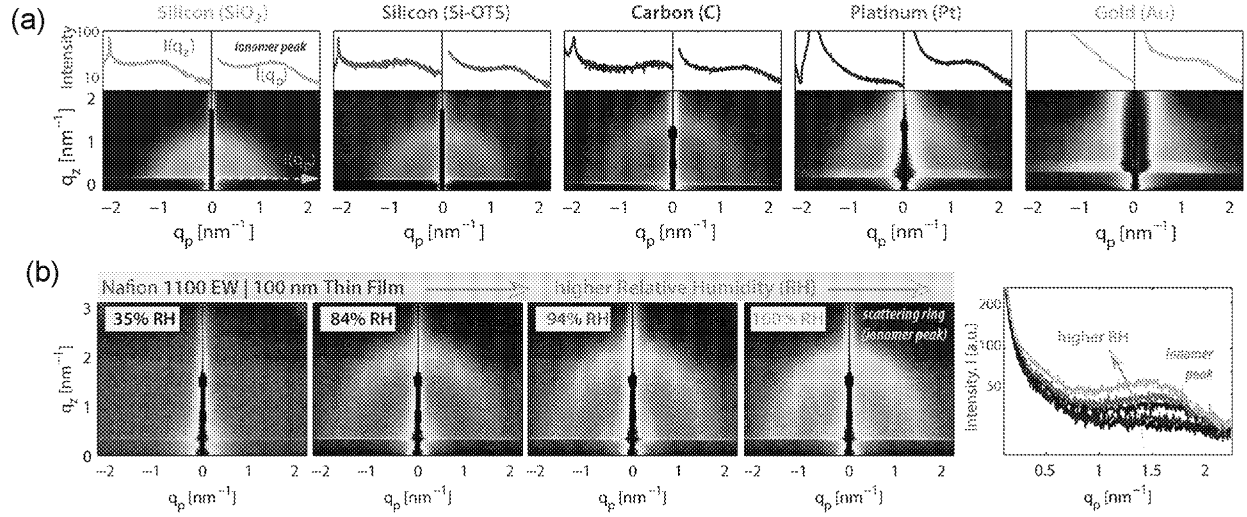

Figure 48. (a) 2D GISAXS patterns for vapor-saturated (100% RH) Nafion films of various thicknesses spin-cast on SiO_2, Si-OTS (from Modestino et al.[366]), and on C, Au, and Pt (from Kusoglu et al.[48,493]) Color scale representing the intensity (I) is the same for each substrate. The intensity line profiles above are the line cuts parallel to the substrate (I-q_p) and perpendicular to the substrate (I-q_z). (b) Evolution of GISAXS spectra during humidification for a 100 nm Nafion film on SiO_2 (from Kusoglu et al.[48]).

$$1 + \underbrace{(\lambda)}_{\text{QCM}} \frac{\bar{V}_{\mathrm{H_2O}}}{\bar{V}_0} - \frac{\bar{V}_{\mathrm{mix}}}{\bar{V}_0} = \frac{V_{RH}}{V_0} = \underbrace{\left(1 + \frac{\Delta L_{RH}}{L_0}\right)^m}_{\text{ellipsometry}} \qquad (65)$$

where the (partial) volume of mixing $\bar{V}_{\mathrm{mix}}$ reflects the contribution due to nonideal mixing[213] and m is the swelling dimension, which is usually assumed to be 1 for thin-films as they are confined on the substrate and swell only in the thickness direction.[487,679,746,752] This value shifts toward 2 as the thickness increases over 200 nm, perhaps due to the fact that some lateral swelling occurs or there are factors not accounted for in the ellipsometry thickness analysis. A dimension of $m = 3$ should eventually be reached as the ionomer reaches the "bulk" regime. As for $\bar{V}_{\mathrm{mix}}$, it is known that at least for bulk membranes, the partial molar volumes change as a function of hydration due to the mechanisms of solvation and swelling, although with relatively minor effects at higher hydration levels (see Section 2.4).[213] A recent investigation showed that the contribution from nonideal mixing is negligible ($\bar{V}_{\mathrm{mix}} \approx 0$) if 1-D swelling is assumed ($m = 1$).[752] Physically, the low volume-of-mixing effect perhaps indicates that confinement impacts the solvation process in the ionomer, which is also evident from the shape of the thin-film uptake isotherm (Figure 47), which appears to lack the primary solvation regime (compare to Figure 7) at low RH (i.e., Langmuir regime discussed in section 2.1 for bulk PFSAs), and warrants further investigation. The thin-film uptake curve exhibits lower water contents for a given RH than for a bulk membrane. This is especially apparent at higher RHs, where the water uptake is driven by entropic effects and not primary solvation.[82,203,206] Thus, it is likely that confinement effects that reduce the swelling of ionomer thin films also change the nature of the associated water (i.e., whether it is strongly bound to an ionic group or freely moving). Overall, the qualitative trends between QCM and ellipsometry are consistent, with the latter being more commonly employed as it works on any substrate, albeit with the caveat of using the correct model for the data analysis.[747]

Due to the large number of parameters controlling ionomer thin-film behavior, the impact of each parameter must be investigated by carefully accounting for its interrelation with other parameters. Thus, even though an overall decrease in swelling is observed due to confinement effects, the reality is more complex due to the interplays among confinement and substrate, casting (processing), and ionomer chemistry. The current state of understanding of confinement-substrate-processing interplay can be summarized as follows:[48,493,763] (i) impact of processing depends on substrate; for example, swelling of self-assembled thin films is higher than spin-cast films on gold but the opposite is true on carbon, which may be due to the substrate-specific interactions changing the adsorption of the Nafion colloids from the solution to the substrate during film formation. (ii) Thermal annealing reduces the swelling of thin films and increases crystallinity, similar to its effect on bulk membranes, although the impact of annealing is substrate dependent where it decreases with decreasing film thickness on gold but increases on carbon (see Figure 47c), perhaps owing to the stronger sulfur interactions with gold than carbon. Also, the annealing-driven decrease in swelling of self-assembled films demonstrated a weaker dependence on thickness compared to spin-cast samples. It appears that the thinner films on metallic substrates (Au and Pt) are possibly pinned to the surface and cannot rearrange under the thermal conditions, which is supported by the GISAXS patterns discussed below.[493] Hence, when it comes to the annealing, processing and substrate effects, the latter could dominate the overall ionomer behavior especially when strong interactions exists between the substrate and the very thin ionomer film. Such interactions also drive the changes in T_α[764] and modulus,[209] which alter the effect of the thermal treatment process. Paul et al.[764] reported that annealing makes hydrophilic thin films more hydrophobic, thereby altering the surface (Figure 46). However, such surface alteration is more restricted in ultrathin films (~10 nm), which require more thermal energy for annealing and therefore a higher annealing temperature. This could explain why the impact of annealing on thin-film swelling changes both with thickness and substrate (interaction). Also, the fact that conductivity decreased more upon heat-treatments than does the swelling reveals the key role of morphology and interactions on transport.[493,751,764]

6.2. Morphology, Interactions, and Properties

Recent studies have demonstrated that confinement effects and wetting interactions result in different morphology for thin films compared to bulk PFSAs as shown by various techniques including grazing-incidence small-angle X-ray scattering (GISAXS),[48,267,360,493,747,752] neutron or XR reflectivity,[716,752,760,768] TEM,[747] XPS,[302,772] cryo-TEM tomography,[358] fluorescence,[746] AFM,[79,393,744,747,762−764,773,774] contact angle,[302,751,762,764] PM-IRRAS,[129] FTIR,[767] and positron annihilation,[302] as summarized in Table 14. GISAXS (Figure 48) and NR in particular have been shown to be extremely useful to investigate the orientation and spacing of the nanodomains at and below the thin-film interfaces (free and substrate).[360,493,745,760,768,775,776] Models obtained from fitting the NR data on Nafion thin films suggest evidence for a hydration-dependent multilamellar nanostructure at the film/substrate interface, where alternating layers of water-rich and polymer-rich domains form.[760,768] Especially on hydrophilic substrates (such as SiO_2), excess water is observed at the substrate/film interface, forming a water-enriched surface with a water-layer thickness of 1−3 nm.[760,763,776] Such ordering at the interface is believed to propagate a significant distance (10s of nm) through subsequent layers in a thin film, inducing a locally ordered structure with alternating layers of SO_3-rich hydrophilic domains and fluorocarbon hydrophobic domains (Figure 49).[48,749,760,763,775,776] A recent FTIR study on a PFSA thin film[767] documented different polarization in and out of the plane, with enhanced z-polarized electric field in thinner films indicative of chain alignment parallel to the surface. Such molecular ordering transitions around 50 nm and was impacted by the process of spin-casting.

The preferential domain alignment is strongest closer to the interface, albeit dependent on the substrate interactions, and disappears along the successive layers toward the film surface.[749,760,768,776] (Figure 49). Such changes in film morphology with the substrate, along with the impact of thickness and humidity, were also witnessed in GISAXS studies.[48,493] Typical GISAXS patterns for Nafion films (of 90 ± 10 nm thickness) on various substrates are compared in Figure 48 and analyzed as illustrated in Figure 45.

Despite the more complex nature of GISAXS analysis compared to transmission SAXS, due to reflections from the substrate, it has been shown to be a powerful technique for polymer thin films.[777] Several features are salient from the GISAXS data on PFSA thin films (Figure 48): (i) a scattering half-ring (i.e., at q = 1.5 to 2 nm^{-1}) indicating phase-separation similar to bulk membranes; (ii) the scattering ring grows inward and becomes more intense with humidification,[360,493] reflecting the swelling of the hydrophilic domains from $d \approx 3$ nm ($q = 2\pi/d \approx 2$ nm^{-1}) up to $d \approx 4.5$ nm ($q \approx 1.5$ nm^{-1}) from ambient humidity to saturation. (iii) patterns exhibit stronger anisotropy as the film thickness decreases. This is seen from the different intensity profiles parallel (I-q_p) and perpendicular (I-q_z) to the substrate (Figure 48), with the latter giving smaller hydrophilic d-spacing, indicative of stronger packing parallel to the substrate[48] (see Figure 49). (iv) Peak intensity, and therefore the degree of phase separation—quantified by the full-width half-max (fwhm) of the peak—decreases with film thickness and almost disappears for ultrathin films.[48,360,493,752] These observations are also in accord with reduced crystallinity in thinner films,[48,493] which become less sensitive to annealing because the chains become topologically confined as the film thickness approaches the crystallite size. Thus, similar to the trends observed with swelling-related properties shown in Figure 46, as the film thickness is reduced below 50 nm, ionomer films begin to exhibit weaker phase separation. This is shown through a less well-defined ionomer peak in GISAXS,[360,493,747] more mixing of smaller ionic domains as observed by TEM (Figure 46),[747] and AFM,[744] and a change from hydrophobic to hydrophilic film surface.[302,762,764]

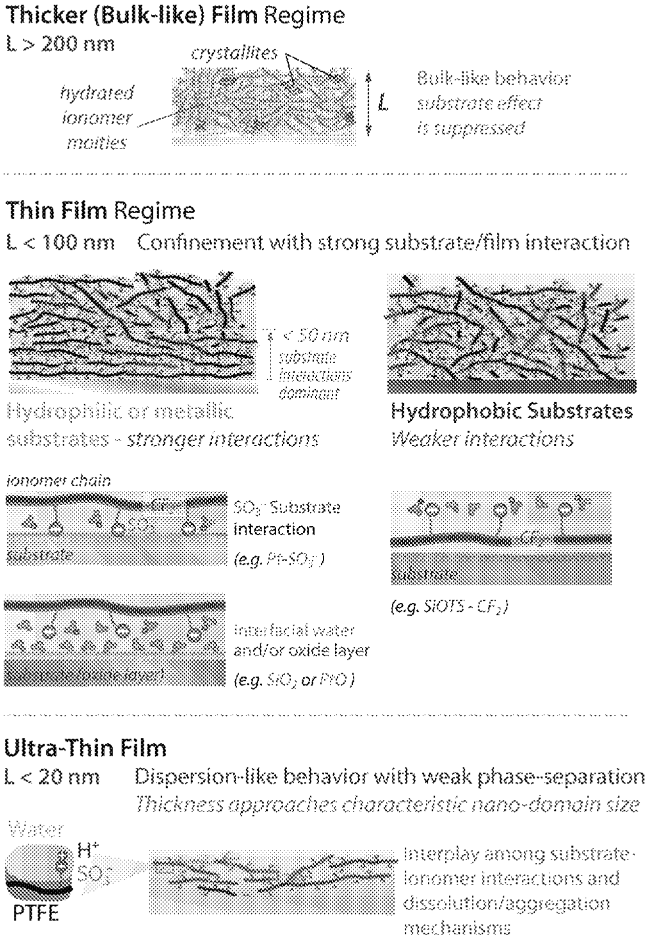
Thicker (Bulk-like) Film Regime
L > 200 nm
crystallites
hydrated ionomer moities
L
Bulk-like behavior
substrate effect is suppressed
Thin Film Regime
L < 100 nm Confinement with strong substrate/film interaction
< 50 nm
substrate interactions dominant
Hydrophilic or metallic substrates - stronger interactions
Hydrophobic Substrates
Weaker interactions
ionomer chain
CF₂
SO₃
substrate
SO₃⁻ Substrate interaction
(e.g. Pt-SO₃⁻)
CF₂
substrate
(e.g. SiOTS - CF₂)
interfacial water and/or oxide layer
(e.g. SiO₂ or PtO)
Ultra-Thin Film
L < 20 nm Dispersion-like behavior with weak phase-separation
Thickness approaches characteristic nano-domain size
Water
H⁺
SO₃⁻
PTFE
Interplay among substrate-ionomer interactions and dissolution/aggregation mechanisms

Figure 49. Illustration of the thickness-substrate interplay controlling the nanostructure of PFSA thin films. Modified from Kusoglu et al.[48,493]

One consequence of these structural changes and ordering is reduced transport properties. For example, swelling kinetics of thin films have been shown to yield time constants[236,360,487,493,494] similar to those found for the interfacial transport of bulk membranes (see section 4.1.5), thus revealing the interfacial nature of thin films. However, one must bear in mind that correlating kinetic effects with confinement and surface interactions is not straightforward, especially when probing transport parallel or perpendicular to the substrate. This is because swelling kinetics is strongly intertwined to dynamic processes of morphological changes, such as formation of interfacial layering.[760] In general, there exists a strong interplay between the film morphology and transport properties, as dictated by confinement and substrate interactions.[129,493,747,749,762] When confined to thin films, Nafion not only exhibits lower diffusion,[129,492,494,748,752,765] but also a few orders of magnitude slower relaxation, suggesting more restricted chain dynamics.[129] Reduced conductivity in thinner PFSA films can be associated with decreased water uptake (QCM),[679,751,764] and the number of conducting sites (from CAFM),[744] as the conductivity-λ relationship was shown to extend to the thin-film regime.[763] Similarly, oxygen-transport resistance was shown to increase in thinner films.[490,739,740,778] For example, Kudo et al.[490,778] showed that the reduced O_2 permeation in thinner films exhibits a thickness dependence, which is governed by the surface interactions of the film, especially at the Pt/ionomer interface.

From GISAXS, comparison among substrates reveals a more well-defined and semicircular ionomer peak on silicon and carbon than on gold and platinum for nominally the same thickness. In addition, the substrate seems to have a stronger impact on nanostructural anisotropy (domain alignment) than on domain spacing. This substrate-induced ordering may be due to the way the polymer interacts with the substrate surface, in agreement with the substrate-dependent impact of annealing mentioned above. Similarly, compared to self-assembled films, spin-cast films exhibited a lower q value and a more ordered ionomer peak,[493] due possibly to the fact that the self-assembly process is governed more strongly by the interaction of dispersed colloids with the substrate surface. This concept also agrees with the more defined structure after annealing with self-assembled films.

The nature of the substrate, including possibly surface oxide layers (e.g., SiO_2 and PtO), is critical for determining thin-film morphology and response.[493,744,745,759] For example, wetting could occur on a hydrophilic substrate even in the absence of a film creating a monolayer of water molecules[760,763] leading to anomalously high water-uptake in the ultrathin films, but not on Au or Pt substrates.[763] Thus, compared to a hydrophilic Si native-oxide surface, films on hydrophobized Si substrates exhibited less water uptake and strong structural anisotropy with domains parallel to the substrate.[360] On carbon, the nature of the substrate becomes critical as well.[302,493,744,745,759] Aging of carbon was shown to cause surface oxidation and rearrangement, concomitant with reduced film thickness and irreversible swelling.[745] Also, when the carbon surface is hydrophobic, the ionomer's adsorption occurs via its apolar CF-rich chains, whereas hydrophilic carbon preferentially interacts with the polar SOH groups.[779] Similarly, on a highly oriented pyrolytic graphite (HOPG) surface, aggregates of PFSA were shown to be randomly absorbed and formed an ordered morphology at the interface.[780] The favorable interactions between SO_3^- groups and a hydrophilic substrate's polar groups,[302,360,744,745,780] becomes strongest on a Pt substrate.[302,744] Yet, in contrast to GISAXS data showing stronger substrate-induced morphological changes on Au and Pt,[493] some NR data indicated lower affinity of $-SO_3^-$ groups on Au and Pt compared to more hydrophilic SiO_2.[760,768]

Nevertheless, PFSA($-SO_3H$)/Pt interactions were substantiated further by electrochemical cell studies to elucidated the effect of electrochemically formed water and oxide-layer formation on ionomer film behavior.[490,738,739,745,759,781−783] Even though Nafion could form an interface adjacent to a Pt substrate, it becomes hydrophilic when in contact with a PtO surface, causing a long-range restructuring of its chains, which was accompanied by the restrictions in SO_3^- vibration mode,[782] changes in ionomer structure,[302,738,759,781,784] and transport therein.[490,738,739,745] PFSA/Pt interactions were shown to be reversible during Pt-oxide formation and reduction such that adsorption of PFSA moieties on the Pt surface weakens and disrupted if surface oxides form (e.g., due to applied potential).[738,759,781−783] These studies confirmed the high chemical affinity of sulfonate $-SO_3^-$ groups to the Pt, which was also supported by FTIR,[782,784] XPS,[302] PALS,[302] and MD studies.[784−787] Subbaraman et al.[781] explained the adsorption/desorption of the SO_3^- onto/from the Pt by the balance between an electrode metal spring (Pt-SO_3^-) and ionomer spring (backbone-SO_3-cation). With increasing potential, SO_3^- approaches Pt, as the Pt-SO_3^- interaction dominates the cation/anion interaction within Nafion. For the same reason, for other cations that interact more strongly with SO_3^-, a higher activation potential is needed to adsorb the cations onto electrode surface.[781] Thus, in essence, SO_3^- responds to electric potential like single counterions (i.e., forming an electric double layer),[782] and affects the backbone (orientation) through the flexible side-chain.[782,784,787] These interactions also change the nature of interfacial water, some of which are relocated to Pt, thereby reducing the hydration of the sulfonate layers (i.e., less H_3O^+)[787] and hydrogen bonding.[784] Hence, even though interfacial water is present on Pt substrates, it is distinct from that on SiO_2 in that it is part of an electrochemically active dynamic layer.[783]

The above substrate-specific changes are in accord with simulation results,[629,786,788] confirming the key role of affinity of water to the substrate in an ionomer's molecular rearrangement that affects the morphology[786] and surface hydrophilicity.[629,764,786,788] As such, the contact angle of water on Nafion thin films also changes, decreasing from 100° to almost 0° around a critical film thickness, L_{cr} = 50 to 60 nm, and then goes up to 20° for a 4 nm film, as demonstrated by Karan and co-workers[751,762,771] (see Figure 46). Below this critical thickness, the film surface is more super hydrophilic and becomes more hydrophobic as the thickness increases toward bulk-like values ($L > L_{cr}$). The hydrophilic nature of thin-film surface was also confirmed by PALS, showing a SO_3-rich surface,[302] and NMR,[393] which demonstrated that the local hydrogen-bonding structure of a 10 nm film is water-rich with a high dissociation of protons and exhibits no further change in ^1H chemical shifts and mobility with temperature.[393] This is in marked contrast with a 160 nm film, which behaves more like a bulk membrane with a temperature-dependent proton mobility, and thus does not suffer from the kinetically trapped state with limited mobility that ultrathin films experience.[393] A noteworthy observation is that L_{cr} decreases as the film is annealed at higher temperatures (T_{ann}); from L_{cr} = 55 nm to L_{cr} = 10 nm (for T_{ann} = 110 °C) and to L_{cr} = 4 nm (for T_{ann} = 146 °C), with the films annealed 160 °C exhibiting hydrophobic surfaces, regardless of the thickness.[764] However, once the annealed film is exposed to liquid water, it becomes hydrophilic again, revealing a surface reorganization that can be switched by means of surface treatment with water and temperature.[751] The fact that switching of the surface wettability from hydrophilic to superhydrophobic requires a higher annealing temperature for thin(ner) films, indicates the highly restrictive mobility of Nafion as its confinement increases drastically. In accord with changes in morphology, conductivity also decreases with thermal annealing accompanied by a reduced surface roughness,[751,764] the impact of which, however, diminishes for very thin (10 nm) films, which exhibits minimal rearrangement in response to heat-treatment processes.[769]

When water-enriched surfaces form near the substrate, it could be easier to solvate SO_3^- groups, with less impact on ionomer backbone, or lower energy cost on its deformation (as evidenced by the availability of non H-bonded water[784]). Hence, the overall distribution of polymer chains (and SO_3^- groups) and sulfonate groups are controlled by both the film/surface and film/substrate interactions, which are expected to change with film thickness (Figure 49). In such a confined geometry, the polymer chains do not have sufficient energy to orient themselves randomly as they do in a bulk volume, and therefore exhibit preferential alignment, thereby impacting transport of ions,[679,680,742,747,769] water,[129,487,493,494,766] and gases.[490,739,740,778] A number of recent studies agree on formation of a partially ordered ionomer domain structure closer to the film/substrate interface,[209,302,493,746,749,762,768] albeit with a strong substrate dependence.[302,360,493,744,768] Such alignment in confined geometries is possible in light of recent evidence on the locally flat, ribbon-like morphology of PFSA[358] (shown in Figure 21 and discussed in section 3.1). In fact, a recent study demonstrated that the growth of water domains in a thin film (inferred from GISAXS peak, $d(\lambda)/d_{\mathrm{dry}}$) scales with thickness swelling ($L(\lambda)/L_{\mathrm{dry}}$, from ellipsometry) in an affine manner, as expected from locally flat domains. The fact that a bulk PFSA ionomer exhibits nonaffine swelling (Figure 20d) indicates that at longer length scales, the ionomer can be considered a mesoscale assembly of locally ordered domains (like thin films), resulting in a multiscale swelling phenomenon (see section 3.2). As such, the anomalies in structure/swelling correlations must be interpreted within the context of a mesoscale water network, which is disrupted below a critical thickness, i.e., when the ionomer is confined with preferential ordering. Moreover, any preferential alignment is expected to result in stiffening, which was evidenced by fluorescence showing antiplasticization[746] and correlates to the observed increase in the modulus of thin films.[209] These changes are consistent with the reduced water uptake due to a stronger mechanical force in the mechanical/chemical energy balance that controls swelling and uptake. In fact, by exploiting this phenomenon and chain orientation in thinner films, confinement-driven stiffening of the PFSA modulus was reproduced (as shown in Figure 46);[716] it should be noted that this change in mechanical energy is due to chain alignment and not crystallinity as is the more common case for bulk membranes. However, with a further decrease in thickness below 20 nm, the lack of structure or phase separation is accompanied by increased swelling as the ionomer exhibits more or less a dispersion-like behavior (Figure 49). Thus, the balance between the transport and mechanical properties, driven by the hydration-induced phase-separation of the ionomer, appears to exist even in the thin-film regime.

In summary, based on the current status of PFSA thin-film research, from the overall trends in Figure 46, three thickness regimes can be identified: (I) a bulk-like regime (from μm to 100s nm) where the ionomer film behaves like a bulk membrane, (II) a thin-film regime where confinement-induced changes are observed in the structure/transport properties resulting in reduced swelling, limited transport, and anisotropic nanostructure in which the specific interactions between the ionomer moieties and substrate induces additional changes in morphology, including local ordering of the domains at the substrate/film interface, and (III) an ultrathin film regime with dispersion-like behavior for the thin(ner) films of less than 15 to 20 nm thick, where the ionomer begins to lose any confinement-driven changes due to the reduced phase separation between hydrophilic and hydrophobic domains and decreased hydrophobic-domain elastic forces, which tend to prevent dissolution of the ionomer.[747] Although the transitions between these regimes are not well-defined, there appears to be a critical thickness of 50 to 60 nm, around which confinement effects manifest themselves even stronger as discussed above (e.g., refs 48, 493, 679, 744, 746, 751, 762, 764, 767, 770, and 771 and Figure 46). It must be noted that this critical thickness (or transitions between regimes) could change in the presence of other effects, such as annealing and substrate interactions, and additional deviations might occur for properties that may be dominated by larger-scale morphological reorganization, such as diffusivity, permeability, and mechanical properties. Thus, for a given substrate, one would expect that EW, annealing and substrates all play key roles in regimes (II) and (III), by controlling the hydrophilic-domain interactions with the substrate, and hydrophobic-domain forces via the main-chain (via EW and crystallinity). Reducing the EW should result in better phase separation and domain orientation by enhancing the favorable interactions between the ionic moieties and the substrate.[48] Also, for regime (III), QCM and ellipsometry data deviate the most, suggesting that the swelling and water-uptake processes are more complicated due to presence of additional mixing effects and water layers at the substrate interface dominating the film behavior.

6.3. Implications

A thin-film's internal and surface morphology could pose significant limitations to transport and overall device performance.[179,267,360,494,744,746,752] Similar transport limitations between the naturally occurring films of Nafion in PEFC electrodes[57,179,236,738,739,743] and Nafion thin films[360,487,493,679,746,752] suggest that thin films can be used as model systems to investigate and model electrode ionomers, as highlighted in recent perspectives.[177−179] Key for electrode performance is good oxygen permeability with adequate proton conductivity across/through an ionomer thin film on and between carbon/Pt agglomerates. As both transport properties deteriorate for nm-thick films, understanding the structure/transport properties therein is of great importance. As discussed above, such transport resistance, while being driven by the confinement, is also impacted by the ionomer/Pt interaction, with structural ordering through chemical affinity of SO_3^- groups onto Pt, which is mitigated by the water at the interface. Although, one strategy that may work for overcoming transport limitations in electrodes is using PFSAs with higher IECs and different side-chain chemistries, their structure/function relationship in thinner films is yet to be explored, in particular for properties such as ion conductivity and gas permeability. For example, a recent MD study reported that increasing the side-chain density enhances the H-bonding and charge-dipole interactions, which impedes water mobility and its self-diffusion.[785] Understanding the impact of ionomer chemistry on transport mechanism in the presence of confinement and substrate effects is among the challenges that need to be tackled. Moreover, application of some of the techniques that probe water dynamics in ionomer interfaces and thin films is yet to be demonstrated. Similarly, it should also be noted that polymer chains could have more conformational freedom in the plane, where their mobility is likely to be less restricted compared to that perpendicular to the nearby substrate. Thus, the impact of morphological

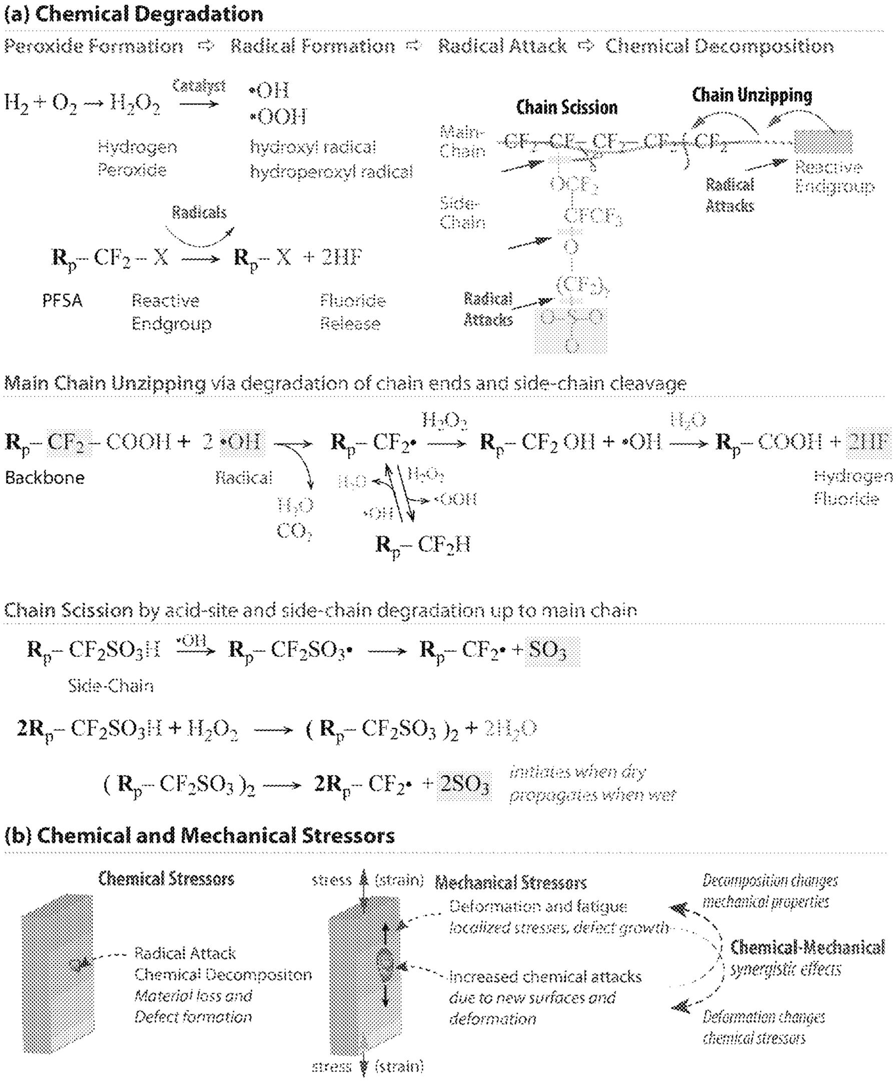
(a) Chemical Degradation
Peroxide Formation ⇨ Radical Formation ⇨ Radical Attack ⇨ Chemical Decomposition
H2 + O2 → H2O2 —Catalyst→ •OH •OOH
Hydrogen Peroxide
hydroxyl radical hydroperoxyl radical
Radicals
Rp− CF2 − X ⟶ Rp− X + 2HF
PFSA
Reactive Endgroup
Fluoride Release
Chain Scission
Chain Unzipping
Main-Chain
Side-Chain
Radical Attacks
Reactive Endgroup
Main Chain Unzipping via degradation of chain ends and side-chain cleavage
Rp− CF2 − COOH + 2 •OH ⟶ Rp− CF2• —H2O2→ Rp− CF2 OH + •OH —H2O→ Rp− COOH + 2HF
Backbone
Radical
H2O CO2
H2O H2O2 •OH •OOH
Rp− CF2H
Hydrogen Fluoride
Chain Scission by acid-site and side-chain degradation up to main chain
Rp− CF2SO3H —•OH→ Rp− CF2SO3• ⟶ Rp− CF2• + SO3
Side-Chain
2Rp− CF2SO3H + H2O2 ⟶ (Rp− CF2SO3)2 + 2H2O
(Rp− CF2SO3)2 ⟶ 2Rp− CF2• + 2SO3
initiates when dry
propagates when wet
(b) Chemical and Mechanical Stressors
Chemical Stressors
Radical Attack
Chemical Decompositon
Material loss and Defect formation
stress (strain)
Mechanical Stressors
Deformation and fatigue
localized stresses, defect growth
increased chemical attacks due to new surfaces and deformation
stress (strain)
Decomposition changes mechanical properties
Chemical-Mechanical synergistic effects
Deformation changes chemical stressors

Figure 50. (a) Chemical degradation of PFSA ionomers with generally accepted chemical decomposition scheme and reactions. (b) Impact of combined chemical and mechanical stressor controlling the failure mechanism in PFSA membranes.[205] (For discussion on mechanical stressors, see section 5.5). The information here are compiled from various references.[11,12,205,726,797,801,804,806]

changes on transport is largely dependent on the direction in which the mechanism is probed. For example, a DPD model of a 5 to 10 nm thick Nafion on carbon demonstrated anisotropic diffusion; higher along the film, lower in thickness direction,[629] in agreement with the morphological changes discussed above. Also, since a higher level of complexity is present in ionomer thin films due to the presence of electrostatic interactions arising from ionic groups responsive to environmental conditions (i.e., humidity, pH, and ionic strength), wetting interactions and thin-film confinement have significant effects in the dynamics of the ionomers' hydrated structure under operation. Thus, additional studies are needed to understand how in-operando stressors such as electrochemical potential impact thin-film morphology and properties of interest.

7. OTHER TOPICS

The various sections above explore the intrinsic properties of PFSAs, from which it is clear that there are a variety of trade-offs. In this section, we explore some topics of interest that are becoming more relevant and explored and that touch on aspects reviewed in the previous sections. In particular, durability and stability are reviewed from both chemical and mechanical degradation standpoints, the impact of additives on PFSA properties and response (i.e., composite membranes), and other cationic forms.

7.1. PFSA Stability and Durability Issues

Most electrochemical devices operate in aggressive hygrothermal and chemical environments, especially at higher potentials, which affect the ionomer's integrity. The complex interactions between the chemical and mechanical failure modes in these devices make it important, yet challenging, to understand the relationship between different stressors and dominant failure modes. Despite their intrinsic chemical and mechanical stability, PFSAs are by no means immune to aging and degradation. There are a multitude of issues to address pertaining to durability of PFSA membranes;[11,12,26,154,205] here we briefly summarize the degradation mechanisms affecting the stability of PFSAs. Overall, the issues regarding stability of PFSA membranes can be listed as

i. Contaminants (i.e., impurities, trace radicals, and foreign cations)

ii. Hygrothermal aging with time (at constant humidity and temperature) inducing morphological changes in the membrane
iii. Chemical degradation in the form of chemical decomposition of PFSA main chain and side-chains
iv. Mechanical stability, which manifests itself when the PFSA membrane is under stress, which is either externally applied (compression or stretching) or, more commonly, internally generated, when the membrane is geometrically constrained within a device platform (e.g., PEFCs or similar electrochemical devices)
v. Thermal stability, which is a measure of membrane's resistance to thermal decomposition at elevated temperatures (>200 °C), which triggers decomposition of PFSA similar to chemical degradation
vi. Other stability factors include, but are not limited to, exposure to UV light and X-synchrotron X-ray induced damage, which, for example, was shown to initiate main-chain cleavage and reduce mechanical stability (by >10% after 60 s of X-ray adsorbed at a rate of 0.63 mJ cm^{-2} s^{-1}[792])

It is worth noting that these factors and stressors are interrelated and often functions of the environment and each other, as well as impacting one another through their effects on morphology and related transport properties (Figure 1). Moreover, even though some of these stressors are naturally occurring (such as storing a PFSA membrane in humid atmosphere that contains trace amounts of contaminants), their real impact is realized when the ionomer is used as the solid electrolyte, where a combination of these stressors simultaneously occurs. Also, as discussed in the previous sections, any parameter controlling the structure−property relationship of PFSA is expected to influence the impact of these stressor (e.g., thermal history of the membrane, EW and side-chain chemistry, environmental conditions (see Figure 5), etc.). Finally, it should be noted that these factors are often explored at the device level through accelerated stress tests (ASTs) that enhance one or two stressors to delineate their specific impact.[12,727,734,793−795] This also allows one to analyze synergistic behavior (e.g., combined chemical and mechanical degradation in PEFCs probed by humidity cycling or membrane and electrodes under hydrogen/air conditions).

7.1.1. Chemical and Mechanical Degradation. PFSA ionomers can chemically decompose via chain-unzipping and/or chain-scission mechanisms due to attack by trace radical species, which can be generated during cell operation. In addition, they can also fail due to the loss of mechanical integrity and pinhole formation, resulting in shorting of the cell due to lack of reactant or electrode (e.g., electronically conductive elements) separation[11,12] (Figure 50). Such degradation has been confirmed through spectroscopic studies in terms of chemical aging[85,90,193] and degradation,[319,377,386,796−799] including degradation product analysis. In terms of chemical degradation, the main culprit is hydroxide radical, •OH, stemming from decomposition of formed hydrogen peroxide (mainly due to reactant gas crossover in PEFCs).[11,26,176,283,291,377,693,705,732,796−798,800,801] Once formed, this highly reactive hydroxide initiate a membrane's chemical decomposition by abstracting a hydrogen atom from a perfluoro-carboxylic acid end-group (R-CF_2COOH) or from a hydrofluorocarbon group, as proposed by Curtin et al.,[176] reviewed,[12] and discussed elsewhere.[11,176,377,797,799,801,802] This degradation mechanism is driven thermodynamically by the formation of strong H−F bonds and continues by releasing 2 HFs while shortening the backbone by one CF_2 unit, thereby unzipping the chain (Figure 50); this process can be monitored by measuring the fluoride release rate (FRR). In fact, higher FRRs have been demonstrated to be related to shorter membrane lifetime in an operating cell, as well as reduced cell performance.[11,12,727,793,803] Gittleman and co-workers[11] revised the degradation mechanisms using kinetic and thermodynamic considerations for the decomposition reactions (Figure 50). In addition, acid sites are also vulnerable to radical attack, which leads to the degradation/fragmentation of the ether linkages in the side-chain and eventually results in chain cleavage.[11,386,797−799,801,804] The strong acidic nature of the side-chain in a PFSA along with the weak C−S bond create a probable pathway for formation of side-chain radicals, degradation of which ultimately leads to the scission of the main chain[11] (Figure 50). This mechanism is more likely to occur in dry conditions, but it can be propagated under hydrated conditions via unzipping, which was attributed to the high residence time of protons on SO_3^- groups at lower water contents (see section 4.4.1).[11]

Spectroscopic analysis of degraded PFSA by Ghassemzedah et al.[386,797] and Danilczuk et al.[804] indicated that OCF_2 groups of the side-chain are the point of attack for the radicals. The side-chain degradation is considered to be more dominant in membranes with reduced −COOH end groups, such as the new generation chemically stabilized PFSAs.[799] The chemical decomposition mechanisms in PFSAs are still a topic of interest, especially for composite and newer SSC PFSA, and are examined thorough either in situ cell testing (e.g., gas crossover, open-circuit voltage (OCV) decay, FRR), a more realistic measure albeit at the expense of additional complexities (arising from contamination, leaching, electrochemical stressors, component interfaces), or ex situ methods (e.g., Fenton's test (see Figure 50)). In Fenton's test the peroxyl/hydroxyl radicals, formed from H_2O_2 in an aqueous solution in the presence of Fe^{2+}/Fe^{3+} (catalyzes H_2O_2 decomposition), react with the PFSA and initiate its chemically decomposition. While the simple Fenton's test has been proven to be a useful method for preliminary screening of a membrane's oxidative stability, and analyzing the fundamentals of the degradation mechanisms,[798] it cannot predict the lifetime in in situ cell testing due to different stressors being present in the latter (e.g., hot and dry conditions). As such, in cell testing, dry-hot operation and higher potentials accelerate chemical-degradation rates due to availability and concentration of radicals among other things.[11,26,724,729,796,803,805]

To protect the PFSA membrane against radical attack and increase chemical stability, chemistry and engineering solutions have been utilized, including capping of the end-groups (e.g., fluorination) to eliminate attack sites, and chemical stabilizers (e.g,, peroxide scavengers) for hybrid composite ionomers.[9,11,76,154,807−809] These latter stabilizers can mitigate chemical decomposition by deactivating the reactive oxo-radicals before they react with the ionomer chain or even react with the crossover gases before they reach the other side.[802,810,811] One particularly effective strategy is to use transition-metal oxides, such as manganese and cerium oxide, which scavenge free radicals and neutralize them.[11,802,809,812−814] For example, cerium cations are effective at decomposing hydrogen peroxide as the two oxidation states of cerium, + 3 and +4, play complementary roles in H_2O_2 decomposition, by reacting first with HO• to produce water and Ce^{4+}, which is then reduced back to Ce^{3+} upon reaction with H_2O_2 or HOO•[11,802,814,815]

$$\text{HO}\bullet + \text{Ce(III)} + \text{H}^+ \rightarrow \text{H}_2\text{O} + \text{Ce(IV)}$$

$$\text{Ce(IV)} + \text{HOO}\bullet \rightarrow \text{O}_2 + \text{H}^+ + \text{Ce(III)}$$

A key issue of this kind of stabilization though is to ensure the stabilization remains at the appropriate locations and deactivates the HO• before it degrades the polymer;[802,815] this is compounded by the fact that the cations can move during operation due to migration and diffusion (see section 7.3), resulting in dramatic changes in their distribution in the membrane during operation.[815] Another way to react the radicals is to add Pt or similar reactive metal into the membrane that can decompose the peroxide with the crossover hydrogen.[802,810,811] In addition to metal cations, other additives can be used but these typically have primary effects in terms of impacting performance more so than durability as discussed in section 7.2.

Chemical and mechanical degradation are inextricably linked as well as coupled to transport phenomena (see section 4.3 and Figure 50b). As the membrane chemically decomposes, depending on the operation and dominant stressors, it could exhibit uniform thinning causing increased overall gas crossover and/or localized physical defects or pinholes. The degree of chemical decomposition has been shown to directly influence the defect sizes and their distribution.[798,816] These changes result in increased rates of crossover,[11,12,26,287,727,817] and thus radical generation that leads to increased chemical degradation and so on in a runaway-type mechanism that leads to catastrophic failure.[26,817−820] Thus, any type of defect or discontinuity in the membrane (e.g., cracks, pinholes) makes the ionomer (i) chemically more vulnerable to radical attacks by opening up more surfaces, (ii) mechanically more prone to damage by creating stress-concentration sites,[708,731,817] and (iii) thermally weaker at higher temperatures (close to T_α) by creating hotspots in the vicinity of defects.[817,820,821] As noted, the environmental conditions also impact this by controlling not only the rates of chemical degradation and radical formation but also by modulating the transport through the defects. For example, a small pinhole could fill with water or swell shut during humid operation, thereby decreasing the crossover flux.[800,817,820] Although initiated in the presence of chemical and thermal attacks, membrane defects could propagate and grow due to mechanical stresses generated in a geometrically constrained membrane where it cannot freely swell with solvent uptake. For mechanical stability considerations, it is the dimensional change rather than water uptake (λ) that is important for cyclical stresses under swelling−deswelling cycles.[154,285,708,822,823] Even though swelling and λ are related, it is possible to modify the swelling ratios and anisotropy for a given RH change (Figure 11), which can be accomplished with composite membranes (see section 7.2). Moreover, a defect's size is related to gas crossover,[800,818] and its impact on performance[820] and durability[708] are related to transport and mechanical properties, respectively. However, along with chemical structure, both transport and mechanical properties also change with chemical decomposition, which, in most cases, reduces the ionomer's water-uptake capacity and increases its brittleness (higher Young's modulus and lower break strain[319,668,724,725,727−729,806,824,825]). Such changes in ionomer properties with degradation could make it less resistant to failure, and provide another means through which the chemical effects influence the stresses. A rather more intriguing effect is that of the mechanical stress on the rate of chemical decomposition as demonstrated by ex situ Fenton's test under mechanical forces,[726,826] which confirm the synergistic nature of chemical-mechanical degradation of ionomers controlling the fate of the defects as discussed in ref 205. Thus, when an ionomer separator undergoes dry/wet cycles during operation, whether driven by environment or electrochemical reactions, changes in transport and mechanical properties, along with the interplay between the gas pressure gradients, chemical stressors, and swelling-induced deformation, all together control the fate of the defect and the membrane's lifetime.

7.1.2. Contamination Effects.

Contamination with trace amount of foreign cations can critically affect a PFSA's transport properties and thermomechanical stability. Foreign contaminants often arise in various devices from balance of stack or cell corrosion (e.g., metallic bipolar-plate corrosion), environmental conditions (e.g., salts or impurities in the incoming reactant flows), or balance-of-system components (e.g., seal or tubing degradation).[12,827,828] In terms of foreign cations, similar to the changes discussed in section 7.3, they typically imbibe into the membrane and affect local morphology and transport properties. In some cases (e.g., Fe cations),[612,829] they are present in small amount as impurities and enhance degradation by acting as catalysts; while in other cases, they are added intentionally to inhibit degradation (e.g., cerium cations, see section 7.1.1).[828] In small concentrations, foreign cations can result in significant changes in electro-osmotic response[830−833] and conductivity[170,834,835] and can even limit cell performance due to blockage of protons.[828,836] For example, more than a 50% decrease in conductivity was reported at levels of 100 ppm of foreign cations due to their higher affinity than H^+ to the sulfonic-acid moieties.[833,835] Overall, contamination becomes a critical issue for higher valence cations (such Fe^{3+}), which have much higher affinity to PFSA side-chains than H^+.[837] As an example, Nafion has higher affinity for Na^+ than for H^+, and with increasing fraction of Na^+, water content, ionic transference number, and conductivity all decrease, because H^+ carries more current than Na^+,[612,832] which was shown to occur even at 0.2 Na^+/SO_3^- levels of contamination.[838] This higher affinity and hence impact scales with valence and size, for example, in terms of transport impact, as $Fe^{3+} > Ni^{2+} > Cu^{2+}$.[833−835,837] It is worth noting that, even though H^+ mobility depends on the foreign cation, the converse is not necessarily true since they are a dilute species.[612,833] An intriguing impact of contaminants is the increase in the onset of thermal decompositions, namely, thermal stability, especially for SO_3 degradation.[825] Also, with increasing concentration (ppm) of contaminant (Ni^{2+}), the mechanical response changes from relaxation (chain motion) to degradation.[825] Such impacts are witnessed with other contaminants, such as ammonia (NH_3^+), which, as a proton acceptor, can readily form NH_4^+ whose reaction with SO_3^- sites results in drastic reductions in conductivity and durability[170,839−841] (see Figure 51).[170] Nevertheless, recent studies demonstrate that contaminants have more pronounced time-dependent effects over longer times, activating mechanisms reminiscent of aging, not only in PEFCs,[824,825] but also in chlor-alkali cells.[182]

7.1.3. Hygrothermal Aging.

As discussed throughout this review, PFSA ionomers are not in true equilibrium and their morphology tends to change over time and under certain environmental conditions; such changes over longer time scales

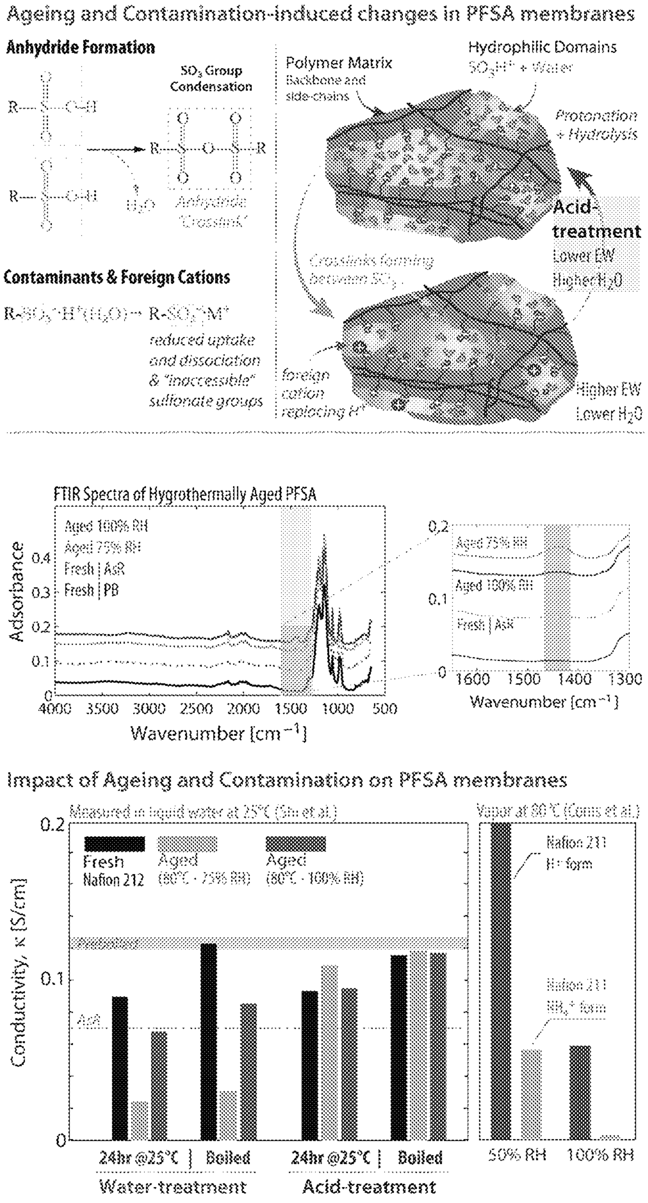

Figure 51. Possible scenarios affecting the phase-separated morphology of PFSA resulting in inaccessible ionic sites, such as ionic cross-linking, contamination or the process of reversible anhydride formation. Impact of hygrothermal aging on FTIR spectra, which shows the formation of the 1440 cm^{-1} peak, and liquid-water conductivity of Nafion 212 membrane (from Shi et al.[90,400]). For comparison, decrease in conductivity of Nafion in the presence of ammonium is shown (from Coms et al.[170]).

is termed aging.[85,86,183,193,648,697] During such aging, a PFSA membrane was observed to exhibit a decay in conductivity,[90,183,193,400,842] gas permeability,[648] water permeance and water uptake,[170] as well as an increase in tensile modulus,[85,86,90,193,400,697] and T_α[90,400] with implications on membrane performance in PEFCs[86,170] and humidifiers.[170] Many of these changes are attributed to the formation of functional species (e.g., anhydrides) that form cross-links between the ionic groups, which are catalyzed by contaminants. A commonly employed method to examine these effect is FTIR, in which some studies reported a new peak around 1440 cm^{-1}, accompanied by a weakening of the peaks associated with H-bonds.[86,90,170,400] This along with a reduction in transport properties and increase in elastic modulus have lead researchers to relate the origin of such peak to a change in local structure. This peak was assigned in some studies to the S−O−S cross-links, believed to be formed via condensation of SO_3^- groups (Figure 51).[85,90,183,193,648] The effect of aging was shown to be more pronounced for membranes aged in higher RH conditions, due possibly to water promoting side-chain mobility;[85,193,400] but less pronopunced in liquid water, due to possible hydrolysis reactions, or increase in SO_3^- separation, reducing the condensation.[193] While such a scenario is in agreement with the higher EW reported for aged memrbanes,[90] due to a reduced fraction of available SO_3^- groups, the origins of aging is not yet understood.

Collette et al. reported an increase in the anhydride content and accelerated aging with a cationic pollutant, such as copper ions, were shown to accelerate the formation of anhydrides.[193] In addition, Clapham et al. found that the intensity of the FTIR band at 1440 cm^{-1} after aging increased with membrane thickness, which can also be interpreted as the existence of other phenomena than anhydride formation.[183] Recently, Coms et al. proposed that the observed changes due to aging are strongly linked to contaminants,[170] in particular trace levels of ammonia in the atmosphere. The ammonia (NH_3^+), as a proton acceptor, can readily form NH_4^+ in the membrane over time, whose reaction with SO_3^- site via acid−base chemistry form degradation products, resulting in drastic reductions in conductivity (Figure 51).[170] As with other aged membranes, full recovery is observed by treatment with strong acid or base solution.[170]

Qiao et al.[319] reported that S−O−S cross-links formed during oxidative degradation of a PFSA reduces also its conductivity, which scales linearly with the reduction in the −OH bending intensity, indicating a disruption in H-bonded water network. It must be noted that cation-exchange[381,843] and annealing[107] of (unaged) PFSA was also shown to give rise to similar peaks around 1440 cm^{-1} band. As such, the decrease in conductivity with degradation and aging could be associated with the changes in local interactions of SO_3^- whether it is driven by anhydride formation (physical cross-links) or contaminants (ionic cross-links), which appear to reduce available SO_3^- groups (thus the increase in EW and mechanical properties) and changes the morphology (Figure 51).

Aging changes result in lower water contents by shifting the underlying chemical/mechanical energy balance that drives water uptake (see section 2.6).[82] However, unlike thermal annealing, aging does not change crystallinity.[193,400] The SAXS data are consistent with this in that after aging the ionomer peak shifts significantly to the right and broadens, implying a wider distribution of smaller and maybe even isolated water domains. Also, the d_w−λ trend (discussed in section 3.2) shifts downward upon aging (d_w decreases more than λ) indicating a break in the hydration vs d-spacing correlation (Figure 51),[400] where the aging-induced cross-links prevent expansion and perhaps connectivity of the water domains.[183,193,257,430,844] This is consistent with the more severe decrease in ionic conductivity than can be solely explained by changes in EW and water uptake as observed by Collette et al.[193] and Clapham et al.,[183] who reported a conductivity loss of 80% versus a 49% increase in EW.

The effect of hygrothermal aging is reversible in that it can be erased completely by boiling in strong acid, but only partially in DI water (Figure 51).[86,90,400] The recovery process is thought to be promoted by protonation of unaccesible SO_3^- groups in acid (whether hydrolysis of S−O−S or removal of contaminants), thereby breaking cross-links, which is corroborated by the disappearance of their fingerprint in FT-IR peaks and recovery of their baseline EW.[90,400] Moreover, the partial recovery in water uptake and conductivity upon heating in water was also observed for *d*-spacing,[90] indicating, once again, a universal correlation between nanostructure and transport properties. In addition, it was recently reported that aging-induced changes in Nafion EW, structure, and properties are more pronounced if the as-received membrane is hot-pressed,[400] and aging rate is slower for Nafion 212, compared to Nafion 112 that has higher concentration of metal ion contaminants.[648]

This correlation and the impact of thermal processing (see section 3.1.4) hold, in that stabilized and pretreated membranes are less prone to aging, which can be attributed to (i) their larger domains with longer distance between the SO_3^- groups making degradation reactions less favorable, and, more importantly, (ii) elimination of cationic contaminants and impurities during pretreatment. Thus, the impact of thermal history seems to have a profound impact on the result of aging, with the membranes possessing contaminants being more sensitive increased propensity for initiation of cross-link formation due to the introduction or exacerbation of potential reactive sites or presence of foreign cations. All these findings support the potential role of contaminants (see previous section), and provide a link among thermal history, foreign cations, and aging, concomitant with changes in time-dependent structure/property relationship (i.e., relaxation). This coupling warrants further study as PFSA membranes are increasingly used in a variety of technologies (e.g., solar-fuel generators, redox flow batteries, etc.) where the environments are rich with electrolytes, additives, and salts and long lifetime is expected.

7.1.4. Thermal Decomposition. Thermal decomposition of PFSA ionomers, usually studied by thermal gravimetric analysis (TGA) combined with mass spectroscopy of the degraded products, occurs in three stages, with each representing the thermolysis of distinct groups (Figure 52): (1) loss of (residual) water (from 100 to 200 ± 20 °C), ending with breakup of the H_3O^+ and protonation of SO_3^- to SO_3H as well as partial decomposition of $SO_3H \rightarrow SO_2 + \bullet OH$ close to 200 °C; (2) cleavage of the C−S bond (280 ± 30 °C to 400 ± 20 °C) resulting in sulfonate-group degradation ending with oxidation of the side-chain terminus; and (3) the final decomposition (oxidation) of perfluorinated matrix (400 ± 20 °C to 600 ± 40 °C).[107,229,231,232,396,845−849] Thermal decomposition initiates and propagates over a temperature range by releasing (1) the last remaining water molecule (H_3O) (with 5 to 7 wt % loss)[228−232] (2) sulfur dioxide, hydrogen sulfide, CO_2 (with 25−30 wt % loss)[231,396] and (3) SOF_2, thionyl fluoride and COF_2, carbonyl fluoride, followed by complete decomposition of PTFE backbone at 600 °C, with over 90% volatilization, releasing compounds of perfluorocarboxylic acids ($C_nF_{(2n+1)}COOH$[845]).[228,230,231,846] Once decomposition starts from the end groups and side-chain, fluorocarbon and $\bullet SOH_3$ radicals form that cleave to produce SO_2 and an $\bullet OH$ radical, which degrade the main backbone by a random scission process (see Figure 50), similar to the degradation of PTFE (which itself degrades also at 500 to 590 °C).[230,231,845,846]

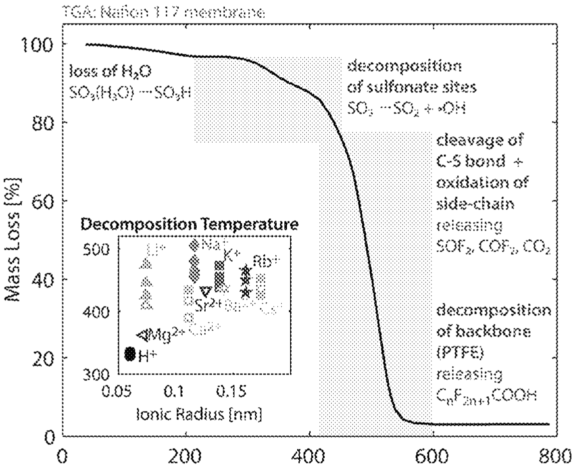

Figure 52. TGA curve of Nafion 117 in N_2 from Feng et al.[845] (heating rate: 20 °C/min). Inset shows the range of decomposition temperatures for second stage from literature studies.[229,394,396,847,850,851]

TGA of PFSAs has been studied in various forms of acid and salts,[229,394,396,397,825,847,850−852] in the presence of fillers,[232] with the effects of casting[848] and thermal treatments.[107,846] From these studies, the decomposition temperature, T_{decomp}, increases with annealing time due to stabilization by the more crystalline backbone and incorporation of alkaline-metal counterions due to the strong ion pairs they form with SO_3^- ($-SO_3^- - M^+$).[229,231,850,851] Overall, the findings suggest that thermal stability improves the best for the Nafion exchanged for alkali-metal counterions (T_{decomp} in order of $H^+ < Li^+ \sim < Cs^+ < Rb^+ < K^+ < Na^+$[394,847,850−852]), followed by divalent ions, then trivalent ions,[851] for which T_{decomp} increases in the order of $Mg^{2+} < Ca^{2+} < Sr^{2+} < Ba^{2+}$, with increasing radius as mentioned in section 7.3 (Figure 52). For alkali-metal cations, reducing the size makes the electrostatic interaction stronger, thus stabilizing the C−S bond, which impedes the thermal decomposition.[229,394,396,847,850,851] The smaller the "effective" size of the alkali-metal cation, the better the thermal stability with the exception of Li^+, which has a large hydration energy like H^+, making its effective diameter larger due to its strong association of water, which it retains at elevated temperatures.[850,851] For alkaline-earth−metal cations, on the other hand, increasing the radius improves stability (T_{decomp} increases in the order of $Mg^{2+} < Ca^{2+} < Sr^{2+} < Ba^{2+}$).[396,851] This anomaly in terms of cation-size effect is attributed to the fact that the stabilization of C−S bonds through the formation of ion pairs is stronger between $-SO_3$ and alkali metal compared to $-SO_3$ and alkaline-earth metal.[851] Lastly, the range of decomposition temperature, ΔT_{decomp}, is inversely proportional to the cationic radius, $\Delta T_{decomp} \propto r_{cation}^{-2}$ and increases with Lewis acid strength (LAS).[397] (See section 7.3.1 for further discussion.)

7.2. Composite Membranes and Modifications

Mitigation strategies aiming at improving membrane durability should encompass good transport properties without sacrificing mechanical stability, thus necessitating a different take on the transport-stability trade-off in PFSAs. Overall, the motivation for developing composite membranes stems from either improving durability by increasing chemical/mechanical stability, increasing performance through transport properties, and/or by extending the operating window of the membrane to higher temperatures and lower humidities, all while mitigating any concomitant deleterious effects.[9,11,30,76,154,205,294]

Such improvements and their potential side-effects include (i) thinner membranes for reduced transport resistance (and cost) which, however, could increase reactant crossover, (ii) lower-EW ionomers, while favorable for transport, usually come at the expense of higher swelling and possibly lower mechanical stability, (iii) higher conductivity in dry/hot conditions (e.g., high-temperature PEFCs) without compromising mechanical and chemical integrity, and (iv) better selectivity, i.e., limiting transport of undesired ions or inactive species, while maintaining high active-ion conductance, including, but not limited to, achieving a higher decrease in solvent permeability than in conductivity with a net effect of increased methanol selectivity in DMFCs, or eliminating crossover of reactants and inactive charged species in redox flow batteries.

Extending the conductivity of a hydrated PFSA to higher temperatures has been an integral part of high-temperature PEM research, which is an ongoing material problem. With increasing temperature, the intrinsic proton mobility increases but this is more than offset by a decrease in PFSA membrane water content. Simply put, the ability to maintain conductivity at elevated temperatures (>100 °C) could be achieved by preventing collapse of interconnected hydrophilic domains (proton channels) and retaining water. Although many other materials solutions are being explored, such as ion-containing block copolymers where there is more morphological control,[672] PFSAs hold their unique position due to their attractive properties that could be exploited to design polymer blends and composites,[30,853,854] as well as their well-demonstrated durability in devices. Furthermore, PFSA ionomers also provide new avenues for many applications, especially when their chemistry is tuned through side-chain modifications and doping, or when they serve as the host material for reinforcements and additives in hybrid ionomers, all of which help expand their structure/performance/stability window.

Over the past decade, an increasing number of membrane modification strategies have been adopted to mitigate degradation and performance problems (Figure 53), including, but not limited to, impregnating/doping the ionomer with (i) radical scavengers such as cerium oxide to prevent radical formation as discussed in section 7.1, (ii) chemically inert hydrophobic mechanical support layers, such as PTFE mesh, to improve the mechanical properties and dimensional stability in response to humidity changes, and (iii) inorganic particles to improve stability and/or inorganic hygroscopic fillers to improve water-retention capacity especially at higher temperature and lower humidity.[30,853,855] It must be noted that when cations or particles are present at low levels they are treated as impurities, which is considered under the contamination section 7.1.2, whereas deliberate doping and impregnation tend to create a true hybrid ionomer membrane. Hence, the overall changes in properties of a composite ionomer depend on (i) the nature of the strategy employed (whether it is an inert, noninteracting reinforcement, or an interacting species such as a doped cation or inorganic filler) and processing (e.g., casting), (ii) the size, distribution, and total amount of the filler, and (iii) the interaction between the ionomer moieties and the added secondary particle (filler).[30,853,854]

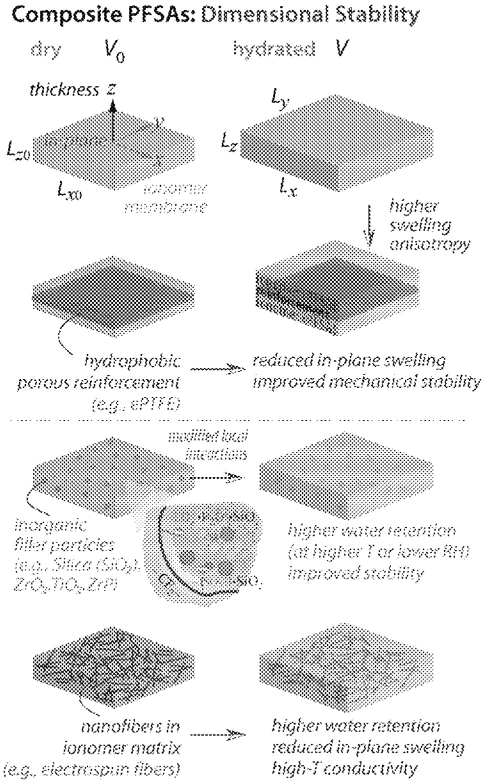
Composite PFSAs: Dimensional Stability
dry V_0
hydrated V
thickness z
y
x
in-plane
L_{z0}
L_{x0}
ionomer membrane
L_y
L_z
L_x
higher swelling anisotropy
hydrophobic porous reinforcement (e.g., ePTFE)
reduced in-plane swelling improved mechanical stability
modified local interactions
inorganic filler particles (e.g., Silica (SiO_2), ZrO_2, TiO_2, ZrP)
SiO_2
higher water retention (at higher T or lower RH) improved stability
nanofibers in ionomer matrix (e.g., electrospun fibers)
higher water retention reduced in-plane swelling high-T conductivity

Figure 53. Strategies used to improve the dimensional and mechanical stability of PFSA membranes and/or to extend its operation window (to higher temperatures, lower humidities).

It is worth noting that some of these strategies are employed in conjunction with efforts toward stabilizing lower-EW ionomers through side-chain-chemistry modifications, doping and processing, or impregnating them with additives to address some of the issues discussed above.[4,7,9,713,807,856] Hence, recent years have witnessed a growing interest in membrane modifications, which include (also see other reviews on related topics[4,9,29,30,853,854]):

- Reinforcement with another polymer, ePTFE,[76,286,287,314,576,614,698,703,708,731,793,823,857−860] or blending with a dissimilar polymer using electrospinning[7,691,713]
- Impregnating the ionomer with metal salts and additives, or hygroscopic inorganic dopant fillers such as silica (SiO_2),[30,133,401,436,721,861−863] zirconium phosphate (ZrO_2),[401,712,863−866] titania (TiO_2),[122,382,863] or secondary particles such as carbon nanotubes (CNTs),[867−870]
- Change in chemistry via doping or polymer blends, such as doping PFSAs with heteropolyacids (HPAs),[10,30,856,871,872] or zeolites.[30]

Regardless of the method, an ionomer filled with secondary particles can be considered and treated as a composite membrane (Figure 53). However, given that PFSA ionomers already possess a complex phase-separated morphology, inclusion of additional particles or support layers creates a true multiphase hybrid material where the interactions of these newly added particles and the ionomer's hydrophilic and hydrophobic phases become critical in controlling not only the efficacy of the composite structure but also the overall properties of the membrane. Of course, since a PFSA's response to electrochemical, mechanical, and environmental stimuli (e.g., ionic potential, stress, RH, T, pH) are interrelated through ionomer morphology, swelling, and transport and mechanical properties, as discussed in previous sections, there is a need to ensure that a multivariable optimization is realized and trade-offs analyzed.

Before proceeding, the scope of this section should be clarified. Literature pertaining to hybrid/composite PFSAs, which have been increasingly explored in the past decade (Figure 3), could be categorized as (i) comparison of PFSAs with other non-PFSA hybrid ionomers, (ii) demonstration of these membranes in devices (commonly PEFCs, DMFCs and redox flow batteries), and (iii) structure/processing/property relationship of composite PFSAs. The focus herein will be on the latter studies.

Another natural outcome of composite PFSAs that need careful attention is an accurate characterization of EW (IEC), or an "effective EW" as the EW, by definition, accounts for the fraction of ionic sites in the polymer, excluding any foreign reinforcement or additives. Given that EW already fluctuates among the batches and/or inaccessibility of some of the sulfonic acid sites, due to processing and thermal history, it remains a challenge to define an EW for the composite PFSAs, as discussed in elsewhere.[3,98,873]

7.2.1. Mechanical Reinforcements. One strategy that has been proven to be effective at improving PFSA performance and lifetime in devices is including a reinforcing layer, typically a microporous expanded-polytetrafluorothylene (ePTFE) mesh. The prototypical commercial composite membrane is known as Gore-Select membrane, manufactured by W.L. Gore & Associates, Inc.[76,287] Despite increased use since 2010, reinforcement of Nafion or PFSAs is not new, as the concept goes back to the 1990s[859,860] and was driven by the need to make thinner, robust membranes. While the porosity of the hydrophobic mesh enables a continuous transport pathway through the thickness (after impregnation), its mechanical stability reduces the dimensional change in the plane of the membrane (Figures 11 and 53), especially during hydration cycles. Reinforced membranes exhibit superior durability as evidenced from longer lifetime without failure under humidity cycling (section 7.1).[11,12,76,154,336,693,734,793] Hence, such reinforcements could possibly allow the use of thinner, lower EW ionomer that would otherwise have insufficient mechanical integrity.

A natural consequence of the reinforcements in such sandwich-composite structures is the dimensional anisotropy, especially thickness vs in-plane. Reinforced membranes have better dimensional stability in the plane, meaning they swell less in favor of higher thickness swelling such that their overall weight or volume uptake could remain relatively unchanged.[154,286,720] Such swelling anisotropy with lower in-plane swelling has been shown to be critical in reducing the swelling-induced mechanical stress during cell operation and especially under cycling operations[118,286,708,822,823] and also effective at increasing a membrane's resistance to defect propagation.[731] Moreover, fatigue stresses with a tensile component were shown to be reduced most by reducing the in-plane swelling, even if the total volume change is the same, as the stresses in the thickness direction are less critical in activating failure mechanisms.[286,822,823] It is interesting to note that although reinforcement increases the mechanical properties in the direction they limit the swelling, it is actually the reduced swelling that is more effective at decreasing the mechanical stresses in the membrane. In fact, modeling studies have shown that a higher modulus alone is not always a favorable outcome of the reinforcement as it increases the stress generated in situ, which brings the deformed membrane closer to its yield strength, i.e., plastic deformation.[123,286,708] However, as the reinforcement also increases the yield strength and reduces swelling, and even more importantly enhances the fracture resistance,[707,731] one could still favorably improve the mechanical response of the composite membrane (see section 5). Thus, it is important to investigate fully the anisotropic swelling behavior and thermo-mechanical properties for newly developed membranes to assess their mechanical and thermal stability accurately. The role of the swelling-resistant reinforcement phase can be interpreted as internally constraining the membrane which limits its expansion, similar to the external constraint and compression effects and prestretched materials discussed in section 3.1.5. In fact, reinforcing a PFSA was shown to cause a shift in domain-size distribution and size toward smaller domains across the whole domain sizes,[98,418] revealing the impact of such internal constraints. Finally, it should be noted that while the reinforcement-induced stability makes the ionomers less sensitive to humidity changes, it does not really change their temperature-dependent stability since the reinforcement too has typically a similar temperature-dependent response.[720]

In terms of transport properties, compared to Nafion, Gore-Select membranes have been shown to have lower H_2 permeability,[287] higher proton diffusion,[314] lower steady-state water diffusion, comparable electro-osmotic coefficient,[614] as well as comparable conductivity[287] and activation energy.[287,314] [Properties are compared at the same RH and T, although it must be noted that ionomers in these two membranes might not have the same EW.] This family of ePTFE-reinforced membranes exhibit improved mechanical stability as investigated in a number of studies; (an order-of magnitude) lower in-plane swelling,[286,287,823] stress−strain behavior with higher modulus and yield strength,[286,287,698,731] and higher critical fracture energy for crack propagation.[707] The above structural and swelling anisotropy also induces anisotropy in transport properties. For example, Gore-Select membranes show a ratio of in-plane to through-plane conductivity of ~1.10 to 1.5, whereas this value is 1.07 for Nafion 212.[576] However, the extent of decrease in through-plane conductivity to in-plane conductivity largely depends on the relative thickness of the ionomer and reinforcement phases.[576]

Despite significant process made in mechanical stability, device demands require better chemical and mechanical durability, which has stimulated development of membranes possessing both mechanical reinforcement and chemical stabilizers. One prominent class of PFSA membrane with improved lifetime compared to regular Nafion membrane is DuPont's Nafion XL,[98] which is both mechanically reinforced by microporous PTFE layers (~10%) and chemically stabilized.[857] Recent studies on Nafion XL reported that, compared to its unreinforced Nafion analogue, it has less shrinkage stress induced by its lower water uptake,[858] lower swelling and higher storage modulus in the plane but with comparable volume change and λ,[708] anisotropic swelling and conductivity (in-plane vs thickness),[708] lower crack initiation and propagation due to the enhanced plastic deformation of PTFE,[705] and higher chemical stability.[793,802,874] More recently, impregnating PFSA ionomers with electrospun nanofibers has been demonstrated to produce composite membranes with improved mechanical properties and water retention.[7,691,713,875] As demonstrated by Pintauro and co-workers, with electrospinning, not only can an ionomer be reinforced by a nanofiber (e.g., poly(phenyl sulfone) (PPS)) network, but ionomer nanofibers could also be embedded in an inert/uncharged polymer nanofiber network; thus enabling morphologies between ePTFE-reinforced PFSAs and Nafion/hydrocarbon polymer blends.[691] The conductivity of nanofiber composite membranes has been shown to scale linearly with the Nafion volume fraction for both structures (i.e., whether Nafion is the host matrix of the filler fiber or vice versa).[691] Volume swelling also increases with PFSA fraction for both structures, which exhibit lower in-plane swelling than Nafion, albeit with different swelling anisotropies due to distinct 3-D connectivity formed in these composite structures. Similar to the other reinforced PFSAs, these composites with electrospun fibers have higher yield strength, modulus, and tensile strength, but slightly lower failure strain, all of which are dependent on the fraction of PFSA. Electrospun composites with lower EW 3M ionomers also exhibited improved conductivity and water weight uptake at higher temperatures; however, their mechanical properties in water were not always superior depending on the PFSA EW used.[7,713] A notable outcome of electrospun PFSA/PPS membrane was that it can be tailored to increase selectivity, by increasing the ratio of proton conductivity to the permeability of reactant species (i.e., selectivity), which makes them an attractive candidate for many different separator applications.[678] Moreover, challenges associated with electrospinning neat Nafion fibers from a Nafion/alcohol solution due to the polymer's rod-like micellar morphology without sufficient chain entanglements (see Section 3.1) have led researchers to add a carrier polymer, e.g., poly(acrylic acid) or poly(ethylene oxide), to the Nafion solution at a high concentration (15 to 30 wt %).[713] Thus, successful electrospinning requires optimizing the trade-off between a high enough polymer concentration in the solution for polymer chain entanglement but low enough to avoid viscosities that are hard to spin.[7,713]

Another filler used in Nafion for both performance and durability enhancements is carbon nanotubes (CNTs), a commonly used reinforcement particle in advanced polymer composites. A critical issue with the use of electrically conductive CNTs is the optimal filling to avoid possible electronic short circuits in applications (i.e., one needs to remain below the percolation threshold, which depends also on the functionalization of the CNT, their dispersion and interaction with the polymer chains through processing effects).[867,870,876] Improvements in Nafion upon incorporation of CNTs are increased strength,[867,868,876] reduced dimensional change,[867] improved thermal stability indicated by a shift in $\tan(\delta)$,[868,876] increased modulus up to 160% with only ~10% decrease in conductivity, increased proton to methanol selectivity,[869] and decreased methanol permeability.[715] While showing increased performance for some applications, the possibility of short circuits as well as expense and use of elongated nanomaterials makes this strategy questionable.

7.2.2. Performance Additives. In addition to forming composite membranes to increase mechanical stability and allow for the use of lower EW ionomer, composite membranes have also been synthesized with additive particles to increase performance. These additives are incorporated to achieve dimensional and thermo-mechanical stability (such as lower in-plane swelling and higher transition temperatures, modulus, and strength), or widen the conductivity range of the ionomer, in particular at lower RHs and higher (>100 °C) temperatures. This strategy is somewhat different than the radical scavengers discussed in section 7.1, where the primary interest and goal is to provide additional chemical stability. With performance additives, however, one can improve membrane properties by tuning its functionality. Of the inorganic fillers used in PFSAs, the most widely studied system is Nafion with metal oxides and, in particular, Nafion-SiO_2.[30,133,401,436,721,854,861−863] Silica in PFSAs is used to exploit its attractive properties such as its tendency to absorb water yet with minimal interaction with hydronium ions at low RHs, to increase crystallinity and mechanical stability, as well as its ability to inhibit methanol permeation.[30] All of these changes, however, are strongly dependent on how much silica is added (i.e., doping level) and how it is added (i.e., processing). Such membranes are prepared via casting from Nafion dispersion with silica nanoparticles or sol−gel polymerization, where the ionomer is imbibed with the Si-containing sol−gel precursors and then annealed where the precursors (SO_2F groups) react with the inorganic molecules that cross-link the polymer chains (via Si−O−Si bridges)[133,861,862] and create a covalently bound inorganic phase.[721,862] Once formed, these groups restrict the mobility within the ionic clusters and therefore increase the modulus[401,862] and shift the transition temperatures,[401,721] although often the membranes could also exhibit more brittle mechanical behavior.[862,877] Overall, these membranes demonstrate higher liquid-water uptake by weight and swelling,[863,877] which leads to better high-temperature conductivity, a larger RH operation window,[401,602,878] higher activation energy for transport,[401] anisotropic water diffusion,[879] and improved thermal stability due to the retardation of thermal degradation by the cross-linked silicon-oxide network.[880] Overall, 3 to 10 wt % of silica loading in Nafion has been employed, giving a range of conductivity from 0.07 to 0.10 S/cm at 80 °C, 100% RH, depending on the processing methods and type of silica (see a review by Herring[30] for more details).

Another hybrid composite with zirconium phosphate, Nafion-ZrP, has been reported to have higher modulus,[401,712,866,881] increased water retention[122,714,864] and dimensional stability over 100 °C,[714,864,881] lower methanol permeability,[866] better high-temperature conductivity,[401,881] albeit, in some cases, at the expense of lower conductivity under moderate humidities and temperatures[122,712,714,864,866] and limited proton mobility, which could be restricted by the ZrP particles.[122,590]

A noteworthy improvement in these hybrid membranes is that the decrease in methanol permeability is usually higher than the decrease in conductivity with a net effect of reduced proton/methanol selectivity, as discussed in section 4.6.[602,866,882] In fact, further enhancements in proton selectivity and methanol permeability has been reported when the inorganic fillers are functionalized (e.g., sulfonated), owing to their dual role of facilitating proton transport while obstructing methanol crossover,[602,882] due to changes in the effective tortuosity of the mesoscale assembly. It was shown through FTIR studies that inorganic fillers could restrict methanol and water transport in a PFSA by reducing the fraction of H-bonding therein, which was facilitated by the interaction of the filler with the fluorinated matrix.[883] In fact, changing nature of water in these hybrid systems could be associated with their higher water self-diffusion in the subzero temperature regime, owing to hygroscopic filler-water interactions.[313]

Similarly, Nafion-titania composites exhibit higher water-uptake capacity,[863] better thermal stability,[382,884] lower permeability,[884] higher modulus and improved mechanical properties,[122,382,402] but also lower[29] or higher[863] conductivity as these properties change with titania wt % in a nonlinear fashion (up to 0.05 S/cm between 115 and 135 °C).[29,382,863] The concentration of fillers and their dispersion affect the interactions between the nanofiller and the host ionomer matrix (both its − SO_3H groups and backbone), thereby changing the strength of the dynamic cross-links therein, leading to the variance in properties.[402]

More recent systematic investigations[401,885,886] that focused on the interactions of Nafion and the inorganic particles (e.g., R-SO_3H··SiO_2 interactions) demonstrated that silica particles exist in both the ionic phase and amorphous matrix, and reduce chain dynamics in a similar manner to thermal annealing (see section 3.1.4).[885] Holdcroft and co-workers showed the formation of Si−O−Si bridges in Nafion, where the inorganic nanoparticles can bind and hold water above 100 °C and thus improve thermal stability. Despite a reduced conductivity in hybrid membranes caused by the restricted mobility of the ionic clusters, such a reduction is not observed at lower RHs and higher temperatures.[861] In a series of recent investigations by Di Noto and co-workers[133,401,886] using broadband dielectric spectroscopy, two distinct interactions between Nafion and the inorganic filler material were identified: (i) silica (or another inorganic particle) clusters interact with Nafion's polar side groups that is predominantly implicated in dynamic cross-links and (ii) silica moieties interacting predominantly with other surrounding oxo-clusters acting as fillers. As the latter interaction increases, the nanoscale homogeneity of the materials is lost, thereby giving rise to a biphasic system where the relative motions between the phases are inhibited more strongly, resulting in more pronounced changes in properties. Such changes are also increased as the basicity of the dopant nanofiller increases (or their amount), which was shown to promote charge delocalization and therefore improve conductivity; the opposite trends were suggested for more acidic fillers.[401] Thus, proton transport and exchange process in hybrid PFSAs is modulated by the amount and types of interstitial water domains, the density of hybrid SiO_2-(HSO_3)-cross-links, and the segmental motions of the ionomer's fluorocarbon backbone.[133,401] Therefore, as expected, the changes in transport and mechanical properties are controlled by the amount[401] and the type of the filler.[401,436] For example, Nafion/$(ZrHf)_x$ has more efficient charge delocalization than Nafion/$(SiHf)_x$ due to their higher basicity, thanks to dynamic bridges, which persists at low RH giving hybrid membranes their advantages.[401]

In a more recent study, using DMA and broadband dynamic dielectric spectroscopy, it was shown that nanopowders of M_xO_y (M = Ti, Zr, Hf, Ta, and W) in a PFSA controls (a) the relaxations of both the hydrophobic and the hydrophilic domains and (b) the thermal stability range of conductivity (i.e., $5\ °C \le T \le 135\ °C$),[436] owing to the dynamic cross-links. In the presence of these dynamic cross-links, proton conduction at high temperature are favored in the hybrid membranes where the long-range charge migration occurs via proton hopping process at the interfaces of the solvated cross-links mediated by the hydroxyl groups.[401] Thus, nanofillers affect the macromolecular dynamics of a PFSA owing to the formation of dynamic cross-links ($R{-}SO_3H \cdots M_xO_y \cdots HSO_3{-}R$) in hydrophilic polar "cages", which modulate the mechanical, thermal and dynamical characteristics of the host ionomer.[401,436]

These studies overall suggest that the nanoscale correlations discussed in section 4.4 change dramatically altering the relationships between the diffusion of water vs protons. As an example, when other cations are introduced into a PFSA containing hygroscopic fillers, the high water-retention capacity increases cation's self-diffusion but reduces their selectivity.[887] Thus, the additional interfaces formed between the PFSA moieties and the inorganic fillers in the proximity of the hydrophilic domains could generate preferential transport pathways for protons, with possible blockage of other species.[401,402,436]

Among other fillers that show promise in altering the properties of PFSA ionomer are zeolites, a class of aluminosilicate framework structures in which the hygroscopic cavities could accommodate cations or water molecules, and heteropoly acids (HPAs), which themselves exhibit high proton conductivity, a property that is exploited in PFSA to increase its operating temperature.[30] The acidic nature of this type of materials creates intimate interactions within the PFSA, and permit achieving high conductivity with less dependence on the ionomer's hydration. Impregnating zeolites in Nafion has been shown to reduce permeability[673] and enhance selectivity with neglibile[676] or positive[673] change in conductivity. Nevertheless, conductivity improves in particular above 120 °C, due to the water present in zeolite cages and at the PFSA-zeolite interphase being more free and noninteracting, which also hinders methanol permeability leading to higher selectivity (up to 50% improvement).[673,674,888] The zeolite size was shown to play a critical role in altering selectivity, with smaller (nanosize) particles being more effective at blocking solvent permeability, thereby effectively increasing proton/methanol selectivity.[673,676,889]

HPAs have also been employed to create hybrid PFSAs, which were shown to improve conductivity[10,30,56,856,871,872] including up to 120 °C.[10,56,872] Herring and co-workers[10] showed that the addition of HPA in PFSA enhances formation of hydrogen-bonding between the HPA particles and promotes Grotthuss-hopping mechanism therein, resulting in higher conductivities, both in the dry and wet state. However, this comes at the expense of lower water self-diffusion, revealing a mismatch between the measured conductivity and those calculated from diffusion (i.e., Nernst−Einstein equation). In addition, doping HPA into a PFSA could improve stability as well, as it was shown to reduce the FRR in a PEFC.[856] These molecular sieves and electrochemically active additives are intriguing avenues for future research with many possibilities.[30,854]

Overall, inorganic fillers can provide stable ionomer functionalities at higher temperatures and lower humidities, yet research into their incorporation into newer PFSAs is still relatively recent and understudied. As with the most other methods, developing an ionomer composite with various techniques relies on developing a delicate formula that accounts for the concentrations, filler/matrix fraction, PFSA chemistry (EW, side-chain) and sufficient impregnation and encapsulation (to ensure additional improvements on stability and/or performance (e.g., conductivity)).[691,713,858] A concern though is also long-term durability and stability of the additives themselves in that they may leach out depending on application environments. Lastly, we note that, even though these strategies for composite membranes are mainly driven by developing better membranes for PEFCs, some of the Nafion-Si composites have found use in actuators,[890,891] which do not share the same functionality requirements as PEFCs.

Table 15. Summary of Trends for Properties of PFSA Membranes Exchanged with Various Cations, Compiled from Various Sources in the Literature[a]

property/mechanism	correlations and order of impact	refs	notes
water transference no.	$H^+ < K^+ \sim < Rb^+ \sim < Cs^+ < Na^+ < Ca^{2+} \sim < Sr^{2+} < Mg^{2+} < Cu^{2+} < Li^+$	44,269,828	
water uptake	$H^+ \sim > Li^+ > Mg^{2+} > Ca^{2+} > Sr^{2+} \sim > Na^+ > K^+ > Rb^+ > Cs^+$	33,185,245,269,329,343,518,538	preboiled membranes absorb more[33,93,106,109]
	$H^+ > Li^+ > Na^+ > K^+ > Cs^+$	211,245	
water self-diffusivity	$H^+ > Na^+ > K^+ > Li^+ \sim > Cs^+ \sim > Rb^+ \gg Mg^{2+} \sim Ca^{2+} \sim Ba^{2+} \sim Sr^{2+}$	44,269,299,510,516,517,531	cation size and interaction
	$Ag^+ > Na^+ > K^+ > Cs^+ \sim Zn^{2+} > Ca^{2+} > Sr^{2+} > Ba^{2+}$		
	H > Li > Ag > ~ Na > K > Rb > Cs[516]	903	
cation self-diffusivity	$Ag^+ > \sim Li^+ > Na^+ > K^+ > Cs^+$; $Zn^{2+} > Ca^{2+} > \sim Sr^{2+} > Ba^{2+}$	896,897,903	
mobility	$H^+ > Na^+ > \sim Li^+ > K^+ > Rb^+ > Ca^{2+} > Cs^+ > Sr^{2+} > Ba^{2+} > Fe^+$	538,828,898	
conductivity	$H^+ > Ag^+ > NH_4^+ > Na^+ > Li^+ > K^+ > Rb^+ >$ divalent cations $> \sim Cs^+ \gg$ trivalent cations $\gg$ tetrabutylammonium	44,308,343	
	$H^+ \gg Na^+ > Li^+ > K^+ > Cs^+ > Cu^{2+} > Zn^{2+} > Mn^{2+} > Fe^{3+}$	211	
selectivity	$Cs^+ > Rb^+ > Ba^{2+} > Sr^{2+} > K^+ > Ca^{2+} > Mg^{2+} > Na^+ > Li^+$	106,608	
sulfonate-cation interaction (cation-SO_3^- bond strength)	$Li^+ > Ca^{2+} > Na^+ > K^+ > H^+$	186,394	
	$Mg^{2+} > K^+ > H^+$	781	
decomposition temperature	$H^+ < Li^+ \sim < Cs^+ < Rb^+ < K^+ < Na^+$	394,847,850−852	
decomposition temperature	$Mg^{2+} < Ca^{2+} < Sr^{2+} < Ba^{2+}$	16,17	
fraction of freezable water	$H^+ > Li^+ \sim Na^+ > K^+ > Cs^+ > Rb^+$	186,269,306	due to cation-interaction energy
thermal transition temperature, T_α	$H^+ \ll Li^+ < Ca^{2+} < Na^+ \sim K^+ \sim Cs^+$	211,394	
	$H^+ \sim TBA^+ < TPA^+ < TEA^+ < TMA^+ \sim Na^+$	91,131	
permeability of gases	$K^+ < H^+ < Na^+ < Li^+ < \sim Ca^{2+}$	394	also affects solubility
tensile strength	$Li^+ > Na^+ > H^+ > K^+ > Ca^{2+} \sim Al > Mg$	689,710,711	controlled by the strength of ionic cross-links formed
Young's modulus	$Li^+ > Na^+ > K^+ > Cs^+ > Ni^{2+} \sim Mg^{2+} > Cu^{2+}$		
storage modulus	$Cs^+ > K^+ > Na^+ > Li^+ > H^+$	211	
activation energy for gas permeation	$H^+ > Li^+ > Ca^{2+} > \sim Na^+ > \sim K^+$	93,394,518	also increase with gas molecule size[394]
hydraulic permeability	$H^+ \gg Li^+ > Na^+ > K^+ > Cs^+$	93,518	
alcohol permeability	$Na^+ > K^+ > Ca^{2+} > Mg^{2+} > Fe^{2+} > Al^{3+} > \sim Ba^{2+} > \sim Cs^+ > \sim Fe^{3+}$	660	negligible effect of R−OH concentration
hydrophilic domain spacing	$H^+ > Cs^+ > Li^+ > Na^+ \sim Rb^+ > K^+$	33	from SAXS (in water)
hydrophilic domain diameter	$H^+ > Li^+ > Na^+ > Cs^+ > Rb^+ > K^+$		calculated
solvation/hydration energy,[b] $-\Delta G_{hyd}$	$H^+ > Cu^+ > Li^+ > Na^+ > K^+ > Rb^+ > Cs^+$	907	based on calculated values[c]
	$Ni^{2+} > Mg^{2+} \sim Cu^{2+} > Co^{2+} \sim Zn^{2+} > Fe^{2+} >$		
	$V^{2+} > Mn^{2+} > Ca^{2+} > Sr^{2+} > Ba^{2+}$		
	$Al^{3+} > V^{3+} \sim Fe^{3+} > Yb^{3+} > Tl^{3+} > Eu^{3+} >$		
	$Ce^{3+} > La^{3+}$		

[a] In cases where the variations in cations and their properties differ, more than multiple trends are included. [b] Listed as a reference for cations commonly used with PFSAs. [c] Experimental values could exhibit slight deviations from the theoretical values.

7.3. Different Ionic Forms and Interactions

Even though PFSAs are most commonly studied in H^+ form (constituting over 90% of publications), the effects of other cations and electrolytes on their properties, such as permselectivity and water transference, have been of interest over the last several decades. Exploration of such effects stems, in part, from studying their performance in specific applications (e.g., solar-fuel generators,[162,892,893] chlor-alkali industry,[1,181,182] aqueous and nonaqueous redox-flow batteries (RFB),[100,105,158,159,894,895] etc.), as well as utilizing the properties they impart for PFSA processing. In many of these applications, alkali, alkaline-earth, and transition-metal ions exist and typically in mixtures, making understanding their impact on PFSA properties very complex due to the coupled nature of the ions and counterions.[100,159,894,895] Overall, PFSA materials are typically relatively nonselective in terms of ion transport and water uptake, which hinders their applicability for such applications as batteries,[159] although as discussed in this review, annealing, processing, and material modifications (see section 7.2) can change that behavior.[100,894] An in-depth review of the various effects of electrolytes and ionic forms for various device-platforms is beyond the scope of this review. However, in this section, we detail some of the changes induced by fully exchanged cationic forms as well as some of the general issues with submersion in electrolytes. Both of these types of studies can help to delineate the nature of the underlying electrostatic interactions and transport processes in PFSA ionomers. It should be noted that, when cations are present in trace amounts, they are treated as foreign cations and investigated within the context of contamination effects (see section 7.1.2).

Before proceeding, it is worth mentioned that the ion-exchange rates must be accounted for when self-diffusion for water and ions are determined from NMR. For example, cation-exchange kinetics from radiotracer measurements indicated diffusion coefficient for reverse exchange (e.g., H^+ replacing another counterion, $M^{n+}_{mem} \leftrightarrow M^{+}_{aq}$) is 10 times slower than that forward forward exchange (of a cation, M^{z+}, with existing counterion, $M^{+}_{mem} \leftrightarrow M^{n+}_{aq}$), which is close to ionic self-diffusion.[896] Self-diffusivity in reverse process is retarded with the cation's slow replacement of the existing counterion due to cation's inability to overcome the strong electrostatic interactions. Thus, ion-exchange kinetics of counterions are dependent on their self-diffusion, which increases with a decrease in their selectivity in the membrane.[896] While Na^+ has higher affinity over H^+, Li^+ has no preference over H^+, which is the only cation that has a higher self-diffusion in forward exchange than in reverse exchange, owing to its weak interaction with the ionic site retarding the displacement of the interchanging ion.[896,897]

7.3.1. Different Cationic Forms.

The literature is rich with studies on PFSA ionomers ion-exchanged with cations (other than protons) (see Table 15). Historically, these studies are related to (i) transport of alkali ions in PFSA (Li^+, K^+, and Na^+), (ii) alkaline-earth metals (Mg^{2+}, Ca^{2+}, Sr^{2+}, and Ba^{2+}), with more of a focus on their impact on thermal stability, and (iii) transition metals (Fe^{3+}, Mn^{2+}, Ni^{2+}, Cu^{2+}, and Zn^{2+}), including their binary compositions in the membrane.[269,538,898,899] Reversible ion-exchange up to 95 to 100% has been shown to occur through immersion of the ionomer into a saturated solution at ambient conditions, with divalent and trivalent cations having a higher exchange level with respect to initial form (99%) vs monovalent ones (~94%),[900] resulting from their stronger interactions as discussed above. There exists a fair amount of studies focusing on the impact of cations on a PFSA membrane's water uptake and structure-sorption relationship,[33,36,106,109,131,145,185,211,245,247,298,299,329,901] thermal decomposition and stability,[229,231,394,396,397,847,850−852] gas permeability,[301,303,394,641] density,[33,538,833] mechanical properties,[131,211,394,689,710,851] thermal transitions,[34,131,135,145,186,211,229,298,301,306,385,394,396,397,852] conductivity, transference numbers, and mobility,[186,211,269,538,646,89,829,305,38,612,832,833,902] ionic self-diffusion,[39,515,903] free volume,[301] water permeability,[269,306,328,518,660] freezable water,[34,186,269,306,308] water uptake in liquid,[33,39,44,93,106,185,210,245,269,299,329,330,343,409,510,515−517,531,538,721,901] and vapor,[210,211,245,247] water diffusivity,[39,180,247,269,298,299,330,416,510,516,517,538,832,901] ion selectivity,[106,306,329,666,903] activation energy,[39,186,282,299,328,394,510] nanostructure,[33,109,142,211,298] as well as molecular-level interactions (e.g., spectroscopy[39,75,373,374,392,396,397]) and modeling.[904,905] Overlaying these issues are those of ionomer chemistry and EW,[33,34,39,180,186,245,329,852,906] pretreatment effects,[93,109,145,900] and other solvents.[142,245,328,343,346,660] Thus, changing cationic form can alter many of the properties discussed throughout this review, although many trends and underlying phenomena (e.g., chemical-mechanical energy balance) hold, albeit with different values (also see Table 15). Overall, there are two interactions controlling the fate of cations in a PFSA; cation (mobile charge) − PFSA (fixed anionic site) electrostatic interaction, and hydration (solvation) energy between cation and solvent. The competition between these two interaction energies have been shown to be the key factor in determining the ionomer behavior.[416,538,583,608]

Multiple cations have been investigated in search for correlating transport properties (e.g., conductivity and diffusivity) with ion size (i.e., radius) and type.[186,211,301,343,531,538,666] PFSAs, although possessing a phase-separated nanostructure, appear to have a more complex morphology since the intermediate region between the backbone and hydrated ionic domains that is occupied by side-chains can be altered in the presence of different cations, which could impact polymer-chain motion[392] (see Figures 54 and 55). Thus, understanding this morphology-interaction interplay (see section 4.4) is critical.

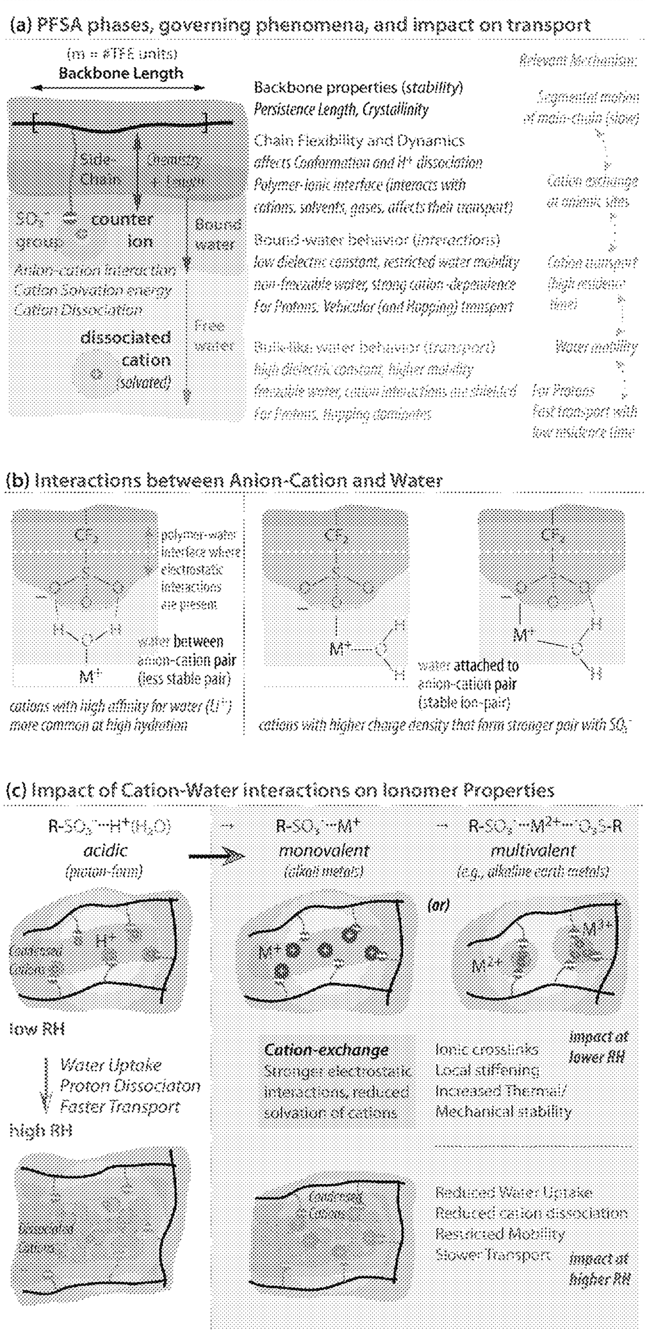
(a) PFSA phases, governing phenomena, and impact on transport
(m = #TFE units)
Backbone Length
Side-Chain
Chemistry + Length
SO_3^- group
counter ion
Bound water
Anion-cation interaction
Cation Solvation energy
Cation Dissociation
dissociated cation (solvated)
Free water
Backbone properties (stability)
Persistence Length, Crystallinity
Chain Flexibility and Dynamics
affects Conformation and H+ dissociation
Polymer-ionic interface (interacts with cations, solvents, gases, affects their transport)
Bound-water behavior (interactions)
low dielectric constant, restricted water mobility
non-freezable water, strong cation-dependence
For Protons: Vehicular (and Hopping) transport
Bulk-like water behavior (transport)
high dielectric constant, higher mobility
freezable water, cation interactions are shielded
For Protons, Hopping dominates
Relevant Mechanism:
Segmental motion of main-chain (slow)
Cation exchange at anionic sites
Cation transport (high residence time)
Water mobility
For Protons Fast transport with low residence time
(b) Interactions between Anion-Cation and Water
CF_2
polymer-water interface where electrostatic interactions are present
water between anion-cation pair (less stable pair)
M^+
cations with high affinity for water (Li^+) more common at high hydration
water attached to anion-cation pair (stable ion-pair)
cations with higher charge density that form stronger pair with SO_3^-
(c) Impact of Cation-Water interactions on Ionomer Properties
$R\text{-}SO_3^-\cdots H^+(H_2O)$
acidic
(proton-form)
$R\text{-}SO_3^-\cdots M^+$
monovalent
(alkali metals)
$R\text{-}SO_3^-\cdots M^{2+}\cdots O_3S\text{-}R$
multivalent
(e.g., alkaline earth metals)
(or)
H^+
M^+
M^{2+}
M^{3+}
Condensed Cations
low RH
Water Uptake
Proton Dissociaton
Faster Transport
high RH
Dissociated Cations
Cation-exchange
Stronger electrostatic interactions, reduced solvation of cations
Ionic crosslinks
Local stiffening
Increased Thermal/ Mechanical stability
impact at lower RH
Reduced Water Uptake
Reduced cation dissociation
Restricted Mobility
Slower Transport
impact at higher RH

Figure 54. (a) Role of cations along with other structural features in controlling various aspects of PFSA behavior. (b) Various configurations for cation−anion pairs that may exist in a PFSA (at lower hydration states).[373] (c) Below is an illustration of ionic cross-links that could form around sulfonate sites and thereby changing local interactions in the presence of monovalent and multivalent cations.

Alkali-metal cations have a higher affinity over H^+ in PFSAs (with a notable exception of Li^+) arising from their stronger interactions with sulfonate groups. And the higher the affinity of the cation or the stronger its interaction, i.e., the strength of the ionic cross-links, the more impactful the decrease in mobility and overall transport (see Figure 54). For this reason, alkali-metal cations tend to reduce the membrane's swelling

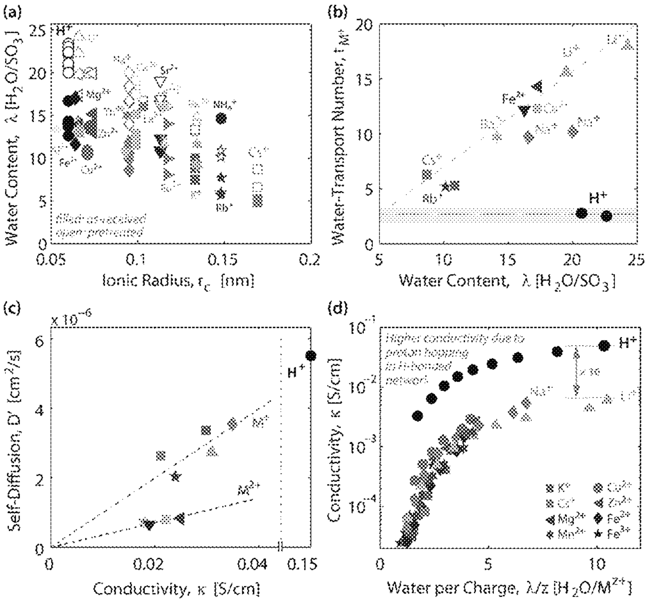

Figure 55. Impact of cations on Nafion: (a) liquid-water uptake vs cation radius,[33,39,44,93,106,269,299,329,330,343,409,510,515−517,531,538,721,901] (b) water-transport number as a function of λ,[44,269,538,612] (c) self-diffusion of water[269,416] vs conductivity,[343,510,612] (in liquid water), and (d) conductivity during humidification in vapor plotted as a function of water content per charge (λ/z).[211]

(Figure 55 and refs therein) and increase its density.[33,538,833,898] As the cation ionic radius increases, its charge density and hydration shell also decreases. While smaller ions with higher charge density could easily be localized in the hydrophilic ionic domains, larger ions (usually multivalent) could more easily interact with the side-chains in the intermediate regions. In fact, divalent and multivalent cations could form stronger ionic cross-links between the SO_3^- sites, and the side-chains, thereby inducing changes in backbone conformation and related thermomechanical properties (Figure 54 and 55a). Hence, the nature of the cation could affect the morphology and even degree of phase-separation, thereby controlling the transport properties of the ions and water.

Overriding the electrostatic effects, although coupled to them, is the impact of water. Not only is the water uptake affected by cation identity but the cation/anion interactions can likewise be impacted by water content due to the separation of ionic charges, i.e., shielding effect, also promoting the dissociation of cations (Figure 55c). This was demonstrated in a recent work, where RH-dependent conductivities of cation-exchanged Nafion exhibit a universal dependence on φ_w, only at RHs exceeding 75%, which marks the dominance of shielding effect of water screening the electrostatic interactions that are dominant at lower RHs.[211] Therefore, transport phenomena depend on a combination of factors including cation size and charge, ionomer water content, and electrostatic interactions that depend on the cation, side-chain, and ionomer EW (SO_3 distribution and spacing). Overall, water uptake and hydration number decrease with increasing cation radius in water (see Figure 55d and refs therein) but also in other polar solvents.[245,247] In what follows below are the implication of such cation-exchange-driven changes in hydration and interactions on morphology, transport, and stability.

7.3.1.1. Morphology. Despite studies on Nafion with different solvents and counterions, investigations on its nanostructure in different acid and salt solutions are very limited.[33,36,109,211,298,306] SAXS profiles of Nafion were examined upon cation-exchange with Cs^+, Li^+, Na^+, and K^+.[33,36,298] Overall, these studies suggest a less apparent ionomer peak and reduced water *d*-spacing in other cation forms compared to that of H^+-form (e.g., d_w decreases from 4.74 nm for H^+ to ~3.5 nm for Rb^+ or Cs^+).[33,36] Gierke et al.[33] attributed this effect to the reduced hydrophilicity of domains in the presence of heavier and larger cations, which change the chemical-mechanical equilibrium in favor of aggregation, thereby resulting in smaller and more separated domains. This morphological change is in fact similar to that induced by increasing EW (in H^+ form), which enhances crystallinity and resistance to domain aggregation and hydration, thus collectively leading to smaller domains. A detailed SANS study by Rollet et al. showed that counterions in Nafion control the size and number of hydrophilic domains by modifying the area per polar head.[109] They observed a linear relationship between the radius of the hydrophilic domains and water volume fraction, φ_w, for monovalent and multivalent ions, with the latter resulting in an additional reduction in size because they are more effective at screening the electrostatic interactions.[109] Also, the hydration number and domain spacing were correlated with the number of water molecules per counterion (not per sulfonic-acid site) regardless of the type and charge number of the counterions.[109,211] Young et al. examined similar cations but also with solvent effects.[346] Recently, the decrease in hydrophilic domain spacing of PFSA exchanged with larger cations was found to scale with cation radius at low water contents, but with Lewis acid strength (LAS) at higher hydration levels.[211] Thus, both φ_w and cation (size and charge) control the hydrophilic domains, although these factors are intrinsically linked. Systematic investigations by Okada and co-workers identified the importance of a cation size in relation to the membrane's nanodomains on the uptake and transport of water molecules.[269,416] It was also suggested that the transport of cations should be related to the size of the transport-pathways (hydrophilic domains), as both are controlled by the cation and its interaction with the ionomer moieties altering the structure-transport correlations.[269]

7.3.1.2. Transport. Changes in transport properties depend on both the electrostatic interactions and water uptake; while the former is more dominant at lower hydration (RH), the properties scale with water volume fraction at higher hydration levels. For example, cations like Na^+ and Ca^{2+} interact with water within the first hydration shell, causing more free-water movement beyond the shell, whereas cations like Ni^{2+} and Cu^{2+} are more strongly bound causing more structured and bound water.[833] Thus, the mobility of transition-metal ions are low, following the order of $Fe^{3+} < Ni^{2+} < Cu^{2+}$, with Fe^{3+} being one of the most detrimental to transport of water and ions.[833,835]

Ionic conductivity has been shown also to correlate well with water permeability, which was investigated in the presence of cations[93,328,518,538,543,546,553] and alcohol[328,543,545−547,551,553,667] and alcohol−water mixtures.[328,346,660,662,666] For example, the activation energy of permeation of the methanol/water mixture was shown to follow: $Rb^+ > K^+ \gg Cs^+ \gg H^+ > Li^+ > Na^+$, without any trend on the ionic radius of the cation.[328] In terms of cation effects, water and methanol permeability in these mixture solutions is higher in the Li^+ and Na^+ forms than it is in the H^+ form, with Na^+ showing the highest water permeability.[550] On the contrary, water permeability in Nafion decreases with the size of the cation, $H^+ \gg Li^+ > Na^+ >$

K^+,[93,518,546] yet still scales with fraction of the solvent,[518] although it was shown to be thickness dependent; the permeability coefficient increases with the size of cation for thicker (>50 μm) membranes, while the opposite trend is observed for thinner membranes.[547]

Since water diffusivity, although independent of ion transport, is also related to the hydrophilic-domain network, the correlation between diffusivity and conductivity provides insight into the nature of the cation transport mechanism (see section 4). Water diffusion exhibits a better correlation with the volume fraction of water[269,510,531] than does the ionic conductivity. In such a D vs κ plot, divalent ions exhibit a slower slope than monovalent (alkali metal) cations, and H^+ is an outlier exhibiting much higher conductivity than expected from diffusivity trends, as discussed in Okada et al.[269,416] (Figure 55c) Also, when the size of conducting channel cross-section was considered, the conductivity for H^+ becomes remarkably high, implying faster migration of smaller ions as well as access to the hydrogen-bond network and associated Grotthuss transport mechanism (see section 4).[269] This was demonstrated in a recent study[211] where conductivities of cation-exchanged Nafion measured as a function of RH were found to exhibit a universal scaling with water molecules per charge, λ/z (instead of per SO_3^-) (Figure 55d). This master curve suggests a cation/water-uptake superposition, where changes in counterion (charger carrier) concentration and λ, driven by cation-solvation effects, govern the conductivity.[211] Compared to the master curve, the conductivity for H^+ exhibits a 10-fold increase due to hopping mechanism (Figure 55d). Also, the fact that both conductivity and d-spacing correlate with water per charge enforces the link between the morphology and transport, as previously discussed for H^+ in section 4.4.

In terms of water transport, however, one can use the transport number of water (defined as the electro-osmotic coefficient in a solely proton-exchange membrane, see section 4.3.1).[538,612,833] The transport number of water in H^+ is the lowest, approaching 1, and increases with increasing fraction of cations, reaching 5 for K^+ and Cs^+, 10 for Na^+, and 15 to 20 for Li^+.[44,269,538,612,833] The water transport number (per cation, M^+), t_{M+}, scales linearly with free(zable) water molecules, indicating that it is the bulk-like water that can pushed by the cations.[269,330] It increases also with cation hydrophilicity, in which case it increases with λ.[269] For hydrophobic cations, however, the transport number is determined by the volume (size) of the cation (more so than λ).[416] It goes up with molar volume or charge density and correlates with hydration enthalpy of cations, i.e., ions with large volume, hydration enthalpy, or charge density tend to transport more water molecules per ion in the absence of concentration gradients (Figure 55d and Table 15).[330,416] H^+ is the least-coupled ion to the water molecules, which manifests itself as a low water-transport number,[269] whereas cations with larger enthalpy (energy) of hydration tend to have lower permeability and also higher selectivity[106,306,330] (Figure 55). In fact, Xie and Okada demonstrated a linear relationship between t_{M+} and hydration enthalpy of the cation, signifying the direct contribution of the hydration to water transport.[330,416] Water transport coefficient has two contributions: Coulombically hydrated/bound water and water (hydro-dynamically) pumped by the ion during ion transport, which is proportional to the cation size due to the cation's volume exclusion effect in the transport channels/pathways of the membrane. Overall, studies on transport of H^+ compared to other cations,[21,44,269,416,606] have indicated cations with stronger interactions have reduced mobility (e.g., Li^+ and Na^+) and slower diffusion, and therefore have higher water transport number than H^+.[44,269,898] When water molecules are strongly associated with a cation, such as Li^+, their mobility and diffusion is restricted, resulting in lower conductivity, and higher transport numbers (>15 for Li^+ vs ~2.5 for H^+). This is also why the cations that interact strongly with the water also reduce the free water in the membrane, which can be evidenced by the lower fraction of freezable water.[186,269,306] As the cationic interactions increase, a higher number of water molecules become bound to the SO_3^- sites, which also exhibits a linear correlation with the increase in selectivity.[306]

The mobility and self-diffusion of cations are intimately related to many other transport properties. For example, selectivity scales with cation self-diffusion coefficient,[106,903] with slower cations such as Cs^+ having high selectivity, as opposed to more mobile Li^+, which has low selectivity. Therefore, another consequence of water/cation interaction is on the cation self-diffusion, which decreases more than 1 order of magnitude from monovalent to trivalent cations yet with almost no effect on the self-diffusion of water, which was attributed to the additional electrostatic friction in the diffusion of cations governed by their charge state.[517] Given the role of cation on water uptake, cation self-diffusion exhibits a good correlation with water volume fraction.[510,896,897,903,908] Hence, ionic mobility is governed by, and decreases with, affinity of cations to SO_3^- groups (electrostatics) and lower water content (domain network connectivity).[538]

Furthermore, gas permeability decreases when H^+ is exchanged with cations (such as Na^+ and K^+) that interact more strongly with the SO_3^- group due to local stiffening and changing free volume due to their larger size, thereby reducing the permeability.[301,303,641] Large cations push away the surrounding molecules thereby making the ionomer stiffer but also opening up additional free volume as inferred PALS[301] (also see section 4.5).

As a result of these interactions, some cations have unique effects on PFSA, such as lithium, which has weak electrostatic interactions with sulfonic-acid sites and favorable interactions with water owing to its large solvation shell.[44,186,538,896] For this reason, Li^+ could carry a lot of water molecules with itself giving rise to its high transport number (electro-osmotic coefficient) in PFSAs,[44,538] and low cationic selectivity.[106,608] This also suggests solvation being critical for electro-osmosis. Given its interesting behavior, the Li^+-form of Nafion has been examined in many studies in terms of its uptake/solubility in liquid water[44,93,328,538] and vapor,[211,245,247] swelling,[188] birefringence,[438] SAXS in various solvents and electrolytes,[142,146,211,406] gas permeability and solubility[394] permeability in water[44,93,328,550] and alcohol,[328,546,550] conductivity,[44,186] cationic self-diffusion,[44,896,897] water self-diffusion,[44,186,516] freezing water,[186] thermal stability,[211,394,851] transport in binary cationic mixtures,[538,608] and interactions (e.g., FTIR).[374] Overall, replacing H^+ with Li^+ deteriorates conductivity and water transport in PFSA, but improves stability, although with similar water uptake.

7.3.1.3. *Stability.* Besides transport properties, the cationic form has a substantial impact on the stability of the membranes, a key issue that is often utilized to allow for different thermal processing.

As discussed in section 5.2, by forming physical cross-links within the cation-sulfonate sites, larger cations reduce the

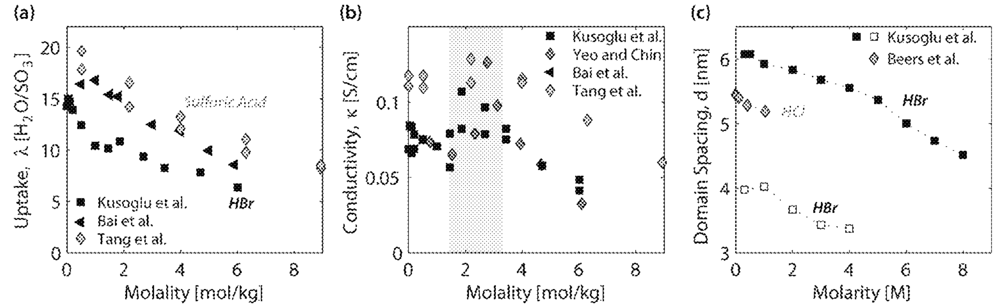

Figure 56. Nafion in electrolytes. (a) Water-uptake and (b) proton conductivity as a function of molality of the external electrolyte concentration, which are sulfuric acid (Tang et al.[895]) and hydrobromic acid (Kusoglu et al.,[407] Yeo and Chin,[913] and Bai et al.[215]). (c) Hydrophilic domain spacing of Nafion equilibrated with various concentration of HBr[407] and HCl[914] obtained from SAXS (open and closed squares are for as-received and preboiled membranes, respectively). (Membranes are N212,[215,407] N115[913] and N117.[215]) Shaded region in (b) highlights the concentration range in which conductivity goes through a maximum.

mobility thereby increasing the resistance to deformation (see Figure 54).[196,689,710,711] The elastic moduli of cation exchange membranes increase linearly with the increase of cation radius,[689,710,711] due to the fact that large cations interact with more sulfonate groups thereby further stabilizing the ionic cross-links and reducing the side-chain mobility, which also improves thermal stability at relatively low energies.[394] The fact that cationic radius is more dominant than the charge number/density is ascribed to limited surface area (between the sites/side-chains) controlling the physical cross-linking.[711]

In general, multivalent ions interact stronger with the ionomer resulting in multiple and stronger ionic cross-links (see Figure 54) that hinder the molecular mobility, shift the transition temperature (T_α) toward higher temperature, increase membrane modulus,[211,689,710,825] strength,[851] and fracture energy,[710] and reduce transport.[852] The cations impact PFSA thermo-mechanical relaxations by restricting the local mobility of ionic moieties, resulting in a shift in thermal-transition temperatures (see section 5.4)[131,135,623] and transport.[301] In fact, this shift in some cases manifest itself a switch from a relaxation response (chain motion) to a degradation response (side-chain).[825,852] In PFSA degradation mechanism, as discussed in section 7.1.4, backbone decomposition T (>500 °C) is less dependent on cations, whereas the onset of sulfonate-group decomposition is most sensitive to cations (see Figure 52) and changes with LAS.[397,825] From TGA and IR data of PFSAs with various cations, two modes of ion interaction effects were found regarding the LAS.[397,852] For LAS > 0.3 (mainly multivalent), the cations have weak polarizing effects on the SO_3^- sites, but strongly interact with the ether-oxide group thereby weakening the chemical C−O−C bond and triggering thermal degradation. Cations with LAS < 0.3, however, interact with both the SO_3^- sites and the ether-oxide groups and tend to stiffen the structure and improve thermal stability.[852] EW and side-chain length was also found to be dominant in the latter regime.[852] Interestingly, for LAS > 0.5, stronger interaction of cations hinders the mobility so much that the T_g shifted toward a temperature beyond the degradation one, meaning that degradation overcomes plasticization.[394,825]

Overall, some properties appear to be strongly related to cation size and radius, where size exclusion effects persist, while some other properties exhibit better correlation with Lewis Acid Strength (LAS) that accounts for both charge density and cationic interactions. In addition, the former effects could be screened in the presence of a large amount of water molecules shielding those interactions[44,135,186,211,373,538,901] but also give rise to secondary effects such as the water/cation interactions influence on transport properties. For example, at low λ, if LAS values of sulfonate anion and cation are dissimilar, water preferentially moves in between and separates them, otherwise it attaches to the cation (Figure 54b).[373] Thus, water insertion between an SO_3^- anion and a cation is minimized when the LAS of the cation is similar to the base strength of the SO_3^- (ca. 0.26), and maximized as it deviates from this value (for example for Li^+ with lower LAS, and for Ni^{2+}, Co^{2+} with higher LAS).[373] However, at high λ, such effects are not discernible due to shielding by water, which was evidenced by the insensitivity of the SO_3^-, $\overline{\nu}_{SO_3^-}$, symmetric stretching vibration in FTIR.[373,374] The λ at which the frequency shifts begin depends on the hydration of the SO_3^- and counterion.[374] Shifts in $\overline{\nu}_{SO_3^-}$ becomes weaker with larger counterions, and is also enhanced by their hydrophilicity due to the induced polarization by the cation electrostatic field, while this polarization diminished upon exchanging with hydrophobic counterions.[41] Thus, LAS is a good indicator of the affinity of cation−anion pair and their resistance to disruption by water,[373,374] which not only impact transport but also thermomechanical[397,825,852] nanostructural[211] properties (Figure 54). In fact, there appears to be a transport/stability trade-off in PFSA ionomers such that a cation that improves thermomechanical stability (via stronger interactions and ionic cross-links) tends to cause detrimental effects on transport, and, in particular, conductivity.[211] Thus, PFSAs exchanged with various cations not only provide a playfield for exploring ionomer interactions but also for modifying material functionality (e.g., doping, see section 7.2).

7.3.2. Interfacial and Electrolyte Effects: Anions.

As noted, many applications involve the use of PFSA membranes in electrolyte solutions that contain multiple cations and anions, notably the renewed interest in redox flow batteries.[158,159,894] In this section, we focus on the impact of different acid solutions on the membrane properties and the next section focuses on multiple cations. Although the impact of individual cations was discussed above, the interaction of salts and even anions warrants a mention, although an in-depth discussion is beyond the scope of this review. Before proceeding, it should be mentioned that one needs to consider how to handle the interface between the PFSA and an electrolyte solution. For ionomer membranes, a discontinuity in the potential (called the Donnan potential) results due to the charged groups on the polymer.[909,910] In this case, care should be taken when defining the potential to be used along with the reference states for electrochemical potentials, if the quasi-electrostatic potential is selected, the boundary relation becomes

$$(RT \ln m_i\Gamma_i + z_iF\Phi)|_{\mathrm{el}} = (RT \ln m_i\Gamma_i + z_iF\Phi)|_{\mathrm{membrane}} \tag{66}$$

where z_i, m_i, and Γ_i are the charge number, molality, and activity coefficient of species *i*, respectively. If electroneutrality does not hold because the electrolyte is dilute, and thus the Debye length is large, one can solve the Poisson–Boltzmann equation to determine the Donnan potential.[911]

Thus, the charged, tethered constituents within PFSAs can impact the local electrostatics at the interface as well as internally, where condensation of the protons could occur. Such effects, known as Manning condensation, will occur especially as the ion concentration within the membrane increases, which can happen in different acid solutions if the anions also enter the internal hydrophilic domains. These effects can help to explain the fact that anions are known to transport through the membrane. Inorganic acids in contact with the PFSA can also greatly impact their properties. For example, the conductivity and properties of PFSA membranes in hydrobromic,[215,407,912,913] hydrochloric,[605,914] phosphoric,[605] and sulfuric acids[605,668,895] was measured as summarized in Figure 56. In the solutions, the proton conductivity increases with acid content at low acid concentrations, despite a decrease in water content, due to ionization of H_2SO_4 that provides additional protons that enhance conductivity. Although even in dilute concentrations the membrane loses water, the proton concentration increase in acid electrolytes could compensate for this loss by acid dissociation.[407,895] At higher concentrations, however, the decrease in water content dominates such that net effect is a loss in conductivity (i.e., free ionic-charge carriers). This results in a peak in the conductivity around 2 to 3M of external concentration, which can be correlated to morphological changes inferred from *d*-spacing.[407] From the data, one can estimate Donnan concentration and try and determine the amount of free protons in the membrane or those available for conduction. Finally, it should be noted that understanding and mitigating the decrease in conductivity with higher acid concentrations is critical for the development of redox flow batteries, seeing as the performance is typically ohmically limited.[158,915] For example, in the HBr system, optimizing the system efficiency revolves around minimizing the concentration of HBr at the membrane interface.[916]

7.3.3. Interfacial and Electrolyte Effects: Multiple Cations.

Another important aspect of transport phenomenon is the coexistence of multiple cations in the PFSAs when they function as an ion-exchange-membrane separator (e.g., in redox flow batteries, reverse osmosis, dialysis, etc.). Such devices require enhanced transport of the desired cations while restricting transport of undesired ones. As with many other competing functionalities discussed in this review, this also presents a trade-off between conductivity and crossover, in that system efficiency is limited by the former at high current density and by the latter at low current density.[105] For example, when the water mobility increases in water-purification membranes, salt rejection decreases while the water flux increases, making water behavior in hydrated nanostructure an important aspect of ion-exchange process.[27] Thus, it was suggested that measuring water motion and probing water–polymer interactions at the necessary length and time scales provides critical information for assessing the factors controlling the performance of these materials and for developing new polymer compositions for clean-water applications.[18]

Although the impact of cationic form was discussed above, the interaction of different cations warrants a mention, although an in-depth discussion is beyond the scope of this review. As stated above, multiple cations can penetrate and change the properties of the PFSA and result in more complicated physics that requires separate ionic-species transport equations and mass balances either in dilute- (e.g., Nernst–Planck) or concentrated-solution theory,[610,836] while one still needs to consider the Donnan potential as well ($\Delta\Phi_{\mathrm{el}} - \Delta\Phi_{\mathrm{membrane}}$ in eq 66).

The mobility of cations change when they coexist with other cations, and their transport behavior is governed the nature of the cationic interactions in the mixture and electrolyte solution.[106,538,583,608,666,833,899,901] Overall, replacing H^+ with cations of higher valence due to their higher affinity to the SO_3^- sites makes the remaining protons less mobile as discussed above.[538,833,835,898] In binary cation mixtures, the specific conductivity decreases almost linearly with a decrease in H^+ fraction.[269,612,832] While multivalent cations tend to have higher charge density and form stronger ionic cross-links despite their lower concentration (per electroneutrality), for monovalent cations, it is the size that appears to be a dominant factor. It has been suggested that the increase in entropy when water is released during exchange of H^+ for a metal ion is the controlling factor in determining the magnitude of selectivity coefficients,[106] whereas Pintauro et al. attributed it to electrostatic interactions ($SO_3^-\cdot\mathrm{cation}^+$) along with the repulsive energy due to the hydration effects.[583,608]

Selectivity and mobility of ions in mixtures are interrelated, and their transport is governed by a multitude of factors such as size (exclusion) effects, valence (charge exclusion) effects, the solvation (shell) of the cation, along with the nature of the nanomorphology within which they reside and move. Thus, cation selectivity can be defined similar to eq 56 as a ratio of ion mobilities, $S_{i/\mathrm{H}^+} = u_i/u_{\mathrm{H}^+}$, which in essence relates the transport of one species over that of the proton. In addition, one can define a separate ion affinity or partition coefficient,

$$K_{i/\mathrm{H}^+} = \frac{c_i}{c_{\mathrm{H}^+}} \tag{67}$$

where due to the ionic charge it has been defined with respect to protons instead of the normal external solution.

Steck and Yeager[106,329] measured the selectivity of cations in mixed-cation forms and found that selectivity increases with the size (radius) of the cation, because cations with smaller hydration energies gain more energy from their electrostatic interactions with the exchange site. The partition coefficient was shown to be governed by the difference in free energies of hydration between the cation and proton, $\Delta H_{i/\mathrm{H}^+}$,[329] which was demonstrated by the fact that log of K_{i/H^+} scales with $\Delta H_{i/\mathrm{H}^+}$, indicating an entropy-controlled process during which entropy is released when a proton is replaced by a metal ion.[106] Pivovar et al. showed that when a PFSA is placed into an external acid concentration, the partition coefficient of the acid increases, leading to higher anion transference numbers, consistent with Donnan exclusion.[605] In such concentrated solutions, size exclusion could be more important than the charge exclusion.[406,894]

Moreover, cation-selectivity is reduced upon hydration. Thus, overall selectivity decreases with higher cation self-diffusion,[903] smaller cations, higher hydration, and larger hydrophilic domains,[106,306,329] all of which contribute to the larger spread in selectivity values in PFSAs. The highest selectivity is for Cs$^+$,[106,329] owing to its large radius and low charge density and strong interaction with SO_3^-.[538] For this reason, Cs$^+$ has very low mobility, diffusion[516,518] and conductivity,[899] permeability,[328,518,547] and swelling,[106,247,329,515,516,546] and is likely to be transferred through the interfacial regions (side-chain) instead of the (weakly hydrated) ionic domains,[508] as suggested by Yeager and Steck.[899] (see Figure 54). Similarly, some solvents such as alcohols (as discussed in section 4.6) or olefins[917] preferentially interact with the fluoroether-rich ionomer side-chain-SO_3^- interface which controls their transport. Thus, cross-linking and fillers are also expected to control selectivity by changing the nature interface surrounding the ionic sites (see section 7.2). Tandon and Pintauro[608] showed that selectivity for monovalent cations scale with cation size as Cs$^+$ > K$^+$ > Li$^+$, but in binary mixtures, it is governed by a multitude of factors, including composition and solvents.[666] The concentrations of divalent cations in these mixtures are low compared to the monovalent cations due to electroneutrality.[608]

A series of papers by Okada, Xie, and co-workers[269,538,612,832,833] studied Nafion with varying binary compositions of counterions, to elucidate the underlying mechanism of transport, including conductivity, self-diffusion coefficient, and transference number (the amount of charge carried by an ion in the absence of concentrations gradients). It was shown that these interactions follow the rule-of-mixture of weakly and strongly interacting species in Nafion-composition.[385] The transference number of a cation in a membrane is a measure of the fraction of ionic current, *i*, carried by that cation, which for a binary mixture is given by

$$t_{\mathrm{H}^+} = \frac{x_{HM} u_{\mathrm{H}^+}}{x_{HM} u_{\mathrm{H}^+} + x_{AM_n} u_{\mathrm{A}^{n+}}} \tag{68}$$

where x_i is the mole fraction of species *i*. The proton transference number decreases in the presence of foreign cations due to the above-mentioned affinity and water-content effects.[833] Measured t_i^m values for Nafion exhibit a strong dependence on the external electrolyte concentration as shown for H$^+$, Na$^+$, and Li$^+$.[181,538,546,612,898,902,908]

In mixed cationic systems of binary compositions, interference between the cations is lessened/screened in the presence of more water molecules. For example, in mixed cationic compositions of Na$^+$/H$^+$, Na$^+$/Cs$^+$, and Cs$^+$/Ba^{2+}, the conductivity-composition relationship is linear, meaning no mutual interaction among the cations that move independent of each other, whereas it is nonlinear for Na$^+$/Ba^{2+}, Li$^+$/K$^+$, and Ca^{2+}/H$^+$, indicating interactions between the cations and water interference.[269,898,899] When less hydrophilic cations (Cs$^+$ and Rb$^+$) are mixed with more hydrophilic cations like Li$^+$, the repulsive interactions between cations are screened and mitigated due to large hydration shell of Li$^+$, which makes it more likely for these cations to mix.[898] Also, while mobility of Li$^+$ is less affected by the presence of other cations (Na$^+$, K$^+$, and Rb$^+$), the mobility of these cations are more affected by Li$^+$.[898]

For practical applications, the changes in water and ion transport properties in various solutions can result in nonintuitive trade-offs between migration and electro-osmosis and thus device performance, as has been shown in all-vanadium[894] and HBr[105] flow batteries. For example, when vanadium is present in membrane (V$^{3+,4+,5+}$), it has a retarding effect on proton transport regardless of the valence state of V.[895] It was suggested that vanadium may disrupt acid and water clustering by replacing acid sites and forming hydration shells with water.[918] Even with the renewed and previous interest in flow batteries, gaps remain in understanding and measuring changes of PFSA with different electrolytes.

8. CONCLUDING REMARKS AND FUTURE DIRECTIONS

This review presents a comprehensive summary of PFSAs, both Nafion and alternate PFSA chemistries, as well as recent progress on composite and stabilized PFSAs. Thanks to an increasing number of modeling and experimental studies with these relatively newer ionomers, there is a need to understand how they differ from traditional Nafion, as discussed throughout this review. Although this review provides several insights into the behavior of PFSAs and uncovers many of their foundational aspects, there are still unanswered questions and areas where further research is required, which are discussed below.

PFSAs have a long and rich history in research, which has not only resulted in significant advances in stable and robust ionomers for many next-generation technologies, including most notably PEM fuel cells, but also provided significant scientific challenges and partially contributed to the development and demonstration of many new modeling and diagnostic techniques, from in situ and operando characterization to imaging with high spatial and temporal resolutions. In PFSA research and applications, technological advances and scientific progress have evolved together, providing a unique cross-disciplinary research field that touches upon electrochemistry, transport phenomena, polymer physics and chemistry, mechanics, and structure/property characterization and multiscale modeling. In an effort to reflect the perspective from such multiple disciplines, a significant effort has been made to collect and analyze the published data, and, more importantly, to develop new correlations from seemingly disparate data sets including property expressions and structural relationships. Such analysis provides new insights into PFSAs. This article reviews some aspects of PFSAs in-depth for the first time including thin films, interfaces, sorption and modeling, various aspects of transport and mechanically related phenomena, along with the aforementioned new correlations based on compiled literature data.

By compiling and combining hundreds of data set from the literature, new structure/property relationships have been presented, from which a fresh understanding of the many topics have emerged. Such findings include the effect of pretreatment, processing, chemistry, cation and electrolytes, and degradation (chemical, mechanical, aging, and contamination). In plotting various data together, clear trends appear in some cases such as crystallinity vs TFE, *d*-spacing vs hydration, and discrepancies in other like the water diffusivity from various techniques showing vastly different values, but which can be rationalized upon accounting for membrane history and understanding what the different experiments are actually measuring (e.g., transport and sorption versus just diffusion). In addition, in conducting measurements, it is vital to recognize the quasi-equilibrium nature of PFSAs, which exhibits multiple relaxation mechanisms across a spectrum of time and length scales. Studies should clearly report thermal history, the processing and pretreatment effects, and equilibrium time (even in steady-state experiments). For modified membranes,

DOI: 10.1021/acs.chemrev.6b00159
Chem. Rev. 2017, 117, 987−1104

baseline comparisons must be included, any processing effect that is integral part of the composite manufacturing should be applied to the bare membrane itself, if possible. Efforts should be made to make thickness, thermal history, processing, measurement conditions, and equilibrium times all identical so as to ensure fair comparisons and move the knowledge base forward among the different studies.

It is clear that there is an underlying structure/function relationship that governs the morphology, transport, and stability of PFSAs. These aspects are rooted in the balance between chemical and mechanical energies that form distinct morphologies and resultant water sorption, which together govern the various transport phenomena, whether it is proton hopping, gas dissolution, water diffusion, etc. The various phenomena are highly coupled, making their measurement and analysis in exclusion hard to accomplish satisfactorily, which is made even more challenging due to the dynamic and indistinct nature of the PFSA phase separation. This phase separation is a result of the chemical/mechanical energy balance where the hydrophobic backbone phase segregates from the hydrophilic sulfonic-acid sites, especially when hydrated. At full hydration, this forms a locally flat nanodomain system that is connected at the mesoscale in a network, which results in the macroscopically observable properties. There is a need to move beyond the cluster-network type pictures of PFSA morphology, which may be valid at low hydration, but are inconsistent with data at higher hydration. Although a PFSA membrane is a phase-separated ionomer, treating it as a two-phase material simplifies its true characteristics and cannot capture the transition phases (interfacial region) that impact its properties. For example, one such issue is the hydrophobic/hydrophilic regions of the side-chain, which interacts with various solvents and cations, and therefore affects the interactions among the ions/solvents within the more hydrophilic domains. There is also consensus on the important role of a dynamic hydrophobic surface layer that is responsive to environment and exhibits drastic changes in favor of transport from vapor- to liquid-equilibrium. As for the differences between the vapor/liquid equilibrium, i.e., Schröder's paradox, or underlying origins of it, the role of interfacial phenomena has been acknowledged, yet how it is modeled is still not suitable, in part, due to challenges associated with the interpretation of experimental observations in a robust theoretical frame. The interface is a crucial property of a PFSA membrane in that it accompanies any change in its structure/property relationship.

A PFSA's remarkable transport properties could primarily be associated with nanoscale phenomena, such as the formation of highly mobile bulk-like water in domains facilitating ion transport. However, many factors controlling the macroscopic transport manifest themselves at higher length scales, e.g., in the nanodomain connectivity. It is this hierarchical morphology that bridges nano- and macroscales, which governs the changes in properties in response to heat-treatments, processing, reinforcements along with macroscopic dimensional changes and swelling anisotropy, although with implications on nanoscale behavior. Thus, there is need to move from domain-level to network-level behavior, or bridge them, whether it is for experimental characterization or modeling. The field has witnessed more examples of such activities that aim to link various length and time scales. While recent molecular simulations tend to model larger scales and more atoms, there is room for improvement to understand macromolecular phenomena especially across the length scale. This is a promising avenue, and in particular with phase-field and coarse-grained techniques (e.g., DPD), although care must be exercised to remain physically consistent across the scales. This is a significant challenge and opportunity to incorporate water uptake and multicomponent transport simulations together such that chemical and mechanical energies are evaluated consistently and simultaneously in the dynamic framework of these materials. This is especially true in that most continuum models on PFSA's swelling and transport behavior still incorporate phenomenological approaches either to idealize the nanostructure or to account for some of the experimental observations (e.g., transport properties). Even so, most models are in fact for Nafion (or even 1100 EW one), and their applicability for, or extension to, other PFSAs is yet to be demonstrated. There is also a need to develop more predictive, holistic models for PFSAs.

As noted throughout, the molar ratio of water to sulfonic-acid sites, λ, is often used to characterize water content, although one could also use the water volume fraction ($\varphi_{w)}$). While the former has proven to be a useful parameter that probes the local behavior of water, the latter is a better representation of the network-level properties. However, the difference between the two appears only when the side-chain and EW changes, due to changing molar volumes, and in fact, changes in the correlation of various structural and transport properties with λ or φ_w reveals insight into the network and mesoscale properties, which has been shown to be valuable in recent studies on these new PFSAs. It must be noted that, despite early studies on non-Nafion chemistries around the 1990s, there is a significant renewed interest in alternative side-chain chemistries in the past decade, driven by different applications or usage (e.g., thin-films). Even though altering the side-chain chemistry brings additional complexities to PFSAs, studying such phenomena also helps to understand the role of side-chain in PFSA's structure/function relationship. Notwithstanding these developments, a generalized picture of the morphology of PFSAs (not just Nafion) accounting for EW and side-chain effects is yet to be developed.

Furthermore, more focus is required on understanding not just beginning of life performance and properties of PFSAs but also the related degradation and durability issues. Thus, additional studies are needed to understand how in-operando stressors such as electrochemical potential impact morphology as well as direct measurements of critical transport properties across scales and how they change with related stressors. Much of the durability depends on the synergistic (electro)chemical-mechanical interactions mentioned above. Detailed knowledge of these interactions would have significant impact on technologies that exploit electrochemical-mechanical phenomena, from shape-memory applications, electro-active polymers, and bioinspired ionomer-based materials, to soft-active materials based on hydrogels exhibiting strong swelling-deformation coupling, as well as defect-detection in advanced roll-to-roll manufacturing of membrane-electrode assemblies.

To solve the durability issues and move PFSAs into more technologies, they are increasingly being found as composites and hybrid ionomers, which not only demonstrate increased lifetime and performance in electrochemical devices, but also provide an opportunity for fundamental research. In fact, most studies seem to fall into either category, i.e., device-level demonstration of a new hybrid PFSA or structure/property characterization of it. An active area of research is elucidating the new interfaces formed within the hybrid PFSAs, where ionomer moieties interact with the inorganic fillers and additives, affecting the overall transport, thermal, and mechanical properties. There is need to merge these activities, not only to understand better the origins of device-level improvements, but also create a knowledge base for developing new materials, and their subsequent optimization. Accomplishing the latter requires more systematic investigations, focusing on both transport and stability, not each of them independently. As discussed throughout, approaches that examine the synergy between the various PFSA properties and phenomena are required since they are tightly coupled, and typically nonlinearly, in these materials. Similarly, the coupling in electro-mechanical phenomena in these materials is likewise in its early stages. Although mechanically-reinforced membranes are providing necessary functionalities for devices such as going toward lower thicknesses, there are still deficiencies in the science and understanding such as what is the definition of EW and domain-network in such composite systems and how can it be evaluated. Furthermore, careful examination of the impact of the additives is not comprehensive, as most studies with composite membrane focus solely on conductivity or stability and not the underlying polymer physics driving those properties. For example, while the concept of water retention has been frequently used in the presence of inorganic fillers, sorption/desorption phenomena in the vapor phase has not been investigated systematically to truly elucidate the underlying origins of the retention mechanism, and its dynamics. Moreover, despite very strong trends toward the use of thinner and chemically/mechanically stabilized hybrid PFSAs, especially in automotive PEFC applications, the literature data and models are lagging.

A related issue that is garnering much more attention is that of PFSA in a thin-film motif, where the polymer chains are confined. Such systems serve as proxies for complex porous electrodes and exhibit phenomena associated with PFSA surface layers and composite materials through mechanical interactions. Even though substrate-specific interactions are known to affect the ionic moieties' distribution at the interface, a complete picture as to how these interactions control the orientation of ionomer's side- and main-chain, and how effectively any ordering in the morphology propagates through the thickness are yet to be determined. Nevertheless, all of these morphological and surface effects can help explain the observed limitations in transport properties when Nafion is topologically confined. For example, PFSAs exhibit anisotropy in morphology and transport properties in composite structures, and more importantly in confined thin films, for which variation in transport resistances parallel and perpendicular to the substrate is directly relevant to ionomer performance. Thus, there is need to move beyond scalar values to direction-dependent properties and even tensor quantities. The thin-films introduce the importance of substrate interactions, especially during operation, which expands the required data needs and science, most of which is still nascent. A similar focus is emerging on the need to tailor and understand selectivity in PFSA membranes used for reinvigorated activities such as redox flow batteries. In these systems, multicomponent ion interactions with the PFSA and each other dominate, and there is a lack of fundamental knowledge on the co-transport issues as well as different cationic forms and exchange.

Overall, PFSAs remain benchmark materials due to their unique transport properties and stability in various applications and environments, and well-demonstrated real-world performance and longevity in various devices, in particular PEFCs. With new applications for PFSA ionomers emerging constantly, there is a need to correlate and understand their transport, structural, and mechanical phenomena and properties. This is especially important in many applications that require multiple functionalities, and such correlations are an area of active research. Even though it is one class of material, research and application on PFSA offers ample opportunity for tuning their properties and functionality for emerging next-generation technologies, setting benchmark material properties for design and development of alternative chemistries of hybrid ion-conductive materials, and adopting and developing advanced modeling and diagnostic techniques due to the disparate length and time scale that occur and dominate PFSA responses from molecular movement to mesoscale transport to dynamic surface layers and relaxation/swellling.

AUTHOR INFORMATION

Corresponding Author

*E-mail: akusoglu@lbl.gov.

ORCID

Ahmet Kusoglu: 0000-0002-2761-1050

Notes

The authors declare no competing financial interest.

Biographies

Ahmet Kusoglu is a research scientist in the Energy Technologies Area at Berkeley Lab (LBNL), working on characterization and fundamental understanding of structure/function relationships of ionomer membranes and thin films for electrochemical devices and related electrochemical-mechanical phenomena for energy applications. He holds B.S. and Ph.D. degrees in Mechanical Engineering, the latter of which he received from University of Delaware, where he studied the mechanical characterization and durability of ionomer membranes and earned a graduate fellowship award. In 2010, he joined Berkeley Lab as a chemist postdoctoral fellow to study ionomer membrane transport and degradation in fuel cells. He has published over 35 peer-reviewed journal publications and a book chapter on ionomer membranes and delivered various invited talks and tutorials on related topics. He is the recipient of 2016 Supramaniam Srinivasan Young Investigator Award of the Energy Technology Division of the Electrochemical Society.

A. Z. Weber received his B.Sc and M.Sc. degrees from Tufts University in 1999 and his Ph.D. from University of California, Berkeley in 2004 under the guidance of J. Newman. He then moved to Lawrence Berkeley National Laboratory where he is now a staff scientist, leader of the Energy Conversion Group, Deputy of the Fuel-Cell − Performance and Durability (FC−PAD) consortium, and thrust coordinator in at the Joint Center for Artificial Photosynthesis. His interests and research focus on electrochemical technologies including flow batteries, fuel cells, and solar-fuel generators, with a focus on advanced diagnostics and mathematical modeling. He has a particular interest in ion-conducting membranes. He has over 90 peer-reviewed publications and 9 book chapters. He received a Presidential Early Career Award for Scientists and Engineers (PECASE) in 2012 and the Charles W. Tobias Young Investigator Award of the Electrochemical Society in 2014.

ACKNOWLEDGMENTS

Part of this work was funded under the Fuel Cell Performance and Durability Consortium (FC-PAD) funded by the Energy

Efficiency and Renewable Energy, Fuel Cell Technologies Office, of the U.S. Department of Energy under Contract No. DE-AC02-05CH11231. The authors are grateful to myriads of meetings and discussions with researchers over the years that helped refine this review; and particular acknowledgements go out to Steve Hamrock, Andy Herring, Michael Hickner, and Klaus-Dieter Kreuer, for helpful discussions and their resourceful comments on various topics, as well as Andrew Crothers, Meron Tesfaye, and Shouwen Shi for proofreading of the article and discussions.

REFERENCES

(1) Mauritz, K. A.; Moore, R. B. State of Understanding of Nafion. *Chem. Rev.* **2004**, *104* (10), 4535−4585.

(2) Giffin, G. A.; Haugen, G. M.; Hamrock, S. J.; Di Noto, V. Interplay between Structure and Relaxations in Perfluorosulfonic Acid Proton Conducting Membranes. *J. Am. Chem. Soc.* **2013**, *135* (2), 822−834.

(3) Moukheiber, E.; De Moor, G.; Flandin, L.; Bas, C. Investigation of Ionomer Structure through Its Dependence on Ion Exchange Capacity (Iec). *J. Membr. Sci.* **2012**, *389*, 294−304.

(4) Hamrock, S. J.; Yandrasits, M. A. Proton Exchange Membranes for Fuel Cell Applications. *J. Macromol. Sci., Polym. Rev.* **2006**, *46* (3), 219−244.

(5) Schaberg, M. S.; Abulu, J. E.; Haugen, G. M.; Emery, M. A.; O'Conner, S. J.; Xiong, P. N.; Hamrock, S. New Multi Acid Side-Chain Ionomers for Proton Exchange Membrane Fuel Cells. *ECS Trans.* **2010**, *33* (1), 627−633.

(6) Kreuer, K. D.; Schuster, M.; Obliers, B.; Diat, O.; Traub, U.; Fuchs, A.; Klock, U.; Paddison, S. J.; Maier, J. Short-Side-Chain Proton Conducting Perfluorosulfonic Acid Ionomers: Why They Perform Better in Pem Fuel Cells. *J. Power Sources* **2008**, *178* (2), 499−509.

(7) Ballengee, J. B.; Haugen, G. M.; Hamrock, S. J.; Pintauro, P. N. Properties and Fuel Cell Performance of a Nanofiber Composite Membrane with 660 Equivalent Weight Perfluorosulfonic Acid. *J. Electrochem. Soc.* **2013**, *160* (4), F429−F435.

(8) Aieta, N. V.; Stanis, R. J.; Horan, J. L.; Yandrasits, M. A.; Cookson, D. J.; Ingham, B.; Toney, M. F.; Hamrock, S. J.; Herring, A. M. Clipped Random Wave Morphologies and the Analysis of the Saxs of an Ionomer Formed by Copolymerization of Tetrafluoroethylene and Cf(2) = Cfo(Cf(2))(4)So(3)H. *Macromolecules* **2009**, *42* (15), 5774−5780.

(9) Hamrock, S. J.; Herring, A. M. In *Encyclopedia of Sustainability Science and Technology*; Meyers, R., Ed.; Springer: New York, 2012, DOI:10.1007/978-1-4419-0851-3_155.

(10) Liu, Y.; Sambasivarao, S. V.; Horan, J. L.; Yang, Y.; Maupin, C. M.; Herring, A. M. A Combined Theoretical and Experimental Investigation of the Transport Properties of Water in a Perfluorosulfonic Acid Proton Exchange Membrane Doped with the Heteropoly Acids, H3pw12o40or H4siw12o40. *J. Phys. Chem. C* **2014**, *118* (2), 854−863.

(11) Gittleman, C. S.; Coms, F. D.; Lai, Y.-H. In *Polymer Electrolyte Fuel Cell Degradation*; Matthew, M., Emin Caglan, K., Veziroglu, T. N., Eds.; Academic Press: Boston, 2012.

(12) Borup, R.; Meyers, J.; Pivovar, B.; Kim, Y. S.; Mukundan, R.; Garland, N.; Myers, D.; Wilson, M.; Garzon, F.; Wood, D.; et al. Scientific Aspects of Polymer Electrolyte Fuel Cell Durability and Degradation. *Chem. Rev.* **2007**, *107* (10), 3904−3951.

(13) Hickner, M. A.; Pivovar, B. S. The Chemical and Structural Nature of Proton Exchange Membrane Fuel Cell Properties. *Fuel Cells* **2005**, *5* (2), 213−229.

(14) Weber, A. Z.; Newman, J. Modeling Transport in Polymer-Electrolyte Fuel Cells. *Chem. Rev.* **2004**, *104* (10), 4679−4726.

(15) Ito, H.; Maeda, T.; Nakano, A.; Takenaka, H. Properties of Nafion Membranes under Pem Water Electrolysis Conditions. *Int. J. Hydrogen Energy* **2011**, *36* (17), 10527−10540.

(16) Kreuer, K.-D.; Paddison, S. J.; Spohr, E.; Schuster, M. Transport in Proton Conductors for Fuel-Cell Applications: Simulations, Elementary Reactions, and Phenomenology. *Chem. Rev.* **2004**, *104* (10), 4637−4678.

(17) Kusoglu, A.; Weber, A. Z. *Polymers for Energy Storage and Delivery: Polyelectrolytes for Batteries and Fuel Cells*; American Chemical Society: Washington, DC, 2012; Vol. *1096*.

(18) Hickner, M. A. Water-Mediated Transport in Ion-Containing Polymers. *J. Polym. Sci., Part B: Polym. Phys.* **2012**, *50* (1), 9−20.

(19) Gebel, G.; Diat, O. Neutron and X-Ray Scattering: Suitable Tools for Studying Lonomer Membranes. *Fuel Cells* **2005**, *5* (2), 261−276.

(20) Weber, A. Z.; Borup, R. L.; Darling, R. M.; Das, P. K.; Dursch, T. J.; Gu, W. B.; Harvey, D.; Kusoglu, A.; Litster, S.; Mench, M. M.; et al. A Critical Review of Modeling Transport Phenomena in Polymer-Electrolyte Fuel Cells. *J. Electrochem. Soc.* **2014**, *161* (12), F1254−F1299.

(21) Pivovar, B. S. An Overview of Electro-Osmosis in Fuel Cell Polymer Electrolytes. *Polymer* **2006**, *47* (11), 4194−4202.

(22) Doyle, M.; Rajendran, G.; Vielstich, W.; Lamm, A.; Gasteiger, H. A. *Handbook of Fuel Cells: Fundamentals Technology and Applications* **2003**.

(23) Paddison, S. J. Proton Conduction Mechanisms at Low Degrees of Hydration in Sulfonic Acid-Based Polymer Electrolyte Membranes. *Annu. Rev. Mater. Res.* **2003**, *33*, 289−319.

(24) Kim, Y. S.; Pivovar, B. S. Moving Beyond Mass-Based Parameters for Conductivity Analysis of Sulfonated Polymers. *Annu. Rev. Chem. Biomol. Eng.* **2010**, *1* (1), 123−148.

(25) Duncan, A. J.; Leo, D. J.; Long, T. E. Beyond Nafion: Charged Macromolecules Tailored for Performance as Ionic Polymer Transducers. *Macromolecules* **2008**, *41* (21), 7765−7775.

(26) Rodgers, M. P.; Bonville, L. J.; Kunz, H. R.; Slattery, D. K.; Fenton, J. M. Fuel Cell Perfluorinated Sulfonic Acid Membrane Degradation Correlating Accelerated Stress Testing and Lifetime. *Chem. Rev.* **2012**, *112* (11), 6075−6103.

(27) Hickner, M. A. Ion-Containing Polymers: New Energy & Clean Water. *Mater. Today* **2010**, *13* (5), 34−41.

(28) Deabate, S.; Gebel, G.; Huguet, P.; Morin, A.; Pourcelly, G. 3 in Situ and Operando Determination of the Water Content Distribution in Proton Conducting Membranes for Fuel Cells: A Critical Review. *Energy Environ. Sci.* **2012**, *5* (10), 8824−8847.

(29) Subianto, S.; Pica, M.; Casciola, M.; Cojocaru, P.; Merlo, L.; Hards, G.; Jones, D. J. Physical and Chemical Modification Routes Leading to Improved Mechanical Properties of Perfluorosulfonic Acid Membranes for Pem Fuel Cells. *J. Power Sources* **2013**, *233*, 216−230.

(30) Herring, A. M. Inorganic-Polymer Composite Membranes for Proton Exchange Membrane Fuel Cells. *J. Macromol. Sci., Polym. Rev.* **2006**, *46* (3), 245−296.

(31) Kim, Y. S.; Lee, K. S. Fuel Cell Membrane Characterizations. *Polym. Rev.* **2015**, *55* (2), 330−370.

(32) Lousenberg, R. D. Molar Mass Distributions and Viscosity Behavior of Perfluorinated Sulfonic Acid Polyelectrolyte Aqueous Dispersions. *J. Polym. Sci., Part B: Polym. Phys.* **2005**, *43* (4), 421−428.

(33) Gierke, T. D.; Munn, G. E.; Wilson, F. C. The Morphology in Nafion Perfluorinated Membrane Products, as Determined by Wide-Angle and Small-Angle X-Ray Studies. *J. Polym. Sci., Polym. Phys. Ed.* **1981**, *19* (11), 1687−1704.

(34) Starkweather, H. W.; Chang, J. J. Water Relaxation in Perfluorosulfonate Ionomers. *Macromolecules* **1982**, *15* (3), 752−756.

(35) Hsu, W. Y.; Gierke, T. D. Ion-Transport and Clustering in Nafion Perfluorinated Membranes. *J. Membr. Sci.* **1983**, *13* (3), 307−326.

(36) Fujimura, M.; Hashimoto, T.; Kawai, H. Small-Angle X-Ray-Scattering Study of Perfluorinated Ionomer Membranes 0.1. Origin of 2 Scattering Maxima. *Macromolecules* **1981**, *14* (5), 1309−1315.

(37) Kumar, S.; Pineri, M. Interpretation of Small-Angle X-Ray and Neutron-Scattering Data for Perfluorosulfonated Ionomer Membranes. *J. Polym. Sci., Part B: Polym. Phys.* **1986**, *24* (8), 1767−1782.

(38) Moore, R. B.; Martin, C. R. Morphology and Chemical-Properties of the Dow Perfluorosulfonate Ionomers. *Macromolecules* **1989**, *22* (9), 3594−3599.

(39) Boakye, E. E.; Yeager, H. L. Water Sorption and Ionic-Diffusion in Short Side-Chain Perfluorosulfonate Ionomer Membranes. *J. Membr. Sci.* **1992**, *69* (1−2), 155−167.

(40) Martin, R. T.; Kevin, P. D.; Katherine, D. L.; Charles, W. M. *Multiphase Polymers: Blends and Ionomers*; American Chemical Society: Washington, DC, 1989; Vol. 395.

(41) Cable, K. M.; Mauritz, K. A.; Moore, R. B. Effects of Hydrophilic and Hydrophobic Counterions on the Coulombic Interactions in Perfluorosulfonate Ionomers. *J. Polym. Sci., Part B: Polym. Phys.* **1995**, *33* (7), 1065−1072.

(42) Liu, Y.; Horan, J. L.; Schlichting, G. J.; Caire, B. R.; Liberatore, M. W.; Hamrock, S. J.; Haugen, G. M.; Yandrasits, M. A.; Seifert, S.; Herring, A. M. A Small-Angle X-Ray Scattering Study of the Development of Morphology in Films Formed from the 3m Perfluorinated Sulfonic Acid Ionomer. *Macromolecules* **2012**, *45* (18), 7495−7503.

(43) Larson, J. M.; Hamrock, S. J.; Haugen, G. M.; Pham, P.; Lamanna, W. M.; Moss, A. B. Membranes Based on Basic Polymers and Perfluorinated Acids for Hotter and Drier Fuel Cell Operating Conditions. *J. Power Sources* **2007**, *172* (1), 108−114.

(44) Saito, M.; Arimura, N.; Hayamizu, K.; Okada, T. Mechanisms of Ion and Water Transport in Perfluorosulfonated Ionomer Membranes for Fuel Cells. *J. Phys. Chem. B* **2004**, *108* (41), 16064−16070.

(45) Ferrari, M. C.; Catalano, J.; Baschetti, M. G.; De Angelis, M. G.; Sarti, G. C. Ftir-Atr Study of Water Distribution in a Short-Side-Chain Pfsi Membrane. *Macromolecules* **2012**, *45* (4), 1901−1912.

(46) Peng, A. Z.; Morin, A.; Huguet, P.; Lanteri, Y.; Deabate, S. Asymmetric Bi-Layer Pfsa Membranes as Model Systems for the Study of Water Management in the Pemfc. *Phys. Chem. Chem. Phys.* **2014**, *16* (38), 20941−20956.

(47) Zawodzinski, T. A.; Springer, T. E.; Davey, J.; Jestel, R.; Lopez, C.; Valerio, J.; Gottesfeld, S. A Comparative-Study of Water-Uptake by and Transport through Ionomeric Fuel-Cell Membranes. *J. Electrochem. Soc.* **1993**, *140* (7), 1981−1985.

(48) Kusoglu, A.; Dursch, T. J.; Weber, A. Z. Nanostructure/Swelling Relationships of Bulk and Thin-Film Pfsa Ionomers. *Adv. Funct. Mater.* **2016**, *26* (27), 4961−4975.

(49) Hensley, J. E.; Way, J. D.; Dec, S. F.; Abney, K. D. The Effects of Thermal Annealing on Commercial Nafion((R)) Membranes. *J. Membr. Sci.* **2007**, *298* (1−2), 190−201.

(50) Economou, N. J.; O'Dea, J. R.; McConnaughy, T. B.; Buratto, S. K. Morphological Differences in Short Side Chain and Long Side Chain Perfluorosulfonic Acid Proton Exchange Membranes at Low and High Water Contents. *RSC Adv.* **2013**, *3* (42), 19525−19532.

(51) Hiesgen, R.; Morawietz, T.; Handl, M.; Corasaniti, M.; Friedrich, K. A. Insight into the Structure and Nanoscale Conductivity of Fluorinated Ionomer Membranes. *J. Electrochem. Soc.* **2014**, *161* (12), F1214−F1223.

(52) Alvarez-Gallego, Y.; de Heer, M. P. Sub-Freezing Conductivity of Pfsa Membranes. *Fuel Cells* **2009**, *9* (4), 421−431.

(53) Edmondson, C. A.; Fontanella, J. J. Free Volume and Percolation in S-Sebs and Fluorocarbon Proton Conducting Membranes. *Solid State Ionics* **2002**, *152*, 355−361.

(54) Halim, J.; Buchi, F. N.; Haas, O.; Stamm, M.; Scherer, G. G. Characterization of Perfluorosulfonic Acid Membranes by Conductivity Measurements and Small-Angle X-Ray-Scattering. *Electrochim. Acta* **1994**, *39* (8−9), 1303−1307.

(55) Lee, D. K.; Saito, T.; Benesi, A. J.; Hickner, M. A.; Allcock, H. R. Characterization of Water in Proton-Conducting Membranes by Deuterium Nmr T-1 Relaxation. *J. Phys. Chem. B* **2011**, *115* (5), 776−783.

(56) Meng, F. Q.; Aieta, N. V.; Dec, S. F.; Horan, J. L.; Williamson, D.; Frey, M. H.; Pham, P.; Turner, J. A.; Yandrasits, M. A.; Hamrock, S. J.; et al. Structural and Transport Effects of Doping Perfluorosulfonic Acid Polymers with the Heteropoly Acids, H3pw12o40 or H4siw12o40. *Electrochim. Acta* **2007**, *53* (3), 1372−1378.

(57) Peron, J.; Edwards, D.; Haldane, M.; Luo, X. Y.; Zhang, Y. M.; Holdcroft, S.; Shi, Z. Q. Fuel Cell Catalyst Layers Containing Short-Side-Chain Perfluorosulfonic Acid Ionomers. *J. Power Sources* **2011**, *196* (1), 179−181.

(58) Siu, A.; Schmeisser, J.; Holdcroft, S. Effect of Water on the Low Temperature Conductivity of Polymer Electrolytes. *J. Phys. Chem. B* **2006**, *110* (12), 6072−6080.

(59) Zawodzinski, T. A.; Springer, T. E.; Uribe, F.; Gottesfeld, S. Characterization of Polymer Electrolytes for Fuel-Cell Applications. *Solid State Ionics* **1993**, *60* (1−3), 199−211.

(60) Ren, X. M.; Gottesfeld, S. Electro-Osmotic Drag of Water in Poly(Perfluorosulfonic Acid) Membranes. *J. Electrochem. Soc.* **2001**, *148* (1), A87−A93.

(61) Zhao, Q.; Benziger, J. Mechanical Properties of Perfluoro Sulfonated Acids: The Role of Temperature and Solute Activity. *J. Polym. Sci., Part B: Polym. Phys.* **2013**, *51* (11), 915−925.

(62) Paddison, S. J.; Elliott, J. A. Molecular Modeling of the Short-Side-Chain Perfluorosulfonic Acid Membrane. *J. Phys. Chem. A* **2005**, *109* (33), 7583−7593.

(63) Wu, D. S.; Paddison, S. J.; Elliott, J. A. A Comparative Study of the Hydrated Morphologies of Perfluorosulfonic Acid Fuel Cell Membranes with Mesoscopic Simulations. *Energy Environ. Sci.* **2008**, *1* (2), 284−293.

(64) Paddison, S. J.; Elliott, J. A. Selective Hydration of the 'Short-Side-Chain' Perfluorosulfonic Acid Membrane. An Oniom Study. *Solid State Ionics* **2007**, *178* (7−10), 561−567.

(65) Dorenbos, G.; Suga, Y. Simulation of Equivalent Weight Dependence of Nafion Morphologies and Predicted Trends Regarding Water Diffusion. *J. Membr. Sci.* **2009**, *330* (1−2), 5−20.

(66) Wu, D. S.; Paddison, S. J.; Elliott, J. A. Effect of Molecular Weight on Hydrated Morphologies of the Short-Side-Chain Perfluorosulfonic Acid Membrane. *Macromolecules* **2009**, *42* (9), 3358−3367.

(67) Wu, D. S.; Paddison, S. J.; Elliott, J. A.; Hamrock, S. J. Mesoscale Modeling of Hydrated Morphologies of 3m Perfluorosulfonic Acid-Based Fuel Cell Electrolytes. *Langmuir* **2010**, *26* (17), 14308−14315.

(68) Clark, J. K., 2nd; Paddison, S. J.; Hamrock, S. J. The Effect of Hydrogen Bond Reorganization and Equivalent Weight on Proton Transfer in 3m Perfluorosulfonic Acid Ionomers. *Phys. Chem. Chem. Phys.* **2012**, *14* (47), 16349−16359.

(69) Clark, J. K.; Paddison, S. J. Proton Dissociation and Transfer in Proton Exchange Membrane Ionomers with Multiple and Distinct Pendant Acid Groups: An Ab Initio Study. *Electrochim. Acta* **2013**, *101* (0), 279−292.

(70) Paddison, S. J.; Elliott, J. A. The Effects of Backbone Conformation on Hydration and Proton Transfer in the 'Short-Side-Chain' Perfluorosulfonic Acid Membrane. *Solid State Ionics* **2006**, *177* (26−32), 2385−2390.

(71) Elliott, J. A.; Paddison, S. J. Modelling of Morphology and Proton Transport in Pfsa Membranes. *Phys. Chem. Chem. Phys.* **2007**, *9* (21), 2602−2618.

(72) Devanathan, R.; Dupuis, M. Insight from Molecular Modelling: Does the Polymer Side Chain Length Matter for Transport Properties of Perfluorosulfonic Acid Membranes? *Phys. Chem. Chem. Phys.* **2012**, *14* (32), 11281−11295.

(73) Paddison, S. J.; Elliott, J. A. On the Consequences of Side Chain Flexibility and Backbone Conformation on Hydration and Proton Dissociation in Perfluorosulfonic Acid Membranes. *Phys. Chem. Chem. Phys.* **2006**, *8* (18), 2193−2203.

(74) Economou, N. J.; Barnes, A. M.; Wheat, A. J.; Schaberg, M. S.; Hamrock, S. J.; Buratto, S. K. Investigation of Humidity Dependent Surface Morphology and Proton Conduction in Multi-Acid Side Chain Membranes by Conductive Probe Atomic Force Microscopy. *J. Phys. Chem. B* **2015**, *119* (44), 14280−14287.

(75) Bawagan, A. D. O.; Hamrock, S. J.; Schaberg, M.; Yousef, I.; Ritter, E.; Schade, U. Far-Infrared Studies on Nafion and Perfluoroimide Acid (Pfia) and Their Alkali Salts. *Vib. Spectrosc.* **2014**, *75* (0), 213−217.

(76) Liu, W.; Suzuki, T.; Mao, H.; Schmiedel, T. Development of Thin, Reinforced Pemfc Membranes through Understanding of

Structure-Property-Performance Relationships. *ECS Trans.* **2013**, *50* (2), 51−64.

(77) Hamrock, S. *HTMWG*; available at http://www.hydrogen.energy.gov, 2010.

(78) Van Nguyen, T.; Nguyen, M. V.; Nordheden, K. J.; He, W. S. Effect of Bulk and Surface Treatments on the Surface Ionic Activity of Nafion Membranes. *J. Electrochem. Soc.* **2007**, *154* (11), A1073−A1076.

(79) Maeda, Y.; Gao, Y.; Nagai, M.; Nakayama, Y.; Ichinose, T.; Kuroda, R.; Umemura, K. Study of the Nanoscopic Deformation of an Annealed Nafion Film by Using Atomic Force Microscopy and a Patterned Substrate. *Ultramicroscopy* **2008**, *108* (6), 529−535.

(80) Kwon, O.; Wu, S. J.; Zhu, D. M. Configuration Changes of Conducting Channel Network in Nafion Membranes Due to Thermal Annealing. *J. Phys. Chem. B* **2010**, *114* (46), 14989−14994.

(81) Wang, J.; Yang, M. K.; Dou, P.; Wang, X. J.; Zhang, H. Influences of Annealing on the Perfluorosulfonate Ion-Exchanged Membranes Prepared by Melt Extrusion. *Ind. Eng. Chem. Res.* **2014**, *53* (36), 14175−14182.

(82) Kusoglu, A.; Savagatrup, S.; Clark, K. T.; Weber, A. Z. Role of Mechanical Factors in Controlling the Structure−Function Relationship of Pfsa Ionomers. *Macromolecules* **2012**, *45* (18), 7467−7476.

(83) Maldonado, L.; Perrin, J. C.; Dillet, J.; Lottin, O. Characterization of Polymer Electrolyte Nafion Membranes: Influence of Temperature, Heat Treatment and Drying Protocol on Sorption and Transport Properties. *J. Membr. Sci.* **2012**, *389*, 43−56.

(84) Elliott, J. A.; Hanna, S.; Newton, J. N.; Elliott, A. M. S.; Cooley, G. E. Elimination of Orientation in Perfluorinated Lonomer Membranes. *Polym. Eng. Sci.* **2006**, *46* (2), 228−234.

(85) Collette, F. M.; Lorentz, C.; Gebel, G.; Thominette, F. Hygrothermal Aging of Nafion (R). *J. Membr. Sci.* **2009**, *330* (1−2), 21−29.

(86) Collette, F. M.; Thominette, F.; Escribano, S.; Ravachol, A.; Morin, A.; Gebel, G. Fuel Cell Rejuvenation of Hygrothermally Aged Nafion (R). *J. Power Sources* **2012**, *202*, 126−133.

(87) Xie, T.; Page, K. A.; Eastman, S. A. Strain-Based Temperature Memory Effect for Nafion and Its Molecular Origins. *Adv. Funct. Mater.* **2011**, *21* (11), 2057−2066.

(88) Alberti, G.; Narducci, R. Evolution of Permanent Deformations (or Memory) in Nafion 117 Membranes with Changes in Temperature, Relative Humidity and Time, and Its Importance in the Development of Medium Temperature Pemfcs. *Fuel Cells* **2009**, *9* (4), 410−420.

(89) Divoux, G. M.; Finlay, K. A.; Park, J. K.; Song, J.-M.; Yan, B.; Zhang, M.; Dillard, D. A.; Moore, R. B. Morphological Factors Affecting the Behavior of Water in Proton Exchange Membrane Materials. *ECS Trans.* **2011**, *41* (1), 87−100.

(90) Shi, S. W.; Dursch, T. J.; Blake, C.; Mukundan, R.; Borup, R. L.; Weber, A. Z.; Kusoglu, A. Impact of Hygrothermal Aging on Structure/Function Relationship of Perfluorosulfonic-Acid Membrane. *J. Polym. Sci., Part B: Polym. Phys.* **2016**, *54* (5), 570−581.

(91) Page, K. A.; Cable, K. M.; Moore, R. B. Molecular Origins of the Thermal Transitions and Dynamic Mechanical Relaxations in Perfluorosulfonate Ionomers. *Macromolecules* **2005**, *38* (15), 6472−6484.

(92) Hinatsu, J. T.; Mizuhata, M.; Takenaka, H. Water-Uptake of Perfluorosulfonic Acid Membranes from Liquid Water and Water-Vapor. *J. Electrochem. Soc.* **1994**, *141* (6), 1493−1498.

(93) Evans, C. E.; Noble, R. D.; Nazeri-Thompson, S.; Nazeri, B.; Koval, C. A. Role of Conditioning on Water Uptake and Hydraulic Permeability of Nafion (R) Membranes. *J. Membr. Sci.* **2006**, *279* (1−2), 521−528.

(94) Onishi, L. M.; Prausnitz, J. M.; Newman, J. Water-Nafion Equilibria. Absence of Schroeder's Paradox. *J. Phys. Chem. B* **2007**, *111* (34), 10166−10173.

(95) Zawodzinski, T. A.; Derouin, C.; Radzinski, S.; Sherman, R. J.; Smith, V. T.; Springer, T. E.; Gottesfeld, S. Water-Uptake by and Transport through Nafion(R) 117 Membranes. *J. Electrochem. Soc.* **1993**, *140* (4), 1041−1047.

(96) Singhal, N.; Datta, A. Reversible Tuning of Chemical Structure of Nafion Cast Film by Heat and Acid Treatment. *J. Phys. Chem. B* **2015**, *119* (6), 2395−2403.

(97) Lee, K.; Ishihara, A.; Mitsushima, S.; Kamiya, N.; Ota, K. Effect of Recast Temperature on Diffusion and Dissolution of Oxygen and Morphological Properties in Recast Nafion. *J. Electrochem. Soc.* **2004**, *151* (4), A639−A645.

(98) Shi, S. W.; Weber, A. Z.; Kusoglu, A. Structure/Property Relationship of Nafion Xl Composite Membranes. *J. Membr. Sci.* **2016**, *516*, 123−134.

(99) Takamatsu, T.; Eisenberg, A. Densities and Expansion Coefficients of Nafion Polymers. *J. Appl. Polym. Sci.* **1979**, *24* (11), 2221−2235.

(100) Xie, W.; Darling, R. M.; Perry, M. L. Processing and Pretreatment Effects on Vanadium Transport in Nafion Membranes. *J. Electrochem. Soc.* **2016**, *163* (1), A5084−A5089.

(101) Luan, Y.; Zhang, Y.; Zhang, H.; Li, L.; Li, H.; Liu, Y. Annealing Effect of Perfluorosulfonated Ionomer Membranes on Proton Conductivity and Methanol Permeability. *J. Appl. Polym. Sci.* **2008**, *107* (1), 396−402.

(102) Cappadonia, M.; Erning, J. W.; Niaki, S. M. S.; Stimming, U. Conductance of Nafion-117 Membranes as a Function of Temperature and Water-Content. *Solid State Ionics* **1995**, *77*, 65−69.

(103) Li, J. S.; Yang, X.; Tang, H. L.; Pan, M. Durable and High Performance Nafion Membrane Prepared through High-Temperature Annealing Methodology. *J. Membr. Sci.* **2010**, *361* (1−2), 38−42.

(104) Hassan, M. K.; Abukmail, A.; Mauritz, K. A. Broadband Dielectric Spectroscopic Studies of Molecular Motions in a Nafion (R) Membrane Vs. Annealing Time and Temperature. *Eur. Polym. J.* **2012**, *48* (4), 789−802.

(105) Tucker, M. C.; Cho, K. T.; Spingler, F. B.; Weber, A. Z.; Lin, G. Y. Impact of Membrane Characteristics on the Performance and Cycling of the Br-2-H-2 Redox Flow Cell. *J. Power Sources* **2015**, *284*, 212−221.

(106) Steck, A.; Yeager, H. L. Water Sorption and Cation-Exchange Selectivity of a Perfluorosulfonate Ion-Exchange Polymer. *Anal. Chem.* **1980**, *52* (8), 1215−1218.

(107) Feng, K.; Hou, L.; Tang, B. B.; Wu, P. Y. Does Thermal Treatment Merely Make a H2o-Saturated Nafion Membrane Lose Its Absorbed Water at High Temperature? *Phys. Chem. Chem. Phys.* **2015**, *17* (14), 9106−9115.

(108) Gebel, G.; Aldebert, P.; Pineri, M. Structure and Related Properties of Solution-Cast Perfluorosulfonated Ionomer Films. *Macromolecules* **1987**, *20* (6), 1425−1428.

(109) Rollet, A. L.; Gebel, G.; Simonin, J. P.; Turq, P. A Sans Determination of the Influence of External Conditions on the Nanostructure of Nafion Membrane. *J. Polym. Sci., Part B: Polym. Phys.* **2001**, *39* (5), 548−558.

(110) Roche, E. J.; Pineri, M.; Duplessix, R.; Levelut, A. M. Small-Angle Scattering Studies of Nafion Membranes. *J. Polym. Sci., Polym. Phys. Ed.* **1981**, *19* (1), 1−11.

(111) von Kraemer, S.; Sagidullin, A. I.; Lindbergh, G.; Furo, I.; Persson, E.; Jannasch, P. Pore Size Distribution and Water Uptake in Hydrocarbon and Perfluorinated Proton-Exchange Membranes as Studied by Nmr Cryoporometry. *Fuel Cells* **2008**, *8* (3−4), 262−269.

(112) Zawodzinski, T. A.; Gottesfeld, S.; Shoichet, S.; Mccarthy, T. J. The Contact-Angle between Water and the Surface of Perfluorosulfonic Acid Membranes. *J. Appl. Electrochem.* **1993**, *23* (1), 86−88.

(113) Luo, Z. P.; Chang, Z. Y.; Zhang, Y. X.; Liu, Z.; Li, J. Electro-Osmotic Drag Coefficient and Proton Conductivity in Nafion (R) Membrane for Pemfc. *Int. J. Hydrogen Energy* **2010**, *35* (7), 3120−3124.

(114) Alberti, G.; Narducci, R.; Sganappa, M. Effects of Hydrothermal/Thermal Treatments on the Water-Uptake of Nafion Membranes and Relations with Changes of Conformation, Counter-Elastic Force and Tensile Modulus of the Matrix. *J. Power Sources* **2008**, *178* (2), 575−583.

(115) Kusoglu, A.; Modestino, M. A.; Hexemer, A.; Segalman, R. A.; Weber, A. Z. Subsecond Morphological Changes in Nafion During

Water Uptake Detected by Small-Angle X-Ray Scattering. *ACS Macro Lett.* **2012**, *1* (1), 33−36.

(116) Gebel, G.; Lyonnard, S.; Mendil-Jakani, H.; Morin, A. The Kinetics of Water Sorption in Nafion Membranes: A Small-Angle Neutron Scattering Study. *J. Phys.: Condens. Matter* **2011**, *23* (23), 234107.

(117) Fumagalli, M.; Lyonnard, S.; Prajapati, G.; Berrod, Q.; Porcar, L.; Guillermo, A.; Gebel, G. Fast Water Diffusion and Long-Term Polymer Reorganization During Nafion Membrane Hydration Evidenced by Time-Resolved Small-Angle Neutron Scattering. *J. Phys. Chem. B* **2015**, *119* (23), 7068−7076.

(118) Patankar, K. A.; Dillard, D. A.; Case, S. W.; Ellis, M. W.; Lai, Y. H.; Budinski, M. K.; Gittleman, C. S. Hygrothermal Characterization of the Viscoelastic Properties of Gore-Select (R) 57 Proton Exchange Membrane. *Mech. Time-Depend. Mater.* **2008**, *12* (3), 221−236.

(119) Liu, D.; Hickner, M. A.; Case, S. W.; Lesko, J. J. Relaxation of Proton Conductivity and Stress in Proton Exchange Membranes under Strain. *J. Eng. Mater. Technol.* **2006**, *128* (4), 503−508.

(120) Casciola, M.; Alberti, G.; Sganappa, M.; Narducci, R. On the Decay of Nafion Proton Conductivity at High Temperature and Relative Humidity. *J. Power Sources* **2006**, *162* (1), 141−145.

(121) Park, M. J.; Downing, K. H.; Jackson, A.; Gomez, E. D.; Minor, A. M.; Cookson, D.; Weber, A. Z.; Balsara, N. P. Increased Water Retention in Polymer Electrolyte Membranes at Elevated Temperatures Assisted by Capillary Condensation. *Nano Lett.* **2007**, *7* (11), 3547−3552.

(122) Satterfield, M. B.; Majsztrik, P. W.; Ota, H.; Benziger, J. B.; Bocarsly, A. B. Mechanical Properties of Nafion and Titania/Nafion Composite Membranes for Polymer Electrolyte Membrane Fuel Cells. *J. Polym. Sci., Part B: Polym. Phys.* **2006**, *44* (16), 2327−2345.

(123) Kusoglu, A.; Tang, Y. L.; Lugo, M.; Karlsson, A. M.; Santare, M. H.; Cleghorn, S.; Johnson, W. B. Constitutive Response and Mechanical Properties of Pfsa Membranes in Liquid Water. *J. Power Sources* **2010**, *195* (2), 483−492.

(124) Majsztrik, P. W.; Bocarsly, A. B.; Benziger, J. B. Viscoelastic Response of Nafion. Effects of Temperature and Hydration on Tensile Creep. *Macromolecules* **2008**, *41* (24), 9849−9862.

(125) Solasi, R.; Zou, Y.; Huang, X. Y.; Reifsnider, K. A Time and Hydration Dependent Viscoplastic Model for Polyelectrolyte Membranes in Fuel Cells. *Mech. Time-Depend. Mater.* **2008**, *12* (1), 15−30.

(126) Satterfield, M. B.; Benziger, J. B. Viscoelastic Properties of Nafion at Elevated Temperature and Humidity. *J. Polym. Sci., Part B: Polym. Phys.* **2009**, *47* (1), 11−24.

(127) Lu, Z. W.; Lugo, M.; Santare, M. H.; Karlsson, A. M.; Busby, F. C.; Walsh, P. An Experimental Investigation of Strain Rate, Temperature and Humidity Effects on the Mechanical Behavior of a Perfluorosulfonic Acid Membrane. *J. Power Sources* **2012**, *214*, 130−136.

(128) Hallinan, D. T.; De Angelis, M. G.; Baschetti, M. G.; Sarti, G. C.; Elabd, Y. A. Non-Fickian Diffusion of Water in Nafion. *Macromolecules* **2010**, *43* (10), 4667−4678.

(129) Davis, E. M.; Stafford, C. M.; Page, K. A. Elucidating Water Transport Mechanisms in Nafion Thin Films. *ACS Macro Lett.* **2014**, *3* (10), 1029−1035.

(130) van der Heijden, P. C.; de la Rosa, A.; Gebel, G.; Diat, O. Relaxation of Drawn Nafion Films Studied with Birefringence Experiments. *Polym. Adv. Technol.* **2005**, *16* (2−3), 102−107.

(131) Page, K. A.; Landis, F. A.; Phillips, A. K.; Moore, R. B. Saxs Analysis of the Thermal Relaxation of Anisotropic Morphologies in Oriented Nafion Membranes. *Macromolecules* **2006**, *39* (11), 3939−3946.

(132) Chen, R. S.; Jayakody, J. P.; Greenbaum, S. G.; Pak, Y. S.; Xu, G.; Mclin, M. G.; Fontanella, J. J. Studies of Water in Nafion Membranes - Using Deuteron and O-17 Nuclear-Magnetic-Resonance, and Dielectric-Relaxation Techniques. *J. Electrochem. Soc.* **1993**, *140* (4), 889−895.

(133) Di Noto, V.; Gliubizzi, R.; Negro, E.; Pace, G. Effect of Sio2 on Relaxation Phenomena and Mechanism of Ion Conductivity of [Nafion/(Sio2)(X)] Composite Membranes. *J. Phys. Chem. B* **2006**, *110* (49), 24972−24986.

(134) Fontanella, J. J.; Mclin, M. G.; Wintersgill, M. C. Electrical Relaxation in in-Situ Dried Acid-Form Nafion. *J. Polym. Sci., Part B: Polym. Phys.* **1994**, *32* (3), 501−507.

(135) Kyu, T.; Eisenberg, A. Underwater Stress-Relaxation Studies of Nafion (Perfluorosulfonate) Ionomer Membranes. *J. Polym. Sci., Polym. Symp.* **1984**, *71* (71), 203−219.

(136) Eikerling, M.; Kornyshev, A. A.; Kucernak, A. R. Water in Polymer Electrolyte Fuel Cells: Friend or Foe? *Phys. Today* **2006**, *59* (10), 38−44.

(137) Satterfield, M. B.; Benziger, J. B. Non-Fickian Water Vapor Sorption Dynamics by Nafion Membranes. *J. Phys. Chem. B* **2008**, *112* (12), 3693−3704.

(138) Patankar, K. A.; Dillard, D. A.; Case, S. W.; Ellis, M. W.; Lai, Y. H.; Gittleman, C. S. Linear Hygrothermal Viscoelastic Characterization of Nafion Nre 211 Proton Exchange Membrane. *Fuel Cells* **2012**, *12* (5), 787−799.

(139) Kim, Y. S.; Welch, C. F.; Hjelm, R. P.; Mack, N. H.; Labouriau, A.; Orler, E. B. Origin of Toughness in Dispersion-Cast Nafion Membranes. *Macromolecules* **2015**, *48* (7), 2161−2172.

(140) Welch, C.; Labouriau, A.; Hjelm, R.; Orler, B.; Johnston, C.; Kim, Y. S. Nafion in Dilute Solvent Systems: Dispersion or Solution? *ACS Macro Lett.* **2012**, *1* (12), 1403−1407.

(141) Aldebert, P.; Dreyfus, B.; Pineri, M. Small-Angle Neutron-Scattering of Perfluorosulfonated Ionomers in Solution. *Macromolecules* **1986**, *19* (10), 2651−2653.

(142) Aldebert, P.; Dreyfus, B.; Gebel, G.; Nakamura, N.; Pineri, M.; Volino, F. Rod Like Micellar Structures in Perfluorinated Ionomer Solutions. *J. Phys. (Paris)* **1988**, *49* (12), 2101−2109.

(143) Gebel, G.; Loppinet, B. Colloidal Structure of Ionomer Solutions in Polar Solvents. *J. Mol. Struct.* **1996**, *383* (1−3), 43−49.

(144) Loppinet, B.; Gebel, G. Rodlike Colloidal Structure of Short Pendant Chain Perfluorinated Ionomer Solutions. *Langmuir* **1998**, *14* (8), 1977−1983.

(145) Moore, R. B.; Martin, C. R. Chemical and Morphological Properties of Solution-Cast Perfluorosulfonate Ionomers. *Macromolecules* **1988**, *21* (5), 1334−1339.

(146) Gebel, G. Structural Evolution of Water Swollen Perfluorosulfonated Ionomers from Dry Membrane to Solution. *Polymer* **2000**, *41* (15), 5829−5838.

(147) Matos, B. R.; Santiago, E. I.; Rey, J. F. Q.; Fonseca, F. C. Origin of Alpha and Ss Relaxations of Nafion. *Phys. Rev. E* **2014**, *89* (5) 10.1103/PhysRevE.89.052601

(148) Moore, R. B.; Martin, C. R. Procedure for Preparing Solution-Cast Perfluorosulfonate Ionomer Films and Membranes. *Anal. Chem.* **1986**, *58* (12), 2569−2570.

(149) Ma, C.-H.; Yu, T. L.; Lin, H.-L.; Huang, Y.-T.; Chen, Y.-L.; Jeng, U. S.; Lai, Y.-H.; Sun, Y.-S. Morphology and Properties of Nafion Membranes Prepared by Solution Casting. *Polymer* **2009**, *50* (7), 1764−1777.

(150) Silva, R. F.; De Francesco, M.; Pozio, A. Solution-Cast Nafion (R) Ionomer Membranes: Preparation and Characterization. *Electrochim. Acta* **2004**, *49* (19), 3211−3219.

(151) Yamaguchi, M.; Matsunaga, T.; Amemiya, K.; Ohira, A.; Hasegawa, N.; Shinohara, K.; Ando, M.; Yoshida, T. Dispersion of Rod-Like Particles of Nafion in Salt-Free Water/1-Propanol and Water/Ethanol Solutions. *J. Phys. Chem. B* **2014**, *118* (51), 14922−14928.

(152) Wang, Z.; Tang, H. L.; Li, J. R.; Zeng, Y.; Chen, L. T.; Pan, M. Insight into the Structural Construction of a Perfluorosulfonic Acid Membrane Derived from a Polymeric Dispersion. *J. Power Sources* **2014**, *256*, 383−393.

(153) Slade, S. M.; Ralph, T. R.; de Leon, C. P.; Campbell, S. A.; Walsh, F. C. The Ionic Conductivity of a Nafion (R) 1100 Series of Proton-Exchange Membranes Re-Cast from Butan-1-Ol and Propan-2-Ol. *Fuel Cells* **2010**, *10* (4), 567−574.

(154) MacKinnon, S. M.; Fuller, T. J.; Coms, F. D.; Schoeneweiss, M. R.; Gittleman, C. S.; Lai, Y. H.; Jiang, R.; Brenner, A. M. In

Encyclopedia of Electrochemical Power Sources; Garche, J., Ed.; Elsevier: Amsterdam, 2009, DOI: 10.1016/B978-044452745-5.00905-9.

(155) Perry, M. L.; Fuller, T. F. A Historical Perspective of Fuel Cell Technology in the 20th Century. *J. Electrochem. Soc.* **2002**, *149* (7), S59−S67.

(156) Mathias, M. F.; Makharia, R.; Gasteiger, H. A.; Conley, J. J.; Fuller, T. J.; Gittleman, C. J.; Kocha, S. S.; Miller, D. P.; Mittelsteadt, C. K.; Xie, T.; et al. Two Fuel Cell Cars in Every Garage? *Electrochem. Soc. Interface* **2005**, *14* (3), 24−35.

(157) Macknight, W. J.; Earnest, T. R. The Structure and Properties of Ionomers. *Macromol. Rev.* **1981**, *16*, 41−122.

(158) Weber, A. Z.; Mench, M. M.; Meyers, J. P.; Ross, P. N.; Gostick, J. T.; Liu, Q. H. Redox Flow Batteries: A Review. *J. Appl. Electrochem.* **2011**, *41* (10), 1137−1164.

(159) Perry, M. L.; Weber, A. Z. Advanced Redox-Flow Batteries: A Perspective. *J. Electrochem. Soc.* **2016**, *163* (1), A5064−A5067.

(160) Modestino, M. A.; Dumortier, M.; Hosseini Hashemi, S. M.; Haussener, S.; Moser, C.; Psaltis, D. Vapor-Fed Microfluidic Hydrogen Generator. *Lab Chip* **2015**, *15* (10), 2287−2296.

(161) Spurgeon, J. M.; Boettcher, S. W.; Kelzenberg, M. D.; Brunschwig, B. S.; Atwater, H. A.; Lewis, N. S. Flexible, Polymer-Supported, Si Wire Array Photoelectrodes. *Adv. Mater.* **2010**, *22* (30), 3277−3281.

(162) Haussener, S.; Xiang, C. X.; Spurgeon, J. M.; Ardo, S.; Lewis, N. S.; Weber, A. Z. Modeling, Simulation, and Design Criteria for Photoelectrochemical Water-Splitting Systems. *Energy Environ. Sci.* **2012**, *5* (12), 9922−9935.

(163) Spurgeon, J. M.; Walter, M. G.; Zhou, J. F.; Kohl, P. A.; Lewis, N. S. Electrical Conductivity, Ionic Conductivity, Optical Absorption, and Gas Separation Properties of Ionically Conductive Polymer Membranes Embedded with Si Microwire Arrays. *Energy Environ. Sci.* **2011**, *4* (5), 1772−1780.

(164) Spurgeon, J. M.; Lewis, N. S. Proton Exchange Membrane Electrolysis Sustained by Water Vapor. *Energy Environ. Sci.* **2011**, *4* (8), 2993−2998.

(165) Ramirez-Garcia, S.; Diamond, D. Biomimetic, Low Power Pumps Based on Soft Actuators. *Sens. Actuators, A* **2007**, *135* (1), 229−235.

(166) Shahinpoor, M. Mechanoelectrical Phenomena in Ionic Polymers. *Math Mech Solids* **2003**, *8* (3), 281−288.

(167) Shahinpoor, M. Ionic Polymer-Conductor Composites as Biomimetic Sensors, Robotic Actuators and Artificial Muscles - a Review. *Electrochim. Acta* **2003**, *48* (14−16), 2343−2353.

(168) Wang, J.; Sato, H.; Xu, C. Y.; Taya, M. Bioinspired Design of Tactile Sensors Based on Flemion. *J. Appl. Phys.* **2009**, *105* (8), 08351510.1063/1.3110768

(169) Park, J. K.; Jones, P. J.; Sahagun, C.; Page, K. A.; Hussey, D. S.; Jacobson, D. L.; Morgan, S. E.; Moore, R. B. Electrically Stimulated Gradients in Water and Counterion Concentrations within Electroactive Polymer Actuators. *Soft Matter* **2010**, *6* (7), 1444−1452.

(170) Coms, F. D.; Fuller, T. J.; Schaffer, C. P. A Mechanistic Study of Perfluorosulfonic Acid Membrane Water Permeance Degradation in Air. *ECS Trans.* **2015**, *69* (17), 189−204.

(171) Fitzgerald, N.; Tyson, J. F.; Leighty, D. A. Reduction of Water Loading Effects in Inductively Coupled Plasma Mass Spectrometry by a Nafion Membrane Dryer Device. *J. Anal. At. Spectrom.* **1998**, *13* (1), 13−16.

(172) Welp, L. R.; Keeling, R. E.; Weiss, R. F.; Paplawsky, W.; Heckman, S. Design and Performance of a Nafion Dryer for Continuous Operation at Co2 and Ch4 Air Monitoring Sites. *Atmos. Meas. Tech.* **2013**, *6* (5), 1217−1226.

(173) Lindbrathen, A.; Hagg, M. B. Membrane Separation of Chlorine Gas. *Chem. Eng. Process.* **2009**, *48* (1), 1−16.

(174) Nagarale, R. K.; Gohil, G. S.; Shahi, V. K. Recent Developments on Ion-Exchange Membranes and Electro-Membrane Processes. *Adv. Colloid Interface Sci.* **2006**, *119* (2−3), 97−130.

(175) Xie, T. Tunable Polymer Multi-Shape Memory Effect. *Nature* **2010**, *464* (7286), 267−270.

(176) Curtin, D. E.; Lousenberg, R. D.; Henry, T. J.; Tangeman, P. C.; Tisack, M. E. Advanced Materials for Improved Pemfc Performance and Life. *J. Power Sources* **2004**, *131* (1−2), 41−48.

(177) Holdcroft, S. Fuel Cell Catalyst Layers: A Polymer Science Perspective. *Chem. Mater.* **2014**, *26* (1), 381−393.

(178) Weber, A. Z.; Kusoglu, A. Unexplained Transport Resistances for Low-Loaded Fuel-Cell Catalyst Layers. *J. Mater. Chem. A* **2014**, *2* (41), 17207−17211.

(179) Kongkanand, A.; Mathias, M. F. The Priority and Challenge of High-Power Performance of Low-Platinum Proton-Exchange Membrane Fuel Cells. *J. Phys. Chem. Lett.* **2016**, *7* (7), 1127−1137.

(180) Yeager, H. L.; Kipling, B.; Dotson, R. L. Sodium-Ion Diffusion in Nafion Ion-Exchange Membranes. *J. Electrochem. Soc.* **1980**, *127* (2), 303−307.

(181) Gronowski, A. A.; Yeager, H. L. Factors Which Affect the Permselectivity of Nafion Membranes in Chloralkali Electrolysis 0.1. *J. Electrochem. Soc.* **1991**, *138* (9), 2690−2697.

(182) Momose, T.; Higuchi, N.; Arimoto, O.; Yamaguchi, K.; Walton, C. W. Effects of Low Concentration Levels of Calcium and Magnesium in the Feed Brine on the Performance of a Membrane Chloralkali Cell. *J. Electrochem. Soc.* **1991**, *138* (3), 735−741.

(183) Clapham, S. M.; Coms, F. D.; Fuller, T. J.; Zou, L. Degradation of Perfluorosulfonic Acid Membrane Water Permeance Via Formation of Sulfonic Acid Anhydrides. *ECS Trans.* **2013**, *50* (2), 1011−1020.

(184) Springer, T. E.; Zawodzinski, T. A.; Gottesfeld, S. Polymer Electrolyte Fuel-Cell Model. *J. Electrochem. Soc.* **1991**, *138* (8), 2334−2342.

(185) Pushpa, K. K.; Nandan, D.; Iyer, R. M. Thermodynamics of Water Sorption by Perfluorosulfonate (Nafion-117) and Polystyrene-Divinylbenzene Sulfonate (Dowex 50w) Ion-Exchange Resins at 298 ± 1-K. *J. Chem. Soc., Faraday Trans. 1* **1988**, *84*, 2047−2056.

(186) Saito, M.; Hayamizu, K.; Okada, T. Temperature Dependence of Ion and Water Transport in Perfluorinated Ionomer Membranes for Fuel Cells. *J. Phys. Chem. B* **2005**, *109* (8), 3112−3119.

(187) Kreuer, K. D.; Weppner, W.; Rabenau, A. Investigation of Proton-Conducting Solids. *Solid State Ionics* **1981**, *3−4* (Aug), 353−358.

(188) Gebel, G.; Aldebert, P.; Pineri, M. Swelling Study of Perfluorosulphonated Ionomer Membranes. *Polymer* **1993**, *34* (2), 333−339.

(189) Yeo, R. S. Dual Cohesive Energy Densities of Perfluorosulfonic Acid (Nafion) Membrane. *Polymer* **1980**, *21* (4), 432−435.

(190) Zhao, Q.; Carro, N.; Ryu, H. Y.; Benziger, J. Sorption and Transport of Methanol and Ethanol in H+-Nafion. *Polymer* **2012**, *53* (6), 1267−1276.

(191) Kidena, K.; Ohkubo, T.; Takimoto, N.; Ohira, A. Pfg-Nmr Approach to Determining the Water Transport Mechanism in Polymer Electrolyte Membranes Conditioned at Different Temperatures. *Eur. Polym. J.* **2010**, *46* (3), 450−455.

(192) Shi, S.; Liu, D.; Liu, D.; Tae, P.; Gao, C. Y.; Yan, L.; An, K.; Chen, X. Mechanical Properties and Microstructure Changes of Proton Exchange Membrane under Immersed Conditions. *Polym. Eng. Sci.* **2014**, *54* (10), 2215−2221.

(193) Collette, F. M.; Thominette, F.; Mendil-Jakani, H.; Gebel, G. Structure and Transport Properties of Solution-Cast Nafion (R) Membranes Subjected to Hygrothermal Aging. *J. Membr. Sci.* **2013**, *435*, 242−252.

(194) Kusoglu, A.; Kienitz, B. L.; Weber, A. Z. Understanding the Effects of Compression and Constraints on Water Uptake of Fuel-Cell Membranes. *J. Electrochem. Soc.* **2011**, *158* (12), B1504−B1514.

(195) Eisenberg, A. Clustering of Ions in Organic Polymers. A Theoretical Approach. *Macromolecules* **1970**, *3* (2), 147−154.

(196) Mauritz, K. A.; Rogers, C. E. A Water Sorption Isotherm Model for Ionomer Membranes with Cluster Morphologies. *Macromolecules* **1985**, *18* (3), 483−491.

(197) Dreyfus, B. Thermodynamic Properties of a Small Droplet of Water around an Ion in a Compressible Matrix. *J. Polym. Sci., Polym. Phys. Ed.* **1983**, *21* (11), 2337−2347.

(198) Hsu, W. Y.; Gierke, T. D. Elastic Theory for Ionic Clustering in Perfluorinated Ionomers. *Macromolecules* **1982**, *15* (1), 101−105.

(199) Choi, P.; Jalani, N. H.; Datta, R. Thermodynamics and Proton Transport in Nafion - I. Membrane Swelling, Sorption, and Ion-Exchange Equilibrium. *J. Electrochem. Soc.* **2005**, *152* (3), E84−E89.

(200) Choi, P.; Jalani, N. H.; Thampan, T. M.; Datta, R. Consideration of Thermodynamic, Transport, and Mechanical Properties in the Design of Polymer Electrolyte Membranes for Higher Temperature Fuel Cell Operation. *J. Polym. Sci., Part B: Polym. Phys.* **2006**, *44* (16), 2183−2200.

(201) Weber, A. Z.; Newman, J. Transport in Polymer-Electrolyte Membranes - Ii. Mathematical Model. *J. Electrochem. Soc.* **2004**, *151* (2), A311−A325.

(202) Freger, V. Elastic Energy in Microscopically Phase-Separated Swollen Polymer Networks. *Polymer* **2002**, *43* (1), 71−76.

(203) Freger, V. Hydration of Ionomers and Schroeder's Paradox in Nafion. *J. Phys. Chem. B* **2009**, *113* (1), 24−36.

(204) Kusoglu, A.; Santare, M. H.; Karlsson, A. M. Mechanics-Based Model for Non-Affine Swelling in Perfluorosulfonic Acid (Pfsa) Membranes. *Polymer* **2009**, *50* (11), 2481−2491.

(205) Kusoglu, A.; Weber, A. Z. Electrochemical/Mechanical Coupling in Ion-Conducting Soft Matter. *J. Phys. Chem. Lett.* **2015**, *6* (22), 4547−4552.

(206) Kreuer, K. D. The Role of Internal Pressure for the Hydration and Transport Properties of Ionomers and Polyelectrolytes. *Solid State Ionics* **2013**, *252* (0), 93−101.

(207) Mangiagli, P. M.; Ewing, C. S.; Xu, K.; Wang, Q.; Hickner, M. A. Dynamic Water Uptake of Flexible Ion-Containing Polymer Networks. *Fuel Cells* **2009**, *9* (4), 432−438.

(208) Eikerling, M. H.; Berg, P. Poroelectroelastic Theory of Water Sorption and Swelling in Polymer Electrolyte Membranes. *Soft Matter* **2011**, *7* (13), 5976−5990.

(209) Page, K. A.; Kusoglu, A.; Stafford, C. M.; Kim, S.; Kline, R. J.; Weber, A. Z. Confinement-Driven Increase in Ionomer Thin-Film Modulus. *Nano Lett.* **2014**, *14* (5), 2299−2304.

(210) Li, Y. L.; Nguyen, Q. T.; Buquet, C. L.; Langevin, D.; Legras, M.; Marais, S. Water Sorption in Nafion (R) Membranes Analyzed with an Improved Dual-Mode Sorption Model Structure/Property Relationships. *J. Membr. Sci.* **2013**, *439*, 1−11.

(211) Shi, S.; Weber, A. Z.; Kusoglu, A. Structure-Transport Relationship of Perfluorosulfonic-Acid Membranes in Different Cationic Forms. *Electrochim. Acta* **2016**, *220*, 517−528.

(212) Reucroft, P. J.; Rivin, D.; Schneider, N. S. Thermodynamics of Nafion (Tm)-Vapor Interactions. I. Water Vapor. *Polymer* **2002**, *43* (19), 5157−5161.

(213) Zawodzinski, T. A.; Sun, C.-N.; Bright, M.; Ghassemi, H.; DiNoto, V.; Fujiwara, T.; Maalouf, M.; Y, B. *Water Phenomena in PEM: Sorption, Swelling and Breakthrough Processes*, Trondheim, Norway, 2013.

(214) Escoubes, M.; Pineri, M.; Robens, E. Application of Coupled Thermal-Analysis Techniques to Thermodynamic Studies of Water Interactions with a Compressible Ionic Polymer Matrix. *Thermochim. Acta* **1984**, *82* (1), 149−160.

(215) Bai, Y.; Papandrew, A. B.; Zawodzinski, T. A. Hydrogen Bromine Redox Flow Battery Cell Performance Study. *ECS Meeting Abstracts* **2012**, *MA2012* (5), 398.

(216) Burnett, D. J.; Garcia, A. R.; Thielmann, F. Measuring Moisture Sorption and Diffusion Kinetics on Proton Exchange Membranes Using a Gravimetric Vapor Sorption Apparatus. *J. Power Sources* **2006**, *160* (1), 426−430.

(217) Kim, M. H.; Glinka, C. J.; Grot, S. A.; Grot, W. G. Sans Study of the Effects of Water Vapor Sorption on the Nanoscale Structure of Perfluorinated Sulfonic Acid (Nafion) Membranes. *Macromolecules* **2006**, *39* (14), 4775−4787.

(218) Fujimura, M.; Hashimoto, T.; Kawai, H. Small-Angle X-Ray-Scattering Study of Perfluorinated Ionomer Membranes 0.2. Models for Ionic Scattering Maximum. *Macromolecules* **1982**, *15* (1), 136−144.

(219) Orfino, F. P.; Holdcroft, S. The Morphology of Nafion: Are Ion Clusters Bridged by Channels or Single Ionic Sites? *J. New Mater. Electrochem. Syst.* **2000**, *3* (4), 285−290.

(220) Gebel, G.; Lambard, J. Small-Angle Scattering Study of Water-Swollen Perfluorinated Ionomer Membranes. *Macromolecules* **1997**, *30* (25), 7914−7920.

(221) James, P. J.; Elliott, J. A.; McMaster, T. J.; Newton, J. M.; Elliott, A. M. S.; Hanna, S.; Miles, M. J. Hydration of Nafion (R) Studied by Afm and X-Ray Scattering. *J. Mater. Sci.* **2000**, *35* (20), 5111−5119.

(222) Gruger, A.; Regis, A.; Schmatko, T.; Colomban, P. Nanostructure of Nafion (R) Membranes at Different States of Hydration - an Ir and Raman Study. *Vib. Spectrosc.* **2001**, *26* (2), 215−225.

(223) Dreyfus, B.; Gebel, G.; Aldebert, P.; Pineri, M.; Escoubes, M.; Thomas, M. Distribution of the Micelles in Hydrated Perfluorinated Ionomer Membranes from Sans Experiments. *J. Phys. (Paris)* **1990**, *51* (12), 1341−1354.

(224) Roche, E. J.; Pineri, M.; Duplessix, R. Phase-Separation in Perfluorosulfonate Ionomer Membranes. *J. Polym. Sci., Polym. Phys. Ed.* **1982**, *20* (1), 107−116.

(225) Haubold, H. G.; Vad, T.; Jungbluth, H.; Hiller, P. Nano Structure of Nafion: A Saxs Study. *Electrochim. Acta* **2001**, *46* (10−11), 1559−1563.

(226) Laporta, M.; Pegoraro, M.; Zanderighi, L. Perfluorosulfonated Membrane (Nafion): Ft-Ir Study of the State of Water with Increasing Humidity. *Phys. Chem. Chem. Phys.* **1999**, *1* (19), 4619−4628.

(227) Wadsö, L.; Jannasch, P. Water Vapor Sorption Thermodynamics of the Nafion Ionomer Membrane. *J. Phys. Chem. B* **2013**, *117* (28), 8561−8570.

(228) Shimoaka, T.; Wakai, C.; Sakabe, T.; Yamazaki, S.; Hasegawa, T. Hydration Structure of Strongly Bound Water on the Sulfonic Acid Group in a Nafion Membrane Studied by Infrared Spectroscopy and Quantum Chemical Calculation. *Phys. Chem. Chem. Phys.* **2015**, *17* (14), 8843−8849.

(229) de Almeida, S. H.; Kawano, Y. Thermal Behavior of Nafion Membranes. *J. Therm. Anal. Calorim.* **1999**, *58* (3), 569−577.

(230) Sun, L.; Thrasher, J. S. Studies of the Thermal Behavior of Nafion((R)) Membranes Treated with Aluminum(Iii). *Polym. Degrad. Stab.* **2005**, *89* (1), 43−49.

(231) Wilkie, C. A.; Thomsen, J. R.; Mittleman, M. L. Interaction of Poly(Methyl Methacrylate) and Nafions. *J. Appl. Polym. Sci.* **1991**, *42* (4), 901−909.

(232) Tiwari, S. K.; Nema, S. K.; Agarwal, Y. K. Thermolytic Degradation Behavior of Inorganic Ion-Exchanger Incorporated Nafion-117. *Thermochim. Acta* **1998**, *317* (2), 175−182.

(233) Pivovar, A. A.; Pivovar, B. S. Dynamic Behavior of Water within a Polymer Electrolyte Fuel Cell Membrane at Low Hydration Levels. *J. Phys. Chem. B* **2005**, *109* (2), 785−793.

(234) Perrin, J. C.; Lyonnard, S.; Volino, F. Quasielastic Neutron Scattering Study of Water Dynamics in Hydrated Nafion Membranes. *J. Phys. Chem. C* **2007**, *111* (8), 3393−3404.

(235) Sondheimer, S. J.; Bunce, N. J.; Lemke, M. E.; Fyfe, C. A. Acidity and Catalytic Activity of Nafion-H. *Macromolecules* **1986**, *19* (2), 339−343.

(236) Kusoglu, A.; Kwong, A.; Clark, K. T.; Gunterman, H. P.; Weber, A. Z. Water Uptake of Fuel-Cell Catalyst Layers. *J. Electrochem. Soc.* **2012**, *159* (9), F530−F535.

(237) Jalani, N. H.; Choi, P.; Datta, R. Teom: A Novel Technique for Investigating Sorption in Proton-Exchange Membranes. *J. Membr. Sci.* **2005**, *254* (1−2), 31−38.

(238) Mittelsteadt, C. K.; Staser, J. Simultaneous Water Uptake, Diffusivity and Permeability Measurement of Perfluorinated Sulfonic Acid Polymer Electrolyte Membranes. *ECS Trans.* **2011**, *41* (1), 101−121.

(239) Gates, C. M.; Newman, J. Equilibrium and Diffusion of Methanol and Water in a Nafion 117 Membrane. *AIChE J.* **2000**, *46* (10), 2076−2085.

(240) Futerko, P.; Hsing, I. M. Thermodynamics of Water Vapor Uptake in Perfluorosulfonic Acid Membranes. *J. Electrochem. Soc.* **1999**, *146* (6), 2049−2053.

(241) Takata, H.; Mizuno, N.; Nishikawa, M.; Fukada, S.; Yoshitake, M. Adsorption Properties of Water Vapor on Sulfonated Perfluoropolymer Membranes. *Int. J. Hydrogen Energy* **2007**, *32* (3), 371−379.

(242) Kim, S. Y.; Park, M. J.; Balsara, N. P.; Jackson, A. Confinement Effects on Watery Domains in Hydrated Block Copolymer Electrolyte Membranes. *Macromolecules* **2010**, *43* (19), 8128−8135.

(243) Park, M. J.; Balsara, N. P.; Jackson, A. Order-Disorder Transitions in Block Copolymer Electrolytes at Equilibrium with Humid Air. *Macromolecules* **2009**, *42* (17), 6808−6815.

(244) Ochi, S.; Kamishima, O.; Mizusaki, J.; Kawamura, J. Investigation of Proton Diffusion in Nafion (R) 117 Membrane by Electrical Conductivity and Nmr. *Solid State Ionics* **2009**, *180* (6−8), 580−584.

(245) Jalani, N. H.; Datta, R. The Effect of Equivalent Weight, Temperature, Cationic Forms, Sorbates, and Nanoinorganic Additives on the Sorption Behavior of Nafion (R). *J. Membr. Sci.* **2005**, *264* (1−2), 167−175.

(246) Morris, D. R.; Sun, X. D. Water-Sorption and Transport-Properties of Nafion-117-H. *J. Appl. Polym. Sci.* **1993**, *50* (8), 1445−1452.

(247) Legras, M.; Hirata, Y.; Nguyen, Q. T.; Langevin, D.; Metayer, M. Sorption and Diffusion Behaviors of Water in Nafion 117 Membranes with Different Counter Ions. *Desalination* **2002**, *147* (1−3), 351−357.

(248) Peron, J.; Mani, A.; Zhao, X. S.; Edwards, D.; Adachi, M.; Soboleva, T.; Shi, Z. Q.; Xie, Z.; Navessin, T.; Holdcroft, S. Properties of Nafion (R) Nr-211 Membranes for Pemfcs. *J. Membr. Sci.* **2010**, *356* (1−2), 44−51.

(249) Broka, K.; Ekdunge, P. Oxygen and Hydrogen Permeation Properties and Water Uptake of Nafion(R) 117 Membrane and Recast Film for Pem Fuel Cell. *J. Appl. Electrochem.* **1997**, *27* (2), 117−123.

(250) Thompson, E. L.; Jorne, J.; Gu, W. B.; Gasteiger, H. A. Pem Fuel Cell Operation at −20 Degrees C. I. Electrode and Membrane Water (Charge) Storage. *J. Electrochem. Soc.* **2008**, *155* (6), B625−B634.

(251) Pineri, M.; Volino, F.; Escoubes, M. Evidence for Sorption Desorption Phenomena During Thermal Cycling in Highly Hydrated Perfluorinated Membranes. *J. Polym. Sci., Polym. Phys. Ed.* **1985**, *23* (10), 2009−2020.

(252) Thampan, T.; Malhotra, S.; Tang, H.; Datta, R. Modeling of Conductive Transport in Proton-Exchange Membranes for Fuel Cells. *J. Electrochem. Soc.* **2000**, *147* (9), 3242−3250.

(253) Choi, P. H.; Datta, R. Sorption in Proton-Exchange Membranes - an Explanation of Schroeder's Paradox. *J. Electrochem. Soc.* **2003**, *150* (12), E601−E607.

(254) Weber, A. Z.; Newman, J. A Theoretical Study of Membrane Constraint in Polymer-Electrolyte Fuel Cells. *AIChE J.* **2004**, *50* (12), 3215−3226.

(255) Bass, M.; Freger, V. Hydration of Nafion and Dowex in Liquid and Vapor Environment: Schroeder's Paradox and Microstructure. *Polymer* **2008**, *49* (2), 497−506.

(256) Zhao, Q.; Majsztrik, P.; Benziger, J. Diffusion and Interfacial Transport of Water in Nafion. *J. Phys. Chem. B* **2011**, *115* (12), 2717−2727.

(257) Kusoglu, A.; Hexemer, A.; Jiang, R. C.; Gittleman, C. S.; Weber, A. Z. Effect of Compression on Pfsa-Ionomer Morphology and Predicted Conductivity Changes. *J. Membr. Sci.* **2012**, *421* (0), 283−291.

(258) Bass, M.; Freger, V. An Experimental Study of Schroeder's Paradox in Nafion and Dowex Polymer Electrolytes. *Desalination* **2006**, *199* (1−3), 277−279.

(259) Schroeder, P. Z. Uber Erstarrungs-Und Quellungerscheinungen Von Gelatine. *Z. Phys. Chem.* **1903**, *45*, 75−117.

(260) Davankov, V. A.; Pastukhov, A. V. Paradoxes of Thermodynamics of Swelling Equilibria of Polymers in Liquids and Vapors. *J. Phys. Chem. B* **2011**, *115* (51), 15188−15195.

(261) Musty, J. W. G.; Pattle, R. E.; Smith, P. J. A. The Swelling of Rubber in Liquid and Vapour (Schroeder's Paradox). *J. Appl. Chem.* **1966**, *16* (8), 221−222.

(262) Vallieres, C.; Winkelmann, D.; Roizard, D.; Favre, E.; Scharfer, P.; Kind, M. On Schroeder's Paradox. *J. Membr. Sci.* **2006**, *278* (1−2), 357−364.

(263) Hwang, G. S.; Kaviany, M.; Nam, J. H.; Kim, M. H.; Son, S. Y. Pore-Water Morphological Transitions in Polymer Electrolyte of a Fuel Cell. *J. Electrochem. Soc.* **2009**, *156* (10), B1192−B1200.

(264) Onishi, L.; Newman, J. Low Temperature Membrane Properties. *ECS Trans.* **2005**, *1* (6), 365−374.

(265) Jeck, S.; Scharfer, P.; Kind, M. Absence of Schroeder's Paradox: Experimental Evidence for Water-Swollen Nafion (R) Membranes. *J. Membr. Sci.* **2011**, *373* (1−2), 74−79.

(266) Bass, M.; Berman, A.; Singh, A.; Konovalov, O.; Freger, V. Surface Structure of Nafion in Vapor and Liquid. *J. Phys. Chem. B* **2010**, *114* (11), 3784−3790.

(267) Bass, M.; Berman, A.; Singh, A.; Konovalov, O.; Freger, V. Surface-Induced Micelle Orientation in Nafion Films. *Macromolecules* **2011**, *44* (8), 2893−2899.

(268) Slade, S.; Campbell, S. A.; Ralph, T. R.; Walsh, F. C. Ionic Conductivity of an Extruded Nafion 1100 Ew Series of Membranes. *J. Electrochem. Soc.* **2002**, *149* (12), A1556−A1564.

(269) Okada, T.; Xie, G.; Gorseth, O.; Kjelstrup, S.; Nakamura, N.; Arimura, T. Ion and Water Transport Characteristics of Nafion Membranes as Electrolytes. *Electrochim. Acta* **1998**, *43* (24), 3741−3747.

(270) Goswami, S.; Klaus, S.; Benziger, J. Wetting and Absorption of Water Drops on Nafion Films. *Langmuir* **2008**, *24* (16), 8627−8633.

(271) Van Nguyen, T.; Nguyen, M. V.; Lin, G. Y.; Rao, N. X.; Xie, X.; Zhu, D. M. Characterization of Surface Ionic Activity of Proton Conductive Membranes by Conductive Atomic Force Microscopy. *Electrochem. Solid-State Lett.* **2006**, *9* (2), A88−A91.

(272) Aleksandrova, E.; Hiesgen, R.; Eberhard, D.; Friedrich, K. A.; Kaz, T.; Roduner, E. Proton Conductivity Study of a Fuel Cell Membrane with Nanoscale Resolution. *ChemPhysChem* **2007**, *8* (4), 519−522.

(273) Noguchi, H.; Taneda, K.; Minowa, H.; Naohara, H.; Uosaki, K. Humidity-Dependent Structure of Surface Water on Perfluorosulfonated Ionomer Thin Film Studied by Sum Frequency Generation Spectroscopy. *J. Phys. Chem. C* **2010**, *114* (9), 3958−3961.

(274) Hiesgen, R.; Helmly, S.; Morawietz, T.; Yuan, X. Z.; Wang, H. J.; Friedrich, K. A. Atomic Force Microscopy Studies of Conductive Nanostructures in Solid Polymer Electrolytes. *Electrochim. Acta* **2013**, *110*, 292−305.

(275) He, Q.; Kusoglu, A.; Lucas, I. T.; Clark, K.; Weber, A. Z.; Kostecki, R. Correlating Humidity-Dependent Ionically Conductive Surface Area with Transport Phenomena in Proton-Exchange Membranes. *J. Phys. Chem. B* **2011**, *115* (40), 11650−11657.

(276) Aleksandrova, E.; Hiesgen, R.; Friedrich, K. A.; Roduner, E. Electrochemical Atomic Force Microscopy Study of Proton Conductivity in a Nafion Membrane. *Phys. Chem. Chem. Phys.* **2007**, *9* (21), 2735−2743.

(277) Kwon, O.; Kang, Y.; Wu, S.; Zhu, D.-M. Characteristics of Microscopic Proton Current Flow Distributions in Fresh and Aged Nafion Membranes. *J. Phys. Chem. B* **2010**, *114* (16), 5365−5370.

(278) O'Hayre, R.; Feng, G.; Nix, W. D.; Prinz, F. B. Quantitative Impedance Measurement Using Atomic Force Microscopy. *J. Appl. Phys.* **2004**, *96* (6), 3540−3549.

(279) Bussian, D. A.; O'Dea, J. R.; Metiu, H.; Buratto, S. K. Nanoscale Current Imaging of the Conducting Channels in Proton Exchange Membrane Fuel Cells. *Nano Lett.* **2007**, *7* (2), 227−232.

(280) Novitski, D.; Holdcroft, S. Determination of O-2 Mass Transport at the Pt I Pfsa Lonomer Interface under Reduced Relative Humidity. *ACS Appl. Mater. Interfaces* **2015**, *7* (49), 27314−27323.

(281) Tang, J.; Yuan, W.; Zhang, J.; Li, H.; Zhang, Y. Evidence for a Crystallite-Rich Skin on Perfluorosulfonate Ionomer Membranes. *RSC Adv.* **2013**, *3* (23), 8947−8952.

(282) Saito, M.; Tsuzuki, S.; Hayamizu, K.; Okada, T. Alcohol and Proton Transport in Perfluorinated Ionomer Membranes for Fuel Cells. *J. Phys. Chem. B* **2006**, *110* (48), 24410−24417.

(283) Uchiyama, T.; Kato, M.; Ikogi, Y.; Yoshida, T. Mechanical Degradation Mechanism of Membrane Electrode Assemblies in Buckling Test under Humidity Cycles. *J. Fuel Cell Sci. Technol.* **2012**, *9* (6), 06100510.1115/1.4007814

(284) Tang, Y. L.; Karlsson, A. M.; Santare, M. H.; Gilbert, M.; Cleghorn, S.; Johnson, W. B. An Experimental Investigation of Humidity and Temperature Effects on the Mechanical Properties of Perfluorosulfonic Acid Membrane. *Mater. Sci. Eng., A* **2006**, *425* (1−2), 297−304.

(285) Li, Y.; Dillard, D. A.; Lai, Y.-H.; Case, S. W.; Ellis, M. W.; Budinski, M. K.; Gittleman, C. S. Experimental Measurement of Stress and Strain in Nafion Membrane During Hydration Cycles. *J. Electrochem. Soc.* **2012**, *159* (2), B173−B184.

(286) Tang, Y. L.; Kusoglu, A.; Karlsson, A. M.; Santare, M. H.; Cleghorn, S.; Johnson, W. B. Mechanical Properties of a Reinforced Composite Polymer Electrolyte Membrane and Its Simulated Performance in Pem Fuel Cells. *J. Power Sources* **2008**, *175* (2), 817−825.

(287) Cleghorn, S.; Kolde, J.; Liu, W. In *Handbook of Fuel Cells − Fundamentals, Technology and Applications*; Wolf, V., Arnold, L., Hubert, G., Eds.; John Wiley & Sons, Ltd.: New York, 2003.

(288) Bauer, F.; Denneler, S.; Willert-Porada, M. Influence of Temperature and Humidity on the Mechanical Properties of Nafion [Registered Trademark] 117 Polymer Electrolyte Membrane. *J. Polym. Sci., Part B: Polym. Phys.* **2005**, *43* (7), 786−795.

(289) Sanders, E. H.; McGrady, K. A.; Wnek, G. E.; Edmondson, C. A.; Mueller, J. M.; Fontanella, J. J.; Suarez, S.; Greenbaum, S. G. Characterization of Electrosprayed Nafion Films. *J. Power Sources* **2004**, *129* (1), 55−61.

(290) Blumenthal, G.; Cappadonia, M.; Lehmann, M. Investigation of the Proton Transport in Nafion (R) Membranes as a Function of Direction, Temperature and Relative Humidity. *Ionics* **1996**, *2* (2), 102−106.

(291) Uchiyama, T.; Kato, M.; Yoshida, T. Buckling Deformation of Polymer Electrolyte Membrane and Membrane Electrode Assembly under Humidity Cycles. *J. Power Sources* **2012**, *206*, 37−46.

(292) Rodgers, M. P.; Berring, J.; Holdcroft, S.; Shi, Z. Q. The Effect of Spatial Confinement of Nafion (R) in Porous Membranes on Macroscopic Properties of the Membrane. *J. Membr. Sci.* **2008**, *321* (1), 100−113.

(293) Hink, S.; Henkensmeier, D.; Jang, J. H.; Kim, H. J.; Han, J.; Nam, S. W. Reduced in-Plane Swelling of Nafion by a Biaxial Modification Process. *Macromol. Chem. Phys.* **2015**, *216* (11), 1235−1243.

(294) Kolde, J.; Bahar, B.; Wilson, M. S.; Zawodzinki, T.; Gottesfeld, S. Proceedings of the First International Symposium on Proton Conducting Membrane. *Fuel Cells* **1995**, 193−201.

(295) Lin, J.; Wu, P.-H.; Wycisk, R.; Pintauro, P. Pem Fuel Cell Properties of Pre-Stretched Recast Nafion®. *ECS Trans.* **2008**, *16* (2), 1195−1204.

(296) Lin, J.; Wu, P. H.; Wycisk, R.; Pintauro, P. N.; Shi, Z. Q. Properties of Water in Prestretched Recast Nafion. *Macromolecules* **2008**, *41* (12), 4284−4289.

(297) Gong, X.; Bandis, A.; Tao, A.; Meresi, G.; Wang, Y.; Inglefield, P. T.; Jones, A. A.; Wen, W. Y. Self-Diffusion of Water, Ethanol and Decafluropentane in Perfluorosulfonate Ionomer by Pulse Field Gradient Nmr. *Polymer* **2001**, *42* (15), 6485−6492.

(298) Yeo, S. C.; Eisenberg, A. Physical-Properties and Supermolecular Structure of Perfluorinated Ion-Containing (Nafion) Polymers. *J. Appl. Polym. Sci.* **1977**, *21* (4), 875−898.

(299) Takamatsu, T.; Hashiyama, M.; Eisenberg, A. Sorption Phenomena in Nafion Membranes. *J. Appl. Polym. Sci.* **1979**, *24* (11), 2199−2220.

(300) Shantarovich, V. P.; Kevdina, I. B.; Yampolskii, Y. P.; Alentiev, A. Y. Positron Annihilation Lifetime Study of High and Low Free Volume Glassy Polymers: Effects of Free Volume Sizes on the Permeability and Permselectivity. *Macromolecules* **2000**, *33* (20), 7453−7466.

(301) Mohamed, H. F.; Kobayashi, Y.; Kuroda, C. S.; Ohira, A. Effects of Ion Exchange on the Free Volume and Oxygen Permeation in Nafion for Fuel Cells. *J. Phys. Chem. B* **2009**, *113* (8), 2247−2252.

(302) Mohamed, H. F.; Kuroda, S.; Kobayashi, Y.; Oshima, N.; Suzuki, R.; Ohira, A. Possible Presence of Hydrophilic So3h Nanoclusters on the Surface of Dry Ultrathin Nafion(R) Films: A Positron Annihilation Study. *Phys. Chem. Chem. Phys.* **2013**, *15* (5), 1518−1525.

(303) Mohamed, H. F. M.; Ito, K.; Kobayashi, Y.; Takimoto, N.; Takeoka, Y.; Ohira, A. Free Volume and Permeabilities of O-2 and H-2 in Nafion Membranes for Polymer Electrolyte Fuel Cells. *Polymer* **2008**, *49* (13−14), 3091−3097.

(304) Guillermo, A.; Gebel, G.; Mendil-Jakani, H.; Pinton, E. Nmr and Pulsed Field Gradient Nmr Approach of Water Sorption Properties in Nafion at Low Temperature. *J. Phys. Chem. B* **2009**, *113* (19), 6710−6717.

(305) Kusoglu, A.; Karlsson, A. M.; Santare, M. H. Structure-Property Relationship in Ionomer Membranes. *Polymer* **2010**, *51* (6), 1457−1464.

(306) Yoshida, H.; Miura, Y. Behavior of Water in Perfluorinated Ionomer Membranes Containing Various Monovalent Cations. *J. Membr. Sci.* **1992**, *68* (1−2), 1−10.

(307) Corti, H. R.; Nores-Pondal, F.; Buera, M. P. Low Temperature Thermal Properties of Nafion 117 Membranes in Water and Methanol-Water Mixtures. *J. Power Sources* **2006**, *161* (2), 799−805.

(308) Asaka, K.; Fujiwara, N.; Oguro, K.; Onishi, K.; Sewa, S. State of Water and Ionic Conductivity of Solid Polymer Electrolyte Membranes in Relation to Polymer Actuators. *J. Electroanal. Chem.* **2001**, *505* (1−2), 24−32.

(309) Thompson, E. L.; Capehart, T. W.; Fuller, T. J.; Jorne, J. Investigation of Low-Temperature Proton Transport in Nafion Using Direct Current Conductivity and Differential Scanning Calorimetry. *J. Electrochem. Soc.* **2006**, *153* (12), A2351−A2362.

(310) Lue, S. J.; Shieh, S. J. Water States in Perfluorosulfonic Acid Membranes Using Differential Scanning Calorimetry. *J. Macromol. Sci., Part B: Phys.* **2009**, *48* (1), 114−127.

(311) Gallagher, K. G.; Pivovar, B. S.; Fuller, T. F. Electro-Osmosis and Water Uptake in Polymer Electrolytes in Equilibrium with Water Vapor at Low Temperatures. *J. Electrochem. Soc.* **2009**, *156* (3), B330−B338.

(312) Cappadonia, M.; Erning, J. W.; Stimming, U. Proton Conduction of Nafion((R))-117 Membrane between 140 K and Room-Temperature. *J. Electroanal. Chem.* **1994**, *376* (1−2), 189−193.

(313) Nicotera, I.; Coppola, L.; Rossi, C. O.; Youssry, M.; Ranieri, G. A. Nmr Investigation of the Dynamics of Confined Water in Nafion-Based Electrolyte Membranes at Subfreezing Temperatures. *J. Phys. Chem. B* **2009**, *113* (42), 13935−13941.

(314) Ma, Z. R.; Jiang, R. C.; Myers, M. E.; Thompson, E. L.; Gittleman, C. S. Nmr Studies of Proton Transport in Fuel Cell Membranes at Sub-Freezing Conditions. *J. Mater. Chem.* **2011**, *21* (25), 9302−9311.

(315) Pineri, M.; Gebel, G.; Davies, R. J.; Diat, O. Water Sorption-Desorption in Nafion (R) Membranes at Low Temperature, Probed by Micro X-Ray Diffraction. *J. Power Sources* **2007**, *172* (2), 587−596.

(316) Plazanet, M.; Bartolini, P.; Torre, R.; Petrillo, C.; Sacchetti, F. Structure and Acoustic Properties of Hydrated Nafion Membranes. *J. Phys. Chem. B* **2009**, *113* (30), 10121−10127.

(317) Mendil-Jakani, H.; Davies, R. J.; Dubard, E.; Guillermo, A.; Gebel, G. Water Crystallization inside Fuel Cell Membranes Probed by X-Ray Scattering. *J. Membr. Sci.* **2011**, *369* (1−2), 148−154.

(318) Teocoli, F.; Paolone, A.; Palumbo, O.; Navarra, M. A.; Casciola, M.; Donnadio, A. Effects of Water Freezing on the Mechanical Properties of Nafion Membranes. *J. Polym. Sci., Part B: Polym. Phys.* **2012**, *50* (20), 1421−1425.

(319) Qiao, J. L.; Saito, M.; Hayamizu, K.; Okada, T. Degradation of Perfluorinated Ionomer Membranes for Pem Fuel Cells During Processing with H2o2. *J. Electrochem. Soc.* **2006**, *153* (6), A967−A974.

(320) Plazanet, M.; Sacchetti, F.; Petrillo, C.; Deme, B.; Bartolini, P.; Torre, R. Water in a Polymeric Electrolyte Membrane: Sorption/Desorption and Freezing Phenomena. *J. Membr. Sci.* **2014**, *453* (0), 419−424.

(321) Kreuer, K. D. On the Development of Proton Conducting Materials for Technological Applications. *Solid State Ionics* **1997**, *97* (1−4), 1−15.

(322) Freger, V.; Korin, E.; Wisniak, J.; Korngold, E. Transport Mechanism in Ion-Exchange Pervaporation Membranes: Dehydration of Water-Ethanol Mixture by Sodium Polyethylene Sulphonate Membranes. *J. Membr. Sci.* **1997**, *133* (2), 255−267.

(323) Park, Y. S.; Hatae, T.; Itoh, H.; Jang, M. Y.; Yamazaki, Y. High Proton-Conducting Nafion/Calcium Hydroxyphosphate Composite Membranes for Fuel Cells. *Electrochim. Acta* **2004**, *50* (2−3), 595−599.

(324) Fatyeyeva, K.; Chappey, C.; Poncin-Epaillard, F.; Langevin, D.; Valleton, J. M.; Marais, S. Composite Membranes Based on Nafion (R) and Plasma Treated Clay Charges: Elaboration and Water Sorption Investigations. *J. Membr. Sci.* **2011**, *369* (1−2), 155−166.

(325) Meyers, J. P.; Newman, J. Simulation of the Direct Methanol Fuel Cell - I. Thermodynamic Framework for a Multicomponent Membrane. *J. Electrochem. Soc.* **2002**, *149* (6), A710−A717.

(326) Choi, P.; Datta, R. Sorption in Proton-Exchange Membranes. An Explanation of Schroeder's Paradox. *J. Electrochem. Soc.* **2003**, *150* (12), E601−E607.

(327) Brunauer, S.; Emmett, P. H.; Teller, E. Adsorption of Gases in Multimolecular Layers. *J. Am. Chem. Soc.* **1938**, *60* (2), 309−319.

(328) Godino, M. P.; Barragan, V. M.; Villaluenga, J. P. G.; Izquierdo-Gil, M. A. Influence of the Cationic Form of an Ion-Exchange Membrane in the Permeability and Solubility of Methanol/Water Mixtures. *Sep. Purif. Technol.* **2015**, *148*, 10−14.

(329) Yeager, H. L.; Steck, A. Ion-Exchange Selectivity and Metal-Ion Separations with a Perfluorinated Cation-Exchange Polymer. *Anal. Chem.* **1979**, *51* (7), 862−865.

(330) Xie, G.; Okada, T. Water Transport Behavior in Nafion-117 Membranes. *J. Electrochem. Soc.* **1995**, *142* (9), 3057−3062.

(331) Flory, P. J. *Principles of Polymer Chemistry*; Cornell University Press: Ithaca, NY, 1953.

(332) Choi, P.; Jalani, N. H.; Datta, R. Thermodynamics and Proton Transport in Nafion - Ii. Proton Diffusion Mechanisms and Conductivity. *J. Electrochem. Soc.* **2005**, *152* (3), E123−E130.

(333) Kreuer, K. D.; Portale, G. A Critical Revision of the Nano-Morphology of Proton Conducting Ionomers and Polyelectrolytes for Fuel Cell Applications. *Adv. Funct. Mater.* **2013**, *23* (43), 5390−5397.

(334) Elliott, J. A.; Hanna, S.; Elliott, A. M. S.; Cooley, G. E. Interpretation of the Small-Angle X-Ray Scattering from Swollen and Oriented Perfluorinated Ionomer Membranes. *Macromolecules* **2000**, *33* (11), 4161−4171.

(335) Cable, K. M.; Mauritz, K. A.; Moore, R. B. Anisotropic Ionic Conductivity in Uniaxially Oriented Perfluorosulfonate Ionomers. *Chem. Mater.* **1995**, *7* (9), 1601−1603.

(336) Spernjak, D.; Mukherjee, P. P.; Mukundan, R.; Davey, J.; Hussey, D. S.; Jacobson, D.; Borup, R. L. Measurement of Water Content in Polymer Electrolyte Membranes Using High Resolution Neutron Imaging. *ECS Trans.* **2010**, *33* (1), 1451−1456.

(337) Borup, R. In *DoE 2010 Annual Merit Review Meeting*; available at http://www.hydrogen.energy.gov, 2011.

(338) Budinski, M. K.; Cook, A. Osmotic Pressure of Water in Nafion®. *Tsinghua Sci. Technol.* **2010**, *15* (4), 385−390.

(339) Colinart, T.; Perrin, J.-C.; Moyne, C. Application of a Micro/Macro-Homogenization Procedure to the Investigation of the Mechanical Behavior of Ionomer Membranes for Fuel Cells. *J. Polym. Sci., Part B: Polym. Phys.* **2014**, *52* (22), 1496−1509.

(340) Villaluenga, J. P. G.; Barragan, V. M.; Izquierdo-Gil, M. A.; Godino, M. P.; Seoane, B.; Ruiz-Bauza, C. Comparative Study of Liquid Uptake and Permeation Characteristics of Sulfonated Cation-Exchange Membranes in Water and Methanol. *J. Membr. Sci.* **2008**, *323* (2), 421−427.

(341) Park, M. J.; Nedoma, A. J.; Geissler, P. L.; Balsara, N. P.; Jackson, A.; Cookson, D. Humidity-Induced Phase Transitions in Ion-Containing Block Copolymer Membranes. *Macromolecules* **2008**, *41* (6), 2271−2277.

(342) Yeo, R. S.; Lee, J.; Chan, S. F. Swelling Behavior of Ion-Exchange Membranes in Non-Aqueous Solvents. *J. Electrochem. Soc.* **1980**, *127* (8), C405−C405.

(343) Doyle, M.; Lewittes, M. E.; Roelofs, M. G.; Perusich, S. A.; Lowrey, R. E. Relationship between Ionic Conductivity of Perfluorinated Ionomeric Membranes and Nonaqueous Solvent Properties. *J. Membr. Sci.* **2001**, *184* (2), 257−273.

(344) Affoune, A. M.; Yamada, A.; Umeda, M. Conductivity and Surface Morphology of Nafion Membrane in Water and Alcohol Environments. *J. Power Sources* **2005**, *148*, 9−17.

(345) Randova, A.; Bartovska, L.; Hovorka, S.; Poloncarzova, M.; Kolska, Z.; Izak, P. Application of the Group Contribution Approach to Nafion Swelling. *J. Appl. Polym. Sci.* **2009**, *111* (4), 1745−1750.

(346) Young, S. K.; Trevino, S. F.; Tan, N. C. B. Small-Angle Neutron Scattering Investigation of Structural Changes in Nafion Membranes Induced by Swelling with Various Solvents. *J. Polym. Sci., Part B: Polym. Phys.* **2002**, *40* (4), 387−400.

(347) Hwang, G. S.; Kaviany, M.; Gostick, J. T.; Kientiz, B.; Weber, A. Z.; Kim, M. H. Role of Water States on Water Uptake and Proton Transport in Nafion Using Molecular Simulations and Bimodal Network. *Polymer* **2011**, *52* (12), 2584−2593.

(348) Jorn, R.; Voth, G. A. Mesoscale Simulation of Proton Transport in Proton Exchange Membranes. *J. Phys. Chem. C* **2012**, *116* (19), 10476−10489.

(349) Daly, K. B.; Benziger, J. B.; Debenedetti, P. G.; Panagiotopoulos, A. Z. Molecular Dynamics Simulations of Water Sorption in a Perfluorosulfonic Acid Membrane. *J. Phys. Chem. B* **2013**, *117* (41), 12649−12660.

(350) Eikerling, M.; Kornyshev, A. A.; Stimming, U. Electrophysical Properties of Polymer Electrolyte Membranes: A Random Network Model. *J. Phys. Chem. B* **1997**, *101* (50), 10807−10820.

(351) Safiollah, M.; Melchy, P. E.; Berg, P.; Eikerling, M. Model of Water Sorption and Swelling in Polymer Electrolyte Membranes: Diagnostic Applications. *J. Phys. Chem. B* **2015**, *119* (25), 8165−8175.

(352) Gostick, J. T.; Weber, A. Z. Resistor-Network Modeling of Ionic Conduction in Polymer Electrolytes. *Electrochim. Acta* **2015**, *179* (0), 137−145.

(353) Gavish, N.; Jones, J.; Xu, Z. F.; Christlieb, A.; Promislow, K. Variational Models of Network Formation and Ion Transport: Applications to Perfluorosulfonate Ionomer Membranes. *Polymers* **2012**, *4* (1), 630−655.

(354) Li, X. F.; Li, F.; Shi, Y.; Chen, Q.; Sun, H. A. Predicting Water Uptake in Poly(Perfluorosulfonic Acids) Using Force Field Simulation Methods. *Phys. Chem. Chem. Phys.* **2010**, *12* (43), 14543−14552.

(355) Feng, S. L.; Savage, J.; Voth, G. A. Effects of Polymer Morphology on Proton Solvation and Transport in Proton-Exchange Membranes. *J. Phys. Chem. C* **2012**, *116* (36), 19104−19116.

(356) Savage, J.; Voth, G. A. Proton Solvation and Transport in Realistic Proton Exchange Membrane Morphologies. *J. Phys. Chem. C* **2016**, *120* (6), 3176−3186.

(357) Feng, S.; Voth, G. A. Proton Solvation and Transport in Hydrated Nafion. *J. Phys. Chem. B* **2011**, *115* (19), 5903−5912.

(358) Allen, F. I.; Comolli, L. R.; Kusoglu, A.; Modestino, M. A.; Minor, A. M.; Weber, A. Z. Morphology of Hydrated as-Cast Nafion Revealed through Cryo Electron Tomography. *ACS Macro Lett.* **2015**, *4* (1), 1−5.

(359) Elfring, G. J.; Struchtrup, H. Thermodynamic Considerations on the Stability of Water in Nafion. *J. Membr. Sci.* **2007**, *297* (1−2), 190−198.

(360) Modestino, M. A.; Kusoglu, A.; Hexemer, A.; Weber, A. Z.; Segalman, R. A. Controlling Nafion Structure and Properties Via Wetting Interactions. *Macromolecules* **2012**, *45* (11), 4681−4688.

(361) McLean, R. S.; Doyle, M.; Sauer, B. B. High-Resolution Imaging of Ionic Domains and Crystal Morphology in Ionomers Using Afm Techniques. *Macromolecules* **2000**, *33* (17), 6541−6550.

(362) Takimoto, N.; Wu, L.; Ohira, A.; Takeoka, Y.; Rikukawa, M. Hydration Behavior of Perfluorinated and Hydrocarbon-Type Proton Exchange Membranes: Relationship between Morphology and Proton Conduction. *Polymer* **2009**, *50* (2), 534−540.

(363) Affoune, A. M.; Yamada, A.; Umeda, M. Surface Observation of Solvent-Impregnated Nafion Membrane with Atomic Force Microscopy. *Langmuir* **2004**, *20* (17), 6965−6968.

(364) Rubatat, L.; Rollet, A. L.; Gebel, G.; Diat, O. Evidence of Elongated Polymeric Aggregates in Nafion. *Macromolecules* **2002**, *35* (10), 4050−4055.

(365) Barbi, V.; Funari, S. S.; Gehrke, R.; Scharnagl, N.; Stribeck, N. Nanostructure of Nafion Membrane Material as a Function of Mechanical Load Studied by Saxs. *Polymer* **2003**, *44* (17), 4853−4861.

(366) Rubatat, L.; Gebel, G.; Diat, O. Fibrillar Structure of Nafion: Matching Fourier and Real Space Studies of Corresponding Films and Solutions. *Macromolecules* **2004**, *37* (20), 7772−7783.

(367) van der Heijden, P. C.; Rubatat, L.; Diat, O. Orientation of Drawn Nafion at Molecular and Mesoscopic Scales. *Macromolecules* **2004**, *37* (14), 5327−5336.

(368) Elliott, J. A.; Wu, D. S.; Paddison, S. J.; Moore, R. B. A Unified Morphological Description of Nafion Membranes from Saxs and Mesoscale Simulations. *Soft Matter* **2011**, *7* (15), 6820−6827.

(369) Li, J.; Park, J. K.; Moore, R. B.; Madsen, L. A. Linear Coupling of Alignment with Transport in a Polymer Electrolyte Membrane. *Nat. Mater.* **2011**, *10* (7), 507−511.

(370) Roche, E. J.; Stein, R. S.; Russell, T. P.; Macknight, W. J. Small-Angle X-Ray-Scattering Study of Ionomer Deformation. *J. Polym. Sci., Polym. Phys. Ed.* **1980**, *18* (7), 1497−1512.

(371) Loppinet, B.; Gebel, G.; Williams, C. E. Small-Angle Scattering Study of Perfluorosulfonated Ionomer Solutions. *J. Phys. Chem. B* **1997**, *101* (10), 1884−1892.

(372) Falk, M. An Infrared Study of Water in Perfluorosulfonate (Nafion) Membranes. *Can. J. Chem.* **1980**, *58* (14), 1495−1501.

(373) Quezado, S.; Kwak, J. C. T.; Falk, M. An Infrared Study of Water-Ion Interactions in Perfluorosulfonate (Nafion) Membranes. *Can. J. Chem.* **1984**, *62* (5), 958−966.

(374) Lowry, S. R.; Mauritz, K. A. An Investigation of Ionic Hydration Effects in Perfluorosulfonate Ionomers by Fourier-Transform Infrared-Spectroscopy. *J. Am. Chem. Soc.* **1980**, *102* (14), 4665−4667.

(375) Chourdakis, N.; Voyiatzis, G. A. Molecular Orientation Study of Uniaxially Drawn Nafion Polymer Electrolyte Membranes Utilizing Polarized Uv-Raman Spectra. *J. Polym. Sci., Part B: Polym. Phys.* **2007**, *45* (17), 2509−2517.

(376) Deabate, S.; Huguet, P.; Morin, A.; Gebel, G.; Lanteri, Y.; Peng, Z.; Sutor, A. K. Raman Microspectroscopy as a Useful Tool for in Situ and Operando Studies of Water Transport in Perfluorosulfonic Membranes for Pemfcs. *Fuel Cells* **2014**, *14* (5), 677−693.

(377) Danilczuk, M.; Lin, L.; Schlick, S.; Hamrock, S. J.; Schaberg, M. S. Understanding the Fingerprint Region in the Infra-Red Spectra of Perfluorinated Ionomer Membranes and Corresponding Model Compounds: Experiments and Theoretical Calculations. *J. Power Sources* **2011**, *196* (20), 8216−8224.

(378) Kunimatsu, K.; Bae, B.; Miyatake, K.; Uchida, H.; Watanabe, M. Atr-Ftir Study of Water in Nafion Membrane Combined with Proton Conductivity Measurements During Hydration/Dehydration Cycle. *J. Phys. Chem. B* **2011**, *115* (15), 4315−4321.

(379) Hallinan, D. T.; Elabd, Y. A. Diffusion and Sorption of Methanol and Water in Nafion Using Time-Resolved Fourier Transform Infrared-Attenuated Total Reflectance Spectroscopy. *J. Phys. Chem. B* **2007**, *111* (46), 13221−13230.

(380) Hallinan, D. T.; Elabd, Y. A. Diffusion of Water in Nafion Using Time-Resolved Fourier Transform Infrared-Attenuated Total Reflectance Spectroscopy. *J. Phys. Chem. B* **2009**, *113* (13), 4257−4266.

(381) Buzzoni, R.; Bordiga, S.; Ricchiardi, G.; Spoto, G.; Zecchina, A. Interaction of H2o, Ch3oh, (Ch3)(2)O, Ch3cn, and Pyridine with the Superacid Perfluorosulfonic Membrane Nafion - an Ir and Raman-Study. *J. Phys. Chem.* **1995**, *99* (31), 11937−11951.

(382) Di Noto, V.; Piga, M.; Lavina, S.; Negro, E.; Yoshida, K.; Ito, R.; Furukawa, T. Structure, Properties and Proton Conductivity of Nanocomposite Membranes. *Electrochim. Acta* **2010**, *55* (4), 1431−1444.

(383) Ostrowska, J.; Narebska, A. Infrared Study of Hydration and Association of Functional-Groups in a Perfluorinated Nafion Membrane 0.1. *Colloid Polym. Sci.* **1983**, *261* (2), 93−98.

(384) Chen, Q.; Schmidt-Rohr, K. Backbone Dynamics of the Nafion Ionomer Studied by F-19-C-13 Solid-State Nmr. *Macromol. Chem. Phys.* **2007**, *208* (19−20), 2189−2203.

(385) Phillips, A. K.; Moore, R. B. Mechanical and Transport Property Modifications of Perfluorosulfonate Ionomer Membranes Prepared with Mixed Organic and Inorganic Counterions. *J. Polym. Sci., Part B: Polym. Phys.* **2006**, *44* (16), 2267−2277.

(386) Ghassemzadeh, L.; Marrony, M.; Barrera, R.; Kreuer, K. D.; Maier, J.; Muller, K. Chemical Degradation of Proton Conducting Perflurosulfonic Acid Ionomer Membranes Studied by Solid-State Nuclear Magnetic Resonance Spectroscopy. *J. Power Sources* **2009**, *186* (2), 334−338.

(387) Page, K. A.; Jarrett, W.; Moore, R. B. Variable Temperature F-19 Solid-State Nmr Study of the Effect of Electrostatic Interactions on Thermally-Stimulated Molecular Motions in Perfluorosulfonate Lonomers. *J. Polym. Sci., Part B: Polym. Phys.* **2007**, *45* (16), 2177−2186.

(388) Korzeniewski, C.; Adams, E.; Liu, D. Responses of Hydrophobic and Hydrophilic Groups in Nafion Differentiated by Least Squares Modeling of Infrared Spectra Recorded During Thin Film Hydration. *Appl. Spectrosc.* **2008**, *62* (6), 634−639.

(389) Buzzoni, R.; Bordiga, S.; Ricchiardi, G.; Lamberti, C.; Zecchina, A.; Bellussi, G. Interaction of Pyridine with Acidic (H-Zsm5, H-Beta, H-Mord Zeolites) and Superacidic (H-Nafion Membrane) Systems: An Ir Investigation. *Langmuir* **1996**, *12* (4), 930−940.

(390) Chen, Q.; Schmidt-Rohr, K. F-19 and C-13 Nmr Signal Assignment and Analysis in a Perfluorinated Ionomer (Nafion) by Two-Dimensional Solid-State Nmr. *Macromolecules* **2004**, *37* (16), 5995−6003.

(391) Blanchard, R. M.; Nuzzo, R. G. An Infrared Study of the Effects of Hydration on Cation-Loaded Nafion Thin Films. *J. Polym. Sci., Part B: Polym. Phys.* **2000**, *38* (11), 1512−1520.

(392) Negro, E.; Vittadello, M.; Vezzu, K.; Paddison, S. J.; Noto, V. The Influence of the Cationic Form and Degree of Hydration on the Structure of Nafion (Tm). *Solid State Ionics* **2013**, *252*, 84−92.

(393) De Almeida, N. E.; Paul, D. K.; Karan, K.; Goward, G. R. 1h Solid-State Nmr Study of Nanothin Nafion Films. *J. Phys. Chem. C* **2015**, *119* (3), 1280−1285.

(394) Fan, Y. F.; Tongren, D.; Cornelius, C. J. The Role of a Metal Ion within Nafion Upon Its Physical and Gas Transport Properties. *Eur. Polym. J.* **2014**, *50*, 271−278.

(395) Tabuchi, Y.; Ito, R.; Tsushima, S.; Hirai, S. Analysis of in Situ Water Transport in Nafion (R) by Confocal Micro-Raman Spectroscopy. *J. Power Sources* **2011**, *196* (2), 652−658.

(396) Lage, L. G.; Delgado, P. G.; Kawano, Y. Vibrational and Thermal Characterization of Nafion (R) Membranes Substituted by Alkaline Earth Cations. *Eur. Polym. J.* **2004**, *40* (7), 1309−1316.

(397) Bas, C.; Reymond, L.; Danerol, A. S.; Alberola, N. D.; Rossinot, E.; Flandin, L. Key Counter Ion Parameters Governing Polluted Nafion Membrane Properties. *J. Polym. Sci., Part B: Polym. Phys.* **2009**, *47* (14), 1381−1392.

(398) Awatani, T.; Midorikawa, H.; Kojima, N.; Ye, J. P.; Marcott, C. Morphology of Water Transport Channels and Hydrophobic Clusters in Nafion from High Spatial Resolution Afm-Ir Spectroscopy and Imaging. *Electrochem. Commun.* **2013**, *30*, 5−8.

(399) Liang, Z. X.; Chen, W. M.; Liu, J. G.; Wang, S. L.; Zhou, Z. H.; Li, W. Z.; Sun, G. Q.; Xin, Q. Ft-Ir Study of the Microstructure of Nafion((R)) Membrane. *J. Membr. Sci.* **2004**, *233* (1−2), 39−44.

(400) Shi, S.; Dursch, T. J.; Borup, R. L.; Weber, A. Z.; Kusoglu, A. Effect of Hygrothermal Ageing on Pfsa Ionomers' Structure/Property Relationship. *ECS Trans.* **2015**, *69* (17), 1017−1025.

(401) Di Noto, V.; Boaretto, N.; Negro, E.; Stallworth, P. E.; Lavina, S.; Giffin, G. A.; Greenbaum, S. G. Inorganic−Organic Membranes Based on Nafion, [(Zro2)·(Hfo2)0.25] and [(Sio2)·(Hfo2)0.28] Nanoparticles. Part Ii: Relaxations and Conductivity Mechanism. *Int. J. Hydrogen Energy* **2012**, *37* (7), 6215−6227.

(402) Di Noto, V.; Bettiol, M.; Bassetto, F.; Boaretto, N.; Negro, E.; Lavina, S.; Bertasi, F. Hybrid Inorganic-Organic Nanocomposite Polymer Electrolytes Based on Nafion and Fluorinated Tio2 for Pemfcs. *Int. J. Hydrogen Energy* **2012**, *37* (7), 6169−6181.

(403) Mendil-Jakani, H.; Pouget, S.; Gebel, G.; Pintauro, P. N. Insight into the Multiscale Structure of Pre-Stretched Recast Nafion (R) Membranes: Focus on the Crystallinity Features. *Polymer* **2015**, *63* (0), 99−107.

(404) Melchior, J. P.; Brauniger, T.; Wohlfarth, A.; Portale, G.; Kreuer, K. D. About the Interactions Controlling Nafion's Viscoelastic Properties and Morphology. *Macromolecules* **2015**, *48* (23), 8534−8545.

(405) Hwang, G. S.; Parkinson, D. Y.; Kusoglu, A.; MacDowell, A. A.; Weber, A. Z. Understanding Water Uptake and Transport in Nafion Using X-Ray Microtomography. *ACS Macro Lett.* **2013**, *2* (4), 288−291.

(406) Su, L.; Darling, R. M.; Gallagher, K. G.; Xie, W.; Thelen, J. L.; Badel, A. F.; Barton, J. L.; Cheng, K. J.; Balsara, N. P.; Moore, J. S.; et al. An Investigation of the Ionic Conductivity and Species Crossover of Lithiated Nafion 117 in Nonaqueous Electrolytes. *J. Electrochem. Soc.* **2016**, *163* (1), A5253−A5262.

(407) Kusoglu, A.; Cho, K. T.; Prato, R. A.; Weber, A. Z. Structural and Transport Properties of Nafion in Hydrobromic-Acid Solutions. *Solid State Ionics* **2013**, *252* (0), 68−74.

(408) Mauritz, K. A. Review and Critical Analyses of Theories of Aggregation in Ionomers. *J. Macromol. Sci., Polym. Rev.* **1988**, *28* (1), 65−98.

(409) Rollet, A.-L.; Diat, O.; Gebel, G. A New Insight into Nafion Structure. *J. Phys. Chem. B* **2002**, *106* (12), 3033−3036.

(410) Termonia, Y. Nanoscale Modeling of the Structure of Perfluorosulfonated Ionomer Membranes at Varying Degrees of Swelling. *Polymer* **2007**, *48* (5), 1435−1440.

(411) Schmidt-Rohr, K.; Chen, Q. Parallel Cylindrical Water Nanochannels in Nafion Fuel-Cell Membranes. *Nat. Mater.* **2008**, *7* (1), 75−83.

(412) Yamamoto, S.; Hyodo, S. A. A Computer Simulation Study of the Mesoscopic Structure of the Polyelectrolyte Membrane Nafion. *Polym. J.* **2003**, *35* (6), 519−527.

(413) Weber, A. Z.; Newman, J. Transport in Polymer-Electrolyte Membranes - I. Physical Model. *J. Electrochem. Soc.* **2003**, *150* (7), A1008−A1015.

(414) Kusoglu, A.; Santare, M. H.; Karlsson, A. M.; Cleghorn, S.; Johnson, W. B. Micromechanics Model Based on the Nanostructure of Pfsa Membranes. *J. Polym. Sci., Part B: Polym. Phys.* **2008**, *46* (22), 2404−2417.

(415) Starkweather, H. W. Crystallinity in Perfluorosulfonic Acid Ionomers and Related Polymers. *Macromolecules* **1982**, *15* (2), 320−323.

(416) Xie, G.; Okada, T. Characteristics of Water Transport in Relation to Microscopic Structure in Nafion Membranes. *J. Chem. Soc., Faraday Trans.* **1996**, *92* (4), 663−669.

(417) Divisek, J.; Eikerling, M.; V, M.; Schmitz, H.; Stimming, U.; Volfkovich, Y. M. A Study of Capillary Porous Structure and Sorption Properties of Nafion Proton-Exchange Membranes Swollen in Water. *J. Electrochem. Soc.* **1998**, *145* (8), 2677−2683.

(418) Kononenko, N. A.; Fomenko, M. A.; Volfkovich, Y. M. Structure of Perfluorinated Membranes Investigated by Method of Standard Contact Porosimetry. *Adv. Colloid Interface Sci.* **2015**, *222*, 425−435.

(419) Koter, S. The Equivalent Pore Radius of Charged Membranes from Electroosmotic Flow. *J. Membr. Sci.* **2000**, *166* (1), 127−135.

(420) Litt, M. A Reevaluation of Nafion(R) Morphology. *Abstr. Pap. Am. Chem. Soc.* **1997**, *213*, 33-Poly.

(421) Kong, X. Q.; Schmidt-Rohr, K. Water-Polymer Interfacial Area in Nafion: Comparison with Structural Models. *Polymer* **2011**, *52* (9), 1971−1974.

(422) Rubatat, L.; Diat, O. Stretching Effect on Nafion Fibrillar Nanostructure. *Macromolecules* **2007**, *40* (26), 9455−9462.

(423) O'Dea, J. R.; Economou, N. J.; Buratto, S. K. Surface Morphology of Nafion at Hydrated and Dehydrated Conditions. *Macromolecules* **2013**, *46* (6), 2267−2274.

(424) Cornet, N.; Diat, O.; Gebel, G.; Jousse, F.; Marsacq, D.; Mercier, R.; Pineri, M. Sulfonated Polyimide Membranes: A New Type of Ion-Conducting Membrane for Electrochemical Applications. *J. New Mater. Electrochem. Syst.* **2000**, *3* (1), 33−42.

(425) Lee, S.-J.; Yu, T. L.; Lin, H.-L.; Liu, W.-H.; Lai, C.-L. Solution Properties of Nafion in Methanol/Water Mixture Solvent. *Polymer* **2004**, *45* (8), 2853−2862.

(426) Lin, H.-L.; Yu, T. L.; Huang, C.-H.; Lin, T.-L. Morphology Study of Nafion Membranes Prepared by Solutions Casting. *J. Polym. Sci., Part B: Polym. Phys.* **2005**, *43* (21), 3044−3057.

(427) Ngo, T. T.; Yu, T. L.; Lin, H.-L. Influence of the Composition of Isopropyl Alcohol/Water Mixture Solvents in Catalyst Ink Solutions on Proton Exchange Membrane Fuel Cell Performance. *J. Power Sources* **2013**, *225* (0), 293−303.

(428) Luan, Y. H.; Zhang, Y. M.; Li, L.; Zhang, H.; Zhang, Q.; Huang, Z. X.; Liu, Y. G. Perfluorosulfonic Ionomer Solution in N,N-Dimethylformamide. *J. Appl. Polym. Sci.* **2008**, *107* (5), 2892−2898.

(429) Berrod, Q.; Lyonnard, S.; Guillermo, A.; Ollivier, J.; Frick, B.; Manseri, A.; Ameduri, B.; Gebel, G. Nanostructure and Transport Properties of Proton Conducting Self-Assembled Perfluorinated Surfactants: A Bottom-up Approach toward Pfsa Fuel Cell Membranes. *Macromolecules* **2015**, *48* (17), 6166−6176.

(430) Wang, C.; Krishnan, V.; Wu, D. S.; Bledsoe, R.; Paddison, S. J.; Duscher, G. Evaluation of the Microstructure of Dry and Hydrated Perfluorosulfonic Acid Ionomers: Microscopy and Simulations. *J. Mater. Chem. A* **2013**, *1* (3), 938−944.

(431) Yakovlev, S.; Balsara, N. P.; Downing, K. H. Insights on the Study of Nafion Nanoscale Morphology by Transmission Electron Microscopy. *Membranes (Basel, Switz.)* **2013**, *3* (4), 424−439.

(432) Roe, R. J. *Methods of X-Ray and Neutron Scattering in Polymer Science*; Oxford University Press: Oxford, U.K., 2000.

(433) Brown, E. N.; Rae, P. J.; Orler, E. B.; Gray, G. T.; Dattelbaum, D. M. The Effect of Crystallinity on the Fracture of Polytetrafluoroethylene (Ptfe). *Mater. Sci. Eng., C* **2006**, *26* (8), 1338−1343.

(434) Brown, E. N.; Rae, P. J.; Dattelbaum, D. M.; Clausen, B.; Brown, D. W. In-Situ Measurement of Crystalline Lattice Strains in Polytetrafluoroethylene. *Exp. Mech.* **2008**, *48* (1), 119−131.

(435) Schlick, S.; Gebel, G.; Pineri, M.; Volino, F. F-19 Nmr-Spectroscopy of Acid Nafion Membranes and Solutions. *Macromolecules* **1991**, *24* (12), 3517−3521.

(436) Noto, V.; Lavina, S.; Negro, E.; Vittadello, M.; Conti, F.; Piga, M.; Pace, G. Hybrid Inorganic-Organic Proton Conducting Membranes Based on Nafion and 5 Wt% of Mxoy (M = Ti, Zr, Hf, Ta and W). Part Ii: Relaxation Phenomena and Conductivity Mechanism. *J. Power Sources* **2009**, *187* (1), 57−66.

(437) Taylor, E. P.; Landis, F. A.; Page, K. A.; Moore, R. B. Counterion Dependent Crystallization Kinetics in Blends of a Perfluorosulfonate Ionomer with Poly(Vinylidene Fluoride). *Polymer* **2006**, *47* (21), 7425−7435.

(438) van der Heijden, P.; Bouzenad, F.; Diat, O. Birefringence Study of Drawn Nafion Films. *J. Polym. Sci., Part B: Polym. Phys.* **2004**, *42* (15), 2857−2870.

(439) Allahyarov, E.; Taylor, P. L. Simulation Study of the Correlation between Structure and Conductivity in Stretched Nafion. *J. Phys. Chem. B* **2009**, *113* (3), 610−617.

(440) Jiang, R.; Mittelsteadt, C. K.; Gittleman, C. S. Through-Plane Proton Transport Resistance of Membrane and Ohmic Resistance Distribution in Fuel Cells. *J. Electrochem. Soc.* **2009**, *156* (12), B1440−B1446.

(441) Lin, J.; Wycisk, R.; Pintauro, P. N.; Kellner, M. Stretched Recast Nafion for Direct Methanol Fuel Cells. *Electrochem. Solid-State Lett.* **2007**, *10* (1), B19–B22.

(442) Dorenbos, G.; Morohoshi, K. Pore Morphologies and Diffusion within Hydrated Polyelectrolyte Membranes: Homogeneous Vs Heterogeneous and Random Side Chain Attachment. *J. Chem. Phys.* **2013**, *138*, 064902.

(443) Malek, K.; Eikerling, M.; Wang, Q.; Liu, Z.; Otsuka, S.; Akizuki, K.; Abe, M. Nanophase Segregation and Water Dynamics in Hydrated Nafion: Molecular Modeling and Experimental Validation. *J. Chem. Phys.* **2008**, *129* (20), 204702.

(444) Gusler, G. M.; Cohen, Y. Equilibrium Swelling of Highly Cross-Linked Polymeric Resins. *Ind. Eng. Chem. Res.* **1994**, *33* (10), 2345–2357.

(445) Blake, N. P.; Petersen, M. K.; Voth, G. A.; Metiu, H. Structure of Hydrated Na-Nafion Polymer Membranes. *J. Phys. Chem. B* **2005**, *109* (51), 24244–24253.

(446) Devanathan, R.; Venkatnathan, A.; Dupuis, M. Atomistic Simulation of Nafion Membrane. 2. Dynamics of Water Molecules and Hydronium Ions. *J. Phys. Chem. B* **2007**, *111* (45), 13006–13013.

(447) Devanathan, R.; Venkatnathan, A.; Dupuis, M. Atomistic Simulation of Nafion Membrane: I. Effect of Hydration on Membrane Nanostructure. *J. Phys. Chem. B* **2007**, *111* (28), 8069–8079.

(448) Venkatnathan, A.; Devanathan, R.; Dupuis, M. Atomistic Simulations of Hydrated Nafion and Temperature Effects on Hydronium Ion Mobility. *J. Phys. Chem. B* **2007**, *111* (25), 7234–7244.

(449) Cui, S.; Liu, J.; Selvan, M. E.; Paddison, S. J.; Keffer, D. J.; Edwards, B. J. Comparison of the Hydration and Diffusion of Protons in Perfluorosulfonic Acid Membranes with Molecular Dynamics Simulations. *J. Phys. Chem. B* **2008**, *112* (42), 13273–13284.

(450) Elliott, J. A.; Hanna, S.; Elliott, A. M. S.; Cooley, G. E. Atomistic Simulation and Molecular Dynamics of Model Systems for Perfluorinated Ionomer Membranes. *Phys. Chem. Chem. Phys.* **1999**, *1* (20), 4855–4863.

(451) Vishnyakov, A.; Neimark, A. V. Molecular Dynamics Simulation of Microstructure and Molecular Mobilities in Swollen Nafion Membranes. *J. Phys. Chem. B* **2001**, *105* (39), 9586–9594.

(452) Cui, S.; Liu, J.; Selvan, M. E.; Keffer, D. J.; Edwards, B. J.; Steele, W. V. A Molecular Dynamics Study of a Nafion Polyelectrolyte Membrane and the Aqueous Phase Structure for Proton Transport. *J. Phys. Chem. B* **2007**, *111* (9), 2208–2218.

(453) Devanathan, R.; Idupulapati, N.; Baer, M. D.; Mundy, C. J.; Dupuis, M. Ab Initio Molecular Dynamics Simulation of Proton Hopping in a Model Polymer Membrane. *J. Phys. Chem. B* **2013**, *117* (51), 16522–16529.

(454) Choe, Y. K.; Tsuchida, E.; Ikeshoji, T.; Yamakawa, S.; Hyodo, S. A. Nature of Water Transport and Electro-Osmosis in Nafion: Insights from First-Principles Molecular Dynamics Simulations under an Electric Field. *J. Phys. Chem. B* **2008**, *112* (37), 11586–11594.

(455) Habenicht, B. F.; Paddison, S. J.; Tuckerman, M. E. Ab Initio Molecular Dynamics Simulations Investigating Proton Transfer in Perfluorosulfonic Acid Functionalized Carbon Nanotubes. *Phys. Chem. Chem. Phys.* **2010**, *12* (31), 8728–8732.

(456) Tse, Y. L. S.; Herring, A. M.; Kim, K.; Voth, G. A. Molecular Dynamics Simulations of Proton Transport in 3m and Nafion Perfluorosulfonic Acid Membranes. *J. Phys. Chem. C* **2013**, *117* (16), 8079–8091.

(457) Petersen, M. K.; Wang, F.; Blake, N. P.; Metiu, H.; Voth, G. A. Excess Proton Solvation and Delocalization in a Hydrophilic Pocket of the Proton Conducting Polymer Membrane Nafion. *J. Phys. Chem. B* **2005**, *109* (9), 3727–3730.

(458) Petersen, M. K.; Voth, G. A. Characterization of the Solvation and Transport of the Hydrated Proton in the Perfluorosulfonic Acid Membrane Nafion. *J. Phys. Chem. B* **2006**, *110* (37), 18594–18600.

(459) Knight, C.; Voth, G. A. The Curious Case of the Hydrated Proton. *Acc. Chem. Res.* **2012**, *45* (1), 101–109.

(460) Wescott, J. T.; Qi, Y.; Subramanian, L.; Capehart, T. W. Mesoscale Simulation of Morphology in Hydrated Perfluorosulfonic Acid Membranes. *J. Chem. Phys.* **2006**, *124* (13), 134702.

(461) Krueger, J. J.; Simon, P. P.; Ploehn, H. J. Phase Behavior and Microdomain Structure in Perfluorosulfonated Ionomers Via Self-Consistent Mean Field Theory. *Macromolecules* **2002**, *35* (14), 5630–5639.

(462) Paddison, S. J.; Zawodzinski, T. A. Molecular Modeling of the Pendant Chain in Nafion (R). *Solid State Ionics* **1998**, *113*, 333–340.

(463) Paddison, S. J.; Paul, R.; Zawodzinski, T. A. A Statistical Mechanical Model of Proton and Water Transport in a Proton Exchange Membrane. *J. Electrochem. Soc.* **2000**, *147* (2), 617–626.

(464) Paddison, S. J.; Paul, R.; Zawodzinski, T. A. Proton Friction and Diffusion Coefficients in Hydrated Polymer Electrolyte Membranes: Computations with a Non-Equilibrium Statistical Mechanical Model. *J. Chem. Phys.* **2001**, *115* (16), 7753–7761.

(465) Paddison, S. J.; Paul, R. The Nature of Proton Transport in Fully Hydrated Nafion (R). *Phys. Chem. Chem. Phys.* **2002**, *4* (7), 1158–1163.

(466) Vishnyakov, A.; Neimark, A. V. Molecular Simulation Study of Nafion Membrane Solvation in Water and Methanol. *J. Phys. Chem. B* **2000**, *104* (18), 4471–4478.

(467) Karo, J.; Aabloo, A.; Thomas, J. O.; Brandell, D. Molecular Dynamics Modeling of Proton Transport in Nation and Hylton Nanostructures. *J. Phys. Chem. B* **2010**, *114* (18), 6056–6064.

(468) Promislow, K.; Jones, J.; Xu, Z.; Gavish, N.; Christlieb, A. Variational Models of Pore Networks in Ionomer Membranes: The Role of Electrostatics. *ECS Trans.* **2013**, *50* (2), 161–173.

(469) Dorenbos, G.; Morohoshi, K. Modeling Gas Permeation through Membranes by Kinetic Monte Carlo: Applications to H2, O2, and N2 in Hydrated Nafion(R). *J. Chem. Phys.* **2011**, *134* (4), 044133.

(470) Habenicht, B. F.; Paddison, S. J.; Tuckerman, M. E. The Effects of the Hydrophobic Environment on Proton Mobility in Perfluorosulfonic Acid Systems: An Ab Initio Molecular Dynamics Study. *J. Mater. Chem.* **2010**, *20* (30), 6342–6351.

(471) Sung, D. W.; Kim, Y. G.; Bae, Y. C. Ionic Conductivities of Perfluorosulfonic Acid Membrane by Group Contribution Method. *Polymer* **2009**, *50* (15), 3686–3692.

(472) Brandell, D.; Karo, J.; Liivat, A.; Thomas, J. O. Molecular Dynamics Studies of the Nafion (R), Dow (R) and Aciplex (R) Fuel-Cell Polymer Membrane Systems. *J. Mol. Model.* **2007**, *13* (10), 1039–1046.

(473) Bae, B.; Kim, D.; Kim, H. J.; Lim, T. H.; Oh, I. H.; Ha, H. Y. Surface Characterization of Argon-Plasma-Modified Perfluorosulfonic Acid Membranes. *J. Phys. Chem. B* **2006**, *110* (9), 4240–4246.

(474) Chen, C.; Levitin, G.; Hess, D. W.; Fuller, T. F. Xps Investigation of Nafion (R) Membrane Degradation. *J. Power Sources* **2007**, *169* (2), 288–295.

(475) Chen, C.; Fuller, T. F. Xps Analysis of Polymer Membrane Degradation in Pemfcs. *J. Electrochem. Soc.* **2009**, *156* (10), B1218–B1224.

(476) Liang, Z. X.; Zhao, T. S.; Xu, C.; Xu, J. B. Microscopic Characterizations of Membrane Electrode Assemblies Prepared under Different Hot-Pressing Conditions. *Electrochim. Acta* **2007**, *53* (2), 894–902.

(477) Lee, W.; Prinz, F. B.; Chen, X.; Nonnenmann, S.; Bonnell, D. A.; O'Hayre, R. P. Nanoscale Impedance and Complex Properties in Energy-Related Systems. *MRS Bull.* **2012**, *37* (07), 659–667.

(478) Hiesgen, R.; Wehl, I.; Aleksandrova, E.; Roduner, E.; Bauder, A.; Friedrich, K. A. Nanoscale Properties of Polymer Fuel Cell Materials-a Selected Review. *Int. J. Energy Res.* **2010**, *34* (14), 1223–1238.

(479) O'Hayre, R.; Lee, M.; Prinz, F. B. Ionic and Electronic Impedance Imaging Using Atomic Force Microscopy. *J. Appl. Phys.* **2004**, *95* (12), 8382–8392.

(480) Hiesgen, R.; Aleksandrova, E.; Meichsner, G.; Wehl, I.; Roduner, E.; Friedrich, K. A. High-Resolution Imaging of Ion Conductivity of Nafion (R) Membranes with Electrochemical Atomic Force Microscopy. *Electrochim. Acta* **2009**, *55* (2), 423–429.

(481) Xie, X.; Kwon, O.; Zhu, D.-M.; Nguyen Trung, V.; Lin, G. Local Probe and Conduction Distribution of Proton Exchange Membranes. *J. Phys. Chem. B* **2007**, *111* (22), 6134−6140.

(482) Kang, Y.; Kwon, O.; Xie, X.; Zhu, D.-M. Conductance Mapping of Proton Exchange Membranes by Current Sensing Atomic Force Microscopy. *J. Phys. Chem. B* **2009**, *113* (45), 15040−15046.

(483) Ge, S. H.; Li, X. G.; Yi, B. L.; Hsing, I. M. Absorption, Desorption, and Transport of Water in Polymer Electrolyte Membranes for Fuel Cells. *J. Electrochem. Soc.* **2005**, *152* (6), A1149−A1157.

(484) Majsztrik, P. W.; Satterfield, M. B.; Bocarsly, A. B.; Benziger, J. B. Water Sorption, Desorption and Transport in Nafion Membranes. *J. Membr. Sci.* **2007**, *301* (1−2), 93−106.

(485) Monroe, C. W.; Romero, T.; Merida, W.; Eikerling, M. A Vaporization-Exchange Model for Water Sorption and Flux in Nafion. *J. Membr. Sci.* **2008**, *324* (1−2), 1−6.

(486) Kienitz, B.; Yamada, H.; Nonoyama, N.; Weber, A. Z. Interfacial Water Transport Effects in Proton-Exchange Membranes. *J. Fuel Cell Sci. Technol.* **2011**, *8* (1), 011013.

(487) Kongkanand, A. Interfacial Water Transport Measurements in Nafion Thin Films Using a Quartz-Crystal Microbalance. *J. Phys. Chem. C* **2011**, *115* (22), 11318−11325.

(488) Daly, K. B.; Benziger, J. B.; Panagiotopoulos, A. Z.; Debenedetti, P. G. Molecular Dynamics Simulations of Water Permeation across Nafion Membrane Interfaces. *J. Phys. Chem. B* **2014**, *118* (29), 8798−8807.

(489) Novitski, D.; Xie, Z.; Holdcroft, S. Time-Dependent Mass Transport for O-2 Reduction at the Pt | Perfluorosulfonic Acid Ionomer Interface. *ECS Electrochem. Lett.* **2015**, *4* (1), F9−F12.

(490) Kudo, K.; Jinnouchi, R.; Morimoto, Y. Humidity and Temperature Dependences of Oxygen Transport Resistance of Nafion Thin Film on Platinum Electrode. *Electrochim. Acta* **2016**, *209*, 682−690.

(491) Gargas, D. J.; Bussian, D. A.; Buratto, S. K. Investigation of the Connectivity of Hydrophilic Domains in Nafion Using Electrochemical Pore-Directed Nanolithography. *Nano Lett.* **2005**, *5* (11), 2184−2187.

(492) Krtil, P.; Trojanek, A.; Samec, Z. Kinetics of Water Sorption in Nafion Thin Films - Quartz Crystal Microbalance Study. *J. Phys. Chem. B* **2001**, *105* (33), 7979−7983.

(493) Kusoglu, A.; Kushner, D.; Paul, D. K.; Karan, K.; Hickner, M. A.; Weber, A. Z. Impact of Substrate and Processing on Confinement of Nafion Thin Films. *Adv. Funct. Mater.* **2014**, *24* (30), 4763−4774.

(494) Ogata, Y.; Kawaguchi, D.; Yamada, N. L.; Tanaka, K. Multistep Thickening of Nafion Thin Films in Water. *ACS Macro Lett.* **2013**, *2* (10), 856−859.

(495) Bird, R. B.; Stewart, W. E.; Lightfoot, E. N. *Transport Phenomena*; J. Wiley: New York, 2007.

(496) Zelsmann, H. R.; Pineri, M.; Thomas, M.; Escoubes, M. Water Self-Diffusion Coefficient Determination in an Ion-Exchange Membrane by Optical Measurement. *J. Appl. Polym. Sci.* **1990**, *41* (7−8), 1673−1684.

(497) Caulk, D. A.; Brenner, A. M.; Clapham, S. M. A Steady Permeation Method for Measuring Water Transport Properties of Fuel Cell Membranes. *J. Electrochem. Soc.* **2012**, *159* (9), F518−F529.

(498) Fuller, T. F. Ph.D. Dissertation, University of California: Berkeley, CA, 1992.

(499) Onishi, L. M.; Prausnitz, J. M.; Newman, J. Steady-State Diffusion Coefficients for Water in Nafion in the Absence of Inert Gas. *J. Electrochem. Soc.* **2012**, *159* (6), B754−B760.

(500) Schneider, N. S.; Rivin, D. Steady State Analysis of Water Vapor Transport in Ionomers. *Polymer* **2010**, *51* (3), 671−678.

(501) Ye, X. H.; LeVan, M. D. Water Transport Properties of Nafion Membranes - Part I. Single-Tube Membrane Module for Air Drying. *J. Membr. Sci.* **2003**, *221* (1−2), 147−161.

(502) Zawodzinski, T. A.; Neeman, M.; Sillerud, L. O.; Gottesfeld, S. Determination of Water Diffusion-Coefficients in Perfluorosulfonate Ionomeric Membranes. *J. Phys. Chem.* **1991**, *95* (15), 6040−6044.

(503) Tsushima, S.; Teranishi, K.; Hirai, S. Water Diffusion Measurement in Fuel-Cell Spe Membrane by Nmr. *Energy* **2005**, *30* (2−4), 235−245.

(504) Kreuer, K.-D.; Dippel, T.; Meyer, W.; Maier, J. Nafion® Membranes: Molecular Diffusion, Proton Conductivity and Proton Conduction Mechanism. *MRS Online Proc. Libr.* **1992**, *293* (273), 210.

(505) Buchi, F. N.; Scherer, G. G. Investigation of the Transversal Water Profile in Nafion Membranes in Polymer Electrolyte Fuel Cells. *J. Electrochem. Soc.* **2001**, *148* (3), A183−A188.

(506) Hussey, D. S.; Spernjak, D.; Weber, A. Z.; Mukundan, R.; Fairweather, J.; Brosha, E. L.; Davey, J.; Spendelow, J. S.; Jacobson, D. L.; Borup, R. L. Accurate Measurement of the through-Plane Water Content of Proton-Exchange Membranes Using Neutron Radiography. *J. Appl. Phys.* **2012**, *112* (10), 10490610.1063/1.4767118

(507) Van Nguyen, T.; Vanderborgh, N. The Rate of Isothermal Hydration of Polyperfluorosulfonic Acid Membranes. *J. Membr. Sci.* **1998**, *143* (1−2), 235−248.

(508) Rivin, D.; Kendrick, C. E.; Gibson, P. W.; Schneider, N. S. Solubility and Transport Behavior of Water and Alcohols in Nafion (Tm). *Polymer* **2001**, *42* (2), 623−635.

(509) Isopo, A.; Albertini, V. R. An Original Laboratory X-Ray Diffraction Method for in Situ Investigations on the Water Dynamics in a Fuel Cell Proton Exchange Membrane. *J. Power Sources* **2008**, *184* (1), 23−28.

(510) Yeager, H. L.; Steck, A. Cation and Water Diffusion in Nafion Ion-Exchange Membranes - Influence of Polymer Structure. *J. Electrochem. Soc.* **1981**, *128* (9), 1880−1884.

(511) Ohkubo, T.; Kidena, K.; Ohira, A. Determination of a Micron-Scale Restricted Structure in a Perfluorinated Membrane from Time-Dependent Self-Diffusion Measurements. *Macromolecules* **2008**, *41* (22), 8688−8693.

(512) Kidena, K. Anisotropic Diffusion of Water in Perfluorosulfonic Acid Membrane and Hydrocarbon Membranes. *J. Membr. Sci.* **2008**, *323* (1), 201−206.

(513) Freger, V.; Korin, E.; Wisniak, J.; Korngold, E.; Ise, M.; Kreuer, K. D. Diffusion of Water and Ethanol in Ion-Exchange Membranes: Limits of the Geometric Approach. *J. Membr. Sci.* **1999**, *160* (2), 213−224.

(514) Jayakody, J. R. P.; Stallworth, P. E.; Mananga, E. S.; Farrington-Zapata, J.; Greenbaum, S. G. High Pressure Nmr Study of Water Self-Diffusion in Nafion-117 Membrane. *J. Phys. Chem. B* **2004**, *108* (14), 4260−4262.

(515) Suresh, G.; Scindia, Y. M.; Pandey, A. K.; Goswami, A. Isotopic and Ion-Exchange Kinetics in the Nafion-117 Membrane. *J. Phys. Chem. B* **2004**, *108* (13), 4104−4110.

(516) Suresh, G.; Scindia, Y. M.; Pandey, A. K.; Goswami, A. Self-Diffusion Coefficient of Water in Nafion-117 Membrane with Different Monovalent Counterions: A Radiotracer Study. *J. Membr. Sci.* **2005**, *250* (1−2), 39−45.

(517) Suresh, G.; Pandey, A. K.; Goswami, A. Self-Diffusion Coefficients of Water in Nafion-117 Membrane with Multivalent Counterions. *J. Membr. Sci.* **2006**, *284* (1−2), 193−197.

(518) Suresh, G.; Pandey, A. K.; Goswami, A. Permeability of Water in Poly(Perfluorosulfonic) Acid Membrane with Different Counterions. *J. Membr. Sci.* **2007**, *295* (1−2), 21−27.

(519) Maalouf, M.; Sun, C. N.; Pyle, B.; Emery, M.; Haugen, G. M.; Hamrock, S. J.; Zawodzinski, T. A. Factors Enabling High Mobility of Protons and Water in Perfluorosulfonate Membranes under Low Hydration Conditions. *Int. J. Hydrogen Energy* **2014**, *39* (6), 2795−2800.

(520) Motupally, S.; Becker, A. J.; Weidner, J. W. Diffusion of Water in Nafion 115 Membranes. *J. Electrochem. Soc.* **2000**, *147* (9), 3171−3177.

(521) Onishi, L. Ph.D. Dissertation, University of California: Berkeley, CA, 2009.

(522) MacMillan, B.; Sharp, A. R.; Armstrong, R. L. An Nmr Investigation of the Dynamical Characteristics of Water Absorbed in Nafion. *Polymer* **1999**, *40* (10), 2471−2480.

(523) Ye, G.; Hayden, C. A.; Goward, G. R. Proton Dynamics of Nafion and Nafion/Sio2 Composites by Solid State Nmr and Pulse Field Gradient Nmr. *Macromolecules* **2007**, *40* (5), 1529–1537.

(524) Slade, R. C. T.; Hardwick, A.; Dickens, P. G. Investigation of H + Motion in Nafion Film by Pulsed H-1-Nmr and Ac Conductivity Measurements. *Solid State Ionics* **1983**, *9–10* (Dec), 1093–1098.

(525) Li, J.; Wilmsmeyer, K. G.; Madsen, L. A. Anisotropic Diffusion and Morphology in Perfluorosulfonate Ionomers Investigated by Nmr. *Macromolecules* **2009**, *42* (1), 255–262.

(526) Neves, L. A.; Sebastiao, P. J.; Coelhoso, I. M.; Crespo, J. G. Proton Nmr Relaxometry Study of Nafion Membranes Modified with Ionic Liquid Cations. *J. Phys. Chem. B* **2011**, *115* (27), 8713–8723.

(527) Boyle, N. G.; Mcbrierty, V. J.; Douglass, D. C. A Study of the Behavior of Water in Nafion Membranes. *Macromolecules* **1983**, *16* (1), 75–80.

(528) MacMillan, B.; Sharp, A. R.; Armstrong, R. L. Nmr Relaxation in Nafion - the Low Temperature Regime. *Polymer* **1999**, *40* (10), 2481–2485.

(529) Perrin, J. C.; Lyonnard, S.; Guillermo, A.; Levitz, P. Water Dynamics in Ionomer Membranes by Field-Cycling Nmr Relaxometry. *Magn. Reson. Imaging* **2007**, *25* (4), 501–504.

(530) Slade, R. C. T.; Barker, J.; Strange, J. H. Protonic Conduction and H-1 Self-Diffusion in Nafion Film Studied by Ac Conductivity and Pulsed Field Gradient Nmr Techniques. *Solid State Ionics* **1989**, *35* (1–2), 11–15.

(531) Suresh, G.; Sodaye, S.; Scindia, Y. M.; Pandey, A. K.; Goswami, A. Study on Physical and Electrostatic Interactions of Counterions in Poly(Perfluorosulfonic) Acid Matrix: Characterization of Diffusion Properties of Membrane Using Radiotracers. *Electrochim. Acta* **2007**, *52* (19), 5968–5974.

(532) Fontanella, J. J.; Edmondson, C. A.; Wintersgill, M. C.; Wu, Y.; Greenbaum, S. G. High-Pressure Electrical Conductivity and Nmr Studies in Variable Equivalent Weight Nafion Membranes. *Macromolecules* **1996**, *29* (14), 4944–4951.

(533) Commer, P.; Cherstvy, A. G.; Spohr, E.; Kornyshev, A. A. The Effect of Water Content on Proton Transport in Polymer Electrolyte Membranes. *Fuel Cells* **2002**, *2* (3–4), 127–136.

(534) Allahyarov, E.; Taylor, P. L.; Lowen, H. Simulation Study of Sulfonate Cluster Swelling in Ionomers. *Phys. Rev. E* **2009**, *80* (6), 061802.

(535) Moilanen, D. E.; Piletic, I. R.; Fayer, M. D. Water Dynamics in Nafion Fuel Cell Membranes: The Effects of Confinement and Structural Changes on the Hydrogen Bond Network. *J. Phys. Chem. C* **2007**, *111* (25), 8884–8891.

(536) Park, J. K.; Li, J.; Divoux, G. M.; Madsen, L. A.; Moore, R. B. Oriented Morphology and Anisotropic Transport in Uniaxially Stretched Perfluorosulfonate Ionomer Membranes. *Macromolecules* **2011**, *44* (14), 5701–5710.

(537) Klein, M.; Perrin, J.-C.; Leclerc, S.; Guendouz, L.; Dillet, J.; Lottin, O. Anisotropy of Water Self-Diffusion in a Nafion Membrane under Traction. *Macromolecules* **2013**, *46* (23), 9259–9269.

(538) Okada, T.; Satou, H.; Okuno, M.; Yuasa, M. Ion and Water Transport Characteristics of Perfluorosulfonated Ionomer Membranes with H+ and Alkali Metal Cations. *J. Phys. Chem. B* **2002**, *106* (6), 1267–1273.

(539) Grossi, N.; Espuche, E.; Escoubes, M. Transport Properties of Nafion (R)/Cyclodextrin Membranes. *Sep. Purif. Technol.* **2001**, *22–23* (1–2), 255–267.

(540) Romero, T.; Merida, W. Water Transport in Liquid and Vapour Equilibrated Nafion (Tm) Membranes. *J. Membr. Sci.* **2009**, *338* (1–2), 135–144.

(541) Adachi, M.; Navessin, T.; Xie, Z.; Li, F. H.; Tanaka, S.; Holdcroft, S. Thickness Dependence of Water Permeation through Proton Exchange Membranes. *J. Membr. Sci.* **2010**, *364* (1–2), 183–193.

(542) Duan, Q. J.; Wang, H. P.; Benziger, J. Transport of Liquid Water through Nafion Membranes. *J. Membr. Sci.* **2012**, *392*, 88–94.

(543) Izquierdo-Gil, M. A.; Barragan, V. M.; Godino, M. P.; Villaluenga, J. P. G.; Ruiz-Bauza, C.; Seoane, B. Salt Diffusion through Cation-Exchange Membranes in Alcohol-Water Solutions. *Sep. Purif. Technol.* **2009**, *64* (3), 321–325.

(544) Adachi, M.; Navessin, T.; Xie, Z.; Frisken, B.; Holdcroft, S. Correlation of in Situ and Ex Situ Measurements of Water Permeation through Nafion Nre211 Proton Exchange Membranes. *J. Electrochem. Soc.* **2009**, *156* (6), B782–B790.

(545) Villaluenga, J. P. G.; Seoane, B.; Barragan, V. M.; Ruiz-Bauza, C. Permeation of Electrolyte Water-Methanol Solutions through a Nafion Membrane. *J. Colloid Interface Sci.* **2003**, *268* (2), 476–481.

(546) Villaluenga, J. P. G.; Barragan, V. M.; Seoane, B.; Ruiz-Bauza, C. Sorption and Permeation of Solutions of Chloride Salts, Water and Methanol in a Nafion Membrane. *Electrochim. Acta* **2006**, *51* (28), 6297–6303.

(547) Izquierdo-Gil, M. A.; Barragan, V. M.; Villaluenga, J. P. G.; Godino, M. P. Water Uptake and Salt Transport through Nafion Cation-Exchange Membranes with Different Thicknesses. *Chem. Eng. Sci.* **2012**, *72*, 1–9.

(548) Barragan, V. M.; Ruiz-Bauza, C.; Villaluenga, J. P. G.; Seoane, B. Simultaneous Electroosmotic and Permeation Flows through a Nafion Membrane - 1. Aqueous Electrolyte Solutions. *J. Colloid Interface Sci.* **2004**, *277* (1), 176–183.

(549) Majsztrik, P.; Bocarsly, A.; Benziger, J. Water Permeation through Nafion Membranes: The Role of Water Activity. *J. Phys. Chem. B* **2008**, *112* (51), 16280–16289.

(550) Godino, M. P.; Barragan, V. M.; Villaluenga, J. P. G.; Ruiz-Bauza, C.; Seoane, B. Water and Methanol Transport in Nafion Membranes with Different Cationic Forms 1. Alkali Monovalent Cations. *J. Power Sources* **2006**, *160* (1), 181–186.

(551) Godino, M. P.; Barragan, V. M.; Izquierdo, M. A.; Villaluenga, J. P. G.; Seoane, B.; Ruiz-Bauza, C. Study of the Activation Energy for Transport of Water and Methanol through a Nafion Membrane. *Chem. Eng. J.* **2009**, *152* (1), 20–25.

(552) Morin, A.; Xu, F. N.; Gebel, G.; Diat, O. Influence of Pemfc Gas Flow Configuration on Performance and Water Distribution Studied by Sans: Evidence of the Effect of Gravity. *Int. J. Hydrogen Energy* **2011**, *36* (4), 3096–3109.

(553) Lang, W. Z.; Niu, H. Y.; Liu, Y. X.; Liu, C. X.; Guo, Y. J. Pervaporation Separation of Dimethyl Carbonate/Methanol Mixtures with Regenerated Perfluoro-Ion-Exchange Membranes in Chlor-Alkali Industry. *J. Appl. Polym. Sci.* **2013**, *129* (6), 3473–3481.

(554) Okada, T. Theory for Water Management in Membranes for Polymer Electrolyte Fuel Cells - Part 1. The Effect of Impurity Ions at the Anode Side on the Membrane Performances. *J. Electroanal. Chem.* **1999**, *465* (1), 1–17.

(555) Suzuki, T.; Tabuchi, Y.; Tsushima, S.; Hirai, S. Measurement of Water Content Distribution in Catalyst Coated Membranes under Water Permeation Conditions by Magnetic Resonance Imaging. *Int. J. Hydrogen Energy* **2011**, *36* (9), 5479–5486.

(556) Cheah, M. J.; Kevrekidis, I. G.; Benziger, J. Effect of Interfacial Water Transport Resistance on Coupled Proton and Water Transport across Nafion. *J. Phys. Chem. B* **2011**, *115* (34), 10239–10250.

(557) Rinaldo, S. G.; Monroe, C. W.; Romero, T.; Merida, W.; Eikerling, M. Vaporization-Exchange Model for Dynamic Water Sorption in Nafion: Transient Solution. *Electrochem. Commun.* **2011**, *13* (1), 5–7.

(558) Zenyuk, I. V.; Das, P. K.; Weber, A. Z. Understanding Impacts of Catalyst-Layer Thickness on Fuel-Cell Performance Via Mathematical Modeling. *J. Electrochem. Soc.* **2016**, *163* (7), F691–F703.

(559) Cooper, K. Progress toward Accurate through-Plane Membrane Resistance and Conductivity Measurement. *ECS Trans.* **2009**, *25* (1), 995–1007.

(560) Springer, T. E.; Wilson, M. S.; Gottesfeld, S. Modeling and Experimental Diagnostics in Polymer Electrolyte Fuel-Cells. *J. Electrochem. Soc.* **1993**, *140* (12), 3513–3526.

(561) Weber, A. Z.; Hickner, M. A. Modeling and High-Resolution-Imaging Studies of Water-Content Profiles in a Polymer-Electrolyte-Fuel-Cell Membrane-Electrode Assembly. *Electrochim. Acta* **2008**, *53* (26), 7668–7674.

(562) Mukundan, R.; Borup, R. L. Visualising Liquid Water in Pem Fuel Cells Using Neutron Imaging. *Fuel Cells* **2009**, *9* (5), 499−505.

(563) Mukundan, R.; Davey, J. R.; Rockward, T.; Spendelow, J. S.; Pivovar, B.; Hussey, D. S.; Jacobson, D. L.; Arif, M.; Borup, R. Imaging of Water Profiles in Pem Fuel Cells Using Neutron Radiography: Effect of Operating Conditions and Gdl Composition. *ECS Trans.* **2007**, *11* (1), 411−422.

(564) Spendelow, J.; Mukundan, R.; Davey, J.; Rockward, T.; Hussey, D. S.; Jacobson, D.; Arif, M.; Borup, R. L. High Resolution Neutron Radiography Imaging of Operating Pem Fuel Cells: Effect of Flow Configuration and Gravity on Water Distribution. *ECS Trans.* **2008**, *16* (2), 1345−1355.

(565) Morin, A.; Xu, F.; Gebel, G.; Diat, O. Evolution of Water Distribution in Pemfc During on/Off Cycling. *Fuel Cells* **2012**, *12* (2), 156−161.

(566) Huguet, P.; Morin, A.; Gebel, G.; Deabate, S.; Sutor, A. K.; Peng, Z. In Situ Analysis of Water Management in Operating Fuel Cells by Confocal Raman Spectroscopy. *Electrochem. Commun.* **2011**, *13* (5), 418−422.

(567) Hara, M.; Inukai, J.; Miyatake, K.; Uchida, H.; Watanabe, M. Temperature Dependence of the Water Distribution inside a Nafion Membrane in an Operating Polymer Electrolyte Fuel Cell. A Micro-Raman Study. *Electrochim. Acta* **2011**, *58*, 449−455.

(568) Zhang, Z.; Marble, A. E.; MacMillan, B.; Promislow, K.; Martin, J.; Wang, H.; Balcom, B. J. Spatial and Temporal Mapping of Water Content across Nafion Membranes under Wetting and Drying Conditions. *J. Magn. Reson.* **2008**, *194* (2), 245−253.

(569) Ouriadov, A. V.; MacGregor, R. P.; Balcom, B. J. Thin Film Mri-High Resolution Depth Imaging with a Local Surface Coil and Spin Echo Spi. *J. Magn. Reson.* **2004**, *169* (1), 174−186.

(570) Tsushima, S.; Ikeda, T.; Koido, T.; Hirai, S. Investigation of Water Distribution in a Membrane in an Operating Pemfc by Environmental Mri. *J. Electrochem. Soc.* **2010**, *157* (12), B1814−B1818.

(571) Albertini, V. R.; Paci, B.; Nobili, F.; Marassi, R.; Di Michiel, M. Time/Space-Resolved Studies of the Nafion Membrane Hydration Profile in a Running Fuel Cell. *Adv. Mater.* **2009**, *21* (5), 578−583.

(572) Quan, P.; Lai, M. C.; Hussey, D. S.; Jacobson, D. L.; Kumar, A.; Hirano, S. Time-Resolved Water Measurement in a Pem Fuel Cell Using High-Resolution Neutron Imaging Technique. *J. Fuel Cell Sci. Technol.* **2010**, *7* (5), 051009.

(573) Hussey, D. S.; Spernjak, D.; Wu, G.; Jacobson, D. L.; Liu, D.; Khaykovich, B.; Gubarev, M. V.; Fairweather, J. D.; Mukundan, R.; Lujan, R.; et al. Neutron Imaging of Water Transport in Polymer-Electrolyte Membranes and Membrane-Electrode Assemblies. *ECS Trans.* **2013**, *58* (1), 293−299.

(574) Bellows, R. J.; Lin, M. Y.; Arif, M.; Thompson, A. K.; Jacobson, D. Neutron Imaging Technique for in Situ Measurement of Water Transport Gradients within Nafion in Polymer Electrolyte Fuel Cells. *J. Electrochem. Soc.* **1999**, *146* (3), 1099−1103.

(575) Hickner, M. A.; Siegel, N. P.; Chen, K. S.; Hussey, D. S.; Jacobson, D. L.; Arif, M. In Situ High-Resolution Neutron Radiography of Cross-Sectional Liquid Water Profiles in Proton Exchange Membrane Fuel Cells. *J. Electrochem. Soc.* **2008**, *155* (4), B427−B434.

(576) Cooper, K. Characterizing through-Plane and in-Plane Ionic Conductivity of Polymer Electrolyte Membranes. *ECS Trans.* **2011**, *41* (1), 1371−1380.

(577) Cooper, K. R. Progress toward Accurate through-Plane Ion Transport Resistance Measurement of Thin Solid Electrolytes. *J. Electrochem. Soc.* **2010**, *157* (11), B1731−B1739.

(578) Paddison, S. J.; Reagor, D. W.; Zawodzinski, T. A. High Frequency Dielectric Studies of Hydrated Nafion (R). *J. Electroanal. Chem.* **1998**, *459* (1), 91−97.

(579) Kreuer, K. D.; Rabenau, A.; Weppner, W. Vehicle Mechanism, a New Model for the Interpretation of the Conductivity of Fast Proton Conductors. *Angew. Chem., Int. Ed. Engl.* **1982**, *21* (3), 208−209.

(580) Kreuer, K. D. Fast Proton Conductivity: A Phenomenon between the Solid and the Liquid State? *Solid State Ionics* **1997**, *94* (1−4), 55−62.

(581) Paul, R.; Paddison, S. J. A Statistical Mechanical Model for the Calculation of the Permittivity of Water in Hydrated Polymer Electrolyte Membrane Pores. *J. Chem. Phys.* **2001**, *115* (16), 7762−7771.

(582) Tuckerman, M.; Laasonen, K.; Sprik, M.; Parrinello, M. Ab-Initio Molecular-Dynamics Simulation of the Solvation and Transport of H3o+ and Oh- Ions in Water. *J. Phys. Chem.* **1995**, *99* (16), 5749−5752.

(583) Bontha, J. R.; Pintauro, P. N. Water Orientation and Ion Solvation Effects During Multicomponent Salt Partitioning in a Nafion Cation-Exchange Membrane. *Chem. Eng. Sci.* **1994**, *49* (23), 3835−3851.

(584) Villaluenga, J. P. G.; Seoane, B.; Barragan, V. M.; Ruiz-Bauza, C. Thermo-Osmosis of Mixtures of Water and Methanol through a Nafion Membrane. *J. Membr. Sci.* **2006**, *274* (1−2), 116−122.

(585) Tsampas, M. N.; Pikos, A.; Brosda, S.; Katsaounis, A.; Vayenas, C. G. The Effect of Membrane Thickness on the Conductivity of Nafion. *Electrochim. Acta* **2006**, *51* (13), 2743−2755.

(586) Sone, Y.; Ekdunge, P.; Simonsson, D. Proton Conductivity of Nafion 117 as Measured by a Four-Electrode Ac Impedance Method. *J. Electrochem. Soc.* **1996**, *143* (4), 1254−1259.

(587) Rieke, P. C.; Vanderborgh, N. E. Temperature-Dependence of Water-Content and Proton Conductivity in Polyperfluorosulfonic Acid Membranes. *J. Membr. Sci.* **1987**, *32* (2−3), 313−328.

(588) Verbrugge, M. W.; Schneider, E. W.; Conell, R. S.; Hill, R. F. The Effect of Temperature on the Equilibrium and Transport-Properties of Saturated Poly(Perfluorosulfonic Acid) Membranes. *J. Electrochem. Soc.* **1992**, *139* (12), 3421−3428.

(589) Dimitrova, P.; Friedrich, K. A.; Stimming, U.; Vogt, B. Modified Nafion((R))-Based Membranes for Use in Direct Methanol Fuel Cells. *Solid State Ionics* **2002**, *150* (1−2), 115−122.

(590) Damay, F.; Klein, L. C. Transport Properties of Nafion (Tm) Composite Membranes for Proton-Exchange Membranes Fuel Cells. *Solid State Ionics* **2003**, *162*, 261−267.

(591) Elabd, Y. A.; Napadensky, E.; Sloan, J. M.; Crawford, D. M.; Walker, C. W. Triblock Copolymer Ionomer Membranes Part I. Methanol and Proton Transport. *J. Membr. Sci.* **2003**, *217* (1−2), 227−242.

(592) Lee, C. H.; Wang, Y. Z. Synthesis and Characterization of Epoxy-Based Semi-Interpenetrating Polymer Networks Sulfonated Polyimides Proton-Exchange Membranes for Direct Methanol Fuel Cell Applications. *J. Polym. Sci., Part A: Polym. Chem.* **2008**, *46* (6), 2262−2276.

(593) Bruggeman, D. A. G. Calculation of Different Physical Constants of Heterogen Substances I Dielectric Constants and Conductibility of Mixtures from Isotrop Substances. *Ann. Phys.* **1935**, *416* (8), 665−679.

(594) Edmondson, C. A.; Fontanella, J. J.; Chung, S. H.; Greenbaum, S. G.; Wnek, G. E. Complex Impedance Studies of S-Sebs Block Polymer Proton-Conducting Membranes. *Electrochim. Acta* **2001**, *46* (10−11), 1623−1628.

(595) Wodzki, R.; Narebska, A.; Nioch, W. K. Percolation Conductivity in Nafion Membranes. *J. Appl. Polym. Sci.* **1985**, *30* (2), 769−780.

(596) Clark, J. K.; Paddison, S. J. The Effect of Side Chain Connectivity and Local Hydration on Proton Transfer in 3m Perfluorosulfonic Acid Membranes. *Solid State Ionics* **2012**, *213*, 83−91.

(597) Beers, K. M.; Balsara, N. P. Design of Cluster-Free Polymer Electrolyte Membranes and Implications on Proton Conductivity. *ACS Macro Lett.* **2012**, *1* (10), 1155−1160.

(598) Peckham, T. J.; Holdcroft, S. Structure-Morphology-Property Relationships of Non-Perfluorinated Proton-Conducting Membranes. *Adv. Mater.* **2010**, *22* (42), 4667−4690.

(599) Park, M. J.; Balsara, N. P. Anisotropic Proton Conduction in Aligned Block Copolymer Electrolyte Membranes at Equilibrium with Humid Air. *Macromolecules* **2010**, *43* (1), 292−298.

(600) Chang, Y.; Brunello, G. F.; Fuller, J.; Hawley, M.; Kim, Y. S.; Disabb-Miller, M.; Hickner, M. A.; Jang, S. S.; Bae, C. S. Aromatic

Ionomers with Highly Acidic Sulfonate Groups: Acidity, Hydration, and Proton Conductivity. *Macromolecules* **2011**, *44* (21), 8458−8469.

(601) Chang, Y.; Mohanty, A. D.; Smedley, S. B.; Abu-Hakmeh, K.; Lee, Y. H.; Morgan, J. E.; Hickner, M. A.; Jang, S. S.; Ryu, C. Y.; Bae, C. Effect of Superacidic Side Chain Structures on High Conductivity Aromatic Polymer Fuel Cell Membranes. *Macromolecules* **2015**, *48* (19), 7117−7126.

(602) Feng, K.; Tang, B. B.; Wu, P. Y. A "H2o Donating/Methanol Accepting" Platform for Preparation of Highly Selective Nafion-Based Proton Exchange Membranes. *J. Mater. Chem. A* **2015**, *3* (36), 18546−18556.

(603) Page, K. A.; Rowe, B. W.; Masser, K. A.; Faraone, A. The Effect of Water Content on Chain Dynamics in Nafion Membranes Measured by Neutron Spin Echo and Dielectric Spectroscopy. *J. Polym. Sci., Part B: Polym. Phys.* **2014**, *52* (9), 624−632.

(604) Kreuer, K. D. On the Development of Proton Conducting Polymer Membranes for Hydrogen and Methanol Fuel Cells. *J. Membr. Sci.* **2001**, *185* (1), 29−39.

(605) Pivovar, B. S.; Smyrl, W. H.; Cussler, E. L. Electro-Osmosis in Nafion 117, Polystyrene Sulfonic Acid, and Polybenzimidazole. *J. Electrochem. Soc.* **2005**, *152* (1), A53−A60.

(606) Ise, M.; Kreuer, K. D.; Maier, J. Electroosmotic Drag in Polymer Electrolyte Membranes: An Electrophoretic Nmr Study. *Solid State Ionics* **1999**, *125* (1−4), 213−223.

(607) Agmon, N. The Grotthuss Mechanism. *Chem. Phys. Lett.* **1995**, *244* (5−6), 456−462.

(608) Tandon, R.; Pintauro, P. N. Divalent/Monovalent Cation Uptake Selectivity in a Nafion Cation-Exchange Membrane: Experimental and Modeling Studies. *J. Membr. Sci.* **1997**, *136* (1−2), 207−219.

(609) Paciaroni, A.; Casciola, M.; Cornicchi, E.; Marconi, M.; Onori, G.; Pica, M.; Narducci, R. Temperature-Dependent Dynamics of Water Confined in Nafion Membranes. *J. Phys. Chem. B* **2006**, *110* (28), 13769−13776.

(610) Newman, J. S.; Thomas-Alyea, K. E. *Electrochemical Systems*; J. Wiley & Sons: New York, 2004.

(611) Siroma, Z.; Fujiwara, N.; Ioroi, T.; Yamazaki, S.; Senoh, H.; Yasuda, K. Potential Difference Caused by Humidity and Temperature Gradients in a Proton-Exchange Membrane. *J. Electroanal. Chem.* **2009**, *633* (1), 268−271.

(612) Okada, T.; Moller-Holst, S.; Gorseth, O.; Kjelstrup, S. Transport and Equilibrium Properties of Nafion (R) Membranes with H+ and Na+ Ions. *J. Electroanal. Chem.* **1998**, *442* (1−2), 137−145.

(613) Fuller, T. F.; Newman, J. Experimental Determination of the Transport Number of Water in Nafion 117 Membrane. *J. Electrochem. Soc.* **1992**, *139* (5), 1332−1337.

(614) Ye, X. H.; Wang, C. Y. Measurement of Water Transport Properties through Membrane-Electrode Assemblies. *J. Electrochem. Soc.* **2007**, *154* (7), B676−B682.

(615) Ge, S. H.; Yi, B. L.; Ming, P. W. Experimental Determination of Electro-Osmotic Drag Coefficient in Nafion Membrane for Fuel Cells. *J. Electrochem. Soc.* **2006**, *153* (8), A1443−A1450.

(616) Peng, Z.; Morin, A.; Huguet, P.; Schott, P.; Pauchet, J. In-Situ Measurement of Electroosmotic Drag Coefficient in Nafion Membrane for the Pemfc. *J. Phys. Chem. B* **2011**, *115* (44), 12835−12844.

(617) Braff, W.; Mittelsteadt, C. K. Electroosmotic Drag Coefficient of Proton Exchange Membrane as a Function of Relative Humidity. *ECS Trans.* **2008**, *16* (2), 309−316.

(618) Berg, P.; Stornes, M. Towards a Consistent Interpretation of Electro-Osmotic Drag in Polymer Electrolyte Membranes. *Fuel Cells* **2016**, n/a, DOI: 10.1002/fuce.201500210.

(619) Kim, S.; Mench, M. M. Investigation of Temperature-Driven Water Transport in Polymer Electrolyte Fuel Cell: Thermo-Osmosis in Membranes. *J. Membr. Sci.* **2009**, *328* (1−2), 113−120.

(620) Balliet, R. J.; Newman, J. Cold Start of a Polymer-Electrolyte Fuel Cell I. Development of a Two-Dimensional Model. *J. Electrochem. Soc.* **2011**, *158* (8), B927−B938.

(621) D'Epifanio, A.; Navarra, M. A.; Weise, F. C.; Mecheri, B.; Farrington, J.; Licoccia, S.; Greenbaum, S. Composite Nafion/Sulfated Zirconia Membranes: Effect of the Filler Surface Properties on Proton Transport Characteristics. *Chem. Mater.* **2010**, *22* (3), 813−821.

(622) Giotto, M. V.; Zhang, J. H.; Inglefield, P. T.; Wen, W. Y.; Jones, A. A. Nanophase Structure and Diffusion in Swollen Perfluorosulfonate Ionomer: An Nmr Approach. *Macromolecules* **2003**, *36* (12), 4397−4403.

(623) Page, K. A.; Park, J. K.; Moore, R. B.; Sakai, V. G. Direct Analysis of the Ion-Hopping Process Associated with the Alpha-Relaxation in Perfluorosulfonate Ionomers Using Quasielastic Neutron Scattering. *Macromolecules* **2009**, *42* (7), 2729−2736.

(624) Volino, F.; Pineri, M.; Dianoux, A. J.; Degeyer, A. Water Mobility in a Water-Soaked Nafion Membrane - a High-Resolution Neutron Quasi-Elastic Study. *J. Polym. Sci., Polym. Phys. Ed.* **1982**, *20* (3), 481−496.

(625) Kabrane, J.; Aquino, A. J. A. Electronic Structure and Vibrational Mode Study of Nafion Membrane Interfacial Water Interactions. *J. Phys. Chem. A* **2015**, *119* (9), 1754−1764.

(626) Ban, S.; Huang, C.; Yuan, X. Z.; Wang, H. Molecular Simulation of Gas Adsorption, Diffusion, and Permeation in Hydrated Nafion Membranes. *J. Phys. Chem. B* **2011**, *115* (39), 11352−11358.

(627) Kim, Y. G.; Bae, Y. C. Predicting the Proton Conductivity of Perfluorosulfonic Acid Membrane Via Combining Statistical Thermodynamics and Molecular Dynamics Simulation. *J. Polym. Sci., Part B: Polym. Phys.* **2011**, *49* (20), 1455−1463.

(628) Vayenas, C. G.; Tsampas, M. N.; Katsaounis, A. First Principles Analytical Prediction of the Conductivity of Nafion Membranes. *Electrochim. Acta* **2007**, *52* (6), 2244−2256.

(629) Dorenbos, G.; Pomogaev, V. A.; Takigawa, M.; Morohoshi, K. Prediction of Anisotropic Transport in Nafion Containing Catalyst Layers. *Electrochem. Commun.* **2010**, *12* (1), 125−128.

(630) Ozmaian, M.; Naghdabadi, R. Molecular Dynamics Simulation Study of Glass Transition in Hydrated Nafion. *J. Polym. Sci., Part B: Polym. Phys.* **2014**, *52* (13), 907−915.

(631) Zhang, L.; Ma, C. S.; Mukerjee, S. Oxygen Permeation Studies on Alternative Proton Exchange Membranes Designed for Elevated Temperature Operation. *Electrochim. Acta* **2003**, *48* (13), 1845−1859.

(632) Kocha, S. S.; Yang, J. D. L.; Yi, J. S. Characterization of Gas Crossover and Its Implications in Pem Fuel Cells. *AIChE J.* **2006**, *52* (5), 1916−1925.

(633) Takata, H.; Nishikawa, M.; Arimura, Y.; Egawa, T.; Fukada, S.; Yoshitake, M. Study on Water Uptake of Proton Exchange Membrane by Using Tritiated Water Sorption Method. *Int. J. Hydrogen Energy* **2005**, *30* (9), 1017−1025.

(634) Catalano, J.; Myezwa, T.; De Angelis, M. G.; Baschetti, M. G.; Sarti, G. C. The Effect of Relative Humidity on the Gas Permeability and Swelling in Pfsi Membranes. *Int. J. Hydrogen Energy* **2012**, *37* (7), 6308−6316.

(635) Chiou, J. S.; Paul, D. R. Gas Permeation in a Dry Nafion Membrane. *Ind. Eng. Chem. Res.* **1988**, *27* (11), 2161−2164.

(636) He, Y. K.; Cussler, E. L. Ammonia Permeabilities of Perfluorosulfonic Membranes in Various Ionic Forms. *J. Membr. Sci.* **1992**, *68* (1−2), 43−52.

(637) Baik, K. D.; Hong, B. K.; Kim, M. S. Novel Technique for Measuring Oxygen Crossover through the Membrane in Polymer Electrolyte Membrane Fuel Cells. *Int. J. Hydrogen Energy* **2013**, *38* (21), 8927−8933.

(638) Cheng, X.; Zhang, J. L.; Tang, Y. H.; Song, C. J.; Shen, J.; Song, D. T.; Zhang, J. J. Hydrogen Crossover in High-Temperature Pem Fuel Cells. *J. Power Sources* **2007**, *167* (1), 25−31.

(639) Sethuraman, V. A.; Khan, S.; Jur, J. S.; Haug, A. T.; Weidner, J. W. Measuring Oxygen, Carbon Monoxide and Hydrogen Sulfide Diffusion Coefficient and Solubility in Nafion Membranes. *Electrochim. Acta* **2009**, *54* (27), 6850−6860.

(640) Schalenbach, M.; Hoefner, T.; Paciok, P.; Carmo, M.; Lueke, W.; Stolten, D. Gas Permeation through Nafion. Part 1: Measurements. *J. Phys. Chem. C* **2015**, *119* (45), 25145−25155.

(641) Ogumi, Z.; Kuroe, T.; Takehara, Z. Gas Permeation in Spe Method 0.2. Oxygen and Hydrogen Permeation through Nafion. *J. Electrochem. Soc.* **1985**, *132* (11), 2601–2605.
(642) Sodaye, H. S.; Pujari, P. K.; Goswami, A.; Manohar, S. B. Measurement of Free-Volume Hole Size Distribution in Nafion-117 Using Positron Annihilation Spectroscopy. *J. Polym. Sci., Part B: Polym. Phys.* **1998**, *36* (6), 983–989.
(643) Baschetti, M. G.; Minelli, M.; Catalano, J.; Sarti, G. C. Gas Permeation in Perflurosulfonated Membranes: Influence of Temperature and Relative Humidity. *Int. J. Hydrogen Energy* **2013**, *38* (27), 11973–11982.
(644) Ren, X. M.; Myles, T. D.; Grew, K. N.; Chiu, W. K. S. Carbon Dioxide Transport in Nafion 1100 Ew Membrane and in a Direct Methanol Fuel Cell. *J. Electrochem. Soc.* **2015**, *162* (10), F1221–F1230.
(645) Sakai, T.; Takenaka, H.; Torikai, E. Gas-Diffusion in the Dried and Hydrated Nafions. *J. Electrochem. Soc.* **1986**, *133* (1), 88–92.
(646) Yoshida, N.; Ishisaki, T.; Watakabe, A.; Yoshitake, M. Characterization of Flemion (R) Membranes for Pefc. *Electrochim. Acta* **1998**, *43* (24), 3749–3754.
(647) Matsuyama, H.; Matsui, K.; Kitamura, Y.; Maki, T.; Teramoto, M. Effects of Membrane Thickness and Membrane Preparation Condition on Facilitated Transport of Co2 through Ionomer Membrane. *Sep. Purif. Technol.* **1999**, *17* (3), 235–241.
(648) Naudy, S.; Collette, F.; Thominette, F.; Gebel, G.; Espuche, E. Influence of Hygrothermal Aging on the Gas and Water Transport Properties of Nafion (R) Membranes. *J. Membr. Sci.* **2014**, *451* (0), 293–304.
(649) Ma, S. A.; Odgaard, M.; Skou, E. Carbon Dioxide Permeability of Proton Exchange Membranes for Fuel Cells. *Solid State Ionics* **2005**, *176* (39–40), 2923–2927.
(650) Ma, S.; Skou, E. Co2 Permeability in Nafion (R) Ew1100 at Elevated Temperature. *Solid State Ionics* **2007**, *178* (7–10), 615–619.
(651) Guerrero-Gutierrez, E. M. A.; Suleiman, D. Supercritical Fluid Co2 Processing and Counter Ion Substitution of Nafion (R) Membranes. *J. Appl. Polym. Sci.* **2013**, *129* (1), 73–85.
(652) Pellegrino, J.; Kang, Y. S. Co2/Ch4 Transport in Polyperfluorosulfonate Ionomers - Effects of Polar-Solvents on Permeation and Solubility. *J. Membr. Sci.* **1995**, *99* (2), 163–174.
(653) Buchi, F. N.; Wakizoe, M.; Srinivasan, S. Microelectrode Investigation of Oxygen Permeation in Perfluorinated Proton Exchange Membranes with Different Equivalent Weights. *J. Electrochem. Soc.* **1996**, *143* (3), 927–932.
(654) Evans, C. M.; Singh, M. R.; Lynd, N. A.; Segalman, R. A. Improving the Gas Barrier Properties of Nafion Via Thermal Annealing: Evidence for Diffusion through Hydrophilic Channels and Matrix. *Macromolecules* **2015**, *48* (10), 3303–3309.
(655) Zhang, Z. X.; Chattot, R.; Bonorand, L.; Jetsrisuparb, K.; Buchmuller, Y.; Wokaun, A.; Gubler, L. Mass Spectrometry to Quantify and Compare the Gas Barrier Properties of Radiation Grafted Membranes and Nafion (R). *J. Membr. Sci.* **2014**, *472*, 55–66.
(656) Sakai, T.; Takenaka, H.; Wakabayashi, N.; Kawami, Y.; Torikai, E. Gas Permeation Properties of Solid Polymer Electrolyte (Spe) Membranes. *J. Electrochem. Soc.* **1985**, *132* (6), 1328–1332.
(657) Kontou, S.; Stergiopoulos, V.; Song, S.; Tsiakaras, P. Ethanol/Water Mixture Permeation through a Nafion (R) Based Membrane Electrode Assembly. *J. Power Sources* **2007**, *171* (1), 1–7.
(658) Godino, M. P.; Barragan, V. M.; Villaluenga, J. P. G.; Izquierdo-Gil, M. A.; Ruiz-Bauza, C.; Seoane, B. Liquid Transport through Sulfonated Cation-Exchange Membranes for Different Water-Alcohol Solutions. *Chem. Eng. J.* **2010**, *162* (2), 643–648.
(659) Dimitrova, P.; Friedrich, K. A.; Vogt, B.; Stimming, U. Transport Properties of Ionomer Composite Membranes for Direct Methanol Fuel Cells. *J. Electroanal. Chem.* **2002**, *532* (1–2), 75–83.
(660) Godino, M. P.; Barragan, V. M.; Izquierdo-Gil, M. A.; Villaluenga, J. P. G.; Seoane, B.; Ruiz-Bauza, C. Methanol-Water Solution Transport in Nafion Membranes with Different Cationic Forms. *Sep. Sci. Technol.* **2011**, *46* (6), 944–949.
(661) Ren, X. M.; Springer, T. E.; Zawodzinski, T. A.; Gottesfeld, S. Methanol Transport through Nafion Membranes - Electro-Osmotic Drag Effects on Potential Step Measurements. *J. Electrochem. Soc.* **2000**, *147* (2), 466–474.
(662) Aldebert, P.; Guglielmi, M.; Pineri, M. Ionic-Conductivity of Bulk, Gels and Solutions of Perfluorinated Ionomer Membranes. *Polym. J.* **1991**, *23* (5), 399–406.
(663) Every, H. A.; Hickner, M. A.; McGrath, J. E.; Zawodzinski, T. A. An Nmr Study of Methanol Diffusion in Polymer Electrolyte Fuel Cell Membranes. *J. Membr. Sci.* **2005**, *250* (1–2), 183–188.
(664) Hietala, S.; Maunu, S. L.; Sundholm, F. Sorption and Diffusion of Methanol and Water in Pvdf-G-Pssa and Nafion (R) 117 Polymer Electrolyte Membranes. *J. Polym. Sci., Part B: Polym. Phys.* **2000**, *38* (24), 3277–3284.
(665) Hallberg, F.; Vernersson, T.; Pettersson, E. T.; Dvinskikh, S. V.; Lindbergh, G.; Furo, I. Electrokinetic Transport of Water and Methanol in Nafion Membranes as Observed by Nmr Spectroscopy. *Electrochim. Acta* **2010**, *55* (10), 3542–3549.
(666) Tandon, R.; Pintauro, P. N. Solvent Effects During Multicomponent Ion Uptake into a Nafion Cation-Exchange Membrane. *J. Membr. Sci.* **2009**, *341* (1–2), 21–29.
(667) Barragan, V. M.; Ruiz-Bauza, C.; Villaluenga, J. P. G.; Seoane, B. Transport of Methanol and Water through Nafion Membranes. *J. Power Sources* **2004**, *130* (1–2), 22–29.
(668) Saarinen, V.; Kreuer, K. D.; Schuster, M.; Merkle, R.; Maier, J. On the Swelling Properties of Proton Conducting Membranes for Direct Methanol Fuel Cells. *Solid State Ionics* **2007**, *178* (7–10), 533–537.
(669) Vishnyakov, A.; Neimark, A. V. Molecular Dynamics Simulation of Nafion Oligomer Solvation in Equimolar Methanol-Water Mixture. *J. Phys. Chem. B* **2001**, *105* (32), 7830–7834.
(670) Rivin, D.; Meermeier, G.; Schneider, N. S.; Vishnyakov, A.; Neimark, A. V. Simultaneous Transport of Water and Organic Molecules through Polyelectrolyte Membranes. *J. Phys. Chem. B* **2004**, *108* (26), 8900–8909.
(671) Chaabane, L.; Dammak, L.; Grande, D.; Larchet, C.; Huguet, P.; Nikonenko, S. V.; Nikonenko, V. V. Swelling and Permeability of Nafion (R) 117 in Water-Methanol Solutions: An Experimental and Modelling Investigation. *J. Membr. Sci.* **2011**, *377* (1–2), 54–64.
(672) Elabd, Y. A.; Hickner, M. A. Block Copolymers for Fuel Cells. *Macromolecules* **2011**, *44* (1), 1–11.
(673) Byun, S. C.; Jeong, Y. J.; Park, J. W.; Kim, S. D.; Ha, H. Y.; Kim, W. J. Effect of Solvent and Crystal Size on the Selectivity of Zsm-5/Nafion Composite Membranes Fabricated by Solution-Casting Method. *Solid State Ionics* **2006**, *177* (37–38), 3233–3243.
(674) Lavorgna, M.; Sansone, L.; Scherillo, G.; Gu, R.; Baker, A. P. Transport Properties of Zeolite Na-X-Nafion Membranes: Effect of Zeolite Loadings and Particle Size. *Fuel Cells* **2011**, *11* (6), 801–813.
(675) Baglio, V.; Arico, A. S.; Di Blasi, A.; Antonucci, P. L.; Nannetti, F.; Tricoli, V.; Antonucci, V. Zeolite-Based Composite Membranes for High Temperature Direct Methanol Fuel Cells. *J. Appl. Electrochem.* **2005**, *35* (2), 207–212.
(676) Tricoli, V.; Nannetti, F. Zeolite-Nafion Composites as Ion Conducting Membrane Materials. *Electrochim. Acta* **2003**, *48* (18), 2625–2633.
(677) Xu, K.; Chanthad, C.; Gadinski, M. R.; Hickner, M. A.; Wang, Q. Acid-Functionalized Polysilsesquioxane-Nafion Composite Membranes with High Proton Conductivity and Enhanced Selectivity. *ACS Appl. Mater. Interfaces* **2009**, *1* (11), 2573–2579.
(678) Park, J. W.; Wycisk, R.; Pintauro, P. N.; Yarlagadda, V.; Nguyen, T. V. Electrospun Nafion (R)/Polyphenylsulfone Composite Membranes for Regenerative Hydrogen Bromine Fuel Cells. *Materials* **2016**, *9* (3), 143.
(679) Paul, D. K.; Fraser, A.; Karan, K. Towards the Understanding of Proton Conduction Mechanism in Pemfc Catalyst Layer: Conductivity of Adsorbed Nafion Films. *Electrochem. Commun.* **2011**, *13* (8), 774–777.
(680) Siroma, Z.; Kakitsubo, R.; Fujiwara, N.; Ioroi, T.; Yamazaki, S. I.; Yasuda, K. Depression of Proton Conductivity in Recast Nafion (R)

Film Measured on Flat Substrate. *J. Power Sources* **2009**, *189* (2), 994−998.

(681) Volkov, V. I.; Vasilyak, S. L.; Park, I. W.; Kim, H. J.; Ju, H.; Volkov, E. V.; Choh, S. H. Water Behavior in Perfluorinated Ion-Exchange Membranes. *Appl. Magn. Reson.* **2003**, *25* (1), 43−53.

(682) Roberti, E.; Carlotti, G.; Cinelli, S.; Onori, G.; Donnadio, A.; Narducci, R.; Casciola, M.; Sganappa, M. Measurement of the Young's Modulus of Nafion Membranes by Brillouin Light Scattering. *J. Power Sources* **2010**, *195* (23), 7761−7764.

(683) Pantelić, N.; Wansapura, C. M.; Heineman, W. R.; Seliskar, C. J. Dynamic in Situ Spectroscopic Ellipsometry of the Reaction of Aqueous Iron(Ii) with 2,2′-Bipyridine in a Thin Nafion Film. *J. Phys. Chem. B* **2005**, *109* (29), 13971−13979.

(684) Leis, A. P.; Schlicher, S.; Franke, H.; Strathmann, M. Optically Transparent Porous Medium for Nondestructive Studies of Microbial Biofilm Architecture and Transport Dynamics. *Appl. Environ. Microb* **2005**, *71* (8), 4801−4808.

(685) Ablat, H.; Yimit, A.; Mahmut, M.; Itoh, K. Nafion Film/K+-Exchanged Glass Optical Waveguide Sensor for Btx Detection. *Anal. Chem.* **2008**, *80* (20), 7678−7683.

(686) Ardo, S.; Park, S. H.; Warren, E. L.; Lewis, N. S. Unassisted Solar-Driven Photoelectrosynthetic Hi Splitting Using Membrane-Embedded Si Microwire Arrays. *Energy Environ. Sci.* **2015**, *8* (5), 1484−1492.

(687) Singh, M. R.; Stevens, J. C.; Weber, A. Z. Design of Membrane-Encapsulated Wireless Photoelectrochemical Cells for Hydrogen Production. *J. Electrochem. Soc.* **2014**, *161* (8), E3283−E3296.

(688) Khandelwal, M.; Mench, M. M. Direct Measurement of through-Plane Thermal Conductivity and Contact Resistance in Fuel Cell Materials. *J. Power Sources* **2006**, *161* (2), 1106−1115.

(689) Kawano, Y.; Wang, T.; Palmer, R. A.; Aubuchon, S. R. Stress-Strain Curves of Nafion Membranes in Acid and Salt Forms. *Polim.: Cienc. Tecnol.* **2002**, *12* (2), 96−101.

(690) Kusoglu, A.; Tang, Y. L.; Santare, M. H.; Karlsson, A. M.; Cleghorn, S.; Johnson, W. B. Stress-Strain Behavior of Perfluorosulfonic Acid Membranes at Various Temperatures and Humidities: Experiments and Phenomenological Modeling. *J. Fuel Cell Sci. Technol.* **2009**, *6* (1), 011012−011018.

(691) Ballengee, J. B.; Pintauro, P. N. Composite Fuel Cell Membranes from Dual-Nanofiber Electrospun Mats. *Macromolecules* **2011**, *44* (18), 7307−7314.

(692) Liu, D.; Kyriakides, S.; Case, S. W.; Lesko, J. J.; Li, Y. X.; McGrath, J. E. Tensile Behavior of Nafion and Sulfonated Poly-(Arylene Ether Sulfone) Copolymer Membranes and Its Morphological Correlations. *J. Polym. Sci., Part B: Polym. Phys.* **2006**, *44* (10), 1453−1465.

(693) Lai, Y. H.; Mittelsteadt, C. K.; Gittleman, C. S.; Dillard, D. A. Viscoelastic Stress Analysis of Constrained Proton Exchange Membranes under Humidity Cycling. *J. Fuel Cell Sci. Technol.* **2009**, *6* (2), 021002.

(694) Silberstein, M. N.; Boyce, M. C. Constitutive Modeling of the Rate, Temperature, and Hydration Dependent Deformation Response of Nafion to Monotonic and Cyclic Loading. *J. Power Sources* **2010**, *195* (17), 5692−5706.

(695) Silberstein, M. N.; Boyce, M. C. Hygro-Thermal Mechanical Behavior of Nafion During Constrained Swelling. *J. Power Sources* **2011**, *196* (7), 3452−3460.

(696) Yoon, W.; Huang, X. Y. A Nonlinear Viscoelastic-Viscoplastic Constitutive Model for Ionomer Membranes in Polymer Electrolyte Membrane Fuel Cells. *J. Power Sources* **2011**, *196* (8), 3933−3941.

(697) Shi, S.; Chen, G.; Wang, Z.; Chen, X. Mechanical Properties of Nafion 212 Proton Exchange Membrane Subjected To hygrothermal Aging. *J. Power Sources* **2013**, *238* (0), 318−323.

(698) Khattra, N. S.; Karlsson, A. M.; Santare, M. H.; Walsh, P.; Busby, F. C. Effect of Time-Dependent Material Properties on the Mechanical Behavior of Pfsa Membranes Subjected to Humidity Cycling. *J. Power Sources* **2012**, *214*, 365−376.

(699) Kai, Y.; Kitayama, Y.; Omiya, M.; Uchiyama, T.; Kato, M. Crack Formation in Membrane Electrode Assembly under Static and Cyclic Loadings. *J. Fuel Cell Sci. Technol.* **2013**, *10* (2), 021007−021001.

(700) Park, I. S.; Kim, S. M.; Kim, K. J. Mechanical and Thermal Behavior of Ionic Polymer-Metal Composites: Effects of Electroded Metals. *Smart Mater. Struct.* **2007**, *16* (4), 1090−1097.

(701) Lu, Z. W.; Santare, M. H.; Karlsson, A. M.; Busby, F. C.; Walsh, P. Time-Dependent Mechanical Behavior of Proton Exchange Membrane Fuel Cell Electrodes. *J. Power Sources* **2014**, *245* (0), 543−552.

(702) Goulet, M.-A.; Khorasany, R. M. H.; De Torres, C.; Lauritzen, M.; Kjeang, E.; Wang, G. G.; Rajapakse, N. Mechanical Properties of Catalyst Coated Membranes for Fuel Cells. *J. Power Sources* **2013**, *234* (0), 38−47.

(703) Moukheiber, E.; Bas, C.; Flandin, L. Understanding the Formation of Pinholes in Pfsa Membranes with the Essential Work of Fracture (Ewf). *Int. J. Hydrogen Energy* **2014**, *39* (6), 2717−2723.

(704) Grohs, J. R.; Li, Y. Q.; Dillard, D. A.; Case, S. W.; Ellis, M. W.; Lai, Y. H.; Gittleman, C. S. Evaluating the Time and Temperature Dependent Biaxial Strength of Gore-Select (R) Series 57 Proton Exchange Membrane Using a Pressure Loaded Blister Test. *J. Power Sources* **2010**, *195* (2), 527−531.

(705) Li, Y. Q.; Dillard, D. A.; Case, S. W.; Ellis, M. W.; Lai, Y. H.; Gittleman, C. S.; Miller, D. P. Fatigue and Creep to Leak Tests of Proton Exchange Membranes Using Pressure-Loaded Blisters. *J. Power Sources* **2009**, *194* (2), 873−879.

(706) Li, Y. Q.; Quincy, J. K.; Case, S. W.; Ellis, M. W.; Dillard, D. A.; Lai, Y. H.; Budinski, M. K.; Gittleman, C. S. Characterizing the Fracture Resistance of Proton Exchange Membranes. *J. Power Sources* **2008**, *185* (1), 374−380.

(707) Patankar, K.; Dillard, D. A.; Case, S. W.; Ellis, M. W.; Li, Y. Q.; Lai, Y. H.; Budinski, M. K.; Gittleman, C. S. Characterizing Fracture Energy of Proton Exchange Membranes Using a Knife Slit Test. *J. Polym. Sci., Part B: Polym. Phys.* **2010**, *48* (3), 333−343.

(708) Kusoglu, A.; Weber, A. Z. A Mechanistic Model for Pinhole Growth in Fuel-Cell Membranes During Cyclic Loads. *J. Electrochem. Soc.* **2014**, *161* (8), E3311−E3322.

(709) Solasi, R.; Zou, Y.; Huang, X.; Reifsnider, K.; Condit, D. On Mechanical Behavior and in-Plane Modeling of Constrained Pem Fuel Cell Membranes Subjected to Hydration and Temperature Cycles. *J. Power Sources* **2007**, *167* (2), 366−377.

(710) Jia, R. L.; Han, B. H.; Levi, K.; Hasegawa, T.; Ye, J. P.; Dauskardt, R. H. Effect of Cation Contamination and Hydrated Pressure Loading on the Mechanical Properties of Proton Exchange Membranes. *J. Power Sources* **2011**, *196* (8), 3803−3809.

(711) Kundu, S.; Simon, L. C.; Fowler, M.; Grot, S. Mechanical Properties of Nafion [Trademark] Electrolyte Membranes under Hydrated Conditions. *Polymer* **2005**, *46* (25), 11707−11715.

(712) Bauer, F.; Willert-Porada, M. Zirconium Phosphate Nafion (R) Composites - a Microstructure-Based Explanation of Mechanical and Conductivity Properties. *Solid State Ionics* **2006**, *177* (26−32), 2391−2396.

(713) Choi, J.; Lee, K. M.; Wycisk, R.; Pintauro, P. N.; Mather, P. T. Nanofiber Composite Membranes with Low Equivalent Weight Perfluorosulfonic Acid Polymers. *J. Mater. Chem.* **2010**, *20* (30), 6282−6290.

(714) Casciola, M.; Capitani, D.; Comite, A.; Donnadio, A.; Frittella, V.; Pica, M.; Sganappa, M.; Varzi, A. Nafion-Zirconium Phosphate Nanocomposite Membranes with High Filler Loadings: Conductivity and Mechanical Properties. *Fuel Cells* **2008**, *8* (3−4), 217−224.

(715) Thomassin, J. M.; Kollar, J.; Caldarella, G.; Germain, A.; Jerome, R.; Detrembleur, C. Beneficial Effect of Carbon Nanotubes on the Performances of Nafion Membranes in Fuel Cell Applications. *J. Membr. Sci.* **2007**, *303* (1−2), 252−257.

(716) Page, K. A.; Shin, J. W.; Eastman, S. A.; Rowe, B. W.; Kim, S.; Kusoglu, A.; Yager, K. G.; Stafford, G. R. In Situ Method for Measuring the Mechanical Properties of Nafion Thin Films During Hydration Cycles. *ACS Appl. Mater. Interfaces* **2015**, *7* (32), 17874−17883.

(717) Li, J. Y.; Nemat-Nasser, S. Micromechanical Analysis of Ionic Clustering in Nafion Perfluorinated Membrane. *Mech. Mater.* **2000**, *32* (5), 303−314.

(718) Majsztrik, P. W.; Bocarsly, A. B.; Benziger, J. B. An Instrument for Environmental Control of Vapor Pressure and Temperature for Tensile Creep and Other Mechanical Property Measurements. *Rev. Sci. Instrum.* **2007**, *78* (10), 103904.

(719) Silberstein, M. N.; Pillai, P. V.; Boyce, M. C. Biaxial Elastic-Viscoplastic Behavior of Nafion Membranes. *Polymer* **2011**, *52* (2), 529−539.

(720) Khattra, N. S.; Lu, Z. W.; Karlsson, A. M.; Santare, M. H.; Busby, F. C.; Schmiedel, T. Time-Dependent Mechanical Response of a Composite Pfsa Membrane. *J. Power Sources* **2013**, *228* (0), 256−269.

(721) Young, S. K.; Mauritz, K. A. Nafion (R)/(Organically Modified Silicate) Nanocomposites Via Polymer in Situ Sol-Gel Reactions: Mechanical Tensile Properties. *J. Polym. Sci., Part B: Polym. Phys.* **2002**, *40* (19), 2237−2247.

(722) Lu, F.; Gao, X.; Xie, S.; Sun, N.; Zheng, L. Chemical Modification of Nafion Membranes by Protic Ionic Liquids: The Key Role of Ionomer-Cation Interactions. *Soft Matter* **2014**, *10* (39), 7819−7825.

(723) Ishikawa, Y.; Morita, T.; Nakata, K.; Yoshida, K.; Shiozawa, M. Behavior of Water Below the Freezing Point in Pefcs. *J. Power Sources* **2007**, *163* (2), 708−712.

(724) Chen, C.; Fuller, T. F. The Effect of Humidity on the Degradation of Nafion (R) Membrane. *Polym. Degrad. Stab.* **2009**, *94* (9), 1436−1447.

(725) Kundu, S.; Simon, L. C.; Fowler, M. W. Comparison of Two Accelerated Nafion (Tm) Degradation Experiments. *Polym. Degrad. Stab.* **2008**, *93* (1), 214−224.

(726) Kusoglu, A.; Calabrese, M.; Weber, A. Z. Effect of Mechanical Compression on Chemical Degradation of Nafion Membranes. *ECS Electrochem. Lett.* **2014**, *3* (5), F33−F36.

(727) Lim, C.; Ghassemzadeh, L.; Van Hove, F.; Lauritzen, M.; Kolodziej, J.; Wang, G. G.; Holdcroft, S.; Kjeang, E. Membrane Degradation During Combined Chemical and Mechanical Accelerated Stress Testing of Polymer Electrolyte Fuel Cells. *J. Power Sources* **2014**, *257* (0), 102−110.

(728) Yoon, W.; Huang, X. Y. Study of Polymer Electrolyte Membrane Degradation under Ocv Hold Using Bilayer Meas. *J. Electrochem. Soc.* **2010**, *157* (4), B599−B606.

(729) Huang, X. Y.; Solasi, R.; Zou, Y.; Feshler, M.; Reifsnider, K.; Condit, D.; Burlatsky, S.; Madden, T. Mechanical Endurance of Polymer Electrolyte Membrane and Pem Fuel Cell Durability. *J. Polym. Sci., Part B: Polym. Phys.* **2006**, *44* (16), 2346−2357.

(730) Froelich, K.; Rauner, H.; Scheiba, F.; Roth, C.; Ehrenberg, H. Welding of Nafion (R) - the Influence of Time, Temperature and Pressure. *J. Power Sources* **2014**, *267*, 260−268.

(731) Kusoglu, A.; Santare, M. H.; Karlsson, A. M. Aspects of Fatigue Failure Mechanisms in Polymer Fuel Cell Membranes. *J. Polym. Sci., Part B: Polym. Phys.* **2011**, *49* (21), 1506−1517.

(732) Tang, H. L.; Shen, P. K.; Jiang, S. P.; Fang, W.; Mu, P. A Degradation Study of Nation Proton Exchange Membrane of Pem Fuel Cells. *J. Power Sources* **2007**, *170* (1), 85−92.

(733) Liu, W.; Ruth, K.; Rusch, G. Membrane Durability in Pem Fuel Cells. *J. New Mater. Electrochem. Syst.* **2001**, *4* (4), 227−232.

(734) Crum, M.; Liu, W. Effective Testing Matrix for Studying Membrane Durability in Pem Fuel Cells: Part 2. Mechanical Durability and Combined Mechanical and Chemical Durability. *ECS Trans.* **2006**, *3* (1), 541−550.

(735) Ding, G.; Santare, M. H.; Karlsson, A. M.; Kusoglu, A. Numerical Evaluation of Crack Growth in Polymer Electrolyte Fuel Cell Membranes Based on Plastically Dissipated Energy. *J. Power Sources* **2016**, *316*, 114−123.

(736) Brown, H. R. A Molecular Interpretation of the Toughness of Glassy-Polymers. *Macromolecules* **1991**, *24* (10), 2752−2756.

(737) Soboleva, T.; Malek, K.; Xie, Z.; Navessin, T.; Holdcroft, S. Pemfc Catalyst Layers: The Role of Micropores and Mesopores on Water Sorption and Fuel Cell Activity. *ACS Appl. Mater. Interfaces* **2011**, *3* (6), 1827−1837.

(738) Jomori, S.; Komatsubara, K.; Nonoyama, N.; Kato, M.; Yoshida, T. An Experimental Study of the Effects of Operational History on Activity Changes in a Pemfc. *J. Electrochem. Soc.* **2013**, *160* (9), F1067−F1073.

(739) Iden, H.; Ohma, A.; Shinohara, K. Analysis of Proton Transport in Pseudo Catalyst Layers. *J. Electrochem. Soc.* **2009**, *156* (9), B1078−B1084.

(740) Ono, Y.; Ohma, A.; Shinohara, K.; Fushinobu, K. Influence of Equivalent Weight of Ionomer on Local Oxygen Transport Resistance in Cathode Catalyst Layers. *J. Electrochem. Soc.* **2013**, *160* (8), F779−F787.

(741) Lopez-Haro, M.; Guétaz, L.; Printemps, T.; Morin, A.; Escribano, S.; Jouneau, P. H.; Bayle-Guillemaud, P.; Chandezon, F.; Gebel, G. Three-Dimensional Analysis of Nafion Layers in Fuel Cell Electrodes. *Nat. Commun.* **2014**, *5*, 522910.1038/ncomms6229

(742) Siroma, Z.; Ioroi, T.; Fujiwara, N.; Yasuda, K. Proton Conductivity Along Interface in Thin Cast Film of Nafion (R). *Electrochem. Commun.* **2002**, *4* (2), 143−145.

(743) Iden, H.; Sato, K.; Ohma, A.; Shinohara, K. Relationship among Microstructure, Ionomer Property and Proton Transport in Pseudo Catalyst Layers. *J. Electrochem. Soc.* **2011**, *158* (8), B987−B994.

(744) Ohira, A.; Kuroda, S.; Mohamed, H. F. M.; Tavernier, B. Effect of Interface on Surface Morphology and Proton Conduction of Polymer Electrolyte Thin Films. *Phys. Chem. Chem. Phys.* **2013**, *15* (27), 11494−11500.

(745) Wood, D. L.; Chlistunoff, J.; Majewski, J.; Borup, R. L. Nafion Structural Phenomena at Platinum and Carbon Interfaces. *J. Am. Chem. Soc.* **2009**, *131* (50), 18096−18104.

(746) Dishari, S. K.; Hickner, M. A. Antiplasticization and Water Uptake of Nafion Thin Films. *ACS Macro Lett.* **2012**, *1* (2), 291−295.

(747) Modestino, M. A.; Paul, D. K.; Dishari, S.; Petrina, S. A.; Allen, F. I.; Hickner, M. A.; Karan, K.; Segalman, R. A.; Weber, A. Z. Self-Assembly and Transport Limitations in Confined Nafion Films. *Macromolecules* **2013**, *46* (3), 867−873.

(748) Bertoncello, P.; Ciani, I.; Li, F.; Unwin, P. R. Measurement of Apparent Diffusion Coefficients within Ultrathin Nafion Langmuir-Schaefer Films: Comparison of a Novel Scanning Electrochemical Microscopy Approach with Cyclic Voltammetry. *Langmuir* **2006**, *22* (25), 10380−10388.

(749) Dishari, S. K.; Hickner, M. A. Confinement and Proton Transfer in Nafion Thin Films. *Macromolecules* **2013**, *46* (2), 413−421.

(750) Koestner, R.; Roiter, Y.; Kozhinova, I.; Minko, S. Afm Imaging of Adsorbed Nafion Polymer on Mica and Graphite at Molecular Level. *Langmuir* **2011**, *27* (16), 10157−10166.

(751) Paul, D. K.; Karan, K. Conductivity and Wettability Changes of Ultrathin Nafion Films Subjected to Thermal Annealing and Liquid Water Exposure. *J. Phys. Chem. C* **2014**, *118* (4), 1828−1835.

(752) Eastman, S. A.; Kim, S.; Page, K. A.; Rowe, B. W.; Kang, S.; Soles, C. L.; Yager, K. G. Effect of Confinement on Structure, Water Solubility, and Water Transport in Nafion Thin Films. *Macromolecules* **2012**, *45* (19), 7920−7930.

(753) Albert, J. N. L.; Epps, T. H. Self-Assembly of Block Copolymer Thin Films. *Mater. Today* **2010**, *13* (6), 24−33.

(754) Segalman, R. A. Patterning with Block Copolymer Thin Films. *Mater. Sci. Eng., R* **2005**, *48* (6), 191−226.

(755) Fasolka, M. J.; Mayes, A. M. Block Copolymer Thin Films: Physics and Applications1. *Annu. Rev. Mater. Res.* **2001**, *31* (1), 323−355.

(756) Russell, T. P.; Lambooy, P.; Kellogg, G. J.; Mayes, A. M. Diblock Copolymers under Confinement. *Phys. B* **1995**, *213* (0), 22−25.

(757) Huang, E.; Russell, T. P.; Harrison, C.; Chaikin, P. M.; Register, R. A.; Hawker, C. J.; Mays, J. Using Surface Active Random Copolymers to Control the Domain Orientation in Diblock Copolymer Thin Films. *Macromolecules* **1998**, *31* (22), 7641−7650.

(758) Mansky, P.; Russell, T. P.; Hawker, C. J.; Pitsikalis, M.; Mays, J. Ordered Diblock Copolymer Films on Random Copolymer Brushes. *Macromolecules* **1997**, *30* (22), 6810−6813.

(759) Masuda, T.; Sonsudin, F.; Singh, P. R.; Naohara, H.; Uosaki, K. Potential-Dependent Adsorption and Desorption of Perfluorosulfonated Ionomer on a Platinum Electrode Surface Probed by Electrochemical Quartz Crystal Microbalance and Atomic Force Microscopy. *J. Phys. Chem. C* **2013**, *117* (30), 15704−15709.

(760) Kim, S.; Dura, J. A.; Page, K. A.; Rowe, B. W.; Yager, K. G.; Lee, H. J.; Soles, C. L. Surface-Induced Nanostructure and Water Transport of Thin Proton-Conducting Polymer Films. *Macromolecules* **2013**, *46* (14), 5630−5637.

(761) Suzuki, T.; Kudo, K.; Morimoto, Y. Model for Investigation of Oxygen Transport Limitation in a Polymer Electrolyte Fuel Cell. *J. Power Sources* **2013**, *222*, 379−389.

(762) Paul, D. K.; Karan, K.; Docoslis, A.; Giorgi, J. B.; Pearce, J. Characteristics of Self-Assembled Ultrathin Nafion Films. *Macromolecules* **2013**, *46* (9), 3461−3475.

(763) Shim, H. K.; Paul, D. K.; Karan, K. Resolving the Contradiction between Anomalously High Water Uptake and Low Conductivity of Nanothin Nafion Films on Sio2 Substrate. *Macromolecules* **2015**, *48* (22), 8394−8397.

(764) Paul, D. K.; Shim, H. K.; Giorgi, J. B.; Karan, K. Thickness Dependence of Thermally Induced Changes in Surface and Bulk Properties of Nafion (R) Nanofilms. *J. Polym. Sci., Part B: Polym. Phys.* **2016**, *54* (13), 1267−1277.

(765) Bertoncello, P.; Wilson, N. R.; Unwin, P. R. One-Step Formation of Ultra-Thin Chemically Functionalized Redox-Active Langmuir-Schaefer Nafion Films. *Soft Matter* **2007**, 3 (10), 1300−1307.

(766) Nadermann, N. K.; Davis, E. M.; Page, K. A.; Stafford, C. M.; Chan, E. P. Using Indentation to Quantify Transport Properties of Nanophase-Segregated Polymer Thin Films. *Adv. Mater.* **2015**, *27*, 4924; DOI: 10.1002/adma.201501880.

(767) Zimudzi, T. J.; Hickner, M. A. Signal Enhanced Ftir Analysis of Alignment in Nafion Thin Films at Sio2 and Au Interfaces. *ACS Macro Lett.* **2016**, *5* (1), 83−87.

(768) Dura, J. A.; Murthi, V. S.; Hartman, M.; Satija, S. K.; Majkrzak, C. F. Multilamellar Interface Structures in Nafion. *Macromolecules* **2009**, *42* (13), 4769−4774.

(769) Paul, D. K.; McCreery, R.; Karan, K. Proton Transport Property in Supported Nafion Nanothin Films by Electrochemical Impedance Spectroscopy. *J. Electrochem. Soc.* **2014**, *161* (14), F1395−F1402.

(770) Abuin, G. C.; Cecilia Fuertes, M.; Corti, H. R. Substrate Effect on the Swelling and Water Sorption of Nafion Nanomembranes. *J. Membr. Sci.* **2013**, *428* (0), 507−515.

(771) Paul, D. K.; Fraser, A.; Karan, K. Understanding the Ionomer Structure and the Proton Conduction Mechanism in Pefc Catalyst Layer: Adsorbed Nafion on Model Substrate. *ECS Trans.* **2011**, *41* (1), 1393−1406.

(772) Paul, D. K.; Giorgi, J. B.; Karan, K. Chemical and Ionic Conductivity Degradation of Ultra-Thin Ionomer Film by X-Ray Beam Exposure. *J. Electrochem. Soc.* **2013**, *160* (4), F464−F469.

(773) Umemura, K.; Wang, T.; Hara, M.; Kuroda, R.; Uchida, O.; Nagai, M. Nanocharacterization and Nanofabrication of a Nafion Thin Film in Liquids by Atomic Force Microscopy. *Langmuir* **2006**, *22* (7), 3306−3312.

(774) Hill, T. A.; Carroll, D. L.; Czerw, R.; Martin, C. W.; Perahia, D. Atomic Force Microscopy Studies on the Dewetting of Perfluorinated Ionomer Thin Films. *J. Polym. Sci., Part B: Polym. Phys.* **2003**, *41* (2), 149−158.

(775) Kalisvaart, W. P.; Fritzsche, H.; Merida, W. Water Uptake and Swelling Hysteresis in a Nafion Thin Film Measured with Neutron Reflectometry. *Langmuir* **2015**, *31* (19), 5416−5422.

(776) DeCaluwe, S. C.; Kienzle, P. A.; Bhargava, P.; Baker, A. M.; Dura, J. A. Phase Segregation of Sulfonate Groups in Nafion Interface Lamellae, Quantified Via Neutron Reflectometry Fitting Techniques for Multi-Layered Structures. *Soft Matter* **2014**, *10* (31), 5763−5776.

(777) Hexemer, A.; Müller-Buschbaum, P. Advanced Grazing-Incidence Techniques for Modern Soft-Matter Materials Analysis. *IUCrJ* **2015**, *2* (1), 106−125.

(778) Kudo, K.; Morimoto, Y. Analysis of Oxygen Transport Resistance of Nafion Thin Film on Pt Electrode. *ECS Trans.* **2013**, *50* (2), 1487−1494.

(779) Andersen, S. M.; Borghei, M.; Dhiman, R.; Ruiz, V.; Kauppinen, E.; Skou, E. Adsorption Behavior of Perfluorinated Sulfonic Acid Ionomer on Highly Graphitized Carbon Nanofibers and Their Thermal Stabilities. *J. Phys. Chem. C* **2014**, *118* (20), 10814−10823.

(780) Masuda, T.; Naohara, H.; Takakusagi, S.; Singh, P. R.; Uosaki, K. Formation and Structure of Perfluorosulfonated Ionomer Thin Film on a Graphite Surface. *Chem. Lett.* **2009**, *38* (9), 884−885.

(781) Subbaraman, R.; Strmcnik, D.; Stamenkovic, V.; Markovic, N. M. Three Phase Interfaces at Electrified Metal-Solid Electrolyte Systems 1. Study of the Pt(Hkl)-Nafion Interface. *J. Phys. Chem. C* **2010**, *114* (18), 8414−8422.

(782) Ayato, Y.; Kunimatsu, K.; Osawa, M.; Okada, T. Study of Pt Electrode/Nafion Ionomer Interface in Hclo4 by in Situ Surface-Enhanced Ftir Spectroscopy. *J. Electrochem. Soc.* **2006**, *153* (2), A203−A209.

(783) Kanamura, K.; Morikawa, H.; Umegaki, T. Observation of Interface between Pt Electrode and Nafion Membrane. *J. Electrochem. Soc.* **2003**, *150* (2), A193−A198.

(784) Kendrick, I.; Kumari, D.; Yakaboski, A.; Dimakis, N.; Smotkin, E. S. Elucidating the Ionomer-Electrified Metal Interface. *J. Am. Chem. Soc.* **2010**, *132* (49), 17611−17616.

(785) Nouri-Khorasani, A.; Malek, K.; Malek, A.; Mashio, T.; Wilkinson, D. P.; Eikerling, M. H. Molecular Modeling of the Proton Density Distribution in a Water-Filled Slab-Like Nanopore Bounded by Pt Oxide and Ionomer. *Catal. Today* **2016**, *262*, 133−140.

(786) Damasceno Borges, D.; Gebel, G.; Franco, A. A.; Malek, K.; Mossa, S. Morphology of Supported Polymer Electrolyte Ultrathin Films: A Numerical Study. *J. Phys. Chem. C* **2015**, *119* (2), 1201−1216.

(787) He, Q. P.; Suraweera, N. S.; Joy, D. C.; Keffer, D. J. Structure of the Lonomer Film in Catalyst Layers of Proton Exchange Membrane Fuel Cells. *J. Phys. Chem. C* **2013**, *117* (48), 25305−25316.

(788) Mashio, T.; Malek, K.; Eikerling, M.; Ohma, A.; Kanesaka, H.; Shinohara, K. Molecular Dynamics Study of Ionomer and Water Adsorption at Carbon Support Materials. *J. Phys. Chem. C* **2010**, *114* (32), 13739−13745.

(789) Ugo, P.; Bertoncello, P.; Vezzà, F. Langmuir−Blodgett Films of Different Ionomeric Polymers Deposited on Electrode Surfaces. *Electrochim. Acta* **2004**, *49* (22−23), 3785−3793.

(790) Ahmed, M.; Morgan, D.; Attard, G. A.; Wright, E.; Thompsett, D.; Sharman, J. Unprecedented Structural Sensitivity toward Average Terrace Width: Nafion Adsorption at Pt{Hkl} Electrodes. *J. Phys. Chem. C* **2011**, *115* (34), 17020−17027.

(791) Koestner, R.; Roiter, Y.; Kozhinova, I.; Minko, S. Effect of Local Charge Distribution on Graphite Surface on Nafion Polymer Adsorption as Visualized at the Molecular Level. *J. Phys. Chem. C* **2011**, *115* (32), 16019−16026.

(792) Roth, J.; Eller, J.; Büchi, F. N. Effects of Synchrotron Radiation on Fuel Cell Materials. *J. Electrochem. Soc.* **2012**, *159* (8), F449−F455.

(793) Rodgers, M. P.; Bonville, L. J.; Mukundan, R.; Borup, R. L.; Ahluwalia, R.; Beattie, P.; Brooker, R. P.; Mohajeri, N.; Kunz, H. R.; Slattery, D. K.; et al. Perfluorinated Sulfonic Acid Membrane and Membrane Electrode Assembly Degradation Correlating Accelerated Stress Testing and Lifetime Testing. *ECS Trans.* **2013**, *58* (1), 129−148.

(794) Zhang, S. S.; Yuan, X. Z.; Wang, H. J.; Merida, W.; Zhu, H.; Shen, J.; Wu, S. H.; Zhang, J. J. A Review of Accelerated Stress Tests of Mea Durability in Pem Fuel Cells. *Int. J. Hydrogen Energy* **2009**, *34* (1), 388−404.

(795) Mukundan, R.; James, G.; Davey, J.; Langlois, D.; Torraco, D.; Yoon, W.; Weber, A. Z.; Borup, R. Accelerated Testing Validation. *ECS Trans.* **2011**, *41* (1), 613−619.

(796) Healy, J.; Hayden, C.; Xie, T.; Olson, K.; Waldo, R.; Brundage, A.; Gasteiger, H.; Abbott, J. Aspects of the Chemical Degradation of Pfsa Ionomers Used in Pem Fuel Cells. *Fuel Cells* **2005**, *5* (2), 302−308.

(797) Ghassemzadeh, L.; Holdcroft, S. Quantifying the Structural Changes of Perfluorosulfonated Acid Ionomer Upon Reaction with Hydroxyl Radicals. *J. Am. Chem. Soc.* **2013**, *135* (22), 8181−8184.

(798) Shi, W. Q.; Baker, L. A. Imaging Heterogeneity and Transport of Degraded Nafion Membranes. *RSC Adv.* **2015**, *5* (120), 99284−99290.

(799) Zhou, C.; Guerra, M. A.; Qiu, Z. M.; Zawodzinski, T. A.; Schiraldi, D. A. Chemical Durability Studies of Perfluorinated Sulfonic Acid Polymers and Model Compounds under Mimic Fuel Cell Conditions. *Macromolecules* **2007**, *40* (24), 8695−8707.

(800) Kreitmeier, S.; Michiardi, M.; Wokaun, A.; Buchi, F. N. Factors Determining the Gas Crossover through Pinholes in Polymer Electrolyte Fuel Cell Membranes. *Electrochim. Acta* **2012**, *80*, 240−247.

(801) Schiraldi, D. A. Perfluorinated Polymer Electrolyte Membrane Durability. *J. Macromol. Sci., Polym. Rev.* **2006**, *46* (3), 315−327.

(802) Danilczuk, M.; Schlick, S.; Coms, F. D. Cerium(Iii) as a Stabilizer of Perfluorinated Membranes Used in Fuel Cells: In Situ Detection of Early Events in the Esr Resonator. *Macromolecules* **2009**, *42* (22), 8943−8949.

(803) Hicks, M.; Pierpont, D.; Turner, P.; Watschke, T. Accelerated Testing and Lifetime Modeling for the Development of Durable Fuel Cell Meas. *ECS Trans.* **2005**, *1* (8), 229−237.

(804) Danilczuk, M.; Lancuki, L.; Schlick, S.; Hamrock, S. J.; Haugen, G. M. In-Depth Profiling of Degradation Processes in a Fuel Cell: 2d Spectral-Spatial Ftir Spectra of Nafion Membranes. *ACS Macro Lett.* **2012**, *1* (2), 280−285.

(805) Endoh, E.; Terazono, S.; Widjaja, H.; Takimoto, Y. Degradation Study of Mea for Pemfcs under Low Humidity Conditions. *Electrochem. Solid-State Lett.* **2004**, *7* (7), A209−A211.

(806) Rodgers, M. P.; Pearman, B. P.; Mohajeri, N.; Bonville, L. J.; Slattery, D. K. Effect of Perfluorosulfonic Acid Membrane Equivalent Weight on Degradation under Accelerated Stress Conditions. *Electrochim. Acta* **2013**, *100*, 180−187.

(807) D'Urso, C.; Oldani, C.; Baglio, V.; Merlo, L.; Arico, A. S. Towards Fuel Cell Membranes with Improved Lifetime: Aquivion (R) Perfluorosulfonic Acid Membranes Containing Immobilized Radical Scavengers. *J. Power Sources* **2014**, *272*, 753−758.

(808) Liu, W.; Crum, M. Effective Testing Matrix for Studying Membrane Durability in Pem Fuel Cells: Part I. Chemical Durability. *ECS Trans.* **2006**, *3* (1), 531−540.

(809) Trogadas, P.; Parrondo, J.; Ramani, V. Degradation Mitigation in Polymer Electrolyte Membranes Using Cerium Oxide as a Regenerative Free-Radical Scavenger. *Electrochem. Solid-State Lett.* **2008**, *11* (7), B113−B116.

(810) Coms, F.; Gittleman, C.; Brenner, A.; Jiang, R.; Patent Assignee: GM Global Technology Operations LLC. #9,083,050, 2015.

(811) MacKinnon, S. M.; Coms, F.; Fuller, T. J.; Gittleman, C. S.; Jiang, R.; Google Patents, 2015.

(812) Trogadas, P.; Parrondo, J.; Ramani, V. Ceo2 Surface Oxygen Vacancy Concentration Governs in Situ Free Radical Scavenging Efficacy in Polymer Electrolytes. *ACS Appl. Mater. Interfaces* **2012**, *4* (10), 5098−5102.

(813) Prabhakaran, V.; Arges, C. G.; Ramani, V. Investigation of Polymer Electrolyte Membrane Chemical Degradation and Degradation Mitigation Using in Situ Fluorescence Spectroscopy. *Proc. Natl. Acad. Sci. U. S. A.* **2012**, *109* (4), 1029−1034.

(814) Gubler, L.; Koppenol, W. H. Kinetic Simulation of the Chemical Stabilization Mechanism in Fuel Cell Membranes Using Cerium and Manganese Redox Couples. *J. Electrochem. Soc.* **2012**, *159* (2), B211−B218.

(815) Stewart, S. M.; Spernjak, D.; Borup, R.; Datye, A.; Garzon, F. Cerium Migration through Hydrogen Fuel Cells During Accelerated Stress Testing. *ECS Electrochem. Lett.* **2014**, *3* (4), F19−F22.

(816) Kundu, S.; Fowler, M. W.; Simon, L. C.; Grot, S. Morphological Features (Defects) in Fuel Cell Membrane Electrode Assemblies. *J. Power Sources* **2006**, *157* (2), 650−656.

(817) Kreitmeier, S.; Lerch, P.; Wokaun, A.; Buchi, F. N. Local Degradation at Membrane Defects in Polymer Electrolyte Fuel Cells. *J. Electrochem. Soc.* **2013**, *160* (4), F456−F463.

(818) Kreitmeier, S.; Schuler, G. A.; Wokaun, A.; Buchi, F. N. Investigation of Membrane Degradation in Polymer Electrolyte Fuel Cells Using Local Gas Permeation Analysis. *J. Power Sources* **2012**, *212*, 139−147.

(819) Weber, A. Z.; Newman, J. Effects of Membrane- and Catalyst-Layer-Thickness Nonuniformities in Polymer-Electrolyte Fuel Cells. *J. Electrochem. Soc.* **2007**, *154* (4), B405−B412.

(820) Weber, A. Z. Gas-Crossover and Membrane-Pinhole Effects in Polymer-Electrolyte Fuel Cells. *J. Electrochem. Soc.* **2008**, *155* (6), B521−B531.

(821) Bender, G.; Felt, W.; Ulsh, M. Detecting and Localizing Failure Points in Proton Exchange Membrane Fuel Cells Using Ir Thermography. *J. Power Sources* **2014**, *253* (0), 224−229.

(822) Kusoglu, A.; Karlsson, A. M.; Santare, M. H.; Cleghorn, S.; Johnson, W. B. Mechanical Behavior of Fuel Cell Membranes under Humidity Cycles and Effect of Swelling Anisotropy on the Fatigue Stresses. *J. Power Sources* **2007**, *170* (2), 345−358.

(823) Kusoglu, A.; Santare, M. H.; Karlsson, A. M.; Cleghorn, S.; Johnson, W. B. Numerical Investigation of Mechanical Durability in Polymer Electrolyte Membrane Fuel Cells. *J. Electrochem. Soc.* **2010**, *157* (5), B705−B713.

(824) Bas, C.; Flandin, L.; Danero, A. S.; Claude, E.; Rossinot, E.; Alberola, N. D. Changes in the Chemical Structure and Properties of a Perfluorosulfonated Acid Membrane Induced by Fuel-Cell Operation. *J. Appl. Polym. Sci.* **2010**, *117* (4), 2121−2132.

(825) Bas, C.; Alberola, N. D.; Flandin, L. Effects of Contaminant on Thermal Properties in Perfluorinated Sulfonic Acid Membranes. *J. Membr. Sci.* **2010**, *363* (1−2), 67−71.

(826) Yoon, W.; Huang, X. Acceleration of Chemical Degradation of Perfluorosulfonic Acid Ionomer Membrane by Mechanical Stress: Experimental Evidence. *ECS Trans.* **2010**, *33* (1), 907−911.

(827) St Pierre, J.; Wilkinson, D. P.; Knights, S.; Bos, M. L. Relationships between Water Management, Contamination and Lifetime Degradation in Pefc. *J. New Mater. Electrochem. Syst.* **2000**, *3* (2), 99−106.

(828) Okada, T. In *Handbook of Fuel Cells*; John Wiley & Sons, Ltd.: New York, 2010, DOI: 10.1002/9780470974001.f303054.

(829) Pozio, A.; Silva, R. F.; De Francesco, M.; Giorgi, L. Nafion Degradation in Pefcs from End Plate Iron Contamination. *Electrochim. Acta* **2003**, *48* (11), 1543−1549.

(830) Chen, F. L.; Su, Y. G.; Soong, C. Y.; Yan, W. M.; Chu, H. S. Transient Behavior of Water Transport in the Membrane of a Pem Fuel Cell. *J. Electroanal. Chem.* **2004**, *566* (1), 85−93.

(831) Okada, T. Theory for Water Management in Membranes for Polymer Electrolyte Fuel Cells - Part 2. The Effect of Impurity Ions at the Cathode Side on the Membrane Performances. *J. Electroanal. Chem.* **1999**, *465* (1), 18−29.

(832) Okada, T.; Nakamura, N.; Yuasa, M.; Sekine, I. Ion and Water Transport Characteristics in Membranes for Polymer Electrolyte Fuel Cells Containing H+ and Ca2+ Cations. *J. Electrochem. Soc.* **1997**, *144* (8), 2744−2750.

(833) Okada, T.; Ayato, Y.; Yuasa, M.; Sekine, I. The Effect of Impurity Cations on the Transport Characteristics of Perfluorosulfonated Ionomer Membranes. *J. Phys. Chem. B* **1999**, *103* (17), 3315−3322.

(834) Kelly, M. J.; Fafilek, G.; Besenhard, J. O.; Kronberger, H.; Nauer, G. E. Contaminant Absorption and Conductivity in Polymer Electrolyte Membranes. *J. Power Sources* **2005**, *145* (2), 249−252.

(835) Kelly, M. J.; Egger, B.; Fafilek, G.; Besenhard, J. O.; Kronberger, H.; Nauer, G. E. Conductivity of Polymer Electrolyte Membranes by Impedance Spectroscopy with Microelectrodes. *Solid State Ionics* **2005**, *176* (25−28), 2111−2114.

(836) Weber, A. Z.; Delacourt, C. Mathematical Modelling of Cation Contamination in a Proton-Exchange Membrane. *Fuel Cells* **2008**, *8* (6), 459−465.

(837) Andersen, S. M. The Importance of Ion Selectivity of Perfluorinated Sulfonic Acid Membrane for the Performance of Proton Exchange Membrane Fuel Cells. *J. Fuel Cell Sci. Technol.* **2015**, *12* (6), 06101010.1115/1.4032430

(838) Bendert, J. C.; Papadias, D. D.; Myers, D. J. The Effect of Na+ Impurities on the Conductivity and Water Uptake of Nafion 115 Polymer Electrolyte Fuel Cell Membranes. *J. Electrochem. Soc.* **2010**, *157* (10), B1486−B1490.

(839) Hongsirikarn, K.; Napapruekchart, T.; Mo, X. H.; Goodwin, J. G. Effect of Ammonium Ion Distribution on Nafion (R) Conductivity. *J. Power Sources* **2011**, *196* (2), 644−651.

(840) St-Pierre, J. Pemfc Contamination Model: Foreign Cation Exchange with Ionomer Protons. *J. Power Sources* **2011**, *196* (15), 6274−6283.

(841) Cho, H. S.; Das, M.; Wang, H. L.; Dinh, H. N.; Van Zee, J. W. The Contamination Mechanism and Behavior of Amide Bond Containing Organic Contaminant on Pemfc. *J. Electrochem. Soc.* **2015**, *162* (4), F427−F435.

(842) Casciola, M.; Alberti, G.; Sganappa, M.; Narducci, R. Factors Affecting the Stability of Nafion Conductivity at High Temperature and Relative Humidity. *Desalination* **2006**, *200* (1−3), 639−641.

(843) Zecchina, A.; Geobaldo, F.; Spoto, G.; Bordiga, S.; Ricchiardi, G.; Buzzoni, R.; Petrini, G. Ftir Investigation of the Formation of Neutral and Ionic Hydrogen-Bonded Complexes by Interaction of H-Zsm-5 and H-Mordenite with Ch3cn and H2o: Comparison with the H-Nafion Superacidic System. *J. Phys. Chem.* **1996**, *100* (41), 16584−16599.

(844) García-Salaberri, P. A.; Hwang, G.; Vera, M.; Weber, A. Z.; Gostick, J. T. Effective Diffusivity in Partially-Saturated Carbon-Fiber Gas Diffusion Layers: Effect of through-Plane Saturation Distribution. *Int. J. Heat Mass Transfer* **2015**, *86* (0), 319−333.

(845) Feng, M.; Qu, R.; Wei, Z.; Wang, L.; Sun, P.; Wang, Z. Characterization of the Thermolysis Products of Nafion Membrane: A Potential Source of Perfluorinated Compounds in the Environment. *Sci. Rep.* **2015**, *5*, 9859.

(846) Samms, S. R.; Wasmus, S.; Savinell, R. F. Thermal Stability of Nafion® in Simulated Fuel Cell Environments. *J. Electrochem. Soc.* **1996**, *143* (5), 1498−1504.

(847) Lage, L. G.; Delgado, P. G.; Kawano, Y. Thermal Stability and Decomposition of Nafion (R) Membranes with Different Cations - Using High-Resolution Thermogravimetry. *J. Therm. Anal. Calorim.* **2004**, *75* (2), 521−530.

(848) Laporta, M.; Pegoraro, M.; Zanderighi, L. Recast Nafion-117 Thin Film from Water Solution. *Macromol. Mater. Eng.* **2000**, *282* (9), 22−29.

(849) Morita, S.; Kitagawa, K. Temperature-Dependent Structure Changes in Nafion Ionomer Studied by Pcmw2d Ir Correlation Spectroscopy. *J. Mol. Struct.* **2010**, *974* (1−3), 56−59.

(850) Feldheim, D. L.; Lawson, D. R.; Martin, C. R. Influence of the Sulfonate Countercation on the Thermal-Stability of Nafion(R) Perfluorosulfonate Membranes. *J. Polym. Sci., Part B: Polym. Phys.* **1993**, *31* (8), 953−957.

(851) Iwai, Y.; Yamanishi, T. Thermal Stability of Ion-Exchange Nafion N117cs Membranes. *Polym. Degrad. Stab.* **2009**, *94* (4), 679−687.

(852) Moukheiber, E.; Bas, C.; Alberola, N. D.; Flandin, L. Infrared and Thermal Behaviour of Proton Exchange Membrane (Pem) after Cationic Contamination. *J. Membr. Sci.* **2013**, *431*, 105−112.

(853) Alberti, G.; Casciola, M. Composite Membranes for Medium-Temperature Pem Fuel Cells. *Annu. Rev. Mater. Res.* **2003**, *33*, 129−154.

(854) Laberty-Robert, C.; Valle, K.; Pereira, F.; Sanchez, C. Design and Properties of Functional Hybrid Organic-Inorganic Membranes for Fuel Cells. *Chem. Soc. Rev.* **2011**, *40* (2), 961−1005.

(855) Li, Q. F.; He, R. H.; Jensen, J. O.; Bjerrum, N. J. Approaches and Recent Development of Polymer Electrolyte Membranes for Fuel Cells Operating above 100 Degrees C. *Chem. Mater.* **2003**, *15* (26), 4896−4915.

(856) Haugen, G. M.; Meng, F. Q.; Aieta, N. V.; Horan, J. L.; Kuo, M. C.; Frey, M. H.; Hamrock, S. J.; Herring, A. M. The Effect of Heteropoly Acids on Stability of Pfsa Pems under Fuel Cell Operation. *Electrochem. Solid-State Lett.* **2007**, *10* (3), B51−B55.

(857) DuPont; *Product Information: Nafion Xl Pfsa Membrane*, 2010

(858) Tang, H. L.; Pan, M.; Wang, F. A Mechanical Durability Comparison of Various Perfluocarbon Proton Exchange Membranes. *J. Appl. Polym. Sci.* **2008**, *109* (4), 2671−2678.

(859) Verbrugge, M. W.; Hill, R. F.; Schneider, E. W. Composite Membranes for Fuel-Cell Applications. *AIChE J.* **1992**, *38* (1), 93−100.

(860) Liu, C.; Martin, C. R. Ion-Transporting Composite Membranes 0.3. Selectivity and Rate of Ion-Transport in Nafion-Impregnated Gore-Tex Membranes Prepared by a High-Temperature Solution Casting Method. *J. Electrochem. Soc.* **1990**, *137* (10), 3114−3120.

(861) Mistry, M. K.; Choudhury, N. R.; Dutta, N. K.; Knott, R.; Shi, Z. Q.; Holdcroft, S. Novel Organic-Inorganic Hybrids with Increased Water Retention for Elevated Temperature Proton Exchange Membrane Application. *Chem. Mater.* **2008**, *20* (21), 6857−6870.

(862) Greso, A. J.; Moore, R. B.; Cable, K. M.; Jarrett, W. L.; Mauritz, K. A. Chemical Modification of a Nafion(R) Sulfonyl Fluoride Precursor Via in Situ Sol-Gel Reactions. *Polymer* **1997**, *38* (6), 1345−1356.

(863) Slade, S. M.; Smith, J. R.; Campbell, S. A.; Ralph, T. R.; de Leon, C. P.; Walsh, F. C. Characterisation of a Re-Cast Composite Nafion (R) 1100 Series of Proton Exchange Membranes Incorporating Inert Inorganic Oxide Particles. *Electrochim. Acta* **2010**, *55* (22), 6818−6829.

(864) Bauer, F.; Willert-Porada, M. Comparison between Nafion (R) and a Nafion (R) Zirconium Phosphate Nano-Composite in Fuel Cell Applications. *Fuel Cells* **2006**, *6* (3−4), 261−269.

(865) Yang, C.; Srinivasan, S.; Bocarsly, A. B.; Tulyani, S.; Benziger, J. B. A Comparison of Physical Properties and Fuel Cell Performance of Nafion and Zirconium Phosphate/Nafion Composite Membranes. *J. Membr. Sci.* **2004**, *237* (1−2), 145−161.

(866) Casciola, M.; Bagnasco, G.; Donnadio, A.; Micoli, L.; Pica, M.; Sganappa, M.; Turco, M. Conductivity and Methanol Permeability of Nafion-Zirconium Phosphate Composite Membranes Containing High Aspect Ratio Filler Particles. *Fuel Cells* **2009**, *9* (4), 394−400.

(867) Liu, Y. H.; Yi, B. L.; Shao, Z. G.; Xing, D. M.; Zhang, H. M. Carbon Nanotubes Reinforced Nafion Composite Membrane for Fuel Cell Applications. *Electrochem. Solid-State Lett.* **2006**, *9* (7), A356−A359.

(868) Cele, N. P.; Ray, S. S.; Pillai, S. K.; Ndwandwe, M.; Nonjola, S.; Sikhwivhilu, L.; Mathe, M. K. Carbon Nanotubes Based Nafion Composite Membranes for Fuel Cell Applications. *Fuel Cells* **2010**, *10* (1), 64−71.

(869) Chang, C. M.; Li, H. Y.; Lai, J. Y.; Liu, Y. L. Nanocomposite Membranes of Nafion and Fe3o4-Anchored and Nafion-Functionalized Multiwalled Carbon Nanotubes Exhibiting High Proton Conductivity and Low Methanol Permeability for Direct Methanol Fuel Cells. *RSC Adv.* **2013**, *3* (31), 12895−12904.

(870) Cele, N. P.; Ray, S. S. Effect of Multiwalled Carbon Nanotube Loading on the Properties of Nafion (R) Membranes. *J. Mater. Res.* **2015**, *30* (1), 66−78.

(871) Tazi, B.; Savadogo, O. Effect of Various Heteropolyacids (Hpas) on the Characteristics of Nafion((R)) - Hpas Membranes and Their H-2 /O-2 Polymer Electrolyte Fuel Cell Parameters. *J. New Mater. Electrochem. Syst.* **2001**, *4* (3), 187−196.

(872) Ramani, V.; Kunz, H. R.; Fenton, J. M. Investigation of Nafion (R)/Hpa Composite Membranes for High Temperature/Low Relative Humidity Pemfc Operation. *J. Membr. Sci.* **2004**, *232* (1−2), 31−44.

(873) Chen, T. Y.; Leddy, J. Ion Exchange Capacity of Nafion and Nafion Composites. *Langmuir* **2000**, *16* (6), 2866−2871.

(874) Karakoti, A.; Singh, S.; Dowding, J. M.; Seal, S.; Self, W. T. Redox-Active Radical Scavenging Nanomaterials. *Chem. Soc. Rev.* **2010**, *39* (11), 4422−4432.

(875) Park, A. M.; Turley, F. E.; Wycisk, R. J.; Pintauro, P. N. Electrospun and Cross-Linked Nanofiber Composite Anion Exchange Membranes. *Macromolecules* **2014**, *47* (1), 227−235.

(876) Chen, S. L.; Bocarsly, A. B.; Benziger, J. Nafion-Layered Sulfonated Polysulfone Fuel Cell Membranes. *J. Power Sources* **2005**, *152* (1), 27−33.

(877) Ke, C. C.; Li, X. J.; Qu, S. G.; Shao, Z. G.; Yi, B. L. Preparation and Properties of Nafion/Sio2 Composite Membrane Derived Via in Situ Sol-Gel Reaction: Size Controlling and Size Effects of Sio2 Nano-Particles. *Polym. Adv. Technol.* **2012**, *23* (1), 92−98.

(878) Pereira, F.; Valle, K.; Belleville, P.; Morin, A.; Lambert, S.; Sanchez, C. Advanced Mesostructured Hybrid Silica-Nafion Membranes for High-Performance Pem Fuel Cell. *Chem. Mater.* **2008**, *20* (5), 1710−1718.

(879) Filipoi, C.; Demco, D. E.; Zhu, X. M.; Vinokur, R.; Conradi, O.; Fechete, R.; Moller, M. Channel Orientation Anisotropy in Perfluorosulfonic Acid/Sio(2) Composite Proton Exchange Membranes: Water Self-Diffusion Study Using Nmr. *Chem. Phys. Lett.* **2011**, *513* (4−6), 251−255.

(880) Huang, L. N.; Chen, L. C.; Yu, T. L.; Lin, H. L. Nafion/Ptfe/Silicate Composite Membranes for Direct Methanol Fuel Cells. *J. Power Sources* **2006**, *161* (2), 1096−1105.

(881) Casciola, M.; Capitani, D.; Donnadio, A.; Frittella, V.; Pica, M.; Sganappa, M. Preparation, Proton Conductivity and Mechanical Properties of Nafion 117-Zirconium Phosphate Sulphophenylphosphonate Composite Membranes. *Fuel Cells* **2009**, *9* (4), 381−386.

(882) Feng, K.; Tang, B. B.; Wu, P. Y. Sulfonated Graphene Oxide-Silica for Highly Selective Nafion-Based Proton Exchange Membranes. *J. Mater. Chem. A* **2014**, *2* (38), 16083−16092.

(883) Park, Y. S.; Yamazaki, Y. Low Water Uptake Content and Low Water/Methanol Transport in Cp/Nafion Hybrid Membrane with High Non-Hydrogen Bonding. *J. Membr. Sci.* **2005**, *261* (1−2), 58−66.

(884) Cele, N. P.; Ray, S. S.; Sikhwivhilu, L. Nafion Titania Nanotubes Nanocomposite Electrolytes for High-Temperature Direct Methanol Fuel Cells. *J. Nanomater.* **2012**, *2012*, 1.

(885) Davis, E. M.; Kim, J.; Oleshko, V. P.; Page, K. A.; Soles, C. L. Uncovering the Structure of Nafion-Sio2 Hybrid Ionomer Membranes for Prospective Large-Scale Energy Storage Devices. *Adv. Funct. Mater.* **2015**, *25* (26), 4064−4075.

(886) Di Noto, V.; Piga, M.; Giffin, G. A.; Vezzu, K.; Zawodzinski, T. A. Interplay between Mechanical, Electrical, and Thermal Relaxations in Nanocomposite Proton Conducting Membranes Based on Nafion and a [(Zro2)Center Dot(Ta2o5)(0.119)] Core-Shell Nanofiller. *J. Am. Chem. Soc.* **2012**, *134* (46), 19099−19107.

(887) Chaudhury, S.; Agarwal, C.; Pandey, A. K.; Aher, V. T.; Panicker, L.; Ramagiri, S. V.; Bellare, J. R.; Goswami, A. Counter-Ions Diffusion Properties of Silica Embedded Poly(Perfluorosulfonic) Acid Membrane. *J. Membr. Sci.* **2011**, *382* (1−2), 262−270.

(888) Mecheri, B.; Felice, V.; Zhang, Z.; D'Epifanio, A.; Licoccia, S.; Tavares, A. C. Dsc and Dvs Investigation of Water Mobility in Nafion/Zeolite Composite Membranes for Fuel Cell Applications. *J. Phys. Chem. C* **2012**, *116* (39), 20820−20829.

(889) Li, X.; Roberts, E. P. L.; Holmes, S. M.; Zholobenko, V. Functionalized Zeolite a-Nafion Composite Membranes for Direct Methanol Fuel Cells. *Solid State Ionics* **2007**, *178* (19−20), 1248−1255.

(890) Guo, D. J.; Ding, H. T.; Wei, H. J.; He, Q. S.; Yu, M.; Dai, Z. D. Hybrids Perfluorosulfonic Acid Ionomer and Silicon Oxide Membrane for Application in Ion-Exchange Polymer-Metal Composite Actuators. *Sci. China, Ser. E: Technol. Sci.* **2009**, *52* (10), 3061−3070.

(891) Nguyen, V. K.; Lee, J. W.; Yoo, Y. Characteristics and Performance of Ionic Polymer-Metal Composite Actuators Based on Nafion/Layered Silicate and Nafion/Silica Nanocomposites. *Sens. Actuators, B* **2007**, *120* (2), 529−537.

(892) Modestino, M. A.; Walczak, K. A.; Berger, A.; Evans, C. M.; Haussener, S.; Koval, C.; Newman, J. S.; Ager, J. W.; Segalman, R. A. Robust Production of Purified H-2 in a Stable, Self-Regulating, and Continuously Operating Solar Fuel Generator. *Energy Environ. Sci.* **2014**, *7* (1), 297−301.

(893) Xiang, C.; Weber, A. Z.; Ardo, S.; Berger, A.; Chen, Y.; Coridan, R.; Fountaine, K. T.; Haussener, S.; Hu, S.; Liu, R.; et al. Modeling, Simulation, and Implementation of Solar-Driven Water-Splitting Devices. *Angew. Chem., Int. Ed.* **2016**, *55* (42), 12974−12988.

(894) Darling, R. M.; Weber, A. Z.; Tucker, M. C.; Perry, M. L. The Influence of Electric Field on Crossover in Redox-Flow Batteries. *J. Electrochem. Soc.* **2016**, *163* (1), A5014−A5022.

(895) Tang, Z.; Keith, R.; Aaron, D. S.; Lawton, J. S.; Papandrew, A. P.; Zawodzinski, T. A. Proton Exchange Membrane Performance Characterization in Vrfb. *ECS Trans.* **2011**, *41* (23), 25−34.

(896) Sodaye, S.; Suresh, G.; Pandey, A. K.; Goswami, A. Interdiffusion of Exchanging Counterions in Poly(Perfluorosulfonic Acid) Membrane. *J. Phys. Chem. B* **2009**, *113* (37), 12482−12488.

(897) Samec, Z.; Trojanek, A.; Langmaier, J.; Samcova, E. Diffusion Coefficients of Alkali Metal Cations in Nafion(R) from Ion-Exchange Measurements - an Advanced Kinetic Model. *J. Electrochem. Soc.* **1997**, *144* (12), 4236−4242.

(898) Okada, T.; Arimura, N.; Satou, H.; Yuasa, M.; Kikuchi, T. Membrane Transport Characteristics of Binary Cation Systems with Li + and Alkali Metal Cations in Perfluorosulfonated Ionomer. *Electrochim. Acta* **2005**, *50* (16−17), 3569−3575.

(899) Chaudhury, S.; Agarwal, C.; Pandey, A. K.; Goswami, A. Self-Diffusion of Ions in Nafion-117 Membrane Having Mixed Ionic Composition. *J. Phys. Chem. B* **2012**, *116* (5), 1605−1611.

(900) Young, S. K.; Trevino, S. F.; Tan, N. C. B.; Paul, R. L. Utilization of Prompt-Gamma Neutron Activation Analysis in the Evaluation of Nafion Membranes. *J. Polym. Sci., Part B: Polym. Phys.* **2003**, *41* (13), 1485−1492.

(901) Xue, T.; Longwell, R. B.; Osseoasare, K. Mass-Transfer in Nafion Membrane Systems - Effects of Ionic Size and Charge on Selectivity. *J. Membr. Sci.* **1991**, *58* (2), 175−189.

(902) Yeager, H. L.; Odell, B.; Twardowski, Z. Transport-Properties of Nafion Membranes in Concentrated-Solution Environments. *J. Electrochem. Soc.* **1982**, *129* (1), 85−89.

(903) Goswami, A.; Acharya, A.; Pandey, A. K. Study of Self-Diffusion of Monovalent and Divalent Cations in Nafion-117 Ion-Exchange Membrane. *J. Phys. Chem. B* **2001**, *105* (38), 9196−9201.

(904) Daly, K. B.; Panagiotopoulos, A. Z.; Debenedetti, P. G.; Benziger, J. B. Viscosity of Nafion Oligomers as a Function of Hydration and Counterion Type: A Molecular Dynamics Study. *J. Phys. Chem. B* **2014**, *118* (48), 13981−13991.

(905) Soolo, E.; Brandell, D.; Liivat, A.; Kasemagi, H.; Tamm, T.; Aabloo, A. Force Field Generation and Molecular Dynamics Simulations of Li+-Nafion. *Electrochim. Acta* **2010**, *55* (8), 2587−2591.

(906) Shi, J.; Vincent, C. A. The Effect of Molecular-Weight on Cation Mobility in Polymer Electrolytes. *Solid State Ionics* **1993**, *60* (1−3), 11−17.

(907) Marcus, Y. Thermodynamics of Solvation of Ions 0.5. Gibbs Free-Energy of Hydration at 298.15-K. *J. Chem. Soc., Faraday Trans.* **1991**, *87* (18), 2995−2999.

(908) Stenina, I. A.; Sistat, P.; Rebrov, A. I.; Pourcelly, G.; Yaroslavtsev, A. B. Ion Mobility in Nafion-117 Membranes. *Desalination* **2004**, *170* (1), 49−57.

(909) Berger, A.; Newman, J. An Integrated 1-Dimensional Model of a Photoelectrochemical Cell for Water Splitting. *J. Electrochem. Soc.* **2014**, *161* (8), E3328−E3340.

(910) Pintauro, P. N.; Bennion, D. N. Mass-Transport of Electrolytes in Membranes 0.2. Determination of Nacl Equilibrium and Transport Parameters for Nafion. *Ind. Eng. Chem. Fundam.* **1984**, *23* (2), 234−243.

(911) Ohshima, H.; Ohki, S. Donnan Potential and Surface Potential of a Charged Membrane. *Biophys. J.* **1985**, *47* (5), 673−678.

(912) Will, F. G. Bromine Diffusion through Nafion Perfluorinated Ion-Exchange Membranes. *J. Electrochem. Soc.* **1979**, *126* (1), 36−43.

(913) Yeo, R. S.; Chin, D. T. Hydrogen-Bromine Cell for Energy-Storage Applications. *J. Electrochem. Soc.* **1980**, *127* (3), 549−555.

(914) Beers, K. M.; Hallinan, D. T.; Wang, X.; Pople, J. A.; Balsara, N. P. Counterion Condensation in Nafion. *Macromolecules* **2011**, *44* (22), 8866–8870.

(915) Kreutzer, H.; Yarlagadda, V.; Nguyen, T. V. Performance Evaluation of a Regenerative Hydrogen-Bromine Fuel Cell. *J. Electrochem. Soc.* **2012**, *159* (7), F331–F337.

(916) Cho, K. T.; Ridgway, P.; Weber, A. Z.; Haussener, S.; Battaglia, V.; Srinivasan, V. High Performance Hydrogen/Bromine Redox Flow Battery for Grid-Scale Energy Storage. *J. Electrochem. Soc.* **2012**, *159* (11), A1806–A1815.

(917) Rabago, R.; Noble, R. D.; Koval, C. A. Effects of Incorporation of Fluorocarbon and Hydrocarbon Surfactants into Perfluorosulfonic Acid (Nafion) Membranes. *Chem. Mater.* **1994**, *6* (7), 947–951.

(918) Lawton, J. S.; Aaron, D. S.; Tang, Z.; Zawodzinski, T. A. Qualitative Behavior of Vanadium Ions in Nafion Membranes Using Electron Spin Resonance. *J. Membr. Sci.* **2013**, *428* (0), 38–45.